12/6-17-96 (1)

NREL/TP-433-8142
SAND96-8225
Vol II
DE96007898

ALKALI DEPOSITS FOUND IN BIOMASS BOILERS

The Behavior of Inorganic Material in Biomass - Fired Power Boilers - Field and Laboratory Experiences

A Joint Effort

- *Sandia National Laboratory Combustion Research Facility*
- *Thomas R. Miles Consulting Design Engineers*
- *National Renewable Energy Laboratory*
- *University of California at Davis*
- *Foster Wheeler Development Corp.*
- *U.S. Bureau of Mines*

SANDIA NATIONAL LABORATORY AND THE NATIONAL RENEWABLE ENERGY LABORATORY ARE PART OF THE NATIONAL LABORATORY SYSTEM OF THE U.S. DEPARTMENT OF ENERGY

FEBRUARY 1996

Available to DOE and DOE contractors from:
Office of Scientific and Technical Information (OSIT)
P.O. Box 62
Oakridge, TN 37831
Prices Available by calling (615) 576-8401

Available to the public from:
National Technical Information Service (NTIS)
U.S. Department of Commerce
5285 Port Royal Road
Springfield, VA 22161
(703)487-4650

Foreword

These two volumes constitute the complete public record of a landmark laboratory and field study of the formation of alkali deposits in boilers firing a variety of real-world biomass fuels. Volume I was published by Thomas R. Miles, Consulting Design Engineers in April of 1995. It presents a broad overview and summary of the main results of both laboratory and field work. Volume II continues the discussion of alkali deposition, giving in greater detail the work of all participants.

Each volume is available from the National Technical Information Service. A limited number of copies are available to active researchers and industry. Please contact Dr. Richard Bain at the National Renewable Energy Laboratory, 1617 Cole Blvd., Golden, Colorado, 80401.

The performers of this work are pleased to acknowledge the industrial participants and the Office of Solar Energy Conversion, Solar Thermal and Biomass Power Division of the DOE for their financial support and for technical and in-kind contributions.

The Behavior of Inorganic Material in Biomass-Fired Power Boilers--Field and Laboratory Experiences: Volume II of Alkali Deposits Found in Biomass Power Plants

Larry L. Baxter
Sandia National Laboratories
Combustion Research Facility
Livermore, CA

Thomas R. Miles and Thomas R. Miles Jr.
Thomas R. Miles Consulting Design Engineers
Portland, OR

Bryan M. Jenkins
University of California, Davis
Department of Biological and Agricultural Engineering
Davis, CA

David C. Dayton, Thomas. A. Milne
National Renewable Energy Laboratory
Golden, CO

Richard W. Bryers
Foster Wheeler Development Corp. (Retired)
Livingston, NJ

Larry L. Oden
Bureau of Mines
Albany Research Center
Albany, OR

March 1996

Table of Contents

List of Figures

List of Tables

Executive Summary

This report documents the major findings of the Alkali Deposits Investigation. This investigation was a collaborative effort to understand the causes of unmanageable ash deposits in biomass-fired electric power boilers. A group of interested industrial institutions and the US DOE Energy Efficiency and Renewable Energy Office's Biomass Power Program through the National Renewable Energy Laboratory jointly sponsored the project. The industries contributed both funding and, in many cases, use of facilities to the project and included Mendota Biomass Power Ltd. and Woodland Biomass Power Ltd. (both associated with Thermo Electron Energy Systems), CMS Generation Operating Co. (formerly Hydra-Co Operations Inc.), Wheelabrator, Shasta, and Hudson Energy Cos., Sithe Energy Co., Delano Energy Co. Inc., the Electric Power Research Institute, Foster Wheeler Development Corp., and Elkraft Power Co. Ltd. of Denmark. Research contracts with Thomas R. Miles Consulting Design Engineers, Sandia National Laboratories, and The National Renewable Energy Laboratories provided the government portion of the funding. In addition, the University of California at Davis and the Bureau of Mines performed significant work in close collaboration with the other researchers. Volume I of this report provides an overview of the project, with selected highlights. This volume provides more detail and discussion of the data and implications

This document includes six sections. The first, the introduction, provides the motivation, context, and focus for the investigation. The remaining sections discuss fuel properties, bench-scale combustion tests, a framework for considering ash deposition processes, pilot-scale tests of biomass fuels, and field tests in commercially operating biomass power generation stations.

Detailed chemical analyses of eleven biomass fuels representing a broad cross-section of commercially available fuels reveal their properties that relate to ash deposition tendencies. The fuels fall into three broad categories: (1) straws and grasses (herbaceous materials); (2) pits, shells, hulls and other agricultural byproducts of a generally ligneous nature; and (3) woods and waste fuels of commercial interest. Woods and wood-derived products represent the most commonly used biomass fuels.

Herbaceous fuels contain silicon and potassium as their principal ash-forming constituents. They are also commonly high in chlorine relative to other biomass fuels. These properties portend potentially severe ash deposition problems at high or moderate combustion temperatures. The primary sources of these problems are subsequently shown to be: (1) the reaction of alkali with silica to form alkali silicates that melt or soften at low temperatures (can be lower than 700 °C, depending on composition), and (2) the reaction of alkali with sulfur to form alkali sulfates on combustor heat transfer surfaces. Alkali material plays a central role in both processes. The mobility of alkali material, defined as its ability to come in physical contact with other materials, is measured using chemical extractive techniques. Potassium is the dominant source of alkali in most biomass fuels. The analyses below indicate that essentially all of the biologically occurring alkali, in particular potassium, has high mobility. The non-biologically occurring alkali is present as soil contaminants and additives to the fuels, such as clay fillers used in paper production. This non-biologically occurring alkali exhibits far lower mobility than the biological fraction. The relative

amounts of biologically vs. non-biologically occurring material depend on fuel type and fuel handling. In the fuels investigated here, the dominant form of alkali was biologically occurring potassium. Some traditional indicators of deposit behavior, most notably ash fusion temperatures, poorly predict ash behavior.

Many of the agricultural byproducts also contain high potassium concentrations with equally high potassium mobility. Some woods, on the other hand, contain far less ash overall, differing by as much as a factor of 40 from high-ash straws, for example. In addition, the ash-forming constituents contain greater amounts of calcium with less silicon. The total amount of potassium in wood is also much lower than in straws, although this is not necessarily the case when expressed as a fraction of total ash. Calcium reacts with sulfur to form sulfates in ways somewhat analogous to potassium, but the mobility of calcium and the properties of the deposits it forms are both more favorable to sustained furnace operation than the ashes formed from straws and grasses.

Chlorine is a major factor in ash formation. Chlorine facilitates the mobility of many inorganic compounds, in particular potassium. Potassium chloride is among the most stable high-temperature, gas-phase, alkali-containing species. Chlorine concentration often dictates the amount of alkali vaporized during combustion as strongly as by the alkali concentration. In most cases, the chlorine appears to play a shuttle role, facilitating the transport of alkali from the fuel to surfaces, where the alkali often forms sulfates. In the absence of chlorine, alkali hydroxides are the major stable gas-phase species in moist, oxidizing environments (combustion gases).

Bench-scale combustion tests coupled with advanced mass spectrometry analytical techniques reveal the major species evolving from biomass samples during combustion. The suite of fuels examined by chemical analyses were also subjected to these combustion tests. The tests indicate that the major release of alkali material occurs during the char combustion phase and that the primary form of alkali-bearing off-gases corresponds with thermodynamic estimates of product stability and vapor pressure. Investigations were performed varying temperature, oxygen concentration, and moisture levels and revealed thermodynamically consistent results; the amount of alkali vaporized increased with temperature and the amount of hydroxide formed increased with increasing moisture content. Details other species released are also presented. Thermogravimetric and differential thermogravimetric analyses of the samples were also performed, the results of which proved to be marginally useful to predicting ash deposition behavior and are presented as an appendix.

A conceptual framework expresses ash deposition as a combination of four mechanisms: inertial impaction, thermophoretic deposition, condensation, and chemical reaction is presented. This conceptual framework serves to organize the remaining discussion and observations of ash deposition during both pilot and commercial scale. The influences of boiler design, boiler operating conditions, and fuel properties on ash deposit behavior reveal themselves as emphasizing or reducing the role of one or more of these mechanisms and thereby changing deposit composition, phase, and properties.

Pilot-scale investigations on the standard suite of fuels were carried out in an entrained-flow furnace. Isokinetically sampled fly ash samples and deposits collected on instrumented, temperature-regulated probes simulating both waterwalls and convection pass provide the basis for *in situ* and subsequent examination of deposits. Deposit properties reveal spatial dependencies on

probe surfaces that are consistent with both the commercial-scale tests and the conceptual framework for deposit growth and property development. In addition, changes in deposit composition with time, temperature, and other operation-relevant variables exhibit the same consistencies with commercial operation and the conceptual framework. Fuels containing high alkali and silica concentrations form alkali silicates that melt or sinter at low temperatures. The rates of deposit growth and sintering/melting increase with increasing temperature and chlorine concentration but are high at all boiler-relevant temperatures and chlorine concentrations for the straws and grasses. Surfaces exposed to impacting particles accumulate silica and alkali silicates at sometimes very rapid rates. Surfaces exposed to combustion gases but less exposed to particle impaction show evidence of thermophoretic accumulation of deposits, vapor condensation, and sulfation of condensed alkali-laden vapors. These processes lead to deposits with markedly different properties (high reflectivity, modest thickness and growth rate) compared to the impacted regions. Fuels containing little alkali or silica indicate far less deposit growth and development of more manageable deposits.

Commercial-scale investigations using nearly every type of commercially significant biomass boiler design provide full scale data for analysis. Bubbling fluid beds, circulating fluid beds, and various grate-based combustors fed by stokers, augers, and a cigar burner provided the data for comparison. Fuel types ranged from wood-derived material with blended agricultural byproducts to straws, sometimes blended with urban wood fuel. Many of the commercial-scale experiments were conducted in the context of commercial operation and employed varying compositions in the fuel. In all cases, comparisons of deposit composition with position in the boiler, type of deposit surface, position on the surface, and fuel properties reveal complete consistency with the fuel analyses, bench-scale combustion results, pilot-scale results, and the conceptual framework. Fuels containing high alkali and silica fractions exhibited the same rapid accumulation of ash deposits with the same sintered/molten character as was observed in the pilot-scale tests. Advanced mineralogical examinations of selected deposits indicate chemical and species compositions consistent with the conceptual framework and are presented as appendix material. The deposit properties are consistent with the conceptual framework for their formation and the observed bench-scale combustion results. Fuels with less alkali, chlorine, and silica, with less total ash-forming material, and with higher calcium contents exhibit more manageable ash deposits. Wood and non-recyclable paper generated the most manageable deposits.

This report presents a systematic and reasonably detailed analysis of fuel property, operating condition, and boiler design issues that dictate ash deposit formation and property development. The span of investigations from bench-top experiments to commercial operation and observations including both practical illustrations and theoretical background provide a self-consistent and reasonably robust basis to understand the qualitative nature of ash deposit formation in biomass boilers. While there remain many quantitative details to be pursued to complete our understanding, this project encapsulates essentially all of the conceptual aspects of the issue. It provides a basis for understanding and potentially resolving the technical and environmental issues associated with ash deposition during biomass combustion.

Introduction

This document reports on activities of the Alkali Deposits Project (see Volume I for a broad overview with selected details). The objective of this collaborative project was to identify the causes of ash deposition in biomass-fired combustors used for electric power generation and suggest ways they can be remedied. The principal collaborators in this effort include T. R. Miles and T. R. Miles Jr. of T. R. Miles Consulting Design Engineers, B. M. Jenkins of UC Davis, L. Oden of the U.S. Bureau of Mines, L. Baxter of Sandia National Laboratory and a group of ten industrial sponsors. T. R. Miles was principal investigator of a project separately funded by NREL and by industrial sponsors formally entitled Alkali Deposits Found in Biomass Power Plants. Larry Baxter is principal investigator in an ongoing Sandia project complementing that of Miles. In addition, the contributions of D. Dayton and T. Milne of the National Renewable Energy Laboratory are included. This collaborative project combines the resources of industry, design engineers, academia, and government-supported laboratories to address ash deposition, arguably the most critical constraint in burning a wide variety of biomass fuels in existing boilers. Progress reported below includes contributions from all of the collaborators.

This volume, together with Volume I, describes fuel characteristics, combustion behavior, and ash deposition characteristics for a wide variety of biomass fuels and commercial biomass-fired boilers. Data are derived from laboratory-, pilot-, and commercial-scale operations. Chemical compositions of deposits from the laboratory experiments are reported, and compared with the composition of deposits from commercial boilers and the composition of key feedstocks tested in the laboratory and field.

The scope of this project includes fuels characterization, laboratory combustion tests, and field combustion tests at several sites. The focus is on major inorganic species, i.e., silicon, potassium, calcium, aluminum, iron, magnessium, sodium, sulfur, phosphorus, titanium, and chlorine. Information on trace metals in combustion systems is available elsewhere (Tillman, 1994). Fuels characterizations include proximate, ultimate, and ash chemistry analyses of fuels either in use by or of interest to the biomass power generating industry. In addition, modifications to advanced analyses were made that allowed the mode of occurrence of inorganic material to be distinguished. Laboratory combustion tests of fuels were conducted in the Multifuel Combustor (MFC) at Sandia. Bryan Jenkins of UC Davis was on sabbatical leave at Sandia during the majority of this project. He helped select and prepare fuels for testing and perform combustion tests. Field tests hosted by most of the industrial sponsors of the T. R. Miles Alkali Deposits Project were conducted to gain field experience with several fuels and to gather commercial-scale data describing formation of ash deposits. Sandia participated in these field tests. In nearly all cases, the field tests were conducted on blends of fuels. The Sandia MFC was used to perform combustion tests on both non-blended fuels and fuel blends from the industrial collaborators. Fuel samples were collected during the tests and pre- and post-test boiler inspections were performed. During post-test inspections, ash deposits were removed from several locations in the boiler and submitted to a variety of chemical and physical analyses.

The first appendix of this report summarizes most of the raw data collected during this project in several formats. The second and third appendixes are reports generated by two of this document's author's and summarize detailed analyses of some of the fuel and deposit characteristics.

Motivation

Biomass-fired electric power generating stations are assuming increasingly prominent positions in energy and environmental issues in many regions of the world (Hustad & Sønju, 1992). Typically, these power stations are small (less than 50 MW_e net output), and rely on indigenous fuel supplies. Fuels for such facilities can be broadly classified into the categories of wood, agricultural residues, urban and municipal waste, and energy crops. Wood commonly represents the fuel of choice and the design fuel for biomass power stations. Wood's use is limited by availability, cost, and permitting agreements but in most cases not by fireside related problems (fouling, slagging, corrosion, etc.) in the boiler. The cost of wood fuel for such power stations has increased in recent years in many regions of the country due in large measure to competition among biomass-fired power plants. For example, the cost of wood fuel in Northern California (USA) has increased by over a factor of two in the last decade (Turnbull, 1993). The availability of wood is beginning to decrease as a result of substantial reductions in logging associated with economic policy and wildlife protection. The probability of high fuel prices and unreliable availability motivate evaluation of new fuels for these combustors.

Following the enactment of the Public Utilities Regulatory Policy Act (PURPA) in 1978, the installed US capacity in biomass fueled power generation increased ten-fold to roughly 7 GW_e. In California alone, 66 independent power generating facilities operated on biomass fuels (excluding solid waste) in 1993, with 47 generating or co-generating electricity and 19 generating steam only (CEC, 1994). All are direct combustion type units. The 47 power stations utilize standard Rankine cycles, and represent a combined generating capacity just under 900 MW_e, or about 2% of the electric generating capacity utilized by the state. The total energy generation from these facilities is close to 6 TWh y^{-1} from 6.6 million dry tons of fuel, with an average electricity generating efficiency of 17% and composite availability of 74%. Net efficiencies on advanced fluidized bed boilers range as high as 23% with availabilities in excess of 90% (Grass and Jenkins, 1994). Private investment in the California industry totals about $3 billion, and power sales amount to roughly $0.5 billion per year. Most of the recent development in biomass power was stimulated by economic incentives provided by favorable contractual arrangements for power sold to utilities (such as "Standard Offer 4" contracts in California), although there exist substantial environmental incentives in the reduction of local air pollution from open burning of crop and forest residues, and mitigation of global climate impacts by rapid carbon recycling when biomass replaces fossil fuel.

The major type of biomass fuel used is wood, including mill wastes, forest thinnings, and urban wood fuels (demolition wastes, yard prunings, and similar materials). Other fuels include agricultural wood as orchard prunings and tree removals, nut shells and hulls, pits, and other processing wastes. Most of the facilities constructed in California operate under permits requiring the reduction or offset of atmospheric emissions from other sources (Grass and Jenkins, 1994). Perhaps one of the biggest disappointments in the development of the biomass power industry in the state was the inadequacy of the technologies employed to utilize straw as fuel, even though

several facilities obtained air permits on the basis of offsetting field burning emissions from field crop residues. Straw firing leads to rapid and excessive fouling of boiler heat transfer surfaces, as well as slagging and agglomeration in furnaces. The exclusion of straw was not intentional by design. Many manufacturers fully expected to be able to handle straw in their facilities. Although there was evidence from coal-fired facilities and small-scale biomass research tests that straw might create substantial problems with slagging and fouling in conventionally designed boilers, the problem was not widely recognized until most of the existing capacity was already in place. Facilities permitted to burn straw are now buying and reselling the straw for non-burning disposal, without benefit of the energy value of the material as fuel. The problem of fouling and slagging is not restricted to straw materials, however. All facilities suffer economic loss from fireside deposits, with those firing more of the agricultural and urban fuels and less of the clean wood fuels incurring greater maintenance costs and availability losses. To remain economically feasible, power plants must increasingly burn lower quality fuels prone to slagging and fouling.

The motivation to develop new fuels for some power stations is driven by regulation and legal agreements more than by economics or availability. For example, under Title I of the U.S. federal Clean Air Act Amendments of 1990, states designate areas within their boundaries as attainment, non-attainment, or unclassifiable for each of six pollutants (1989). Designations are based on either federal or state air quality standards. Operating permits for all biomass-fired power stations are based in part on their impacts on air quality. For power stations in or near non-attainment areas, permits often require a net *reduction* in the amount of pollutant (NO_x, particulate matter, etc.) generated in that area. This is accomplished by use of offset fuels, straw representing a common example. In these permits, power stations agree to dispose of straw that would otherwise be burned in the field. Combustion of straw in this manner can reduce the amount of pollutant generated from field burning to such an extent that it more than compensates for the residual pollution from the power plant.

Economic, long-term-planning, environmental, regulatory, and legal motivations can be strong for using offset or alternative fuels in biomass combustors. In addition, large and reasonably stable supplies of these fuels can be secured in many regions of the country. In practice, combustion of these fuels has proven difficult. Problems vary from fuels handling and storage to seasonal variations in both the amount and the quality of the supply. Arguably the most daunting issue, and the subject of this investigation, is the inorganic material in the fuel and its impact on the combustor. For example, essentially all biomass-fired power stations in California that were designed and permitted based on using straw as an offset fuel opt to dispose of straw by other means. These decisions are driven by the consistent experience of unmanageable bed agglomeration, slagging deposits, and convection pass fouling when burning straw. Several international studies have been completed in the general area of straw combustion (FEC Consultants Ltd., 1988; Livingston, 1991; Martindale, 1982; Martindale, 1984). In many cases, addition of as little as 10 % straw to the boiler fuel supply for a electric power-generating facility causes an unscheduled shutdown within a few hours. Field experience with some other offset or alternative fuels (orchard prunings, nut shells or hulls, fruit pits, etc.) demonstrates borderline operation, with blend ratios limited to only 10-15 % when fired with wood (Miles, 1992; Miles & Miles, 1993; Miles, Miles, Baxter, Jenkins, & Oden, 1993).

Context and Focus of this Project

General mechanisms of ash deposition and laboratory/pilot-scale tests of bed agglomeration during straw combustion are discussed elsewhere (Baxter, 1993; Salour, Jenkins, Vafaei, & Kayhanian, 1993). The current investigation combines laboratory and field data in examining the causes of fireside problems during straw combustion in a mechanistic way. Laboratory tests were conducted in a pilot-scale combustor and incorporated both *in situ* and *post mortem* analyses of ash deposit morphology, composition, and rate of accumulation. In addition to the pilot-scale tests, field tests were conducted in an independently owned (non-utility) power station under known and controlled conditions of feed composition. Samples from various locations of the power station combustor, all of which were extracted after a controlled test burn, were collected for analysis. These sets of data are analyzed both separately and in comparison to demonstrate several of the most important aspects of ash behavior during straw combustion.

Elements from the fuel deposit in several different forms in boilers. High silica slags frequently form in the high temperature furnace regions as alkali and alkaline earth metals react with silica or sulfur to form molten composites and glasses. Slag masses can form and accumulate on grates or running slags may form on walls — especially refractory walls with high surface temperatures — but also on water-walls. Wall slags are commonly seen in the vicinity of the fuel feed ports. Slags can form as rock-like, ribbon-like, hair-like, or other structural forms. Agglomerates also occur, composed of sand and ash particles bound by fused, glassy materials arising from reactions between the fuel elements or other compounds in the furnace. Agglomeration is a common problem in fluidized bed combustors, where reactions in the bed can lead to the formation of large aggregated composites of bed media and ash, with eventual defluidization of the bed and plant shut-down. Fireside fouling deposits occur on all heat transfer surfaces, but especially on cross-flow tubes situated in the convection passes of boilers. Fouling of furnace water-walls in fluidized beds typically has not been of concern because of the active abrasion by bed media particles. Fouling of water-walls in the convection passes occurs routinely, however, although not generally with the same severity as cross-flow tube surfaces. Particle separation devices, such as cyclones, located at the furnace exit in circulating fluidized beds are also subject to severe fouling.

The apparent mechanisms of fouling deposit formation on boiler surfaces include condensation of inorganic vapors, inertial impaction and sticking of particles, thermophoresis and possibly electrophoresis, and chemical reaction (Baxter, 1993; Raask, 1985). The order in which these occur, and the relative rates, are important to the morphology and mechanical properties of the deposits. There are four principal undesirable effects of deposits: (1) deposits retard heat transfer and lead to an eventual decline in boiler efficiency and capacity if they cannot be removed according to the design assumptions for the boiler, (2) deposits can grow to the extent that flow through the boiler is restricted, often bridging across tubes and tube bundles, and causing mechanical damage, (3) deposits accumulate, for example in hoppers and on grates, in forms or quantities unmanageable by the facility, leading to premature shutdown for maintenance and associated loss in unit availability, and 4) deposits are associated with corrosion. Deposits which are less tenacious and easily removed (e.g., by soot blowing), represent less of a problem to facility operators than those which are hard to remove and require shutting down the boiler for cleaning.

Alkali and alkaline earth metals in the fuel ash are important to the formation of fireside deposits. For biomass, potassium is the major alkali element of concern. By contrast, sodium is the most troublesome alkali component for most coal-fired systems. Both potassium and calcium are important in the formation of sulfate deposits on boiler surfaces. Straws, other grasses and herbaceous species, younger tissues of woody species, nut hulls and shells, and other annual biomass, contain about 1% potassium dry weight.

Potassium is a macronutrient for plants. Along with potassium, straw invariably contains a substantial amount of chlorine, usually at levels greater than 0.2% and up to 3% dry weight (Jenkins, 1989). Straw also contains substantial amounts of silica, usually in macronutrient concentrations, although its role in plant nutrition is not entirely clear. The role of minerals in plant nutrition has been described by (Marschner, 1986). Rice straw, for example, contains about 10% of dry weight as silica. By itself, silica does not present much of a problem for biomass boilers. Rice hull, which may contain 20% by weight silica, does not easily slag and foul in boilers when fired alone because the ash is relatively pure in silica (> 95% SiO_2 in ash, typically) and the melting point is high (> 1650°C), although there exist other problems related to crystalline transformations and the atmospheric emission of cristobalite, a known respiratory hazard, if combustion conditions are not properly controlled. Silica in combination with alkali and alkaline earth metals, however, especially with the readily volatilized forms of potassium present in biomass, can lead to the formation of low melting point compounds which readily slag and foul at normal biomass boiler furnace temperatures (800 - 900°C). Chlorine can be an important facilitator in fouling, leading to the condensation of alkali chlorides on heat transfer surfaces in the boiler, and promoting the development of alkali sulfates. Chlorine may be an important element in the vaporization of alkali species, leading to the formation of more severe deposits. Sugar cane bagasse, which has long been used successfully as boiler fuel, and which is derived from another high potassium, high silica herbaceous crop, does not exhibit the same fouling tendencies as straw and sugar cane trash (tops and leaves) because both potassium and chlorine are substantially leached from the fuel in the process of extracting sugar.

Unlike straw, wood contains very little silicon, and the mature stem wood that makes up the majority of wood fuel, including urban wood fuel, also contains substantially lower amounts of potassium, usually only about 0.1% dry weight. Potassium is a highly mobile element in plants, and moves to younger, actively developing tissues, leaving the mature stem wood depleted in potassium. Facilities burning the leaf and branch fractions of wood, or coppice materials from short rotation woody cultures (SRWC), will also encounter higher levels of potassium (as well as nitrogen and sulfur) in the fuel. This is already apparent in the agricultural wood fuels (e.g. annual prunings) currently burned in boilers. Although wood fuels are inherently low in silica, adventitious material such as clays and other soil components brought in with the fuel include silica and can lead to fouling, although usually at reduced rates compared to straw. Urban wood fuels can include substantial amounts of adventitious materials from manufactured products. The chemistry of inorganic transformations in boilers is quite complex, involving multiple physicochemical pathways among alkali, alkaline earth, and other inorganic and organic species in the fuel. The principal components of interest include silicon, potassium, chlorine, sulfur, iron, phosphorous, magnesium, calcium, titanium, carbon, hydrogen, and oxygen. Sodium and aluminum, which are not normally found in inherently high concentrations, may be introduced as soil or through prior processing operations, as with sodium in olive pits, and may also influence

the fouling behavior. For most biomass fuels, the elements silicon, potassium, calcium, chlorine, sulfur, and to some extent, phosphorous, appear to be the principal elements involved in the fouling of boiler surfaces.

Deposit formation also depends on the boiler design and operation. Differences in slagging and fouling behavior have been observed for the various types of grate, fluidized bed, and suspension boiler designs. Superheater fouling depends to a large extent on the furnace exit gas temperature, a feature recognized by industry in the control of fouling deposits. Many existing biomass boilers were designed with furnace exit gas temperatures of 900 °C or higher. Coupled with cross-flow superheaters typically employed, severe fouling is frequently observed in such units. Reducing the temperature to control deposits can lead to derating the boiler with undesirable economic consequences. Other designs utilizing extended parallel flow heat exchangers or tube walls have been used with some success to reduce the fouling severity, as noted below.

This document presents the essential fuel, combustion, and deposition characteristics needed to understand the formation of ash deposits in a wide range of boiler designs operated on a wide range of fuels.

Fuel Analyses

Figure 1 illustrates the relationship of biomass to other common fuels in terms of the atomic hydrogen-to-carbon (H:C) and oxygen-to-carbon (O:C) ratios. Illustrated in the figure are approximate boundaries between different classes of solid fuels. This type of diagram, known as a coalification diagram in the coal science literature, can be used to infer the chemical structure and some combustion and inorganic aspects of the fuels. For example, increasing H:C or O:C ratio implies decreasing aromaticity of the fuel. Increasing O:C ratio implies increasing hydroxyl, carboxyl, ether, and ketone functional groups in the fuel. Both the aromaticity and the oxygen-containing functional groups influence the modes of occurrence of inorganic material in fuels and its transformation during combustion.

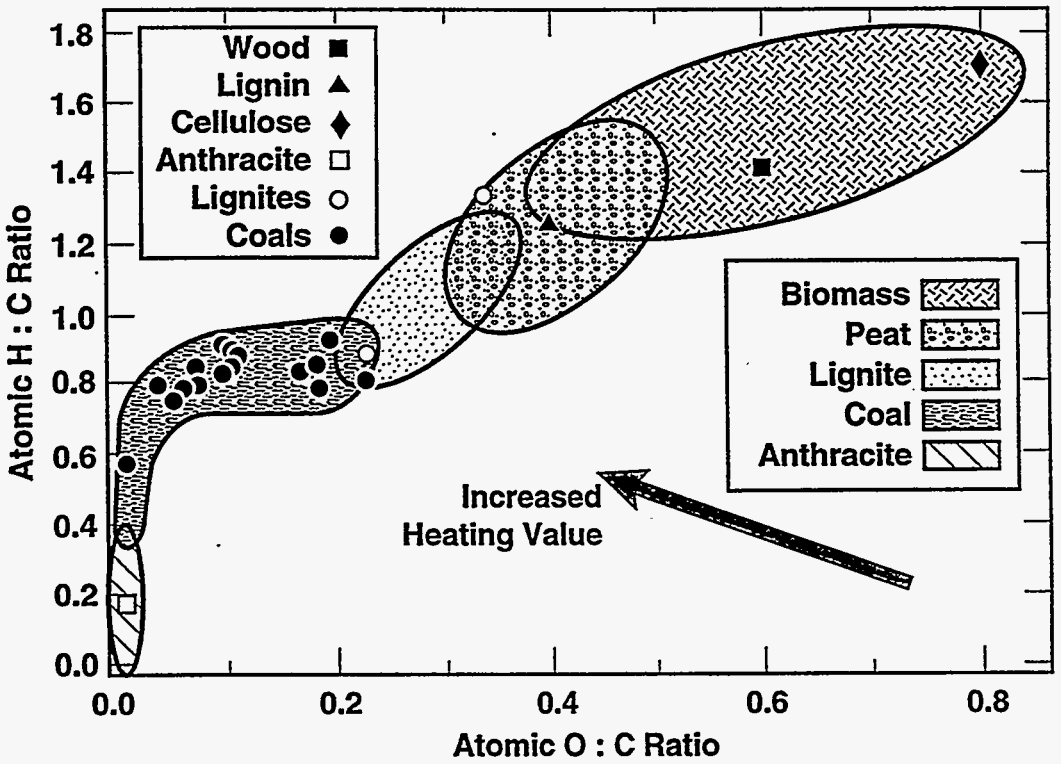

Figure 1 Coalification diagram indicating the relationship between a variety of solid fuels in terms of their chemical composition. The labeled regions represent qualitative boundaries for different fuels. The points represent quantitative results of chemical analyses for various materials.

Inorganic material in solid fuels can be divided into two fractions, one of which is inherent in the fuel and the other of which is added to the fuel through geologic or processing steps. A large fraction of the inherent inorganic material in lignites, and probably the dominant fraction in many biomass fuels, is associated with oxygen-containing functional groups. These functional groups provide sites for inorganic material to become incorporated in the fuel matrix as, for example, chelates and cations. The potential amount of this type of inorganic material is greater in biomass than in most coals due, in large measure, to the far higher oxygen content.

The release of this atomically dispersed inorganic material from a fuel particle is influenced both by its inherent volatility and the reactions of the organic portions of the fuel. Material that is inherently volatile at combustion temperatures includes derivatives of some of the alkali and alkaline earth metals, most notably sodium and potassium. Other, nonvolatile material can be released by convective transport during rapid pyrolysis. The amount of fuel lost during the pyrolysis stage of combustion increases with increasing hydrogen to carbon ratio and, to a lesser extent, with increasing oxygen to carbon ratio (see Figure 1). Anthracites typically lose less than 10 percent of their mass by pyrolysis. Bituminous coals lose between 5 and 65 percent of their mass by this process. Lignites, peats, and biomass can lose over 90 percent of their mass in this first stage of combustion. The large quantities of gases or tars leaving coals, lignites, and biomass fuels can convectively carry inorganic material out of the fuel, even if the inorganic material itself is nonvolatile (Baxter, Mitchell, & Fletcher, 1995 (to appear)). The combination of high oxygen content and high organic volatile matter in biomass indicates a potential for creating large amounts of inorganic vapors during combustion. The modes of occurrence of this material and amounts of inorganic material released during combustion are reviewed below, together with the impact of the material on ash deposits.

The second class of inorganic material in solid fuels includes material that is added to the fuel from extraneous sources. In the case of biomass, fuel processing in the field is likely to contribute the majority of it. This adventitious material is often particulate in nature (by contrast to the atomically dispersed material) and is the dominant contributor to fly ash particles larger than about 10 μm. Most of the true minerals, as opposed to atomically dispersed inorganic material, are introduced in fuels as adventitious material. Examples include silica, pyrite, calcite, kaolinite, illite, and other silicates.

The fate of this second class of inorganic material differs substantially from that of the inherent material. The minerals undergo chemical reactions and phase changes determined by their thermochemistry as well as interacting with other inorganic components and the organic material. Components of the minerals may be released from the fuel by either thermal decomposition or vaporization during combustion.

The variability in both inorganic and organic properties of biomass fuels is large. The underlying theme of this discussion is that the behavior of the inorganic matter and the properties of the deposits that are formed from it can be described in terms of a small number of mechanisms. The discussion below outlines this mechanistic approach to describing the fate of inorganic material in solid fuels with a particular focus on the mechanisms of ash deposition. This mechanistic approach has the potential of embracing a large range of fuel variations, combustor types, and operating conditions without the need of developing extensive databases or testing procedures for

each new situation. The approach has been successfully demonstrated for coal combustion, and examples from coal experiments will be used as illustrations. The same methodology and logic can be applied to biomass combustion.

Fuels Used in This Investigation

Comprehensive analyses were performed for the series of eleven fuels summarized in Table 1. These fuels were each tested at Sandia's Multifuel Combustor (MFC). Those designated as commercial fuels were also tested at commercial facilities. The wood/almond shell blend was tested at Mendota and the wood/wheat straw blend at Hydra-Co, results from which are discussed later. The nonrecyclable paper was tested at Wheelabrator primarily for emissions purposes. No ash-related, commercial-scale results were collected during these tests as part of this project, although the laboratory results were available to Wheelabrator during their successful bid to obtain a permit to burn such fuels. Samples of many of the fuels were also sent to NREL for mass spectrometry measurements (discussed below), to Foster Wheeler Development Corp. for thermal decomposition and differential thermal decomposition analyses (see appendix), to the US Bureau of Mines for ash chemistry analyses, and to other participating organizations. In this report, non-qualified names of fuels represent different aliquots of the eleven fuels from the MFC laboratory. The scientific names indicated in the table are, in some cases, presumptions. It is not know precisely which woods are included in the commercial fuels, for example, but it is probably ponderosa pine and douglas fir (two typical sources of lumber).

There are additional fuels of similar names that were used in some tests. The dominant sources of these fuels were field tests conducted during the initial phase of the Alkali Deposits Program. To avoid confusion, samples derived from field tests all have qualifiers in their names. For example, the wheat straw blended with wood during tests at Hydra-Co differs from the wheat straw in the MFC tests. References to wheat straw imply the latter whereas the former is indicated as wheat straw – Hydra-Co or some similar qualifier. Information regarding the sources, forms, treatments, and botanical names of the eleven base fuels is available in the appendices.

This section of the report contains summaries of most of the data with some interpretation. Appendixes are also provided that contain the raw data in several forms (tabular, graphical, on several different bases, etc.).

For the purposes of later discussion, the fuels are separated into three groups: grasses, ligneous materials, and commercial boiler feedstocks. Grasses include switchgrass, rice straw, and wheat straw. Ligneous fuels include shells, pits, and hulls. And commercial fuels include fuels that either were in use by or were being evaluated as candidates for commercial boilers. The Mendota and Hyrdra-Co fuels are blends of urban wood fuels and almond shells (Mendota) or wheat straw (Hydra-Co). In both cases, nominally 85 weight % of the fuel mass is urban wood fuel. Nonrecyclable paper is under evaluation as a boiler fuel. Two samples of the same nominal fuel have been evaluated. Analyses for samples prepared by shredding (paper i) and by cutting (paper ii) are reported separately. As expected, there is very little difference in the results from these two samples.

Table 1 Summary of fuels used during MFC combustion tests.

Fuel common/ *scientific name*	Moisture (% fuel)	Ash (% dry fuel)	Higher Heating Value (MJ/kg, daf)
	Straws and Grasses (Herbaceous Fuels)/ Family *Gramineae*		
Rice Straw/ *Oryza sativa*	11.22	19.17	18.74
Wheat Straw/ *Triticum aestivum*	8.39	8.08	19.31
Switchgrass/ *Panicum virgatum*	12.98	5.86	19.91
	Shells, Pits, and Hulls (Ligneous Fuels)/ Families *Anacardiaceae* (Pistachio), *Oleaceae* (Olive), *Rosaceae* (almond)		
Almond Shells/ *Prunus dulcis*	7.52	2.87	19.83
Pistachio Shells/ *Pistacia vera*	8.08	1.28	19.90
Olive Pits/ *Olea europaea*	6.97	1.83	21.97
Almond Hulls/ *Prunus dulcis*	8.02	5.75	20.00
	Wood and Commercial Fuels Families *Pinaceae*		
Wood/Almond Shell Blend (Mendota Fuel)/ *Pinus ponderosa/* Pseudotsuga menziesii*/Prunus dulcis*	8.62	7.54	19.97
Nonrecyclable Paper i (Wheelabrator Fuel)/ *Pinus ponderosa/ Pseudotsuga menziesii*	5.95	8.21	23.44
Nonrecyclable Paper ii (Wheelabrator Fuel)/ *Pinus ponderosa/ Pseudotsuga menziesii*	5.95	8.21	23.44
Wood/Wheat Straw Blend (Hydra-Co Fuel) *Pinus ponderosa/ Pseudotsuga menziesii/Triticum aestivum*	9.25	7.33	20.56

Results of Standardized Fuel Analyses

The analyses discussed below were reported by a variety of laboratories using sometimes differing procedures. The laboratories and primary contacts at these laboratories include CONSOL Inc. (Vince Conrad and Murray Abbott), Hazen Research Inc. (Jerry Cunningham), US Bureau of Mines Albany Research Center (Larry Oden), and Foster Wheeler Development Corporation (Dick

Bryers). There are clear indications of laboratory-to-laboratory and procedure-to-procedure differences in the results. A discussion of the differences, and our estimate of the best values of analyses, are also included.

Ultimate Analyses and Total Chlorine

The composition of the organic fractions of these materials (ultimate analyses) are indicated in Figure 2 through Figure 4, together with the total chlorine content. In many cases, several duplicate analyses have been completed on samples of the same fuel. The results illustrated in the figures represent the averages of these duplicates. Sample-to-sample variations among these duplicates are discussed later.

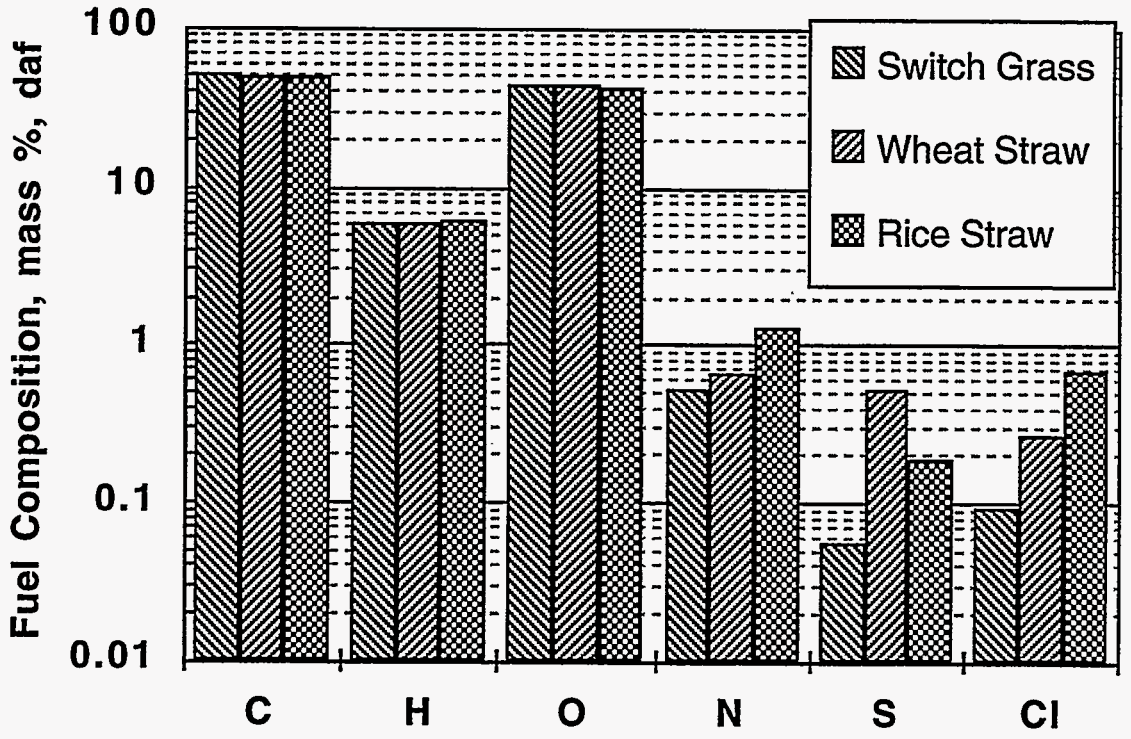

Figure 2 Ultimate analyses of the herbaceous fuels used in the MFC tests.

The data are conveniently discussed in two groups. Major elements (C, O, H) are the dominant components of all organic portions of biomass and form the dominant portion of the dry, ash-free portion of biomass. In these data, over 97 % of the dry, ash-free weight of the biomass is contributed by these three elements. Minor elements (N, S, Cl, and P) are all essential for plant growth and play critical roles in plant metabolism and physiology. However, soil conditions often

influence their ultimate concentrations in biomass as much or more than their roles in plant physiology. No measurement of organic phosphorus was performed on these fuels.

Plant physiology and agricultural practices influence the results of ultimate analyses from these fuels. A brief discussion of the sources and roles of the major and minor species in plants is included here to help interpret and anticipate the measured trends with respect to fuel type.

Major Elements (C, H, O)

Essentially no variation is evident in major organic components (carbon, hydrogen, and oxygen) of the herbaceous fuels on a dry, ash-free basis (Figure 2). Comparisons with Figure 3 and Figure 4 indicate that the carbon, hydrogen, and oxygen contents of the fuels on a dry, ash-free basis are conspicuously consistent for all of the fuels. Paper is the most processed fuel and stands out in the data as being slightly different from the remaining fuels. These differences are difficult to appreciate when displayed on a logarithmic scale. Figure 5 illustrates the consistently higher carbon contents of paper compared to the other fuels. There are significant differences in the oxygen concentrations in the types of organic materials of which biomass is composed. For example, lignin and cellulose have atomic oxygen to carbon ratios of approximately 0.4 and 0.83, respectively. Paper processing removes most lignin from biomass, which should increase oxygen and decrease carbon relative to the feedstock. The observation that carbon is higher and oxygen lower than the remaining fuels indicates that considerations, other than lignin content, are dominating the analysis. For example, the oxygen to carbon ratio of the feedstock that was used to make the paper is unknown and the paper contains a number of non-paper additives (plastics, coatings, filler, etc.).

The data illustrated in Figure 2 through Figure 4 indicate atomic oxygen to carbon ratios of approximately 0.62. This suggests that about half of the material in the fuels is composed of relatively low oxygen content materials whereas the other half is composed of cellulosic material. Lignin typically accounts for a minor fraction of many biomass materials (10 % or less for herbaceous fuels, 20-30 % for woods). Given the diversity in texture and macromolecular composition of the fuels represented in these figures, the consistency of the carbon, hydrogen, and oxygen data was unexpected.

Minor Elements (N, S, Cl, P)

Minor element (nitrogen, sulfur, and chlorine) concentrations vary more significantly among the fuels. Nitrogen is an important plant nutrient and is often concentrated in the most rapidly growing regions of plants. It is introduced in two primary forms in plants: nitrates and ammonium. A portion of the nitrate material remains in solution and is mobile in plants. In order to be incorporated into plant structures, nitrate is reduced to ammonia by the enzyme nitrate reductase (molecular weight of about 200,000 Daltons in the types of plants commonly used as biomass fuels). The enzymes half life is only a few hours. Ammonia, which is quite toxic to most plants, is converted to amino acids, amides, etc. All portions of plants are expected to have significant nitrogen concentrations due to the ubiquitous nature of amino acids, amides, and other essential nitrogen-containing materials in plant structures and the high mobility of nitrogen-containing ions. Consistent with these observations, there is no clear relationship between fuel structure and nitrogen concentrations among the fuels. The significant variation in the nitrogen levels of the

plants is probably best explained by nutrient levels in the soils. Indeed, those plants having the highest nitrogen contents (straws and agricultural byproducts) also are the most heavily fertilized.

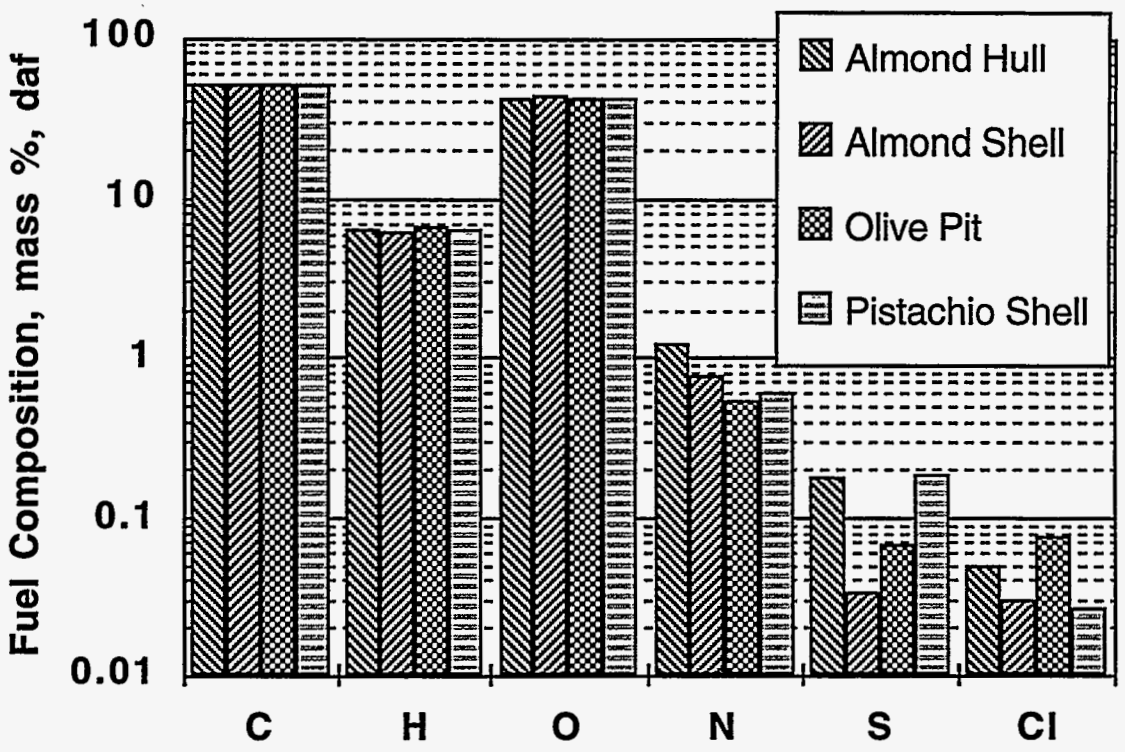

Figure 3 Ultimate analyses for the ligneous fuels used in the MFC combustion tests.

Most (many researchers say all) nitrogen in coal is incorporated in the form of in-ring nitrogen in aromatic compounds. In biomass fuels, on the other hand, nitrogen is found as amines and nitrates in addition to in-ring aromatic and nonaromatic forms. The amines and nitrates are likely to evolve from the biomass much earlier in the devolatilization process than the in-ring nitrogen compounds. Furthermore, the number of rings comprising an aromatic cluster in coal is often larger than those in biomass (the latter typically being one). The amines, nitrates, and single-member rings are both less thermally stable or more volatile than the often large structures in which nitrogen exists in coals. These trends lead us to hypothesize that significant differences exist in nitrogen release rates during biomass combustion as compared with coal combustion. In particular, some nitrogen would be expected to be released earlier in the combustion process of biomass fuels as compared to coals and nitrogen would be expected to be released in a broader variety of forms, including NO, from biomass. This has potentially significant impact on NO_x formation and control during biomass. Overall nitrogen content of coals exceeds that of biomass, with the former ranging from 1 to 1.5 % of dry fuel and the latter ranging from 0.4 to 1 %.

Sulfur can be incorporated by plants both by absorption and assimilation of atmospheric SO_2 and by sulfate absorption by roots. The latter process is the most important. The principal roles of sulfur in plants are similar to those of nitrogen: amino acids, proteins, coenzymes, etc. Unlike nitrogen, sulfur can be directly incorporated in many structures, capable of being used as sulfate without reduction and being reoxidized after reduction. The two principal chemical forms of sulfur in plants are sulfates and organic sulfur. The former form increases with increasing sulfate in the nutrient supply. The latter is far less sensitive to sulfate supply in most plants.

The data indicate no obvious trends of sulfur level with plant type. Sulfur concentrations do not correlate strongly with those of nitrogen. The nutrients available in the local soil have as much influence on these concentrations as plant physiology (both straw samples came from Yolo County in California).

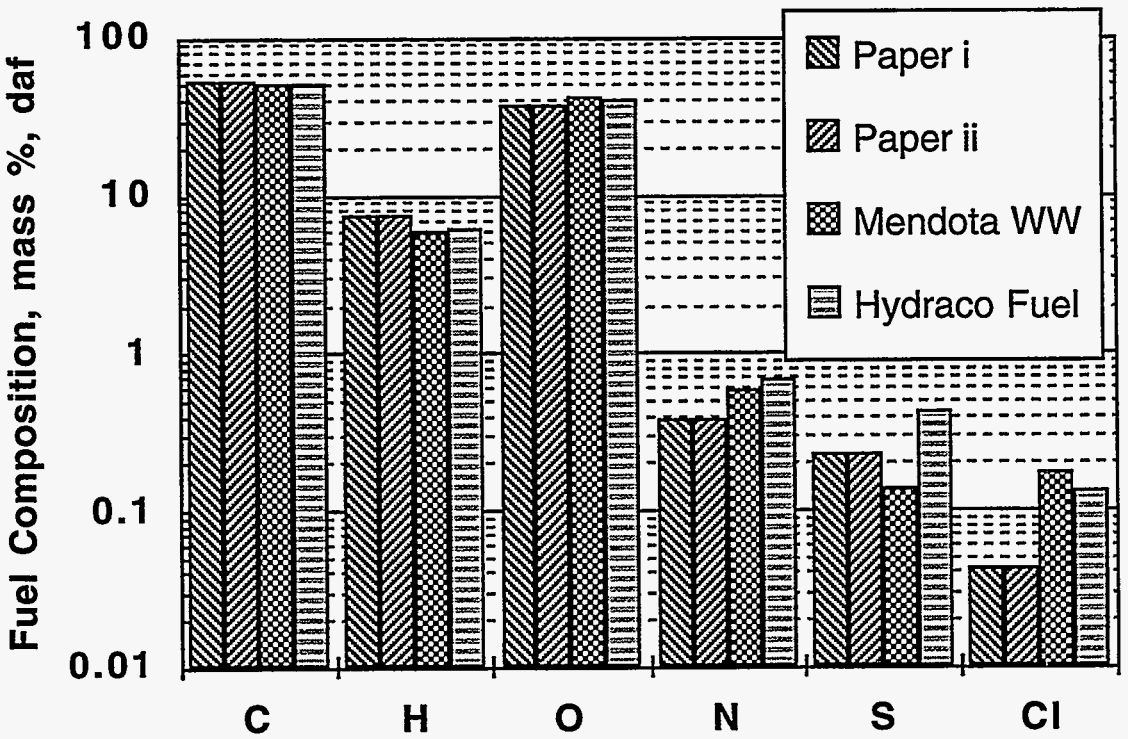

Figure 4 Ultimate analyses of fuels used in MFC combustion tests and derived from field test sites.

Chlorine in biomass appears to occur dominantly in the form of chloride ion and serves the primary role of balancing charge. Its concentration is closely related to the nutrient composition of the soils. The levels of chlorine required for optimal plant growth are usually far less than the levels available in the nutrients. Therefore, chlorine levels observed in these and other data are likely more indicative of local soil conditions than plant physiology.

Phosphorus levels in these fuels are not available. However, phosphorus is found in some concentration in the ash produced from the fuels (see below). Phosphorus exists in its most oxidized form in biomass fuels and is not reduced during plant metabolism. It is primarily introduced in the form of dihydrogen phosphate ions ($H_2PO_4^-$) and either remains in inorganic form or is incorporated in organic structures by forming esters or pyrophosphates. The organic phosphorous is expected to be among the less thermally stable components. Phosphorous will also form stable, inorganic ash deposits when it combines with alkali, alkaline earth or (less probably) other inorganic compounds. Phosphorous-based ash deposits are uncommon during coal combustion, largely due to the lack of phosphorus in coal.

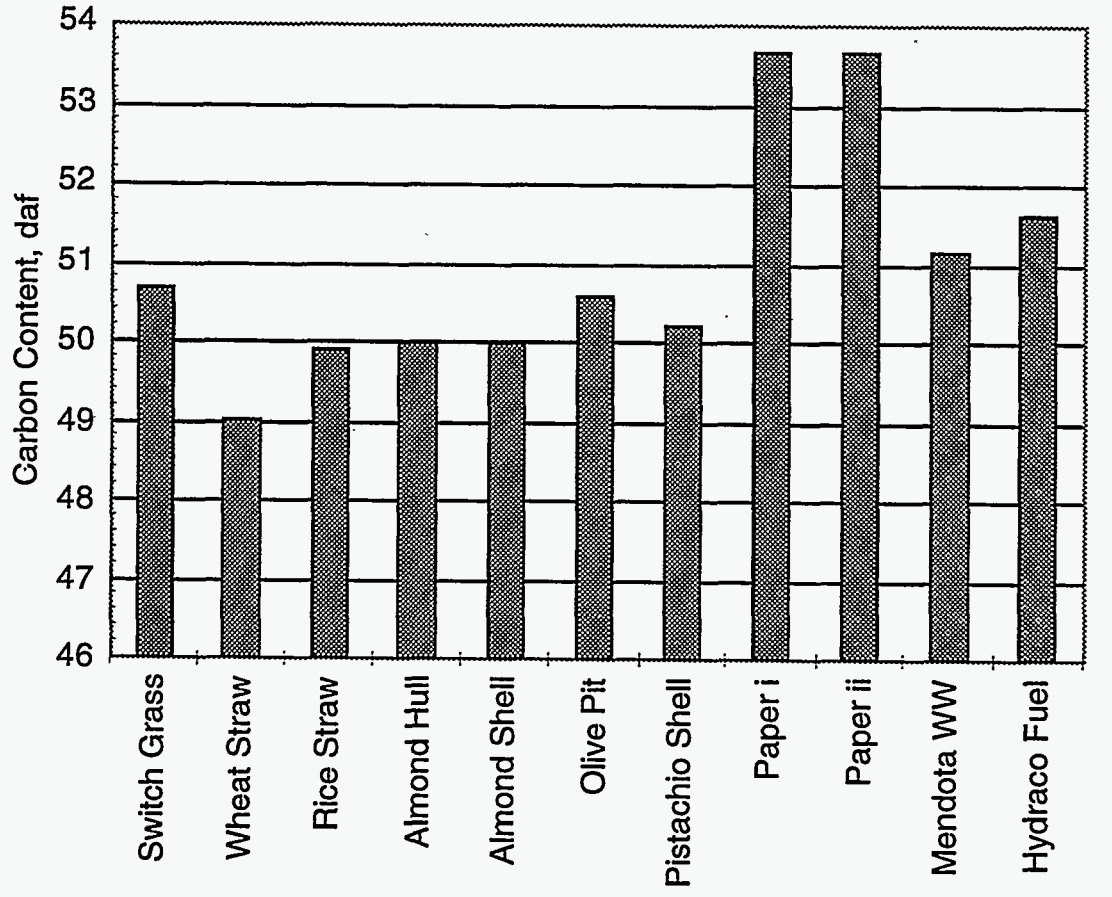

Figure 5 Variation of carbon content among all of the fuels illustrating their conspicuous consistency on a dry, ash-free basis and the consistent difference between paper and the remaining fuels.

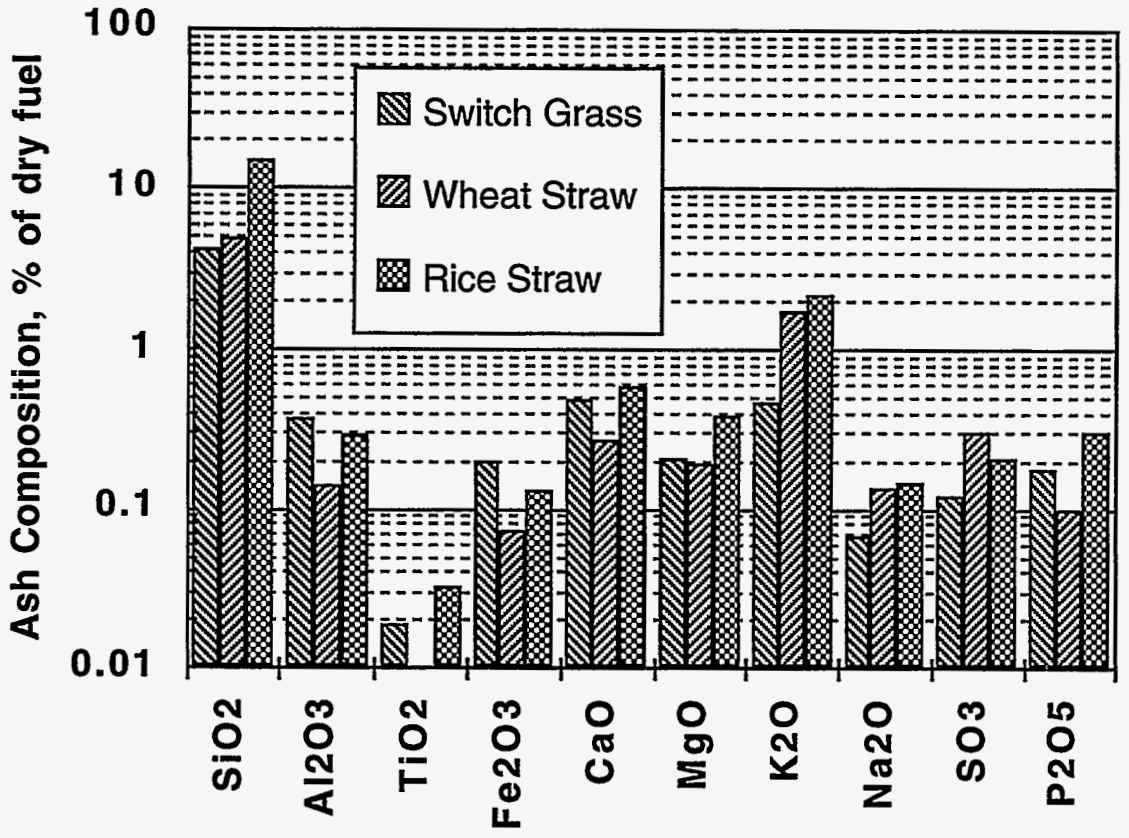

Figure 6 Elemental ash composition (expressed as oxides) of herbaceous fuels used in MFC test burns. Values below 0.01 were below detection limits.

Ash Composition

The composition of the inorganic portion of the fuels was determined by ashing the fuels at 750 °C and measuring the elemental composition of the resulting ash. The ashing technique favors formation of oxides from each of the elements. Therefore, the elemental composition is traditionally represented on an oxide basis. An overall mass balance can be performed by comparing the measured ash fraction of the fuel with the sum of the elements expressed as oxides. With biomass fuels, there are legitimate concerns regarding the temperature at which the fuel is ashed and the validity of assuming all ash components are completely oxidized at any given temperature. These issues will be addressed here after reviewing the results of the ash chemistry analyses.

Figure 6 through Figure 8 illustrate the elemental composition of the ash, expressed as oxides, for each of the three classes of fuels. Results are presented as percent of dry fuel. Because there is

such large variation in concentrations, results are presented on a logarithmic scale. The logarithmic scale allows values of greatly different magnitudes to be displayed meaningfully on a single graph. It also tends to obscure the magnitude of the variations. There are, in many cases, over four orders of magnitude difference in the concentrations of the most and least abundant inorganic component in the fuel.

The most immediate observation is that there is far greater diversity in ash composition than in organic composition in these fuels. Slightly over 16 % of the rice straw (on a dry, fuel basis) is composed of silica, for example, whereas less than 0.4 % of the almond shells and hulls is composed of silica. This is due in part to the significant differences in the overall ash contents of the fuels. When expressed as a percent of ash rather than a percent of fuel, there is still over an order of magnitude difference in the amount of silica in rice straw as compared to almond hull.

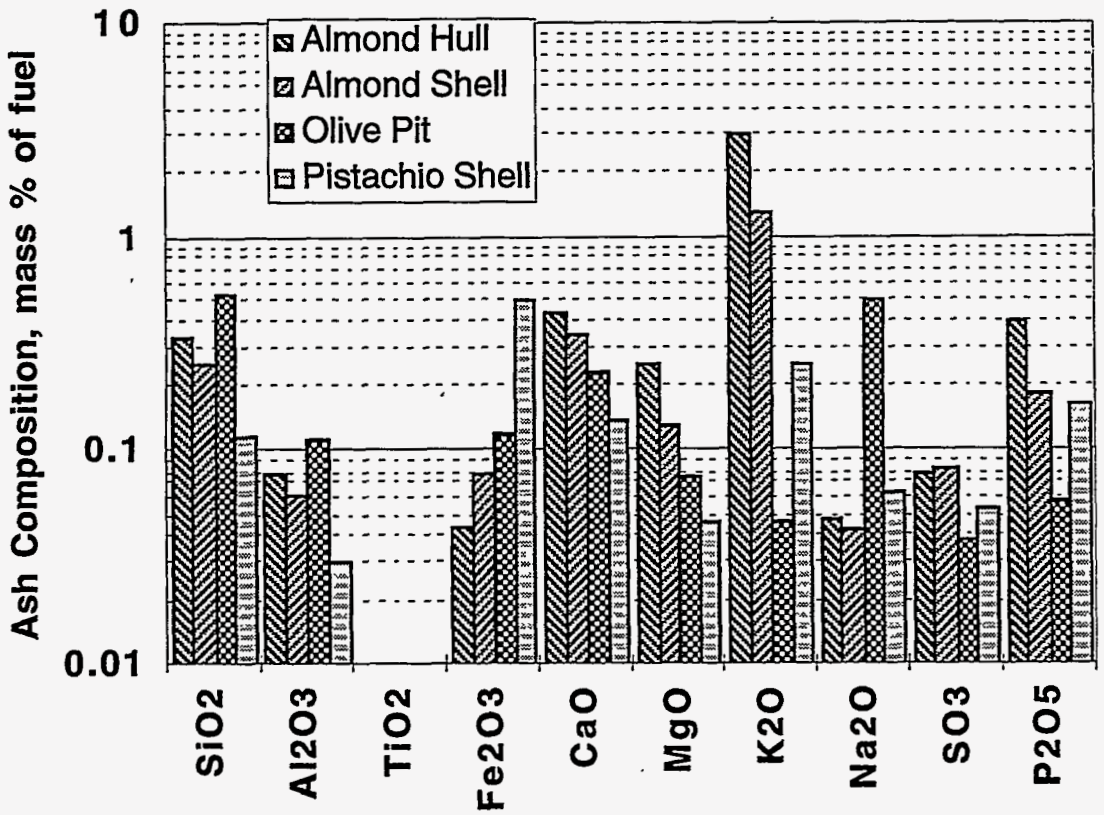

Figure 7 Elemental ash composition (expressed as oxides) of ligneous fuels used in MFC test burns. Values below 0.01 are below detection limits.

Silicon

The most prevalent inorganic component of each of the three fuels (other than oxygen) is silicon. Silicon is incorporated in plants by absorption of silicic acid from the soil solution. There is controversy as to whether silicon is an essential element for plant growth. Silicon is present in

most plants at macronutrient levels (0.1-10 % dry basis). Rice straw is noted by some investigators for its ability to concentrate silicon, primarily in apoplastic forms, as a structural component of the plant (Marschner, 1986). Silicon is deposited as a hydrated oxide ($SiO_2 \cdot nH_2O$) usually in amorphous, but occasionally in crystalline forms. The ratio of silicon found in rice straw to the amount that would be deposited based on the rate of transpiration varies from 54:1 to 3:1, with a typical value being about 10:1. Wheat straw also concentrates silicon, but to a lesser extent, with silicon ratios varying from 5:1 to 1:1. The behavior of switchgrass is not well established. The literature does illustrate that other plants preferentially exclude silicon. For example, soybean silicon ratios vary from 1:1 to 0.1:1. In all cases, the highest ratios are observed when the silicon concentration in the nutrient solution is low.

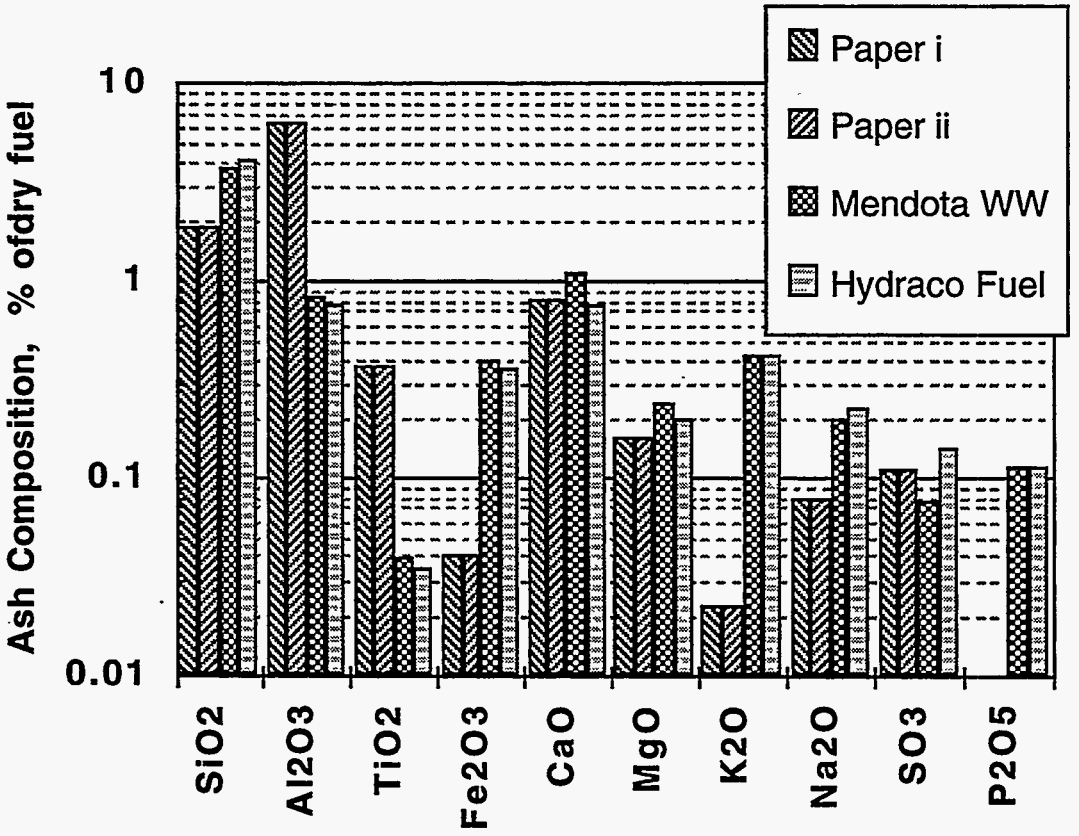

Figure 8 Elemental ash composition (expressed as oxides) of fuels used in MFC test burns that were obtained from field sites.

Potassium

Potassium is the second most prevalent component of the straws and a significant component of switchgrass. Potassium in plants occurs in a distinctly different form compared to silicon. Potassium occurs as a univalent ion (K^+) that is highly mobile with little structural function.

Potassium uptake is highly selective and correlates with plant metabolic activity. Osmotic potentials across membranes and ionic potentials in the cytoplasm are regulated to a large degree by potassium. Potassium also plays important roles in enzyme activation, membrane transport, and stomatal regulation. Because of these metabolic and transport roles, potassium is often found in regions where plant growth is most vigorous (Marschner, 1986).

Sodium

Sodium is not considered an essential element for plant growth, although in low concentrations it may be beneficial to some plants, substituting for potassium in certain roles. At higher concentrations, sodium is usually toxic and is not usually found in concentrations over about 2 % in the plant.

Calcium

Calcium occurs almost exclusively in the apoplasm. It forms exchangeable bonds with the cell walls and has significant function in cell wall stiffening and the structural integrity of plants. It also helps regulate growth.

Aluminum

Aluminum is toxic to most plants and occurs in small quantities, particularly in plants grown under alkaline soil conditions. Aluminum concentrations in plant tissue seldom exceed 300 ppm on a dry weight basis. Aluminum ranks among the most common elements in soils and is usually in the form of an aluminosilicate clay. Kaolinite, illite, and montmorillinite are the most common clays. The significant levels of aluminum in switchgrass are believed to be associated with dust, dirt, or other soil impurities in the sample and not an inherent part of the plant material.

Iron

Iron has two principal roles in plants. It forms coordination compounds (chelates) that are active in transport and is active in reversible oxidation-reduction reactions in which it transforms from Fe (II) to Fe (III). Iron is concentrated in leaves. About 80 % of the iron in the leaves is located in the chloroplasts, and is critical for photosynthesis.

Other Inorganic Components

The remaining inorganic elements exist only in trace quantities in the fuels. Several play specialized roles in enzyme production along with other elements not measured (copper, manganese, etc.). Their concentrations and roles in ash deposition are both relatively insignificant.

Proximate Analyses

The results of proximate analyses for each of the fuels are illustrated in Figure 9. While these fuels produce large amounts of volatiles, the heating value of the volatiles is often quite low. There is a preferential release of oxygen as volatiles are produced, resulting in chars with lower oxygen to

carbon ratios than the parent fuels and volatiles with higher ratios. These partially oxidized volatiles have generally low heating values.

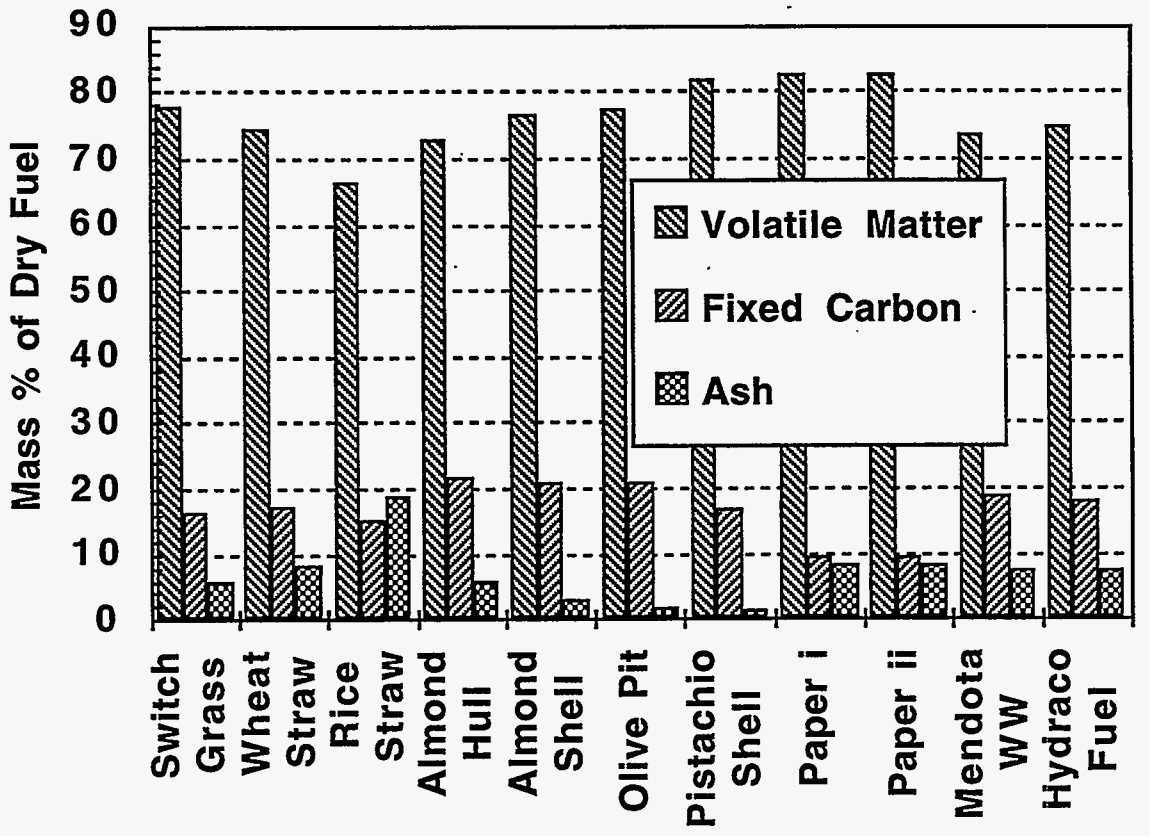

Figure 9 Proximate analyses for the fuels used in the MFC combustion tests.

Ash Fusion Temperatures

Ash fusion temperatures have been determined for all fuels used in the MFC. These results are illustrated in Figure 10 and Figure 11. The four critical temperatures classically used in this test are initial deformation, spherical, hemispherical, and fluid temperatures. The tests are traditionally carried out under both reducing and oxidizing conditions. Differences in the temperatures between these two conditions are usually due to changes in the oxidation state of iron. Fuels that contain little iron typically have similar fusion temperatures under both reducing and oxidizing conditions. These fuels, none of which contains significant iron, show similar fusion temperatures under both reducing and oxidizing conditions, consistent with this expectation.

Fusion temperatures represent the primary means of anticipating ash slagging problems for many boiler operators and manufacturers. A careful comparison between the results illustrated in Figure

10 and the observations from our experiments indicates that the traditional fusion temperature tests are not reliable indicators of ash behavior. Ash fusion tests require only a few minutes to conduct. This is insufficient time for chemical reactions between, for example, alkali and silica to be completed. The actual softening temperatures of the alkali-silica-based ashes are low compared to the results from the fusion tests.

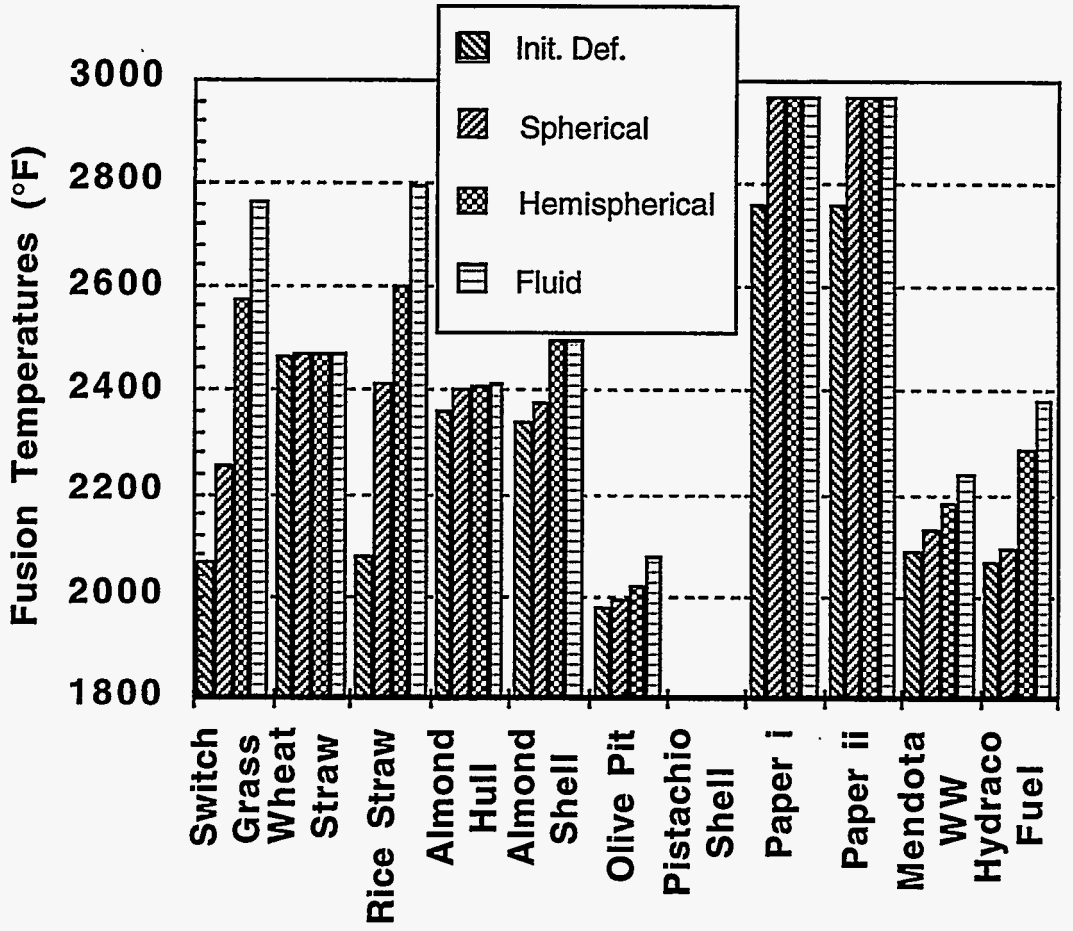

Figure 10 Results of fusion temperature analyses conducted on the fuels used in the MFC tests under reducing conditions. Compare with results obtained under oxidizing conditions (Figure 11).

Heating Value

Variations in heating value among the several fuels are illustrated in Figure 12. Biomass fuel heating values are much lower than coal heating values. However, extrapolations of equations that accurately predict coal heating values based on the elemental composition of the coal (indicated as Dulong values in Appendix 1) consistently underpredict biomass experimental results. This, we believe, is a consequence of the greater aliphatic and lesser aromatic nature of the chemical bonds in biomass compared to coal.

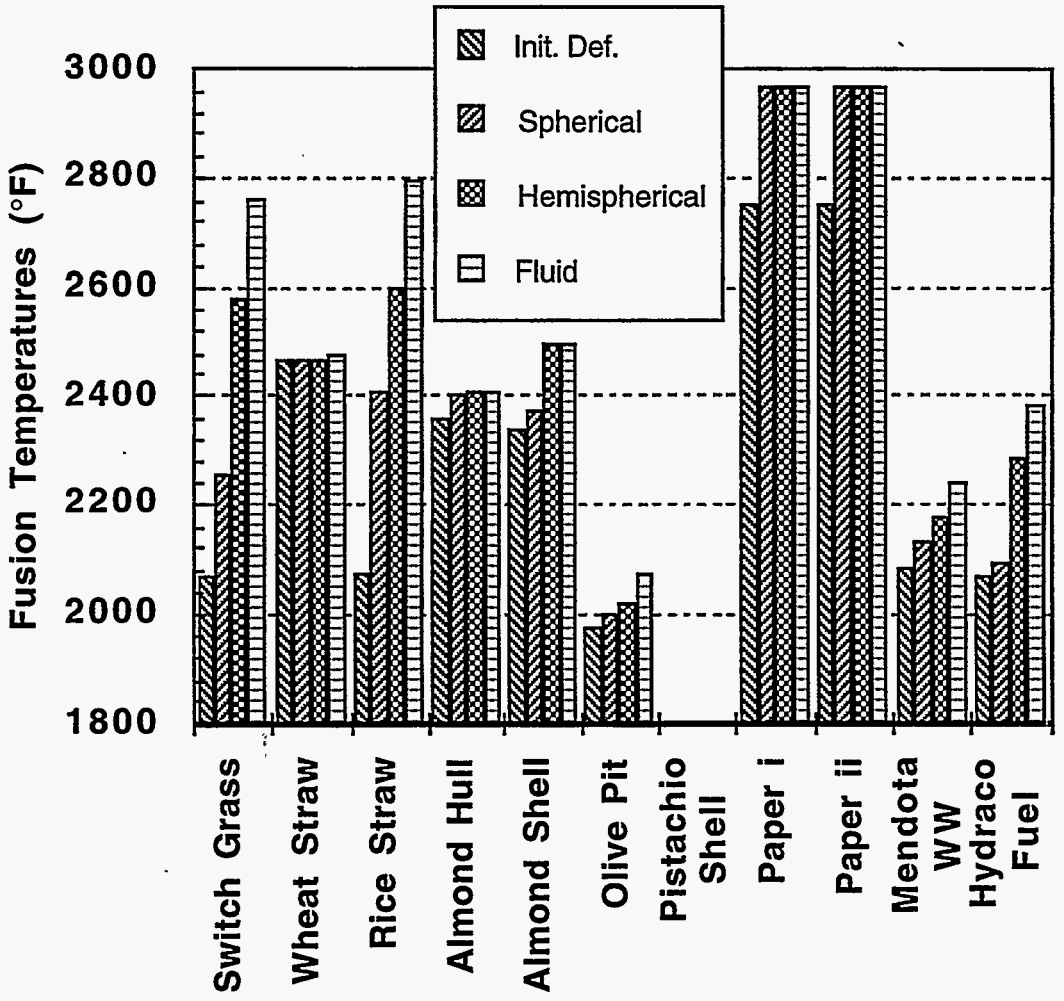

Figure 11 Results of fusion temperature analyses conducted on the fuels used in the MFC tests under oxidizing conditions. Compare with results obtained under reducing conditions (Figure 10).

Heating value, as traditionally determined, can be a poor measure of the comparitive thermal performance of different fuels if they contain different oxygen concentrations. Traditionally, heating value is defined as the amount of heat released during complete oxidation of the fuel divided by the mass of fuel. A more useful number for comparing the thermal contribution of fuels to boilers is the amount of heat released during complete oxidation of a fuel divided by the sum of fuel and oxidizer, or alternatively, divided by the total mass of products. The data labeled Modified in Appendix 1 indicate this latter value. Fuel-bound oxygen decreases the amount of air required to burn a fuel. Dry air is nearly 80 % nitrogen and other inerts. These inert gases tend to dilute the heat released

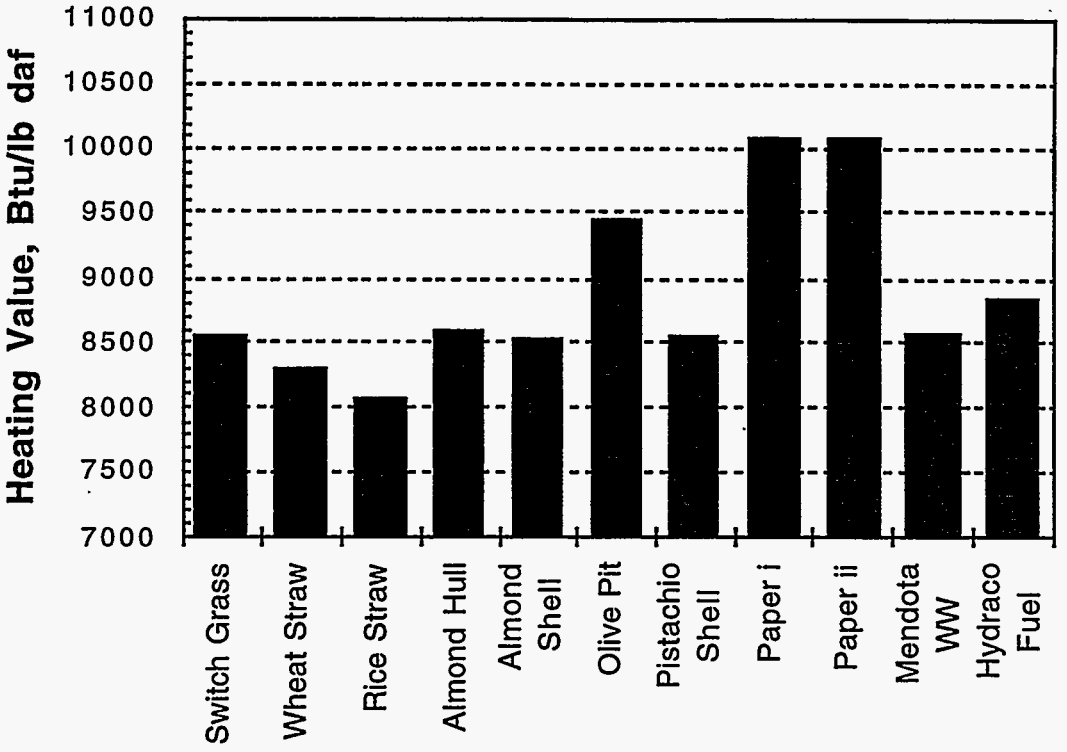

Figure 12 Variation of fuel heating value with fuel type for the biomass fuels fired in the MFC. All values are presented on a dry, ash-free (daf) basis.

by the fuel, and any decrease in the amount of air introduced in the boiler represents an increase in combustion gas temperature.

Accuracy and Precision of Standard Analyses

The accuracy and precision of the measurements has been investigated by comparing duplicate analyses submitted both the the same laboratory and to different laboratories. The results from the proximate and ash chemistry analyses are used to illustrate the discussion on accuracy and precision.

Mass balances between the sum of the oxides and the total ash did not close as well for some of these fuels as they normally do for coal. In particular, the undetermined ash (Figure 13) fractions of the almond shells and hulls exceed the concentrations of many of the other major components and account for 15 to 20 % of the total ash. In addition, there are large negative undetermined ash concentrations for paper, again accounting for about 20% of the total ash. Undetermined ash is determined by summing the concentrations of the measured elements on an oxide basis and comparing the result with the measured ash concentration.

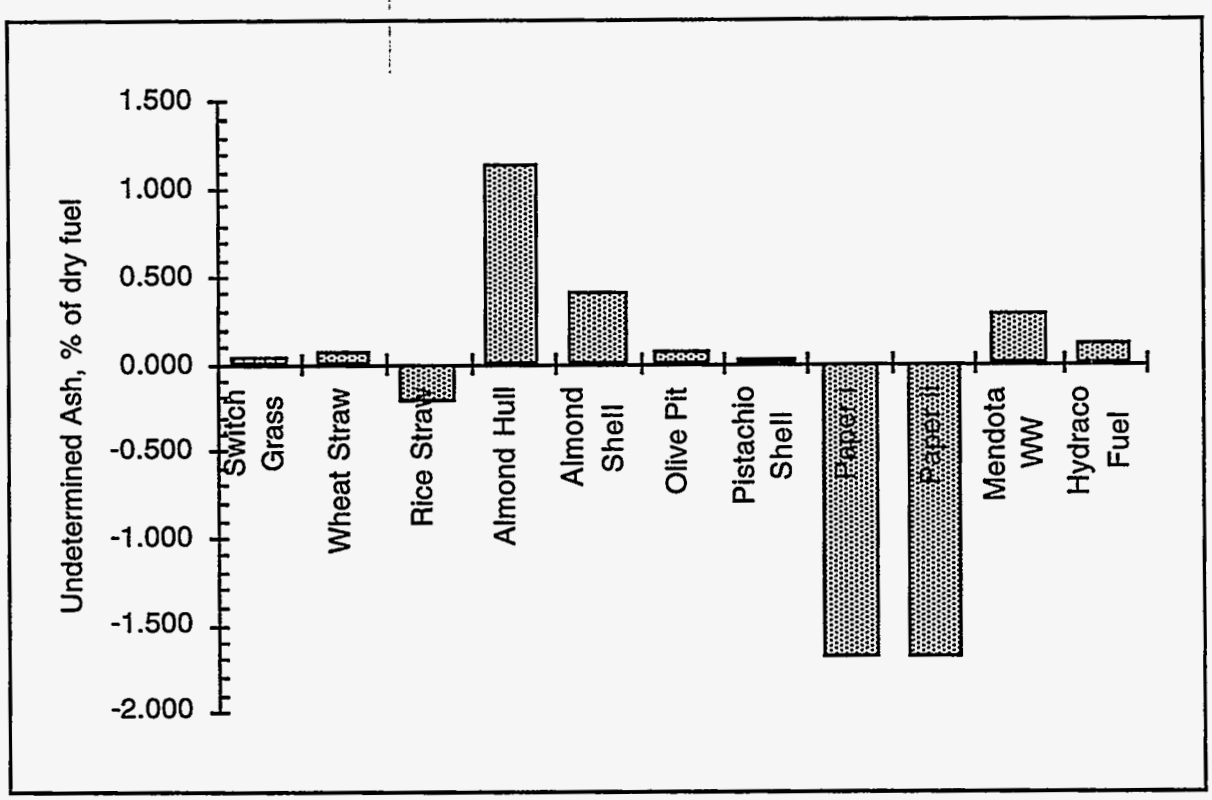

Figure 13 Undetermined ash concentrations as mass percent of dry fuel.

Aside from experimental error, this undetermined ash includes components not reported among the other ten elements (residual carbon, other metals, etc.). If the inorganic components are not completely converted to oxides in the ashing procedure, the mass balance will also not close, sometimes yielding negative and sometimes positive undetermined ash concentrations. In these samples, subsequent analyses indicated that the negative undetermined ash in the paper samples was dominated by incompletely oxidized aluminum foil (Al weighs less per aluminum atom than does Al_2O_3, yielding a negative undetermined ash concentration). More commonly, if there are carbonates or chlorides that survive the ashing procedure, the amount of material measured as ash will exceed the sum of the oxides (carbonates contain more weight per metal atom than oxides). The most likely candidates for carbonate formation are the alkali and alkaline earth elements. Since the dominant portion of the almond fuel ash is potassium, it is possible that this is the reason for the lack of closure of the mass balance.

There is good reason to believe that a portion of the more volatile inorganics could vaporize during high-temperature ashing. Some biomass fuels, in particular those with high amounts of potassium or other volatile components, are particularly susceptible to this behavior. Upon further investigation, the amount of ash was found to increase as the ashing temperature decreased from 950 °C to near room temperature. Room temperature ashes were formed by chemical means in a microwave oven.

While the amount of ash increased, the dominant effect was the formation of carbonates, sulfates, and incomplete oxidation of other compounds, as opposed to an increase in the amount of alkali. Anhydrous potassium carbonate melts at 891 °C and decomposes upon further heating. Potassium sulfate chemistry is more complex but begins to decompose at temperatures near 900 °C. There was a general, but not universal nor exceptionally large, increase in the amount of potassium with decreasing ashing temperature. For biomass fuels, we find the most useful data to come from room-temperature ashing, realizing that the sum of the oxides thus measured will rarely add up to the amount of ash as determined by high-temperature (900 °C +) ashing.

The chemical analyses at one of the laboratories are typically performed in duplicate. Also, multiple samples of the fuels have been submitted to various laboratories for analysis. The analyses themselves are accurate within about ± 3 % and reproducible within tighter tolerances when performed on coals. We do not have as much history with biomass fuels to determine if the analyses have the same accuracy, but the techniques and physics are the same so we assume the accuracy and precision should be similar. Variations between analyses that exceed ± 3 % are usually regarded as true sample-to-sample variations rather than experimental uncertainty. In the case of the biomass fuels, the sample-to-sample variations have, on occasion, been large. Switchgrass results are used here to illustrate the variations (Figure 14 to Figure 16).

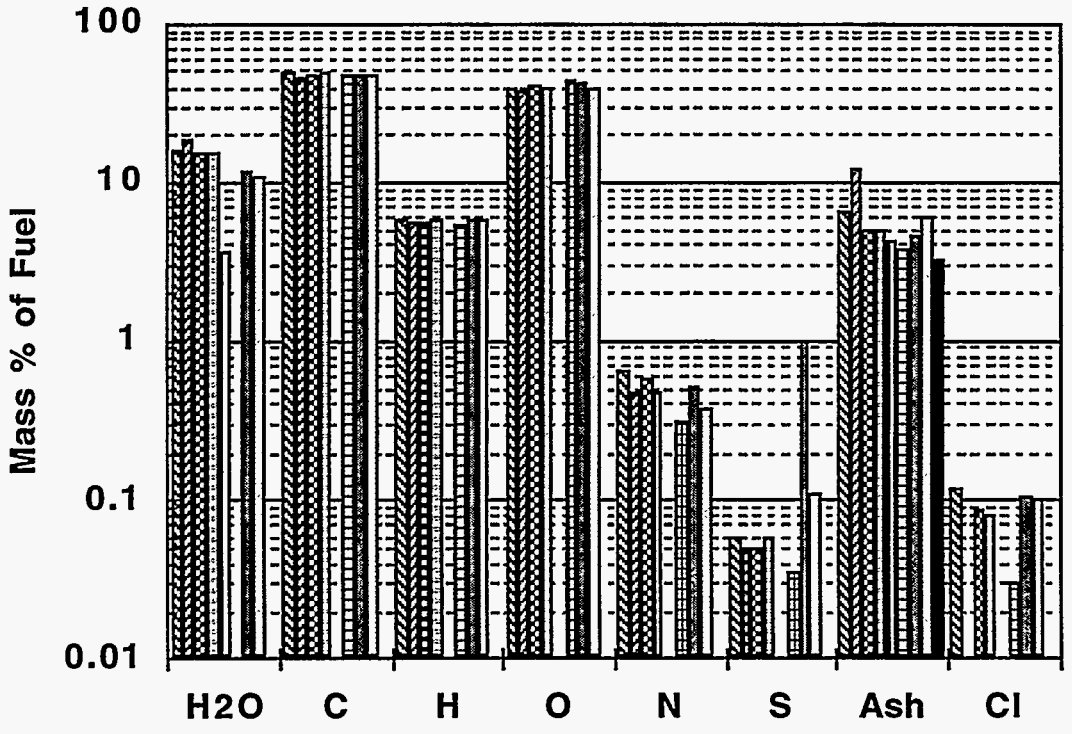

Figure 14 Comparison of ultimate analyses for duplicate samples of switchgrass. Seven complete analyses were performed. Two additional partial analyses were performed.

Figure 14 illustrates the results from seven to nine duplicate analyses for switchgrass. Six of the analyses were performed by the same laboratory but at different times and, in most cases, for different reasons. These results include the analyses performed for standard fuel characterizations as well as chemical fractionation. Most of the data are consistent with only typical variations. For example, the coefficients of variations (standard deviation divided by mean) of the samples is less than 0.05 for carbon, hydrogen, and oxygen. The analysis precision for identical samples is expected to produce of coefficient of variation of no greater than 0.025. The indication is that there are true sample-to-sample variations that are slightly larger than the uncertainty in the measurement, but they are of the same order of magnitude as the analysis precision.

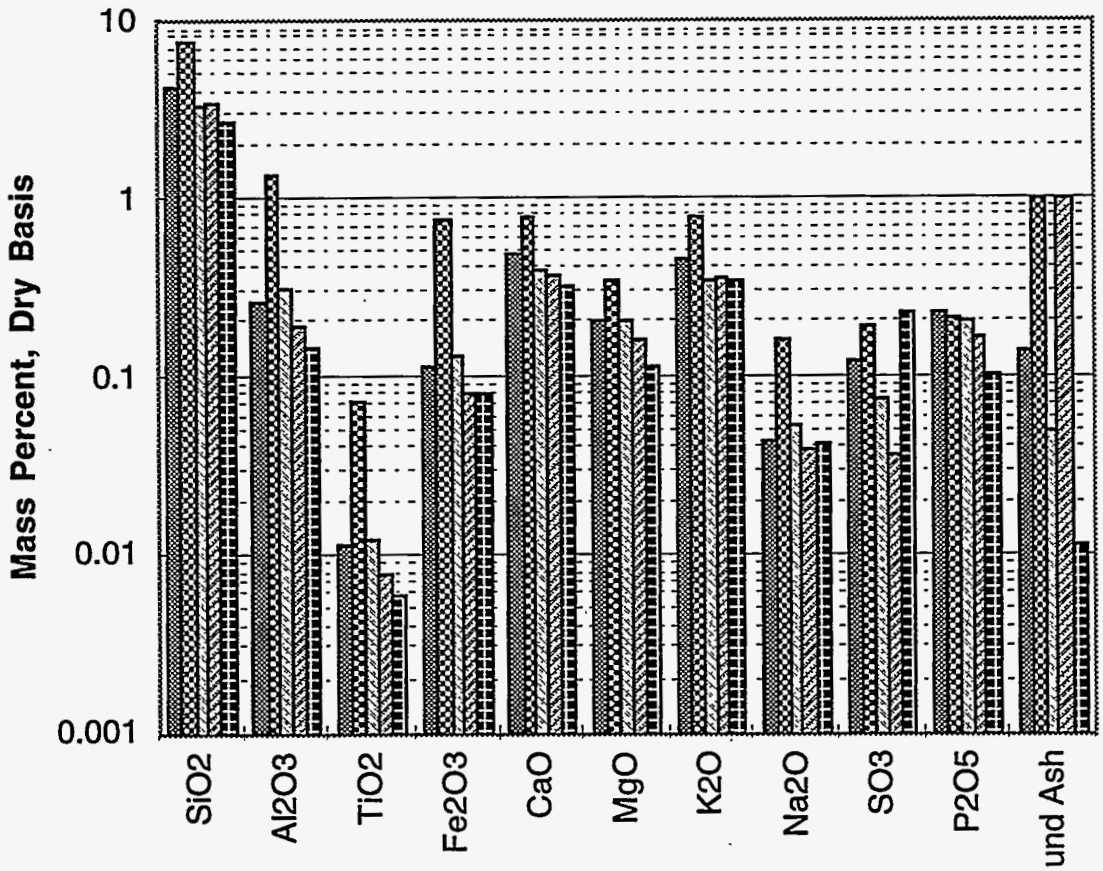

Figure 15 Comparison of replicated samples of ash analyses as a percent of dry fuel for the switchgrass sample. Compare with Figure 16.

By contrast, the minor elements N, S, and Cl have coefficients of variation of 0.24, 0.63, and 0.36, respectively. These coefficients of variation are much larger than is expected from analysis uncertainty alone. Finally, the coefficients of variation of moisture and ash are 0.38 and 0.46, respectively. These are very large values. The moisture variation is expected since moisture levels

are known to change with changing environmental and laboratory conditions. The ash result indicates very large sample-to-sample variations. One result (the second one illustrated) is particularly different from the others and appears to be an outlier. However, it cannot be eliminated as a bad point on a sound statistical basis. The remaining ash values show significantly more variation than the other major components even when the second point is discounted.

Some clues as to the source of the variations are evident in the analysis of the ash chemistry (Figure 15). The results of the composition analyses of the ash, expressed as a percent of dry fuel, are illustrated here for each of the five samples of the same switchgrass. Note that the variations are quite large. Coefficients of variation for these data are illustrated in Figure 16. The highest values (elements showing the greatest amount of variation among samples) are for species associated with soils (Al, Ti, Fe and, to some extent, Na) and typically in very small concentrations in biomass. The variation of values for these species is also dominated by the results of the second analysis, in which the total ash content is much higher than for the other samples (Figure 14). One interpretation of these data is that the second sample contained significant adventitious or extraneous ash in the form of soil contaminant. While this seems likely, it is not a complete explanation.

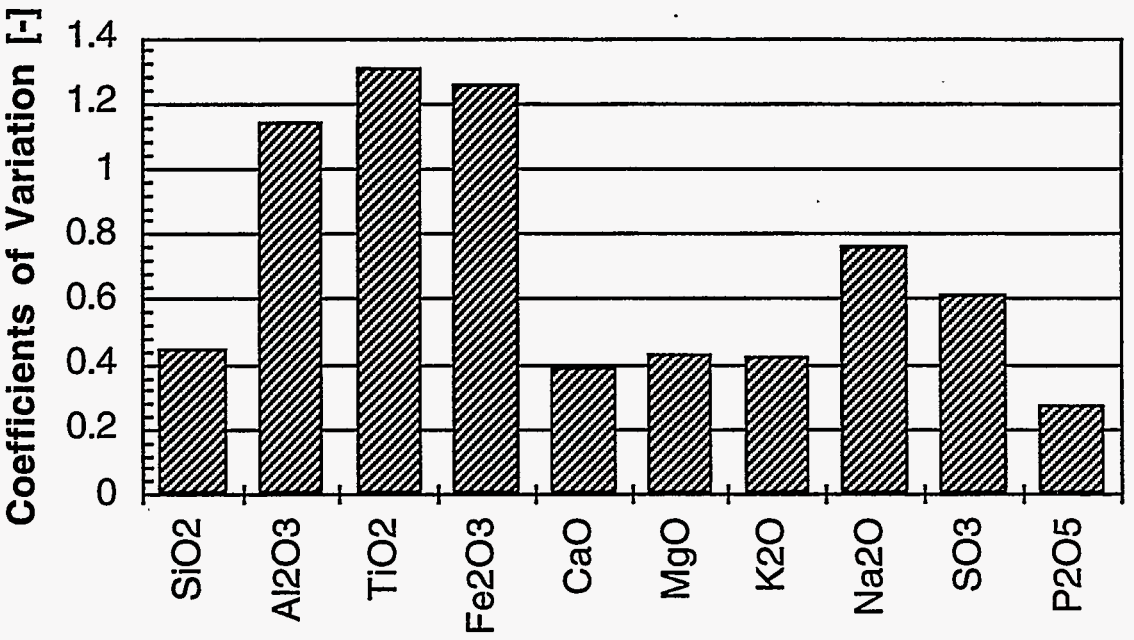

Figure 16 Coefficients of variation for the ash chemistry measurements as a function of element for the switchgrass. Compare with Figure 17.

Examining the coefficients of variation when calculated on a percent of ash basis reveals that all values decrease, that the values for aluminum, iron, and titanium are by far the largest, and that values for silicon, potassium, and calcium are comparable to those for the organic (ultimate) analyses. These data suggest that, while there is significant contribution to the samples (in particularly the second sample) by dirt, there is also significant variation in the amount of inherent ash in the switchgrass. That is, if all the variation were attributed to differences in amount but not composition of the inherent ash, the coefficients of variation would decrease when plotted as percent of ash rather than percent of fuel. Since a general decrease is observed, we believe that a portion of the variation has to do with inherent ash whereas a portion also has to do with soil contaminants.

Similar trends are observed for the other fuels, most of which have been analyzed several times by several laboratories. There are several practical implications of these data. The importance of homogenizing the samples prior to characterization or combustion testing is clear. We have been careful to maintain the correct fraction of fines and coarse material in the samples. The fines contain far greater fractions of ash than the coarse material. Even so, sample-to-sample variations persist in the data. Efforts should be made to avoid these variations by homogenizing the fuels prior to their analysis.

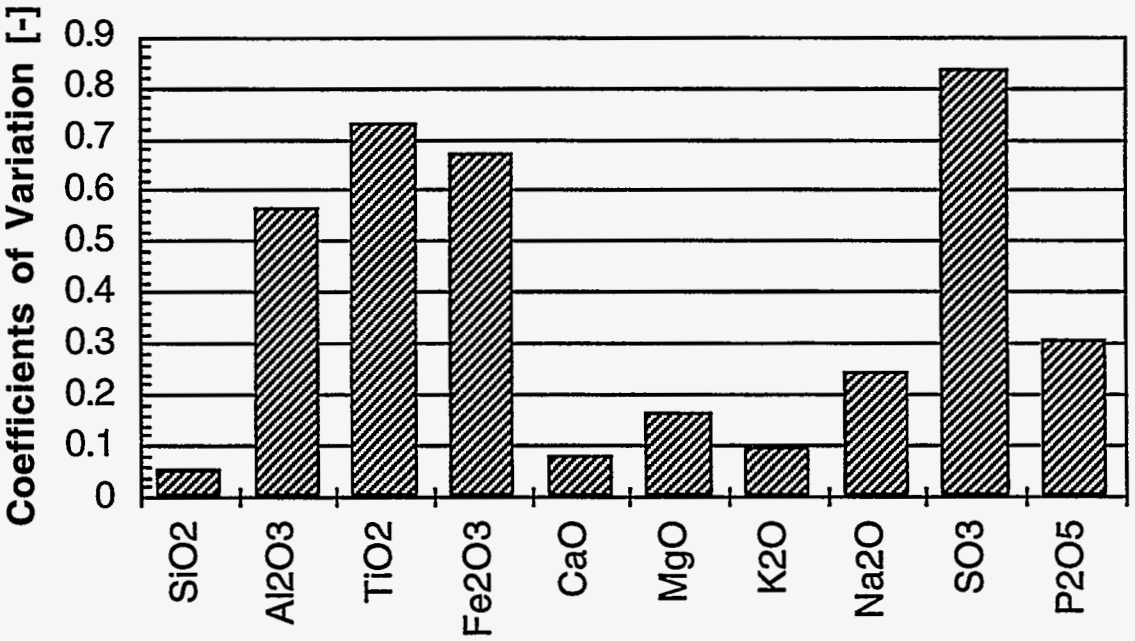

Figure 17 Coefficients of variation as a function of element for the components of the ash when computed as percent ash, as opposed to percent fuel. Compare with Figure 16.

Summary of Standard Analyses and Recommendations

Fuel-to-fuel variations in the major elements in the organic portion (C, H, and O) are slight and show no consistent trends with fuel type. Variations in the minor components of the organic fraction (N, S, and Cl) are larger than for the major components but are believed to be dominated by the local soil conditions in most cases. Organic phosphorus was not always measured but is expected to show similar variation to the other minor organic components.

Variations in inorganic fractions of materials follow expected trends with respect to the role of inorganics in plant growth. Differences in ash composition are large among the fuels being tested. Herbaceous fuels have ashes that are dominated by silica whereas the ligneous fuels analyzed to date have ashes that are dominated by potassium. Both the amount and composition of the ashes have large impacts on the operation of combustion facilities (see Volume I).

Sample-to-sample variations in analyses were studied by replicating analyses performed at one laboratory and by performing analyses at several laboratories. Laboratory-to-laboratory variations were found to be large. Within one laboratory, sample-to-sample variations were found to substantially exceed analytical precision for minor components of the organic structure and all components of the ash. Analyses of the variations indicate that sample inhomogeneity is the dominating contributor to the variations within one laboratory. Between laboratories, analytical skill and procedural variations both contribute to differences in the analyses.

Proper sample handling is of great importance in obtaining representative analyses of biomass fuels. Sample to sample variations in composition are easily introduced by the tendency of many fuels to separate into fine and coarse fractions when in containers. Homogenization of the sample is critical to obtaining reproducible results. In addition, there are indications that standard ashing temperatures (700 °C +) effect some vaporization of potassium and other volatile components of the ash. Ashing should be done at low temperatures, with the most useful data being developed near room temperature using chemical digestion techniques. Total ash determined by this method should not be expected to add to the sum of the oxides, as is traditional with higher temperature ashing.

Results of Nonstandard Fuel Analyses

Chemical Fractionation

Analyses presented thus far represent standardized tests that result in total elemental concentrations but provide little indication of mode of occurrence. We are keenly interested in the modes of occurrence of the inorganics because the chemical form of the materials determines, to a large extent, the transformations that it will undergo during combustion. To this end, we have applied a procedure called chemical fractionation to help distinguish among, for example, alkali in silicates, alkali in carbonates, and atomically dispersed alkali. Chemical fractionation data are available for almond hulls, almond shells, urban wood fuel blended with wheat straw, urban wood fuel blended with almond shells, olive pits, rice straw, switchgrass, nonrecyclable paper, and wheat straw. Duplicate samples conducted using the same technique are available for switchgrass and duplicate samples using different techniques are available for switchgrass, almond shells, and wheat straw. In total, 15 analyses were completed.

The procedure used for most of these samples is presented in detail in Appendix 1 and schematically outlined in Figure 18. Increasingly aggressive solvents leach the same sample in a series of three sequential leachings, producing four samples (including the raw material) for characterization. Because many of the leaching steps require many hours or overnight, the overall process requires about a week of elapsed time even though it only requires an hour or two of technician time. An alternative method involving application of the leaching agents to three nominally identical samples in parallel was proposed to decrease the elapsed time required for the analysis. In this section, we examine the results of chemical fractionation analyses for a series of biomass fuels, including comparisons of the parallel vs. sequential procedure.

The chemical fractionation technique distinguishes different types of inorganic material according to their solubility in a series of increasingly aggressive solvents. Those materials soluble in the two least aggressive solvents (water soluble and ion exchangeable by ammonium acetate) are the most likely to vaporize during combustion. Those soluble in hydrochloric acid are typically carbonates or sulfates. Those not soluble in any of these materials are commonly in the form of oxides, silicates, or sulfides. The mode of occurrence of the materials are important in anticipating their behavior.

Three laboratories (US Bureau of Mines, Albany Research Center; CONSOL Inc.; and Hazen Research) were used in performing these analyses. Most of the analyses were performed by Hazen using the same procedure. These samples have no designations after their names. The fuels designated with letters B, C1, and C2 are duplicate analyses performed at different laboratories. Duplicates designated B were performed using a modified procedure. Duplicates designated C1 and C2 were each performed at the same laboratory, but a different laboratory than either the undesignated samples or those designated by B. Samples C1 and C2 were analyzed using the same procedure as the undesignated samples. Generally, there is reasonable agreement among the three laboratories. In cases of disagreement, the results from laboratory B tend to be the outlier. Nowhere is this more evident than in the titanium results for rice straw. Laboratory B suggests that titanium in rice straw is completely soluble in water, unlike titanium in any other biomass (or fossil) fuel we have tested and unlike titanium in the same fuel analyzed by a different laboratory. We regard the titanium results for rice straw from Laboratory B as flawed.

Figure 19 through Figure 30 illustrate results for the 11 most prevalent inorganic components of biomass fuels (Al, Ca, Cl, Fe, K, Mg, Na, Si, Ti, S, and P). The results fall naturally into four types of elements: (1) refractory materials with little solubility (Si, Ti, and Al); (2) alkali and alkaline earth elements with varying degrees of solubility (K, Na, Ca, and Mg); (3) nonmetallic (anionic) materials typically occurring as biomass nutrients (Cl, S, and P); and (4) iron. Some of these elements are present in only trace quantities in some of the fuels.

Refractory Materials (Si, Ti, and Al)

The refractory materials Si, Al, and Ti occur in plants primarily in the form of oxides. Of the three, silicon is the dominant component. These materials are not expected to be soluble in any of the materials and should appear predominantly in the residual fraction. They also should show very little tendency to vaporize or otherwise mobilize at combustion temperatures. The data

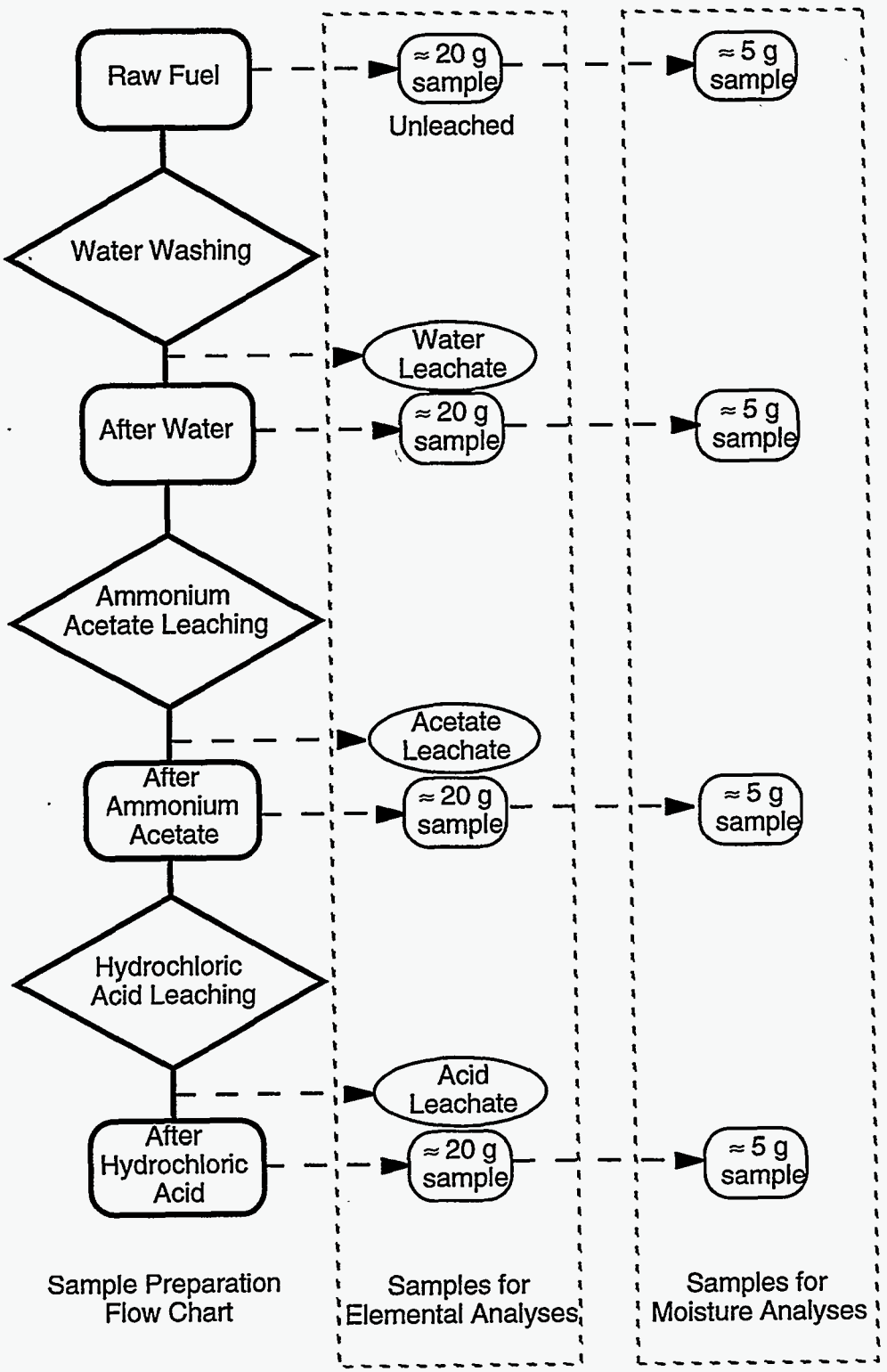

Figure 18 Schematic diagram of the chemical fractionation procedure.

generally support this thesis. Essentially all of each of these elements is found in the residual fraction of the fuel. While these materials are reasonably refractory, silicon plays an essential biological role in many herbaceous plants. It is incorporated into the plant through biological processes, although it occurs dominantly in inorganic forms in the plant. It plays a large role in a plants resistance to lodging (ability to remain upright in winds and rain) and overall strength and possibly a smaller role in photosynthesis.

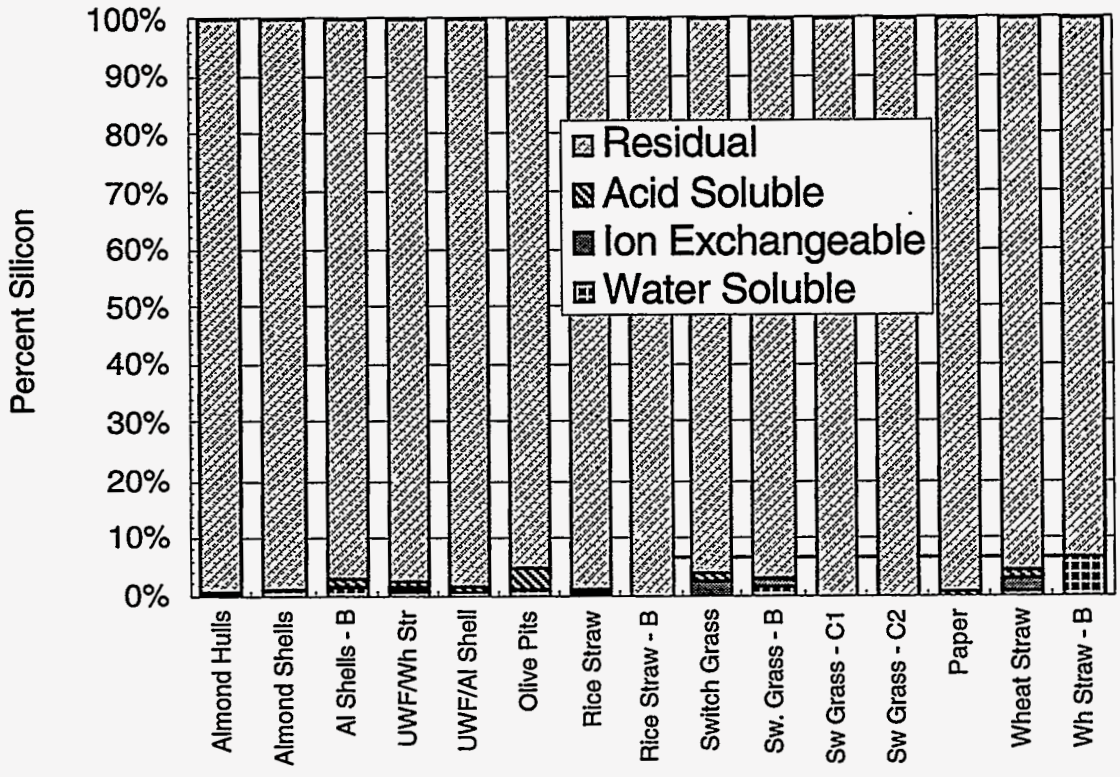

Figure 19 Silicon modes of occurrence, as determined by chemical fractionation analysis, as a function of fuel type. Silicon is a refractory material in biomass and occurs primarily as an oxide, consistent with these data.

Alkali and Alkaline Earth Materials (K, Na, Ca, Mg)

Some of the alkali and alkaline earth materials play essential roles in plant metabolism and occur in organic structures or very mobile, inorganic forms. Potassium and calcium are the most common examples. As illustrated in Figure 22 through Figure 25, chemical fractionation results are consistent with the biological functions of these materials. Over 90% of the potassium of most of the clean (nonsoiled) fuels occurs as either water soluble or ion exchangeable material. Potassium

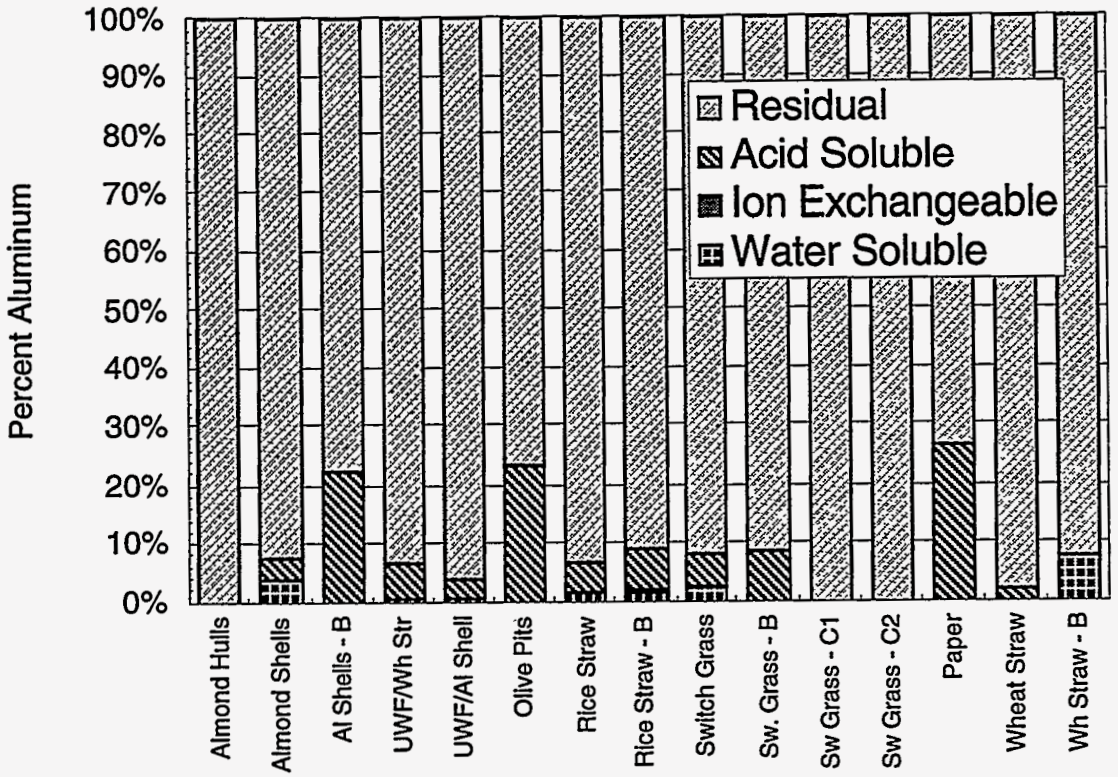

Figure 20 Aluminum modes of occurrence, as determined by chemical fractionation analysis, as a function of fuel type.

is an essential nutrient in many plants and occurs primarily a facilitator of osmotic processes, as indicated by these data. Over 90% of the potassium in clean (non-soiled) fuels occurs as either water soluble or ion exchangeable material. Sodium is minor component of most biomass, substituting for potassium in small quantities. Calcium is a common constituent of cell walls and other organic components of cell structures, consistent with its largely ion exchangeable and acid soluble character. Magnesium occurs in minor to trace quantities in most biomass material.

Both of the urban wood fuel samples were derived from commercially operating biomass boilers and contained soil contamination. Potassium and sodium are common constituents of illite, the most prevalent form of clay in soils. Nonrecyclable paper includes a large fraction of glossy print from magazines and similar publications. Similar clays are used as filler in producing these glossy prints. These are the probable sources of residual potassium in most samples.

The data in Figure 22 and Figure 23 indicate that much of the alkali material is found in forms that are susceptible to vaporization. In many biomass fuels, especially herbaceous fuels, potassium is the most prevalent of these materials. Its vaporization and subsequent chemical reactions are

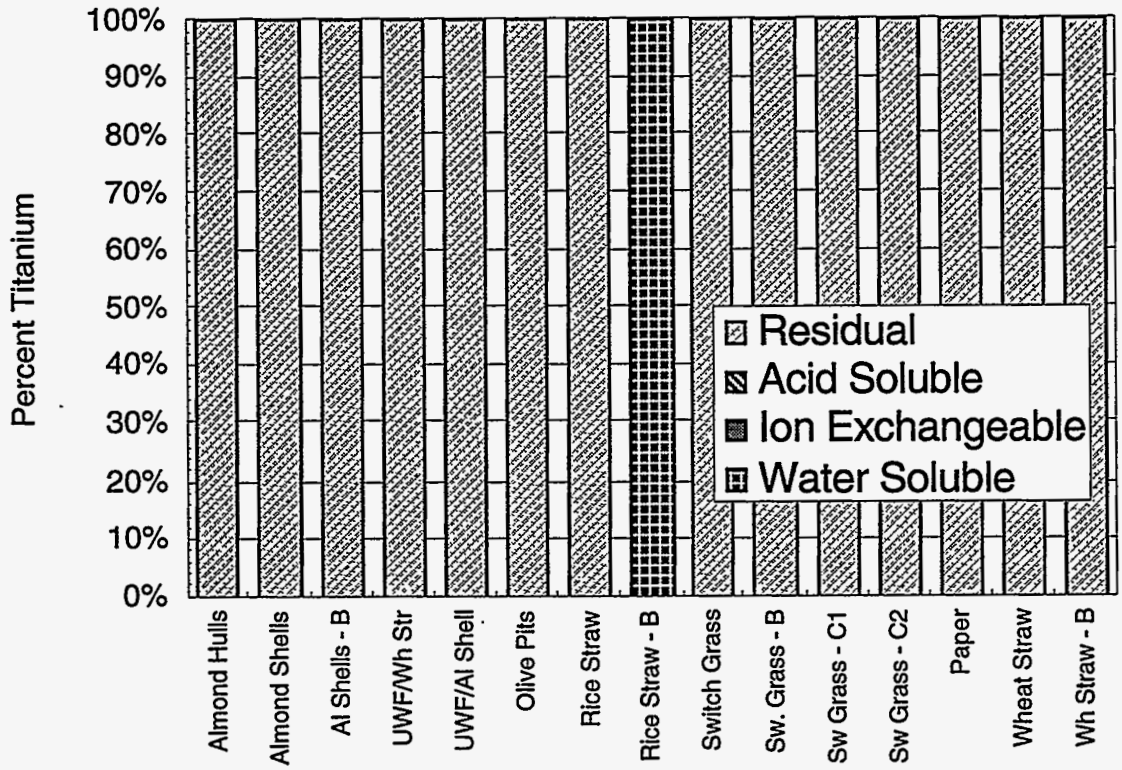

Figure 21 Titanium modes of occurrence, as determined by chemical fractionation analysis, as a function of fuel type. Titanium is a refractory material in biomass.

responsible for much of the fouling, sulfation, corrosion, and silicate formation found in biomass boilers.

Alkaline earth materials are found in forms in biomass less likely to lend themselves to volatilization. Furthermore, the stable compounds they are likely to form during combustion are less volatile than for alkali materials. This explains, in part, why ligneous materials such as wood, with ash containing large fractions of calcium, pose far less fouling problems than herbaceous materials, such as straws and grass, with ash containing higher concentrations of alkali material.

Nonmetallic Materials (Cl, S, P)

Nonmetallic (anionic) materials such as chlorine and sulfur occur as plant nutrients. The classification of nonmetallic is somewhat misleading in that none of the inorganic constituents occur as metals (i.e., in neutral oxidation states). The nonmetallic compounds tend to become anions when oxidized, by contrast to metals that dominantly form cations. However, much of the material in biomass is not ionically bound.

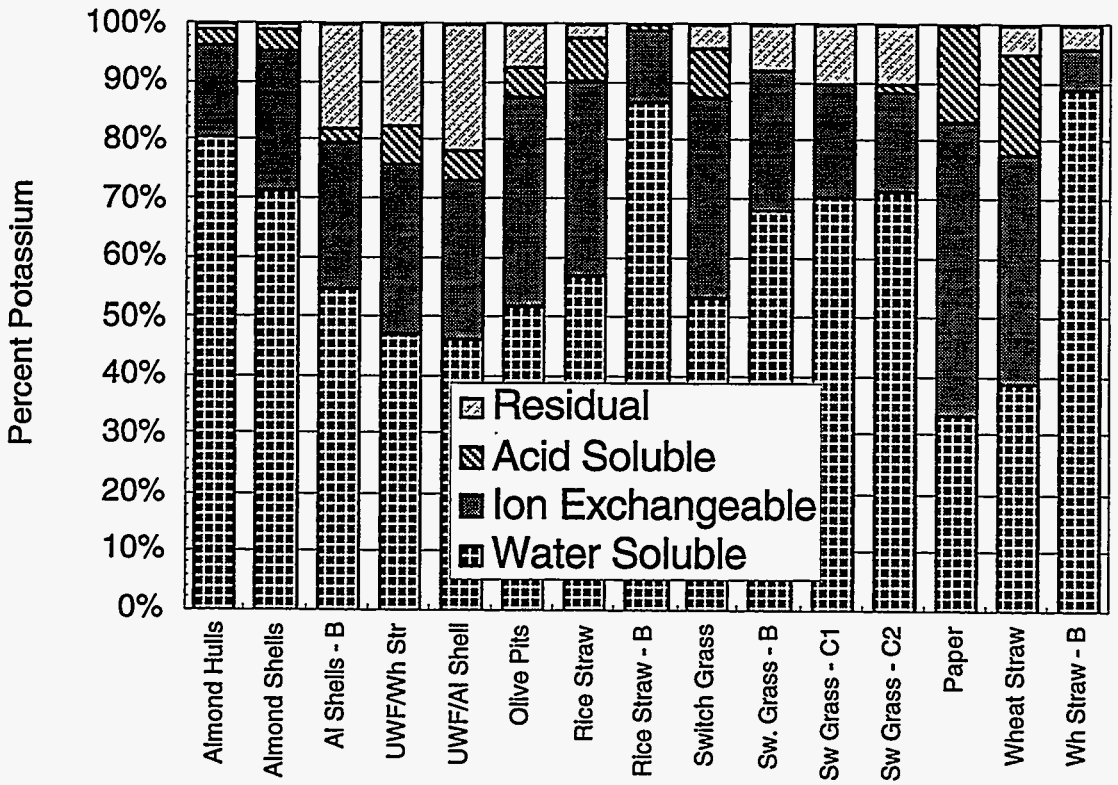

Figure 22 Potassium modes of occurrence, as determined by chemical fractionation analysis, as a function of fuel type. Potassium is an essential nutrient in many plants and occurs primarily a facilitator of osmotic processes, consistent with these data.

Chlorine plays a key role in the transformations of inorganic materials during combustion. Chlorine reacts with alkali material to form relatively volatile and stable alkali chlorides. In this process, it is commonly chlorine concentration rather than alkali concentration that limits the amount of vaporization. Condensation of the chlorides on relatively cool surfaces in the presence of sulfur often leads to the formation of sulfates. At high temperatures on many metals, this leads to a corrosive situation. Chlorine also leads to low temperature corrosion through the formation of acid gases. As indicated in the data, essentially all chlorine is in a vaporizable form for essentially all fuels. The data from laboratory B regarding chlorine are inconsistent with all of the other data and are viewed as erroneous. There are small quantities of plastic in nonrecyclable paper that contribute to forms of chlorine different than is found in traditional biomass fuels.

Sulfur is also a major player in ash deposition. Many convection pass deposits are based on sulfate formation on tube surfaces. The general rule, that water soluble and ion exchangeable forms of material most easily vaporize, does not apply to sulfur. Sulfur, in essentially all of its forms, quantitatively oxidizes during combustion. Some of it then reacts with alkali materials to form sulfates.

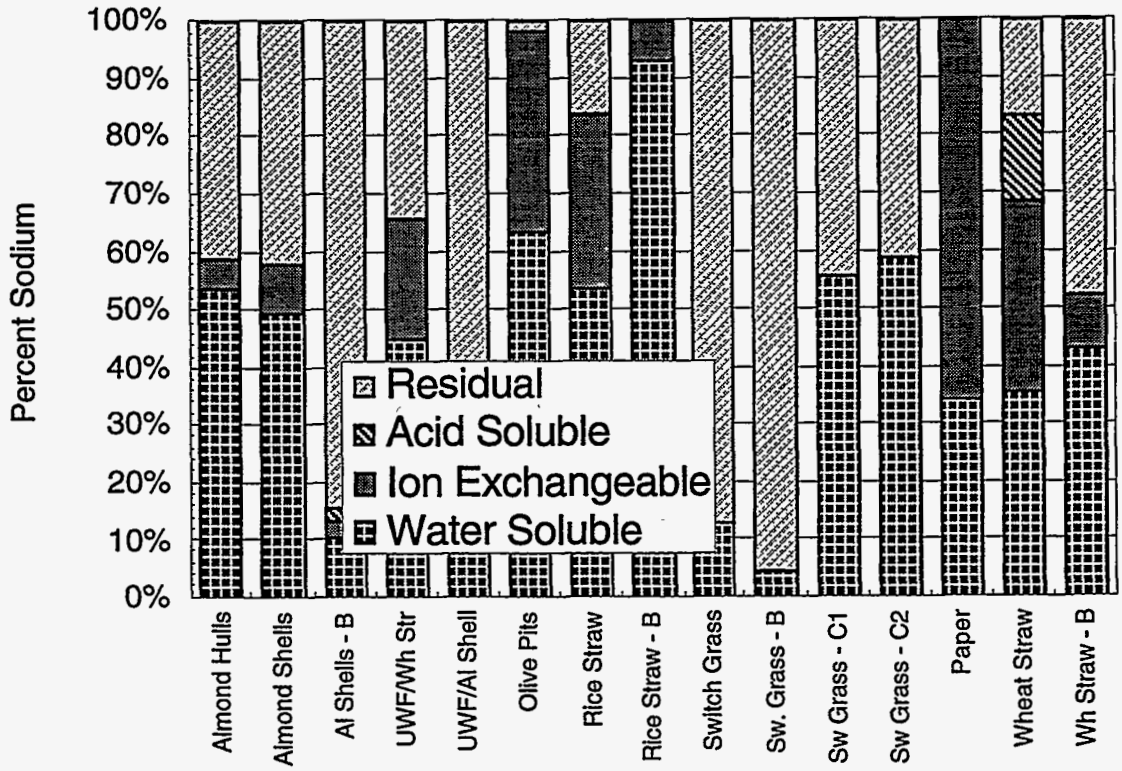

Figure 23 Sodium modes of occurrence, as determined by chemical fractionation analysis, as a function of fuel type. Sodium is minor component of most biomass, substituting for potassium in small quantities.

The behavior of phosphorus is not well characterized during combustion of these biomass fuels. It forms only a small fraction of the fuel and appears to behave as a relatively refractory material. Phosphorus is an important contributor to ash deposits from some manures and litters.

Iron (Fe)

In coal-based systems, iron plays a major role in deposit properties as an effective flux for silicate materials. In particular, the oxidation state of iron in silicates is sensitive to local conditions, with ferric iron being prevalent under oxidizing conditions and increasing amounts of ferrous iron being formed under reducing conditions. Ferrous iron incorporated in silicates leads to lower melting points than ferric iron. The typical forms of iron in coal include, in decreasing order of importance, sulfides such as pyrite, sulfates, oxides, silicates, and carbonates.

Similar behavior is expected in biomass ash deposits. However, there is very little iron in the samples of biomass we have tested to date. Therefore, iron plays a minor role in ash deposits except in special circumstances. The forms of iron in biomass indicate a greater extent of ion exchangeable material than is common in coal.

The conclusions from these results are: (1) chemical fractionation results show general agreement with known forms of inorganic material in biomass that is useful for anticipating the reactions such materials will undergo during combustion; (2) replicate samples show good, but not outstanding, agreement when performed within the same laboratory; (3) laboratory-to-laboratory variations can be large, although they may be attributable to lack of standard protocols at individual labs; (4) trends in chemical fractionation results with fuel type are rational and often reflect different processing, impurities, and other features.

The procedure followed by laboratory B in this study was an attempt to make the chemical fractionation analysis faster, although not cheaper. The difference in the procedures was essentially to process the fuel through the various stages in parallel rather than sequentially. In principal, the parallel approach should be fine. In practice, it appears to have significantly compromised the results. This may be because of inherent sample-to-sample variations in biomass – a concern noted at the outset. However, the first step of both processes (water washing) is essentially identical. Many of the differences in results from laboratory B appeared in this first step. This suggests that the problem lies more in the laboratory analyses than in the procedure.

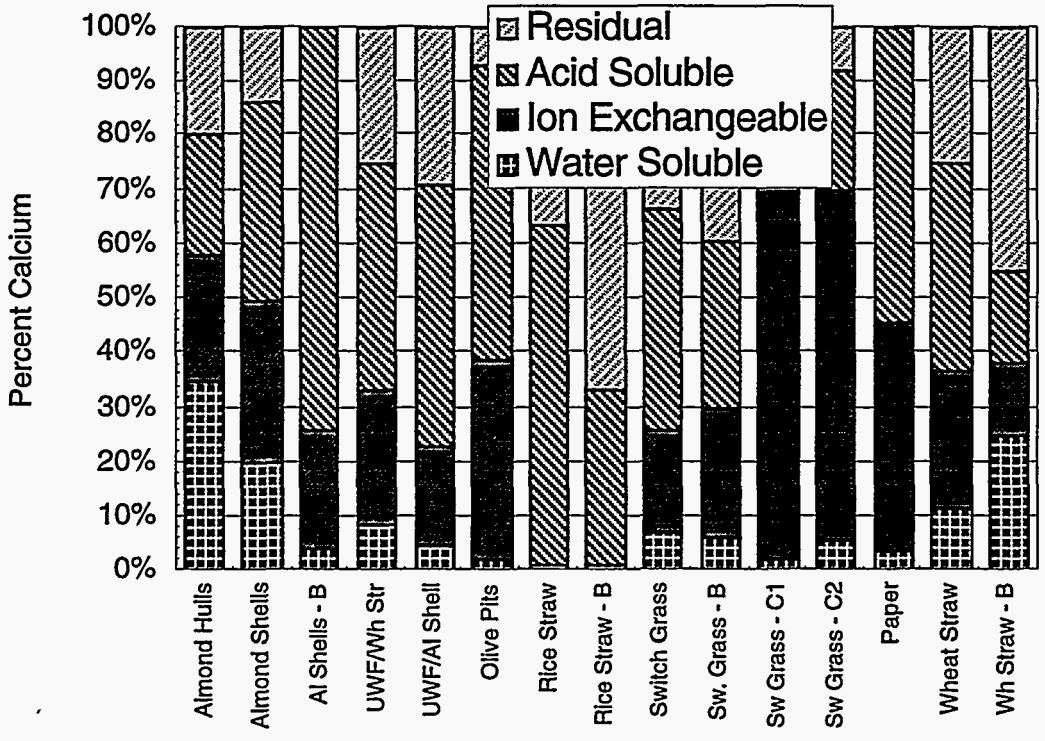

Figure 24 Calcium modes of occurrence, as determined by chemical fractionation analysis, as a function of fuel type. Calcium is a constituent of cell walls and other organic components of cell structures, consistent with its largely ion exchangeable and acid soluble character.

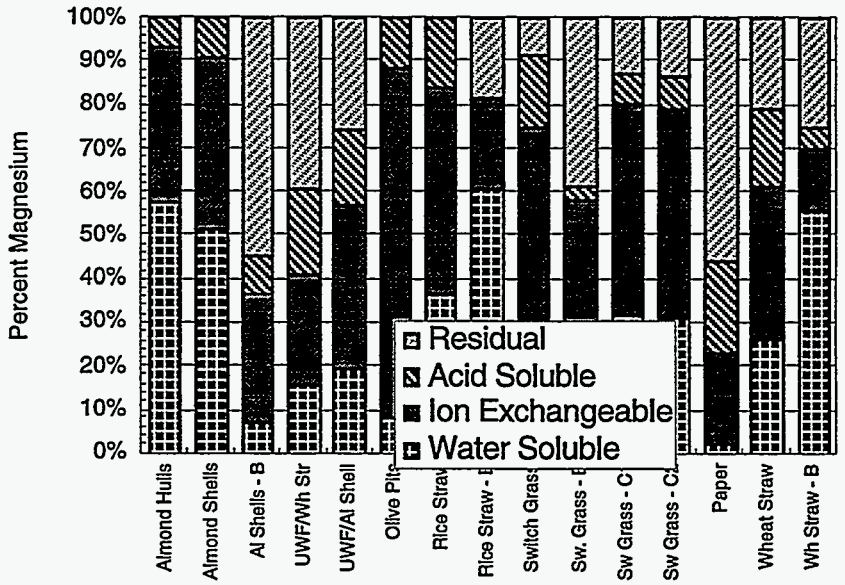

Figure 25 Magnesium modes of occurrence, as determined by chemical fractionation analysis, as a function of fuel type. Magnesium occurs in minor to trace quantities in most biomass material.

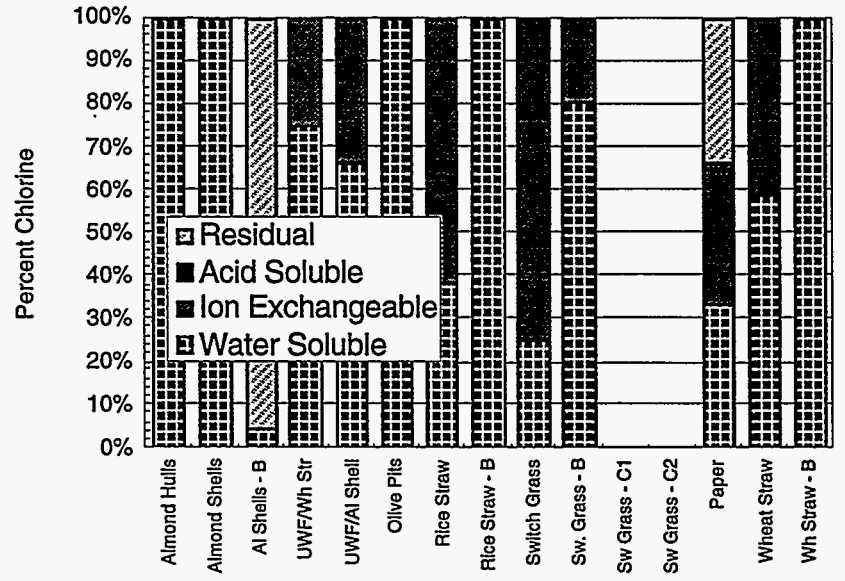

Figure 26 Chlorine modes of occurrence, as determined by chemical fractionation analysis, as a function of fuel type. Chlorine occurs in volatile forms in essentially all biomass fuels.

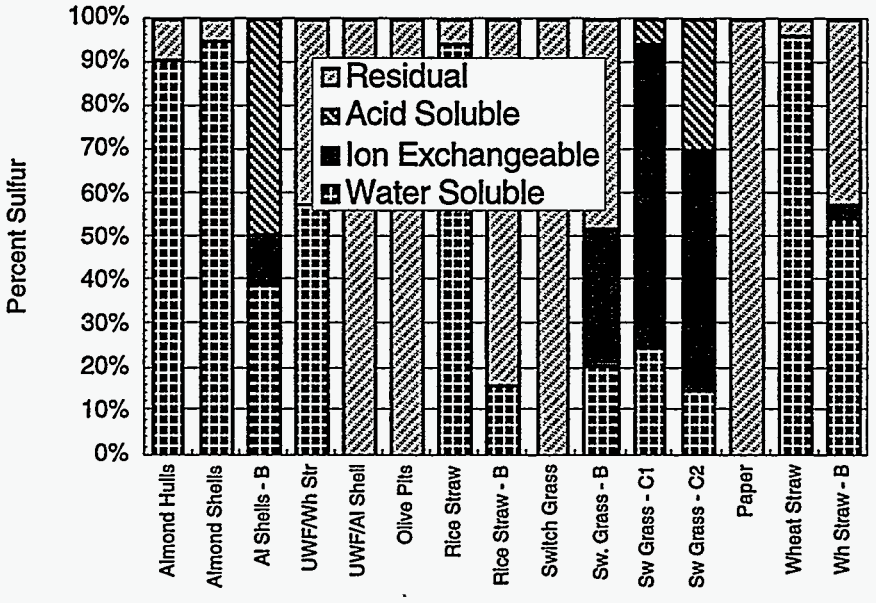

Figure 27 Sulfur modes of occurrence, as determined by chemical fractionation analysis, as a function of fuel type. Sulfur is a trace component of many biomass fuels but a more significant component in straws and some woods.

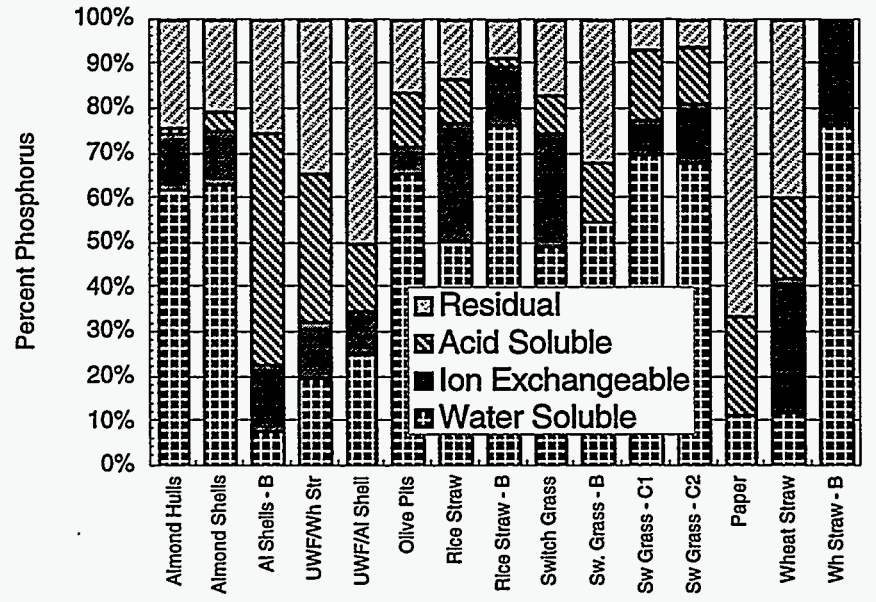

Figure 28 Phosphorus modes of occurrence, as determined by chemical fractionation analysis, as a function of fuel type. Phosphorus is a trace component of most biomass fuels.

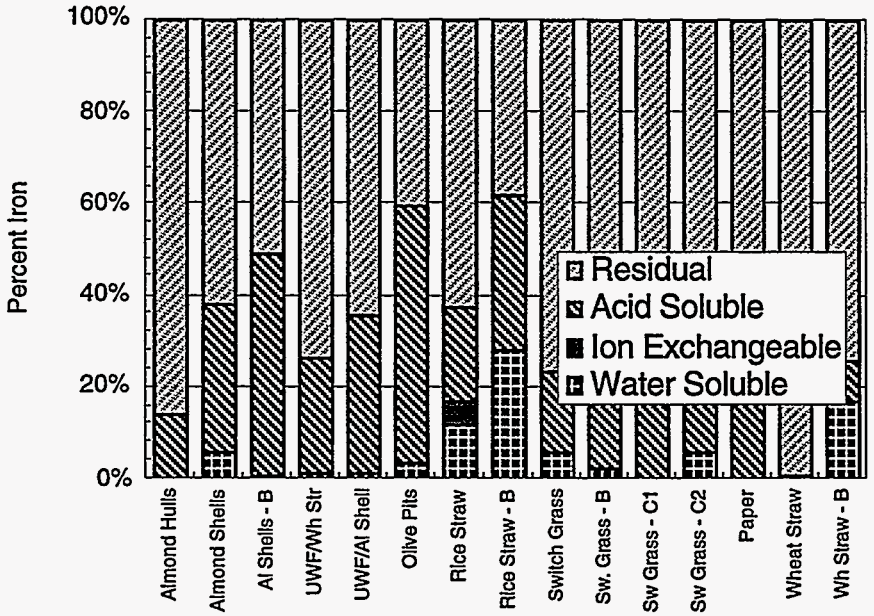

Figure 29 Iron modes of occurrence, as determined by chemical fractionation analysis, as a function of fuel type. Iron is a trace component of most biomass fuels.

Bench-Scale Combustion Investigations

Experimental Approach

The release of alkali vapor species during the combustion of selected forms of biomass was monitored and studied using a direct sampling, molecular beam mass spectrometer (MBMS) system. The MBMS system is ideally suited for studying the high-temperature, ambient pressure environments encountered during the present alkali screening studies. The integrity of the sampled, high-temperature combustion gases is preserved by the free-jet expansion by effectively quenching chemical reactions and inhibiting condensation. As a result, reactive and condensable alkali species remain in the gas phase at temperatures far below their condensation point for long periods of time in comparison to reaction rates. This apparatus (Evans & Thomas A. Milne, 1987a; Evans & Thomas A. Milne, 1987b) and the application of MBMS to the study of alkali transport and speciation during biomass combustion (Dayton, French, & Milne, 1995; French, Dayton, & Milne, 1994) have been described in detail in the literature so only a brief discussion is presented below.

The biomass samples screened during this study include those used in the Alkali Deposits Project being conducted in the Multifuel Combustor at Sandia National Laboratories, Livermore, CA. The biomass feedstocks consist of the following: wheat straw, rice straw, (Sandia) switchgrass, pistachio shells, almond shells, almond hulls, waste paper, wood fuel, and wood straw blend (see Table 1, page 14). This group consists of a grass, straws, agricultural wastes or residues, and waste products. Wood waste #1 is a blend of 20 % wheat straw in urban waste wood and wood waste #2 is a blend of 10 % almond shells in urban wood fuel. Except for the switchgrass, straws, and the wood wastes, the samples are finely ground. The wastepaper is finely shredded to a consistency that is not as dense as the other feedstocks.

Twenty to fifty milligrams of the biomass sample of interest is loaded into hemi-capsular quartz boats which are placed in a platinum mesh basket attached to the end of a quarter inch (6.35 mm) diameter quartz rod. This quartz rod can be inserted and translated into the heated zone of a quartz tube reactor enclosed in a two-zone variable temperature furnace as shown in Figure . In regards to an actual continuously fed combustor, this could be considered a batch combustion event. However, the experiments simulate the continuous combustion of biomass from initial heating to ignition to complete char burnout and ash formation.

Furnace temperatures during these screening studies were maintained at 1100 °C and 800 °C, respectively. Gas temperatures near the quartz boat were measured with a type K thermocouple inserted through the quartz rod. The actual boat temperature and the flame temperature of the combustion event were not measured. The atmosphere in the reactor consisted of a flowing mixture of helium and oxygen (5%, 10% or 20%) at a total flow rate of 4.4 standard liters per minute. For several experiments 20% steam was also added to the gas mixture by injecting water into the rear of the reactor through a needle fed by a

syringe pump. The tip of the needle was packed in stainless steel shot to provide an increased surface area for evaporation. Steam simulates the moisture included in most biomass fuels and plays an important role in the formation of some alkali vapors, most notably hydroxides.

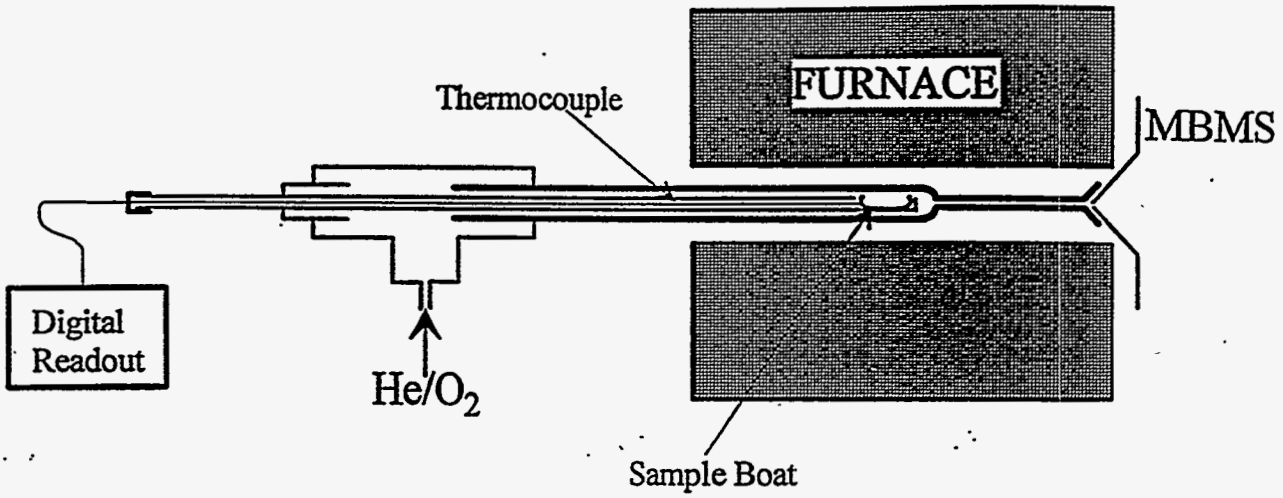

Figure 30 Schematic representation of the high temperature reactor used to study alkali metal release during biomass combustion.

The molecular beam sampling system consists of a three stage, differentially pumped vacuum chamber (Dayton, et al., 1995) as depicted in Figure 31. A conical, stainless steel molecular beam sampling orifice is positioned at the downstream end of the quartz tube reactor to sample the high-temperature, ambient-pressure biomass combustion gases. The tip of the sampling orifice protrudes into the furnace keeping it at an elevated temperature (not measured) to prevent alkali metals and other species from condensing on the orifice. Sampled gases undergo a free jet expansion into the first stage of the vacuum system. A molecular beam is formed by collimating the gas stream with a conical skimmer located at the entrance to the second stage of the vacuum system. The molecular beam was directed into the ionization region of the mass spectrometer located in the third stage of the vacuum system. Electron impact ionization of the species in the molecular beam yields ions that were filtered by a triple quadrupole mass analyzer and detected with an off axis electron multiplier. Comprehensive detection of stable and transient species liberated during biomass combustion was achieved with the MBMS system.

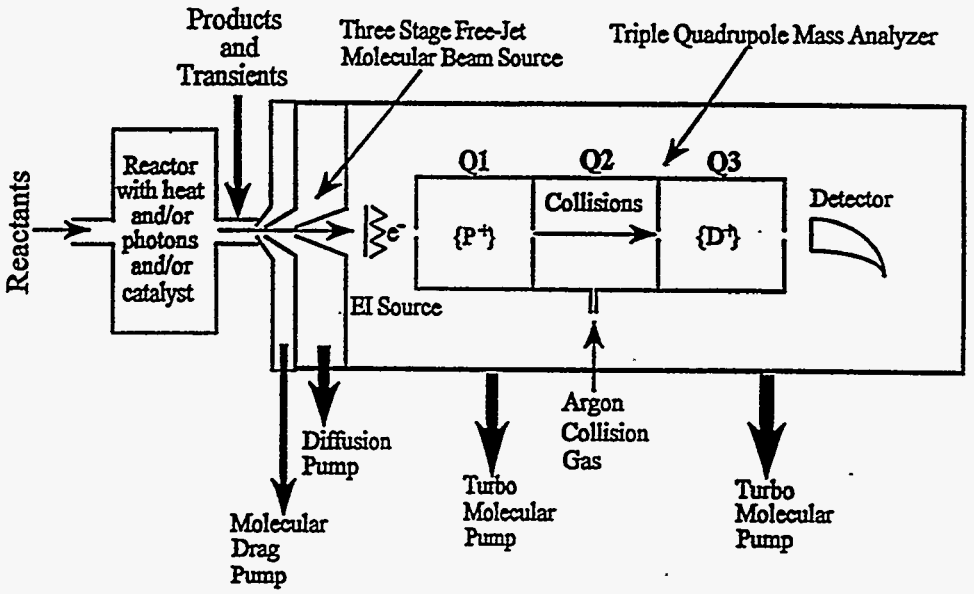

Figure 31 Schematic representation of the molecular beam sampling/mass spectrometer system.

As discussed in a previous report, the combustion of these 20-50 mg biomass samples occurs in three distinct phases (Dayton, et al., 1995; French, et al., 1994). A typical experimental run consisted of loading the quartz boat containing the sample into the cool end of the reactor and waiting a short time for air to be flushed from the system. Data collection was then initiated to record a background for 18-30 seconds. The sample was then inserted into the furnace as quickly as possible (typically 6 to 9 seconds). After insertion, the sample underwent rapid heating and ignition occurred almost immediately. Devolatilization and subsequent gas-phase combustion lasted for about 6 seconds. This stage of reaction is labelled "Combustion" in several following figures. Data were collected for at least an additional minute, encompassing all three phases of reaction that are observed. These phases are distinguished in Figure 32, which shows the total ion current as a function of time measured during reaction of 40 mg of switchgrass in 20% O_2 in helium at 1100 °C. The data points in the total ion current plot represent complete mass spectra scanned over the interval from m/z = 15 through m/z = 130. Masses $^{18}(H_2O)$, $^{32}O_2$ and $^{44}(CO_2)$ were skipped to avoid overloading the detector.

Following a period of time during which background spectra were collected, the sample is inserted into the high temperature zone of the reactor. Combustion was initiated very rapidly once the sample is inserted. The first phase, called the combustion or devolatilization phase, was dominated by the production of CO, CO_2, and H_2O while O_2 was consumed. SO_2 and NO were also detected during the combustion phase. Depending on the combustion conditions, such as oxygen concentration and gas temperature, this phase can be dominated by the evolution of organic hydrocarbons that do not completely convert to products. As a result, the mass spectrum averaged over the combustion phase

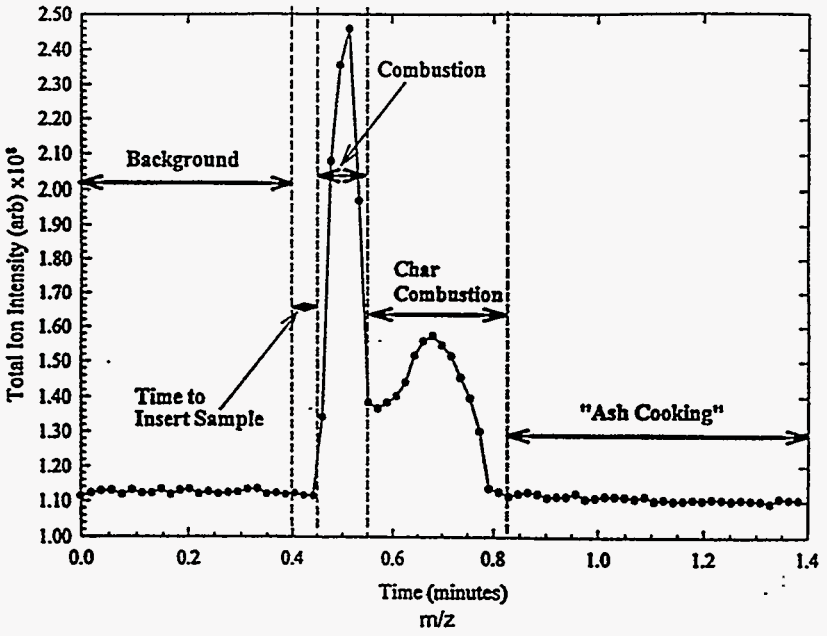

Figure 32 Temporal profile of the total ion current measured during switchgrass combustion at 1100 °C in He/O_2 (20%).

can be complicated by the presence of hydrocarbon fragment ions making it very difficult to monitor trace amounts of alkali released during this phase.

After the volatile species have been completely liberated, the char combustion phase begins. Most of the alkali is released into the gas phase during the char combustion phase (Dayton, et al., 1995). In the absence of organic hydrocarbons, it is relatively simple to identify the alkali species in the mass spectrum averaged over the char combustion phase. Consequently, the char combustion phase contains the most useful information concerning alkali release and speciation. The final phase of the combustion process is termed the "ash cooking" phase. Most of the volatile matter has been liberated by the beginning of this phase. However, the remaining ash is left in the high temperature reactor to insure that all of the volatile matter has been released. In entrained combustion, this phase will be limited to, at most, a few seconds. However, it could be much longer in a moving or fluidized bed combustor.

The nine feedstocks listed above were screened for alkali release and speciation at four different combustion conditions: 1100 °C in He/O_2 (20%); 800 °C in He/O_2 (20%); 1100 °C in He/O_2 (5%) and; 1100 °C in He/O_2 (10%) / Steam (20%). These conditions were chosen to study the effect of temperature, oxygen concentration, and gas composition (dry vs. moist) on alkali release and speciation.

Experimental Results

Baseline Results

Alkali release and speciation during biomass combustion is investigated by examining the mass spectra averaged over the char combustion phase for the reasons discussed above and in the literature (Dayton, et al., 1995). Figure 33 through Figure 45 display the mass spectra averaged over the char combustion phase during the combustion of the following feedstocks in a 20 % O_2 in helium atmosphere at 1100 °C: wheat straw, rice straw, Sandia switchgrass, pistachio shells, almond shells, almond hulls, waste paper, wood/wheat straw blend, and wood/almond shell blend, respectively. Masses 18, 32, and 44 were not scanned during these experiments to avoid saturating the detector. The ion intensities in these and all subsequent mass spectra have been normalized to the background $^{34}O_2^+$ signal. Relative ion intensities are, therefore, semi-quantitative and it is reasonable to compare the relative ion signal intensities between spectra. Uncertainties of a factor of two, however, can arise because of day-to-day variations in mass spectrometer tuning, varying time intervals of spectral averaging, and different sample weights. The insets in the figures are the compositions of the feedstock of interest as determined in the ultimate analysis of the sample as received except where noted.

The wheat straw has a relatively high chlorine content and moderately high alkali content. The mass spectrum recorded during the char phase of wheat straw combustion shown in Figure 33 contains peaks assigned to K^+ (m/z = 39) and KCl^+ (m/z = 74 and m/z = 76) as expected from a high-chlorine-containing feedstock. It is also possible to identify the KCl dimer fragment (K_2Cl^+ at m/z = 113 and m/z = 115). Very little HCl is detected in the char combustion phase, however, there was a significant amount of HCl released during the combustion phase.

The rice straw sample has a very high chlorine (the highest chlorine content compared to the other eight feedstocks) and alkali content and a high percentage of sulfur and bound nitrogen. The mass spectrum averaged over the char phase during rice straw combustion shown in Figure 33 exhibits large signals resulting from CO and CO_2, as before, but the K^+ signal at m/z = 39 is considerably more intense than the NO^+ and SO_2^+ peaks. There are also many features in the spectrum that can be attributed to alkali chlorides. Two peaks at m/z = 74 and m/z = 76 are assigned to KCl^+ while the two peaks at m/z = 113 and m/z = 115 are assigned to K_2Cl^+, a fragment ion of the KCl dimer (Hastie, Zmbov, & Bonnell, 1984; Milne & Klein, 1960). Sodium chloride was also released during rice straw combustion as indicated by the peaks at m/z = 58 and m/z = 60 corresponding to $NaCl^+$.

Although an abundance of alkali chlorides appeared to be released during the combustion of this high-alkali-metal-containing feedstock, there was no evidence of other alkali containing species being released during the char combustion phase. As a result, the increased intensity of the K^+ and Na^+ signals is mostly due to fragmentation of the parent chloride species. One curious feature was observed, however, in the char phase mass spectra of rice straw shown in Figure 34. Two unique peaks were evident at m/z = 97 and m/z = 99

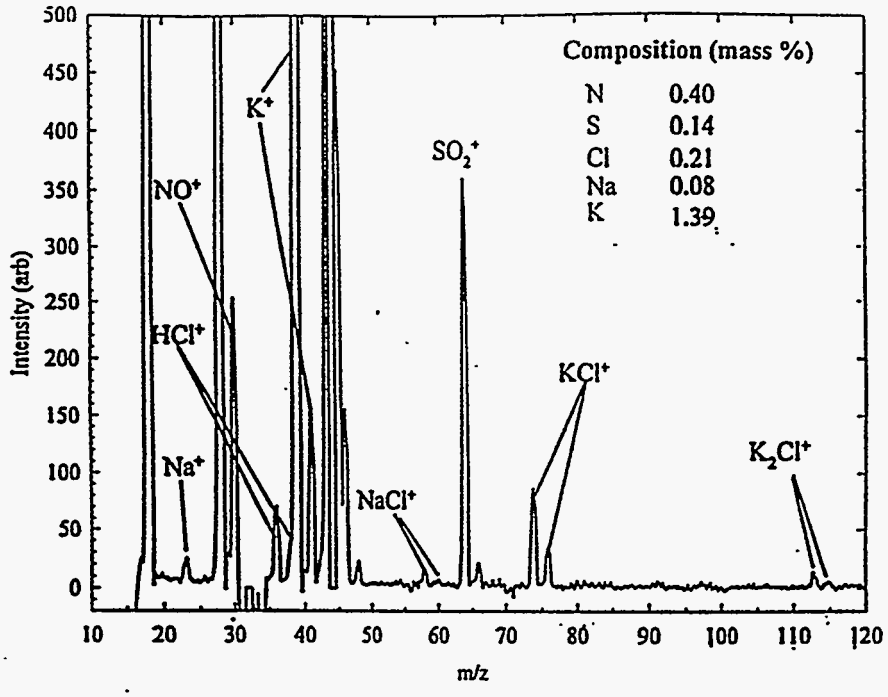

Figure 33 Mass spectrum averaged during the char phase of wheat straw combustion at 1100 °C in He/O_2 (20%).

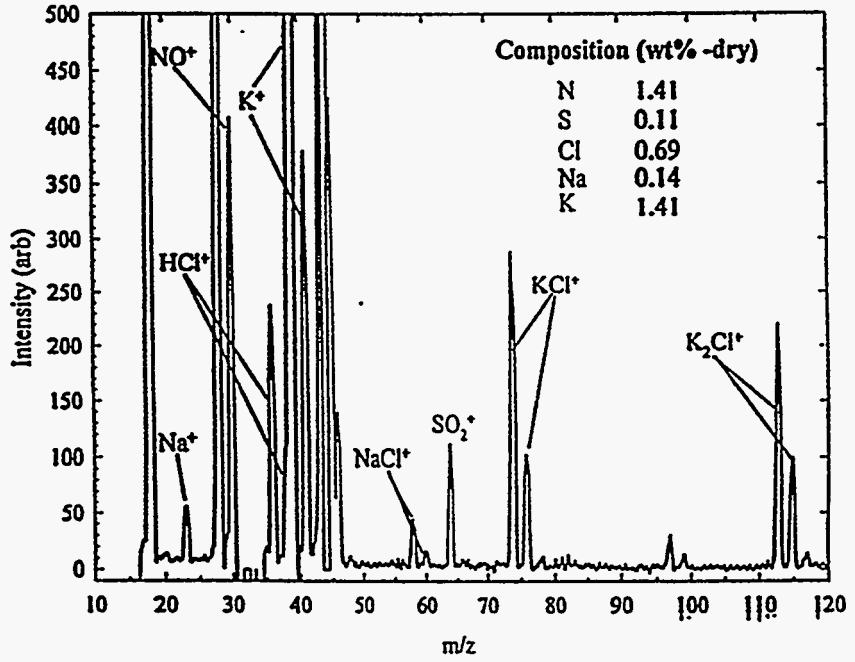

Figure 34 Mass spectrum averaged during the char phase of rice straw combustion at 1100 °C in He/O2 (20%).

that appeared to have the characteristic intensity pattern of a species containing one chlorine atom. Given the high potassium and sodium content of this feedstock, these peaks are tentatively assigned to $KNaCl^+$, a fragment of the mixed dimer of sodium and potassium chloride.

Figure 35 shows the mass spectrum averaged over the char combustion phase of Sandia switchgrass combustion in 20% O_2 in helium at 1100 °C. The production of CO and CO_2 is obvious given the intense peaks at m/z = 28 and m/z = 45 (mass 44, the most abundant isotopic species of CO_2, was skipped to avoid overloading the detector). There is also an indication of the formation of NO at m/z = 30 and SO2 at m/z = 64. According to the ultimate analysis of this switchgrass sample shown in the inset, it contains much less chlorine (by a factor of 7) and three times less potassium compared to a different switchgrass sample (NREL Switchgrass Time 0, sample # 877-051) screened in a previous study (Dayton, et al., 1995). This is also reflected in the char phase mass spectrum. The HCl^+ (m/z = 36 and m/z = 38) and KCl^+ (m/z =74 and 76) peaks which were prominent in the char phase spectra recorded during the combustion of NREL switchgrass are absent in Figure 35 and the only indication of alkali release is the K^+ peak at m/z = 39. This is probably a fragment ion from an unidentified parent alkali species and not the result of potassium being released as the free metal.

The mass spectrum averaged over the char combustion phase of pistachio shells is shown in Figure 35. Combustion products similar to those identified in the Sandia switchgrass char phase spectrum (Figure 35) are also observed in Figure 36, however, the K^+ signal at m/z = 39 is almost twice as large. The parent alkali species responsible for this potassium fragment ion, however, cannot be identified in the char phase mass spectrum. Although the potassium content of the two feedstocks as determined from the ultimate analyses are similar (see insets), more alkali (potassium) was released into the gas phase during combustion of pistachio shells compared to Sandia switchgrass. Surprisingly, the ultimate analyses indicate that the sulfur content of the pistachio shells is four times greater than that of the Sandia switchgrass, yet no sulfur species are observed in the char phase mass spectrum for the pistachio shells. These two observations suggest that the mechanism of alkali release during the combustion of these two feedstocks is different.

The char phase mass spectra of the other two agricultural wastes, almond shells and almond hulls, are presented in Figure 37 and Figure 38 , respectively. The almond hulls have the highest potassium content of the feedstocks studied. The almond hulls are also high in nitrogen and very low in chlorine. These factors play an important role in the alkali release mechanism observed during almond hulls combustion. These mass spectra are rich in comparison with those presented thus far. Significantly more NO (m/z = 30) was liberated during the char combustion of almond shells and almond hulls. Twice as much NO was released during almond hulls combustion compared to almond shells combustion. By comparison, these feedstocks have significantly higher amounts of potassium, based on the ultimate analysis data, and this was reflected in the char phase mass spectra. In fact, the almond hulls have the highest potassium content of any feedstock studied to date.

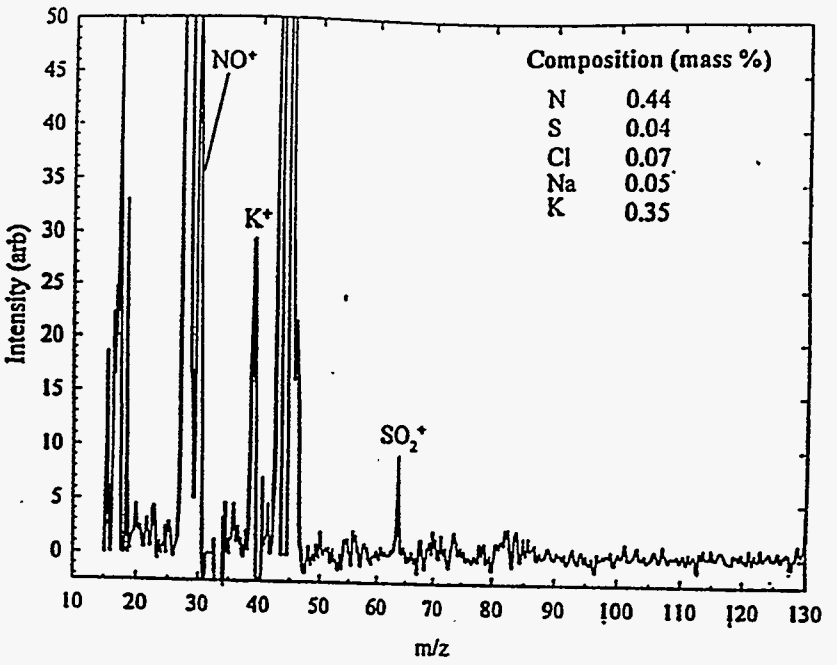

Figure 35 Mass spectrum averaged during the char phase of Sandia switchgrass combustion at 1100 °C in He/O_2 (20%).

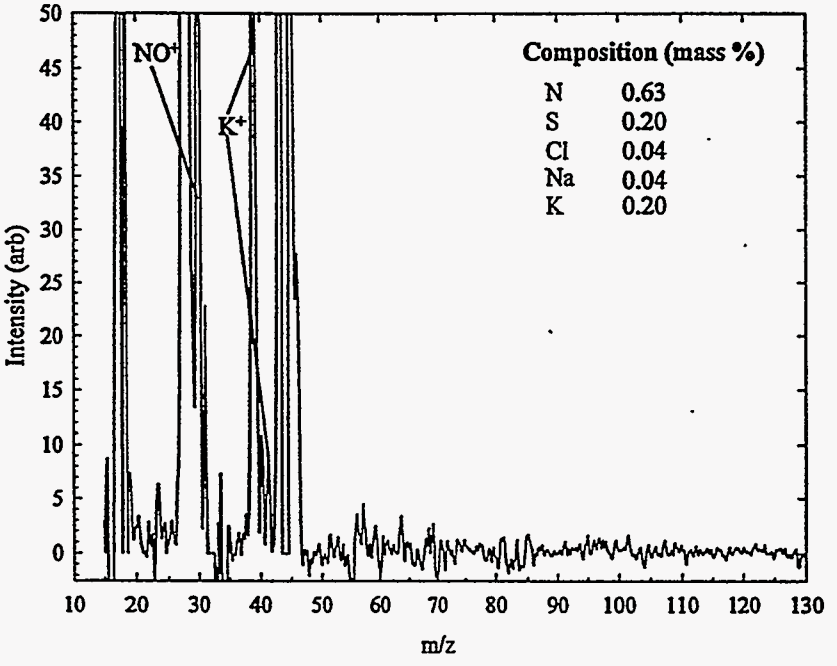

Figure 36 Mass spectrum averaged during the char phase of pistachio shells combustion at 1100 °C in He/O_2 (20%).

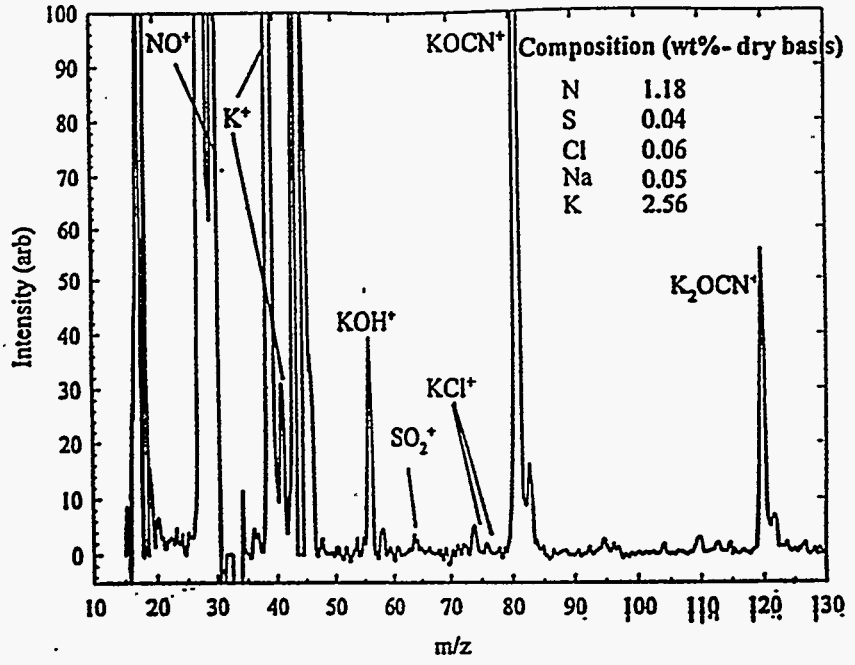

Figure 37 Mass spectrum averaged during the char phase of almond shells combustion at 1100 °C in He/O_2 (20%).

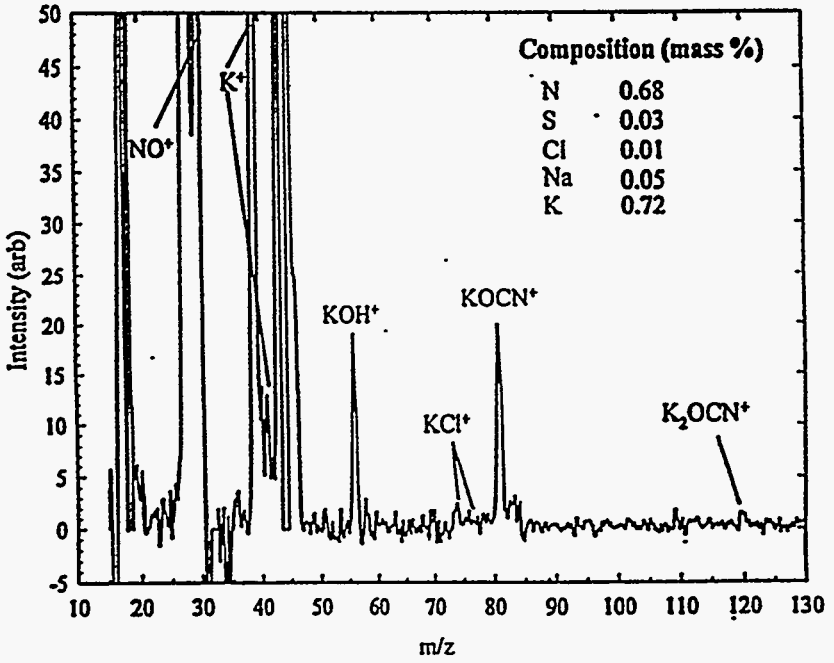

Figure 38 Mass spectrum averaged during the char phase of almond hulls combustion at 1100 °C in He/O_2 (20%).

The intensity of the K^+ ion (m/z = 39) is slightly larger in the char phase mass spectrum of almond shells (Figure 37) compared to the pistachio shells char phase spectrum. In the almond shells char phase spectrum, however, it was possible to identify individual alkali species. The strong signal at m/z = 56 was assigned to KOH^+ and the weaker signals at m/z = 74 and m/z = 76 were assigned to KCl^+. These species were also observed in the char phase mass spectrum of almond hulls combustion, however, almost twice as much KOH was released during almond hulls char combustion. The dominant alkali release mechanism during almond hulls combustion was the release of potassium cyanate as observed by the intense peak at m/z = 81, corresponding to $KOCN^+$. The potassium cyanate dimer fragment ion, K_2OCN^+ at m/z = 120 was also observed. The identity of the peak at m/z = 81 was confirmed by recent collision induced dissociation experiments (Dayton & Wang, 1995).

The final three feedstocks screened are categorized as wastes. The waste paper exhibited a unique combustion behavior compared to the other feedstocks screened to date. A distinct devolatilization phase was observed during which CO_2, H_2O, CO, HCl, and SO_2 were liberated. After this phase, the total ion current (TIC) recorded with the MBMS decayed very rapidly indicating a comparatively short char combustion phase. The duration of the char combustion phase for the waste paper is approximately 5 seconds compared to 12 seconds for the Sandia switchgrass and almond hulls char combustion phases. The mass spectrum averaged over the char combustion phase of waste paper combustion is shown in Figure 39. The prominent species detected are CO^+ and CO_2^+ with smaller amounts of NO^+ and SO_2^+. In terms of alkali, however, the sample is relatively clean. Only K^+ at m/z = 39 was observed and no definitive alkali species can be identified. This is not surprising considering the ultimate analysis results shown in the inset.

The two wood wastes are blends of wheat straw and almond shells, respectively with wood waste. The char phase mass spectra of the wood/wheat straw blend and wood/almond shell blend combustion are shown in Figure 40 and Figure 41. Comparing the two spectra, more K^+ and NO were released during the combustion of the wood/wheat straw blend compared to the combustion of the wood/almond shell blend. There was also an indication of KCl^+ in the wood/wheat straw blend char phase mass spectrum while individual alkali species cannot be identified in the wood/almond shell blend char phase mass spectrum. These two feedstocks have a similar alkali content according to the ultimate analyses, but the wood/wheat straw blend has four times more chlorine. This explains the greater release of alkali into the gas phase during combustion of wood/wheat straw blend and is further evidence that chlorine facilitates the release of alkali. Considering that these feedstocks are classified as wastes, the char phase mass spectra indicate that these samples are relatively clean in terms of alkali released into the gas phase.

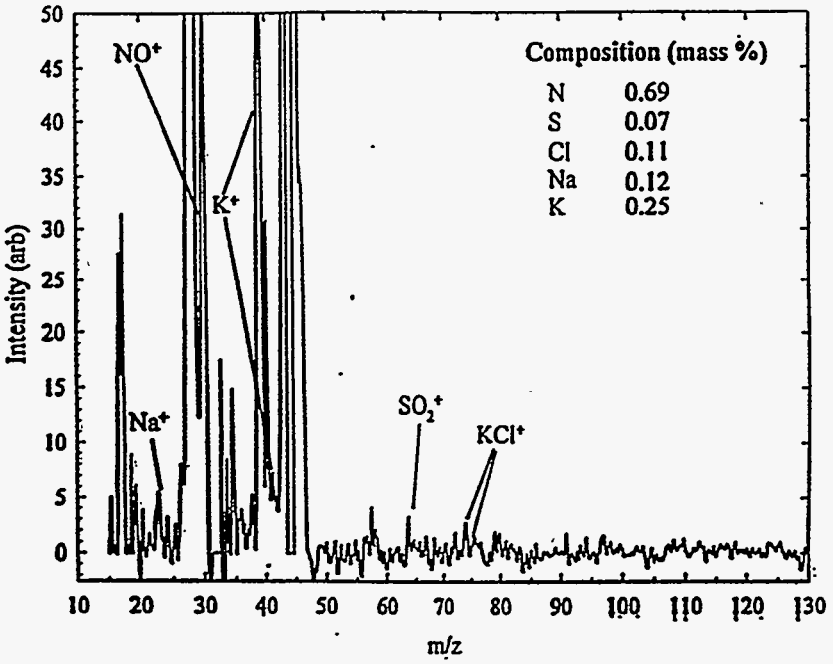

Figure 39 Mass spectrum averaged during the char phase of waste paper combustion at 1100 °C in He/O_2 (20%).

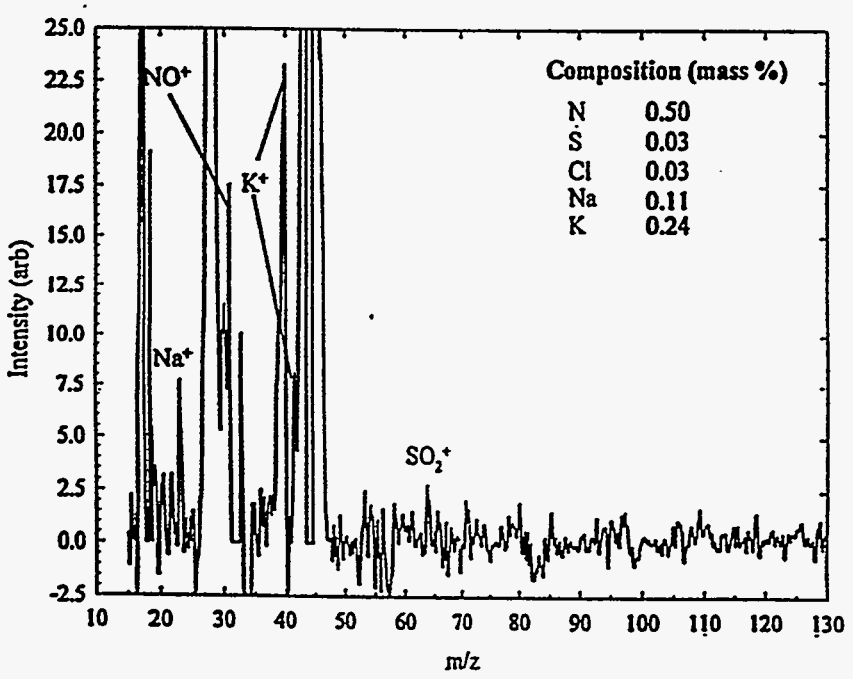

Figure 40 Mass spectrum averaged during the char phase of the wood/wheat straw blend combustion at 1100 °C in He/O_2 (20%).

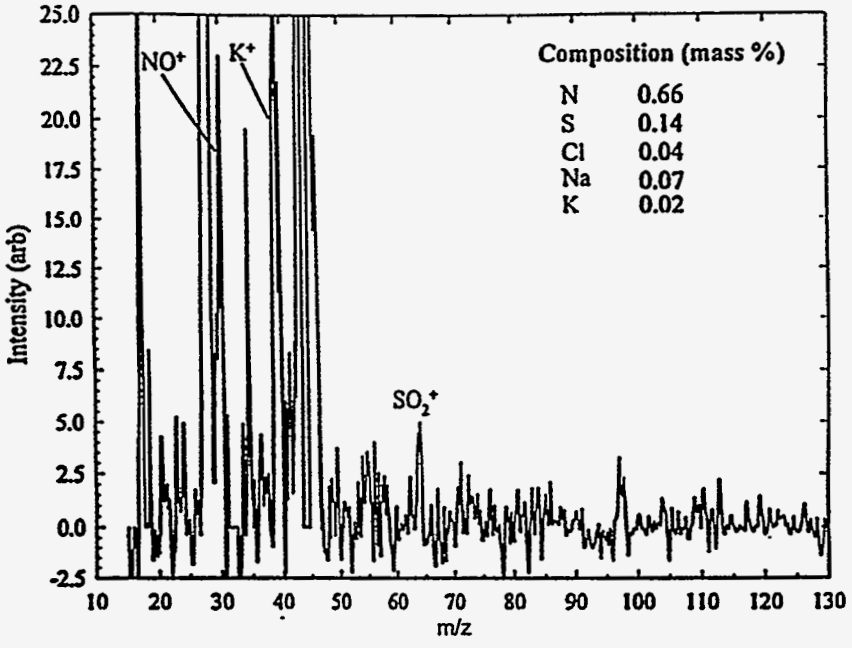

Figure 41 Mass spectrum averaged during the char phase of the wood/almond shell blend combustion at 1100 °C in He/O_2 (20%).

The Effect of Temperature

Investigating the combustion behavior of the nine feedstocks screened above at 800 °C in 20% O_2 in helium reveals the effect of temperature on the release of alkali during biomass combustion. Despite which feedstock undergoes combustion, the devolatilization phase was dominated by the release of organic hydrocarbons at the lower combustion temperature. The mass spectrum recorded over this phase for a given feedstock was complicated and congested by the fragmentation of these organic hydrocarbons. Identification of alkali species liberated during this phase was obscured by the dominant mass spectral fingerprints of the hydrocarbon species. In general, the amount of alkali released into the gas phase appears to be less at the lower furnace temperature.

The char phase mass spectra recorded during combustion of the nine feedstocks listed above at the lower furnace temperature are presented in Figure 42 through Figure 50. Lowering the furnace temperature has little effect on wheat straw combustion. The most noticeable difference between the char phase spectra for wheat straw combustion at 1100 °C (Figure 33) and at 800 °C (Figure 42) is the relative intensity of the SO_2^+ peak at m/z = 64. At the lower furnace temperature the SO_2^+ signal intensity is comparable to the KCl^+ signals whereas at the higher furnace temperature the SO_2^+ signal is 7 times larger than the KCl^+ signals. Similar results are observed in the char phase spectrum recorded during rice straw combustion at the lower furnace temperature shown in Figure 43. In addition, the mixed NaCl/KCl dimer fragment ion at m/z =97 and m/z = 99 is not observed in the char phase spectrum recorded at the lower furnace temperature.

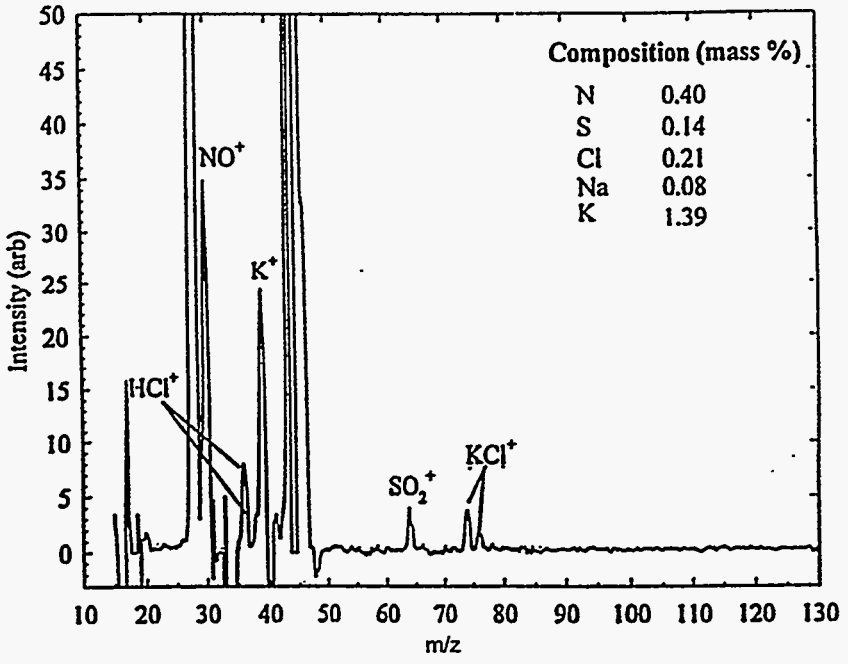

Figure 42 Mass spectrum averaged during the char phase of wheat straw combustion at 800 °C in He/O_2 (20%).

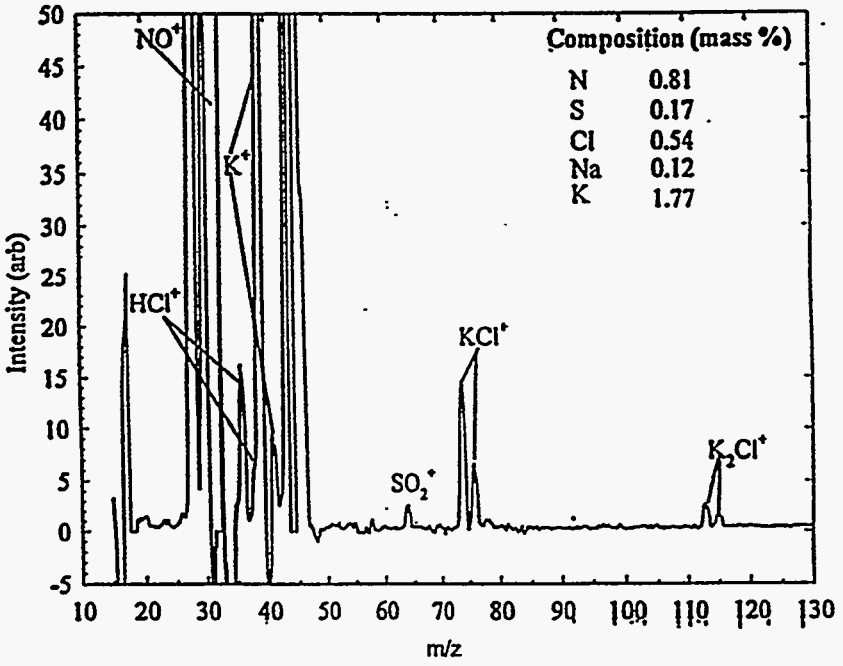

Figure 43 Mass spectrum averaged during the char phase of rice straw combustion at 800 °C in He/O_2 (20%).

The char phase spectrum for Sandia switchgrass combustion at 800 °C shown in Figure 44 is compared to the higher temperature results presented in Figure 35. The K^+ signal intensity is significantly reduced and the peak at m/z = 64 corresponding to SO_2^+ is absent from the lower temperature char phase spectrum. This is consistent with arguments that correlate these observations with the decomposition of condensed phase potassium sulfate (French, et al., 1994). Indeed, the lower furnace temperature is below the decomposition temperature of K_2SO_4 explaining why less alkali was released at the lower furnace temperature. It also appears that slightly less NO was liberated during the char combustion phase of Sandia switchgrass at the lower temperature. Similar conclusions can be drawn from the char phase mass spectrum of pistachio shells combustion at 800 °C (Figure 45).

The effect of furnace temperature on the combustion of almond shells and almond hulls can be seen by comparing the char phase spectra in Figure 46 and Figure 47 to the higher temperature results in Figure 37 and Figure 38. For the almond shells, the K^+ intensity in the char phase spectrum recorded under the 800 °C furnace temperature conditions is a factor of four lower compared to the K^+ signal in Figure 37. This correlates with a lower KOH^+ signal intensity at the lower furnace temperature as well as the absence of KCl^+ at m/z = 74 and m/z = 76. The $KOCN^+$ and K_2OCN^+ signal intensities recorded during almond shell char combustion were relatively insensitive to furnace temperature. A similar decrease in the K^+ and KOH^+ signals was observed in the 800 °C char phase spectrum of almond hulls combustion. In contrast to the almond shells, however, the $KOCN^+$ and K_2OCN^+ signals were dramatically affected by the lower furnace temperature. This difference is currently unexplainable but it might suggest that the mechanism for the release of the parent alkali species of these two fragment ions differs in almond shell combustion versus almond hull combustion.

The char phase mass spectra of waste paper, wood/wheat straw blend, and wood/almond shell blend combustion at 800 °C in He/O_2 (20%) are presented in Figure 48 through Figure 50, respectively. The char phase spectrum of waste paper combustion at 800 °C exhibits a lower K^+ signal intensity compared to the higher temperature results shown in Figure 39. SO_2^+ was also absent from the char phase spectrum in Figure 48 consistent with the above arguments regarding the decomposition of K_2SO_4. The intensity of the NO^+ signal was relatively temperature insensitive. Similar observations can be made in the char phase mass spectra of the two wood wastes. The K^+ signals in the char phase mass spectra of the wood/wheat straw blend and the wood/almond shell blend were consistently smaller at the lower furnace temperature and the SO_2^+ peak at m/z = 64 was absent.

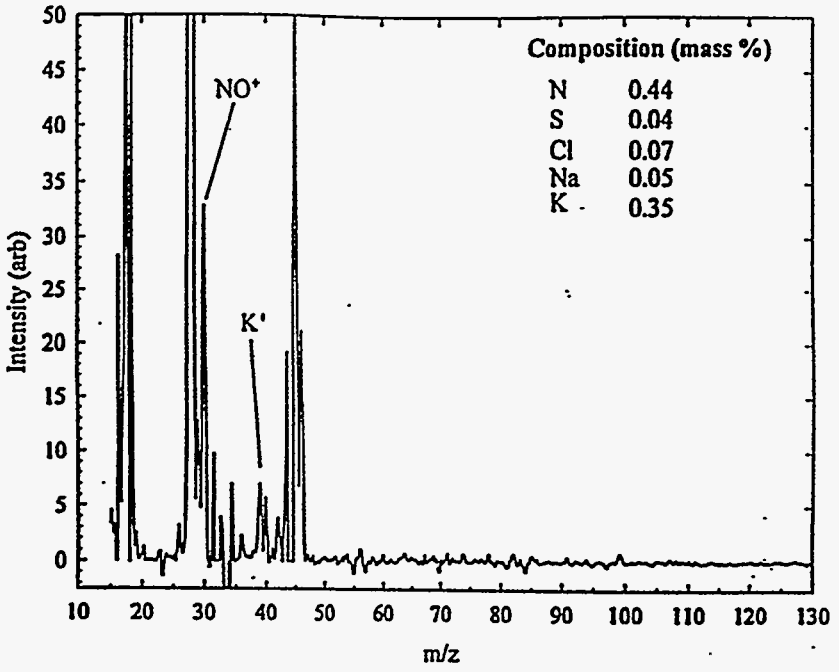

Figure 44 Mass spectrum averaged during the char phase of Sandia switchgrass combustion at 800 °C in He/O_2 (20%).

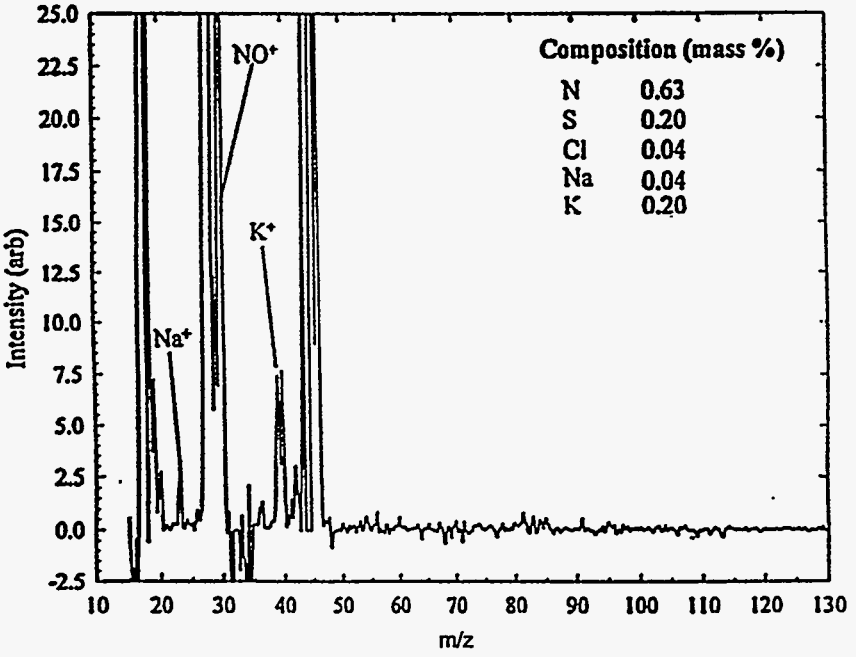

Figure 45 Mass spectrum averaged during the char phase of pistachio shells combustion at 800 °C in He/O_2 (20%).

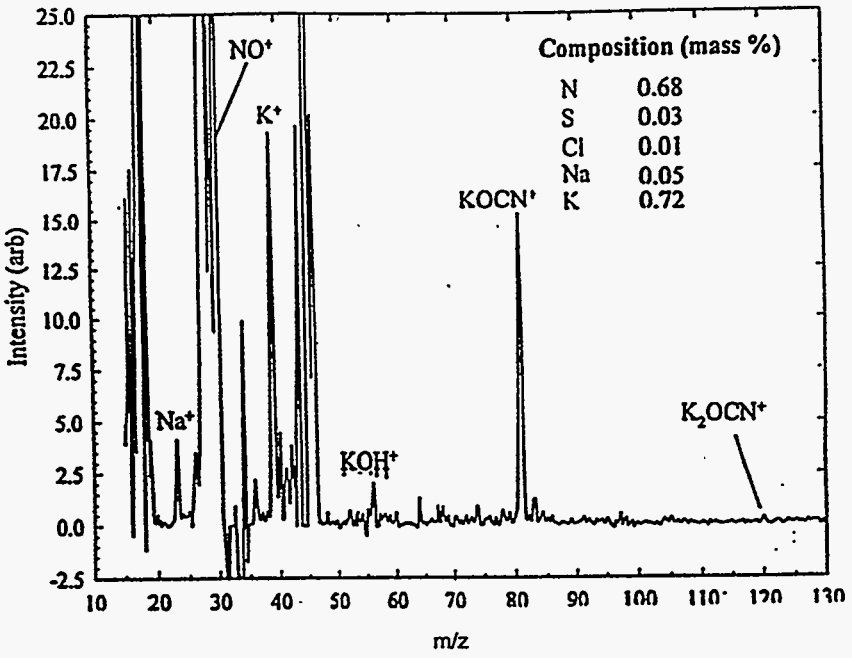

Figure 46 Mass spectrum averaged during the char phase of almond shells combustion at 800 °C in He/O_2 (20%).

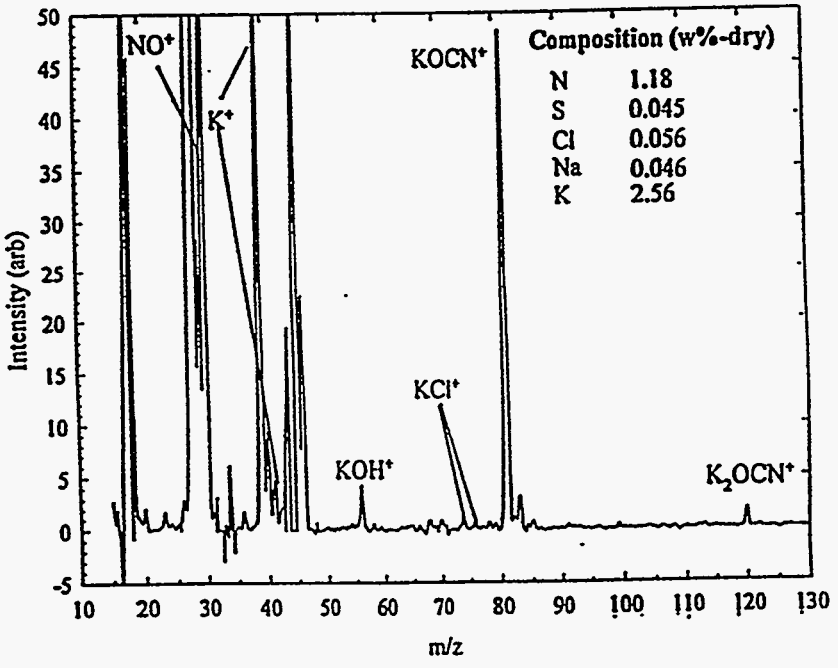

Figure 47 Mass spectrum averaged during the char phase of almond hulls combustion at 800 °C in He/O_2 (20%).

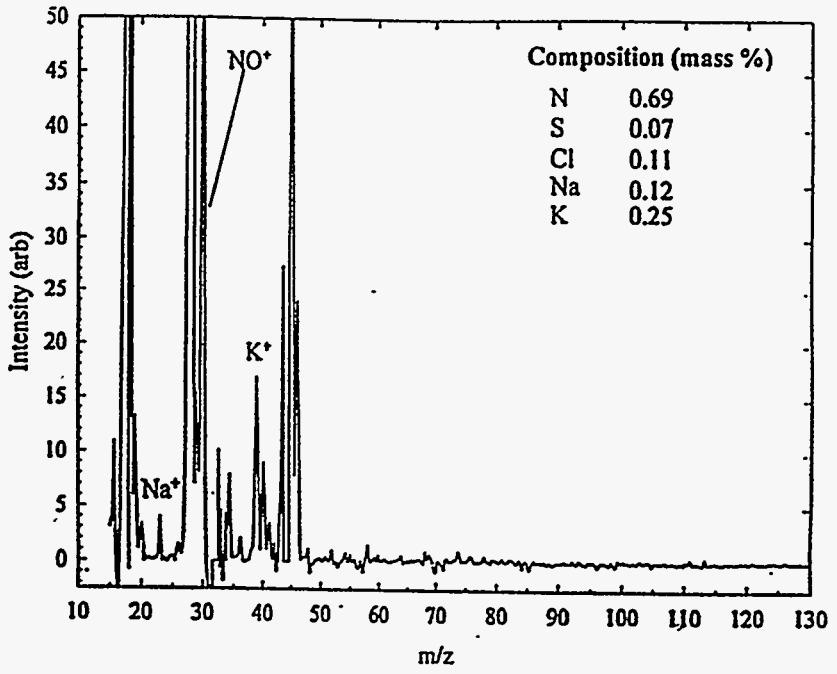

Figure 48 Mass spectrum averaged during the char phase of waste paper combustion at 800 °C in He/O_2 (20%).

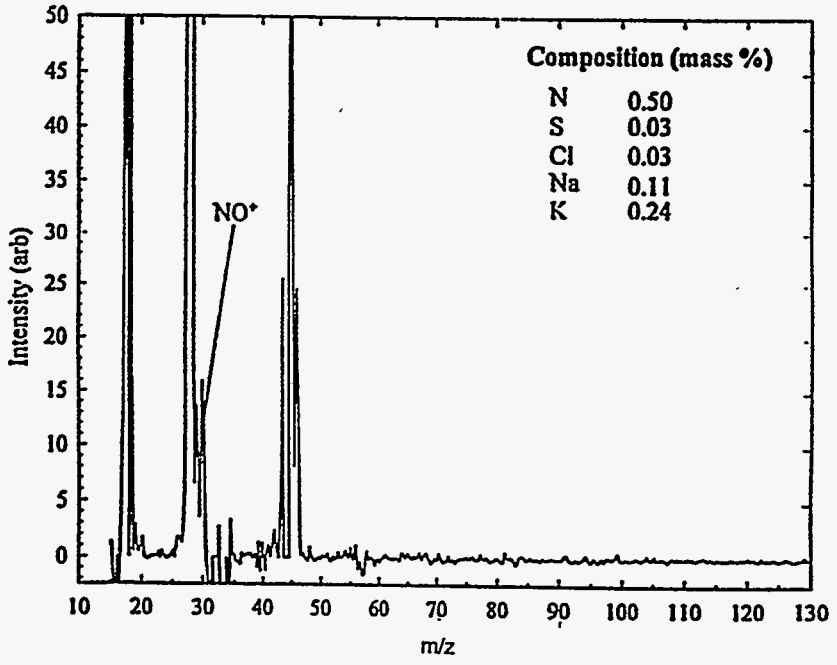

Figure 49 Mass spectrum averaged during the char phase of wood/wheat straw blend combustion at 800 °C in He/O_2 (20%).

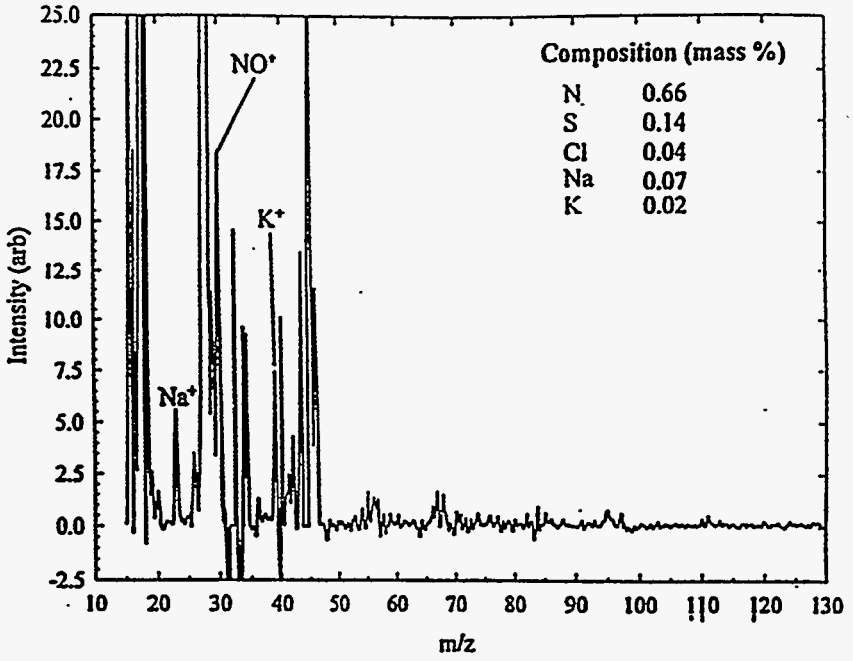

Figure 50 Mass spectrum averaged during the char phase of wood/almond shell blend combustion at 800 °C in He/O_2 (20%).

The Effect of Oxygen Concentration

The oxygen concentration in the reactor atmosphere was reduced to 5% O_2 in helium to investigate the effect this might have on alkali release during combustion of the nine feedstocks screened for alkali metal release. The furnace temperature was maintained at 1100 °C to compare these results with the initial screening of the feedstocks at 20% O_2 in helium. Reducing the oxygen concentration in the reactor atmosphere has a major effect on the devolatilization or combustion phase of biomass combustion. The reduced oxygen concentration prevents complete conversion of the released volatile materials to combustion products. As a result, the mass spectra averaged over the combustion phase were dominated by the presence of organic hydrocarbons, similar to what happens when the furnace temperature was lowered. Few differences were observed, however, in the spectra averaged over the char combustion phase. For all of the feedstocks, similar species were identified in the char phase spectra, shown in Figure 51 through Figure 59 compared to the higher oxygen concentration results.

The effects of changes in oxygen concentration are confounded to some extent with those of changes in temperature. Increased oxygen concentration leads to increased sample temperature associated with more vigorous combustion. While furnace temperature is maintained at 1100 °C while lowering oxygen concentration to 5% O_2 in these experiments, the sample temperature also dropped by an unknown amount. The observations reported here result from the combined effects of oxygen concentration change and sample temperature change.

A reduced oxygen concentration does not appear to significantly affect the combustion properties of the straws. Peaks at m/z = 26 and m/z = 81 were observed in the char phase mass spectra of rice straw and wheat straw (Figure 51 and Figure 52). The peak at m/z = 26 was tentatively assigned to the $C_2H_2^+$ ion. Apparently some hydrocarbons survive even during the char combustion phase. The HCl^+ peaks at m/z =36 and m/z = 38 were observed in the char phase spectra of wheat straw and rice straw and the relative intensity of these peaks appeared to be unaffected by the change in oxygen concentration. The relative intensity of the NO^+ and K^+ peaks also appeared to be unaffected by the change in oxygen concentration during combustion of the herbaceous feedstocks. An apparent result of the lower oxygen concentration was an increased release of NaCl (Na^+ at m/z = 23 and $NaCl^+$ at m/z = 58 and m/z = 60) during the char phase combustion.

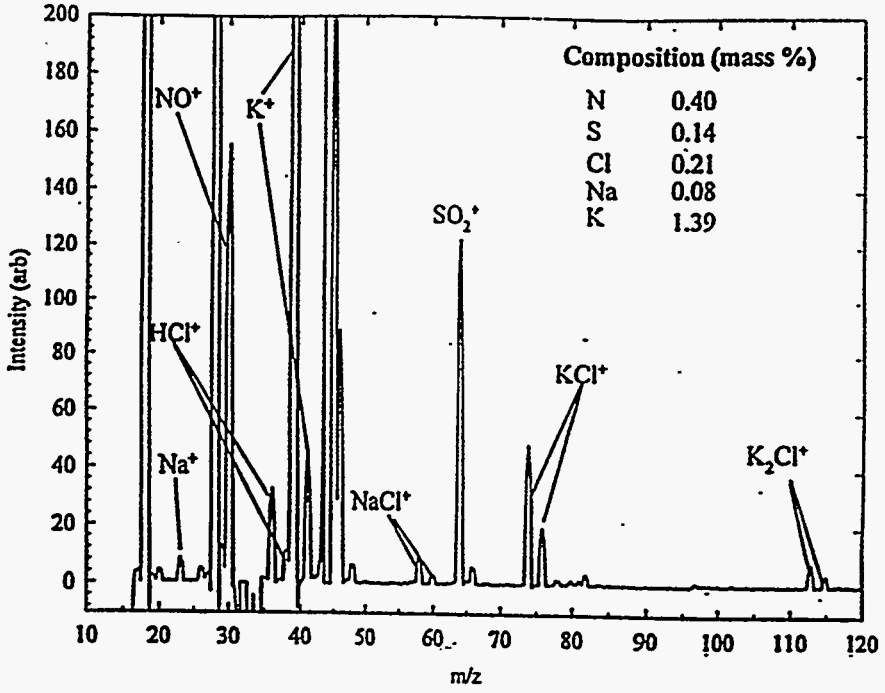

Figure 51 Mass spectrum averaged during the char phase of wheat straw combustion at 1100 °C in He/O_2 (5%).

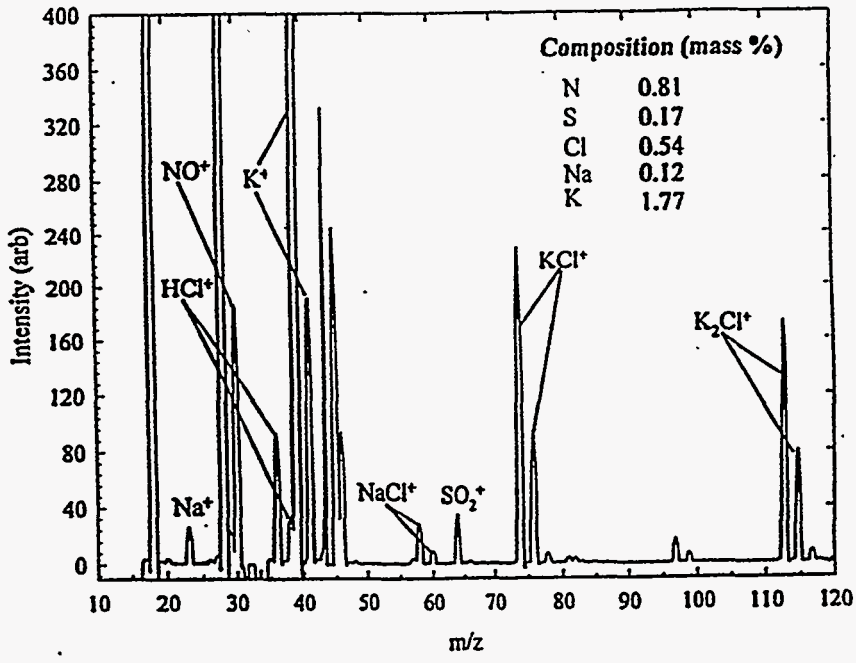

Figure 52 Mass spectrum averaged during the char phase of rice straw combustion at 1100 °C in He/O_2 (5%).

The mass spectrum averaged over the char combustion phase of Sandia switchgrass combustion at 1100 °C in He/O_2 (5%) is presented in Figure 53. Compared to the results shown in Figure for Sandia switchgrass combustion in 20% O_2 in helium, it appears that the amount of alkali released was less at the lower oxygen concentration. The K^+ signal intensity was lower in the 5% O_2 char phase spectrum, however, it was now possible to identify KCl as a gas phase alkali species and HCl could also be identified. The SO_2^+ signal intensity was also lower at the lower oxygen concentration. Comparing the relative intensities of various peaks in Figure 35 and Figure 53, it appeared that only the overall intensity has changed and this was probably just a discrepancy in scaling the spectral intensities. For instance, the ratio of the NO^+:K^+ signals is about 2:1 in each case. Without quantifying the signals it was not possible to determine whether there was less of a given species being liberated into the gas phase or whether it was an effect of normalizing the spectra.

Similar conclusions can be drawn for the pistachio shells combustion results at the two oxygen concentrations. Comparing the signal intensities in the char phase mass spectra for pistachio shells in Figure 51 and Figure 54, it appears that less alkali is liberated into the gas phase at lower oxygen concentrations. The K^+ signal intensity is lower by a factor of 10 at the lower oxygen concentration and the NO^+ signal is considerably smaller. The K^+:NO^+ ratio at the 20% O_2 in helium condition is 1:1 while at the lower oxygen concentration this same ratio is 1:3. Unfortunately, it was not possible to determine whether this corresponds to less alkali released. At a lower oxygen concentration it does not seem likely, however, that more NO would be formed.

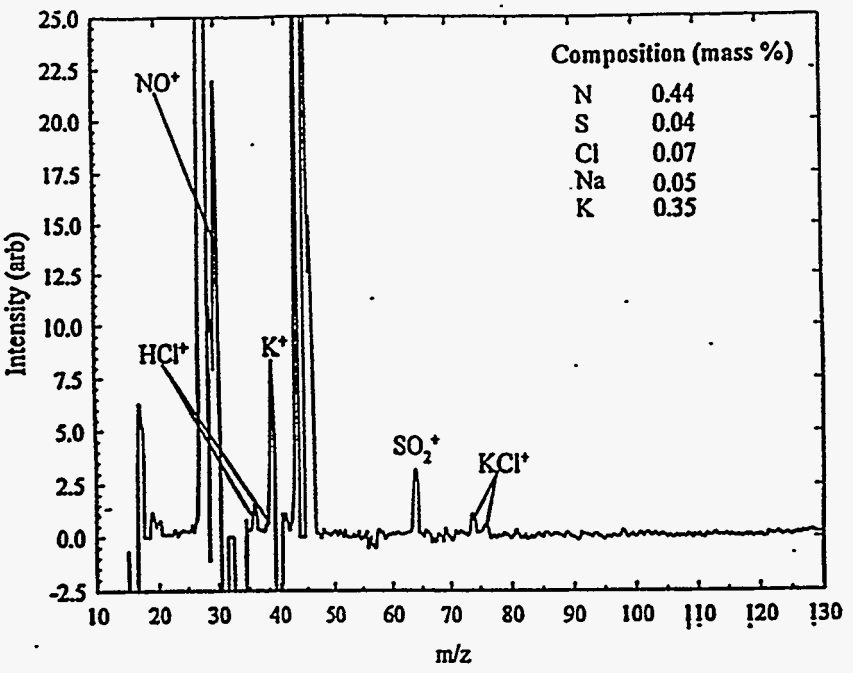

Figure 53 Mass spectrum averaged during the char phase of Sandia switchgrass combustion at 1100 °C in He/O_2 (5%).

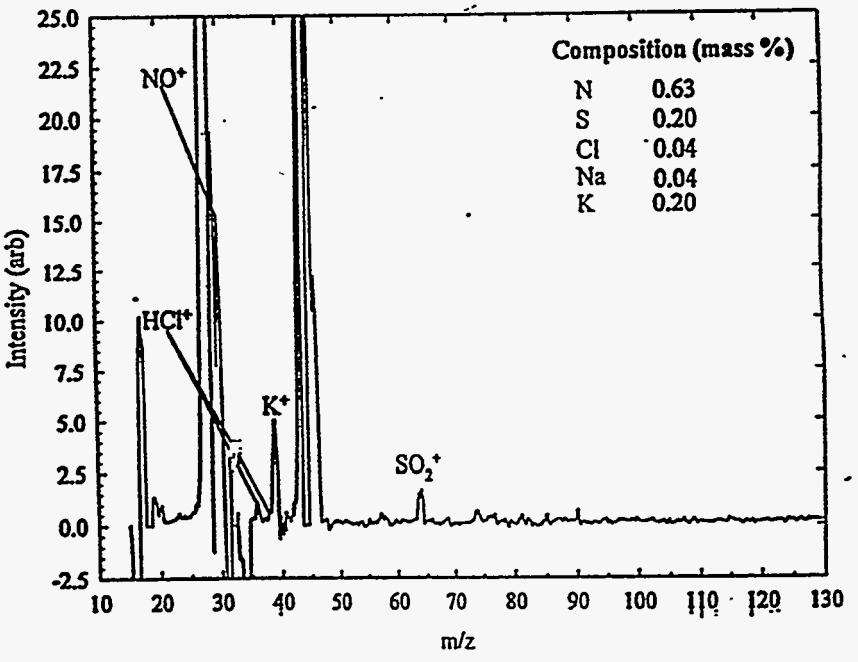

Figure 54 Mass spectrum averaged during the char phase of pistachio shells combustion at 1100 °C in He/O_2 (5%).

The mass spectra recorded during the char combustion phase of almond shell and almond hull combustion in He/O_2 (5%) at 1100 °C are presented in Figure 55 and Figure 56. For the almond shells, it also appears that less alkali is released during char combustion at lower oxygen concentrations. The K^+ signal is three times smaller and the KOH^+ signal is almost a factor of ten smaller at the lower oxygen concentration. The $KOCN^+$ signal is also smaller at the lower oxygen concentration. In the case of the almond hulls, it also appears that less alkali is released into the gas phase. Like the almond shells, both the K^+ and KOH^+ signal intensities are reduced at the lower oxygen concentration. The ratio of the K_2OCN^+ and $KOCN^+$ signals as well as the absolute signal intensities are also dramatically affected by the reduced oxygen concentration. The $KOCN^+$ signal is a factor of six smaller at a lower oxygen concentration and the ratio of the signals is dramatically reduced. It also appears that less NO is released at the lower oxygen concentration.

Lowering the oxygen concentration in the reactor atmosphere had a similar effect on combustion of the waste feedstocks. The char phase mass spectra for waste paper, the wood/wheat straw blend, and wood/almond shell blend are shown in Figure 57 through Figure 59. The K^+ signal intensity is smaller at the lower oxygen concentration and the ratio of the K^+:NO^+ signals decreases.

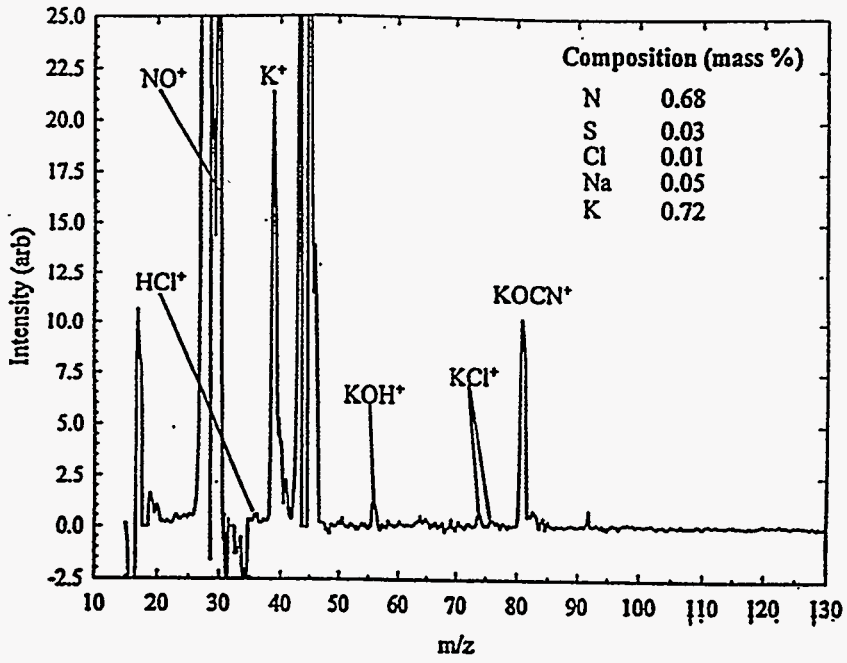

Figure 55 Mass spectrum averaged during the char phase of almond shells combustion at 1100 °C in He/O_2 (5%).

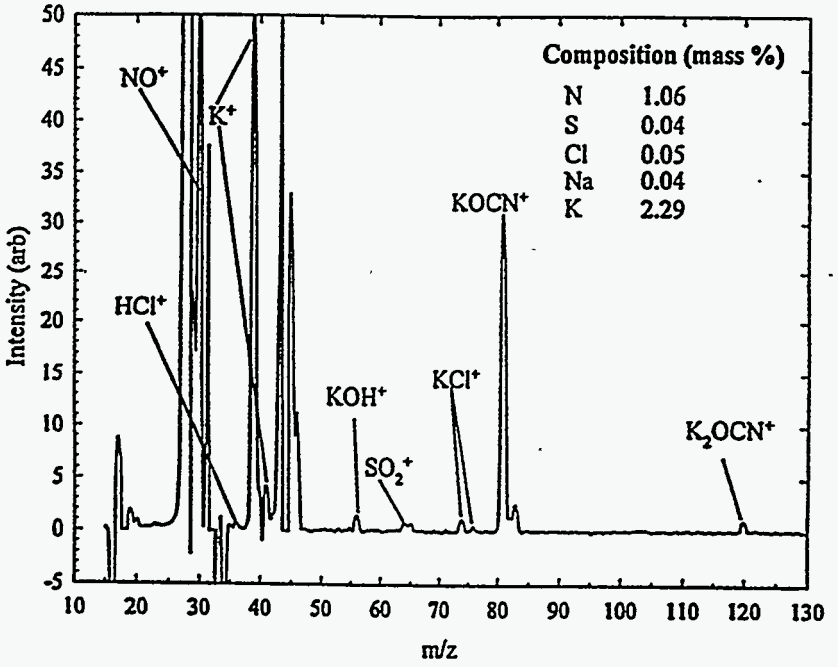

Figure 56 Mass spectrum averaged during the char phase of almond hulls combustion at 1100 °C in He/O_2 (5%).

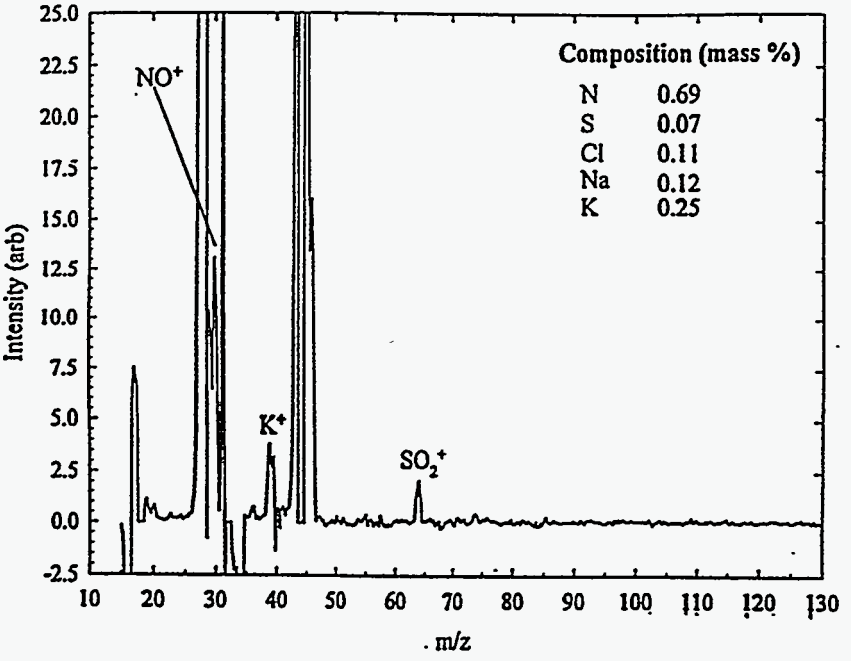

Figure 57 Mass spectrum averaged during the char phase of waste paper combustion at 1100 °C in He/O_2 (5%).

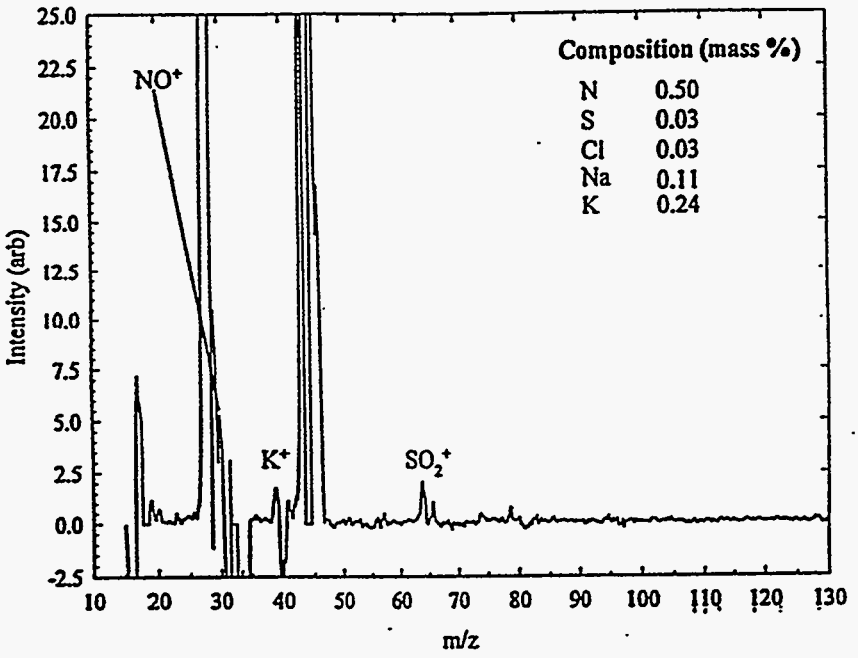

Figure 58 Mass spectrum averaged during the char phase of wood/wheat straw blend combustion at 1100 °C in He/O_2 (5%).

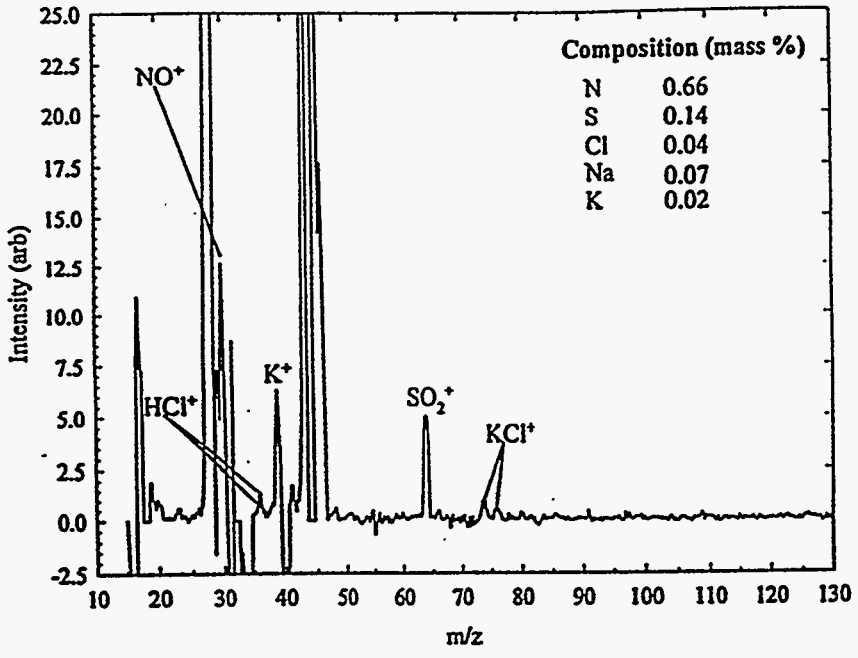

Figure 59 Mass spectrum averaged during the char phase of wood/almond shell blend combustion at 1100 °C in He/O_2 (5%).

The Effect of Excess Steam

Excess steam was added to the reactor atmosphere to simulate an environment in which water vapor is continuously being supplied by the combustion of multiple biomass particles. Such an environment is one that would occur in an industrial boiler or combustor in which biomass is constantly fed. All nine feedstocks were subjected to combustion in an excess steam environment and the corresponding mass spectra averaged over the respective char combustion phases are presented in Figure 60 through Figure 68. The combustion conditions established for the purpose of studying the effect of added steam were 10% O_2 and 20% steam in helium at a furnace temperature of 1100 °C.

The char phase spectra recorded during the combustion of wheat straw and rice straw in the presence of excess steam are shown in Figure 60 and Figure 61. The K^+/HCl^+ signal intensity is dramatically reduced when steam is added to the reactor atmosphere during combustion of the straws and indicates that more HCl was being released. It also appeared

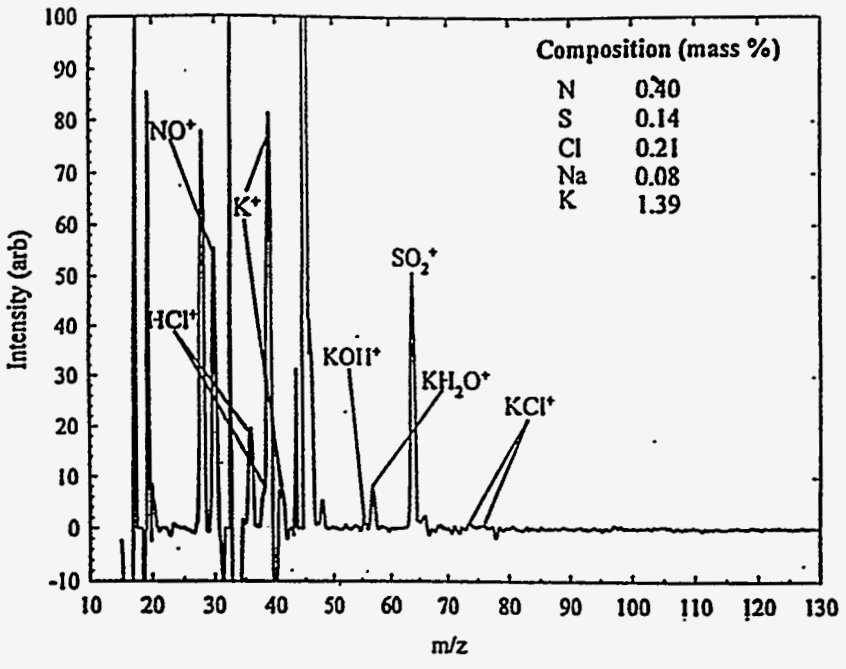

Figure 60 Mass spectrum averaged during the char phase of wheat straw combustion at 1100 °C in He/O_2 (10%)/Steam (20%).

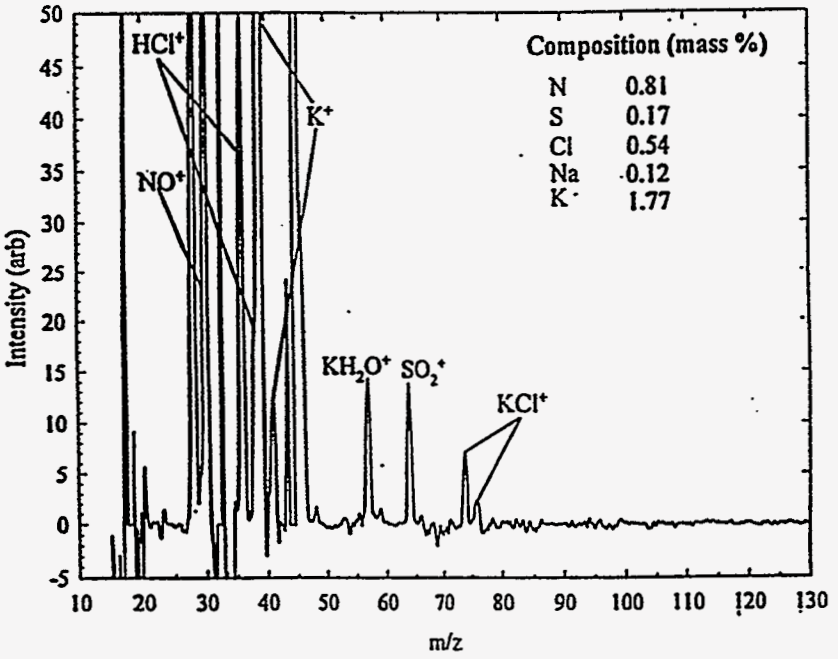

Figure 61 Mass spectrum averaged during the char phase of rice straw combustion at 1100 °C in He/O_2 (10%)/Steam (20%).

that less alkali is released as potassium chloride. The intensity of the KCl^+ peaks at m/z = 74 and m/z = 76 are considerably reduced and the K_2Cl^+ peaks that were observed in the char phase spectra recorded without steam are not observed. Given the high potassium content of these two feedstocks, it is not surprising that a prominent peak at m/z = 57 (KH_2O^+) is observed in char phase spectra of rice and wheat straw combustion in excess steam. Given the high concentration of water vapor in the combustion atmosphere and the high potassium content of the straws, it is possible that this species is an artifact of the free jet expansion during which a K-species/H_2O cluster is formed and subsequently fragments upon ionization. KOH was not released during rice straw combustion, suggesting that the primary alkali release is still through the chloride for this feedstock. Some potassium hydroxide is released during the combustion of wheat straw indicating that alkali release during combustion of this feedstock was shifted in the excess steam atmosphere.

The char phase spectrum recorded during combustion of Sandia switchgrass with steam at 1100 °C is shown in Figure 62. Comparing this spectrum to the one recorded during the char phase of Sandia switchgrass combustion without steam suggests that the amount of alkali released decreases when steam is added. This can be verified by quantifying the KCl^+ signals observed with and without steam in the reactor atmosphere. HCl is clearly liberated during Sandia switchgrass combustion with steam in the reactor atmosphere, while in the absence of steam it was not released. The release of NO and SO_2 does not appear to be affected by the addition of steam.

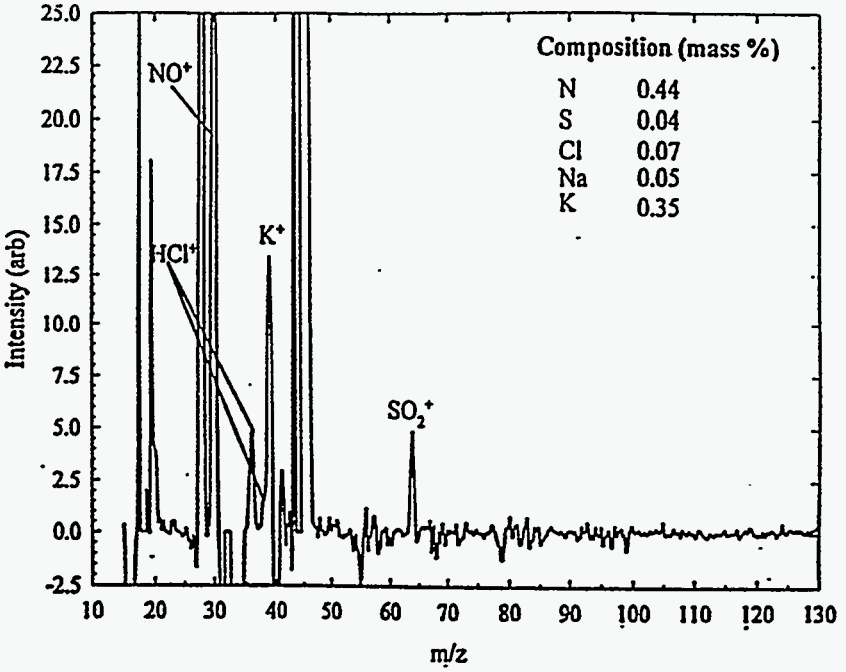

Figure 62 Mass spectrum averaged during the char phase of Sandia switchgrass combustion at 1100 °C in He/O_2 (10%)/Steam (20%).

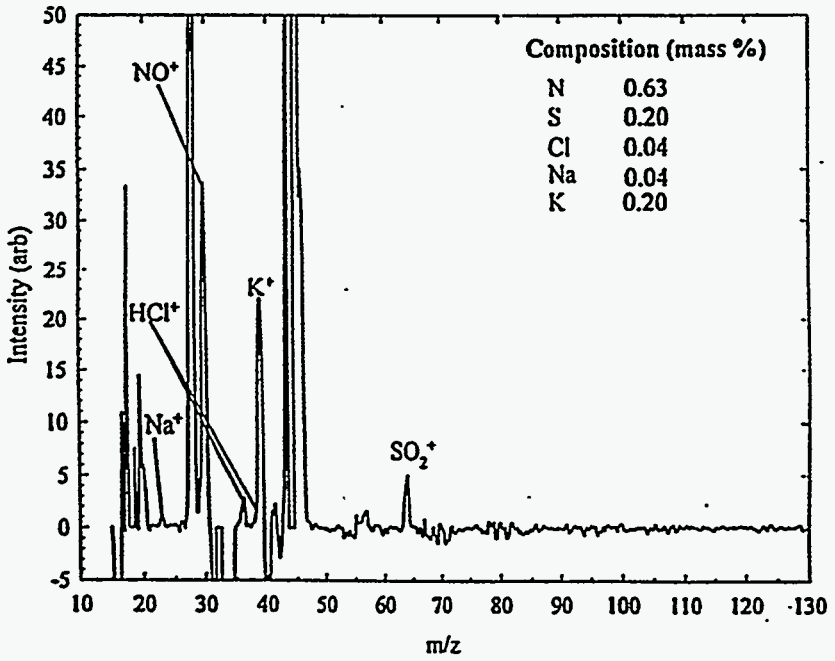

Figure 63 Mass spectrum averaged during the char phase of pistachio shells combustion at 1100 °C in He/O_2 (10%)/Steam (20%).

Adding 20% steam to the reactor atmosphere during the char combustion phase of pistachio shells (Figure 63) affects the ratio of K^+ to HCl^+ observed in the char phase mass spectrum as discussed above. The decrease in the NO^+ and K^+ signal intensities are the only other significant differences. The addition of steam appears to have a substantial effect on the combustion of almond shells and almond hulls. The char phase spectra recorded during combustion of almond shells and almond hulls with steam are shown in Figure 64 and Figure 65. The features at m/z = 81, assigned to $KOCN^+$, and m/z = 120, assigned to K_2OCN^+, which were so prominent in the absence of steam (see Figure 37 and Figure 38) were dramatically affected by the presence of excess steam during combustion. The $KOCN^+$ and K_2OCN^+ were absent from the char phase spectrum of almond shells and there is only a hint of a $KOCN^+$ peak in the almond hulls char phase spectrum. The peak at m/z = 64, corresponding to SO_2^+, also appeared to increase in the char combustion phase of almond shells and almond hulls combustion in the presence of water vapor. Given the low chlorine levels of these two feedstocks, it is not surprising that the amount of HCl liberated during almond shell and almond hull combustion is unaffected by the presence of steam in the reactor atmosphere. The amount of KOH released was also not significantly affected by the addition of steam, however, KH_2O^+ (m/z = 57) was detected in the char phase spectra recorded during almond shell and almond hull combustion with steam.

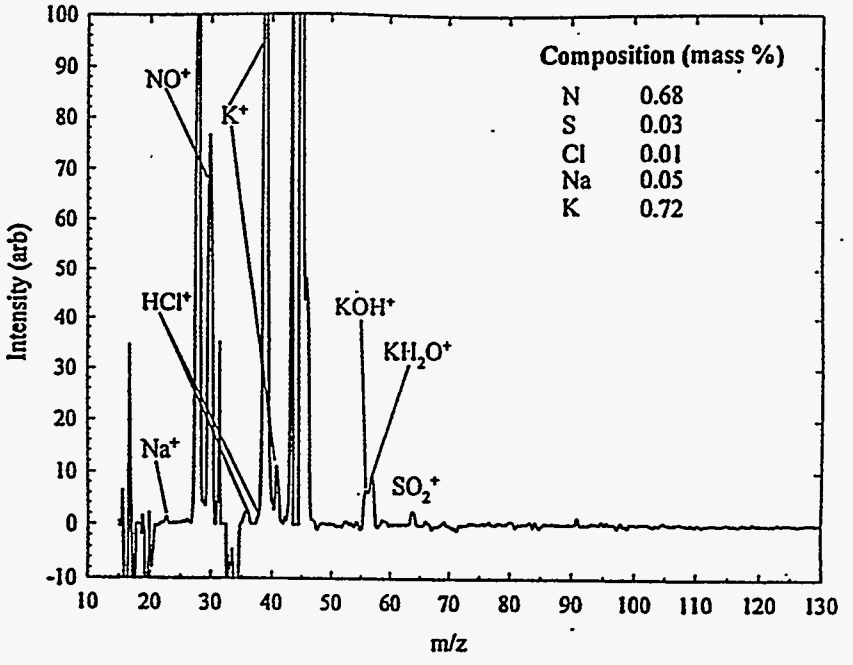

Figure 64 Mass spectrum averaged during the char phase of almond shells combustion at 1100 °C in He/O_2 (10%)/Steam (20%).

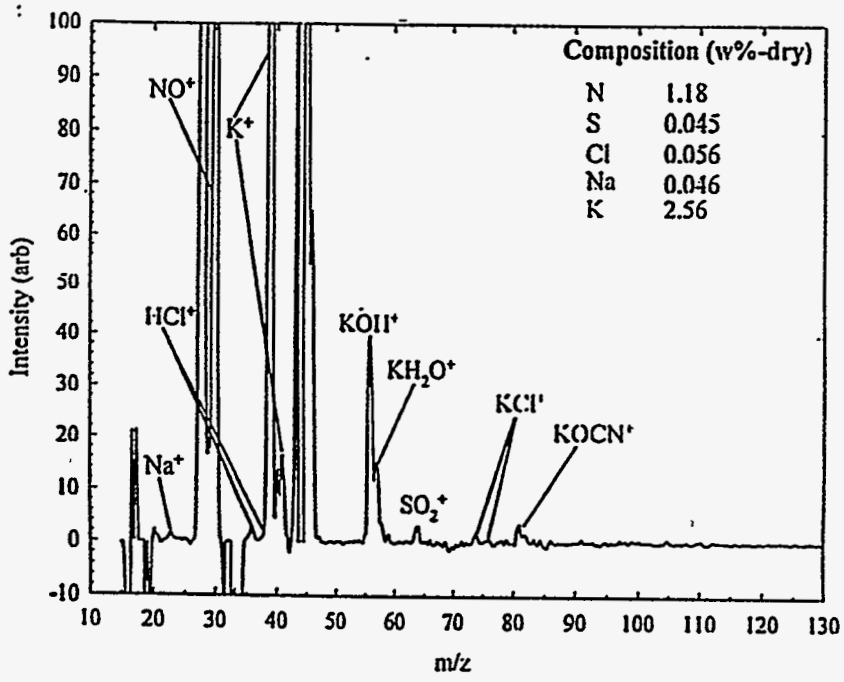

Figure 65 Mass spectrum averaged during the char phase of almond hulls combustion at 1100 °C in He/O_2 (10%)/Steam (20%).

The addition of 20% steam to the reactor atmosphere has little effect on the combustion of the waste feedstocks; waste paper, the wood/wheat straw blend, and the wood/almond shell blend. The char phase spectra recorded during combustion of waste paper, the wood/wheat straw blend, and the wood/almond shell blend in the presence of steam are presented in Figure 66 through Figure 68, respectively. More HCl is liberated during waste paper combustion in excess steam compared to dry combustion. This is evident in the char phase spectrum for waste paper combustion in excess steam shown in Figure 66. There also appears to be less K^+ signal intensity in the char combustion phase in excess steam. Similar conclusions can be drawn for combustion of the two wood wastes in the presence of excess steam.

Discussion of Molecular Beam Mass Spectrometry Results

The conclusions determined in previous investigations (Dayton, et al., 1995; French, et al., 1994) have been confirmed by the results of this investigation. The current subset of feedstocks screened contains different varieties of biomass compared to the previous subset, which contained both woody and herbaceous feedstocks. Adding to the list of feedstocks screened for alkali release in the present investigation are agricultural residues (pistachio shells, almond shells, and almond hulls) and urban waste feedstocks (wood/wheat straw blend, wood/almond shell blend, and waste paper). The char combustion phase of biomass combustion generates the highest particle temperatures in these experiments and consequently is the most interesting in terms of alkali release and

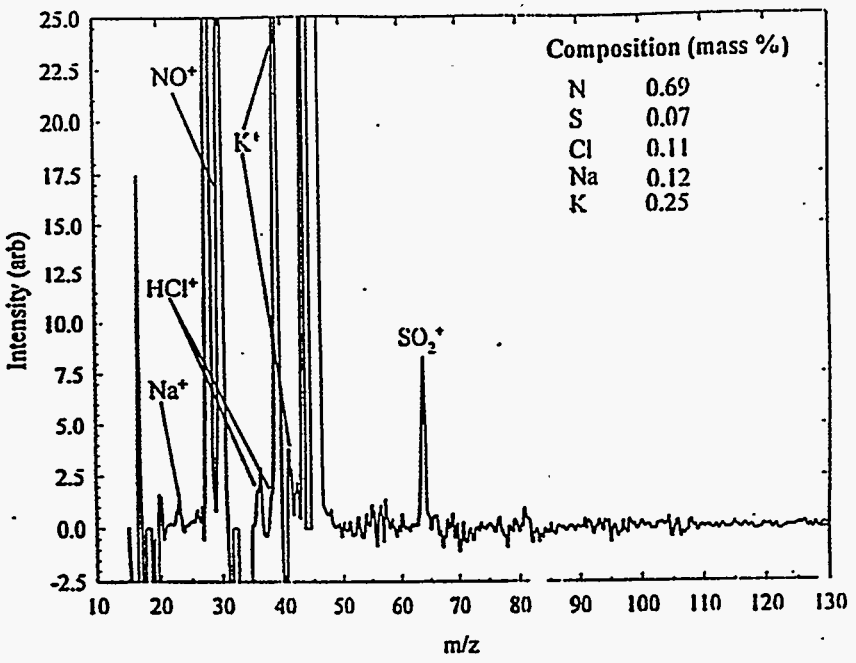

Figure 66 Mass spectrum averaged during the char phase of waste paper combustion at 1100 °C in He/O_2 (10%)/Steam(20%).

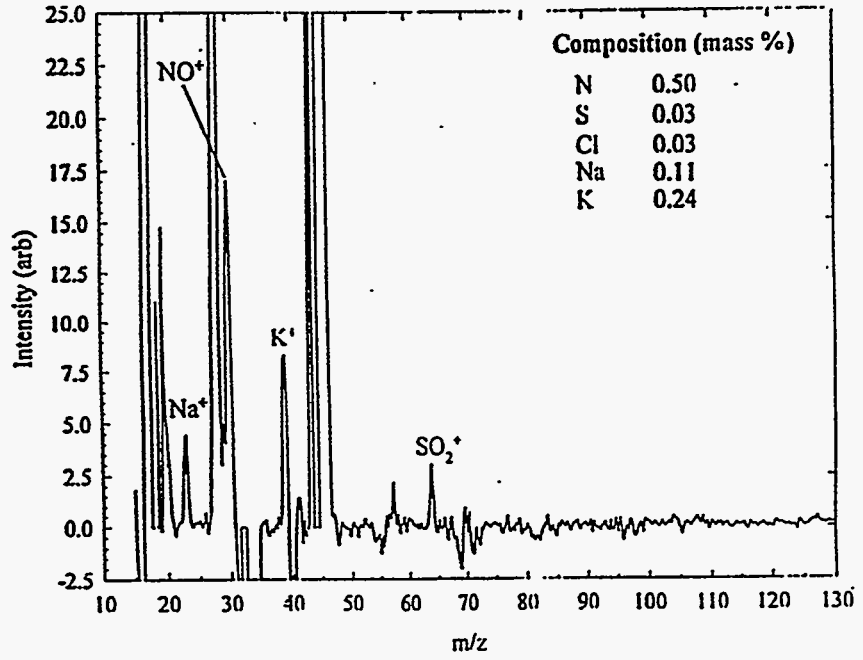

Figure 67 Mass spectrum averaged during the char phase of the wood/wheat straw blend combustion at 1100 °C in He/O_2 (10%)/Steam (20%).

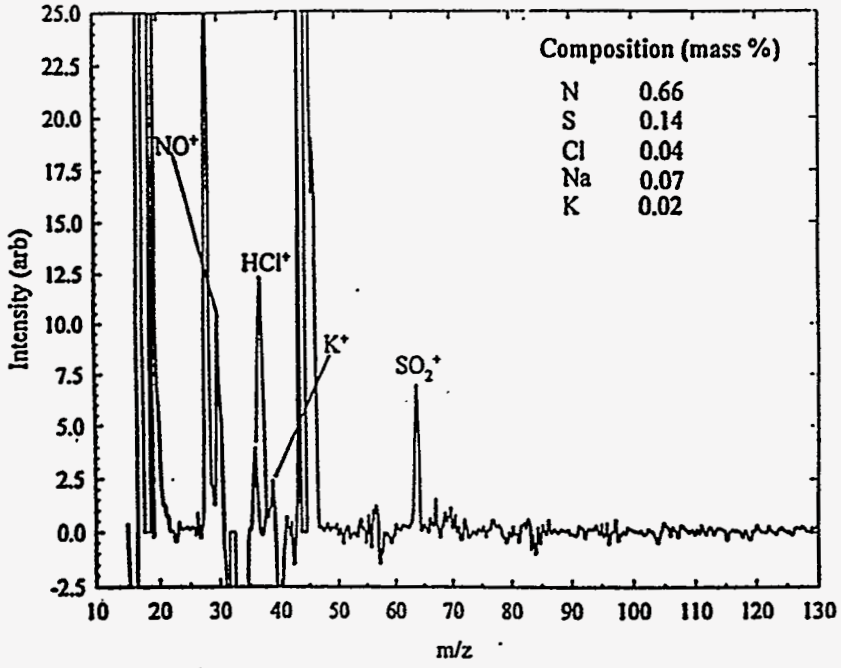

Figure 68 Mass spectrum averaged during the char phase of the wood/almond shell blend combustion at 1100 °C in He/O_2 (10%)/Steam (20%).

vaporization. The mass spectrum averaged over a given char phase of biomass combustion qualitatively reflects the feedstock composition as determined in the ultimate analysis. While the ultimate analysis is important for determining the total amount of alkali in a given feedstock, it does not reflect how much alkali is released into the gas phase nor the form of the alkali released. For this reason, the MBMS technique continues to be a valuable technique for directly studying alkali release during biomass combustion. A high potassium and high chlorine content in a given feedstock translates into significant alkali vapor release in the form of alkali chloride as observed for wheat straw and rice straw combustion. This prevails even when excess steam is present during combustion, however, the alkali release under these conditions is shifted partly, but not completely, to the hydroxide.

Feedstocks with high potassium but low chlorine levels (almond shells and almond hulls) still exhibit significant alkali vapor release during combustion. These feedstocks exhibit alkali vapor released as potassium hydroxide. In fact, the potassium hydroxide identified in the char phase mass spectra recorded during almond shell and almond hull combustion marks the first incidence of major alkali release in the form of the hydroxide in the absence of excess steam. A new mode of alkali metal release was also observed during the combustion of these two feedstocks. The most prominent potassium species observed in the char phase spectra recorded during almond shells and almond hulls combustion was potassium cyanate.

Changing combustion conditions has little effect on the release of alkali vapor. Reducing the furnace temperature and the oxygen concentration in the reactor appears to slightly

hinder the release of alkali vapor compared to the baseline combustion condition of 1100 °C in He/O_2 (20%). In terms of the lower furnace temperatures, less alkali is expected to be released based on the lower vapor pressure of potassium chloride at lower temperatures and less decomposition of potassium sulfate. This could be confirmed by quantifying the alkali species released. The most significant combustion condition which affects alkali release was the addition of excess steam to the reactor atmosphere. The alkali released during the combustion of the high chlorine containing species is shifted partly from potassium chloride to potassium hydroxide. The presence of excess steam during combustion of high-chlorine-containing feedstocks also increases the amount of HCl released. This has important implications in terms of high temperature corrosion in boilers, turbines and industrial combustors. Excess steam in the reactor atmosphere also dramatically affects the release of potassium cyanate during the combustion of almond shells and almond hulls.

The results of the alkali screening studies are relevant to the fouling and slagging observed in larger scale combustion facilities and industrial power generating facilities. Clearly the herbaceous feedstocks, with high potassium and chlorine content, represent the highest probability for severe fouling and slagging in industrial boilers. Herbaceous feedstocks also release three orders of magnitude too much alkali for these feedstocks to be considered for use in direct fired turbine applications. Release of alkali vapors has been proven to accelerate fouling and slagging and a mechanism for deposit formation has been reported by Baxter (Baxter, 1993; Baxter and DeSollar, 1993). Thermodynamics favors the release of alkali chlorides under most combustion conditions if chlorine is available in the gas. In the absence of chlorine, hydroxides are the next most likely alkali species to be released. In the absence of hydrogen, alkali oxides form. The form of the alkali vapor species is also a function of temperature. At lower temperatures the alkali sulfates are stable, however, as concluded from the alkali screening studies, alkali sulfates decompose at combustion temperatures. Deposit formation, therefore, is strongly dependent on the alkali species composition in the gas phase as well as the temperature of the surface on which the deposits form. Baxter (Baxter, 1993) has described four modes of deposit formation; inertial impaction, thermophoresis, condensation, and chemical reaction. In terms of these deposit formation mechanisms, combustion of herbaceous feedstocks pose the greatest threat, not only because of the high alkali and chlorine content, but because of the high ash and moisture contents as well. Herbaceous feedstocks tend to be 5% to 18% (rice straw) ash which tends to be predominantly silica, SiO_2. In a typical boiler, these ash particles become entrained in the hot gas flow and stick to heat transfer surfaces by inertial impaction. The silica alone does not pose too great a threat for deposit formation because it has a melting point of 1700 °C. Fouling and slagging is accelerated by the alkali vapors, primarily potassium, that condense on or react with the silica on the surfaces forming potassium silicates. The melting point of this potassium/silica mixture is dramatically reduced, thus enhancing the tenacity and fluidity of the deposit, even on relatively hot surfaces. Alkali condensation on cooler surfaces is more rapid, which increases the rate of accumulation of the deposit. Given this mechanism for deposit formation, it is clear that even a small amount of alkali vapor can dramatically alter the rate of deposit formation and the nature of the deposit that is formed.

Ash Deposit Formation Background

Among the issues that determine the design and operation of boilers, ash deposition on combustor surfaces plays a significant, in many cases dominant, role. The historical role of ash deposition as a motivation for major new coal combustion technologies concludes that "it is ... inevitable that there will be always some problems with ash, whatever the system of coal combustion" (Raask, 1985). The role of ash deposition in the emerging field of biomass combustion is likely to be similar. Nevertheless, the fate of inorganic material during combustion remains less well understood than the behavior of the organic material. While there are several indices of ash behavior, there is no complete model that describes ash deposition in a comprehensive way. The results of this investigation draw heavily on experience and concepts developed for ash deposition during coal combustion. The concepts and approach are fundamental and are demonstrated below to apply to both coal and biomass combustion.

Significant experimental and theoretical work has been directed at developing a better understanding of ash deposition and the resulting deposit properties, focused primarily on coal combustion. Quantitative data addressing deposit properties as a function of fuel properties, location within an experimental facility, and operating conditions have been published by several investigators (Baxter, 1990a; Baxter, 1992a; Baxter, Abbott, & Douglas, 1991; Baxter & DeSollar, 1991; Baxter & Dora, 1992; Baxter, Hencken, & Harding, 1990; Chow & Lexa, 1987; Durant, Kwasnik, & Lexa, 1989; Griffith, Lexa, & Teigen, 1988; Harb, Munson, & Richards, 1993; Harding & Mai, 1990; Helble, Neville, & Sarofim, 1986; Helble & Sarofim, 1989a; Helble & Sarofim, 1989b; Helble, Srinivasachar, & Boni, 1990; Loehden, Walsh, Sayre, Béer, & Sarofim, 1989; Quann, Neville, & Sarofim, 1990; Richards, Harb, Baxter, Bhattacharya, Bupta, & Wall, 1994; Srinivasachar & Boni, 1989; Srinivasachar, Helble, & Boni, 1990b; Srinivasachar, Helble, Boni, Shah, Huffman, & Huggins, 1990c; Srinivasachar, Senior, Helble, & Moore, 1992; Wall, Baxter, Richards, & Harb, 1994a; Wall, Bhattacharya, Zhang, Gupta, & He, 1994b; Wibberley & Wall, 1986; Zygarlicke, Ramanathan, & Erickson, 1992b). However, there are fewer published ash deposition data from facilities larger than pilot scale.

Fly ash formation models are in various states of development by several researchers. Many investigators working independently at several laboratories have developed a consensus view of the major mechanisms of fly ash formation, as illustrated in Figure (Baxter, 1994; Baxter, 1995; Loehden, et al., 1989; Srinivasachar, et al., 1992; Zygarlicke, McCollor, Toman, Erickson, Ramanathan, & Folkedahl, 1992a; Zygarlicke, et al., 1992b). These models, combined with fundamental results (Friedlander & Johnstone, 1957; Israel & Rosner, 1983; Loehden, et al., 1989; Rosner, 1989) pose a unified view of the formation of fly ash in terms of the size and elemental composition distributions of the entrained particulate phase resulting from the combustion of pulverized coal. Similar concepts are applied here to biomass.

Figure 69 schematically summarizes the fate of the inorganic material in solid fuel in terms of producing a fly ash. The solid fuel is illustrated on the left in the form in which it is fired into a combustor. In general, there may be mineral grains imbedded in the fuel, as illustrated, or

extraneous to the fuel itself. The transformations are divided into two types: release mechanisms and the fate of the residual ash.

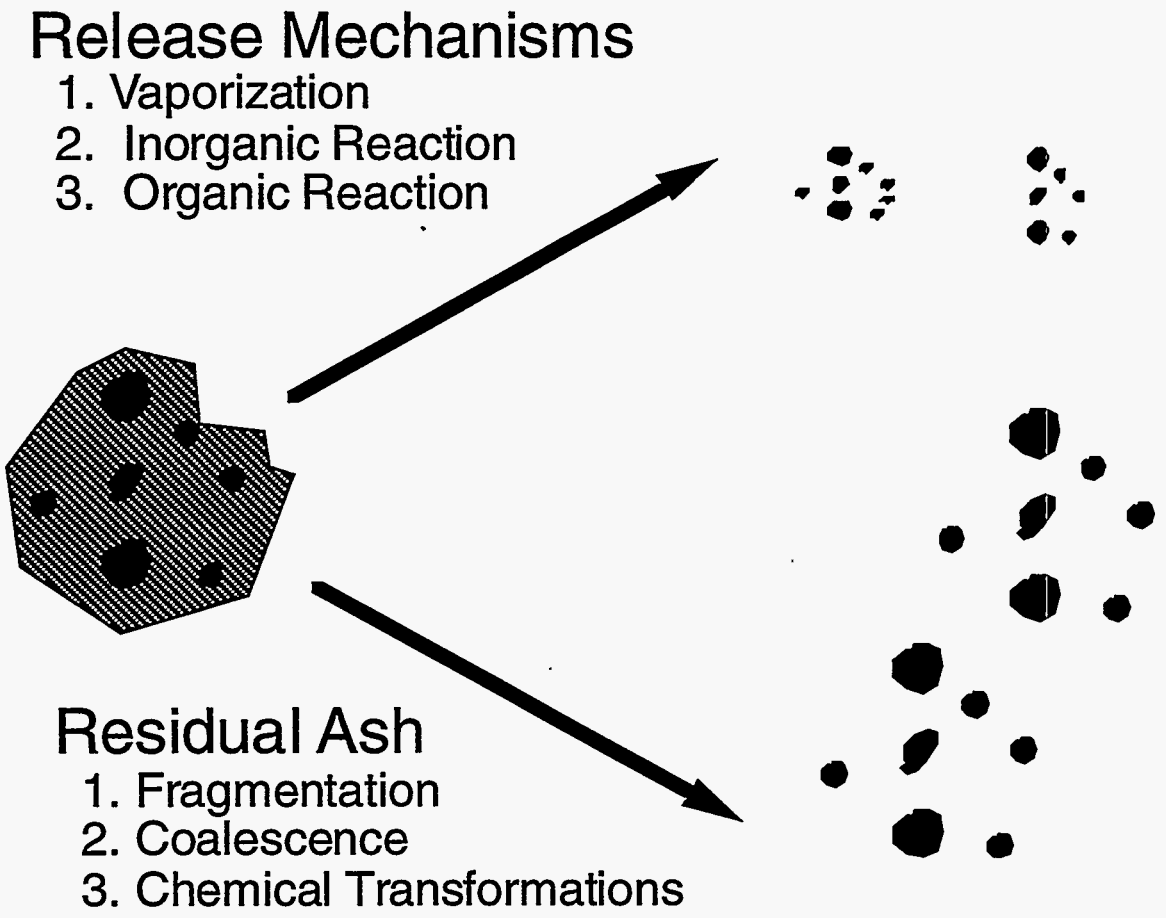

Figure 69 Schematic illustration of the fate of inorganic material in solid fuels during combustion. Inorganic material in the raw fuel may be atomically dispersed or in grains. The grains may be imbedded in the fuel (as illustrated) or extraneous to it.

Release mechanisms are indicated as vaporization, thermal or chemical disintegration of the inorganic material (inorganic reaction), or convection during rapid devolatilization or other organic reactions. These mechanisms tend to produce small (< 0.1 μm) particulate or vapors. The residual ash may undergo fragmentation either as a mineral grain or in conjunction with fragmentation of burning char particle, may coalesce with some or all of the remaining inorganic material, and it may undergo significant chemical or physical transformations. This material tends to produce larger ash particles. Depending on the type of inorganic material and the combustion

conditions, the ash produced during combustion is composed of varying amounts of vapor, fume (< 1 μm diameter), and larger particulate.

A great deal of information is available on rates and mechanisms of ash deposition. In this investigation, we consider four major mechanisms of deposition, or mass transport to a surface: (1) inertial transport including impaction and sticking, (2) thermophoresis, (3) condensation, and (4) chemical reaction. In general, the rates of inertial impaction on cylinders in cross flow are well established. Rates on walls with parallel flows are less well established. The capture efficiency, a measure of the propensity of material to stick to a surface upon impaction, is far less well established. The rates of thermophoretic deposition are reasonably well established when local temperature gradients and the functional form of the thermophoretic force on the particle (or the thermophoretic velocity) are known. Condensation rates can be predicted reasonably well given accurate vapor pressure and concentration data. The accuracy to which rates of chemical reaction are known is often inadequate, especially those involving sulfation and alkali adsorption in silicates.

The approach used in understanding ash deposit properties is illustrated for both pilot- and full-scale, biomass-fired facilities and for biomass fuels with widely varying types of inorganic material. Much of this discussion is relevant in analyzing high temperature corrosion, degradation of ceramic material in combustion environments, and other combustor-surface-related issues, although these are not highlighted in the discussion.

Both ash deposition rate and the properties of ash deposits are important considerations in the operation of a combustor. The properties of ash deposits most important to the successful operation of a combustor include: (1) the ease of removal from a combustor surface (this is referred to as the deposit tenacity in this paper); (2) viscosity; (3) effective thermal conductivity; (4) effective emissivity; and (5) deposit strength (this reflects strength of the bulk material, as opposed to tenacity). Additional deposit properties whose importance may be less obvious to the operator but that strongly influence properties 1-5 above include: (1) elemental composition; (2) morphology; (3) porosity; and (4) chemical species composition.

The discussion in the previous section briefly outlined the transformation of inorganic material during combustion. The discussion below focuses on deposition and the connection between deposit properties (and rate of accumulation) and fuel properties. This relationship depends strongly on combustor type, location within the combustor, and operating conditions. The relationship also depends on what is termed a mineralogical description of the inorganic material. The term mineralogical is used in a broad sense that includes the specification of atomically dispersed material (that is not actually mineral in a strict sense) and granular material of a true mineral nature.

It is significant that a mineralogical description of the inorganic material in the fuel is required, as opposed to an ASTM ash analysis. ASTM procedures can be used to generate much of the required information. For example, pyritic sulfur can be used to quantitatively estimate the fraction of pyritic iron in the fuel, and free silicon (silicon in the form of silica) can be estimated from the

ratio of silicon to aluminum in the ash. Other fuel mineralogies cannot be easily estimated from ASTM procedures. Principal among these are calcitic calcium, atomically dispersed species of any type, and the precise composition of silicates. The behavior of different minerals with similar elemental composition varies markedly. For example, the behavior of a mixture of silica and alumina has little resemblance to that of an alumino-silicate.

Frame of Reference

The frame of reference for this discussion is that of inorganic material traveling through a combustor from its injection to its removal. The inorganic material responds to the changing environment encountered along this path. These changes are cast in the form of a series of coupled, ordinary differential equations, the solutions to which indicate temperature, velocity, and position of the material as a function of its residence time. Also included in these equations is the rate of accumulation of ash on combustor surfaces. The solutions to the differential equations are used to predict the rate of deposition and deposit properties.

The four processes that contribute to deposit formation are: (1) inertial impaction (and particle capture), (2) thermophoresis, (3) condensation, and (4) heterogeneous reaction. These processes are assumed to have additive influences on the total deposit mass. That is, the mass rate of deposition of ash at residence time t is given by

$$\frac{dm_i}{dt} = I_i(\tau,t)G_i(\tau,t) + T_i(\tau,t) + C_i(\tau,t) + R_i(\tau,t) \qquad (1)$$

In this equation, m_i represents the mass of component i in the deposit. The factor I_i represents the rate of inertial impaction, G_i the particle capture efficiency, T_i the rate of thermophoretic deposition, C_i the rate of condensation, and R_i the rate of chemical reaction. The subscript i refers to each of the inorganic components in the fuel. These include, for example, pyritic iron, other forms of iron, silica, silicates, calcite, atomically dispersed species (sodium, calcium, potassium, magnesium, and titanium), etc.

The variable t is a material time scale, designating residence time relative to the time of injection of the fuel. It typically varies between 0 and 3 seconds. The variable τ designates elapsed or laboratory (clock) time, i.e., time relative to an arbitrary time of day independent of the residence time. It represents, for example, the time between soot blowing cycles and typically varies between 0 and 20 hours. In a steady-state or stationary system, the only relevant time scale is t and ash deposition rates, composition, and all other characteristics of the process would have the same mean values at all times at a given location. However, ash deposition clearly is a non-stationary process (Baxter, 1990a; Baxter, 1990b; Baxter, 1992b). Therefore, both the material and elapsed time scales must be addressed. Equation 1 can be thought of as an ordinary differential equation parameterized by the variable τ.

Practical illustrations can be used to clarify the differences in the two time scales. Changes in deposit composition from one location to another in a combustor are indicative of variation of one or more of the terms in Equation 1 with particle residence time (t). For example, biomass fly ash formed from herbaceous feedstocks often contains particles composed primarily of silica and potassium. Initially, the silica and potassium are poorly mixed since they derive from separate portions of the biomass. As the particles are maintained at high temperatures for long times, silica reacts with potassium to form a potassium silicate. The latter has a much lower melting temperature than the silica and can result in pronounced changes in the propensity for particles to remain on surfaces after collision. This leads to different particle capture efficiencies during the lifetime of a particle, generating different ash deposit compositions in different regions of the boiler. This change in deposit composition with location is a reflection of the residence time (t) dependence of the inertial impaction and particle capture efficiency terms in Equation 1.

Changes in deposit composition as a function of deposit thickness are indicative of variation of one of the terms in Equation 1 with clock time (τ). For example, deposits formed in the convection pass of boilers typically show pronounced variation in composition between the combustor surface and the outside of the deposit. These composition changes are often associated with variation in the condensation rate with τ. As the deposit accumulates, its surface temperature increases and the rate of condensation decreases.

Each of the major mechanisms of ash deposition indicated in Equation 1 is conceptually reviewed below. A cylinder in cross flow is used to illustrate several of the mechanisms, although the same mechanistic processes describe deposition on both cylinders and walls.

Inertial Impaction $I(t, \tau)$

Inertial impaction (see Figure 70) is most often the process by which the bulk of the ash deposit is transported to the combustor surface. Particles depositing on a surface by inertial impaction have sufficient inertia to traverse the gas stream lines and impact on the surface. The particle capture efficiency describes the propensity of these particles to stay on the surface once they impact. The rate of inertial impaction depends almost exclusively on target geometry, particle size and density, and gas flow properties. The capture efficiency depends strongly on these parameters and on particle composition and viscosity (Srinivasachar, Helble, & Boni, 1990a; Srinivasachar, et al., 1992). It also depends on deposit surface composition, morphology, and viscosity (Smouse & Wagoner, 1991; Wagoner & Yan, 1991).

The relative magnitudes of the characteristic times and dimensions of particle and fluid relaxation processes control the rate of inertial impaction. Specifically, inertial impaction occurs when the distance a particle travels before it fully adjusts to changes in the fluid velocity is larger than the length scale of an object, or target, submerged in the fluid. The particle Stokes number is defined as the ratio of these length scales.

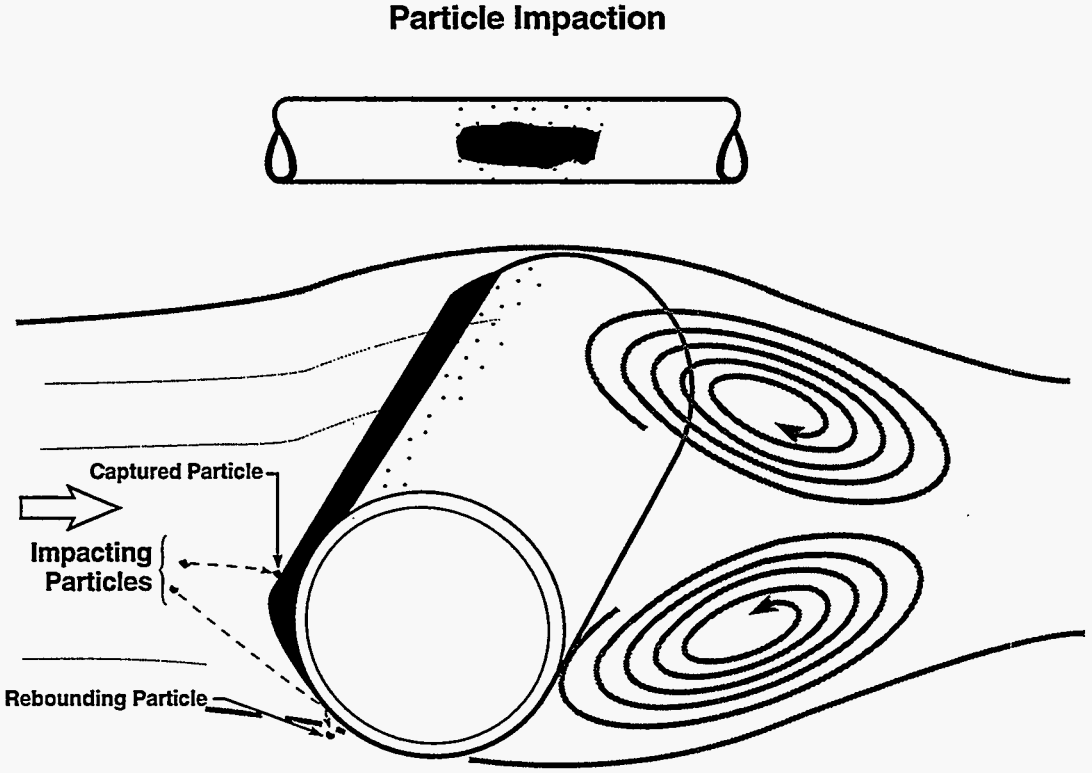

Figure 70 Conceptual illustration of inertial impaction mechanism on a cylinder in cross flow. One rebounding and one sticking particle are also illustrated.

Inertial impaction is illustrated schematically in Figure 70 for the case of a cylinder in cross flow. Two particles are illustrated as they approach the cylinder. Both respond to the gas flow field around the cylinder by beginning to move around the cylinder on approach. The inertia of both particles overwhelms the aerodynamic drag forces, and they impact on the cylinder. One is shown rebounding and the other sticking to the surface. Gas stream lines, including recirculation zones, are shown in light gray.

This process is most important for large particles (10 μm or larger) and results in a coarse-grained deposit. The impaction rates are highest at the cylinder stagnation point, decreasing rather rapidly with angular position along the surface as measured from this stagnation point. At angular displacements larger than about 50° (as measured from the forward stagnation point), the rate of inertial impaction drops to essentially zero under conditions typical of combustor operation.

The particle capture efficiencies can be estimated from global empirical correlations based on particle residence time and composition. The product of the capture and impaction efficiencies yields the collection efficiency. Therefore, the deposition rate of each inorganic component on the surface is directly proportional to its capture efficiency. There are wide variations in capture efficiency among different chemical components.

The impaction efficiency is indicated in Figure 71 and is defined as the ratio of number of particles that impact the tube surface to the number that are directed at the tube in the free stream. Predictions of the impaction efficiency as a function of particle, gas, and tube properties have been published, at various levels of approximation, by numerous investigators (Baxter & DeSollar, 1991; Beér, Monroe, Barta, & Sarofim, 1990; Israel & Rosner, 1983; Laitone, 1981; Rosner & Tassopoulos, 1989). The figure indicates that inertial impaction can be characterized as a function of the particle Stokes Number, which is defined for a cylinder in cross flow as

$$St^c \equiv \frac{\rho_p d_p^2 \langle u_p \rangle}{9 \mu_g d_c} \Psi \qquad (2)$$

where ρ_p, d_p, and $\langle u_p \rangle$ represent particle density, diameter, and mean velocity, respectively, and μ_g and d_c represent gas viscosity and tube diameter, respectively. Ψ is a correction factor that is only important when the particles do not obey Stokes' law, i.e., large particles with high velocities relative to the gas. Under typical conditions at the entrance of a convection pass (gas temperature 1580 K, gas velocity 16 m/s, tube diameter 7.62 cm or 3 in, particle specific gravity = 2), a 40 μm particle ash particle has a Stokes Number of about 1.2 and a 10 μm particle has a Stokes number of approximately 0.07.

Further investigation of the influence of the boundary layer, thermophoresis, and turbulence on this impaction efficiency is discussed elsewhere (Baxter & Hardesty, 1990). Figure 71 illustrates typical impaction efficiency results as a function of Stokes number. The details of the corrleation between Stokes number and impaction efficiency are available elsewhere (Baxter & Hardesty, 1990; Israel & Rosner, 1983).

Material within an ash deposit that accumulates by inertial deposition normally comprises relatively refractory particulate material. In biomass combustors, this would commonly involve many silica-, calcium-, and phosphorus-containing species. Biomass contaminants such as soil (clays) or inorganics in processed fuels, such as foil in non-recyclable paper, may contibute aluminum-, magnesium- and titanium-containing species to the inertially impacted fraction of an ash deposit.

Thermophoresis $T(t, \tau)$

Thermophoresis is a process of particle transport in a gas due to local temperature gradients. Under some circumstances, thermophoretic deposition accounts for a dominant fraction of the submicron particulate on a surface. Under most conditions relevant to biomass combustion, however, the other mechanisms of deposition contribute a larger fraction of the total deposit mass than thermophoresis.

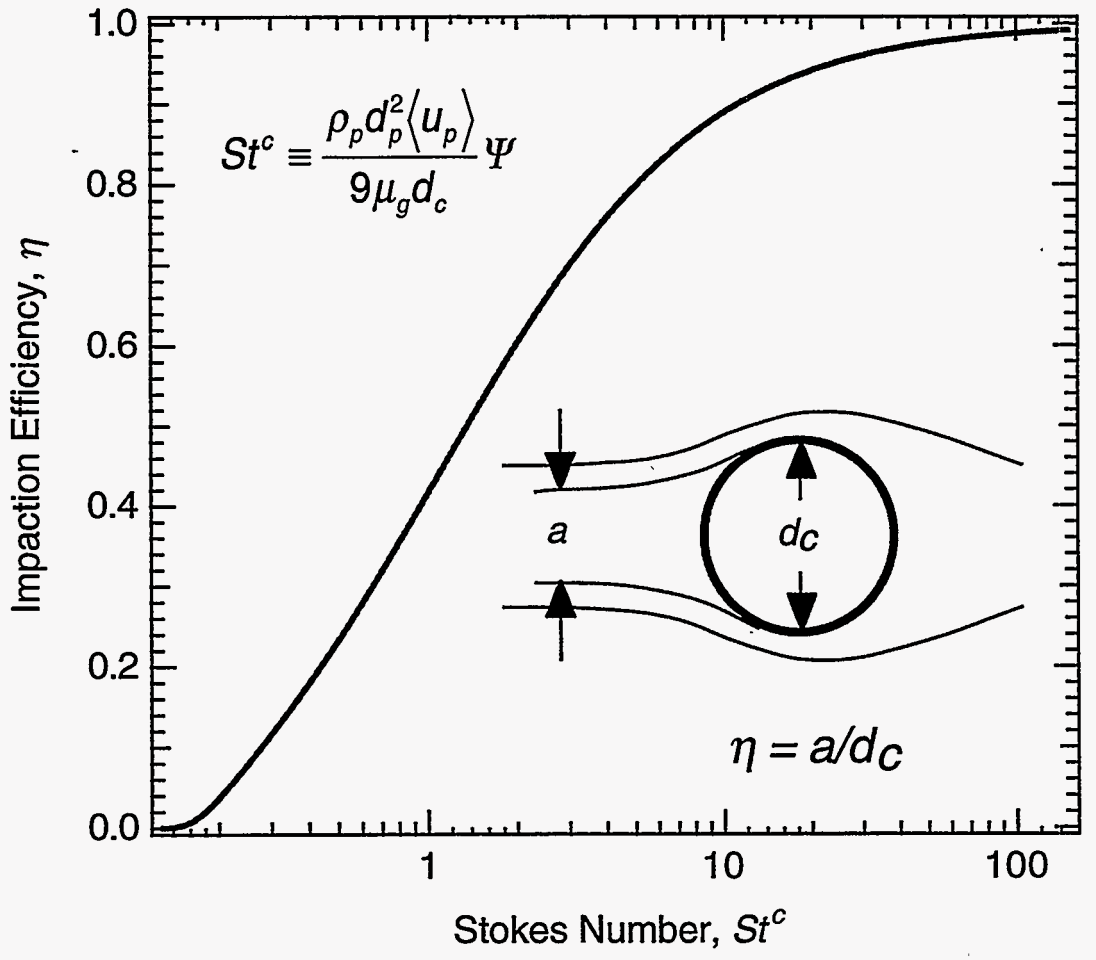

Figure 71 Correlation of particle impaction efficiency on a tube in cross flow as a function of Stokes number. A more detailed discussion of correlations is available in the literature (Baxter & Hardesty, 1990; Israel & Rosner, 1983).

Thermophoretic forces on a particle may be induced either by the temperature gradient in the gas in which the particle is suspended or as a consequence of a temperature gradient in the particle itself (Byers & Calvert, 1969; Fuchs, 1964; Gökoglu & Rosner, 1984; Gökoglu & Rosner, 1985; Gökoglu & Rosner, 1986). The origin of thermophoretic forces on a particle can be appreciated from the following, overly simplified argument. A particle suspended in a fluid with a strong temperature gradient interacts with molecules that have higher average kinetic energies on the side with the hot fluid than on the side with the cold fluid. The energetic collisions of the high energy molecules on the hot side of the particle create a stronger force than those of the low energy molecules on the cold side. This gives rise to a net force on the particle. In general, these forces

act in the direction opposite to that of the temperature gradient, although they can act in the direction of the gradient under certain conditions of particle surface temperature.

An illustration of thermophoretic deposition as it is manifest in biomass combustion equipment is presented in Figure 72. Thermophoretic deposits are finer grained and more evenly distributed around the tube surface than deposits formed by inertial impaction, as indicated. With increasing deposit accumulation on the tube surface, there is a decrease in the temperature gradient in the thermal boundary layer, decreasing the rate of thermophoresis.

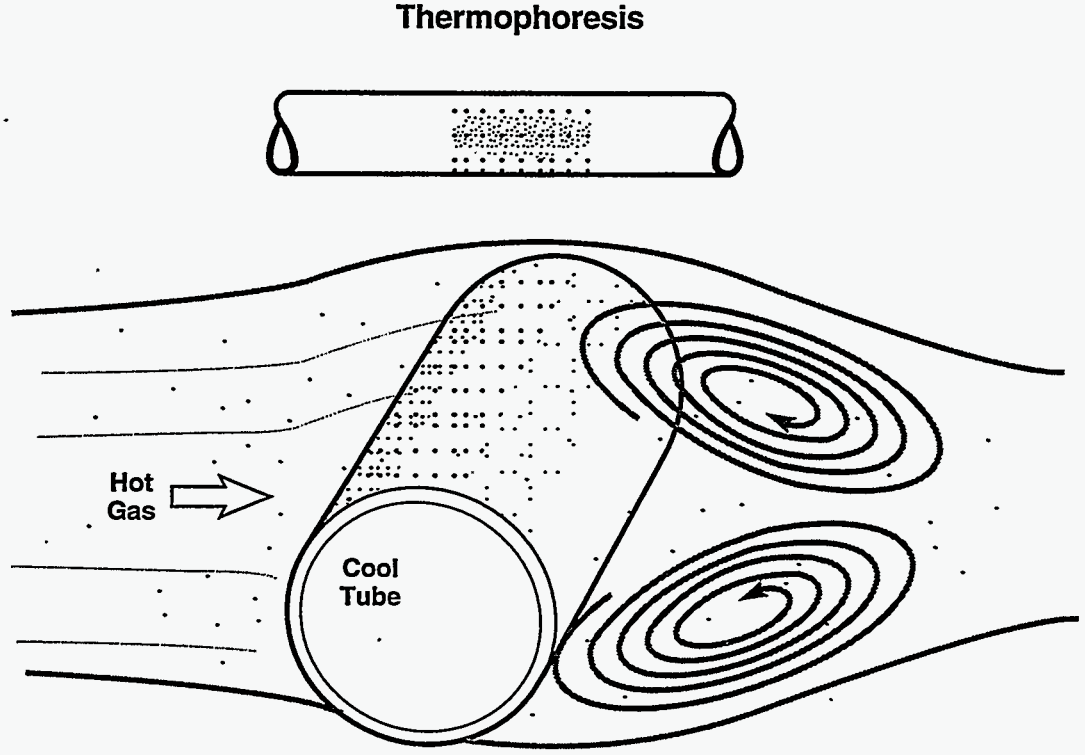

Figure 72 Schematic illustration of thermophoretic deposition on a tube in cross flow.

One functional form for the thermophoretic force that should apply over a broad range of Knudsen numbers (ratio of the gas mean-free-path to the particle diameter) is given below (Eq. 3). It is based on an integration of particle-gas momentum exchange over the surface of the particle (Jacobsen & Brock, 1965) and has been used by other investigators with some success (Im & Chung, 1983). The thermophoretic force, as used in this model, is given by

$$F_T = -6\pi\mu_g d_p f(Kn)\nabla T_g \qquad (3)$$

where $f(Kn)$ depends on particle diameter, Knudsen number, and several material-specific properties. Further discussion about thermophoresis is included elsewhere (Baxter & Hardesty, 1990; Baxter & Hardesty, 1992a; Baxter & Hardesty, 1992b).

Thermophetically deposited material is dominated by small (< 1μm) material, often formed through vapor nucleation, condensation, and agglomeration processes. This material typically is enriched in volatile species which, in the case of biomass, often includes potassium, chloine, and sometimes sodium and sulfur.

Condensation C (t, τ)

Condensation is the mechanism by which vapors are collected on surfaces cooler than the local gas. An illustration of deposition by condensation on a tube in cross flow is presented in Figure 73. The amount of condensate in a deposit depends strongly on the mode of occurrence of the inorganic material in the biomass. Low rank coals, lignites, biomass, and other similar fuels have the potential of producing large quantities of condensable material. Furthermore, the role of condensate in determining deposit properties can be substantially greater than the mass fraction of the condensate in the deposit might suggest. For example, condensate increases the contacting area between an otherwise granular deposit and a surface by several orders of magnitude. This increases by the difficulty of removing the deposit from the surface by a similar amount. Condensate can also increase the contacting area between particles by many orders of magnitude, having profound influences in the bulk strength, thermal conductivity, mass diffusivity, etc. of the deposit. Condensation is a relatively minor contributor to the development of deposits and their properties for most high-rank coals. However, in lower grade fuels such as lignites, biomass, etc., condensation becomes a significant or even dominant contributor.

All vapors that enter the thermal boundary layer around a cool surface and subsequently are deposited on the surface can be thought of as condensate. Condensation occurs by at least three mechanisms: (1) vapors may traverse the boundary layer and heterogeneously condense on the surface or within the porous deposit; (2) vapors may homogeneously nucleate to form a fume and subsequently deposit by thermophoresis on the surface; and (3) vapors may heterogeneously condense on other particles in the boundary layer and arrive at the surface by thermophoresis (Castillo & Rosner, 1988; Helble, et al., 1986; Rosner & Nagarajan, 1985).

Condensation deposits have no granularity at length scales larger than 0.5 μm and are more uniformly deposited on the tube than either thermophoretically or inertially deposited material. The deposits are tacky and have a strong influence on the surface capture efficiency.

The condensation flux is described by the following equation

$$C_i = \zeta_i \theta \, k_m \left(x_{i,b} - x_{i,s} \right) + x_{i,b} \sum_j C_j \qquad (4)$$

where ζ_i is the condensation efficiency, θ is a blowing factor (which will be very near unity for this application), k_m is a mass transfer coefficient (that depends in known ways on geometry, Reynolds number, and fluid properties), and x represents a mole fraction of species i in the bulk gas (subscript b) and at the tube surface (subscript s). The second term on the right side of the equation represents convective transport to the surface.

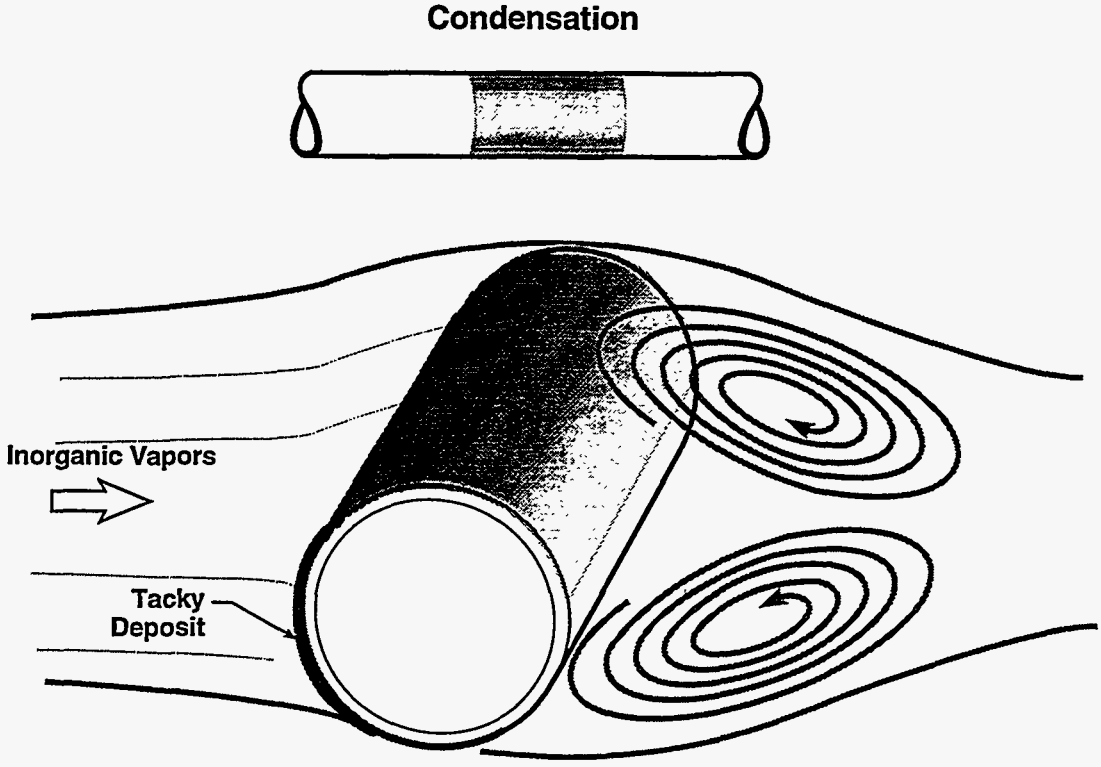

Figure 73 Schematic illustration of condensation on a tube in cross flow.

Thermophetically deposited material is dominated by small (< 1μm) material, often formed through vapor nucleation, condensation, and agglomeration processes. This material typically is enriched in volatile species which, in the case of biomass, includes potassium, chloine, and sometimes sodium.

Condensates are derived from vapors and other volatile material. This material typically is enriched in potassium, chloine, and sometimes sodium.

Chemical Reaction $R(t, \tau)$

Inertial impaction and thermophoresis describe the two most significant mechanisms for transporting particulate material to a surface for biomass- and coal-fired systems. Condensation involves transportation of vapors to a surface by means of a physical reaction and phase change. Chemical reactions (Figure 74) complete the mechanisms by which mass can be accumulated in a deposit. These involve the heterogeneous reaction of gases with materials in the deposit or, less commonly, with the deposition surface itself. Some of the chemical species found in deposits are not stable at gas temperatures, alkali sulfates being typical examples. The sole source of these species is heterogeneous reactions between gas phase constituents and constituents of the lower temperature deposits.

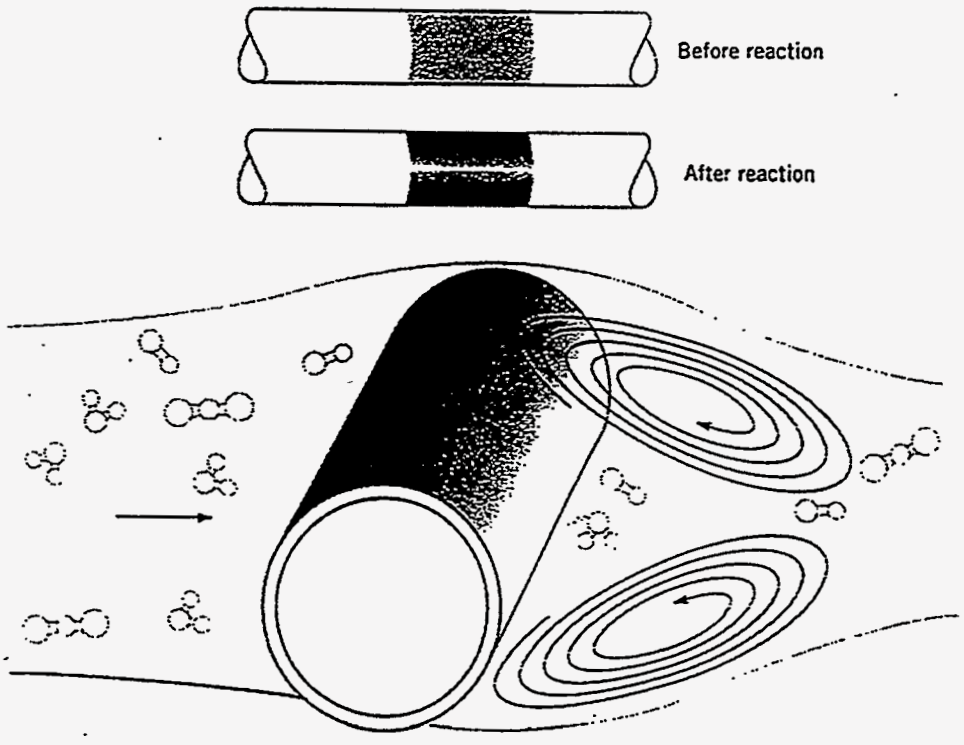

Figure 74 Schematic illustration of chemical reaction on a tube in cross flow.

Among the most important chemical reactions with respect to ash deposition are (1) sulfation, (2) alkali absorption, and (3) oxidation. The principal sulfating species of concern are compounds containing the alkali metals, sodium and potassium. Sodium and potassium in the forms of condensed hydroxides and possibly chlorides are susceptible to sulfation.

Silica absorbs alkali material to form silicates. Silicates are less rigid and melt at lower temperatures than silica. The transformations of silica to silicates in deposits can induce sintering and significant changes in deposit properties. These reactions are relatively slow compared to sulfation.

Residual char often deposits with the inorganic material on combustor surfaces. However, the char oxidizes with locally available oxygen to produce deposits with very little residual carbon. In biomass combustion, carbon typically accounts for less than 2 % of the overall deposit mass.

Chemical reactions, such as sulfation of alkali species and combustion of residual carbon in the ash, are similar to condensation in their mathematical treatment (Baxter & Hardesty, 1990). Both condensation and chemical reactions are strongly temperature dependent and give rise to spatial variation in ash deposit composition.

Chemical reactions of greatest importance to deposit formation include sulfation of alkali species, incorporation of alkali into silica, combustion of residual carbon, and sometimes formation and decomposition of carbonates. In addtion, almost all species on a surface will utlimately react with each other if temperature is sufficiently high and deposits mature for long periods of time.

Pilot-Scale Deposition Results

Experimental Facilities

Deposit samples were obtained by burning various biomass fuels in the Multifuel Combustor (MFC) at the Combustion Research Facility of Sandia National Laboratories in California. The MFC was originally designed to simulate combustion and ash deposition in pulverized-coal-fired boilers. It was used to perform laboratory- and pilot-scale tests on ash deposition during combustion of the solid fuels. The MFC is a pilot-scale (30 kW), 4.2 m high, down-fired, turbulent flow reactor that simulates the gas temperature and composition histories experienced by particles in combustion systems (Figure 75). A gas burner may be used to provide a vitiated air to the remainder of the combustor, although the more typical experiment involves self-supported flames. Gases flow through a series of modular sections that include guard heaters, fuel insertion ports, and thermocouple insertion ports. At the end of these modular heaters is the test section of the combustor. In this section, several air-cooled deposition surfaces that simulate waterwalls and convection pass tubes are inserted in the particle-laden, vitiated flow. In the experiments described here, surface temperatures of these tubes are measured using thermocouples. Surface temperature was held constant in each individual experiment but varied from 350 to 650°C among the several experiments performed. Advanced diagnostics are used to measure deposit chemical composition and emissivity as a function of time during ash deposition. Deposits are also sampled from the furnace and submitted for SEM-based analyses as well as elemental analyses using atomic emission/absorption spectroscopy with an inductively coupled plasma following digestion. Details regarding the application of the combustor and its advanced diagnostics for coal-related work are available elsewhere (Baxter, 1993). During these investigations, milled biomass fuel passing a 10 mesh sieve or finer was injected pneumatically via a water-cooled lance inserted through the side of the furnace just below the gas burner at the top. The fuel was fired downward from a position about 4 m above the test section, producing a particle residence time of 1 to 2 s, depending of fuel type and other operating conditions. This provided for essentially complete carbon conversion of the fuels within the combustor. For most tests reported here, the furnace wall temperature was set at 900 °C to simulate a typical biomass combustor furnace exit gas temperature ahead of the superheaters. Typically, the gas burner was not used to preheat the air, with some exceptions when simulating very high temperature systems.

The fuels used for the MFC experiments reported here (Table 2) included almond hull, almond shell, olive pits, rice straw, switchgrass, wheat straw, and a blend of urban and agricultural wood fuel with almond shell. The fuels selected provided a wide range of inorganic element concentrations.

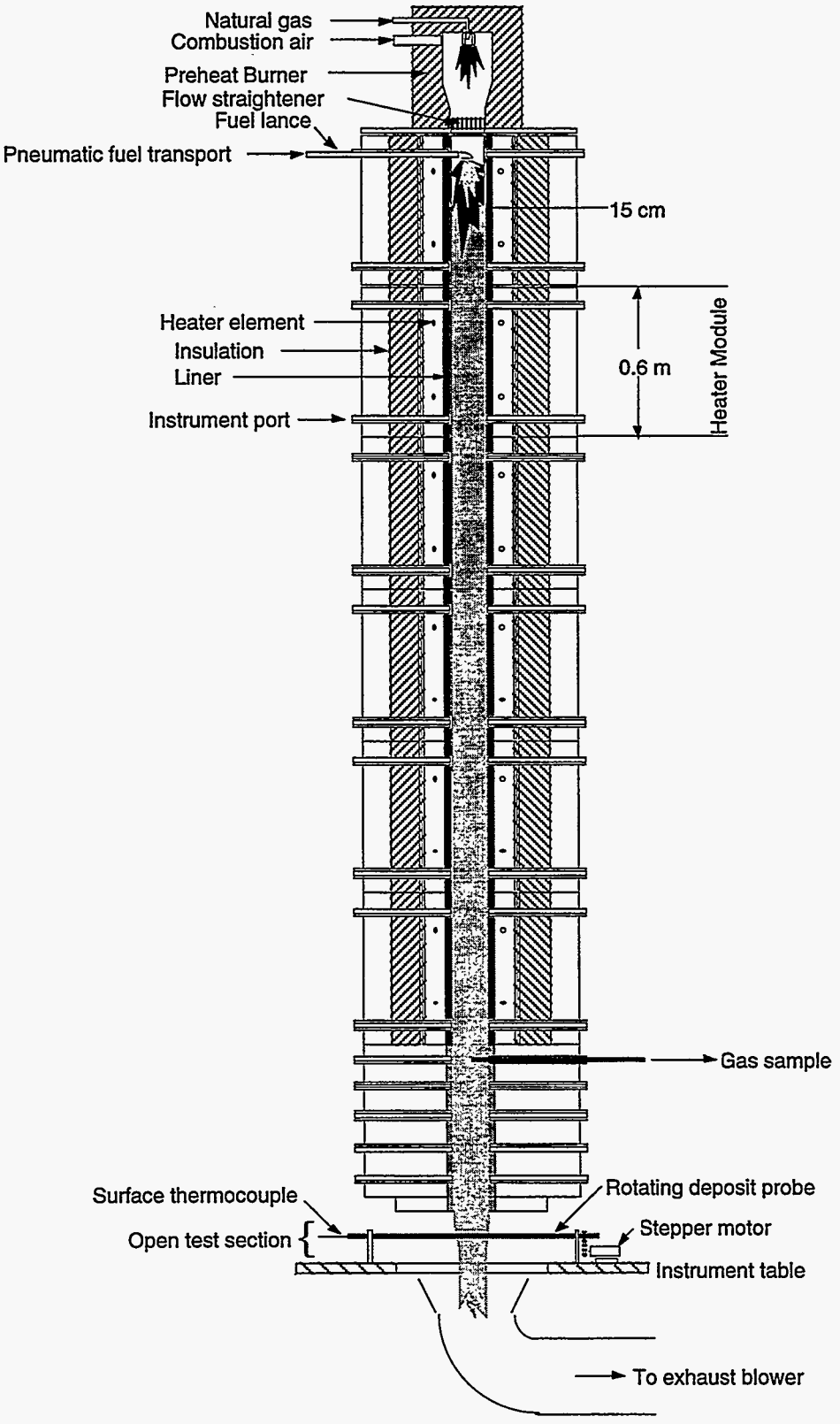

Figure 75 Schematic diagram of the Sandia Multifuel Combustor used in these combustion tests.

Deposits were collected on a horizontal 16 mm o.d. stainless steel tube situated across the furnace exit flow (Figure 76). In most experiments, this deposit probe was continuously rotated for the purposes of obtaining emission spectra from the deposit for analysis by FTIR and generating axisymmetric deposits for heat transfer analysis. The non-destructive FTIR spectroscopy technique provides time resolved, *in situ* information on deposit composition and other properties, but is developmental for biomass and the results are not discussed in this document. Alongside the rotating probe, a stationary horizontal tubular probe of the same diameter was inserted to collect additional deposit and to better simulate the stationary superheater surfaces in commercial boilers. Two waterwall probes were constructed, one low alloy and one stainless steel, and placed in the combustor test section extending upwards into the furnace. The water-wall probes consisted of a serpentine steel tube with membranes between each bend. All probes were air cooled and thermocouple instrumented, with surface temperatures maintained in the range of 400 to 500°C, to simulate the wall temperatures of heat exchangers in full-scale units.

Fly ash particles were collected with a rapid-quench, isokinetic probe on a polycarbonate filter, and were generally analyzed separately. When empty, this filter passes particles less than one micron in diameter. As the filter becomes more loaded, the collection efficiency of the submicron particulate increases. Often large, partially oxidized fuel particles were collected loose in the filter holder, and were generally analyzed separately. Such particles were also frequently collected on the horizontal surfaces of the water-wall probe, and were analyzed separately.

Each test lasted three to six hours, and consumed 3 to 15 kg of fuel. Deposit samples were collected from the probes at the end of each experiment and submitted for chemical analysis.

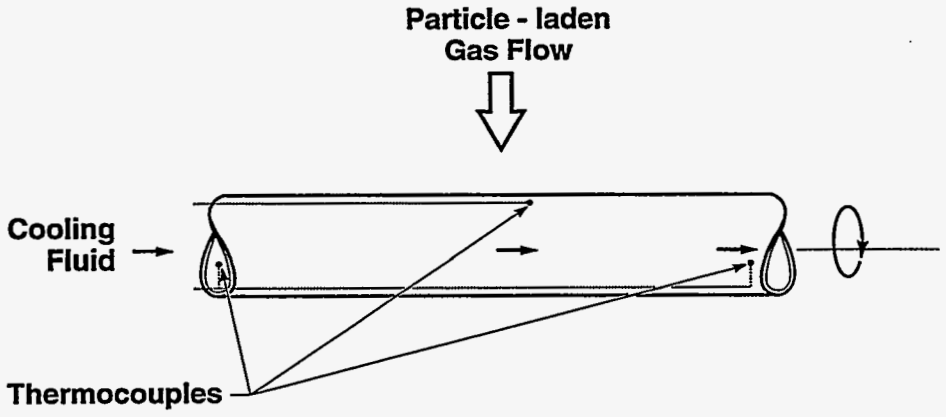

Figure 76 Schematic diagram of the horizontal tube in cross flow deposition probe used during MFC experiments.

Combustion of Straw and Straw Blends

In all laboratory straw combustion tests, fuel was inserted into the MFC at a height of approximately 4.3 m (14 ft.) above the beginning of the test section. Ash deposits were collected from a simulated water wall and convection pass tube as well as from the internal ceramic liner of the MFC. Straw and grass fuels produced rather heavy deposits on the furnace wall downstream from the fuel injection point. In the case of rice straw, these deposits grew inwards to a point where aerodynamic drag or furnace vibration caused them to fall from the wall. Deposit attrition from wall deposits falling and impacting the probes caused a second rice straw test to be aborted. Wall deposits were collected and analyzed separately.

Compositions for fuel ash, probe deposits, and fly ash from seven laboratory combustion experiments are reported in Table 2 through Table 8. The fuel ash composition indicated in these tables are as measured for the specific test burn and differ slightly from the averages presented earlier in this document. The undetermined fractions of these materials are indicated under the column labeled Und in the figures and are abnormally high. With the exception of fuel, none of the samples was ashed prior to analyzing for inorganic composition. Ashing generally decomposes carbonates, some sulfates, and removes residual carbon from samples. The lack of ashing results in high undetermined fractions.

Relative enrichments or depletions of the elements in the deposits and fly ash are clues to the chemistry that influences both their transformations during combustion and their reactions on surfaces.

Rice Straw

Rice straw combines high chlorine with a high silica fuel ash (Figure 2 and Table 2). Two tests with rice straw were conducted, the second of which was terminated early due to tube deposit attrition from loose furnace wall deposits. The only air-cooled deposition target used for these tests was the rotating, horizontal probe. The deposit on this tube formed initially as a uniform white layer, a universal characteristic of the laboratory experiments on alkali-laden fuels. Subsequently, the deposit grew as a porous sintered matrix, which was readily brushed from the tube at the end of the experiment. The outer deposit layer from the second test was somewhat enriched in potassium and depleted in silicon compared to the bulk probe deposit from the first test. All deposits were depleted in sulfur compared to the fuel.

Furnace wall deposits from the heated silicon carbide liner of the MFC were also collected and analyzed during straw combustion. Heavy deposits formed on the wall of the furnace below the fuel injection point. Samples were recovered both during the experiment and after cooling and cleaning the furnace. The wall deposits were highly porous with a sintered sponge-like appearance, white in color where they were attached to the wall, and dark (shading from purple to black) extending away from the wall. The white and dark portions were analyzed separately. The white portion was enriched in aluminum, titanium, and iron compared to the dark deposit, as illustrated in Figure 77, which may be due to the influence of the furnace wall material, a mullite

Table 2 Inorganic composition of fuel and ash deposits generated during MFC combustion tests of rice straw.

Sample Type	SiO2	Al2O3	TiO2	Fe2O3	CaO	MgO	Na2O	K2O	P2O5	SO3	Und
Fuel Ash	80.15	1.46	0.06	0.85	2.03	2.11	0.91	8.51	1.68	1.22	1.02
Flyash (2)	58.59	2.65	0.13	1.56	2.07	1.93	0.88	17.63	1.64	1.10	11.82
Furnace wall, black (2)	79.01	1.13	0.04	0.79	4.56	1.04	0.70	12.20	1.54	0.03	-1.04
Furnace wall-white (2)	73.50	9.56	0.47	6.87	2.28	1.41	0.67	5.19	0.65	0.14	-0.74
Probe, outer layer (2)	67.06	2.10	0.23	1.18	3.73	1.60	0.68	14.60	4.56	0.67	3.59
Probe, rotating (1)	76.57	0.70	0.04	0.92	2.12	1.45	0.41	9.65	1.16	0.82	6.16

Test number indicated in parentheses. Und = undetermined.

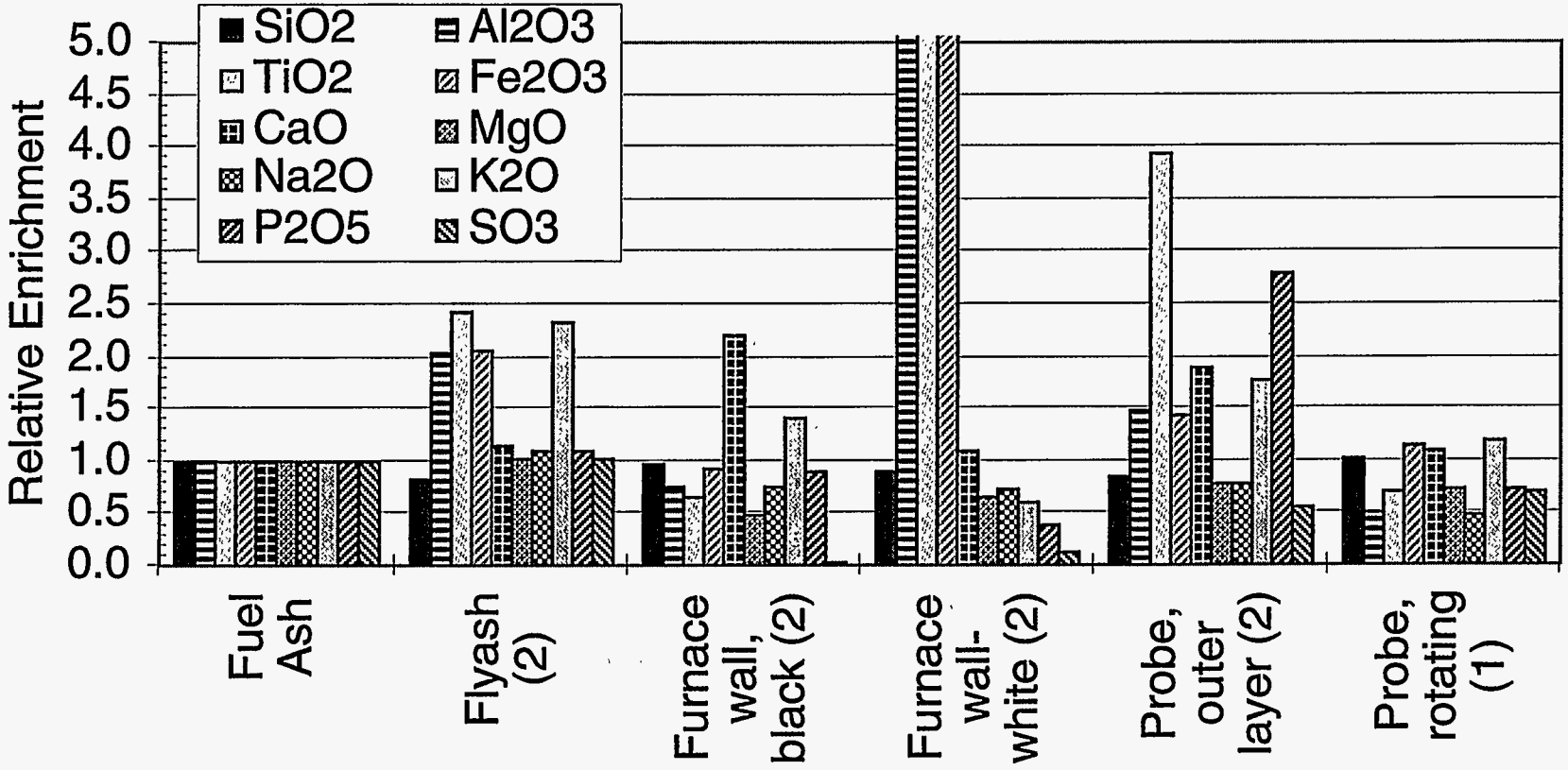

Figure 77 Relative enrichment of various deposit and fly ash samples collected during MFC investigations on rice straw.

($3Al_2O_3 \cdot 2SiO_2$) ceramic and possible contamination from residual coal ash deposited on the wall in the tests previous to this experiment. The fly ash was also enriched in aluminum, titanium, and iron, as well as potassium. The absolute amounts are small and do not suggest substantial contamination. The fly ash also has a high undetermined fraction, which may account in part for the enrichment ratios observed. Alternatively, the undetermined fraction may include chlorine or carbon. Regardless, the probe deposit has a composition very similar to the composition of the fuel ash.

X-ray analysis during scanning of the wall deposits with SEM did not detect chlorine. SEM analyses of probe deposits did show evidence of chlorine, but quantitative concentrations were not obtained. The rice straw wall deposits show distinctly a glassy matrix in which lie imbedded porous silica particles. These particles are nearly pure silicon (94%) with potassium making up most of the residual, and almost certainly derive directly from the fuel. The glassy phase binding the silica particles is 64% silicon, with 19% potassium, and smaller amounts of calcium, magnesium, sodium and other elements (Baxter, et al., 1993). The glass appears to have formed over time by reaction of silica with potassium vapor and other elements to form a low melting point silicate. The bulk composition of the glass is consistent with a melting point between 900 and 1200°C at equilibrium (Levin, et al., 1964). The liquidus surface is steep in the region of this composition, and the observation of a molten phase is consistent with the possible range in furnace gas temperatures. Relative concentrations of chlorine show the layer of the probe deposit next to the tube surface to be chlorine enriched relative to the outer deposit layer. Potassium and sulfur are also enriched in the inner layer, while silicon is depleted.

Figure 78 is a scanning electron micrograph of a deposit produced during combustion of rice straw in the MFC. The deposit was generated on the wall of the MFC combustor and accumulated over a 3 hour test period. The wall temperature was 900 °C, the gas temperature was 1000 °C, and the gas composition is estimated to contain 6 % oxygen. Most of the deposit has a glassy appearance, with occasional nodules under the otherwise smooth surface.

The deposit composition is determined as a function of location on the surface using electron dispersive spectroscopy in a scanning electron microscope. The compositions of the glassy and nodular phases are summarized in Figure 79 on an oxygen-free, mass basis. Both phases are composed principally of silicon. By comparison with the nodules, the glassy phase contains more nonsilaceous material. More than half of the nonsilaceous fraction is potassium.

Figure 78 and Figure 79 illustrate how incorporation of alkalis and other materials changes the physical properties of silica-based deposits. For example, the melting point of silica decreases from about 1700 °C to less than 750 °C as potassium is introduced to form potassium silicates. Incorporation of additional materials, in particular other alkalis and alkaline earth materials, usually lowers the melting point further still. The silicon to potassium ratio observed in the glassy portions of the deposit illustrated in Figure 78 is about 3.4 on a mass basis, or about 81 % SiO_2 to 19 %

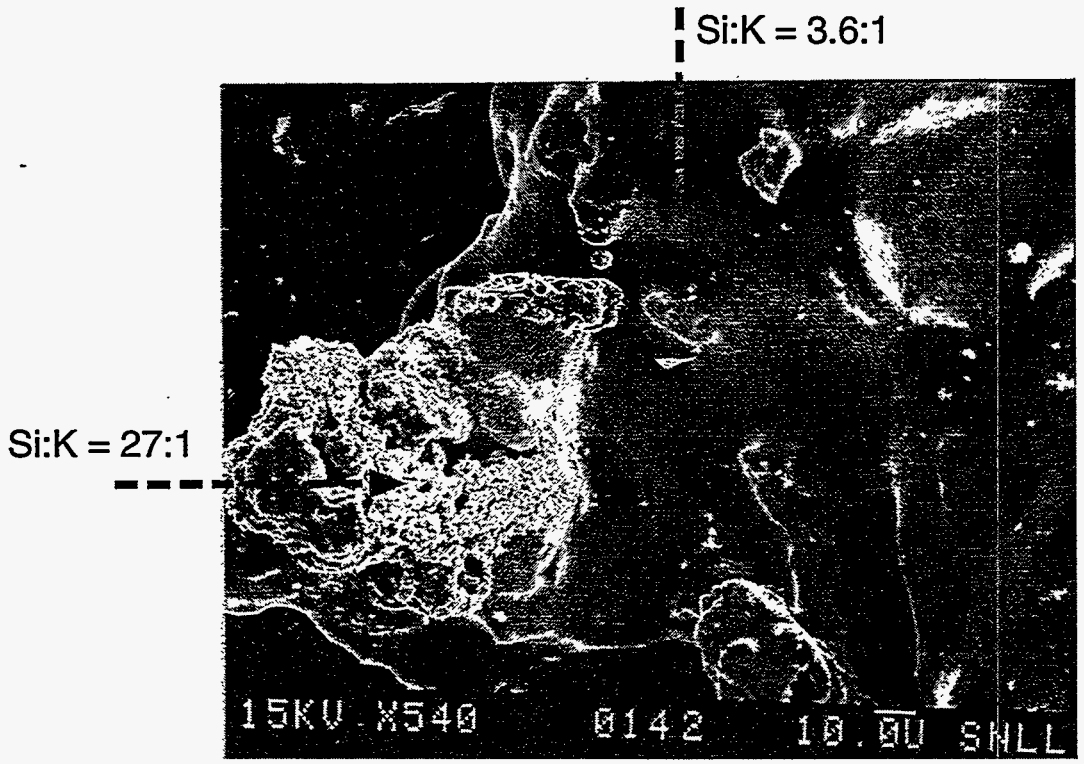

Figure 78 Scanning electron micrograph of a portion of a rice straw deposit collected from a ceramic surface in the MFC. The porous, silica based material was exposed by fracturing the deposit though one of the nodules evident in many locations on the smooth, glassy surface.

K_2O. An equilibrium mixture of such material becomes completely molten at approximately 1300 °C. This is slightly above the temperature of deposit, but the addition of calcium and other heteroatoms to this mixture reduces the melting point significantly (Levin, Robbins, & McMurdie, 1964). The nodular material, on the other hand, has a much higher melting point.

The data support the following hypothesized mechanism for the formation of the deposit. Alkali material (predominately potassium) is released from the fuel during the early stages of combustion. Mechanisms of release include vaporization and convective transport with volatiles (Baxter, et al., 1995 (to appear)). Silaceous material dehydrates and becomes porous silica particles, but neither vaporizes nor melts. The silica particles arrive on a surface by inertial impaction. Potassium (and other vapors) arrive either by condensation or chemical reaction with the silica. Chemical reaction

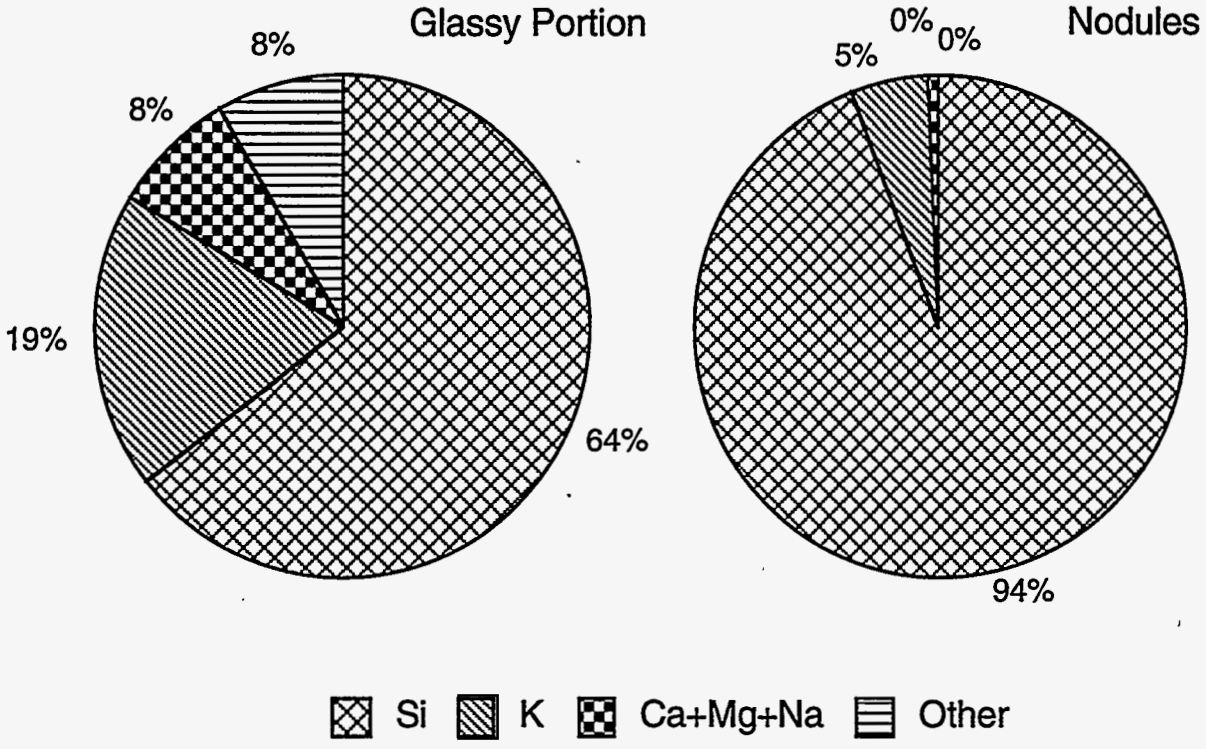

Figure 79 Average compositions of the glassy and nodular regions of the rice straw deposit illustrated in Figure 78.

is believed to be the dominant mechanism in this case, since the deposit temperature is near or above the estimated dew point for potassium-containing vapors under these conditions. As silica grains become impregnated by potassium and other material, the melting point of the mixture drops rapidly. As the mixture becomes increasingly molten, the originally granular silica sinters, developing strength and tenacity. Impregnation of surfaces by potassium occurs most readily on exposed surfaces and more slowly in interior regions, creating the coating of glass around the nodules seen in the micrograph.

Nodules of calcium oxide and iron oxide present in several locations in the deposit do not exhibit the same behavior as silica. These nodules show little evidence of melting, although they are thoroughly impregnated with potassium silicate. This observation underscores the role of high temperature chemistry in formation of the deposit.

Wheat Straw

The wheat straw deposits are in many respects similar to the rice straw deposits. Two tests were conducted without hindrance from dislodged wall deposits. The fuel chlorine concentration of the wheat straw was about 40% that of the rice straw fuel, but wheat straw is also a high chlorine, high silica fuel. Chlorine concentrations in wheat straw have often been observed at substantially higher levels. The vertical water-wall probe was used along with the rotating horizontal probe. The deposits collected were segregated into different parts for analysis. During the second test, the horizontal probe rotation was stopped and the deposit collected with the probe stationary. The deposit built up in three distinct layers beginning with a uniform fine textured white deposit next to the probe surface, a more porous intermediate layer which was brushed from the tube, and an upper crown deposit with the appearance of sintered fuel ash particles. The latter portion of the deposit was only loosely bonded and was removed simply by inverting the tube. Various types of deposits were collected from the water-wall probe. On the upper horizontal surfaces of this probe, deposits were formed which were similar in character to the crown deposit on the horizontal probe. These varied in hardness and color. On the vertical face of the water-wall, a fine textured white layer formed next to the surface, followed by a darker layer building outward, but considerably finer textured than any of the crown deposits. The compositions of the deposits, including one removed from the furnace wall, are listed along with the fuel and fly ash compositions in Table 3. The relative abundance is shown in Figure 81 and Figure 82 for selected samples.

Silicon was the major species in all samples. The inner deposit layers from both probes were depleted in silicon relative to the outer layers. Potassium enrichment was evident in all of the deposit samples as well as the fly ash. The deposit layers showed increasing potassium and sulfur concentrations moving inward towards the probe surfaces, although sulfur was depleted relative to the fuel. SEM/X-ray analyses gave qualitatively higher chlorine concentrations in the inner layers as well, although no quantitative determinations for chlorine were made. Phosphorous was enriched in the outer deposit layers compared to the inner layers, and was enriched in the fly ash as well. Furnace wall deposits did not show any evidence for contamination as with rice straw. The iron enrichment in the inner layers of the water-wall deposit may have been the result of tube metal contamination when sampling, however.

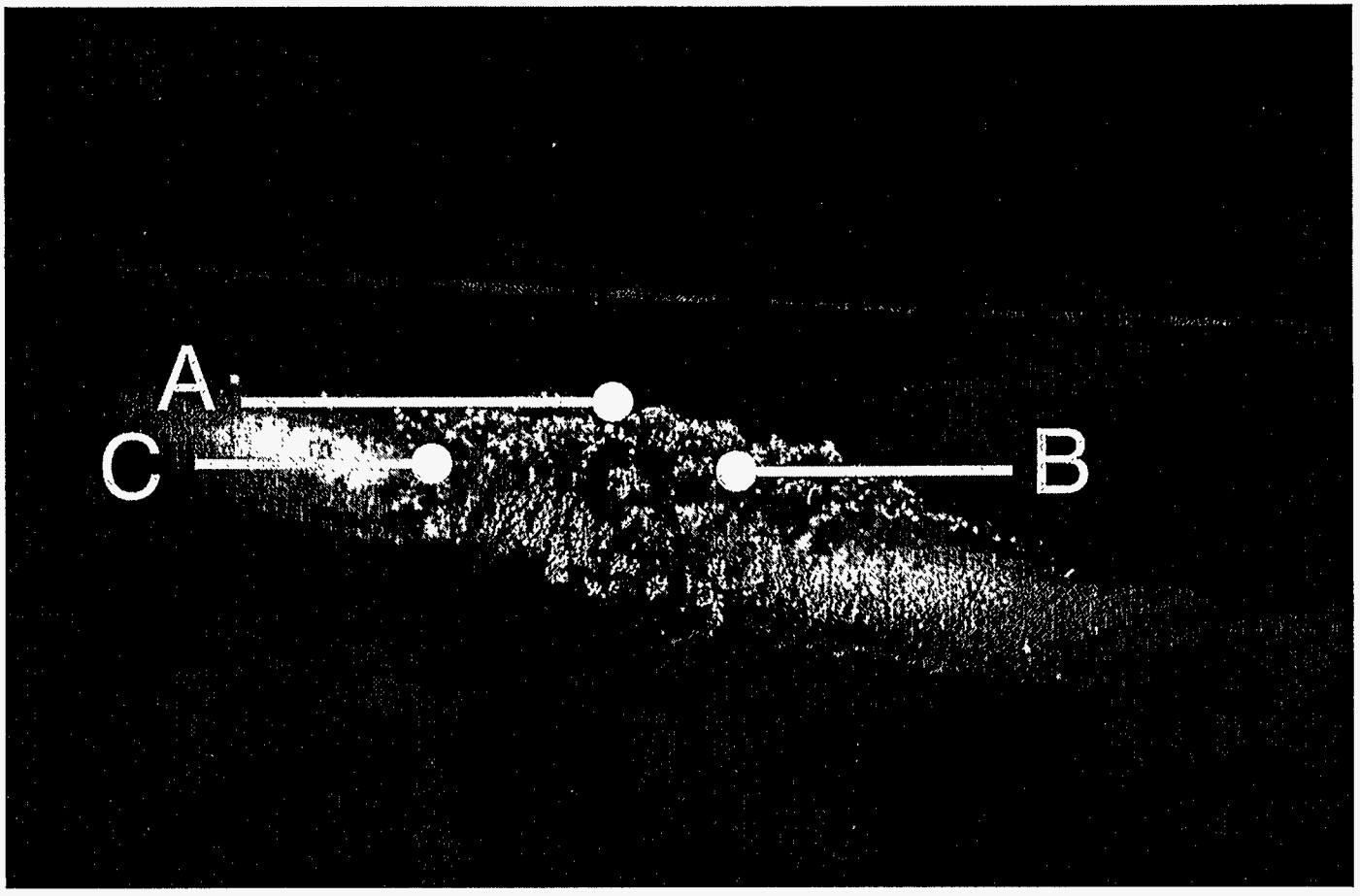

Figure 80 Photograph of deposit forming from wheat straw on a simulated boiler tube in the test section of the MFC. The three locations labeled A through C represent the deposit crown, outer layer, and inner layer, respectively (see Table 3 and Figure 77). A red laser beam measuring the size and speed of entrained particles is shown above the probe.

Table 3 Inorganic composition of fuel and ash deposits generated during MFC combustion tests of wheat straw.

Sample Type	SiO2	Al2O3	TiO2	Fe2O3	CaO	MgO	Na2O	K2O	P2O5	SO3	Und
Fuel Ash	67.54	2.14	0.10	1.22	3.08	2.88	2.05	14.38	1.41	5.02	0.18
Flyash (2)	50.49	1.35	0.04	1.40	5.28	1.10	1.09	23.10	3.35	5.77	7.03
Furnace Wall (2)	66.28	1.26	0.11	0.99	4.48	2.67	0.90	18.40	2.16	1.23	1.52
Probe, stationary, crown (2)	58.90	2.08	0.04	1.18	4.85	2.40	0.86	19.50	4.51	1.59	4.09
Probe, stationary, inner layer (2)	49.96	2.78	0.14	1.48	4.30	4.07	1.20	24.80	2.02	4.39	4.86
Probe, stationary, intermediate (2)	57.13	3.01	0.15	1.32	5.74	3.04	1.01	21.10	3.79	2.04	1.67
Water wall, crown (1)	56.82	1.36	0.08	0.90	2.70	2.49	0.67	19.80	1.23	2.28	11.67
Water wall, crown, brown (2)	67.46	2.46	0.14	1.30	3.52	3.15	0.87	16.14	1.57	2.61	0.78
Water wall, crown, hard black (2)	53.92	5.45	0.33	3.31	8.16	3.10	0.59	14.10	3.64	2.72	4.68
Water wall, crown, soft black (2)	61.04	2.40	0.08	1.16	4.67	1.73	0.86	19.30	3.48	1.38	3.90
Water wall, inner white layer (2)	43.49	1.63	0.08	2.86	2.89	2.55	0.83	27.50	1.34	6.37	10.46
Water wall, inner white layer (1)	41.60	2.00	0.12	4.27	3.06	2.55	0.95	28.40	1.28	7.37	8.40
Water wall, outer dark layer (1)	50.68	1.50	0.15	1.30	4.65	1.60	0.87	23.90	3.75	3.44	8.16
Water wall, outer layer, (2)	52.85	1.44	0.08	1.42	5.03	1.86	0.90	24.20	3.77	3.11	5.34

Test number indicated in parentheses. Und = undetermined.

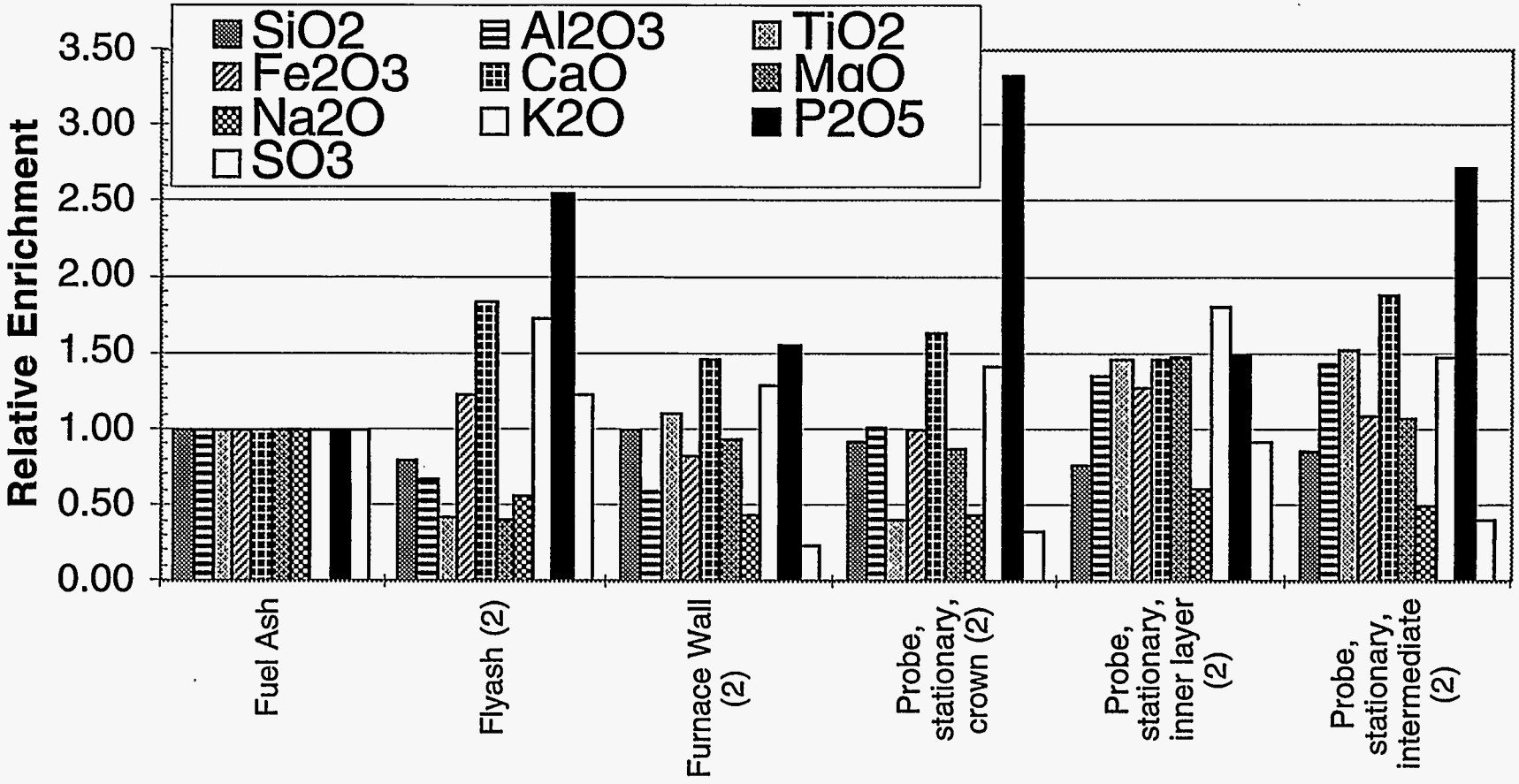

Figure 81 Relative enrichment of various deposit and fly ash samples collected during MFC investigations on wheat straw (continued on Figure 82).

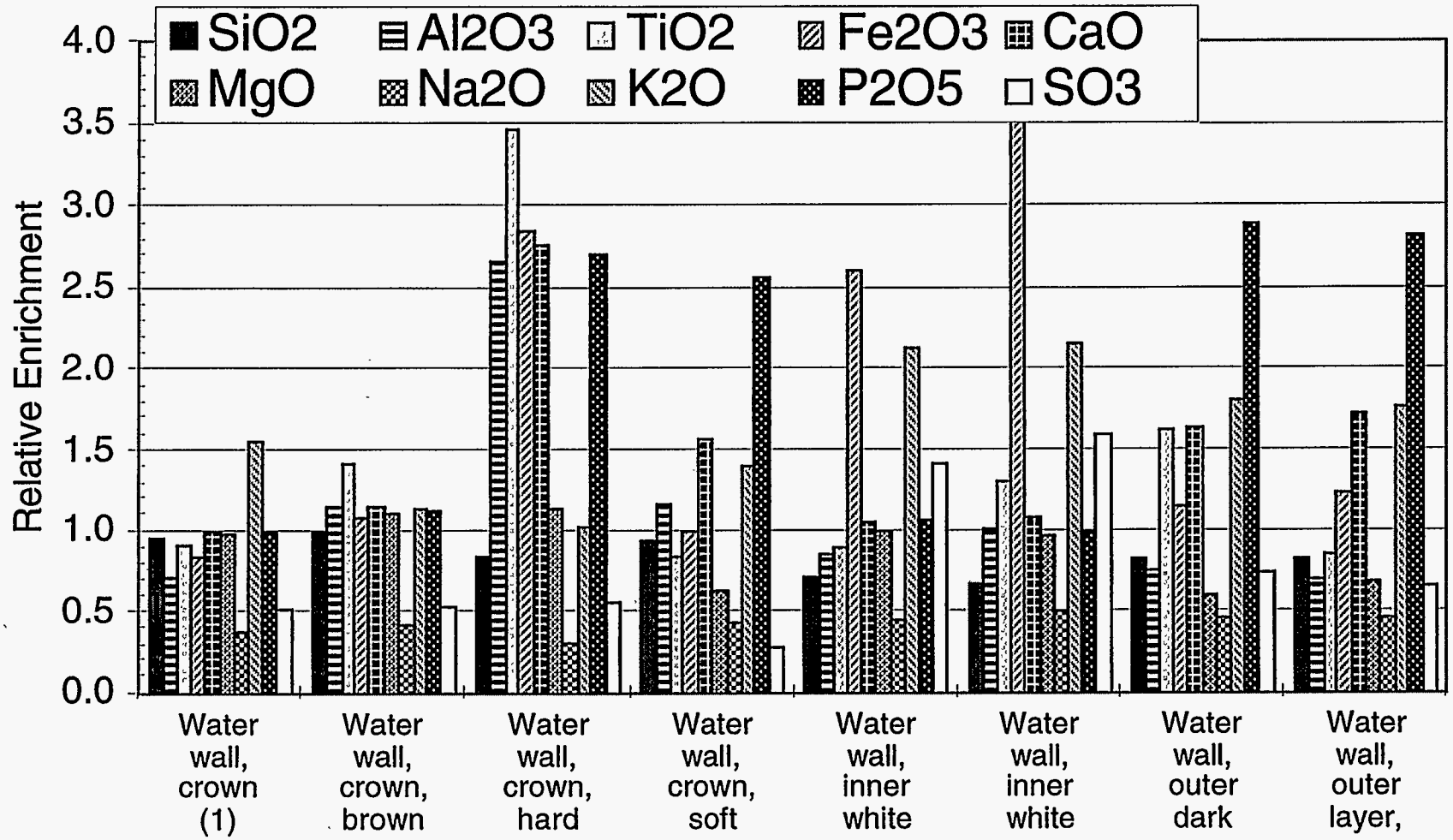

Figure 82 Relative enrichment of various deposit samples collected during MFC investigations on wheat straw (continued from Figure 81).

Switchgrass

Results for switchgrass are illustrated in Table 4 and Figure 83. Two tests were completed. The rotating horizontal probe results are shown for both. The water-wall probe and a stationary probe were utilized during one of the tests. Switchgrass, like the straws, contains high concentrations of chlorine and silicon, although its total ash content is only one quarter that of rice straw. The calcium concentration was higher than rice or wheat straw ash by a factor of 3 to 4, although this may be due to the inclusion of adventitious materials (soil), suggested by the high aluminum concentration. The presence of aluminum in quantity is typically an indicator of soil contamination because aluminum in plants is normally present at low levels.

Deposit compositions from switchgrass were in many respects similar to those from the straws, although the deposits were not segregated in the same way as for wheat straw. All contained high concentrations of silica in combination with potassium. The sulfate enrichment in the switchgrass deposits was substantially greater, however, when contrasted against the straw deposits, even though switchgrass has a sulfur concentration about one quarter that of wheat straw and roughly the same as rice straw. The sulfur enrichment was highest in the stationary horizontal probe deposit. This deposit also had the greatest potassium enrichment, nearly four times the level of the fuel ash, which in combination with the sulfur implies the presence of an alkali sulfate. The fly ash was somewhat depleted in silicon, but the undetermined fraction was high for this sample, possibly as a result of undetermined carbon. Normalizing the silica concentration in the fly ash to the total determined species yields a silica concentration of roughly 60%. The deposit collected from the top of the water-wall was not enriched in sulfur as was the stationary probe deposit, possibly indicating the instability of the potassium sulfate at furnace temperature. The furnace wall deposit, like the wall deposits from straw, was greatly depleted in sulfur.

Table 4 Inorganic composition of fuel and ash deposits generated during MFC combustion tests of switchgrass.

Sample Type	SiO2	Al2O3	TiO2	Fe2O3	CaO	MgO	Na2O	K2O	P2O5	SO3	Und
Fuel Ash	69.51	3.84	0.14	1.52	8.17	3.48	0.82	7.26	3.63	1.49	0.14
Flyash (1)	47.97	6.60	0.34	2.00	7.70	2.66	0.82	7.39	2.76	1.58	20.18
Furnace wall (1)	68.85	3.58	0.21	1.52	9.10	3.76	0.46	9.07	3.58	0.37	-0.50
Probe, rotating (1)	42.42	3.88	0.22	14.72	6.85	2.62	0.74	11.85	3.12	3.87	9.71
Probe, rotating (2)	53.92	5.45	0.33	3.31	8.16	3.10	0.59	14.10	3.64	2.72	4.68
Probe, stationary (1)	32.35	3.02	0.19	7.13	6.25	2.39	1.25	25.52	3.64	8.94	9.32
Water wall (1)	63.70	5.70	0.34	3.60	9.99	3.57	0.64	7.59	3.08	1.15	0.64
Water wall (1)	55.17	6.18	0.34	3.54	10.05	3.30	0.75	9.33	2.91	3.96	4.47

Test number indicated in parentheses. Und = undetermined.

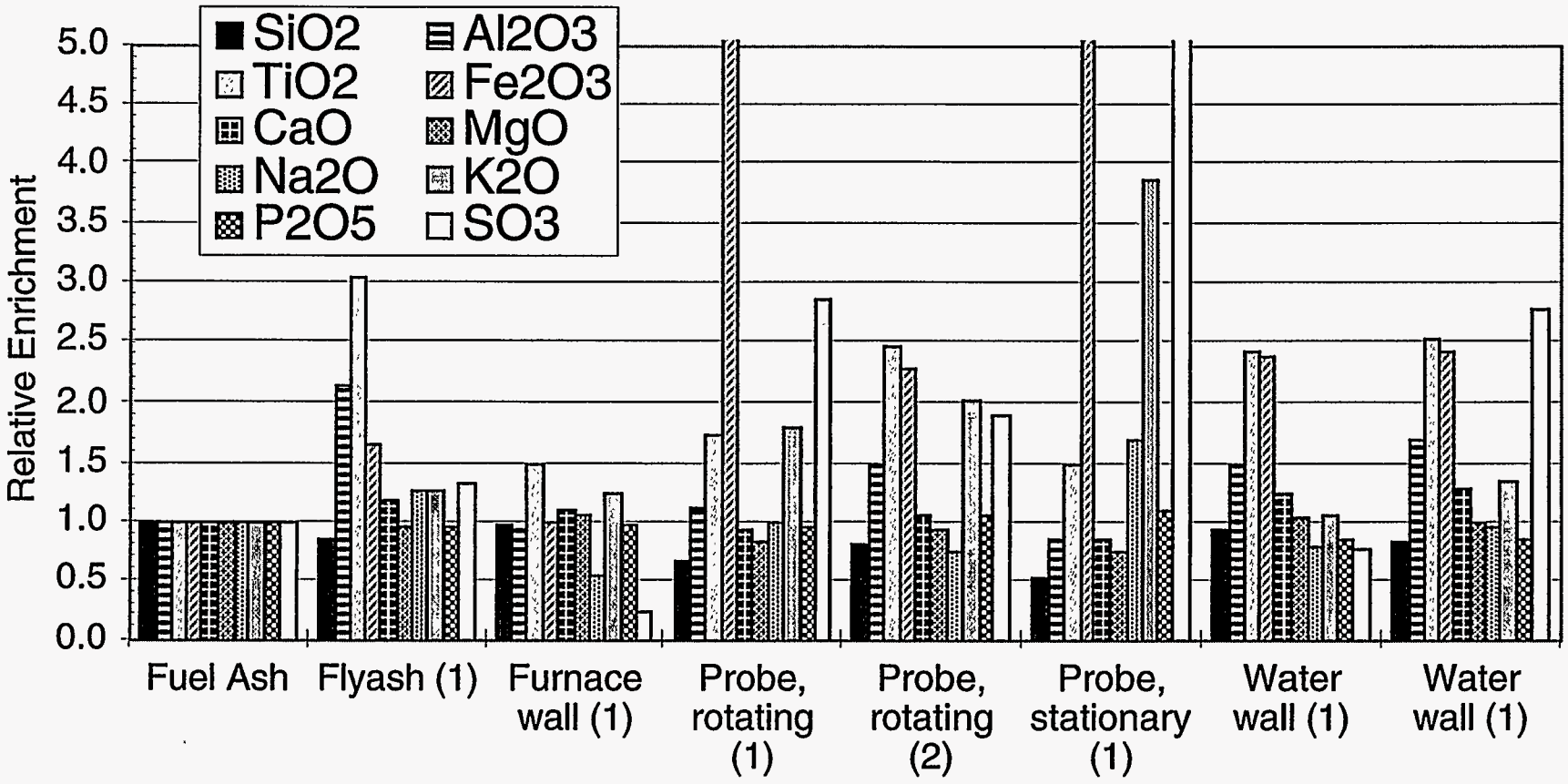

Figure 83 Relative enrichment of various deposit and fly ash samples collected during MFC investigations on switchgrass.

Condensation and the Role of Chlorine

The herbaceous materials present an opportunity for examination of the role of chlorine in formation of ash deposits. Chlorides represents among the most stable alkali-bearing species in the gas phase. Essentially all of the fuel chlorine is released early in the combustion process and much of it combines with available alkali to form alkali chloride vapors. In many cases, the amount of alkali vaporized during biomass combustion is determined more by the amount of chlorine available to form stable vapors than by the amount of alkali in the fuel. Equilibrium vapor pressures of representative materials illustrate this tendency. Figure 84 illustrates predicted equilibrium concentration of gas-phase, potassium-containing species under conditions typical of many biomass combustors. The overall stoiciometry of this calculation assumes excess air and moisture and sufficient sulfur to convert all potassium to sulfate. In terms of gas-phase chemistry, few biomass fuels contain this much sodium. (The rationale for chosing these conditions will be explained shortly). Even at these conditions of high sulfur concentration, gas-phase sulfate is seen to play a relatively minor role in potassium chemistry. Peak sulfate concentrations represent about 10 % of the total gas-phase potassium and occur at about 1100 °C. At lower temperatures, potassium sulfate vapor condenses to form liquid or solid sulfate. At higher temperatures, it decomposes.

The dominant gas-phase, potassium bearing species at flame temperatures (>1400 °C) is potassium hydroxide, followed by the chloride. In the absence of significant chlorine for reaction, only the hydroxide is present. As temperatures cool to convection-pass values (<1000 °C), hydroxides convert to chlorides, which represents the only potassium-bearing species in significant quantities. In these calculations, there is sufficient total chlorine to convert half of the potassium to chloride. The fact that nearly all of the gas-phase potassium exists as a chloride at intermediate and low temperatures indicates that chlorine is a strong controller of the total gas-phase potassium budget at these temperatures. This is verified by MBMS results, where total potassium release is measured as a function of fuel potassium content and fuel chlorine content. Figure 85 illustrates the measured correlation between fuel potassium content and total potassium released to the gas-phase as determined by the MBMS technique. The correlation is generally positive, as would be expected, but it is not linear. A better correlation, that is one that has less scatter and is more linear, is seen between released potassium and fuel chlorine contents (Figure 86). Essentially all of the chlorine in a fuel is released early in the combustion process. This chlorine has a strong influence on the amount of potassium that is found in the vapor.

The condensed-phase behavior of potassium-containing compounds is illustrated in Figure 87 as a function of temperature. In performing these calculations, we have assumed that there is sufficient sulfur to convert all of the potassium to sulfate. Most biomass fuels have less sulfur than the stoichiometric amount required for such a conversion. However, an ash deposit on a surface interacts with a continuous gas stream, providing a continuous source of sulfur. Often, the rate of accumulation of alkali in the deposit is slow compared to the rate of diffusion of sulfur from the bulk gas stream to the deposit surface. Under these conditions, the deposit has opportunity to react with a much larger amount of sulfur than the elemental composition of the fuel may suggest. We

also intended to illustrate that sulfates are the preferred condensed-phase species, even in the presence of abundant chlorine and carbon dioxide.

As illustrated in the figure, sulfur is completely converted to sulfate at the low temperatures, even though there are ample reactants to form carbonates and chlorides. If there is less sulfur in the gas phase than is required to convert all of the alkali to sulfate, chlorides and carbonates form, in that order. The laboratory data and the field data reflect these trends

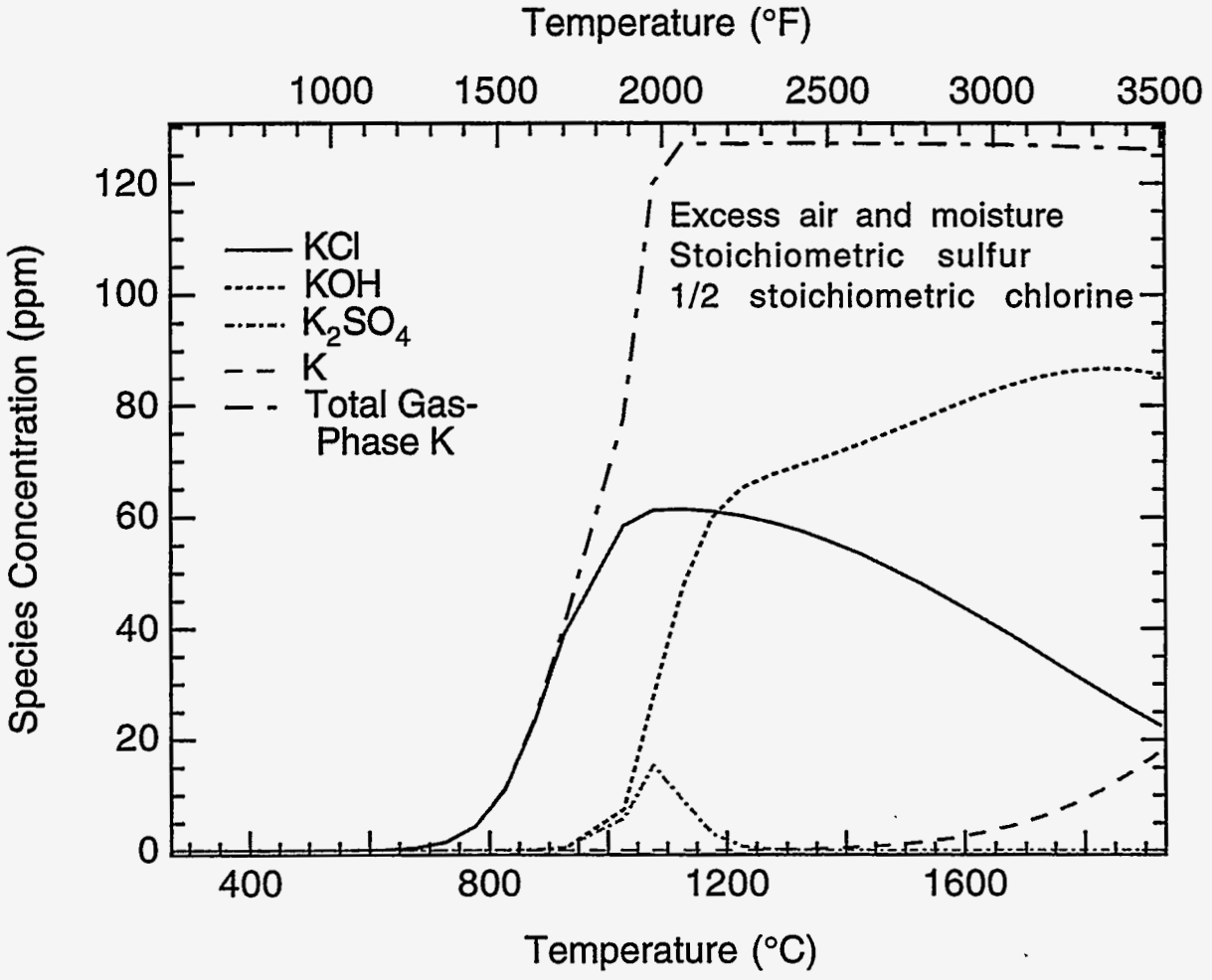

Figure 84 Equilibrium species concentrations for the major potassium-containing, gas-phase species present under typical biomass combustion conditions. Compare with condensed-phase behavior illustrated in Figure 87.

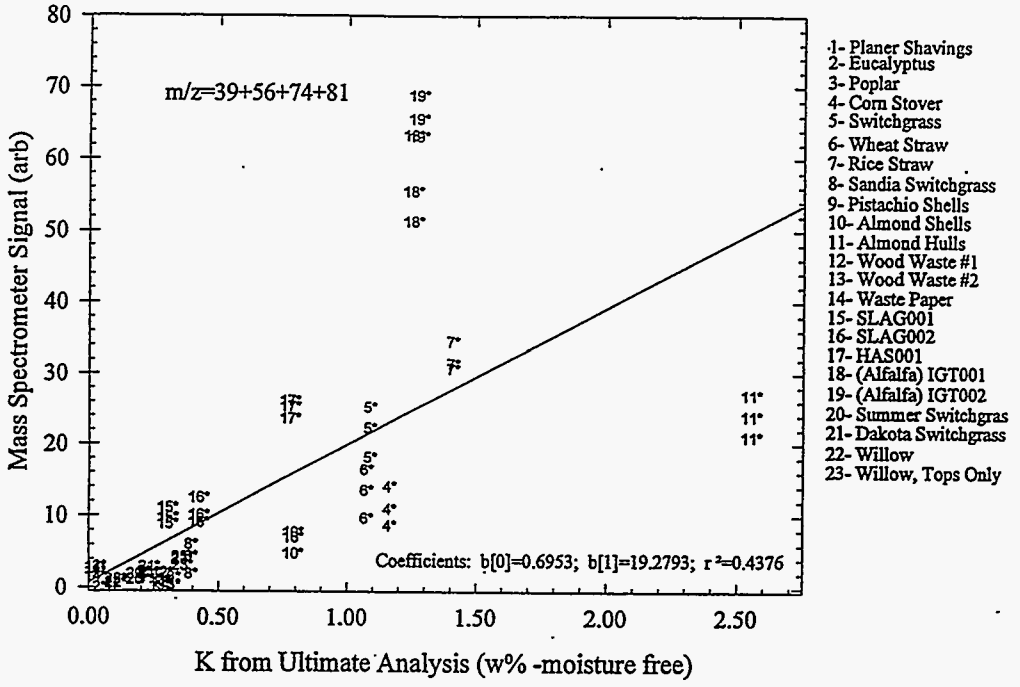

Figure 85 Correlation between fuel potassium content and total potassium released to the gas-phase as determined by the MBMS technique. Compare with Figure 86.

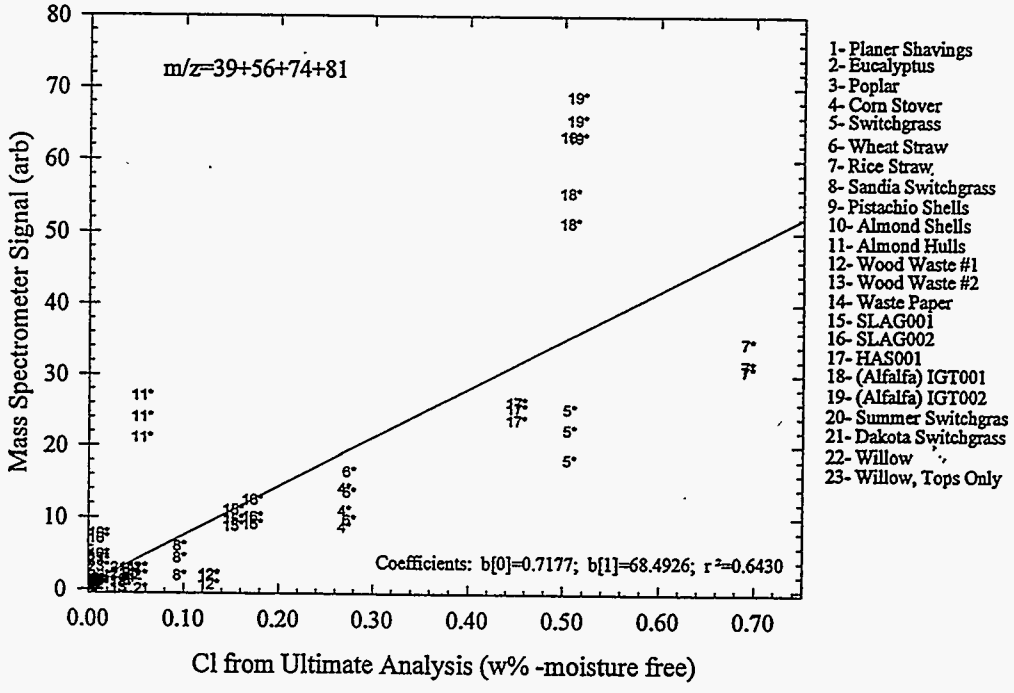

Figure 86 Correlation between fuel chlorine content and total potassium released to the gas-phase as determined by the MBMS technique. Compare with Figure 85.

The sample illustrated in Figure 78 was deposited on a relatively hot, ceramic surface. On cooler surfaces, alkali condensation is more rapid. An example of deposit formation on cool surfaces is illustrated by scanning electron micrographs in Figure 88 and Figure 89. These wheat straw deposits were collected from a carbon steel, air-cooled (surface temperature = 370 °C), sampling probe in the test section of the MFC. Figure 88 illustrates the portion of the deposit directly on the tube surface, shown in greater detail in Figure 89.

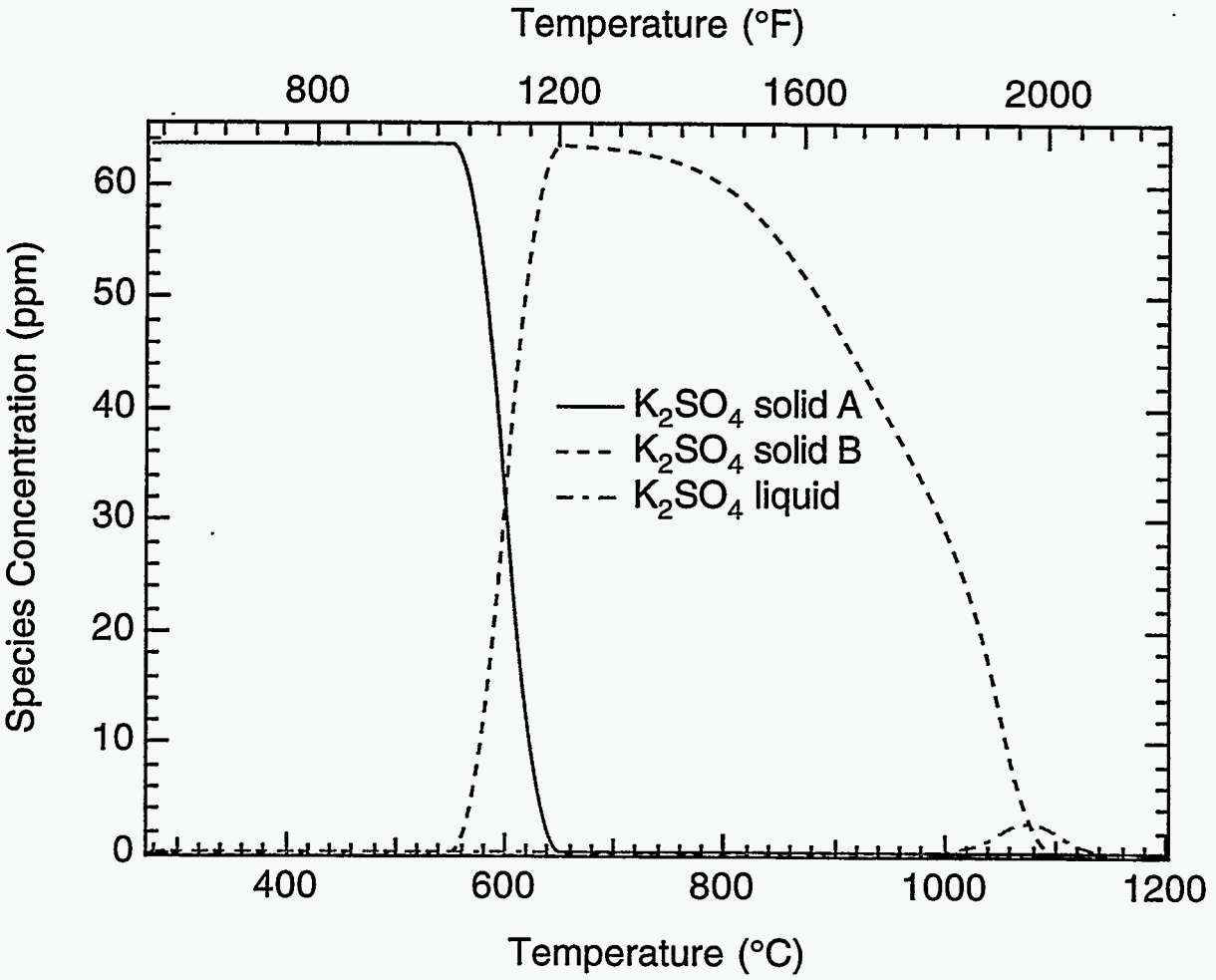

Figure 87 Condensed-phase equilibrium behavior of potassium-containing species as a function of temperature under conditions similar to those in many biomass boilers. Compare with gas-phase behavior illustrated in Figure 84.

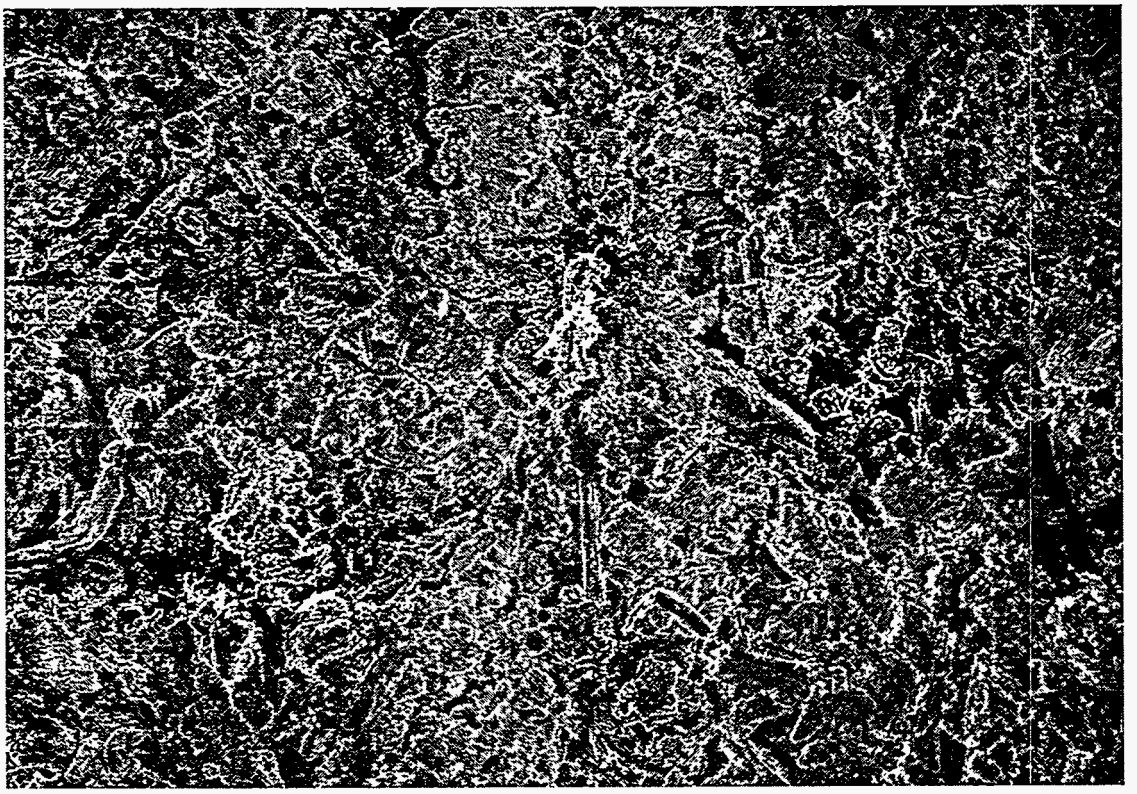

Figure 88 Scanning electron micrograph of a portion of a rice straw deposit collected from a metallic surface in the MFC. This surface is the section of the deposit adjacent to the deposition probe. More detail is illustrated in Figure 89.

The chemical compositions of the interface region and the bulk deposit differ in that the interface contains approximately 25 to 30 % higher amounts of chlorine and potassium than the bulk of the deposit. These observations illustrate additional aspects of deposit formation. Vapors condense on cool surfaces as they respond to the thermal boundary layer. In these experiments, inorganic vapors are dominated by alkali-containing species. In the presence of hydrogen, oxygen, and halides (chlorine), the predominant form of the alkali vapors include chlorines, hydroxides, and oxides. Thermodynamics favors chlorides under most combustion conditions if chlorine is available in the gas. In the absence of chlorine, hydroxides are favored. In the absence of hydrogen, oxides form. At low temperatures, sulfates are thermodynamically favored. Alkali sulfates decompose at combustion temperatures.

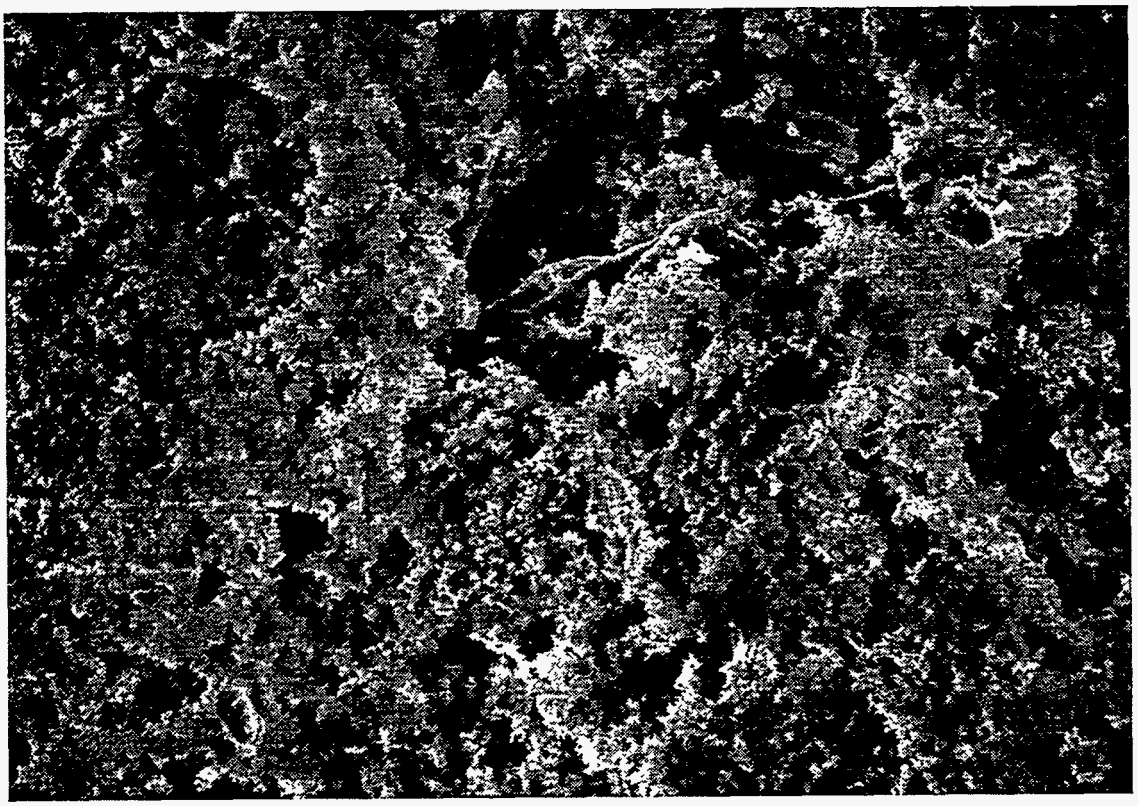

Figure 89 Scanning electron micrograph of a portion of a rice straw deposit collected from a metallic surface in the MFC. This surface is the section of the deposit adjacent to the deposition probe. The flat layers of condensate can be seen in the foreground, with the bulk deposit in the background.

As an ash deposit develops, the deposit surface temperature increases (tube surface temperature is constant). Potassium and chlorine condense most rapidly on the relatively cool probe surface. As the deposit develops, its surface temperature approaches the gas temperature. This increase in surface temperature causes a decrease in the rate of condensation but little change in the rate of inertial impaction. Rates of thermophoresis, which also decrease with a rise in surface temperature, are small compared to those of inertial impaction. This produces the observed decrease in potassium and chlorine concentrations (materials that condense) with increasing deposit thickness.

Shells, Pits, and Hulls (Ligneous Fuels)

Almond Shells

Fuel ash, fly ash, and deposit compositions from an MFC test with almond shells are listed in Table 5, with relative concentration ratios (normalized to the determined fraction) illustrated in Figure 90. Almond shells, as with almond hulls, are distinctive in their high potassium concentrations in the ash (Figure 7). K_2O accounted for almost half the fuel ash. Unlike the straws and grass, the silica concentration in almond shell ash was low, about 10%. Calcium and phosphorous were the other major constituents of shell ash. The chlorine concentration was low at 0.03% of dry fuel, whereas the ash sulfate concentration was not substantially different from rice straw or switchgrass.

Two tests with almond shells were conducted using all three probes. Fly ash samples were segregated into coarse particles collected loose in the filter holder and representing partially reacted fuel particles, and a fine fraction collected on the filter. The analytical results were combined on the basis of the respective sample weights to give an average fly ash composition. Loose particles were also collected on the horizontal surfaces of the water-wall probe, and a lightly sintered deposit formed on the top of this probe. The undetermined fractions were very high in almost all cases, almost certainly as the result of large amounts of unburned carbon. Based on the determined fraction only, the silica concentration of the coarse fly ash was in excess of 30%. The coarse particles collected on the water-wall probe, as well as the crown deposit collected on this probe, also showed elevated silica concentrations. Sulfate in the fine fly ash fraction was enriched over that in the coarse fly ash fraction, possibly due to sulfate condensing on the filter.

The initial deposits were gray-white in color, but brightened over time, and all were fine textured. A few partially burned, carbon containing fuel particles adhered to the deposit after impact, and may account for some of the undetermined fraction in these deposits. The deposit potassium and sulfur concentrations were not particularly enriched relative to the fuel, and potassium continued to make up the majority of the deposit mass. Ca, Mg, Na, and P were all depleted in the deposits relative to the fuel. The mass ratio of K_2O to SO_3 is consistently on the order of 20, and well in excess of the equivalent mass ratio for potassium sulfate (2.35). The contribution from chlorine in this case is unknown, but is in insufficient concentration in the fuel to account for the residual potassium as KCl. In the absence of sufficient sulfur and chlorine, the potassium may have deposited as a hydroxide or carbonate. The crown deposit on the water-wall probe was quite similar in composition to the fuel ash.

Table 5 Inorganic composition of fuel and ash deposits generated during MFC combustion tests of almond shells.

Sample Type	SiO2	Al2O3	TiO2	Fe2O3	CaO	MgO	Na2O	K2O	P2O5	SO3	Und
Fuel Ash	9.82	2.44	0.10	2.46	11.95	4.35	1.61	44.72	6.52	1.41	14.63
Coarse Flyash	4.15	0.93	0.03	0.34	1.07	0.25	0.23	5.91	0.30	0.10	86.70
Fine Flyash	14.11	6.93	0.37	2.27	4.85	1.72	0.85	30.04	2.11	2.56	34.22
Combined Flyash	6.14	2.13	0.10	0.73	1.83	0.54	0.35	10.74	0.66	0.59	76.20
Probe, rotating (1)	4.24	1.10	0.05	1.70	3.88	1.47	0.75	46.07	2.36	2.16	36.22
Probe, rotating (2)	5.06	1.27	0.07	2.00	4.22	1.69	0.93	53.46	2.85	1.91	26.54
Probe, stationary (1)	6.61	1.82	0.11	6.92	4.97	1.85	0.69	34.92	2.78	1.86	37.47
Probe, stationary (2)	2.72	0.76	0.06	1.15	3.19	1.28	0.83	53.92	2.17	1.94	31.98
Water wall, crown (2)	11.75	3.76	0.16	3.46	11.87	4.43	1.11	33.63	6.29	1.36	22.18
Water wall, loose particles (2)	12.73	3.32	0.17	3.91	8.76	3.42	0.85	32.61	4.77	0.75	28.71
Water wall, loose particles, back (2)	20.97	4.93	0.24	2.91	7.53	2.49	0.94	21.37	2.92	0.74	34.96
Water wall, surface (1)	5.82	1.53	0.07	6.02	7.49	2.58	0.69	35.64	3.59	2.43	34.14
Water wall, surface (2)	3.18	1.04	0.06	2.80	5.85	2.04	0.86	50.40	3.03	2.41	28.33

Test number indicated in parentheses. Und = undetermined.

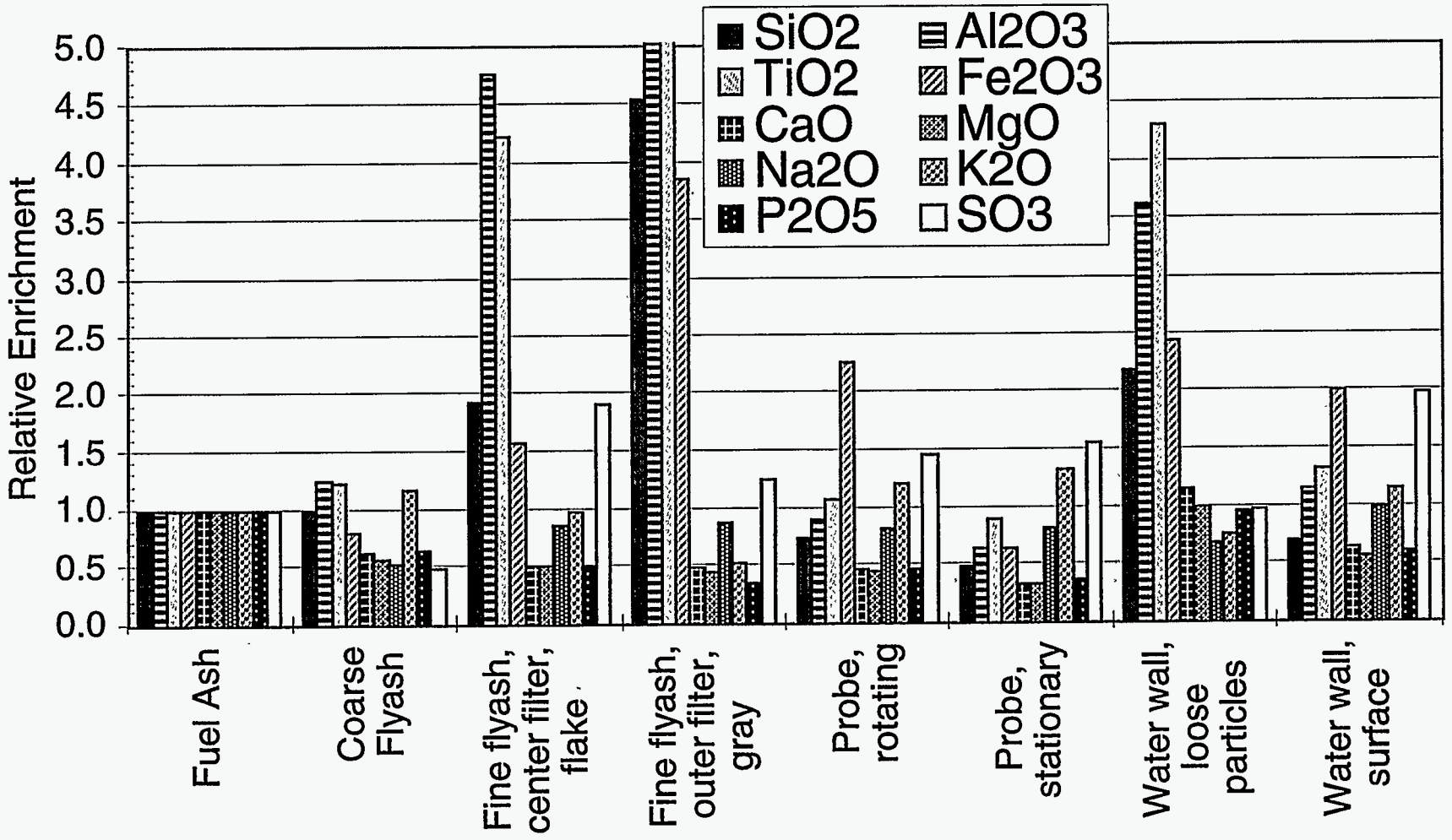

Figure 90 Relative enrichment of various deposit and fly ash samples collected during MFC investigations on almond shells.

Almond Hulls

The characteristics of the almond hull deposits (Table 6 and Figure 91) were similar to those for almond shell. Potassium accounted for more than half the fuel ash, with total ash and chlorine concentrations twice those for shell. The initial deposit was again gray-white in color, indicating the presence of carbon, but brightened to a brilliant white after approximately 3 h and remained so for the remainder of the experiment. The deposit was fine textured throughout, with a superficial coating of partially reacted fuel particles sticking after impact. The deposit enrichment ratios for potassium and sulfur were quite similar to those for almond shell, again suggesting the presence of potassium hydroxide or carbonate on the probe surfaces. The fly ash collected on the filter surface showed a distinct segregation by color and texture, with the center portion having a brighter tint and flake-like appearance compared to the gray, powdery outer deposit. The outer portion had substantially higher silica and iron concentrations, but a lower undetermined fraction suggesting unreacted carbon was not the reason for the difference in color.

Olive Pits

Olive pits had a uniquely high sodium concentration as a result of the olive processing. Pits had moderate chlorine (0.08%), and a low total ash content (Figure 7). The silica concentration in the ash was also moderate, but the potassium concentration was very low, likely as a result of leaching during processing. The deposit and fly ash compositions are included in Table 7 and Figure 92. The deposits were enriched in both potassium and sulfur, and depleted in sodium compared to the fuel. All analyses had high undetermined fractions, again the likely result of undetermined carbon. Sodium, although somewhat depleted relative to the fuel, was still the predominant alkali species present in the deposits. The total sulfur and chlorine in the fuel would account for roughly 30% of fuel sodium if present as sulfate and chloride, again suggesting the possible presence of hydroxides or carbonates.

Wood and Commercial Fuels

The results for the commercial wood and almond shell blend are listed in Table 8 and the concentration ratios illustrated in Figure 93. This fuel had high silicon and aluminum concentrations due to the inclusion of soil contaminants, which is typical for power plant fuels of this type. The chlorine concentration was quite low at 0.03%. The fuel had a moderate total ash content, with low alkali and moderate calcium concentrations.

A visible deposit developed within 2 min after starting, white in color, fine textured, and sticky as larger particles could be seen to adhere to it after impact. The color darkened somewhat over the course of the test, developing a grayish cast, but the deposit thickness did not develop as fast as with straw and the deposit remained fine textured. Relative to the fuel, the deposit composition showed little enrichment except in potassium and sulfur. The greatest enrichment occurred on the stationary horizontal probe, and at intermediate enrichment on the vertical face of the water-wall probe. Partially burned fuel particles collected loose on the water-wall were depleted in sulfur, but the fly ash overall was not. The ratio $(CaO+Na_2O+K_2O)/SO_3$ in the deposits is generally consistent with the deposition of these elements as sulfates, particularly in the case of the stationary horizontal probe.

Table 6 Inorganic composition of fuel and ash deposits generated during MFC combustion tests of almond hulls.

Sample Type	SiO2	Al2O3	TiO2	Fe2O3	CaO	MgO	Na2O	K2O	P2O5	SO3	Und
Fuel Ash	6.03	1.28	0.07	0.83	8.66	5.01	0.99	53.60	7.33	1.46	14.74
Coarse Flyash	1.39	0.37	0.02	0.15	1.23	0.66	0.12	14.48	1.06	0.16	80.36
Fine flyash, center filter, flake	8.27	4.32	0.21	0.93	3.17	1.78	0.61	36.47	2.62	1.99	39.63
Fine flyash, outer filter, gray	23.15	12.06	0.58	2.71	3.42	1.84	0.74	23.65	2.19	1.54	28.12
Probe, rotating	2.97	0.77	0.05	1.26	2.61	1.45	0.54	43.75	2.25	1.43	42.92
Probe, stationary	2.33	0.65	0.05	0.42	2.34	1.36	0.64	56.47	2.12	1.84	31.78
Water wall, loose particles	12.28	4.29	0.28	1.88	9.24	4.63	0.63	37.98	6.43	1.30	21.06
Water wall, surface	3.68	1.27	0.08	1.44	4.71	2.46	0.85	52.55	3.82	2.50	26.64

Und = undetermined.

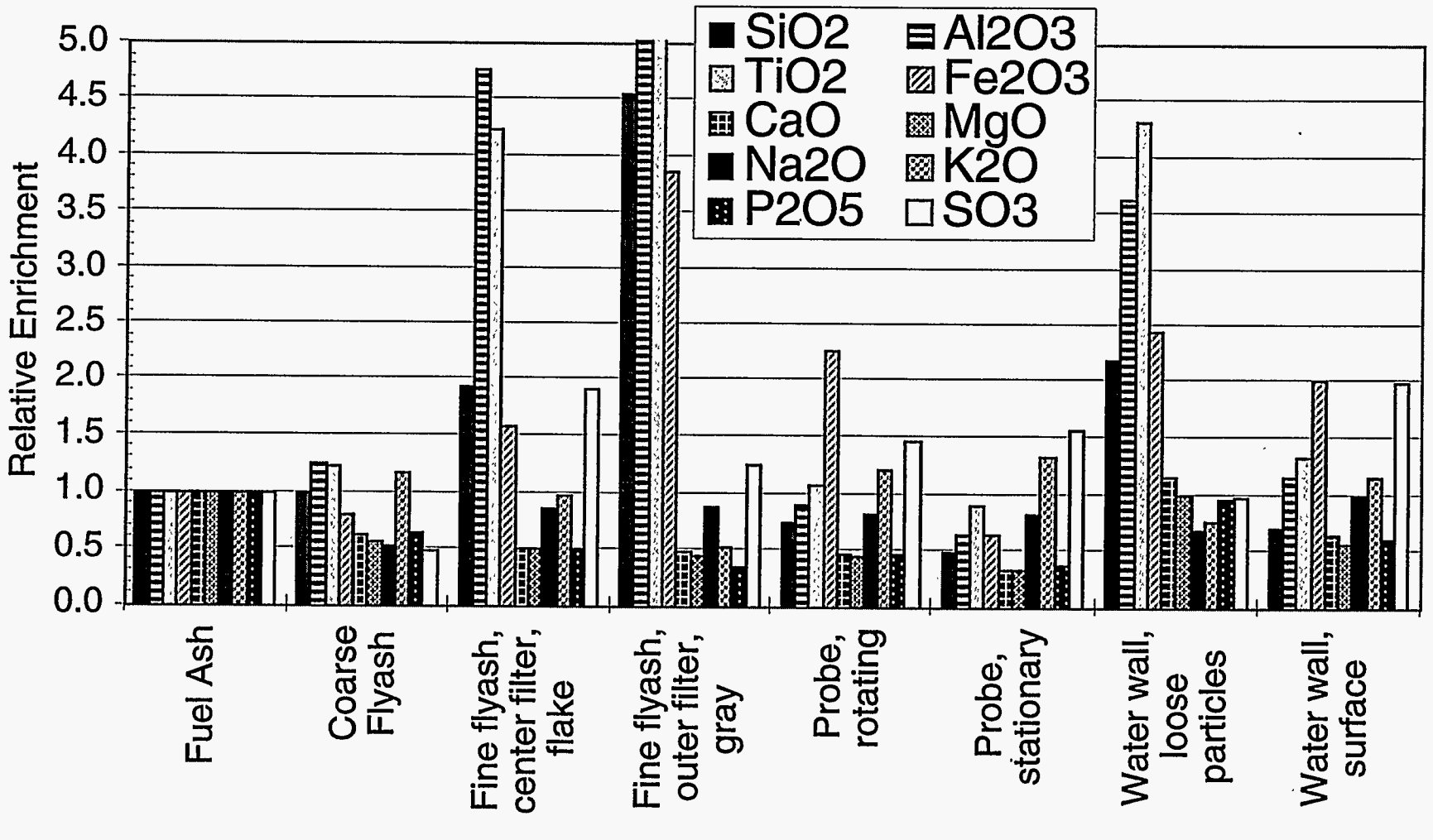

Figure 91 Relative enrichment of various deposit and fly ash samples collected during MFC investigations on almond hulls.

Table 7 Inorganic composition of fuel and ash deposits generated during MFC combustion tests of olive pits.

Sample Type	SiO2	Al2O3	TiO2	Fe2O3	CaO	MgO	Na2O	K2O	P2O5	SO3	Und
Fuel Ash	31.47	6.45	0.31	6.97	13.66	4.48	27.43	1.77	3.34	1.98	2.12
Flyash	4.12	2.62	0.16	1.76	5.25	1.15	2.54	0.64	0.50	1.53	79.73
Probe, rotating	13.14	3.16	0.17	12.37	8.15	2.68	21.20	7.31	2.73	7.36	21.73
Probe, stationary	18.78	4.56	0.23	13.93	10.06	3.23	18.25	5.73	3.20	5.91	16.12
Water wall	32.62	6.59	0.33	11.09	6.69	2.09	11.29	4.46	1.24	4.07	19.53

Und = undetermined.

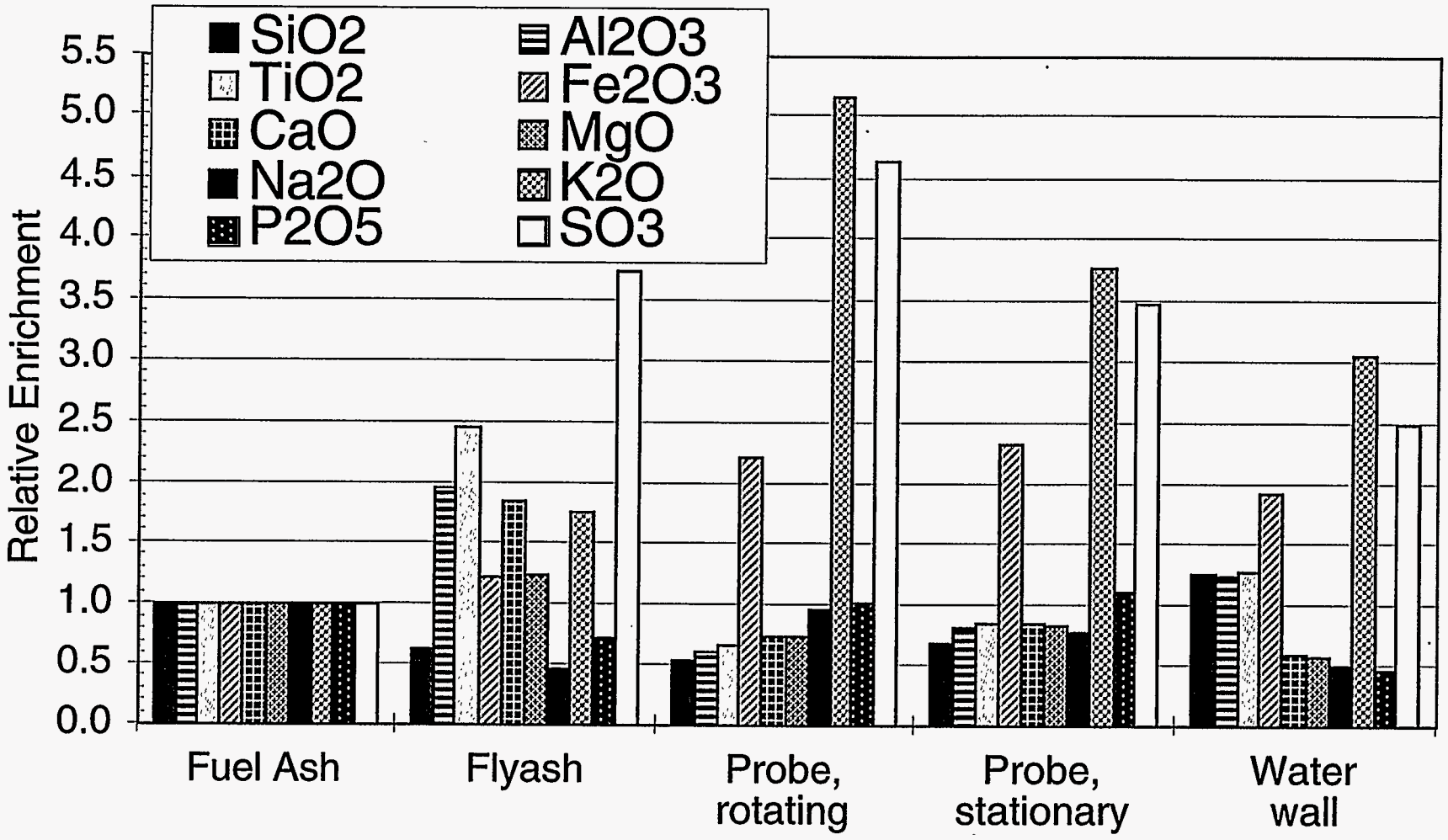

Figure 92 Relative enrichment of various deposit and fly ash samples collected during MFC investigations on olive pits.

Table 8 Inorganic composition of fuel and ash deposits generated during MFC combustion tests of wood/almond shell blend.

Sample Type	SiO2	Al2O3	TiO2	Fe2O3	CaO	MgO	Na2O	K2O	P2O5	SO3	Und
Fuel Ash	55.69	10.75	0.52	4.72	14.04	3.01	2.17	4.39	1.54	1.11	2.06
Flyash	35.61	11.97	0.63	3.86	10.49	2.03	1.51	5.73	0.99	1.68	25.50
Probe, rotating	50.56	11.19	0.53	8.34	10.10	2.83	2.69	7.87	1.67	3.76	0.46
Probe, stationary	42.88	9.54	0.49	7.68	11.97	3.02	2.48	11.40	1.94	6.29	2.31
Water wall, surface	42.79	9.90	0.44	4.30	16.09	3.29	2.40	9.83	1.96	4.56	4.44
Water wall, loose particles	63.44	12.05	0.54	4.13	8.33	1.86	2.56	3.92	0.71	0.45	2.01

Und = undetermined.

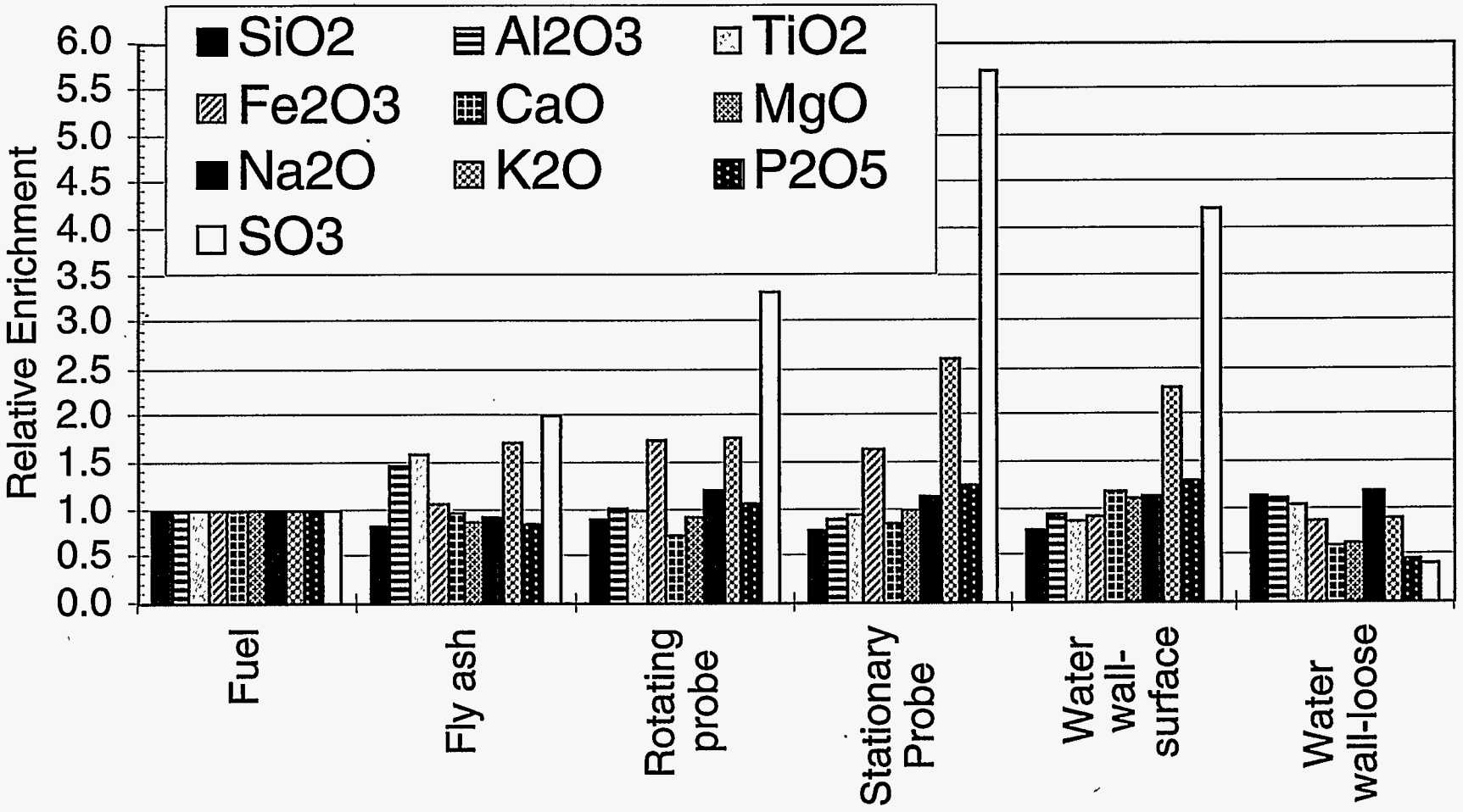

Figure 93 Relative enrichment of various deposit and fly ash samples collected during MFC investigations on wood/almond shell blend.

Commercial-Scale Deposition Results

Host Sites

Each of the industrial sponsors of the Alkali Deposits Investigation that operates a power generating station was a potential host site for a field test. The locations, names, and types of boilers at each of these seven industrial sponsor's sites are indicated in Figure 94. Field tests were not conducted at Wheelabrator.

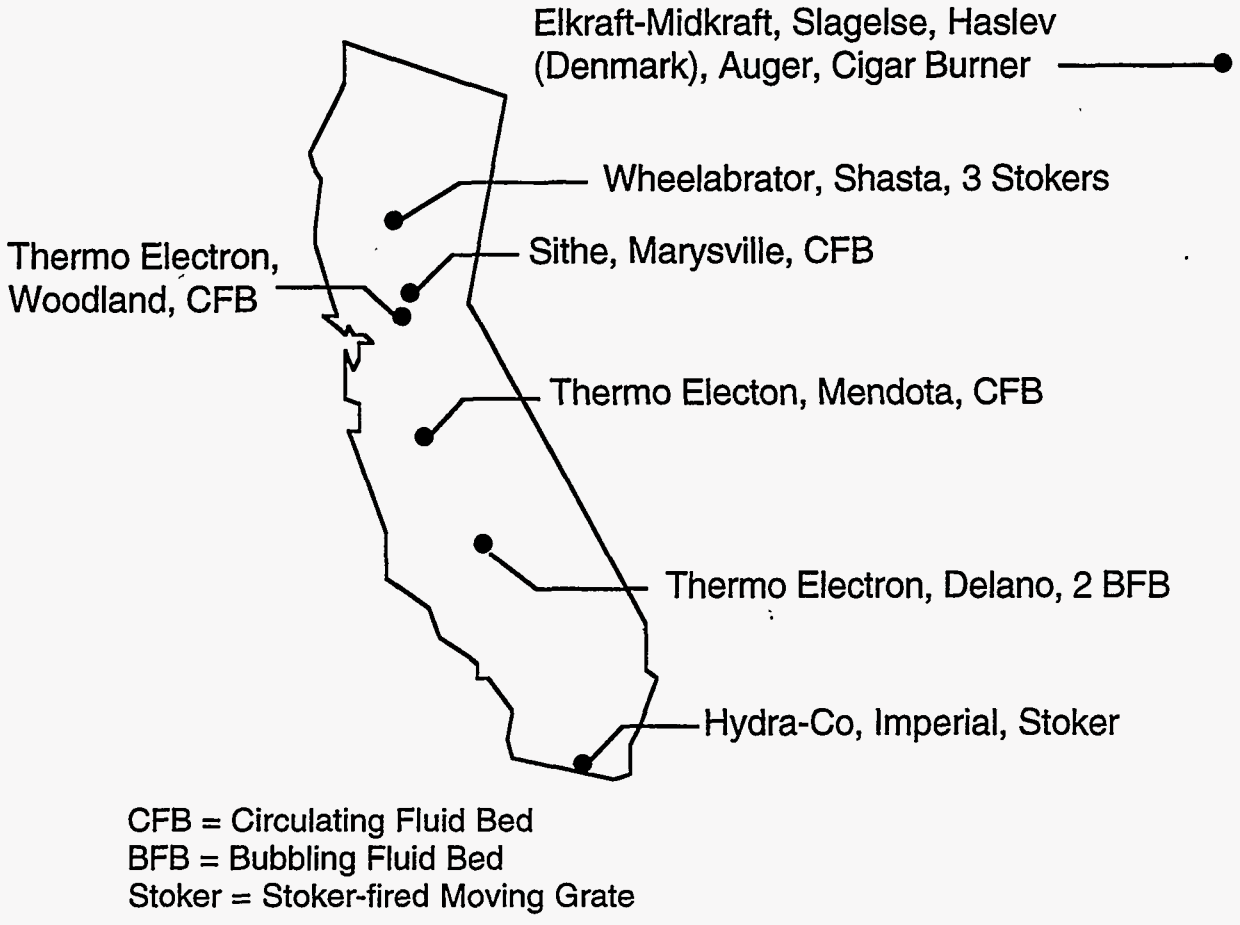

Figure 94 Diagram of the locations, names, boiler designs, and owners of the biomass power plants involved in this project. Details of boiler design and operation are provided in Figure 94.

Figure 95 presents the schedule of the commercial test burns conducted during this project. Danish tests were conducted at two sites, Slagelse and Haslev, under the direction of Erik Winther of Elkraft, an industrial sponsor of the Alkali Deposits Investigation. Some samples and data were collected by Thomas R. Miles Jr. during a personal visit to the Danish sites. All deposit analyses from the commercial tests were performed by Hazen Research Inc. for the Alkali Deposits Investigation. This report focuses on Hydra-Co, the Danish results and the results from Sithe, Woodland, and Delano. Data from the Hydra-Co (1992) and Mendota tests were reported earlier. Hydra-Co (Dec. 1992, March 1993).

Field Tests

Hydraco:	12/92, <15 % wheat straw (≈2% Cl) and wood
	3/93 20% wheat straw (≈0.2% Cl) and wood
Haslev:	10/93
Slagelse:	9/93
Mendota:	1-14-93 to 4-10-93, deposit samples collected 4-12-93 by plant personnel
Delano:	6-17-93 to 7-1-93, samples collected 7-10-93, boiler cleaned
	7-11-93 to 9-3-93, samples collected 9-4-93
Woodland:	5-1-93 to 9-6-93, samples collected 9-7-93
Marysville:	4-22-93 to 5-26-93, samples collected 5-30-93

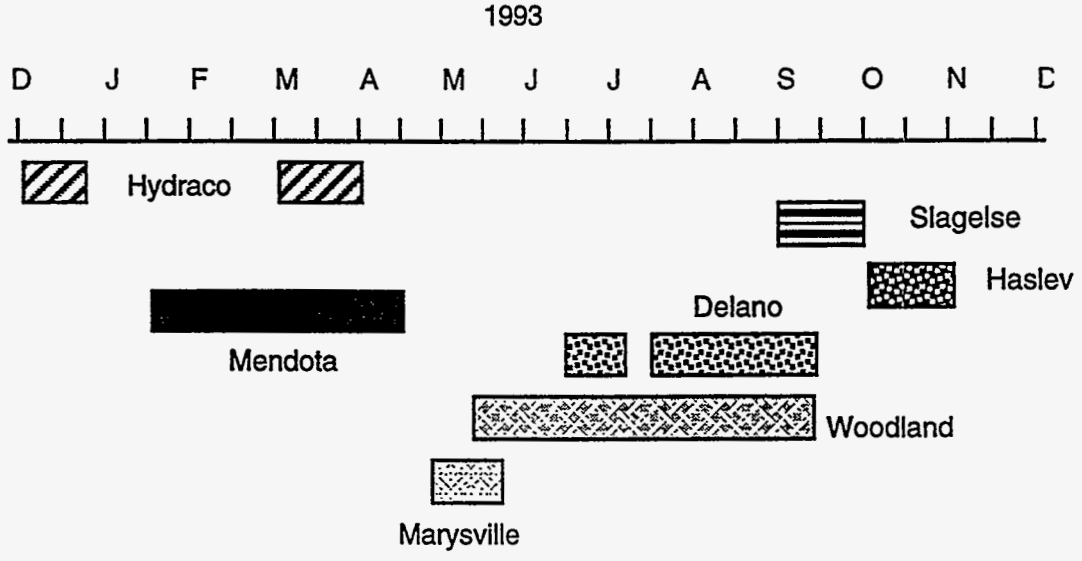

Figure 95 Schedule of field tests conducted during this project.

Investigations were conducted at 7 different commercial biomass power stations. Three of the boilers employed grate-type furnaces, one was a bubbling fluidized bed, and three were circulating fluidized beds. The plants ranged in capacity from 5 to 25 MW_e. Two of the grate units were located in Denmark and fired straw, principally wheat straw. All other boilers were located in California.

Fuel supplies for all of the units vary with season and availability. During these tests, Hydra-Co (grate-fired) fired a mixture of wood (80%) blended with wheat straw (20%). The bubbling fluidized bed unit (Delano) fired a blend of 60% urban wood fuel, 37% agricultural wood, and 3% almond shell. One of the circulating fluidized beds (Mendota) fired a blend of wood (from urban and agricultural sources) with 6% almond shell, another (Sithe) fired a blend of sawdust with 20% pits, shells, and hulls in varying concentrations, and Woodland fired a variable blend based on wood with additions of pits and shells. For Woodland, composite fuel samples were collected during each week and analyzed only for chlorine, sulfur, and water soluble calcium, potassium, and sodium.

The essential configurations of the boilers are similar, with water-wall furnaces followed by cross-flow superheaters, economizers, and air-heaters in the convection passes. The circulating fluidized beds are distinctive in the inclusion of particle separation devices at the furnace exit for the purposes of recirculating bed material and partially burned fuel back to the bed. Woodland and Mendota are identical designs of identical capacity, and utilize twin cyclones for particle separation. Sithe utilized a series of cross-flow impaction surfaces (U-tubes) to disengage particles from the furnace exit flow. A more important distinction lies in the folded furnace design of the two Danish units, by which the furnace section is extended and the gas temperatures ahead of the cross-flow superheaters reduced substantially compared to the California units.

Deposits were collected following routine operation of the boilers for periods of up to 4 months. Fuel and ash samples were collected throughout the experiments. For the purposes of conducting the investigation, an attempt was made by the operators of Mendota and Delano to maintain the fuel composition reasonably constant. The fuel composition for Hydra-Co was strictly controlled. Fuel mix was adjusted routinely for the other facilities. As a result of firing only straw, the fuel compositions for Haslev and Slagelse were essentially fixed. The greatest variability in fuel mix occurred with Mendota. Sithe was operated on an intermittent basis, running at peak capacity under utility dispatch, and curtailed off-peak. The other facilities were all operated at or near their peak capacities.

Results of deposit composition assays are described here for the purposes of direct interpretation and comparison with the results from the laboratory experiments. As shown later, laboratory results, although from tests of much shorter duration and with only general similarity in combustion and flow conditions to the full-scale boilers, appear to be consistent when interpreted in light of the major mechanisms proposed for the formation of fouling deposits. Extensive details of the full-scale experiments will be reported later.

Table 9 provides general operation, design, and location information for each of the industri facilities involved in these investigations. Since this project began, several corporate changes ha occurred.

Table 9 General information on commercial boilers involved in this investigation.

Name	Delano	Haslev	Hydra-Co	Mendota	Sithe	Slagelse	Wheelabrator	Woodland
Boiler Type	Bubbling Fluid Bed	Auger-fed Grate	Stoker-fired Grate	Circulating Fluid Bed	Circulating Fluid Bed	Cigar-burner-fed Grate	Stoker-fired Grate	Circulating Fluid Bed
Gross Generating Capacity MWe (MWt for cogen plants)	27	5 (13)	20	28	18	12 (28)	55	28
Steam Flow metric t/h	116	26	84	118	77	40	82x3	118
1000 lb/h	256	57	185	260	170	88	180x3	260
Steam Pressure kPa	9308	6701	6378	6240	6206	6701	6206	6240
psi	1350	972	925	905	900	972	900	905
Steam Temperature °C	513	450	421	454	482	450	485	482
°F	955	842	790	849	900	842	905	900
Furnace Exit Gas Temperature °C	960	760	850	882	900	640	650-816	882
°F	1760	1400	1562	1620	1652	1184	1200-1500	1620
Fuel Consumption metric t/h	30	6	22	30	22	8	80	30
1000 lb/h	66	13	48	66	48	18	176	66
Fuel Type	uwf, ag prunings	straw	uwf, straw	wood, ag nuts, shells	uwf, ag	straw	wood, nonrecylable paper	uwf, ag fuel
Location	Delano	Denmark	Imperial	Mendota	Marysville	Denmark	Shasta, CA	Woodland
Operator	Delano Energy Co., Inc. (Thermo Ecotek)	Elkraft-Midkraft	CMS Generation Operating Co. (Imperial Resource Recovery)	Mendota Biomass Power, Ltd. (Thermo Ecotek)	Sithe Energies, Inc. (shut down)	Elkraft-Midkraft	Wheelabrator Shasta & Hudson Energy Co.	Woodland Biomass Power, Ltd. (Thermo Ecotek)

uwf = urban wood fuel (demolition wood, yard clippings, tree trimmings etc.)
ag = agricultural

The facility at Sithe is presently closed. Hydra-Co was bought by CMS Generation Operating Co. Thermo Electron, which was involved with Delano, Mendota, and Woodland, underwent restructuring. These three plants are now partners with Thermo Eko, a subsidiary of Thermo Electron. The investigation involved facilities of diverse designs (bubbling fluid beds, circulating fluid beds, stoker-fired grates, auger-fed grates, and cigar-burner-fed grates), diverse sizes (5-50 MW_e, with most approximately 20 MW_e), a range of operating conditions (furnace exit gas temperatures range from 640 to 960 °C), and diverse fuel types (wood, straw, agricultural wastes, etc.).

The operators of the facilities cooperated in supplying samples for analysis, providing access to most of the boilers before and after test burns, helping finance the project, and reviewing progress and results during the project. Plant personnel cooperated in interpreting results and providing historical perspectives on plant operation. All of the field tests were done within the context and budget of normal plant operation. As is typical for commercial tests, characterization of the feed stream and of specific operating parameters during a test was done on a best-effort basis, with some gaps in the data.

Hydra-Co

Field tests were performed in an 18 MW_e (gross), stoker-fired traveling grate combustor (Figure 96). The stoker has a split grate, the top of which travels toward the stokers (to the left in the left view and toward the reader in the right view). Field tests on wood fuel alone and on a 20%-straw-80%-wood blend were conducted. During the wood tests, fouling and slagging deposits were observed but were manageable by standard practices. The flame structure indicated in the figure is representative of conditions while burning the straw-wood blend. Operations with wood alone result in a flame that extends to approximately half the distance from the grate to the slag screen (half the size of the straw-wood flame). Particle mechanics and aerodynamics of the stokers and the furnace contribute to the increase in flame height during straw combustion. A significant fraction of the straw is entrained in the gas before it reaches the grate because of its low density. The entrained portion of the straw burns in suspension, creating a larger luminous flame.

Field tests were conducted with a blend of urban wood fuel and wheat straw. The characteristics of the individual fuels and of the blend fired during the field tests were also previously discussed. The wheat straw used in the Hydra-Co tests was specially procured based on its abnormally low chlorine content. The analyses of the two components of the fuel and the fuel blend are presented in Table 10. Also shown is a calculated composition of the blend based on the approximate 20 % straw by mass blend ratio. The computed and measured properties generally are in good agreement. The nature of the fuels, fuel handling systems, and the scale of the operation provide greater opportunities for contamination with extraneous materials than in the laboratory test data. Sources of these extraneous inorganics, sometimes referred to as adventitious material, include residual building material (wall board, nails, etc.), and soil. This is a primary reason that the wood ash is significantly higher than the 0.5 to 2 % ash typically reported as the inherent ash content of woods (Atkins & Donovan, 1993; Jenkins, 1989).

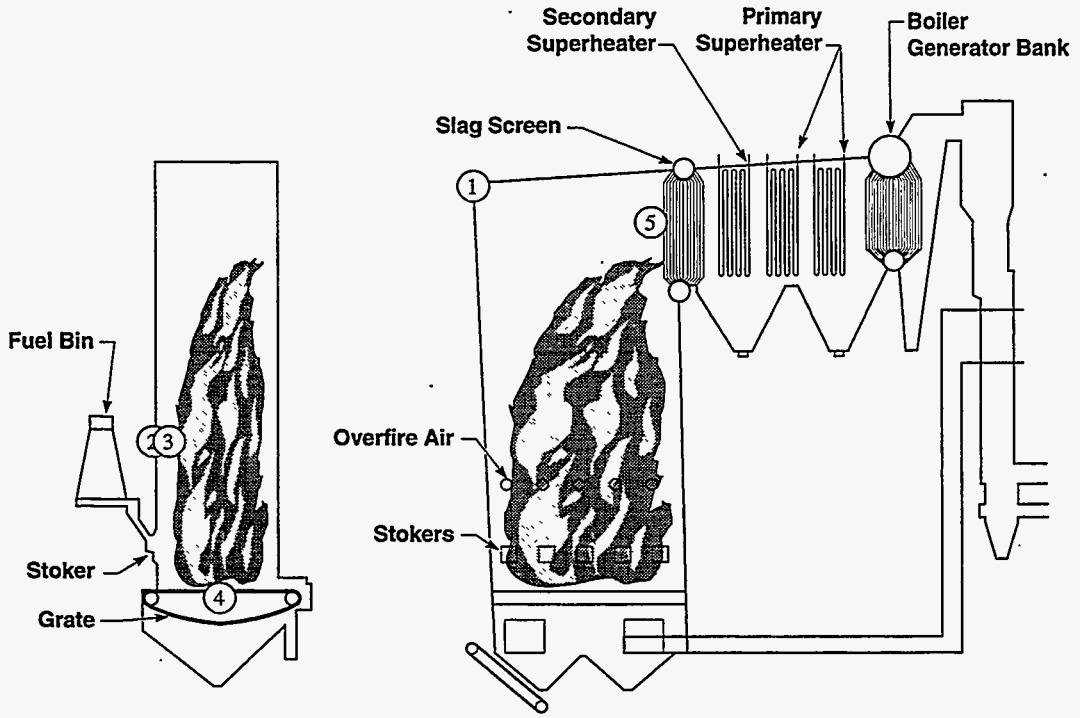

Figure 96 Two schematic side views of the 18 MW_e (gross), stoker-fired traveling grate combustor used in field tests of straw firing in biomass combustors. The stoker has a split grate, the top of which travels toward the stokers (to the left in the left view and toward the reader in the right view).

The particular urban wood fuel used in these tests comprised mostly construction waste, with small amounts of demolition wood and residential yard waste (plant trimmings and prunings). The particular straw used in the field tests was chosen in part on the basis of its low chlorine content, consistent with fuel specifications for the boiler. In this respect, it is not necessarily representative of straws generally or of straws most conveniently available to this boiler.

The general conclusions from the detailed characterizations of the laboratory fuels are applicable here. Urban wood fuel is composed principally of stem-wood- or bole-wood-derived material. This portion of the tree does not experience rapid growth, nor is it involved in photosynthesis or other activities that rely on large amounts of inorganic material. It is expected to have relatively low levels of overall ash. This expectation is consistent with the measurements when one considers that a significant fraction of the observed ash is adventitious. Inorganics in the straw should be similar to the inorganics discussed above in conjunction with laboratory data, except that the straw in the field tests possibly contains larger amounts of adventitious material. Evidence for this higher level of adventitious material is found in the measured concentrations of aluminum, iron, and titanium, all of which occur in straws in trace quantities, several times smaller than the levels indicated in the table.

Table 10 Chemical and combustion properties of the fuels and the blend used in the field combustion tests.

	Urban Wood Waste	*Wheat Straw*	*20 % Straw Blend (Meas.)*	*20 % Straw Blend (Calc.)*
H_2O (mass %)	20.31	12.78	17.94	18.80
Ash (mass %, dry)	5.09	5.59	6.68	5.19
Ultimate Analysis (mass %, dry basis)				
C	38.21	40.05	38.44	38.58
H	4.52	5.02	4.64	4.62
O	31.58	36.07	31.93	32.48
N	0.22	0.40	0.27	0.26
S	0.07	0.10	0.10	0.08
Ash Chemistry (% of Ash)				
SiO_2	53.71	62.46	57.58	55.59
Al_2O_3	11.88	3.96	10.16	10.17
TiO_2	0.56	0.23	0.48	0.49
Fe_2O_3	5.28	1.96	3.98	4.56
CaO	14.04	8.10	11.29	12.76
MgO	3.43	2.39	2.96	3.21
K_2O	4.34	14.17	6.89	6.46
Na_2O	3.02	1.85	3.04	2.77
SO_3	3.30	2.33	2.26	3.09
P_2O_5	0.86	1.96	1.07	1.10
undetr. Ash	-0.42	0.59	0.29	-0.20
Total	100	100	100	100
Cl (mass %, dry basis)	0.06	0.18	0.13	0.08
HHV (dry basis) (MJ/kg)	19.25	18.28	18.51	19.06

The mechanisms of ash deposition in solid-fuel-fired boilers include inertial impaction, condensation, chemical reactions, and thermophoresis (Baxter, 1993). Data collected from both the MFC and the stoker indicate how these mechanisms produce different types of deposits under different operating conditions and at different locations in the boiler.

Samples from full-scale equipment also illustrate the mechanisms of ash deposit formation. In the full-scale test, wheat straw was combined with wood in a 20 % mass ratio. Total mass feedrate was 20 tons/hour. The boiler operated three days on this fuel at partial load (furnace gas exit temperature $\approx$ 750 °C). During the final two days of the test, the furnace operated at full capacity (furnace exit gas temperature $\approx$ 850 °C). The test was aborted after five days due to

unmanageable ash deposits running off the walls and accumulating on the grate and subsequent failure of bottom ash removal conveyers.

Sulfation

Initially, a reflective, nearly white ash deposit formed in the upper half of the furnace and in the convection pass. At partial load, granular deposits accumulated on the walls and on the convection pass tubes, but no molten deposits were observed. Upon reaching full load, flowing deposits were observed on the refractory wind boxes around the stokers. Deposits on the grate agglomerated to sizes too large to pass through the conveyer. Deposits on the water walls accumulated more rapidly, although they were not molten. Large deposits began to accumulate in the convection pass entrance. The thin, white layer of ash observed during partial load persisted on the ceiling and in the corner of the furnace opposite the convective pass entrance.

Figure 97 indicates the composition of the white layer of ash. Also shown in the figure is the average fuel ash composition. There is very little correspondence between the fuel ash composition and that of the deposits found in the region of the combustor. The enrichment in potassium and sodium in the ash deposit are indicative of ash condensation. The high sulfur concentration indicates that the alkalis are in the form of sulfates. The absence of appreciable silicon, aluminum, iron, titanium or other refractory components indicates very few particles from the fuel accumulate in this region of the boiler.

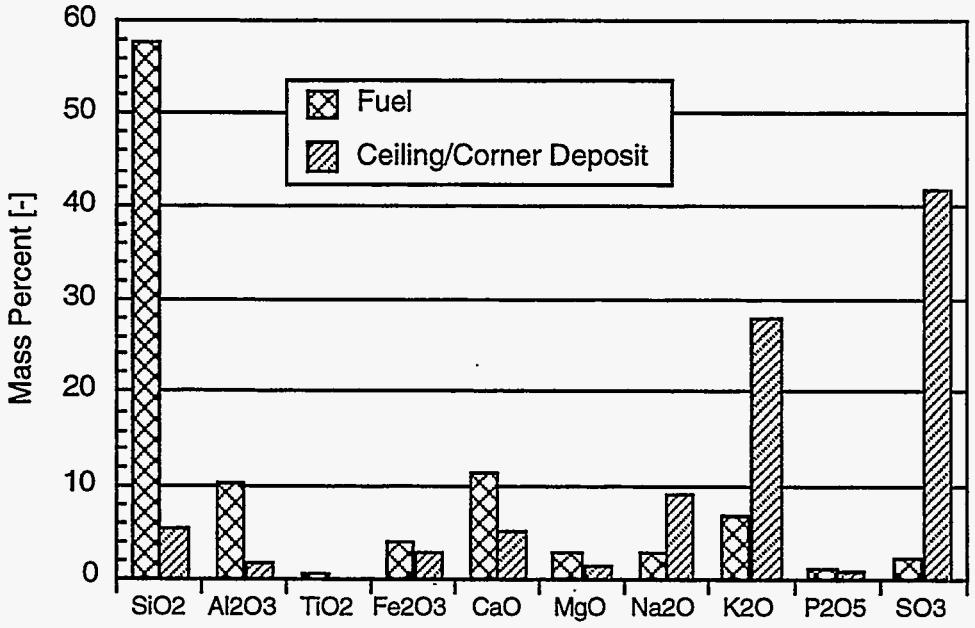

Figure 97 Comparison between elemental composition of the fuel ash and a thin layer of reflective ash deposited on the ceiling and upper corner of the furnace (Position 1 in Figure 96). All compositions are expressed as oxides.

The analysis of the mode of occurrence of the inorganic material in the fuel and the design and operation of the boiler provide the background to identify the mechanism of formation for this deposit. The atomically dispersed potassium in the fuel is principally derived from the straw and forms a vapor during combustion. The alkali vapor condenses on water walls, convection pass tubes, and other cool heat transfer surfaces throughout the boiler. The alkali chemically reacts with gas-phase sulfur to form a sulfate, the principal constituent of the deposit. This is the origin of the thin white layer of deposit observed early in the combustion test throughout the boiler. The chemical analysis of the deposit from the upper section of the furnace illustrates the enrichment of potassium, sodium, and sulfur resulting from condensation and reaction of these species. The thin white layer persists on the roof and in the upper corner of the boiler because there are no other significant mechanisms for ash deposition in these regions. Particle impaction is minimal in this region because the gases and fly ash flow into the convection pass (see Figure 96). The deposits in the upper corner opposite the convection pass and on the roof are formed primarily through condensation and chemical reaction, in contrast with deposits formed in other regions.

Particle Impaction

Lower on the furnace wall, in the region exposed to entrained particles as well as vapors, the ash deposits assume a different character. The entire deposit is granular and porous. The inner deposit (portion closest to the water wall) exhibits a somewhat compact and random ordering of particles. The outer deposit (fire side portion) is more porous and exhibits a chain-linked particle structure described as "angel hair" by some of the observers. The chemical composition (Figure 98) of both deposits more closely resembles that of the fuel than does the white layer on the ceiling and walls of the upper corner opposite the convection pass entrance.

The outer wall deposit is slightly enriched in silica and depleted in potassium compared to the fuel ash. The potassium levels in the deposit are similar to those in the wood fuel and substantially less than the potassium concentration in the straw. The potassium in the wood is primarily in the form of silicates. Potassium in this form does not readily vaporize. Potassium in the straw is atomically distributed and intimately mixed with the organic structure. This form of potassium vaporizes during combustion. The silicon in the fuel does not appreciably vaporize under these conditions, whether it originates from the wood or the straw.

The composition and formation of the wall deposits are dominated by the particle-portion of the ash. The silicon portion of the straw ash and most of the wood ash form fly ash particles during combustion. The fly ash impacts on the wall and is the major contributor to the total deposit mass. Vapor condensation contributes a relatively small portion of the total ash deposit, and this is limited to the inner-most deposit layer next to the cool water wall. The same general features of deposits from the grate (collected from under the stokers) are observed (Figure 99).

Combinations of Mechanisms

The deposits on the slag screen in the entrance to the convection pass exhibit a combination of alkali/alkaline earth sulfation and particle impaction. The composition of these deposits is

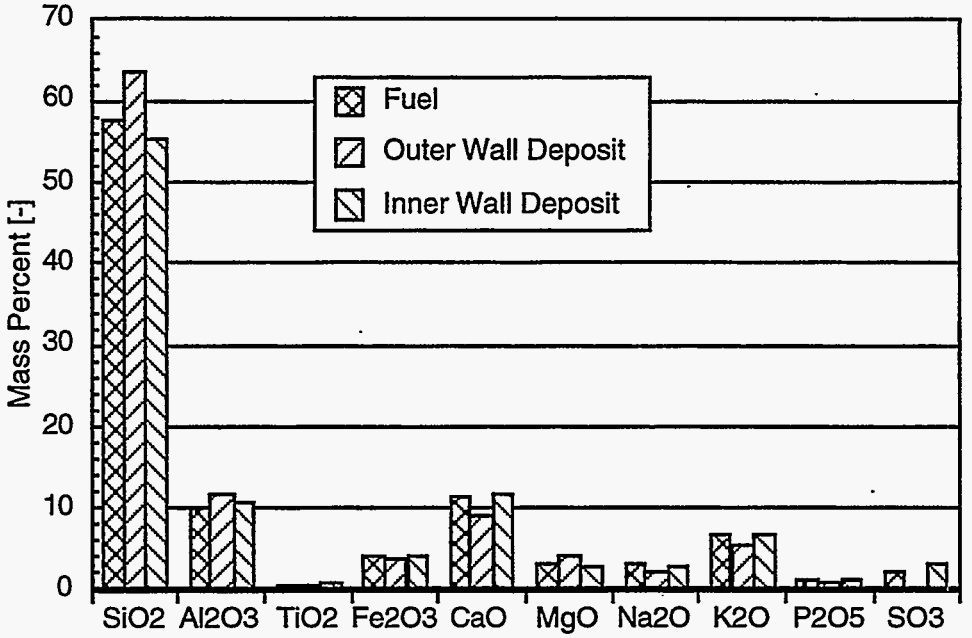

Figure 98 Comparison among elemental composition of ash deposits on the upper walls (positions 2 and 3 in Figure 96) and fuel ash composition. All compositions are expressed as oxides.

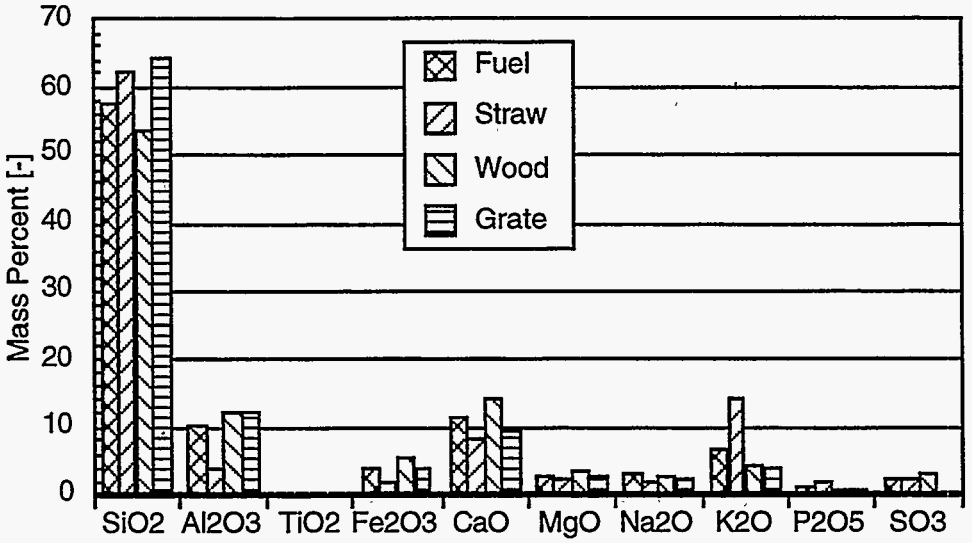

Figure 99 Comparison among elemental composition of ash deposits from the grate (position 4 in Figure 96) and fuel ash composition. All compositions are expressed as oxides.

intermediate to the particle-dominated wall deposits and the condensate-dominated ceiling deposit (Figure 100). This is consistent with the mechanism of deposit formation, with significant contributions from all mechanisms of deposition (particle impaction, condensation, thermophoresis, and chemical reactions). The formation of sulfates in these particle-dominated deposits can dramatically change deposit tenacity (Baxter, 1992a).

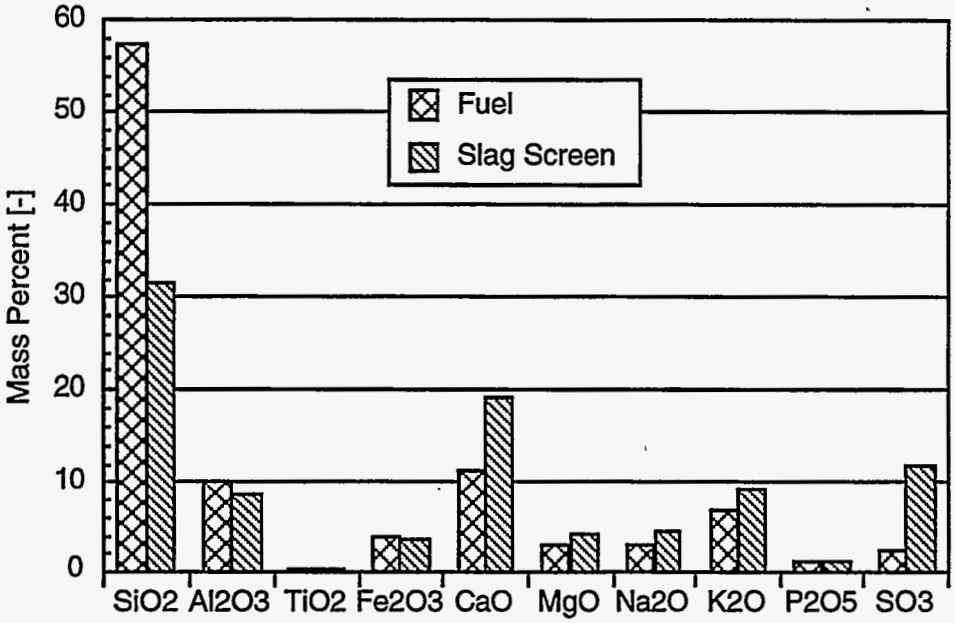

Figure 100 Comparison among elemental composition of ash deposits from the slag screen in the convection pass entrance (position 5 in Figure 96) and fuel ash composition. All compositions are expressed as oxides.

These data from pilot- and commercial-scale boiler operation illustrate the mechanisms of ash deposit formation and their sensitivity to fuel properties, boiler design, and operating conditions. Specifically, fuels with similar elemental ash compositions may behave quite differently during combustion depending on the mode of occurrence of the inorganics in the fuel. Alkali that is atomically distributed or in another potentially volatile form has a potential large effect on ash deposition. This alkali condenses on surfaces and reacts with silica to form molten silicates. Because of its tendency to preferentially accumulate on heat transfer surfaces and its ability to substantially alter melting temperatures, its impact on deposit properties is significantly greater than its mass fraction in the ash may lead one to anticipate. That is, a small percent of releasable alkali in the fuel can change deposit tenacity, fluidity, and rate of accumulation by large amounts.

Boiler design and operation also contribute to the nature of the deposits formed in different regions of the boiler. The effect of boiler design is seen by comparing the ceiling, wall, grate, and superheater deposits illustrated above. Boiler operating conditions control local values of

temperature, gas composition, and particle loading in the boiler. For example, as furnace exit gas temperature decreases in a boiler, the rate of particle sintering and slag formation in the superheater region decreases. This is illustrated by the observed changes in ash deposit character between the boiler at partial load and at full load during the field tests.

A series of laboratory and field tests illustrate the principal mechanisms of ash deposit formation during combustion of biomass fuels. Relationships among the amount and mode of occurrence of inorganic material in the fuel, boiler design, and boiler operating conditions that influence the type of ash deposit formed are discussed. Specific examples of ash deposit formation during combustion of straw are used to illustrate the mechanisms.

Important attributes of ash deposits are determined by the relative rates of particle impaction on surfaces, condensation, and chemical reactions. Deposit morphology, composition, tenacity, porosity, and reflectivity are influenced by the mechanism of deposition. For a specific fuel, the dominant deposition mechanisms vary with location in the boiler and with boiler operating conditions.

Distinguishing characteristics of straw combustion include the large amount of silica and vaporizable alkali in the ash and the tendency of the silica and alkali to combine chemically on heat transfer surfaces. Alkali vapors condense on cool surfaces to form thin, reflective, alkali-based deposits. The alkali chemically combines with sulfur to form sulfates. In regions where silicon-based fly ash particles accumulate on surfaces, alkali combines with the silica to form silicates. These alkali-silicates have melting temperatures near or below the prevailing gas temperatures. This leads to sintering and formation of molten phases in the deposit. The rate of sintering depends on both deposit temperature and the amount of alkali in the gas phase.

Slagelse

The Slagelse boiler in Denmark (Figure 101) is designed to produce both electricity (5 MW_e) and steam from straw. Fuel is augured onto a sloping, reciprocating grate, with underfire air. Immediately above the grate the walls of the combustor form a pinch point. Additional air is introduced above the neck. The boiler features a long convection pass, a trademark of European-designed boilers. Nominal gas temperatures are indicated in the figure. During the field test, the boiler was fired with a blend of straws (90% wheat, 9% barley, 1% rape).

Ash deposits were collected from the locations indicated by numbers in the figure. The elemental compositions of these deposits are presented in Figure 102. An obvious trend in the results is the formation of chloride-based deposits in the sections of the boiler with the lowest gas temperatures

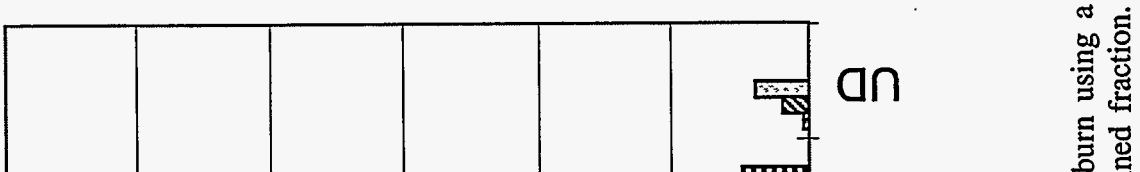

indication of sulfate formation is evident on the coolest waterwalls (locations 3 through 5), although it is minimal. In the furnace region (locations 1, 2, 3, and 5), impaction of silica-based fly ash particles is evident in the elemental compositions. Silica is the dominant inorganic component in straw.

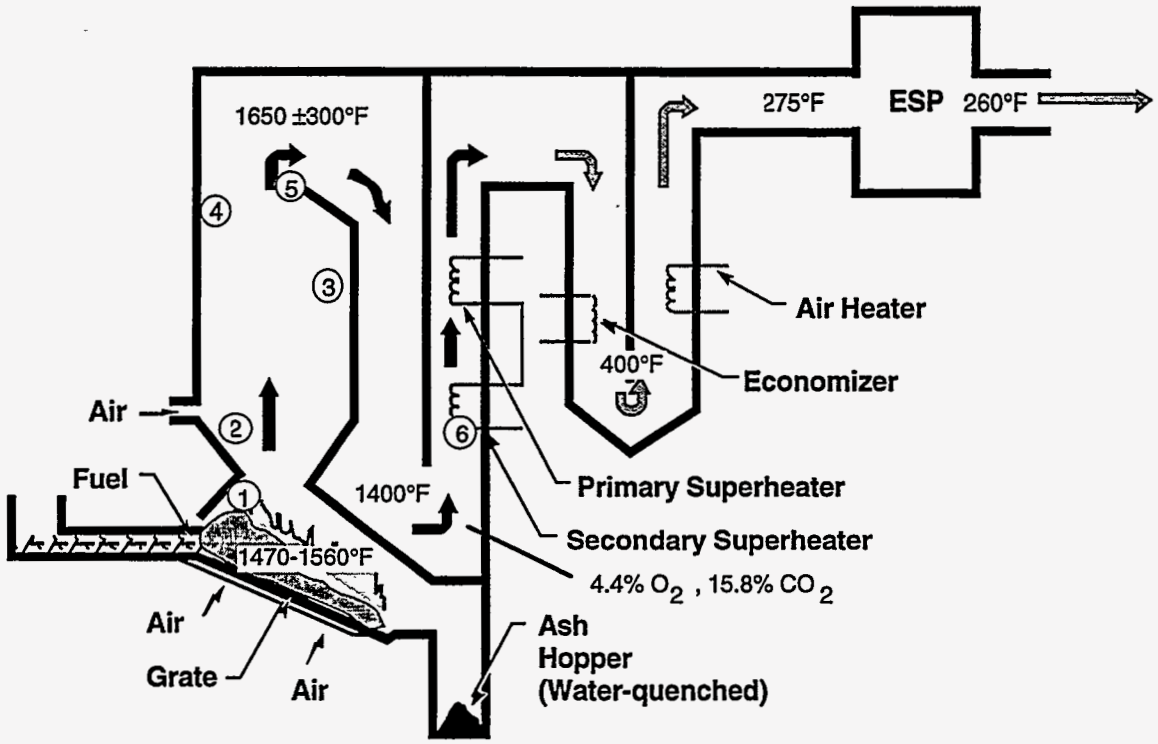

Figure 101 Schematic diagram of the Slagelse boiler in Denmark showing principal components and operation conditions. The boiler is fired with a blend of straws. Deposit samples were removed from the numbered locations.

Ash deposits were collected from the locations indicated by numbers in the figure. The elemental compositions of these deposits are presented in Figure 102. An obvious trend in the results is the formation of chloride-based deposits in the sections of the boiler with the lowest gas temperatures (locations 4 and 6). The boiler design also minimizes particle loading in these regions. The cool temperatures and low particle concentrations favor condensation as the primary deposition mechanism. Potassium is the most volatile inorganic species and potassium chloride is the most stable potassium-bearing vapor under typical biomass combustion systems. The elemental composition of the deposits at locations 4 and 6 indicate that over half of the deposit is composed of potassium chloride. At lower temperatures, sulfates form in preference to chlorides. Some indication of sulfate formation is evident on the coolest waterwalls (locations 3 through 5), although it is minimal. In the furnace region (locations 1, 2, 3, and 5), impaction of silica-based fly ash particles is evident in the elemental compositions. Silica is the dominant inorganic component in straw.

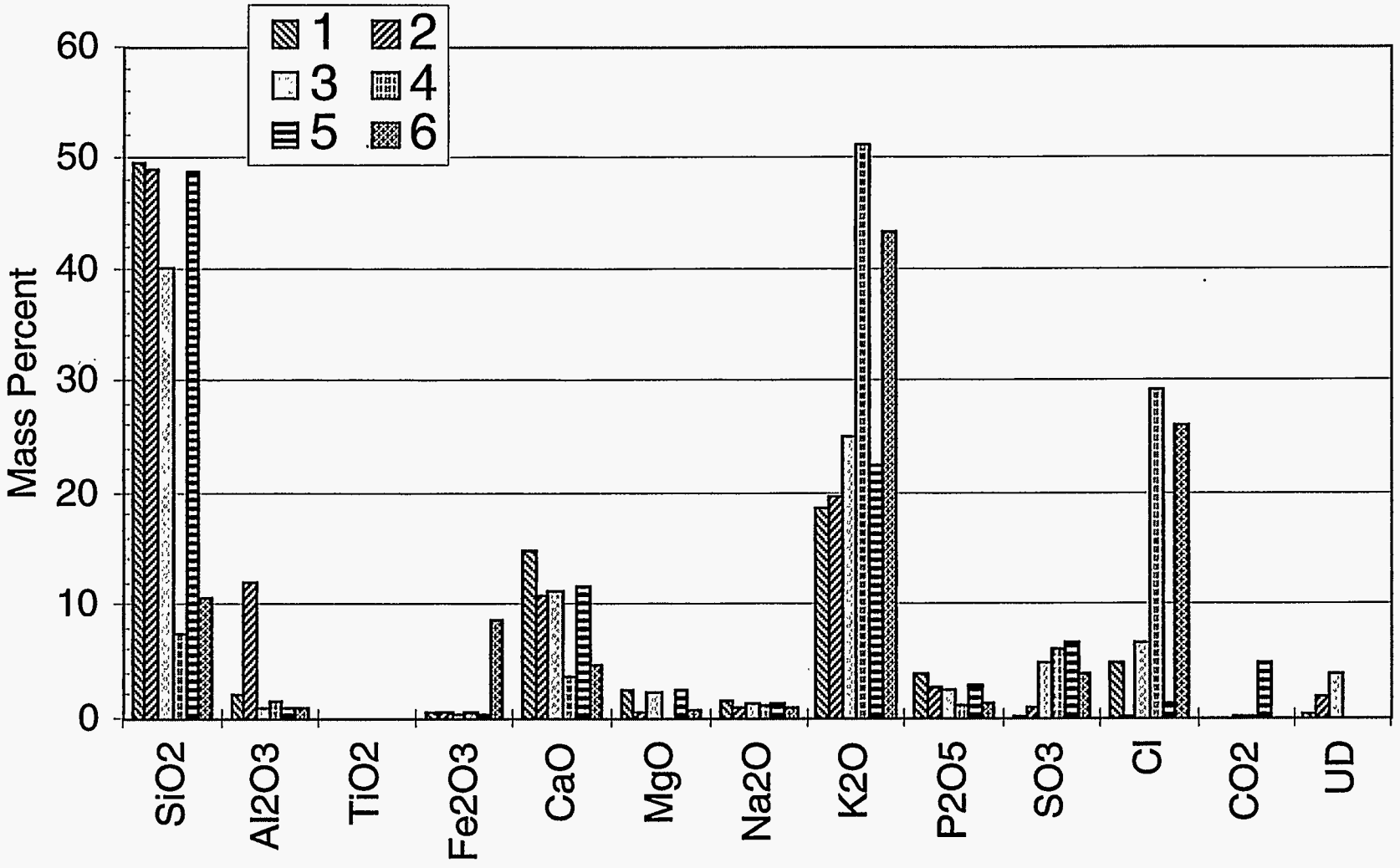

Figure 102 Elemental composition of ash deposits sampled from the Slagelse boiler in Denmark during a test burn using a blend of straws. All values are given in percent of deposit mass. UD represents the undetermined fraction. Numbers correspond to those in Figure 101.

Haslev

The Haslev CHP plant (Figure 103) features a straw burning system sometimes referred to as a cigar burner. Bales of straw are introduced into the boiler by conveyors, as illustrated. The end of the bale ignites as it is introduced into the high temperature region and the flame is supported in part by high-velocity air jets that help break up the bale. The bale tumbles onto a water-cooled, sloping grate. Ash and slag from the grate are collected in an ash hopper. The remainder of the boiler is of conventional European design, with a relatively long convection pass. Nominal gas temperatures are also indicated in the figure.

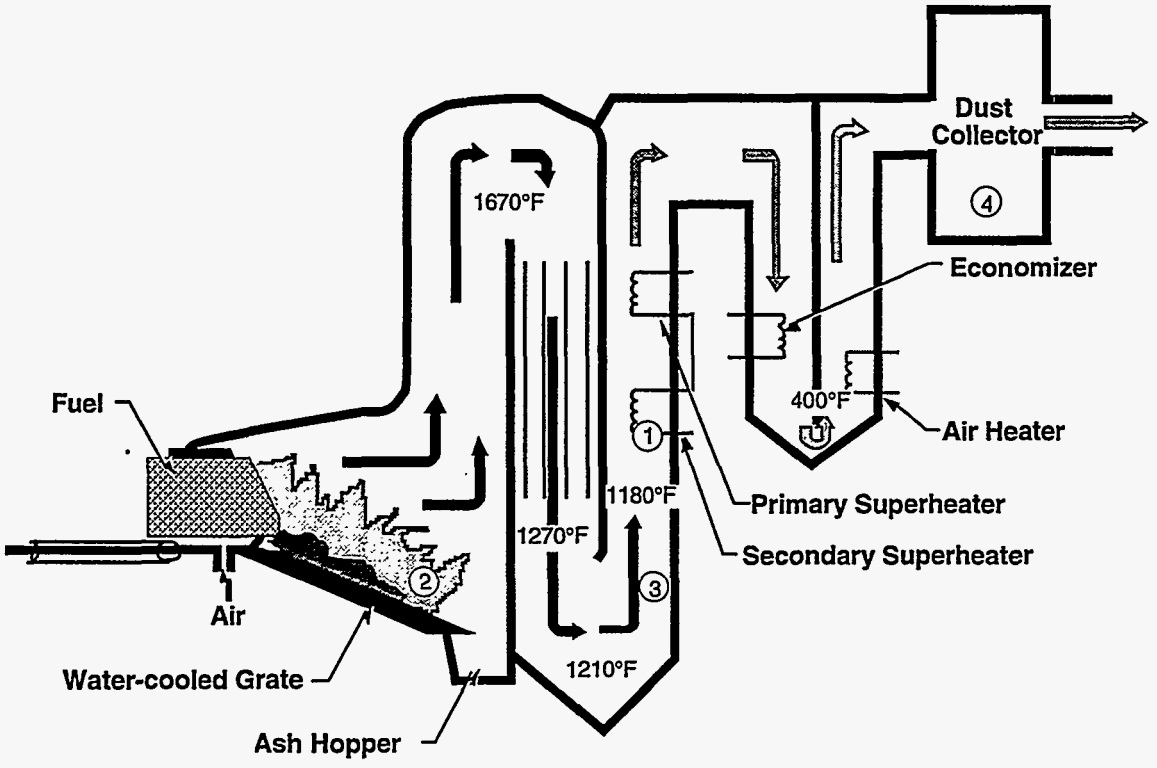

Figure 103 Schematic diagram of the Haslev boiler in Denmark showing design and nominal operating conditions. The boiler is fired by straw. Deposits were removed from labeled locations and analyzed from elemental composition and physical structure.

During the field test, the Haslev boiler was fired with 100% wheat straw. Ash deposits from this boiler were collected at the locations indicated by numbers in Figure 103. One sample was taken of the grate slag and three were obtained from locations in the convective pass. The elemental compositions of these deposits are indicated in Figure 104. The grate slag composition contrasts strongly with the compositions of deposits in the convection pass. In particular, the grate slag is higher in silica and lower in chlorine than the other deposits, more closely resembling the

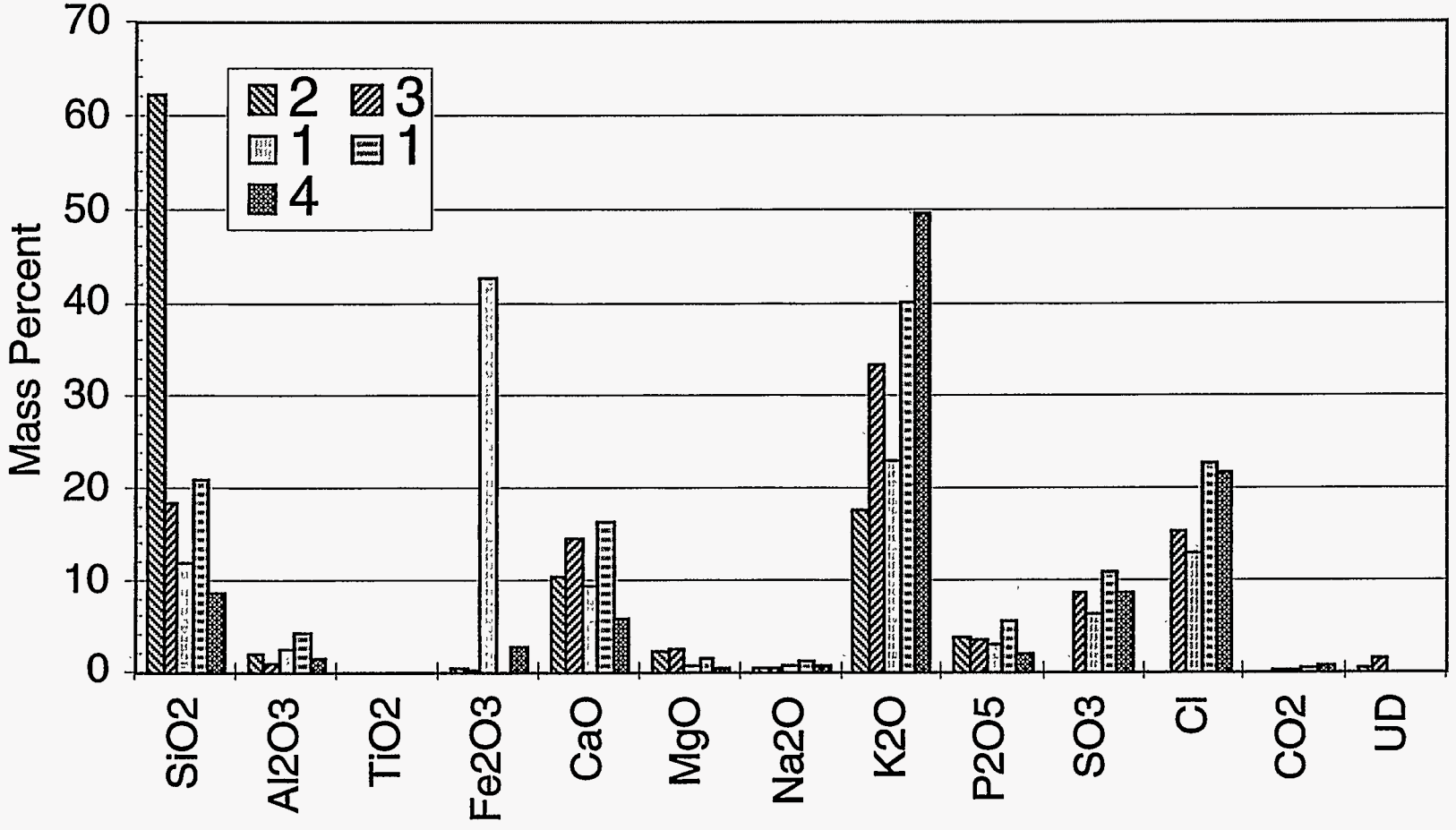

Figure 104 Elemental compositions of deposits obtained from the Haslev boiler. Numbers correspond to sample locations indicated in Figure Figure 103. The second set of data for location 1 are normalized assuming the iron content is an impurity from the tube surface. UD represents the undetermined fraction.

composition of ash from a typical wheat straw. Enrichment of chlorine, potassium, and sulfur in the remaining deposits indicates they are formed by condensation and subsequent reaction. The high iron content in the deposit from the secondary superheater is most likely an impurity or a portion of the superheater tube. A second set of results are illustrated in which iron has been removed and the remaining data normalized.

Sithe

The Sithe boiler (Figure 105) is an atmospheric-pressure, circulating fluid bed system featuring wing walls in the bed and U-tubes for particle separation devices (Gotteverken design). Fuel is augured into the bottom of the bed and entrained by high velocity air into the remaining bed media. Bed media and fuel are separated from gases at the top of the boiler by U-tubes. The U-tubes are not water-cooled and should reach high temperatures, approaching the gas temperature, during operation. Particles are returned to the bed through an L-valve while gases and some small, entrained particles pass through the convection pass. Peak temperatures usually occur at the top of the boiler.

Beginning mid-April, 1993, operating staff at the Sithe Energy Co. plant in Marysville, California began collecting fuel and ash samples. The test lasted through the end of May 1993. The plant was operated at full load during the week and turned down during the non-peak hours of the weekend. Four deposit samples were collected on 30 May, including one (labeled 1 in Figure 105) from the U-beams, one from the access doorway (labeled 2) to the U-beam section, and one each from the primary (4) and secondary (3) superheaters in the convection pass. The deposit taken from the U-beams was an off-white aggregate, sandy in appearance. A dark brown granular deposit was collected from the doorway. The deposit from the secondary superheater was a hard deposit, developing towards the typical "shark's tooth" in appearance. The deposit collected from the primary superheater was a fine textured powder, dark brown in color.

During the test burn, a blend of fuels was fired with the dominant fuel being saw dust and wood chips (80 %), and the balance comprised of pits, almond shells and hulls, and sander dust in varying quantities. Ash deposits were sampled from the locations indicated by numbers in Figure 105. The elemental compositions of these deposits are indicated in Figure 106. The bed material is composed of aluminosilicates, with a high alumina content. The deposit analyses indicate the presence of sulfates, specifically calcium sulfate, on the secondary superheater. The primary superheater deposit indicates essentially no sulfate formation. Sulfates are stable only at relatively low temperature, typical of temperatures of steel surfaces, but not of surrounding gas phase. It is likely that the deposit sampled from the primary superheater was removed from some region other than next to the steel surface. In addition, the samples were collected by plant personnel and there is some question about whether we have identified these two sample locations properly.

The fuels used in this testburn are dominated by wood. Wood has little chlorine content and lower potassium compared to straw and grass. These data contrast with those from the straw-fired tests in that strong preferential deposition of alkali chlorides is not observed.

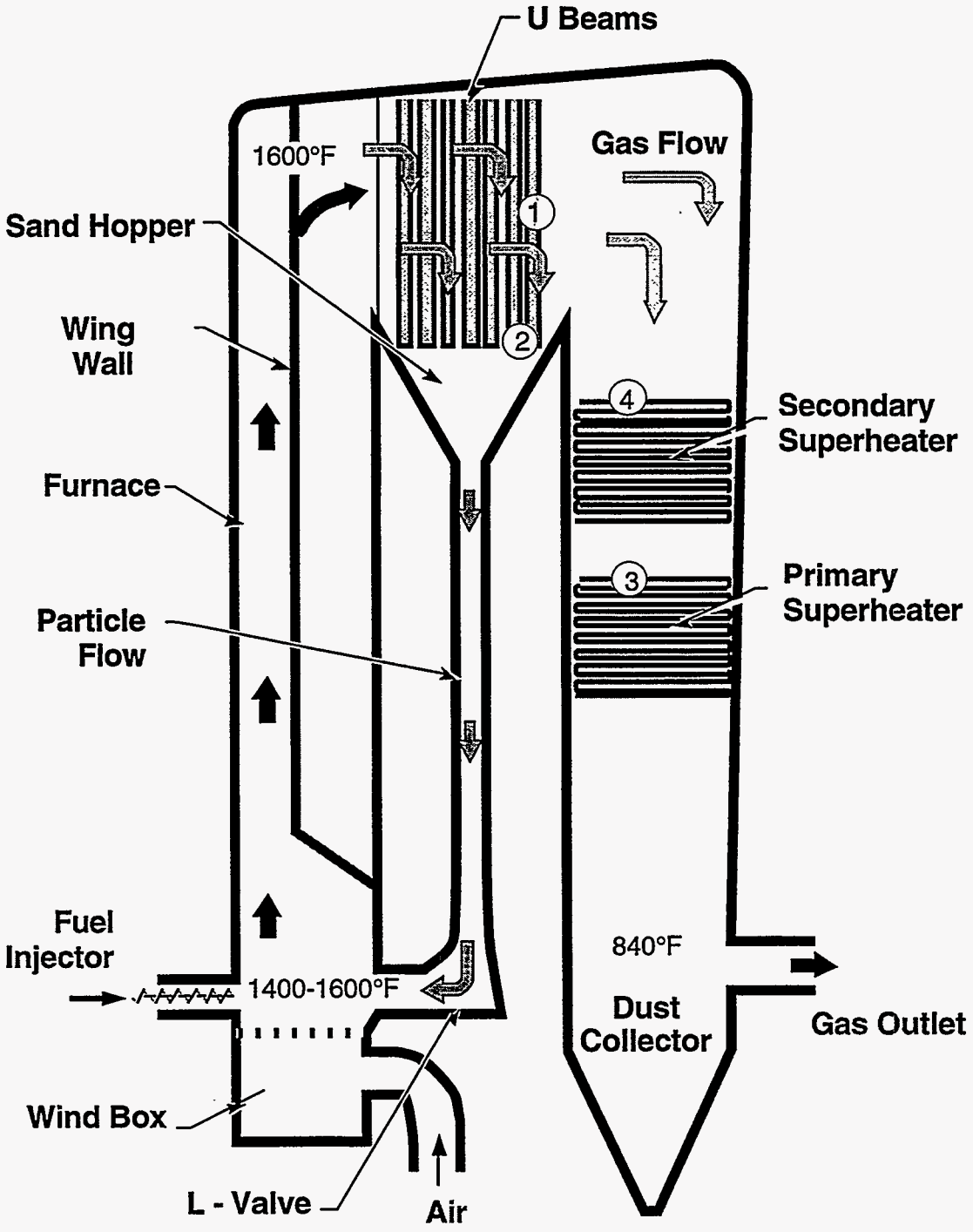

Figure 105 Schematic diagram of the Sithe Energy Systems plant located in Marysville, California. This boiler is fired with a blend of wood-derived products and a minority of agricultural products. Numbers represent locations from which ash deposit samples were obtained.

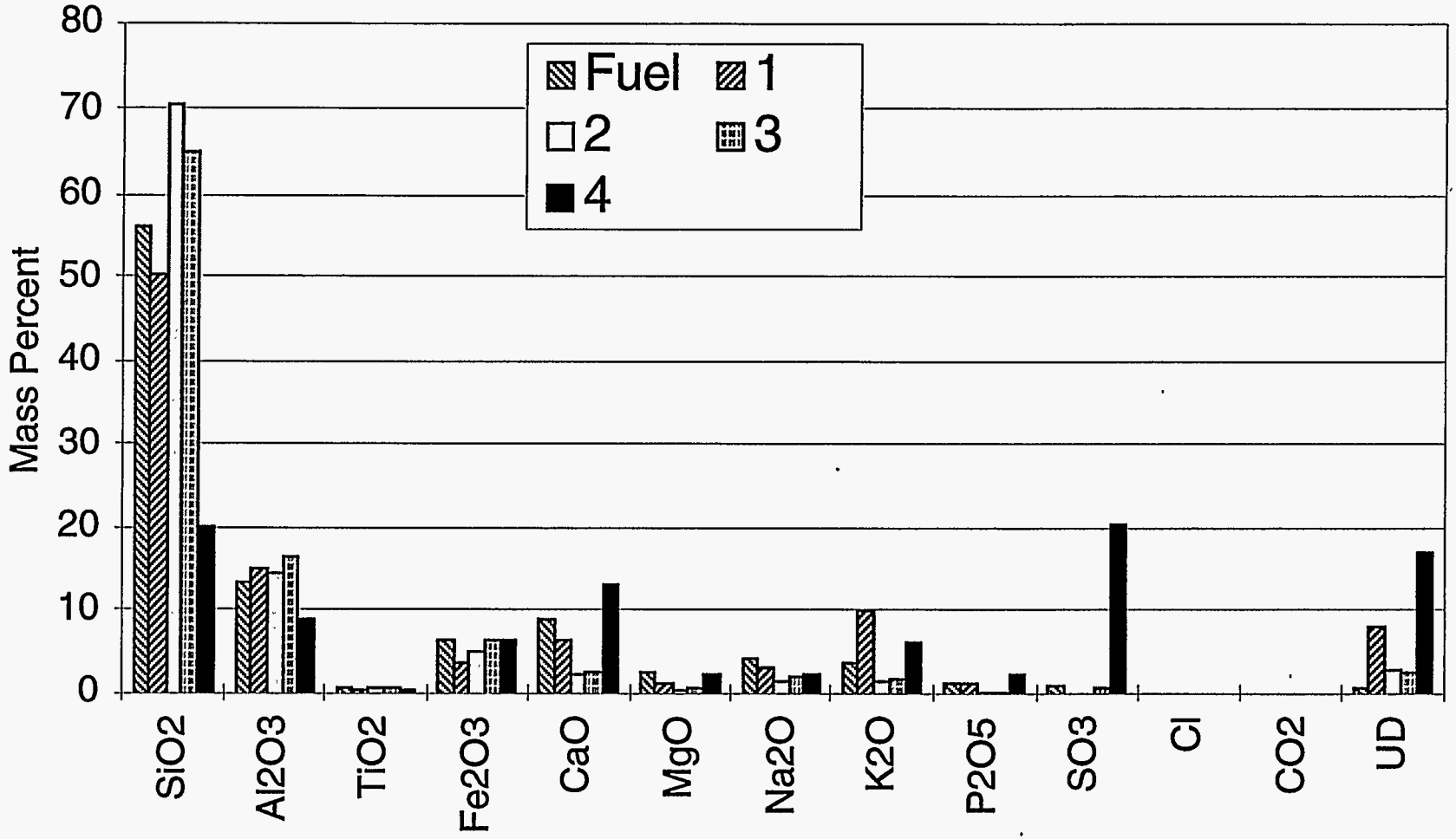

Figure 106 Elemental composition of deposits sampled from the Sithe boiler after the testburn. All values represent percent of total deposit, with UD representing the undetermined fraction as measured by difference between the sum of the oxides and total ash. Samples correspond to locations indicated in Figure 105.

Woodland

The Woodland boiler (Figure 107) is an atmospheric-pressure, circulating fluid bed with cyclone rather than U-beam design to disengage particles from the gas flow. The cyclone is not water cooled. A loop seal (J-valve) is used to reintroduce particles into the bed media. The gases pass through a series of superheater and generator banks before entering the cleanup systems. Fuel is augured into the base of the bed and air is introduced somewhat above the fuel injection port.

The Woodland facility was started up near the end of April and continued operation until 6 September with only three short unscheduled outages around 14 and 30 May and 5 June. The boiler was inspected on 7 September and 18 deposit samples were collected as indicated in Figure 107. The amount of deposition was considered moderate and similar to that at Delano. Hard, tenacious deposits were removed from the top or tertiary superheater. Well developed "shark's teeth," dark brown on the upper surface and lighter behind, were observed on the top tubes of this superheater. Vertical deposit bridging (growth of deposit from the backside of the upstream tubes to the front side of the downstream tubes) was seen in the tube bundles of this superheater, but not much horizontal bridging. Two samples (2 and 3) were collected from the wall of the convection pass above the tertiary superheater for comparison with the tube deposits. Sample 2 was collected from a short horizontal shelf extending from the wall. Hard, tenacious deposits of the "shark's teeth" type were also removed from the top tubes of the secondary and primary superheaters. The bottom tubes of the primary superheater and the tubes below this point were relatively clean.

A number of deposit samples were collected from the two loop seals at the bottom of the cyclones. These were all sandy agglomerates, ranging in color from green to brown. Sample 16 was mostly of this type, but situated on the side was a distinctly different form consisting of a dark brown fine textured agglomerate, which was analyzed separately. Samples 10 and 11 were removed directly from the wall of the loop seal. Samples 12, 14, 16, and 17 were loose deposits found in the loop seals, and their site of origin is not known, although they are believed to have come from the dipleg wall. Samples 13 and 18 consisted of sand drained from the loop seal windboxes on the east and west cyclones, respectively. Sample 8 was collected from the floor of the cross-over duct between the furnace and the cyclones. This was also a sandy agglomerate, more friable than some of those removed from the loop seals. Sample 15 was collected from the floor of the cross-over duct between the west cyclone outlet and the convection pass. This was a light brown colored, fine-textured sandy agglomerate with a hard upper layer.

A wide variety of fuels were used during this field test. These are summarized in Figure 108. A primary component of the fuels is urban wood fuel, sometimes referred to as urban wood waste and designated UWW in Figure 108. There are higher concentrations of sulfur in these fuels than in many pristine biomass fuels, such as straws or wood chips. The variety of fuels fired during this field test indicates how variable the feed to these boilers can be. Samples of ash deposits were collected primarily from the convection pass and the particle return leg of the circulating bed. The locations from which deposits were sampled are indicated in Figure 107.

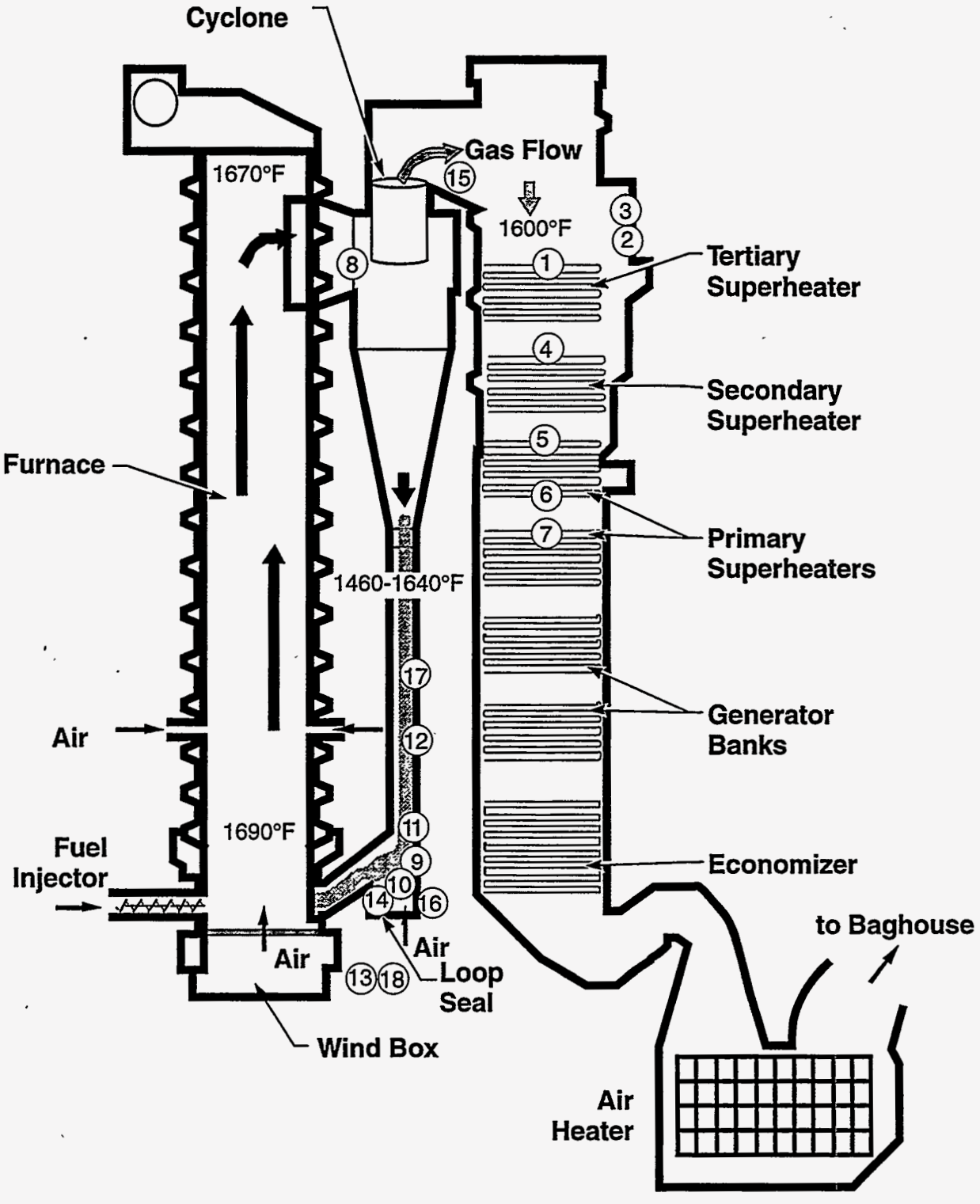

Figure 107 Schematic diagram of the Woodland boiler (Mendota boiler is identical). The boiler is fired by a wide variety of fuels (see Figure 108).

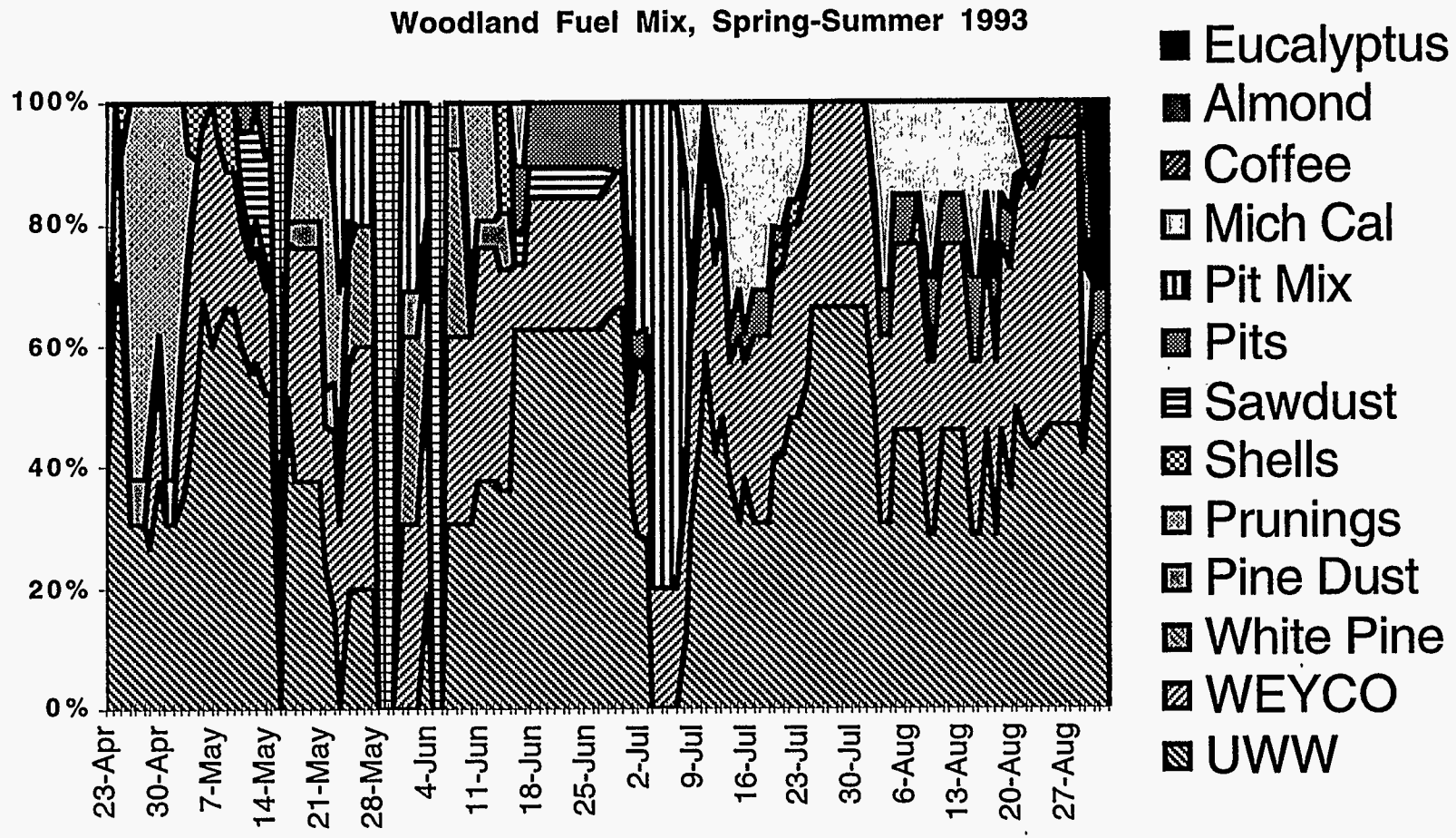

Figure 108 Fuel log for the Woodland boiler. Fuel is primarily urban wood fuel but includes contributions from many other sources.

Superheater deposits show a strong tendency to form sulfates, as indicated by their elemental analyses (Figure 109). The sulfates formed appear to be combinations of alkali and alkaline earth salts. The formation of the sulfates occurs both on the superheater tubes and on nearby walls and other structures (Figure 110). There is only minor variation in composition along the length of the superheater tube.

The analyses of the deposits formed at the entrance and exit of the cyclone indicate an enrichment of soil fines or bed material, as indicated by aluminum, on the outlet side (Figure 111). Soil fines are smaller than bed material and pass through the cyclone more easily. This accounts for the abnormally high aluminum contents observed in the convection pass (Figure 111).

Deposits in the particle down-comer are quite consistent in composition. Figure 112 illustrates a comparison between the samples collected at several locations and with different visual appearances. There is little significant difference in their composition with the exception of the deposit with the very high (57 %) undermined ash composition.

Delano

The Delano boiler (Figure 113) is an atmospheric-pressure bubbling fluid bed design. Fuel is introduced to the top of the bed through a chute type feeder. Heat is extracted from the bed by in-bed tubes. In addition, there are heat exchangers running along the sides of furnace. The gases leave the furnace and pass through the superheater banks in the convection pass. Screen tubes that act as a generator are located prior to the superheaters.

Staff at the Delano facility initiated fuel and ash sampling on 17 June and continued until 1 July when the plant was shut down due to tube leaks in the No. 1 Superheater (Figure 113). The boiler was cleaned (hydroblasted) during the outage period. The plant was restarted on or about 11 July, and continued without interruption until 3 September.

During the first outage and prior to cleaning, five deposit samples were collected from the combustor, screen tubes, and superheaters. One sample was taken from the south wall of the combustor (labeled 17). This deposit was a gray, sandy agglomerate composed mostly of what appeared to be bed media. One sample (18) was collected from the lower screen tubes (lower, middle, and upper sections of the screen tubes and superheaters were identified by the locations of access doors in the side wall of the convection pass). The screen tube deposit was a hard, deposit, about 10 mm thick. Another hard, thin deposit (19) was collected from the upper No. 2 superheater, while a brittle deposit (20) was collected from the lower section of this superheater. A loose, fine textured powdery deposit (21), brown in color, was taken form the lower No. 3 superheater. No samples could be collected from the No. 1 superheater during the inspection visit due to steam and hot water leaking from the tubes at this time.

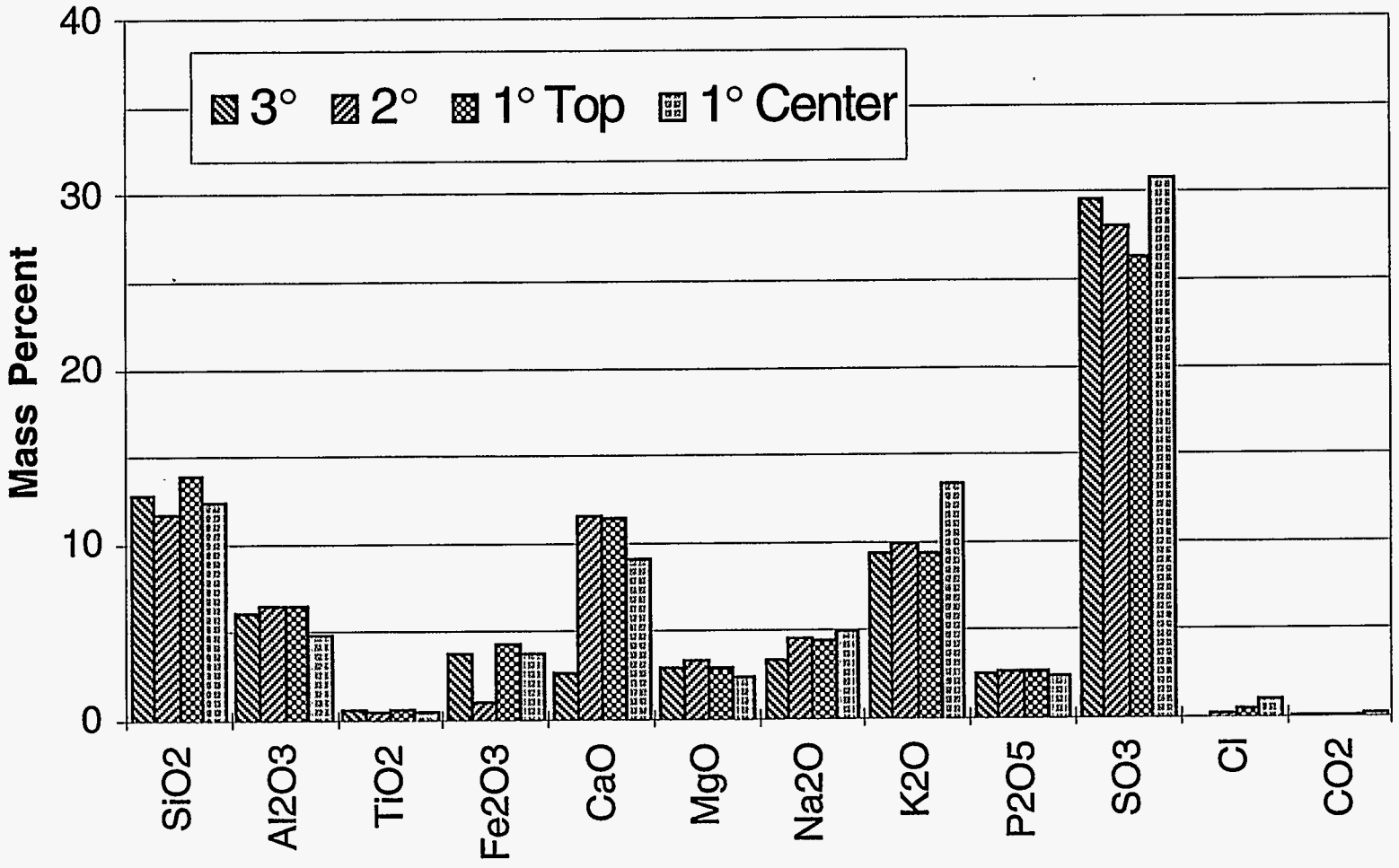

Figure 109 Composition of superheater deposits in the Woodland boiler as a function of location in the gas flow direction. Samples correspond to locations 1, 4, 5, and 7 in Figure 107.

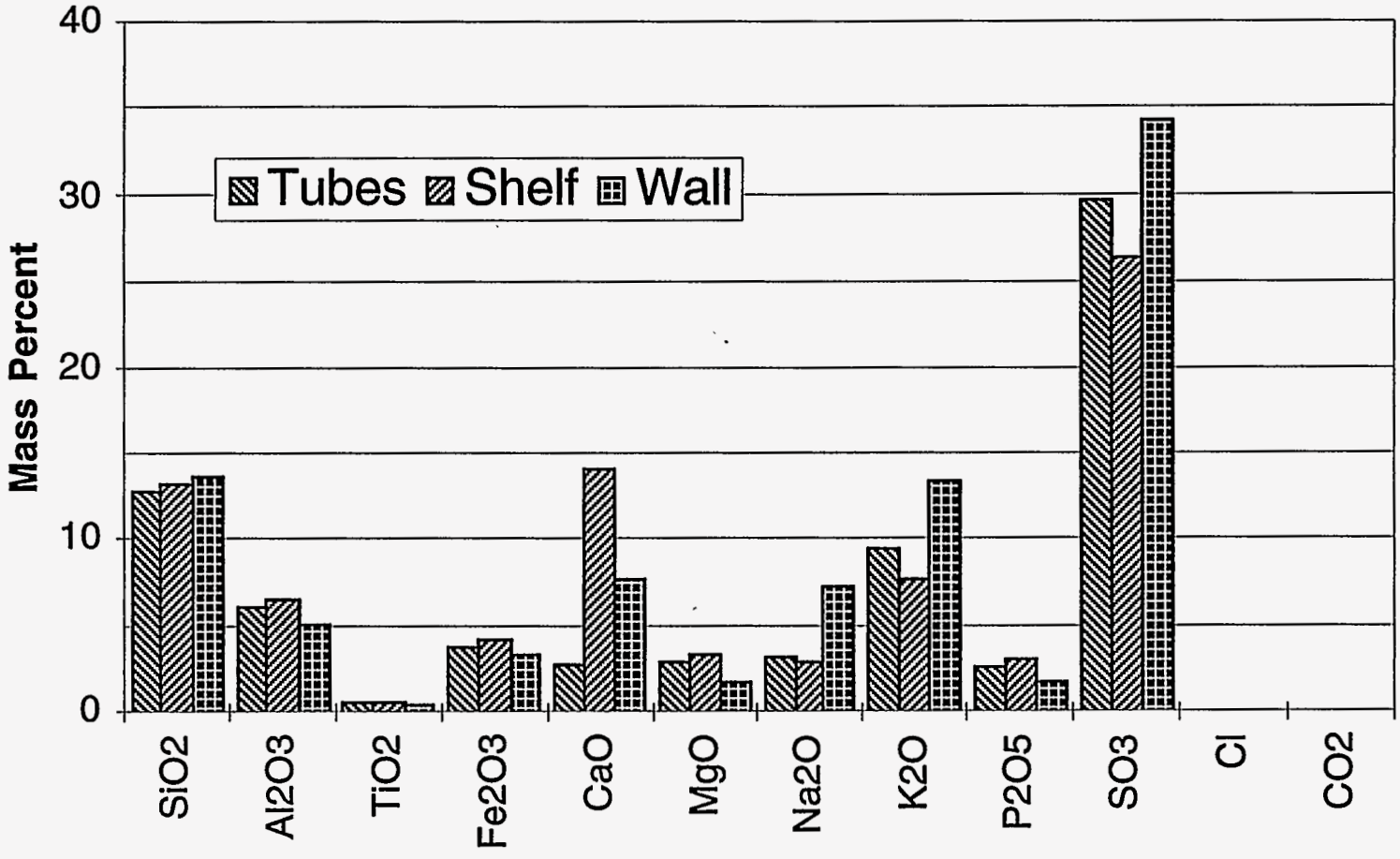

Figure 110 Elemental composition of deposits removed from various surfaces near the tertiary superheater in the Woodland boiler. Deposits indicate a strong tendency to form sulfates irrespective of the surface on which they are found. Samples correspond to locations 1, 2, and 3 in Figure 107, in that order.

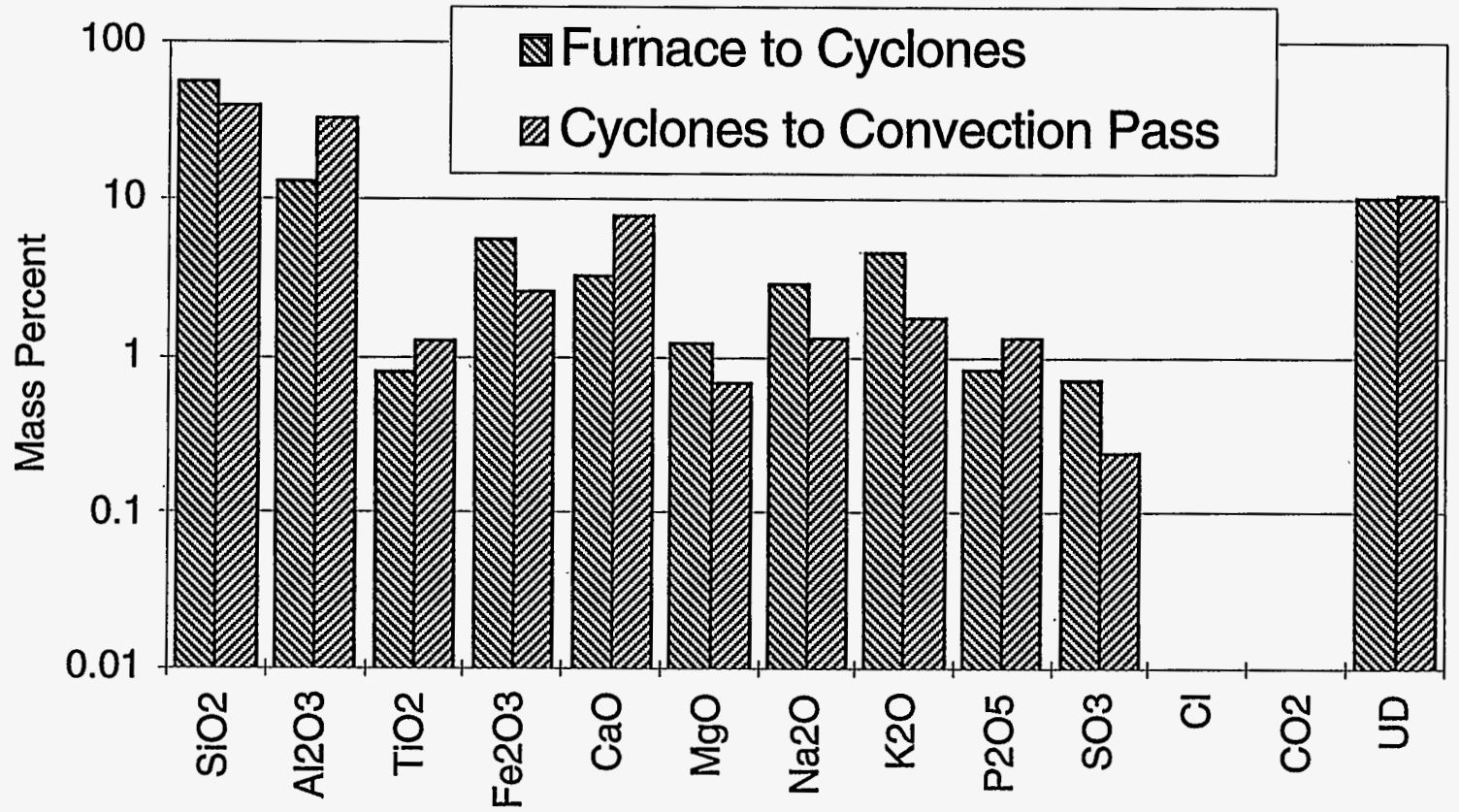

Figure 111 Elemental composition of deposits formed in the cross ducts of the Woodland boiler. The substantial enrichment in aluminum in the deposits formed after the cyclone indicate that either soil or bed material is preferentially passing through the cyclone. Small sizes of soil clays suggest that they are the likely source of the aluminum. Samples correspond to locations 8 and 15 in Figure 107. All values represent percent of total deposit, with UD representing the undetermined fraction as measured by difference between the sum of the oxides and total ash.

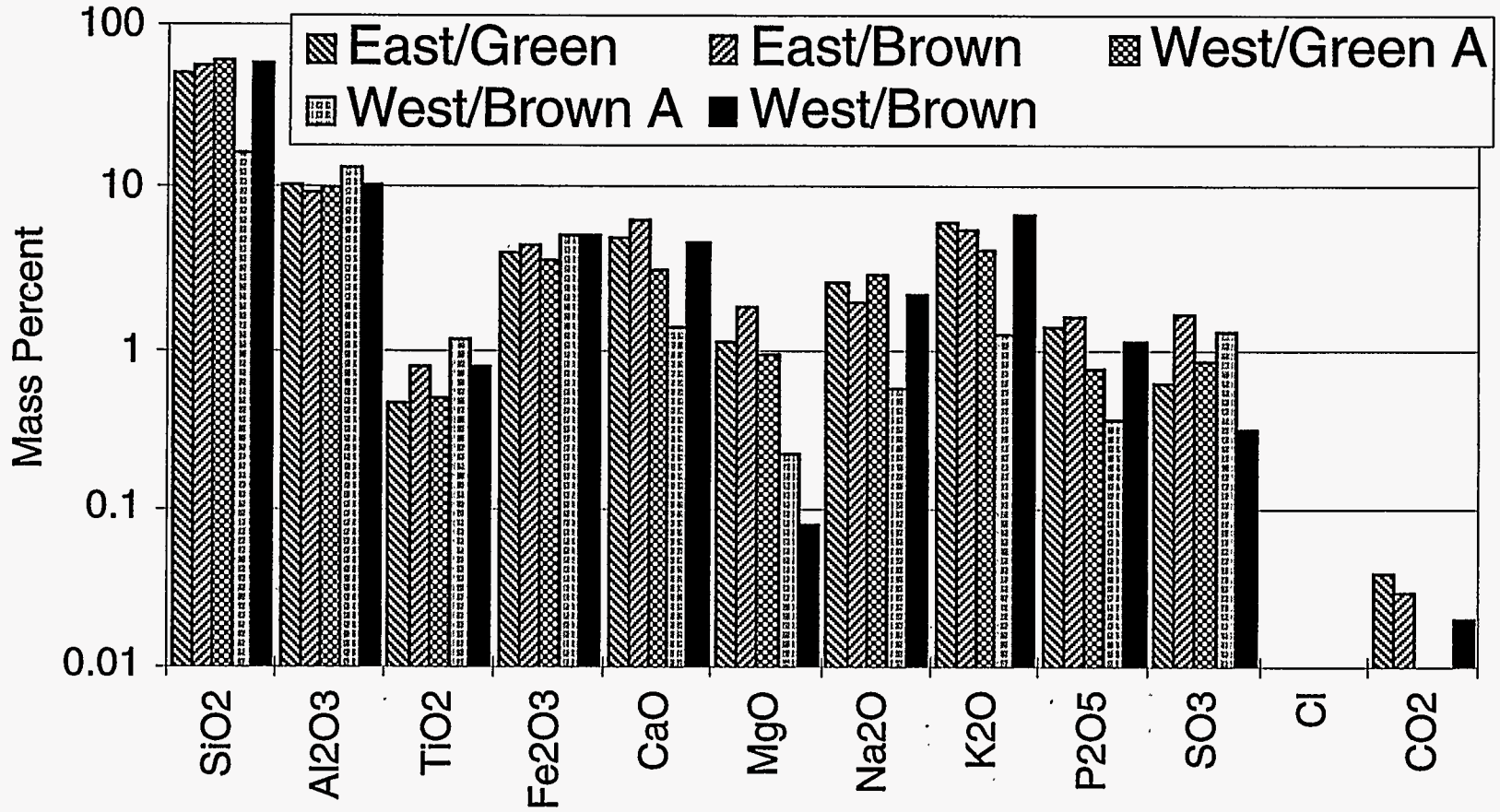

Figure 112 Elemental compositions of deposits removed from the loopseal in the Woodland boiler. Compositions are similar with the exception of one outlier. Deposits differ in color more significantly than in composition. Samples collected from locations 9, 10, 11, 14, and 16 in Figure 107.

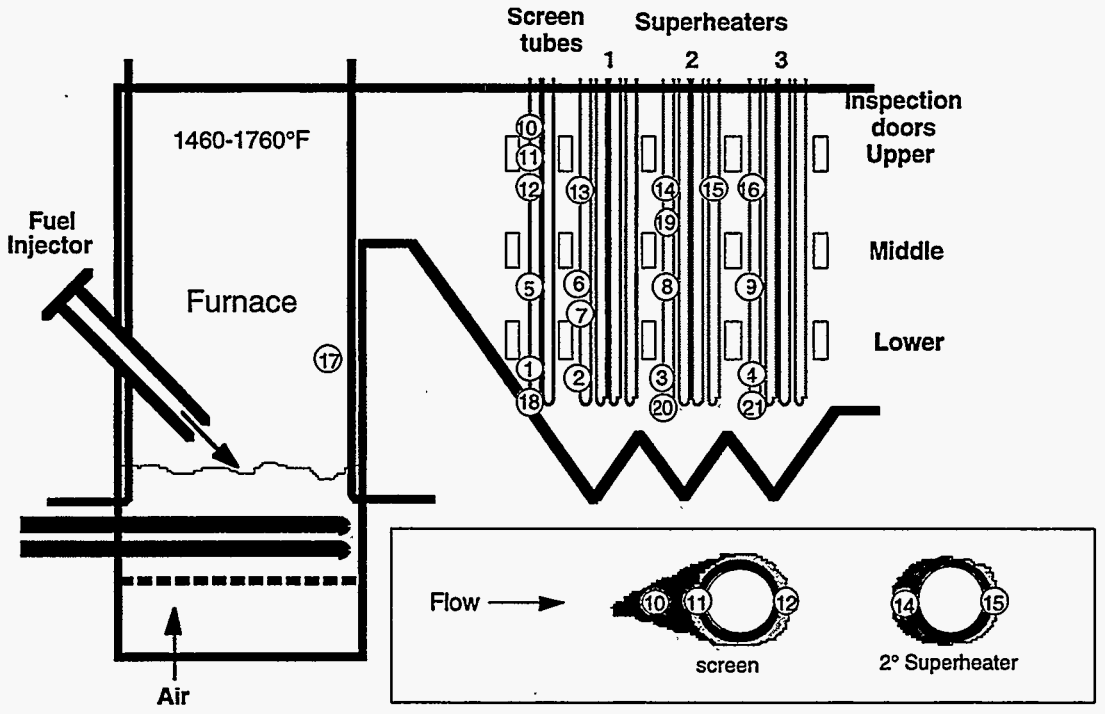

Figure 113 Schematic diagram of the Delano bubbling bed biomass boiler showing major components. This facility was fired primarily by wood during the test burn. Samples were obtained from the regions labeled with numbers, with samples 17-21 being collected after the first shutdown and prior to boiler cleaning (collected on July 10, 1993) and samples 1-16 being collected after the final shutdown (collected on September 4, 1993).

The final inspection of the Delano facility was made on 4 September. Sixteen deposit samples were collected from the screen tube and superheater sections. These are labeled 1 through 16 in Figure 113. The amount of deposition in the convection pass was moderate. Well developed deposits of the typical "shark's teeth" type appeared on the screen tubes. These deposits were better developed in the upper sections of the screen tubes than in the lower, possibly as a result of the flow patterns in the convection pass and greater tube deflections and mechanical loss in the lower end of these pendant tube assemblies. Samples 10, 11, and 12 were collected from the outer front, inner front, and back regions of the screen tubes. Hard, tenacious deposits ranging in thickness from 6 to 10 mm were removed from the front (upstream) side of the tubes in the No. 1 superheater immediately behind the screen tubes. The back side deposits were loose and fine textured. Similar deposits were found in the No. 2 superheater. An undulous appearance was more apparent in the fine textured back side deposits in the No. 2 superheater. Samples 14 and 15 were collected from the front and back sides respectively of the upper No. 2 superheater as shown in Figure 113. Almost no deposit was found on the No. 3 superheater, and the samples collected

were extremely small, consisting principally of tube material scraped from the surface. Spalling and flaking of the No. 3 superheater tube metal were noticeable. The furnace appeared to be relatively free of deposits, and no samples were collected. During the field test, the Delano facility was fired primarily with wood (60 % urban wood fuels and 37 % agricultural wood) and almond shells (3 %).

Figure 114 illustrates the relative consistency of deposit composition as a function of vertical position along a given superheater tube. All of the deposits are enriched in potassium, sulfur, and chlorine, indicating the mechanisms of condensation and chemical reaction are significant in deposit formation. Mass and heat transfer rates are much faster at the front of the tube than at the back. This is reflected in the composition of the deposits, as spatially resolved around the tube. The mechanism of condensation enriches a deposit in condensable vapors such as chlorides. The mechanism of chemical reaction transforms alkali and alkaline earth material into sulfates. Both mechanisms depend on good mass transfer rates. As shown in Figure 115, in regions were mass transfer rates are high, sulfation and alkali enrichment are high. In regions of low mass transfer (back of tube), alkali and sulfate enrichment are less pronounced. A similar trend is seen in the superheater deposits that are spatially resolved (Figure 116). The front deposits exhibit consistent compositions, independent of their vertical height along the tube, whereas the backside deposit is less enriched in potassium, sulfur, and chlorine, the three elements most strongly affected by condensation and chemical reaction mechanisms.

Evidence that the carbon in the deposits derives from carbonates and not from residual carbon in impacting fly ash particles is drawn from an analysis of the fly ash. Figure 117 illustrates that the fly ash contains essentially no carbon, very little chlorine, and very little sulfur. Formation of carbonates, chlorides, and sulfates requires somewhat lower temperatures and long residence times associated with ash deposits on heat transfer surfaces. The fly ash composition differs significantly from the superheater deposit composition, even though the superheater deposits are derived from the selective deposition of fly ash components and vapors.

The progression of deposit chemistry with temperature is also observable in these samples. At the highest temperatures, chlorides are the most stable form of alkali. As the temperature drops, thermodynamics begin to favor sulfates and finally carbonates. This transition is evident in the samples collected after the boiler shutdown and cleaning (Figure 118). There is also less consistency along the length of a given superheater tube than in the previous results, as is seen by comparing the upper and lower superheater #2 samples.

The bottom ash deposits indicate little enrichment in alkali, chlorine, or sulfur (Figure 119). This material has a consistent composition, composed of relatively benign particles that tend not to adhere to surfaces when they collide. The comparison between the furnace wall deposit and the bottom ash indicates similar compositions, consistent with the idea that deposits in regions with high particle concentrations (in the fluid bed) are dominated by inertially impacted particles.

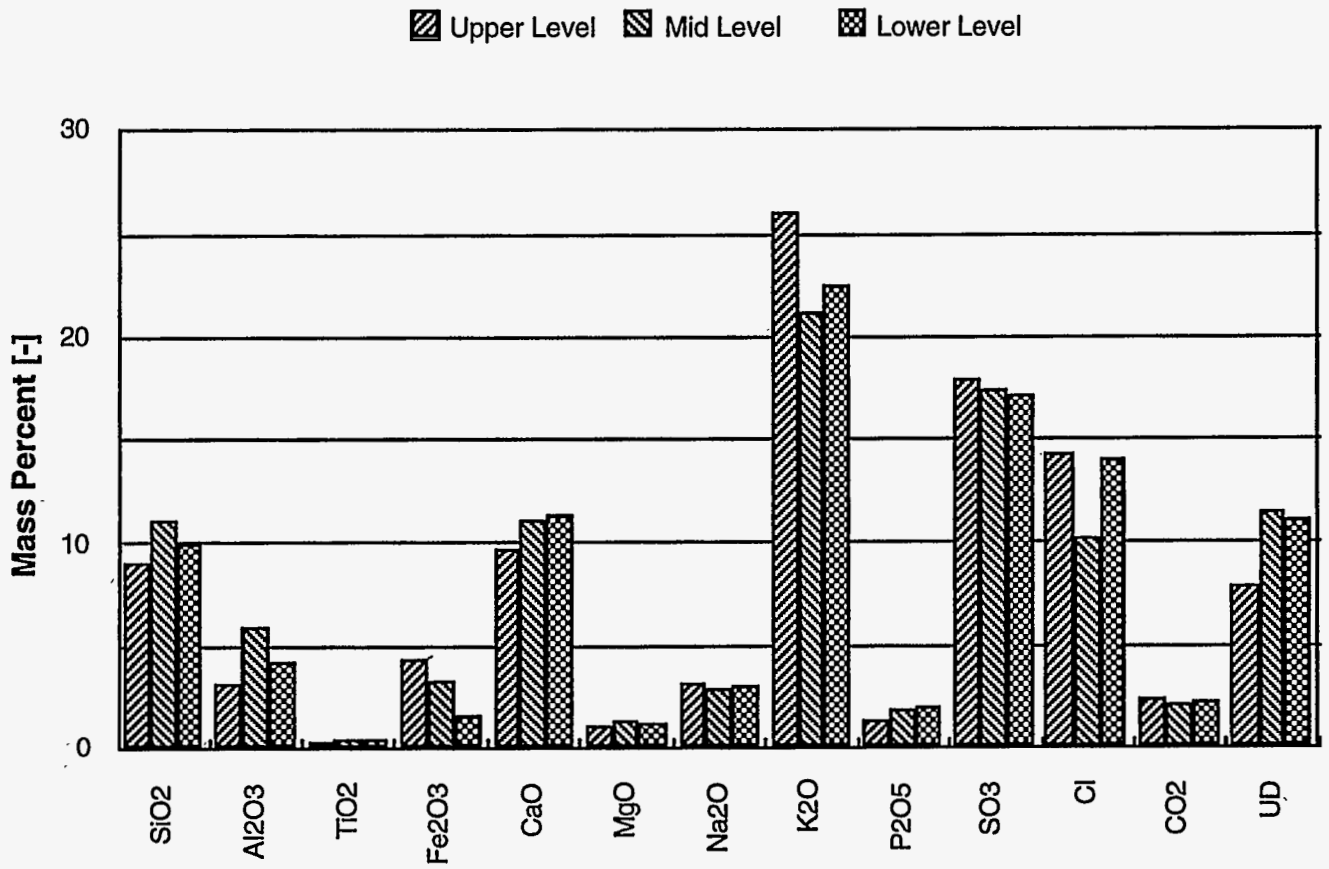

Figure 114 Elemental composition of deposits located on Superheater #1 of the Delano boiler as a function of vertical position along the tube. Samples were collected during the second boiler shutdown. Enrichment in potassium, sulfur, and chlorine is indicative of condensation and chemical reaction playing a significant role in deposit formation. Samples correspond to locations 13, 6 and 2, in that order, in Figure 113. All values represent percent of total deposit, with UD representing the undetermined fraction as measured by difference between the sum of the oxides and total ash.

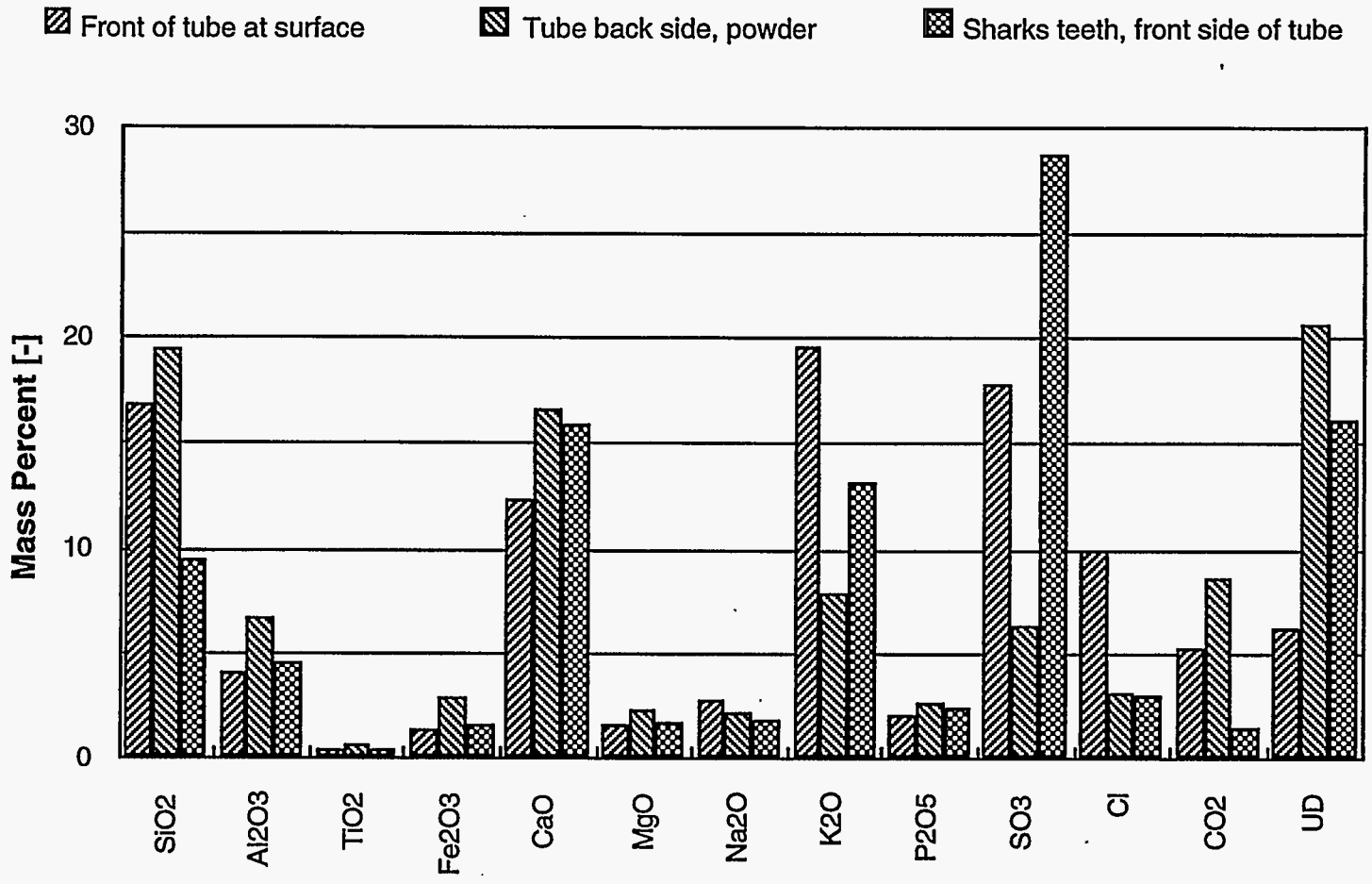

Figure 115 Spatially resolved deposit composition on screen tubes in the Delano boiler. Deposit composition reflects the impact of mass transfer rates on deposit properties. Samples correspond to locations 11, 12, and 10 (left to right) in Figure 113. All values represent percent of total deposit, with UD representing the undetermined fraction as measured by difference between the sum of the oxides and total ash.

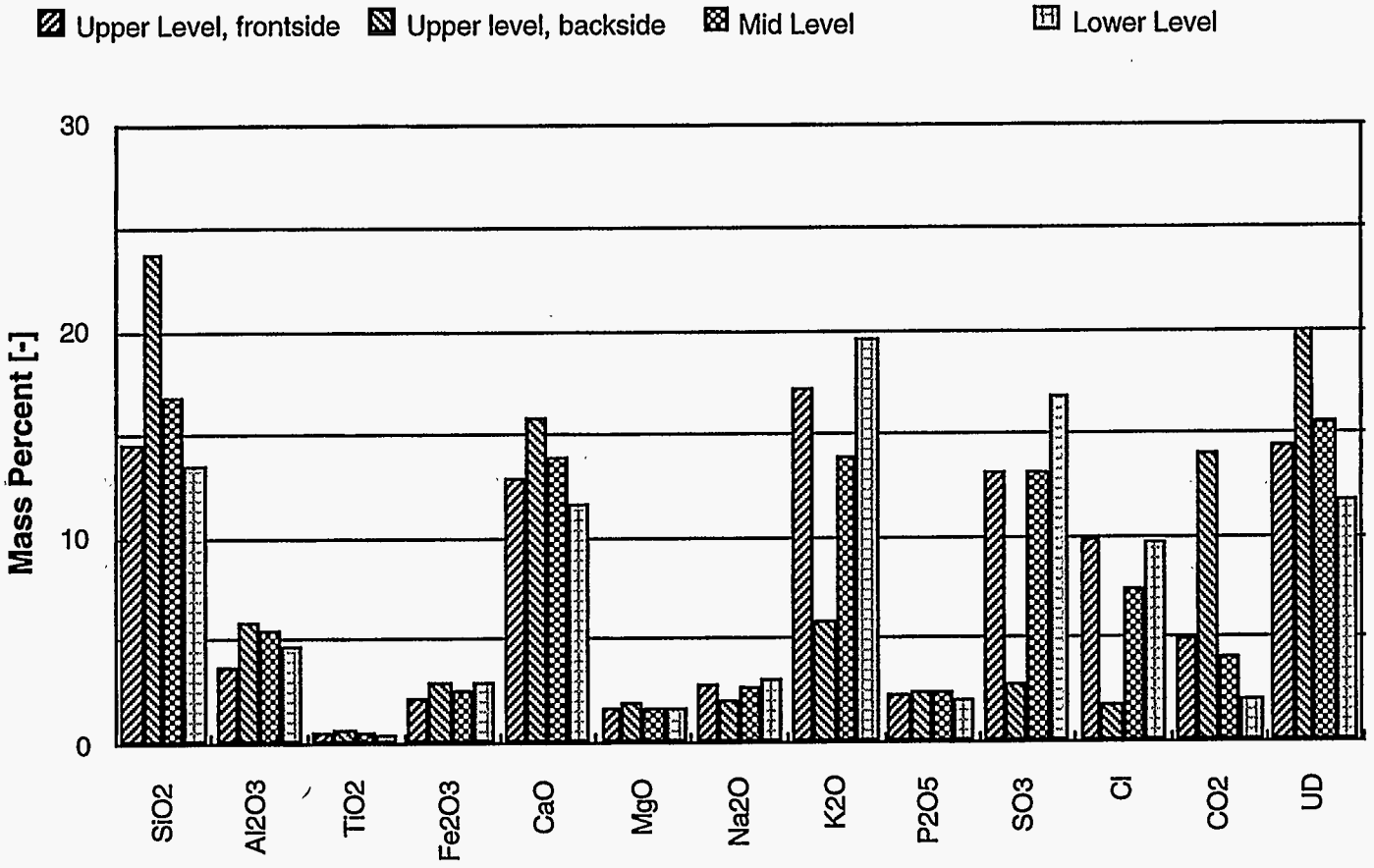

Figure 116 Elemental composition of ash deposit samples collected from the Delano plant on Superheater #2. These spatially resolved results illustrate the dependence of deposit composition on mass transfer rates (high transfer rates at front of tube lead to greater enrichment in sulfur, and chlorine). Results as displayed left to right correspond to locations 14, 15, 8 and 3 in Figure 113 . All values represent percent of total deposit, with UD representing the undetermined fraction as measured by difference between the sum of the oxides and total ash.

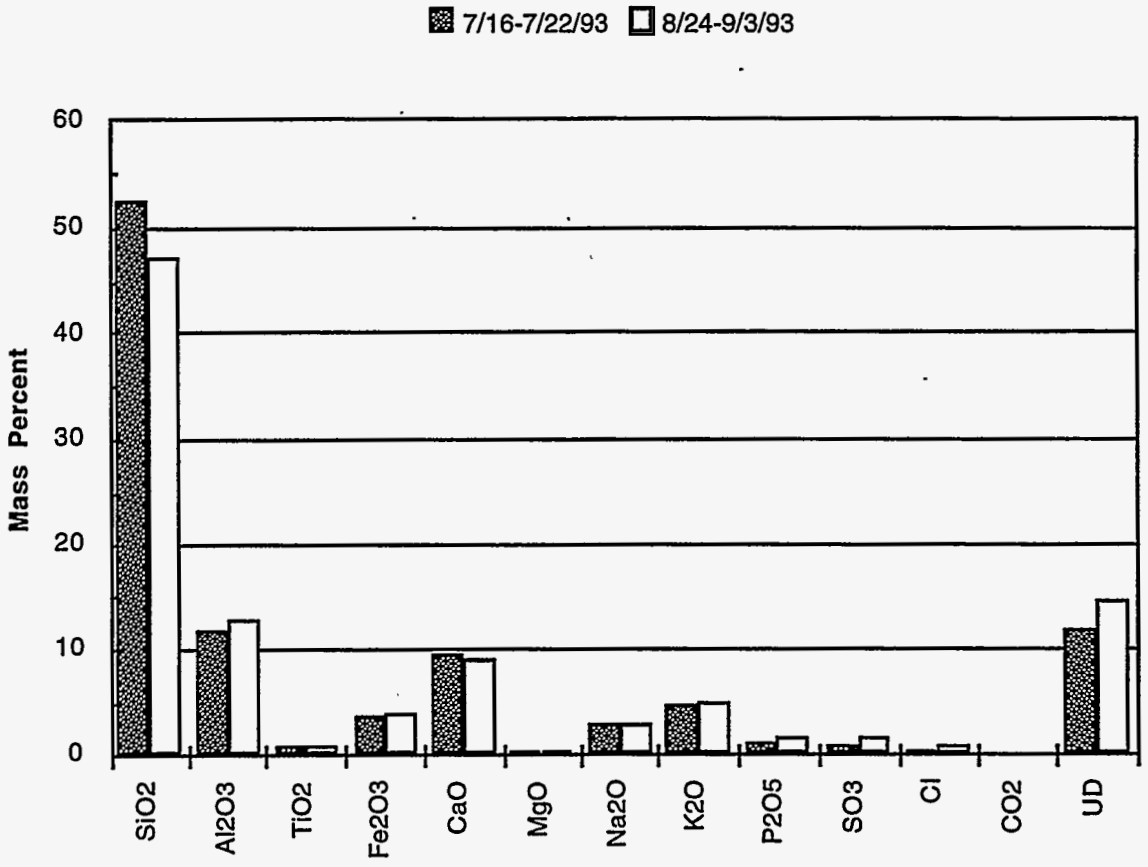

Figure 117 Fly ash composition from the Delano boiler sampled at both boiler shutdowns. The fly ash contains essentially no unburned carbon and differs in elemental composition from the superheater deposits, but is reasonably similar to the bottom ash and boiler wall deposits. All values represent percent of total deposit, with UD representing the undetermined fraction as measured by difference between the sum of the oxides and total ash.

A comparison of the furnace deposit with the convective pass deposit illustrates the substantially different composition of the deposits in different regions of the boiler (Figure 120). These samples show a similar pattern in composition to those illustrated in Figure 118, with the exception that carbonates in the deposits are universally lower in the data illustrated in Figure 120. This is presumably due to differences in operating conditions. The convective pass deposits with compositions indicated in Figure 120 were collected prior to the boiler washing.

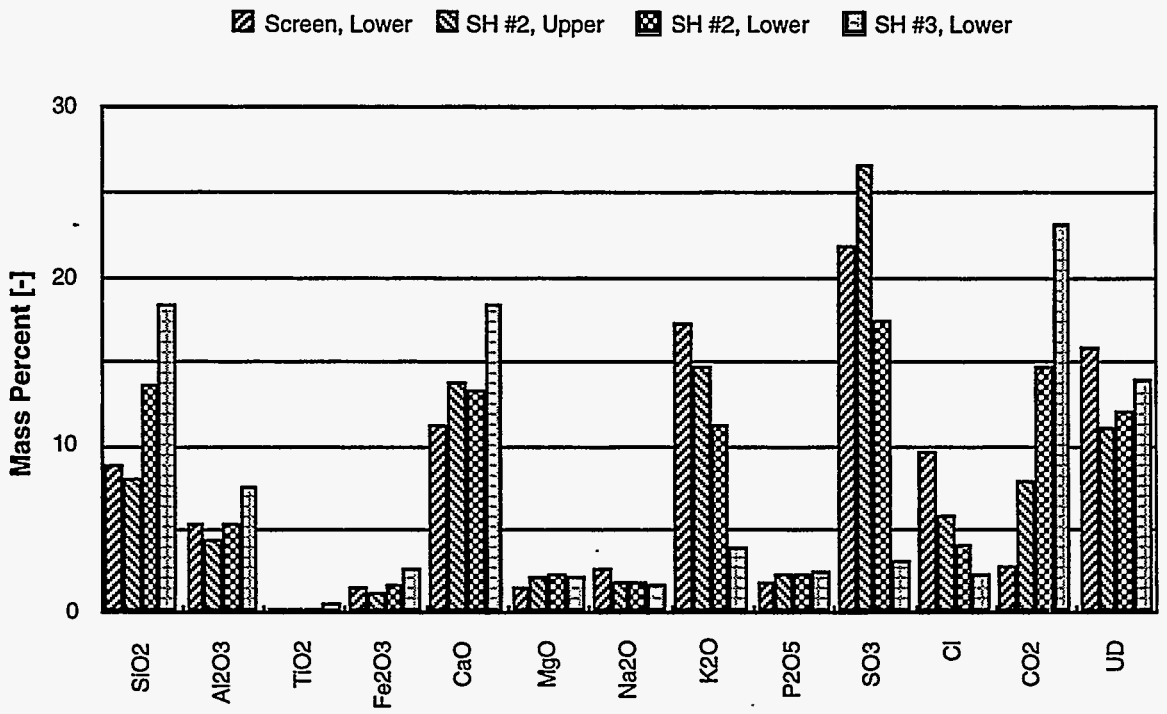

Figure 118 Elemental composition of deposits collected from the Delano boiler at the second shutdown (after boiler washing). Note the progression in deposit chemistry from chlorides to sulfates to carbonates with decreasing gas temperature. Less consistency in deposit composition with vertical distance along the tube is evident here compared with Figure 114. Results as displayed left to right correspond to locations 18, 19, 20, and 21 in Figure 113. All values represent percent of total deposit, with UD representing the undetermined fraction as measured by difference between the sum of the oxides and total ash.

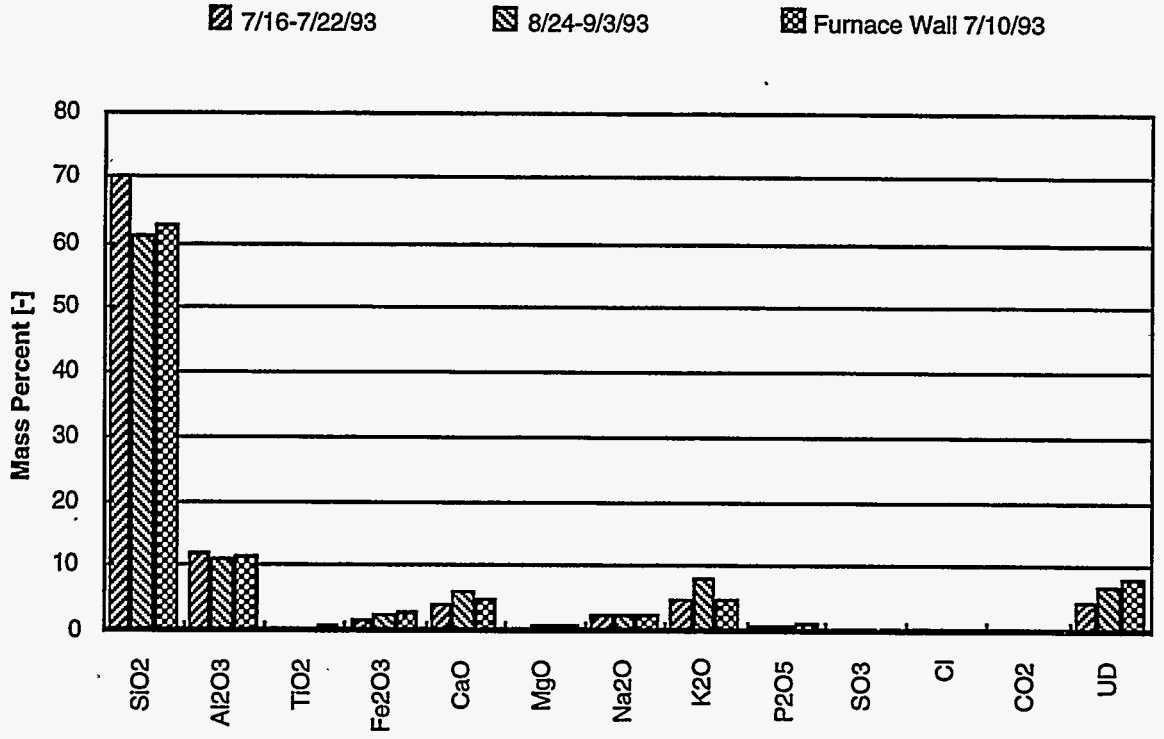

Figure 119 Elemental composition of bottom ash and furnace wall deposit samples obtained from the Delano boiler. Furnace wall deposit corresponds to location 17 in Figure 113. All values represent percent of total deposit, with UD representing the undetermined fraction as measured by difference between the sum of the oxides and total ash.

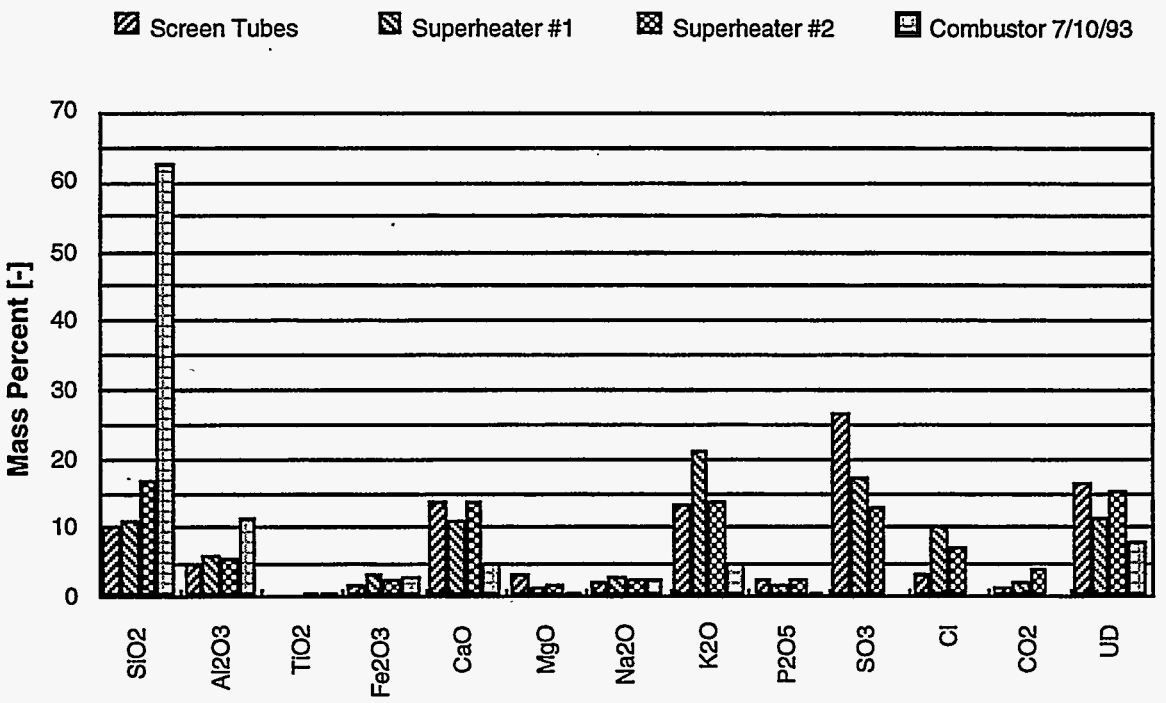

Figure 120 Elemental compositions of superheater deposits collected at midlevel compared with boiler wall deposits. Differences between boiler wall and convective pass deposits are evident and indicate different mechanisms responsible for ash deposition in different regions of the boiler. More subtle differences in convective pass deposits with position and temperature are also evident. Results displayed left to right correspond to samples 5, 6, 8, and 17 in Figure 113. All values represent percent of total deposit, with UD representing the undetermined fraction as measured by difference between the sum of the oxides and total ash.

Summary and Conclusions

Boiler deposits form in a complex interplay of elements from the fuel, additives, bed media, and the boiler structures themselves. The results of the full-scale and laboratory tests show distinctively the influences of fuel composition, limestone addition, and fluidized bed media. The stoker fired unit (Grate-1) burning a blend of wood with straw and the bubbling fluidized bed (FBC-1) burning wood and shell developed superheater deposits enriched in potassium and sulfate. Superheater deposits from the latter facility were also enriched in chlorine and carbonate. The concentrations of sulfates, chlorides, and carbonates vary along the convection pass in a manner apparently consistent with the stability of the compounds, that is, as the temperature increases, the alkali species decompose in the order of carbonates, sulfates, and chlorides. The grate units firing straw produced superheater deposits enriched in potassium and chlorine, with lower concentrations of sulfates and carbonates. The fluidized beds are distinctive for the production of superheater deposits enriched not in potassium, but in calcium, as calcium sulfates. The calcium enrichment is probably related to the addition of limestone or lime to the bed during operation, but one unit not adding limestone also had deposits enriched in calcium sulfate. The superheater deposits from the bubbling fluidized bed had much higher concentrations of chlorides than did those from the circulating fluidized beds, which may be related to differences in fuel composition but also is indicative of differences due to recirculation. Grate and bed deposits were dominated in composition by fuel ash and bed media, with loss of volatile sulfur, as in the case of the MFC furnace wall deposits.

The laboratory experiments reveal the influences of fuel composition and structure. Probe deposits from straw were enriched in potassium and chorine next to the probe surface, developing outwards into a matrix of sintered silicate-rich fly ash particles. Switchgrass deposits also showed potassium enrichment, and greater enrichment in sulfate compared to the straws. The high-potassium almond shells and hulls formed fine textured deposits, rich in potassium, suggesting the deposition of hydroxides or carbonates. A similar result was obtained for olive pits, high in sodium rather than potassium, and again suggesting sodium depositing as other species in addition to sulfates and chlorides. The deposits formed from the commercial wood and almond shell blend were enriched in potassium and sulfate, as in the full-scale deposits, but contained more silicon and less calcium. Greater direct fly ash capture and the lack of calcium from limestone likely account for the differences in the laboratory and full-scale deposit compositions in the latter case. Differences in combustion and flow regimes between the laboratory multi-fuel combustor and the full-scale circulating fluidized bed are likely also responsible, but the initial deposition of alkali sulfate species appears consistent between pilot- and full-scale facilities.

The manner in which fuel elements and elements from other sources come to be incorporated into deposits on boiler heat transfer surfaces is not entirely understood, but physical mechanisms and

conceptual chemical pathways have been developed. A highly simplified and abbreviated conceptual scheme for various chemical interactions among major biomass fuel elements appears in Figure 121. Several possible routes are illustrated for the alkali metal, potassium, and the alkaline earth metal, calcium, to deposit on a surface. The species shown appear to account for much of the superheater deposit mass identified in the full-scale experiments. Other elements, such as sodium or magnesium, may follow generally similar pathways. Not shown in the figure are the physical conditions, which greatly influence the deposit composition and properties.

Potassium can exist in the original biomass in different forms, including ionic and organo-metallic forms, and salts. For all biomass it is atomically dispersed in the fuel, unless present through contamination. By contrast, silicon occurs primarily as hydrated silica grains. Upon combustion, potassium may be released from the fuel in numerous ways. Potassium is likely volatilized with organic species, and may be released as metallic K, although the latter is subject to rapid chemical reaction and its life time short. If the fuel contains chlorine, potassium likely appears as the salt, KCl. Without chlorine, the hydroxide, KOH, or alternatively potassium oxides, sulfates, or carbonates may be formed.

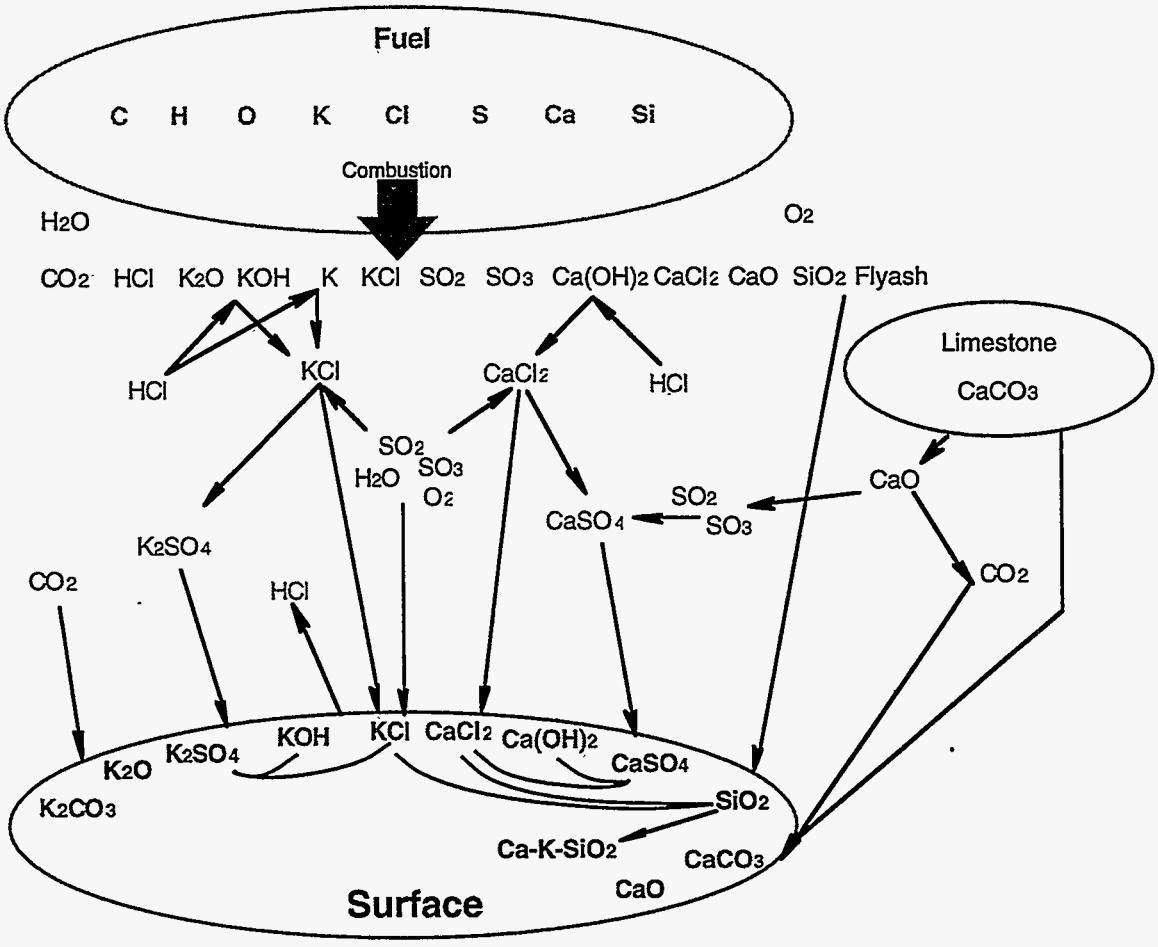

Figure 121 Simplified conceptual interactions among selected fouling elements in biomass.

Nearly all the inherent potassium in biomass is either water soluble or ion exchangeable (Baxter, Miles, Miles, Jenkins, Richards, & Oden, 1993). This mobile material is readily volatilized, although only a fraction (≈25%) of it typically does volatilize and much remains in the fly ash and boiler bottom ash. Calcium, contained primarily in cell walls, is more refractory and less readily volatilized. Calcium may also enter through the introduction of limestone to the furnace. Under attack from chlorine, vaporized as HCl if the fuel contains it, volatilized potassium likely forms KCl in the gas phase. Chlorine is an important facilitator in the deposition of alkali species on heat transfer surfaces. Starting with a clean surface, KCl, or KOH if chlorine is absent, is deposited on the surface through heterogeneous condensation or small particle transport following homogenous condensation and nucleation, either in the bulk gas if sufficiently cooled or in the thermal boundary layer adjacent to heat transfer surfaces.

Thermophoretic mechanisms, in addition to condensation, are important to the deposit formation at this point due to the large thermal gradients above the surface (Baxter, et al., 1993; Raask, 1985). Past the flame, if the gas is sufficiently cooled, KCl or KOH may react with SO_2 or SO_3 in the gas to form potassium sulfate, K_2SO_4, which can condense and deposit (Raask, 1985). Sulfation of the alkali and alkaline earth species also occurs once they are deposited on the surface by reaction with gaseous sulfur oxides, losing chlorine from the deposit in the process. There is some question as to which sulfation route is dominant, but the condensed phase process appears more likely. In this manner the surface initially acquires a characteristic thin, dense, and reflective deposit layer nearly universally observed.

Following the initial deposit formation, particle impaction becomes the dominant mechanism for incorporating inorganic elements into the deposit. Condensation, phoretic forces, and chemical reaction still contribute to the deposit formation while suitable conditions exist. Fly ash particles containing silicates and other species, and limestone or other additives, deposit by impaction if within a suitable size range. Particles smaller than about 5 μm tend to follow the streamlines around the tubes, while for larger particles rebound from the surface is enhanced because of the high kinetic energy of the particles. Large particles have been observed rebounding from the upper tube surface in the MFC even after formation of a deposit. The particle size for which rebound becomes important has not been investigated for biomass.

For tubes in cross flow, the deposit develops as a characteristic aerodynamic wedge on the upstream or leading edge of the tube, as in Figure 113. Heat transfer through the deposit is reduced as it thickens, and the deposit surface temperature increases towards the gas temperature. Condensation is no longer important where the deposit surface temperature exceeds the dew point, and thermophoresis becomes less important as the temperature gradient across the thermal boundary layer declines. Heterogeneous and homogeneous reactions cause continuing sulfation and the formation of complex silicates within the deposit. The less stable carbonates deposit in the cooler regions, downstream in the convection pass and in the wake regions of the tubes, as in the case of the bubbling fluidized bed unit at Delano. Continuing sulfation leads to increased deposit tenacity, making soot blowing less effective in removing deposits. Formation and deposition of alkali sulfates and chlorides also contributes to tube metal corrosion. This conceptual model is grossly simplified, but aids in the interpretation of the results obtained in both the full-scale and

laboratory experiments. Features of the deposits from the different facilities appear consistent with these mechanisms.

None of the California units currently burn straw. The fouling rates with straw, even in low concentrations, have proved too high for economic operation. In contrast, the two Danish grate units described here are fueled entirely with straw, and operate several thousand hours each year, although deposition remains a concern. Despite the problems associated with slagging and fouling from straw fuels, Denmark has established a major program in straw combustion for district heating, electric power, and combined heat and power (CHP) generation. Currently about 70 plants, mostly small heating facilities, but including larger scale power units, burn straw from wheat, rye, and rape alone or in combination with coal or wood. Although fuel costs are high, as much as \$70 t^{-1} (Nikolaisen, 1992), and the cost of electric power from these plants around \$0.10 kWh^{-1}, the sale of thermal energy improves the economic performance, and Danish CO_2 laws provide subsidies to "alleviate any negative consequences caused by the conversion to biomass fuels." Many of the plants utilize the folded furnace design shown in Figure 113, providing greater surface area, and reducing gas temperatures ahead of the critical cross-flow superheater surfaces to below 750°C (1400°F) or lower, which mitigates the problem of superheater fouling. The design utilizes parallel heat exchangers in the folded section following the radiant furnace to reduce the deposition by impaction. All of the California facilities investigated for this study normally operate with furnace exit gas temperatures in the range of 850 to 950°C (1600 to 1750°F) to achieve peak capacity. Reducing furnace exit gas temperature might help reduce the severity of superheater and convection pass fouling in the California facilities, but the impact on capacity and economy of the plants is not yet known. In this sense, the boilers erected to burn agricultural fuels in California appear to have been underdesigned. The concepts employed in the Danish boilers are not unique, and were adapted from boilers burning solid waste and other high fouling fuels.

The reduction of furnace exit gas temperature to reduce the severity of superheater fouling follows from the mechanisms of deposit formation discussed above, although operators know empirically that fouling is generally reduced by lowering the exit gas temperature. If the alkali and other fouling compounds are homogeneously condensed, or heterogeneously condensed on fly ash, prior to crossing the superheaters, particle transport along the streamlines of the flow reduces the amount of substance depositing. For particles diffusing to or impacting the surface, rapid cooling and solidification while crossing the thermal boundary layer reduces the number of particles adhering to the surface. If the exit temperature is low enough, the particles will solidify in the bulk gas. Reduced temperatures also result in reduced chemical reaction rates. The strength of the deposit formed is reduced, which makes it easier to remove by soot blowing. Disadvantages of the method are associated with the costs of building larger furnaces to accommodate the reduced heat transfer coefficients on the parallel heat exchangers, loss of efficiency if high superheat temperatures cannot be attained, and possible derating of capacity and loss of revenue for existing units. Deposit-related corrosion may also be enhanced at lower temperatures. As a short term remedial problem for existing units, the technique may be effective, employed either continuously or on an intermittent basis. Intermittent operation at lower temperature may contribute to weakening of deposit through thermal cycling, also making soot blowing more effective.

Of some interest is the recent Danish experience with so-called "gray" straw, or straw that has been exposed to rain in the field. In the last year, much of the straw was washed by natural precipitation, and problems with boiler fouling were reduced. Plant capacity was also reduced due to higher moisture and reduced organic matter content of the fuel. However, as with bagasse, leaching of the straw appears to offer substantial benefit in the control of fouling deposits in the boilers, and emphasizes the role of potassium and chlorine, which are both readily leached. In California, rain leached, spring harvested, rice straw might be acceptable for existing boilers, but likely only when blended at low concentration with more conventional fuels. Artificial straw washing has not been investigated and the feasibility of such a technique is unknown.

Additives may hold some promise for reducing the rate of fouling. Fluidized bed combustion power plants, as in the units described here, routinely employ limestone injection for control of sulfur emissions, with additional benefits in reduced bed agglomeration. Limestone addition is involved in the formation of calcium sulfate deposits on superheaters and other convection pass surfaces. Other additives, such as kaolin, dolomite, or magnesium oxide, have been used to reduce bed agglomeration and slagging, but they have so far not been widely employed in the industry, and are generally particularly effective only with fluidized beds because of the good mixing. The effect of additives is frequently debated, but so far no systematic study of their potential for biomass combustors has been undertaken. Standardized methods to test the effect of additives on biomass fuel ash behavior are not developed, and standard ash fusibility tests to determine deformation and fusion temperatures of ash are now commonly accepted as being of little value in predicting the behavior of ash in biomass boilers. Such tests generally fail because they do not properly simulate elemental composition and enrichment in deposits, nor the physical conditions leading to deposit formation.

For the existing facilities, retrofit designs can be conceived to increase the number of acceptable fuels, but without major capital investment, strategies are limited principally to changing boiler operating conditions in concert with changes in fuel properties (e.g., furnace exit gas temperature control with fuel selection). Design changes might include the addition of a thermal gasifier on-site to essentially pretreat the fuel ahead of the boiler. Gasifying high fouling fuels and only burning the gas in the boiler might alleviate or reduce ash fouling. The purpose would be to retain inorganic materials, including alkali, in the char phase, which would be disposed of in some other fashion. If sufficiently depleted in carbon, the char could be land applied for its fertilizer value, although there are significant unresolved questions concerning the feasibility and suitability of the technology. The success of such measures depends on gasifying the fuel at lower temperatures than combustion, otherwise, under reducing conditions, the vaporization of fouling elements can be enhanced, exacerbating the problem of deposition. Other pretreatment options include fermenting the fuel and burning the residual solids, which should be leached of potassium and chlorine. At least one facility has already been proposed in California employing a fermentation option for rice straw, although not specifically as a pretreatment for combustion. The feasibility of the technology has not yet been demonstrated in a full-scale unit.

Many of the problems encountered with ash fouling in existing units accrue from the lack of prior experience in the industry in burning the wide variety of fuels, particularly those that are not commonly used as fuel or contain high concentrations of alkali and silica. Improved and advanced

combustor designs and concepts are available, although many have not been adequately tested. Other concepts, such as integrated gasifier combined cycles and numerous variations, are under active development and include research into the control of alkali species. Substantial improvements should be possible as existing units are retired and replaced, although fouling problems are not likely to become fully mitigated. Economic analyses should make careful accounting of operating costs in addition to capital costs for the facilities.

Conclusions

Many agricultural fuels have proved unsuitable for use in existing biomass boilers. Straw and other annual herbaceous plant materials cause rapid fouling of heat transfer surfaces, furnace slagging, and agglomeration of fluidized beds. Excessive deposition results from the incompatibility of fuel composition with boiler design and operation. Superheater fouling is perhaps the most critical problem for existing units. Clearly, deposit formation occurs as a result of complex interactions among many compounds, and cannot be described on the basis of potassium, silicon, or any other element alone.

Full-scale experiments and laboratory simulations show the composition of deposits to be consistent with postulated mechanisms of deposit formation and growth. In biomass, unlike coal, and with a few exceptions, the major alkali species of concern is potassium instead of sodium. In herbaceous species, including straws and grasses, canes and stovers, inherent potassium concentrations are about 1% of the fuel dry weight, almost all of which potentially could vaporize during combustion. These same fuels are frequently rich in chlorine, silicon, and sulfur, which in combination with potassium represent the primary fouling agents when these fuels are burned. Chlorine is an important facilitator, leading to the condensation of potassium chloride salt on surfaces, which often reacts with sulfur oxides to form potassium sulfate, and leads to the creation of sticky coatings for enhanced particle attachment following inertial impaction. Potassium, sometimes in combination with alkaline earth metals like calcium, reacts with silicates deposited as fly ash to form molten glassy phases leading to tightly sintered structures. In the furnace, glass reactions lead to the formation of heavy slag deposits resembling fuel ash in composition but substantially depleted in sulfur. On superheater surfaces in boilers firing wheat straw, chlorides represented a major portion of the deposit mass.

When firing wood fuels, either in combination with agricultural fuels such as hulls, shells, and pits, or woods derived from urban sources with potentially large amounts of adventitious material contamination, the role of potassium may be reduced and that of the alkaline earth metals such as calcium more pronounced. Fuels comprised principally of mature stem wood have relatively low inherent potassium concentrations, around 0.1%, and low inherent silicon and chlorine concentrations. Initial deposition, probably as condensation of hydroxides, is followed by sulfation of alkali and alkaline earth elements, increasing the tenacity of the deposits. If large amounts of adventitious materials in the form of clays or other soil contaminants are present, the role of silicon may still be quite pronounced in secondary deposit growth by particle impaction following the initial formation of condensed layers on surfaces. Complex alkali-alkaline earth-aluminosilicates form or are incorporated into superheater deposits in this manner. Although mature wood is low in silicon, urban and agricultural wood fuels used commercially all had

substantial silicon concentrations in the ash. Injection of limestone into fluidized bed combustors leads to the formation of calcium sulfate deposits on superheaters where sulfur is present in the fuel. Wood fuels and blends fired commercially, although generally low in sulfur, had adequate amounts to cause substantial sulfation of deposits. Calcium sulfate was especially pronounced in the superheater deposits in fluidized beds, compared with the grate units.

Laboratory simulations confirmed the enrichment of alkali species in the early phases of deposit formation. For straws and grasses, initial deposits containing alkali chlorides can be expected. A wood blend with small amounts of almond shell produced a sulfated deposit similar to that observed in commercial units burning similar fuels. Potassium rich almond hulls and shells generated deposits containing more potassium than could be accounted for as sulfates and chlorides. Sodium rich olive pits produced a similar result. With such fuels, initial deposition as alkali hydroxides or carbonates may be important.

References

Federal Register: Part III; Air Contaminants (Final Rule No. 29 CFR Part 1910). (1989).

Atkins, R. S., & Donovan, C. T. *Wood Products in the Waste Stream: Characterization and Combustion Emissions* (Final Report No. Energy Authority Report 92-8). New York State Energy Research and Development Authority. (1993).

Baxter, L. L. Ash Composition Prediction as a Function of Coal Type, Operating Conditions, and Boiler Location. In A. K. Mehta & N. S. Harding (Ed.), *EPRI conference on the Effects of Coal Quality on Power Plants*, (pp. 5/59-5/74). St. Louis, Missouri: Electric Power Research Institute. (1990a).

Baxter, L. L., *Progress in Energy and Combustion Sciences, 16*, 261-266. (1990b).

Baxter, L. L. Boiler Performance with Blends of Eastern and Western Coals. In *EPRI Conference on The Effects of Coal Quality on Power Plants*, . San Diego, CA: (1992a).

Baxter, L. L., *Combustion and Flame, 90*, 174-184. (1992b).

Baxter, L. L., *Biomass and Bioenergy, 4*(2), 85-102. (1993).

Baxter, L. L. Experimental and Theoretical Comparisons of the Combustion and Ash Deposition Behavior of Blended Coals and that of the Blend Components. In R. W. Bryers & N. S. Harding (Eds.), Coal-Blending and Switching of Low-Sulfur Western Coals (pp. 255-264). New York: ASME. (1994).

Baxter, L. L. Ash. In Encyclopecia of Energy Technology and the Environment (pp. 306-321). New York: John Wiley & Sons, Inc. (1995).

Baxter, L. L., Abbott, M. F., & Douglas, R. E. Dependence of Elemental Ash Deposit Composition on Coal Ash Chemistry and Combustor Environment. In S. A. Benson (Ed.), *Engineering Foundation Conference on Inorganic Transformations and Ash Deposition During Combustion*, (pp. 679-698). Palm Coast, Florida: The American Society of Mechanical Engineers. (1991).

Baxter, L. L., & DeSollar, R. W. Ash Deposition as a Function of Coal Type, Location in a Boiler, and Boiler Operating Conditions: Predictions Compared to Observations. In *International Conference on Environmental Control of Combustion Processes*, . Honolulu, HA: (1991).

Baxter, L. L., & DeSollar, R. W., *Fuel, 72*(10), 1411-1418. (1993).

Baxter, L. L., & Dora, L., *ASME Paper No. 92-JPGC-FACT-14*. (1992).

Baxter, L. L., & Hardesty, D. R. *The Fate of Mineral Matter During Pulverized Coal Combustion* (Quarterly Report No. SAND90-8223). Sandia National Laboratories. (1990).

Baxter, L. L., & Hardesty, D. R. *The Fate of Mineral Matter During Pulverized Coal Combustion: April - June* (Quarterly Report No. SAND92-8227). Sandia National Laboratories. (1992a).

Baxter, L. L., & Hardesty, D. R. *The Fate of Mineral Matter During Pulverized Coal Combustion: January-March* (Quarterly Report No. SAND92-8210). Sandia National Laboratories. (1992b).

Baxter, L. L., Hencken, K. R., & Harding, N. S. The Dynamic Variation of Particle Capture Efficiency During Ash Deposition in Coal-Coal Fired Combustors. In *Twenty-Third Symposium (International) on Combustion*, (pp. 993-999). Orleans, France: (1990).

Baxter, L. L., Miles, T. R., Miles, T. R., Jr., Jenkins, B. M., Richards, G. R., & Oden, L. L. Transformations and Deposition of Inorganic Material in Biomass Boilers. In M. G. Carvalho (Ed.), *Second International Conference on Combustion Technologies for a Clean Environment*, 1 (pp. Biomass II: 9-15). Lisbon, Portugal: Commission of European Communities. (1993).

Baxter, L. L., Mitchell, R. E., & Fletcher, T. H., *Combustion and Flame*. (1995 (to appear)).

Beér, J. M., Monroe, L. S., Barta, L. E., & Sarofim, A. F. From Coal Mineral Matter Properties to Fly Ash Deposition Tendencies; a Modeling Approach. In *The Seventh International Pittsburgh Coal Conference*, . Pittsburgh, PA: (1990).

Byers, R. L., & Calvert, S., *Industrial and Engineering Chemistry Fundamentals*, *8*(4), 646-655. (1969).

Castillo, J. L., & Rosner, D. E., *International Journal of Multiphase Flow*, *14*, 99-120. (1988).

Chow, O. K., & Lexa, F. F. *Combustion Characterization of the Kentucky No. 9 Cleaned Coals* (Final Report No. CS-4994 Research Project 2425-1). Electric Power Research Institute. (1987).

Dayton, D. C., French, R. J., & Milne, T. A., *Energy & Fuels, (to appear)*. (1995).

Dayton, D. C., & Wang, D. CID Studies of Inorganic Species Released During BiomassCombustion. In *43rd ASMS Conference on Mass Spectrometry and Allied Topics*, (pp. Poster TPA 034). Atlanta, GA: (1995).

Durant, J. F., Kwasnik, A. F., & Lexa, G. F. *Impacts of Cleaning Texas Lignite on "Boiler Performance and Economics* (Final Report No. GS-6517). Electric Power Research Institute. (1989).

Evans, R. J., & Thomas A. Milne, T. A., *Energy & Fuels*, *1*, 123-127. (1987a).

Evans, R. J., & Thomas A. Milne, T. A., *Energy & Fuels*, *1*, 311-319. (1987b).

FEC Consultants Ltd., O. *Straw Firing of Industrial Boilers* (Contractor Report No. ETSU B 1158). Energy Technology Support Unit: Department of Energy: United Kingdom. (1988).

French, R. J., Dayton, D. C., & Milne, T. A. *The Direct Observation of Alkali Vapor Species in Biomass Combustion and Gasification* No. NREL Technical Report (NREL/TP-430-5597)). NREL. (1994).

Friedlander, S. K., & Johnstone, H. F., *Industrial and Engineering Chemistry, 49*, 1151-1156. (1957).

Fuchs, N. A. The Mechanics of Aerosols. (R. E. Daisley and M. Fuchs, Trans.). New York: Dover. (1964).

Gökoglu, S. A., & Rosner, D. E., *International Journal of Heat and Mass Transfer, 27*, 639-646. (1984).

Gökoglu, S. A., & Rosner, D. E., *Industrial and Engineering Chemistry Fundamentals, 24*, 208-214. (1985).

Gökoglu, S. A., & Rosner, D. E., *AIAA Journal, 24*, 172-179. (1986).

Griffith, B. F., Lexa, F. G., & Teigen, B. C. *Pilot-Scale Combustion Characterization of Two Illinois Coals* (Final Report No. CS-6009, Research Project 2425-1). Electric Power Research Institute. (1988).

Harb, J. N., Munson, C. L., & Richards, G. H., *Energy & Fuels, 7*, 208-214. (1993).

Harding, N. S., & Mai, M. C. Elemental Partitioning during Pilot-Scale Combustion Tests — Effects on Ash Deposit Composition. In R. W. Bryers & K. S. Vorres (Eds.), Mineral Matter and Ash Deposition from Coal (pp. 375-399). Engineering Trustees, Inc. (1990).

Hastie, J. W., Zmbov, K. F., & Bonnell, D. W., *High Temperature Science, 17*, 333-364. (1984).

Helble, J. J., Neville, M., & Sarofim, A. F. Aggregate Formation from Vaporized Ash During Pulverized Coal Combustion. In *Twenty-First Symposium (International) on Combustion*, (pp. 411-417). Technical University of Munich, Germany: The Combustion Institute. (1986).

Helble, J. J., & Sarofim, A. F., *Journal of Colloid and Interface Science, 128*(2), 348-362. (1989a).

Helble, J. J., & Sarofim, A. F., *Combustion and Flame, 76*, 183-196. (1989b).

Helble, J. J., Srinivasachar, S., & Boni, A. A., *Progress in Energy and Combustion Science, 16*, 267-279. (1990).

Hustad, J. E., & Sønju, O. K., *Biomass and Bioenergy, 2*(1-6), 239-261. (1992).

Im, K. H., & Chung, P. M., *AIChE Journal, 29*(3), 498-505. (1983).

Israel, R., & Rosner, D. E., *Aerosol Science and Technology, 2*, 45-51. (1983).

Jacobsen, S., & Brock, J. R., *Journal of Colloid Science, 20*, 544-554. (1965).

Jenkins, B. M. Physical Properties of Biomass. In O. Kitani & C. Hall (Eds.), Biomass Handbook New York: Gordon and Breach. (1989).

Laitone, J. A., *Jounal of Applied Mechanics, 48*, 465-471. (1981).

Levin, E. M., Robbins, C. R., & McMurdie, H. F. Phase Diagrams for Ceramists. (. Columbus, OH: American Ceramic Society. (1964).

Livingston, W. R. *Straw Ash Characteristics* (Contractor Report No. ETSU B 1242). Energy Technology Support Unit: Department of Energy: United Kingdom. (1991).

Loehden, D., Walsh, P. M., Sayre, A. N., Béer, J. M., & Sarofim, A. F., *Journal of the Institute of Energy, 62*, 119-127. (1989).

Marschner, H. Mineral Nutrition of Higher Plants. (. London: Harcourt Brace Jovanovich. (1986).

Martindale, L. P. *The Potential for Large Scale Projects Featuring Straw as a Fuel in the UK* No. ETSU. (1982).

Martindale, L. P. *The Potential for Straw as a Fuel in the UK* No. ETSU. (1984).

Miles, T. R. Operating Experience with Ash Deposition in Biomass Combustion Systems. In *Biomass Combustion Conference*, . Reno, NV: (1992).

Miles, T. R., & Miles, T. R., Jr. Alkali Deposits in Biomass Power Plant Boilers. In *Biomass Power Program*, . Washington, DC: (1993).

Miles, T. R., Miles, T. R., Jr., Baxter, L. L., Jenkins, B. M., & Oden, L. L. Alkali Slagging Problems with Biomass Fuels. In *First Biomass Conference of the Americas: Energy, Environment, Agriculture, and Industry*, 1 (pp. 406-421). Burlington, VT: National Renewable Energy Laboratory. (1993).

Milne, T. A., & Klein, H. M., *Journal of Chemical Physics, 33*, 1628-1637. (1960).

Quann, R. J., Neville, M., & Sarofim, A. F., *Combustion Science and Technology, 74*, 245-265. (1990).

Raask, E. Mineral Impurities in Coal Combustion. (. Washington: Hemisphere Publishing Corporation. (1985).

Richards, G. H., Harb, J. N., Baxter, L. L., Bhattacharya, S., Bupta, R. P., & Wall, T. F. Radiative Heat Transfer in PC-Fired Boilers — Development of the Absorptive/Reflective Character of Initial Ash Deposits on Walls. In *Twenty-Fifth Symposium (International) on Combustion*, . Irvine, CA: The Combustion Institute. (1994).

Rosner, D. E., *AIChE Journal, 35*(1), 164-167. (1989).

Rosner, D. E., & Nagarajan, R., *Chemical Engineering Science, 40*(2), 177-186. (1985).

Rosner, D. E., & Tassopoulos, M., *AIChE Journal, 35*(9), 1497-1508. (1989).

Salour, D., Jenkins, B. M., Vafaei, M., & Kayhanian, M., *Biomass and Bioenergy, 4*(2), 117-133. (1993).

Smouse, S. M., & Wagoner, C. L. Deposit Initiation: Part 2 — Experimental Verification of Hypothesis Using a Simulated Superheater Tube. In S. A. Benson (Ed.), *Conference on Inorganic Transformations and Ash Deposition During Combustion*, (pp. 625-637). Palm Coast, Florida: ASME. (1991).

Srinivasachar, S., & Boni, A. A., *Fuel, 68*(7), 829-836. (1989).

Srinivasachar, S., Helble, J. J., & Boni, A. A. An Experimental Study of the Inertial Deposition of Ash Under Coal Combustion Conditions. In *Twenty-Third Symposium (International) on Combustion*, (pp. 1305-1312). The University of Orléans, Orléans, France: The Combustion Institute. (1990a).

Srinivasachar, S., Helble, J. J., & Boni, A. A., *Progress in Energy and Combustion Science, 16*, 281-292. (1990b).

Srinivasachar, S., Helble, J. J., Boni, A. A., Shah, N., Huffman, G. P., & Huggins, F. E., *Progress in Energy and Combustion Science, 16*, 293-302. (1990c).

Srinivasachar, S., Senior, C. L., Helble, J. J., & Moore, J. W. A Fundamental Approach to the Prediction of Coal Ash Deposit Formation in Combustion Systems. In *The Twenty-Fourth Symposium (International) on Combustion*, (pp. 1179-1187). The University of Sydney, Australia: The Combustion Institute. (1992).

Tillman, D. A. Trace Metals in Combustion Systems. (. San Diego: Academic Press. (1994).

Turnbull, J. H., *Biomass and Bioenergy, 4*(2), 75-84. (1993).

Wagoner, C. L., & Yan, X.-X. Deposit Initiation via Thermophoresis: Part 1 — Insignt on Deceleration and Retention of Inertially-transported particles. In S. A. Benson (Ed.), *Conference on Inorganic Transformations and Ash Deposition During Combustion*, (pp. 607-623). Palm Coast, Florida: ASME. (1991).

Wall, T. F., Baxter, L. L., Richards, G., & Harb, J. N. Ash Deposits, Coal Blends and the Thermal Performance of Furnaces. In R. W. Bryers & N. S. Harding (Eds.), Coal-Blending and Switching of Low-Sulfur Western Coals (pp. 453-463). New York: ASME. (1994a).

Wall, T. F., Bhattacharya, S. P., Zhang, D. K., Gupta, R. P., & He, X. The Properties and Thermal Effects of Ash Deposits in Coal-Fired Furnaces. In J. Williamson & F. Wigely (Eds.),

The Impact of Ash Deposition on Coal-Fired Plants (pp. 463-477). Washington, D.C.: Taylor & Francis. (1994b).

Wibberley, L. J., & Wall, T. F., *Combustion Science and Technology, 48*, 177-190. (1986).

Zygarlicke, C. J., McCollor, D. P., Toman, D. L., Erickson, T. A., Ramanathan, M., & Folkedahl, B. S. *Combustion Inorganic Transformations* (Semiannual Technical Progress Report No. Cooperative Agreement No. DE-FC21-86MC10637). University of North Dakota Energy and Environmental Research Center. (1992a).

Zygarlicke, C. J., Ramanathan, M., & Erickson, T. A. Fly Ash Particle-Size Distribution and Composition: Experimental and Phenomenological Approach. In S. A. Benson (Eds.), Inorganic Transformations and Ash Deposition During Combustion (pp. 525-544). New York: American Society of Mechanical Engineers. (1992b).

APPENDIX 1

Fuel Properties

This appendix contains mainly tabulated data reviewed in the bulk of the report. Data on additional fuels are being collected by several of the authors of the report under continued sponsorship. Also, some additional analyses the same or similar fuels are underway. The suite of fuels highlighted here represents a broad range of commercially and scientifically interesting biomass fuels. Results of replicated, standardized (ASTM) analyses are presented first, followed by nonstandardized analyses.

Almond Hulls

Proximate Analysis

Table 11 Proximate analysis of almond hulls with statistics.

Proximate	Dry	As Rec'd	Standard Deviation (dry basis)	Number of Analyses	95% Confidence Interval (±, Dry Basis)
Fixed Carbon	21.47	19.75	2.21	3	3.18
Volatile Matter	72.80	66.96	1.49	3	2.13
Moisture		8.02	1.46	5	0.81
Ash	5.75	5.29	0.59	5	0.33
Total	100.01	100.01			

Ultimate Analysis

Table 12 Ultimate analysis of almond hulls, with statistics.

Ultimate	Dry (mass %)	As Rec'd (mass %)	Standard Deviation (dry basis)	Number of Analyses	95% Confidence Interval (±, Dry Basis)		Mole % (dry, ash free)
C	47.13	43.35	0.51	5	0.28	C	31.62
H	5.96	5.48	0.05	5	0.03	H	47.63
O (by diff)	39.80	36.61	0.74	5	0.41	O (by diff)	20.04
N	1.14	1.05	0.19	5	0.10	N	0.66
S	0.17	0.16	0.26	5	0.14	S	0.04
Cl	0.05	0.04	0.02	5	0.01	Cl	0.01
Ash	5.75	5.29	0.59	5	0.33		
Moisture		8.02	1.46	5	0.81		
Total	100.00	100.00					100

Heating Value

Table 13 Heating value analysis of almond hulls, with statistics.

Higher Heating Value	Btu/lb, dry	Btu/lb, as rec'd	Standard Deviation (dry basis)	Number of Analyses	95 % Confidence Interval (±, dry basis)	MJ/kg, dry	MJ/kg, as rec'd
ASTM	8105	7455	111	4	88	19	17
Modified*	1206	1109	16	4	13	2.81	2.58
Dulong	7472	7363	117	5	65	17	17

*Modified value is based on heat release per unit mass total combustion products (reactants).
It represents a more useful measure of energy content when comparing fuels of differing oxygen cont

Ash Chemistry

Table 14 Ash chemistry analysis of almond hulls, with statistics.

Ash Chemistry	% dry fuel	% ash	Standard Deviation (% dry fuel basis)	Number of Analyses	95 % Confidence Interval (±, dry fuel basis)		Elemental Composition (% ash)
SiO2	0.335	5.83	0.126	3	0.181	Si	4.57
Al2O3	0.076	1.32	0.011	3	0.016	Al	1.17
TiO2	0.003	0.05	0.003	3	0.004	Ti	0.05
Fe2O3	0.042	0.74	0.020	3	0.029	Fe	0.87
CaO	0.432	7.51	0.163	3	0.234	Ca	9.01
MgO	0.251	4.37	0.095	3	0.137	Mg	4.43
K2O	3.005	52.29	0.375	4	0.298	K	72.84
Na2O	0.046	0.80	0.025	4	0.019	Na	1.00
SO3	0.079	1.38	0.018	3	0.026	S	0.92
P2O5	0.403	7.01	0.118	3	0.170	P	5.14
Cl	n/a	n/a	n/a	0	n/a	Cl	n/a
Undetermined	1.142	19.87	0.243	3	0.348		
Total	5.81	101.16					100.00

Ash Fusion Temperature

Table 15 Ash Fusion Temperature analysis of almond hulls, with statistics.

Fusion Temperatures	°F	Standard Deviation (°F)	Number of Analyses	95 % Confidence Interval (±, °F)	°C
Reducing Conditions					
Initial Deformation	2359	n/a	1	n/a	1293
Spherical	2401	n/a	1	n/a	1316
Hemispherical	2408	n/a	1	n/a	1320
Fluid	2410	n/a	1	n/a	1321
Oxidizing Conditions					
Initial Deformation	2328	325	2	2066	1276
Spherical	2468	472	2	2996	1353
Hemispherical	2540	393	2	2498	1393
Fluid	2575	347	2	2206	1413

Almond Shells

Proximate Analysis

Table 16 Proximate analysis of almond shells with statistics.

Proximate	*Dry*	*As Rec'd*	*Standard Deviation (dry basis)*	*Number of Analyses*	*95% Confidence Interval (±, Dry Basis)*
Fixed Carbon	20.79	19.23	0.88	3	1.26
Volatile Matter	76.40	70.66	0.52	3	0.74
Moisture		7.52	0.83	5	0.46
Ash	2.87	2.65	0.42	5	0.23
Total	100.06	100.06			

Ultimate Analysis

Table 17 Ultimate analysis of almond shells, with statistics.

Ultimate	Dry (mass %)	As Rec'd (mass %)	Standard Deviation (dry basis)	Number of Analyses	95% Confidence Interval (±, Dry Basis)		Mole % (dry, ash free)
C	48.58	44.92	1.47	5	0.82	C	32.19
H	5.89	5.45	0.08	5	0.04	H	46.55
O (by diff)	41.86	38.71	1.79	5	0.99	O (by diff)	20.82
N	0.74	0.69	0.12	5	0.07	N	0.42
S	0.03	0.03	0.01	5	0.00	S	0.01
Cl	0.03	0.03	0.02	5	0.01	Cl	0.01
Ash	2.87	2.65	0.42	5	0.23		
Moisture		7.52	0.83	5	0.46		
Total	100.00	100.00					100.00

Heating Value

Table 18 Heating value analysis of almond shells, with statistics.

Higher Heating Value	Btu/lb, dry	Btu/lb, as rec'd	Standard Deviation (dry basis)	Number of Analyses	95 % Confidence Interval (±, dry basis)	MJ/kg, dry	MJ/kg, as rec'd
ASTM	8281	7658	108	4	86	19	18
Total Mass B	1349	1247	18	4	14	3.14	2.90
Dulong	7477	7415	394	5	219	17	17

*Modified value is based on heat release per unit mass total combustion products (reactants).
It represents a more useful measure of energy content when comparing fuels of differing oxygen contents.

Ash Chemistry

Table 19 Ash chemistry analysis of almond shells, with statistics.

Ash Chemistry	% dry fuel	% ash	Standard Deviation (% dry fuel basis)	Number of Analyses	95 % Confidence Interval (±, dry fuel basis)		Elemental Composition (% ash)
SiO2	0.255	8.89	0.136	3	0.195	Si	6.76
Al2O3	0.062	2.16	0.027	3	0.038	Al	1.87
TiO2	0.003	0.09	0.002	3	0.003	Ti	0.09
Fe2O3	0.079	2.77	0.045	3	0.064	Fe	3.15
CaO	0.351	12.24	0.185	3	0.265	Ca	14.25
MgO	0.131	4.56	0.071	3	0.102	Mg	4.48
K2O	1.300	45.33	0.267	5	0.148	K	61.27
Na2O	0.042	1.45	0.027	5	0.015	Na	1.76
SO3	0.083	2.88	0.031	3	0.044	S	1.87
P2O5	0.181	6.32	0.137	3	0.197	P	4.49
Cl	n/a	n/a	n/a	0	n/a	Cl	n/a
Undetermined	0.409	14.26	0.128	3	0.183		
Total	2.90	100.96					100.00

Ash Fusion Temperature

Table 20 Ash Fusion Temperature analysis of almond shells, with statistics.

Fusion Temperatures	°F	Standard Deviation (°F)	Number of Analyses	95 % Confidence Interval (±, °F)	°C
Reducing Conditions					
Initial Deformation	2340	n/a	1	n/a	1282
Spherical	2372	n/a	1	n/a	1300
Hemispherical	2495	n/a	1	n/a	1368
Fluid	2497	n/a	1	n/a	1369
Oxidizing Conditions					
Initial Deformation	2448	n/a	1	n/a	1342
Spherical	2449	n/a	1	n/a	1343
Hemispherical	2487	n/a	1	n/a	1364
Fluid	2704	n/a	1	n/a	1484

Nonrecyclable Paper i

Proximate Analysis

Table 21 Proximate analysis of nonrecyclable paper i with statistics.

Proximate	Dry	As Rec'd	Standard Deviation (dry basis)	Number of Analyses	95% Confidence Interval (±, Dry Basis)
Fixed Carbon	9.35	8.79	0.27	5	0.15
Volatile Matter	82.50	77.59	0.53	5	0.29
Moisture		5.95	1.39	7	0.49
Ash	8.21	7.72	0.32	8	0.09
Total	100.06	100.05			

Ultimate Analysis

Table 22 Ultimate analysis of nonrecyclable paper i, with statistics.

Ultimate	Dry (mass %)	As Rec'd (mass %)	Standard Deviation (dry basis)	Number of Analyses	95% Confidence Interval (±, Dry Basis)		Mole % (dry, ash free)
C	49.26	46.32	0.79	7	0.27	C	31.06
H	6.97	6.56	0.17	7	0.06	H	52.38
O (by diff)	34.45	32.40	0.60	5	0.33	O (by diff)	16.31
N	0.35	0.33	0.22	7	0.08	N	0.19
S	0.21	0.19	0.20	7	0.07	S	0.05
Cl	0.04	0.04	0.01	7	0.00	Cl	0.01
Ash	8.21	7.72	0.32	8	0.09		
Moisture		5.95	1.39	7	0.49		
Total	99.48	99.51					100

Heating Value

Table 23 Heating value analysis of nonrecyclable paper i, with statistics.

Higher Heating Value	Btu/lb, dry	Btu/lb, as rec'd	Standard Deviation (dry basis)	Number of Analyses	95 % Confidence Interval (±, dry basis)	MJ/kg, dry	MJ/kg, as rec'd
ASTM	9250	8700	246	3	353	22	20
Modified*	1221	1149	33	3	47	2.84	2.67
Dulong	8957	8424	167	7	58	21	20

*Modified value is based on heat release per unit mass of total combustion products (reactants).

It represents a more useful measure of energy content when comparing fuels of differing oxygen contents.

Ash Chemistry

Table 24 Ash chemistry analysis of nonrecyclable paper i, with statistics.

Ash Chemistry	% dry fuel	% ash	Standard Deviation (% dry fuel basis)	Number of Analyses	95 % Confidence Interval (±, dry fuel basis)		Elemental Composition (% ash)
SiO2	1.913	23.29	0.093	5	0.051	Si	16.88
Al2O3	6.295	76.64	1.080	5	0.600	Al	62.90
TiO2	0.374	4.56	0.147	5	0.082	Ti	4.24
Fe2O3	0.041	0.50	0.018	5	0.010	Fe	0.54
CaO	0.824	10.03	0.029	5	0.016	Ca	11.13
MgO	0.165	2.01	0.008	5	0.004	Mg	1.88
K2O	0.023	0.28	0.013	6	0.005	K	0.35
Na2O	0.082	1.00	0.021	6	0.009	Na	1.15
SO3	0.113	1.37	0.047	5	0.026	S	0.85
P2O5	0.010	0.12	0.006	5	0.003	P	0.08
Cl	n/a	n/a	n/a	0	n/a	Cl	n/a
Undetermine	-1.693	-20.61	1.367	5	0.759		
Total	8.15	99.18					100.00

Ash Fusion Temperature

Table 25 Ash Fusion Temperature analysis of nonrecyclable paper i, with statistics.

Ash Chemistry	% dry fuel	% ash	Standard Deviation (% dry fuel basis)	Number of Analyses	95 % Confidence Interval (±, dry fuel basis)		Elemental Composition (% ash)
SiO2	1.913	23.29	0.093	5	0.051	Si	16.88
Al2O3	6.295	76.64	1.080	5	0.600	Al	62.90
TiO2	0.374	4.56	0.147	5	0.082	Ti	4.24
Fe2O3	0.041	0.50	0.018	5	0.010	Fe	0.54
CaO	0.824	10.03	0.029	5	0.016	Ca	11.13
MgO	0.165	2.01	0.008	5	0.004	Mg	1.88
K2O	0.023	0.28	0.013	6	0.005	K	0.35
Na2O	0.082	1.00	0.021	6	0.009	Na	1.15
SO3	0.113	1.37	0.047	5	0.026	S	0.85
P2O5	0.010	0.12	0.006	5	0.003	P	0.08
Cl	n/a	n/a	n/a	0	n/a	Cl	n/a
Undetermine	-1.693	-20.61	1.367	5	0.759		
Total	8.15	99.18					100.00

Nonrecyclable Paper ii

Proximate Analysis

Table 26 Proximate analysis of nonrecyclable paper ii with statistics.

Proximate	Dry	As Rec'd	Standard Deviation (dry basis)	Number of Analyses	95% Confidence Interval (±, Dry Basis)
Fixed Carbon	9.35	8.79	0.27	5	0.15
Volatile Matter	82.50	77.59	0.53	5	0.29
Moisture		5.95	1.39	7	0.49
Ash	8.21	7.72	0.32	8	0.09
Total	100.06	100.05			

Ultimate Analysis

Table 27 Ultimate analysis of nonrecyclable paper ii, with statistics.

Ultimate	*Dry (mass %)*	*As Rec'd (mass %)*	*Standard Deviation (dry basis)*	*Number of Analyses*	*95% Confidence Interval (±, Dry Basis)*		*Mole % (dry, ash free)*
C	49.26	46.32	0.79	7	0.27	C	31.06
H	6.97	6.56	0.17	7	0.06	H	52.38
O (by diff)	34.45	32.40	0.60	5	0.33	O (by diff)	16.31
N	0.35	0.33	0.22	7	0.08	N	0.19
S	0.21	0.19	0.20	7	0.07	S	0.05
Cl	0.04	0.04	0.01	7	0.00	Cl	0.01
Ash	8.21	7.72	0.32	8	0.09		
Moisture		5.95	1.39	7	0.49		
Total	99.48	99.51					100

Heating Value

Table 28 Heating value analyses of nonrecyclable paper ii, with statistics.

Higher Heating Value	*Btu/lb, dry*	*Btu/lb, as rec'd*	*Standard Deviation (dry basis)*	*Number of Analyses*	*95 % Confidence Interval (±, dry basis)*	*MJ/kg, dry*	*MJ/kg, as rec'd*
ASTM	9250	8700	246	3	353	22	20
Modified*	1221	1149	33	3	47	2.84	2.67
Dulong	8957	8424	167	7	58	21	20

*Modified value is based on heat release per unit total mass of combustion products (reactants).
It represents a more useful measure of energy content when comparing fuels of differing oxygen contents.

Ash Chemistry

Table 29 Ash chemistry analysis of nonrecyclable paper ii, with statistics.

Ash Chemistry	% dry fuel	% ash	Standard Deviation (% dry fuel basis)	Number of Analyses	95 % Confidence Interval (±, dry fuel basis)		Elemental Composition (% ash)
SiO2-	1.913	23.29	0.093	5	0.051	Si	16.88
Al2O3	6.295	76.64	1.080	5	0.600	Al	62.90
TiO2	0.374	4.56	0.147	5	0.082	Ti	4.24
Fe2O3	0.041	0.50	0.018	5	0.010	Fe	0.54
CaO	0.824	10.03	0.029	5	0.016	Ca	11.13
MgO	0.165	2.01	0.008	5	0.004	Mg	1.88
K2O	0.023	0.28	0.013	6	0.005	K	0.35
Na2O	0.082	1.00	0.021	6	0.009	Na	1.15
SO3	0.113	1.37	0.047	5	0.026	S	0.85
P2O5	0.010	0.12	0.006	5	0.003	P	0.08
Cl	n/a	n/a	n/a	0	n/a	Cl	n/a
Undetermine	-1.693	-20.61	1.367	5	0.759		
Total	8.15	99.18					100.00

Ash Fusion Temperature

Table 30 Ash Fusion Temperature analysis of nonrecyclable paper ii, with statistics.

Fusion Temperatures	°F	Standard Deviation (°F)	Number of Analyses	95 % Confidence Interval (±, °F)	°C
Reducing Conditions					
Initial Deform:	2753	54	3	78	1512
Spherical	2970	52	3	75	1632
Hemispherical	2970	52	3	75	1632
Fluid	2970	52	3	75	1632
Oxidizing Conditions					
Initial Deform:	2748	112	3	161	1509
Spherical	2861	200	3	286	1571
Hemispherical	2970	52	3	75	1632
Fluid	2970	52	3	75	1632

Olive Pits

Proximate Analysis

Table 31 Proximate analysis of olive pits with statistics.

Proximate	*Dry*	*As Rec'd*	*Standard Deviation (dry basis)*	*Number of Analyses*	*95% Confidence Interval (±, Dry Basis)*
Fixed Carbon	20.76	19.31	0.23	4	0.18
Volatile Matter	77.43	72.03	0.26	4	0.21
Moisture		6.97	0.83	5	0.46
Ash	1.83	1.70	0.19	5	0.11
Total	100.01	100.01			

Ultimate Analysis

Table 32 Ultimate analysis of olive pits, with statistics.

Ultimate	*Dry (mass %)*	*As Rec'd (mass %)*	*Standard Deviation (dry basis)*	*Number of Analyses*	*95% Confidence Interval (±, Dry Basis)*		*Mole % (dry, ash free)*
C	49.64	46.18	6.62	5	3.67	C	31.53
H	6.39	5.95	0.13	5	0.07	H	48.38
O (by diff)	41.47	38.58	6.80	5	3.78	O (by diff)	19.77
N	0.53	0.49	0.10	5	0.06	N	0.29
S	0.07	0.06	0.05	5	0.03	S	0.02
Cl	0.07	0.07	0.02	5	0.01	Cl	0.02
Ash	1.83	1.70	0.19	5	0.11		
Moisture		6.97	0.83	5	0.46		
Total	100.00	100.00					100

Heating Value

Table 33 Heating value analysis of olive pits, with statistics.

Higher Heating Value	*Btu/lb, dry*	*Btu/lb, as rec'd*	*Standard Deviation (dry basis)*	*Number of Analyses*	*95 % Confidence Interval (±, dry basis)*	*MJ/kg, dry*	*MJ/kg, as rec'd*
ASTM	9271	8625	131	3	188	22	20
Modified*	1310	1219	19	3	27	3.05	2.83
Dulong	7972	7416	1550	5	861	19	17

*Modified value is based on heat release per unit total mass of combustion products (reactants).
It represents a more useful measure of energy content when comparing fuels of differing oxygen contents.

Ash Chemistry

Table 34 Ash chemistry analysis of olive pits, with statistics.

Ash Chemistry	% dry fuel	% ash	Standard Deviation (% dry fuel basis)	Number of Analyses	95 % Confidence Interval (±, dry fuel basis)		Elemental Compositio n (% ash)
SiO2	0.540	29.55	0.137	4	0.109	Si	23.64
Al2O3	0.113	6.17	0.023	4	0.018	Al	5.59
TiO2	0.005	0.27	0.002	4	0.002	Ti	0.27
Fe2O3	0.119	6.52	0.028	4	0.022	Fe	7.81
CaO	0.237	12.97	0.048	4	0.038	Ca	15.88
MgO	0.075	4.13	0.020	4	0.016	Mg	4.26
K2O	0.045	2.49	0.024	4	0.019	K	3.54
Na2O	0.507	27.74	0.043	4	0.034	Na	35.23
SO3	0.038	2.06	0.002	4	0.002	S	1.41
P2O5	0.058	3.18	0.011	4	0.009	P	2.38
Cl	n/a	n/a	n/a	0	n/a	Cl	n/a
Undetermine	0.077	4.22	0.074	4	0.059		
Total	1.82	99.29					100.00

Ash Fusion Temperature

Table 35 Ash Fusion Temperature analysis of olive pits, with statistics.

Fusion Temperatures	°F	Standard Deviation (°F)	Number of Analyses	95 % Confidence Interval (±, °F)	°C
Reducing Conditions					
Initial Deformation	1977	23	2	148	1080
Spherical	1996	21	2	135	1091
Hemispherical	2021	15	2	94	1105
Fluid	2075	5	2	31	1135
Oxidizing Conditions					
Initial Deformation	1970	103	2	656	1077
Spherical	1992	132	2	836	1089
Hemispherical	2004	131	2	831	1095
Fluid	2247	144	2	912	1230

Pistachio Shells

Proximate Analysis

Table 36 Proximate analysis of pistachio shells with statistics.

Proximate	Dry	As Rec'd	Standard Deviation (dry basis)	Number of Analyses	95% Confidence Interval (±, Dry Basis)
Fixed Carbon	16.95	15.58	n/a	1	n/a
Volatile Matter	81.64	75.04	n/a	1	n/a
Moisture		8.08	0.78	2	4.94
Ash	1.34	1.23	0.11	2	0.67
Total	99.93	99.93			

Ultimate Analysis

Table 37 Ultimate analysis of pistachio shells, with statistics.

Ultimate	Dry (mass %)	As Rec'd (mass %)	Standard Deviation (dry basis)	Number of Analyses	95% Confidence Interval (±, Dry Basis)		Mole % (dry, ash free)
C	49.55	45.54	0.91	2	5.80	C	31.63
H	6.29	5.78	0.03	2	0.18	H	47.85
O (by diff)	42.02	38.63	1.24	2	7.87	O (by diff)	20.14
N	0.60	0.55	0.12	2	0.76	N	0.33
S	0.19	0.17	0.05	2	0.31	S	0.04
Cl	0.03	0.02	0.02	2	0.15	Cl	0.01
Ash	1.34	1.23	0.11	2	0.67		
Moisture		8.08	0.78	2	4.94		
Total	100.00	100.00					100

Heating Value

Table 38 Heating value analysis of pistachio shells, with statistics.

Higher Heating Value	Btu/lb, dry	Btu/lb, as rec'd	Standard Deviation (dry basis)	Number of Analyses	95 % Confidence Interval (±, dry basis)	MJ/kg, dry	MJ/kg, as rec'd
ASTM	8445	7763	34	2	216	20	18
Modified*	1204	1107	5	2	31	2.80	2.57
Dulong	7857	7222	7857	2	1578	18	17

*Modified value is based on heat release per unit mass of total combustion products (reactants).

It represents a more useful measure of energy content when comparing fuels of differing oxygen contents.

Ash Chemistry

Table 39 Ash chemistry analysis of pistachio shells, with statistics.

Ash Chemistry	% dry fuel	% ash	Standard Deviation (% dry fuel basis)	Number of Analyses	Confidence Interval (±, dry fuel basis)		Elemental Composition (% ash)
SiO2	0.116	8.68	n/a	1	n/a	Si	5.99
Al2O3	0.031	2.29	n/a	1	n/a	Al	1.79
TiO2	0.003	0.21	n/a	1	n/a	Ti	0.19
Fe2O3	0.499	37.36	n/a	1	n/a	Fe	38.60
CaO	0.141	10.57	n/a	1	n/a	Ca	11.17
MgO	0.046	3.44	n/a	1	n/a	Mg	3.07
K2O	0.257	19.22	n/a	1	n/a	K	23.57
Na2O	0.063	4.75	n/a	1	n/a	Na	5.21
SO3	0.053	4.00	n/a	1	n/a	S	2.37
P2O5	0.166	12.46	n/a	1	n/a	P	8.04
Cl	n/a	n/a	n/a	0	n/a	Cl	n/a
Undetermined	0.035	2.62	n/a	1	n/a		
Total	1.41	105.62					100.00

Ash Fusion Temperature

Table 40 Ash Fusion Temperature analysis of pistachio shells, with statistics.

Fusion Temperatures	°F	Standard Deviation (°F)	Number of Analyses	95 % Confidence Interval (±, °F)	°C
Reducing Conditions					
Initial Deformation	n/a	n/a	0	n/a	#VALUE!
Spherical	n/a	n/a	0	n/a	#VALUE!
Hemispherical	n/a	n/a	0	n/a	#VALUE!
Fluid	n/a	n/a	0	n/a	#VALUE!
Oxidizing Conditions					
Initial Deformation	2425	n/a	1	n/a	1329
Spherical	2467	n/a	1	n/a	1353
Hemispherical	2519	n/a	1	n/a	1382
Fluid	2588	n/a	1	n/a	1420

Rice Straw

Proximate Analysis

Table 41 Proximate analysis of rice straw with statistics.

Proximate	*Dry*	*As Rec'd*	*Standard Deviation (dry basis)*	*Number of Analyses*	*95% Confidence Interval (±, Dry Basis)*
Fixed Carbon	14.11	12.40	0.18	2	1.12
Volatile Matte	65.65	57.70	0.04	2	0.27
Moisture		12.12	0.54	2	3.46
Ash	20.25	17.79	0.13	2	0.85
Total	100.00	100.00			

Ultimate Analysis

Table 42 Ultimate analysis of rice straw, with statistics.

Ultimate	Dry (mass %)	As Rec'd (mass %)	Standard Deviation (dry basis)	Number of Analyses	95% Confidence Interval (±, Dry Basis)		Mole % (dry, ash free)
C	39.20	34.45	0.06	2	0.36	C	31.38
H	4.96	4.36	0.01	2	0.09	H	47.32
O (by diff)	33.77	29.68	0.16	2	1.03	O (by diff)	20.29
N	1.22	1.07	0.08	2	0.49	N	0.83
S	0.05	0.04	0.07	2	0.45	S	0.01
Cl	0.56	0.50	0.08	2	0.49	Cl	0.15
Ash	20.25	17.79	0.13	2	0.85		
Moisture		12.12	0.54	2	3.46		
Total	100.00	100.00					100

Heating Value

Table 43 Heating value analysis of rice straw, with statistics.

Higher Heating Value	Btu/lb, dry	Btu/lb, as rec'd	Standard Deviation (dry basis)	Number of Analyses	95 % Confidence Interval (±, dry basis)	MJ/kg, dry	MJ/kg, as rec'd
ASTM	6339	5571	n/a	1	n/a	15	13
Modified*	1107	973	n/a	1	n/a	2.57	2.26
Dulong	6162	5415	32	2	206	14	13

*Modified value is based on heat release per unit mass of total combustion products (reactants).

It represents a more useful measure of energy content when comparing fuels of differing oxygen contents.

Ash Chemistry

Table 44 Ash chemistry analysis of rice straw, with statistics.

Ash Chemistry	% dry fuel	% ash	Standard Deviation (% dry fuel basis)	Number of Analyses	Confidence Interval (±, dry fuel basis)		Elemental Composition (% ash)
SiO2	16.296	80.49	0.009	2	0.060	Si	74.82
Al2O3	0.301	1.48	0.005	2	0.033	Al	1.56
TiO2	0.013	0.06	0.001	2	0.009	Ti	0.08
Fe2O3	0.174	0.86	0.002	2	0.011	Fe	1.20
CaO	0.406	2.01	0.010	2	0.063	Ca	2.85
MgO	0.420	2.08	0.013	2	0.081	Mg	2.49
K2O	1.629	8.05	0.144	2	0.914	K	13.28
Na2O	0.178	0.88	0.010	2	0.062	Na	1.30
SO3	0.291	1.44	0.072	2	0.458	S	1.14
P2O5	0.298	1.47	0.071	2	0.451	P	1.28
Cl	n/a	n/a	n/a	0	n/a	Cl	n/a
Undetermine	0.239	1.18	0.044	2	0.281		
Total	20.25	100.00					100.00

Ash Fusion Temperature

Table 45 Ash Fusion Temperature analysis of rice straw, with statistics.

Fusion Temperatures	°F	Standard Deviation (°F)	Number of Analyses	95 % Confidence Interval (±, °F)	°C
Reducing Conditions					
Initial Deformation	2128	n/a	1	n/a	1164
Spherical	2575	n/a	1	n/a	1413
Hemispherical	2742	n/a	1	n/a	1506
Fluid	2950	n/a	1	n/a	1621
Oxidizing Conditions					
Initial Deformation	2327	n/a	1	n/a	1275
Spherical	2514	n/a	1	n/a	1379
Hemispherical	2756	n/a	1	n/a	1513
Fluid	2950	n/a	1	n/a	1621

Ash Fusion Temperature

Table 50 Ash Fusion Temperature analysis of switchgrass, with statistics.

Fusion Temperatures	°F	Standard Deviation (°F)	Number of Analyses	95 % Confidence Interval (±, °F)	°C
Reducing Conditions					
Initial Deformation	2065	5	2	31	1129
Spherical	2253	16	2	99	1234
Hemispherical	2578	93	2	593	1414
Fluid	2764	39	2	247	1518
Oxidizing Conditions					
Initial Deformation	2120	1	2	9	1160
Spherical	2311	19	2	121	1266
Hemispherical	2510	7	2	45	1377
Fluid	2732	24	2	153	1500

Wheat Straw

Proximate Analysis

Table 51 Proximate analysis of wheat straw with statistics.

Proximate	*Dry*	*As Rec'd*	*Standard Deviation (dry basis)*	*Number of Analyses*	*95% Confidence Interval (±, Dry Basis)*
Fixed Carbon	17.25	15.80	2.78	4	2.21
Volatile Matter	74.49	68.24	2.00	4	1.59
Moisture		8.39	0.89	5	0.50
Ash	8.08	7.40	1.01	8	0.30
Total	99.82	99.84			

Ultimate Analysis

Table 52 Ultimate analysis of wheat straw, with statistics.

Ultimate	*Dry (mass %)*	*As Rec'd (mass %)*	*Standard Deviation (dry basis)*	*Number of Analyses*	*95% Confidence Interval (±, Dry Basis)*		*Mole % (dry, ash free)*
C	45.05	41.27	1.67	7	0.58	C	32.01
H	5.43	4.98	0.29	7	0.10	H	45.99
O (by diff)	40.35	36.96	2.64	7	0.92	O (by diff)	21.52
N	0.61	0.56	0.22	7	0.08	N	0.37
S	0.19	0.17	0.03	6	0.01	S	0.05
Cl	0.24	0.22	0.03	7	0.01	Cl	0.06
Ash	8.08	7.40	1.01	8	0.30		
Moisture		8.39	0.89	5	0.50		
Total	99.96	99.96					100

Heating Value

Table 53 Heating value analysis of wheat straw, with statistics.

Higher Heating Value	*Btu/lb, dry*	*Btu/lb, as rec'd*	*Standard Deviation (dry basis)*	*Number of Analyses*	*95 % Confidence Interval (±, dry basis)*	*MJ/kg, dry*	*MJ/kg, as rec'd*
ASTM	7632	6992	121	5	67	18	16
Modified*	1215	1113	19	5	11	2.83	2.59
Dulong	6799	6229	514	7	180	16	14

*Modified value is based on heat release per unit mass of total combustion products (reactants).
It represents a more useful measure of energy content when comparing fuels of differing oxygen contents.

Ash Chemistry

Table 54 Ash chemistry analysis of wheat straw, with statistics.

Ash Chemistry	% dry fuel	% ash	Standard Deviation (% dry fuel basis)	Number of Analyses	95 % Confidence Interval (±, dry fuel basis)		Elemental Composition (% ash)
SiO2	4.848	60.00	0.621	5	0.345	Si	58.15
Al2O3	0.140	1.73	0.026	5	0.015	Al	7.03
TiO2	0.007	0.08	0.004	5	0.002	Ti	0.39
Fe2O3	0.072	0.89	0.031	6	0.013	Fe	4.74
CaO	0.268	3.32	0.102	6	0.044	Ca	9.71
MgO	0.188	2.33	0.065	6	0.028	Mg	3.64
K2O	1.700	21.04	0.458	6	0.196	K	11.05
Na2O	0.133	1.65	0.058	6	0.025	Na	1.45
SO3	0.307	3.80	0.134	4	0.107	S	1.52
P2O5	0.100	1.24	0.015	6	0.007	P	2.33
Cl	n/a	n/a	n/a	0	n/a	Cl	n/a
Undetermine	0.072	0.89	0.483	5	0.268		
Total	7.84	96.97					100.00

Ash Fusion Temperature

Table 55 Ash Fusion Temperature analysis of wheat straw, with statistics.

Fusion Temperatures	°F	Standard Deviation (°F)	Number of Analyses	95 % Confidence Interval (±, °F)	°C
Reducing Conditions					
Initial Deformation	2464	n/a	1	n/a	1351
Spherical	2466	n/a	1	n/a	1352
Hemispherical	2467	n/a	1	n/a	1353
Fluid	2474	n/a	1	n/a	1357
Oxidizing Conditions					
Initial Deformation	1911	n/a	1	n/a	1044
Spherical	1913	n/a	1	n/a	1045
Hemispherical	2238	n/a	1	n/a	1226
Fluid	2316	n/a	1	n/a	1269

Wood/Almond Shell Blend

Proximate Analysis

Table 56 Proximate analysis of wood/almond shell blend with statistics.

Proximate	Dry	As Rec'd	Standard Deviation (dry basis)	Number of Analyses	Confidence Interval (±, Dry Basis)
Fixed Carbon	18.73	17.12	1.71	3	2.45
Volatile Matte	73.88	67.52	0.71	3	1.01
Moisture		8.62	0.74	5	0.41
Ash	7.54	6.89	2.72	7	0.95
Total	100.15	100.14			

Ultimate Analysis

Table 57 Ultimate analysis of wood/almond shell blend, with statistics.

Ultimate	Dry (mass %)	As Rec'd (mass %)	Standard Deviation (dry basis)	Number of Analyses	Confidence Interval (±, Dry Basis)		Mole % (dry, ash free)
C	47.31	43.23	0.73	6	0.31	C	33.07
H	5.51	5.04	0.05	6	0.02	H	45.90
O (by diff)	39.33	35.94	2.57	6	1.10	O (by diff)	20.64
N	0.54	0.49	0.09	6	0.04	N	0.32
S	0.13	0.12	0.19	6	0.08	S	0.03
Cl	0.16	0.15	0.33	6	0.14	Cl	0.04
Ash	7.54	6.89	2.72	7	0.95		
Moisture		8.62	0.74	5	0.41		
Total	100.51	100.47					100

Heating Value

Table 58 Heating value analysis of wood/almond shell blend, with statistics.

Higher Heating Value	Btu/lb, dry	Btu/lb, as rec'd	Standard Deviation (dry basis)	Number of Analyses	Confidence Interval (±, dry basis)	MJ/kg, dry	MJ/kg, as rec'd
ASTM	7938	7254	111	4	89	18	17
Modified*	1207	1103	17	4	13	2.81	2.57
Dulong	7254	6629	206	6	88	17	15

*Modified value is based on heat release per unit mass of total combustion products (reactants).
It represents a more useful measure of energy content when comparing fuels of differing oxygen contents.

Ash Chemistry

Table 59 Ash chemistry analysis of wood/almond shell blend, with statistics.

Ash Chemistry	% dry fuel	% ash	Deviation (% dry fuel basis)	Number of Analyses	Confidence Interval (±, dry fuel		Elemental Composition (% ash)
SiO2	3.667	48.66	1.162	5	0.645	Si	58.15
Al2O3	0.848	11.25	0.224	5	0.124	Al	7.03
TiO2	0.039	0.52	0.009	5	0.005	Ti	0.39
Fe2O3	0.404	5.36	0.086	5	0.048	Fe	4.74
CaO	1.106	14.68	0.217	5	0.121	Ca	9.71
MgO	0.243	3.22	0.049	5	0.027	Mg	3.64
K2O	0.425	5.63	0.073	5	0.040	K	11.05
Na2O	0.200	2.65	0.045	5	0.025	Na	1.45
SO3	0.077	1.02	0.044	5	0.024	S	1.52
P2O5	0.113	1.50	0.026	5	0.015	P	2.33
Cl	n/a	n/a	n/a	0	n/a	Cl	n/a
Undetermine	0.284	3.77	0.183	4	0.146		
Total	7.41	98.26					100.00

Ash Fusion Temperature

Table 60 Ash Fusion Temperature analysis of wood/almond shell blend, with statistics.

Fusion Temperatures	°F	Standard Deviation (°F)	Number of Analyses	Confidence Interval (±, °F)	°C
Reducing Conditions					
Initial Deformatior	2084	n/a	1	n/a	1140
Spherical	2130	n/a	1	n/a	1166
Hemispherical	2178	n/a	1	n/a	1192
Fluid	2239	n/a	1	n/a	1226
Oxidizing Conditions					
Initial Deformatior	2085	18	2	117	1141
Spherical	2115	27	2	171	1157
Hemispherical	2219	62	2	391	1215
Fluid	2296	47	2	301	1258

Wood/Wheat Straw Blend

Proximate Analysis

Table 61 Proximate analysis of wood/wheat straw blend with statistics.

Proximate	*Dry*	*As Rec'd*	*Standard Deviation (dry basis)*	*Number of Analyses*	*95% Confidence Interval (±, Dry Basis)*
Fixed Carbon	17.95	16.29	0.66	3	0.95
Volatile Matter	74.71	67.80	0.81	3	1.16
Moisture		9.25	1.19	3	1.70
Ash	7.33	6.65	0.38	3	0.55
Total	100.00	100.00			

Ultimate Analysis

Table 62 Ultimate analysis of wood/wheat straw blend, with statistics.

Ultimate	*Dry (mass %)*	*As Rec'd (mass %)*	*Standard Deviation (dry basis)*	*Number of Analyses*	*95% Confidence Interval (±, Dry Basis)*		*Mole % (dry, ash free)*
C	47.83	43.40	1.14	3	1.63	C	32.74
H	5.78	5.25	0.04	3	0.05	H	47.18
O (by diff)	38.26	34.72	1.06	3	1.53	O (by diff)	19.66
N	0.62	0.57	0.14	3	0.20	N	0.37
S	0.08	0.07	0.00	2	0.00	S	0.02
Cl	0.12	0.11	0.00	3	0.01	Cl	0.03
Ash	7.33	6.65	0.38	3	0.55		
Moisture		9.25	1.19	3	1.70		
Total	100.03	100.02					100

Heating Value

Table 63 Heating value analysis of wood/wheat straw blend, with statistics.

Higher Heating Value	*Btu/lb, dry*	*Btu/lb, as rec'd*	*Standard Deviation (dry basis)*	*Number of Analyses*	*95 % Confidence Interval (±, dry basis)*	*MJ/kg, dry*	*MJ/kg, as rec'd*
ASTM	8192	7434	40	2	252	19	17
Modified*	1205	1093	6	2	37	2.80	2.54
Dulong	7580	6878	236	3	338	18	16

*Modified value is based on heat release per unit mass of total combustion products (reactants).
It represents a more useful measure of energy content when comparing fuels of differing oxygen contents.

Ash Chemistry

Table 64 Ash chemistry analysis of wood/wheat straw blend, with statistics.

Ash Chemistry	% dry fuel	% ash	Standard Deviation (% dry fuel basis)	Number of Analyses	95 % Confidence Interval (±, dry fuel basis)		Elemental Composition (% ash)
SiO2	4.163	56.77	0.185	3	0.265	Si	49.51
Al2O3	0.776	10.58	0.057	3	0.081	Al	10.45
TiO2	0.035	0.48	0.003	3	0.004	Ti	0.53
Fe2O3	0.361	4.93	0.016	3	0.023	Fe	6.43
CaO	0.768	10.48	0.045	3	0.065	Ca	13.97
MgO	0.199	2.72	0.015	3	0.022	Mg	3.06
K2O	0.432	5.89	0.094	3	0.135	K	9.13
Na2O	0.222	3.03	0.061	3	0.087	Na	4.19
SO3	0.145	1.97	0.052	3	0.075	S	1.47
P2O5	0.112	1.53	0.030	3	0.044	P	1.25
Cl	n/a	n/a	n/a	0	n/a	Cl	n/a
Undetermined	0.119	1.62	0.050	3	0.071		
Total	7.33	100.00					100.00

Ash Fusion Temperature

Table 65 Ash Fusion Temperature analysis of wood/wheat straw blend, with statistics.

Fusion Temperatures	°F	Standard Deviation (°F)	Number of Analyses	95 % Confidence Interval (±, °F)	°C
Reducing Conditions					
Initial Deformation	2065	n/a	1	n/a	1129
Spherical	2096	n/a	1	n/a	1147
Hemispherical	2288	n/a	1	n/a	1253
Fluid	2384	n/a	1	n/a	1307
Oxidizing Conditions					
Initial Deformation	2070	21	2	130	1132
Spherical	2114	13	2	81	1157
Hemispherical	2281	59	2	373	1249
Fluid	2490	13	2	85	1365

Chemical Fractionation Procedure

The following instructions for the chemical fraction procedure are divided into six parts: sample preparation, analysis of the unleached materials, analysis of the sample after each of three leachings, and characterization of the inorganics in the solid samples from each of the four stages of the procedure. An optional analysis of the leachates is also discussed which allows a mass balance to be made at each step of the procedure.

Chemicals: 1 M Nitric Acid

1 M Hydrochloric Acid (HCl)

1 M Ammonium Acetate (NH_4OAc)

Sample Preparation

1. All samples must be small enough to be completely permeated by leaching agents (water, ammonium acetate, and hydrochloric acid). Normally this requires that the sample pass through at least a 200 mesh screen.

2. Homogenize sample by mixing in suitable container.

Unleached Material

There should be ≈ 100 g of sample (on a dry basis) at this point. At the end of this step there should be ≈ 75 g of material left for the remaining leachings, ≈ 20 g of sample labeled and saved for later inorganic analysis, the weight of the total sample before any leaching, and the moisture of the sample as weighed.

1. Weigh enough material into beaker to provide at least 100 g of dry sample.

2. Determine total weight of sample.

3. Remove and weigh approximately 1/4 (at least 20 g) of sample.

4. Determine the moisture with a portion (< 5 g) of removed material immediately.

5. Label remaining removed material *Unleached* and set aside.

Water Wash

There should be ≈ 75 g of sample (on a dry basis) at this point. At the end of this step there should be ≈ 50 g of sample (on a dry basis) left for the remaining leachings, ≈ 20 g of sample labeled and saved for later inorganic analysis, the weight of the total sample after water washing, and the moisture of the sample as weighed. From this information

and the initial dry weight of the sample, the change in the dry weight induced by water washing can be calculated.

1. Add 3 ml of H_2O per gram of sample remaining in the beaker.
2. Stir overnight at room temperature.
3. Filter and rinse with distilled H_2O.
4. Determine total weight of sample.
5. Remove and weigh approximately 1/3 (at least 20 g) of moist sample.
6. Determine moisture with a portion (< 5 g) of removed material immediately.
7. Label remaining removed material *After H_2O* and set aside.

Ammonium Acetate Wash (NH_4OAc)

There should be ≈ 50 g of sample (on a dry basis) at this point. At the end of this step there should be ≈ 25 g of sample (on a dry basis) left for the remaining leachings, ≈ 20 g of sample labeled and saved for later inorganic analysis, the weight of the total sample after acetate leaching, and the moisture of the sample as weighed. From this information and the dry weight of the sample at the beginning of the acetate leaching step, the change in the dry weight induced by acetate leaching can be calculated.

1. Add 3 ml NH_4OAc per gram of water-leached sample remaining in beaker.
2. Stir overnight at room temperature.
3. Filter and rinse with distilled H_2O.
4. Repeat steps 1 through 3 twice.
5. Determine total weight of sample.
6. Remove and weigh approximately 1/2 (at least 20 g) of moist sample.
7. Determine moisture with a portion (< 5 g) of the removed material immediately.
8. Label remaining removed material *After NH_4OAc* and set aside.

Hydrochloric Acid Wash (HCl)

There should be ≈ 25 g of sample (on a dry basis) at this point. At the end of this step there should be essentially no sample left to be leached, ≈ 20 g of sample labeled and saved for later inorganic analysis, the weight of the total sample after acetate leaching,

and the moisture of the sample as weighed. From this information and the dry weight of the sample at the beginning of the acid leaching step, the change in the dry weight induced by acid leaching can be calculated.

1. Add 3 ml HCl per gram of water- and acetate-leached sample to beaker.

2. Stir overnight at 70° C.

3. Filter and rinse with distilled H_2O.

4. Repeat steps 1 through 3.

5. Determine total weight of sample.

6. Remove and weigh at least 20 g of moist sample. All of the sample may be used in this step.

7. Determine moisture with a portion (< 5 g) of the removed material immediately.

8. Label remaining removed material *After HCl* and set aside.

Ash Chemistry Analyses

There should now be four samples labeled *Unleached, After H_2O, After NH_4OAc*, and *After HCl*. The composition of the inorganic portion of these samples will allow an estimation of the modes of occurrence of each of the major inorganic elements. These analyses should be done by an atomic emission or absorption technique using an inductively coupled plasma (ICP/AA or ICP/AE), for example, in the analysis. Cheaper but less accurate XRF procedures can be substituted where ICP/AA or ICP/AE are not available.

1. Submit all four samples (*Unleached, After H_2O, After NH_4OAc*, and *After HCl*) for ash analyses.

2. Submit all four samples ashed samples for inorganic analysis, which should include Si, Al, Fe, Ti, Ca, Mg, Na, K, S, P, and residual, all expressed on an oxide basis. The 'residual' is determined by difference between the sum of the oxides of the previous ten elements and the results of the total ash analysis.

Option of Analyzing Leachates in Addition to Solid Samples

At each step, the leachate and rinse water are saved in single container, weighed, and submitted to total dissolved solids and inorganic elemental analysis for the same ten elements (Si, Al, Fe, Ti, Ca, Mg, Na, K, S, and P) as are used in the ash chemistry analysis. This provides means by which a mass balance can be closed for each step.

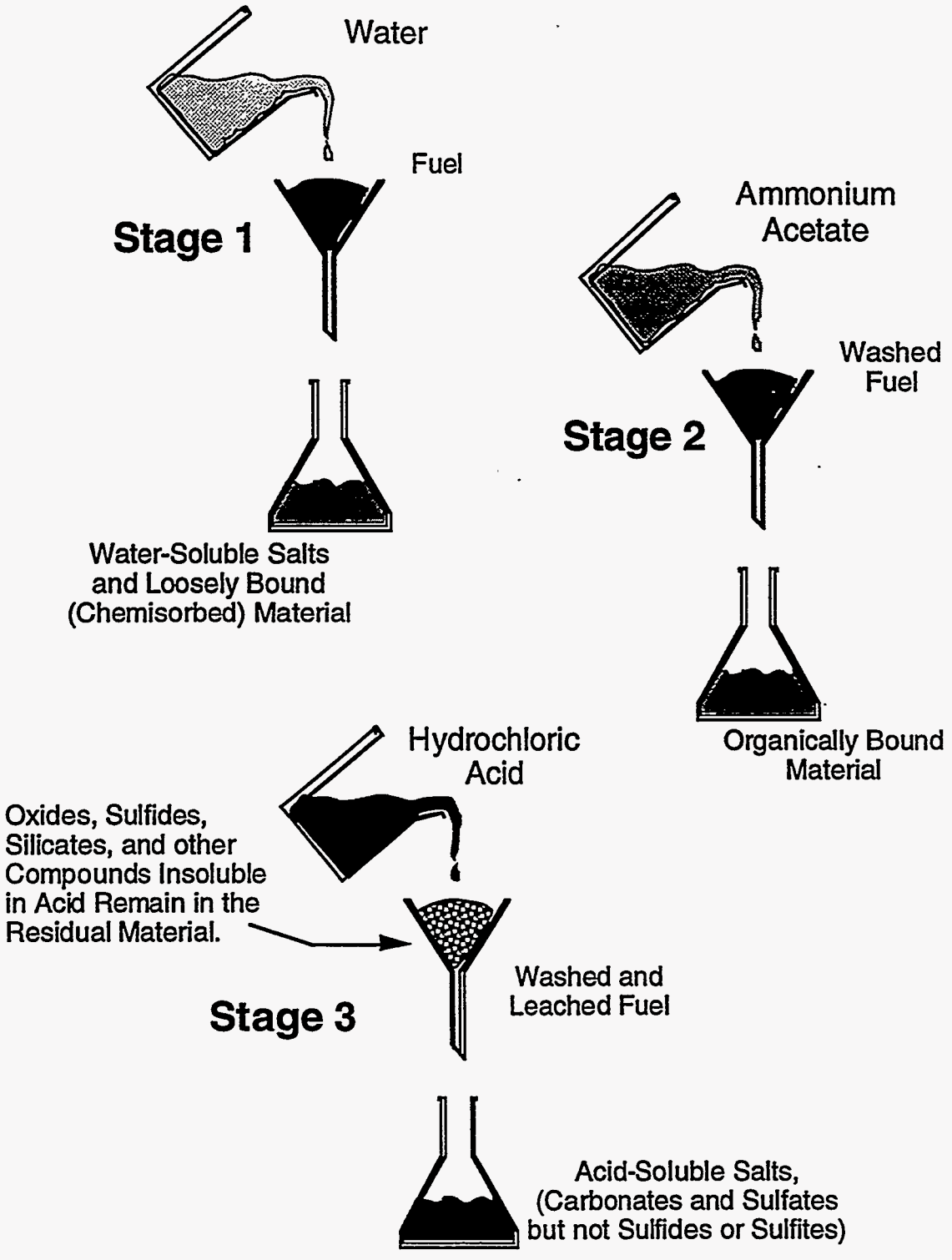

Figure 122 Illustration of the chemical fractionation procedure.

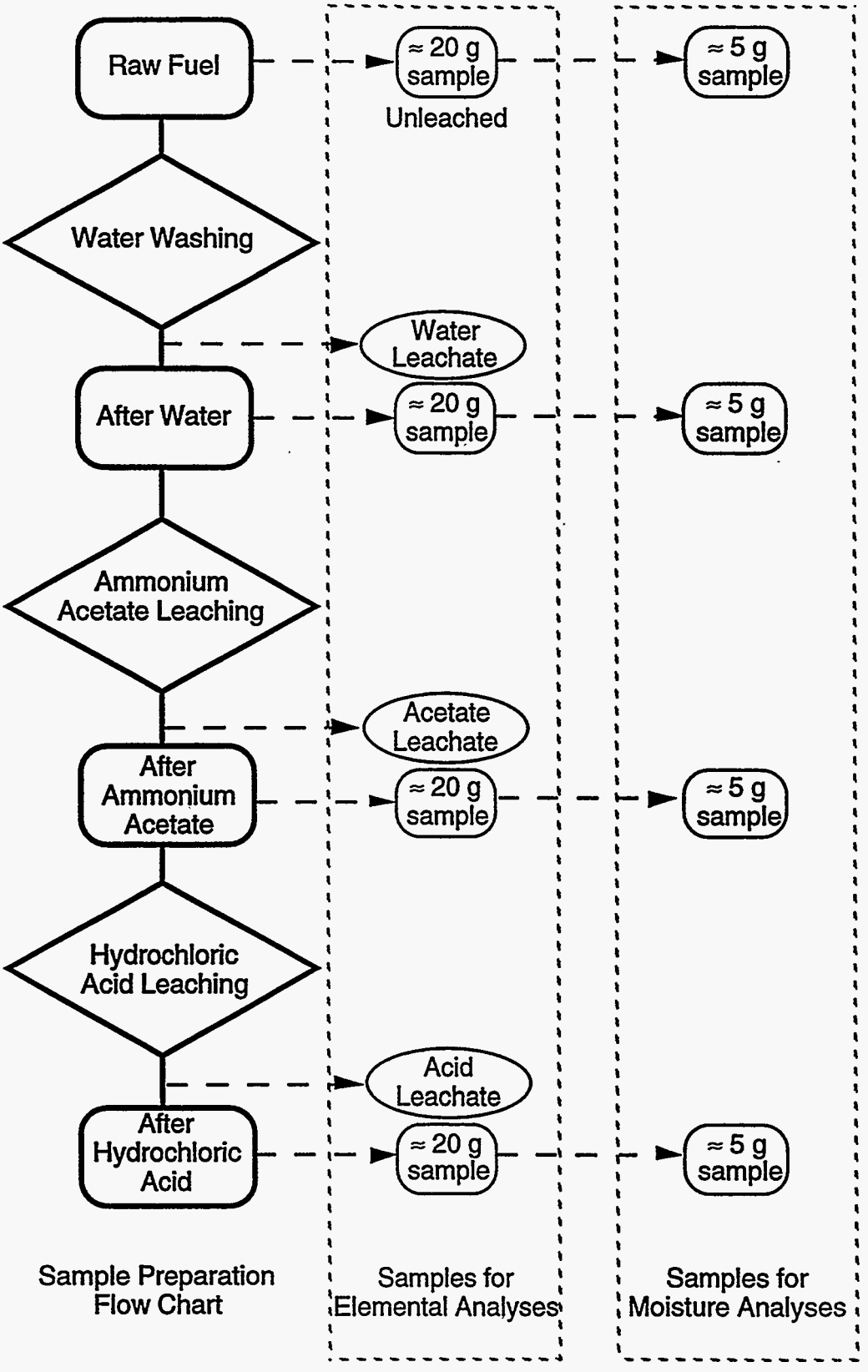

Figure 123 Flow diagram for the chemical fractionation procedure.

Legend of Symbols and Lines

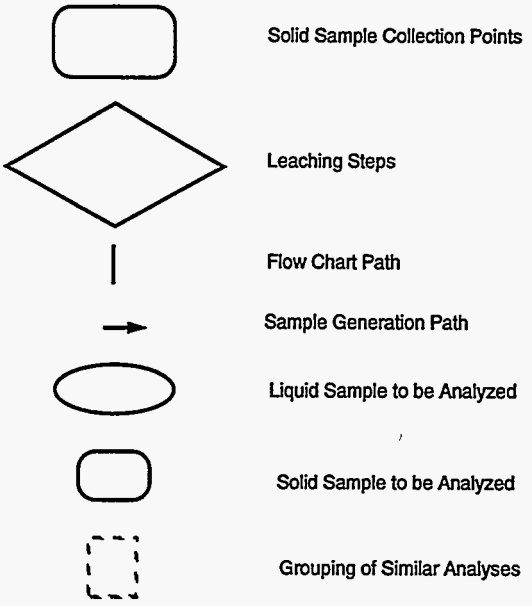

Figure 124 Key to symbols and lines used in flow diagram for chemical fractionation procedure (Figure 123).

Chemical Fractionation Results by Element

The column labeled Sum in each of the following tables represents an independent mass balance of the element in the residual fraction. Departures from unity represent lack of mass closure from the two independent balances. No independent analyses were available for the data from lab B (samples with designation B in sample name), and the closure is indicated as unity. Departures from unity are small for elements in large concentrations but can be sizable for trace elements. In all cases, mass balance closures are worse than are typical for similar analyses of coal. The difficulty of the procedure is much greater with most biomass fuels because they absorb large quantities of leachate that is difficult to separate from the sample. This is possibly the largest single contributor to the sometimes poor mass closures.

The data presented in the discussion earlier in this report are based on normalizing these results with the independently determined mass closure result. That is, the numbers were renormalized such that the sum is unity.

Silicon

Table 66 Chemical fractionation results for silicon for selected biomass fuels.

Sample Name	*Water Soluble*	*Ion Exchangeable*	*Acid Soluble*	*Residual*	***Sum***
Almond Hulls	0.00	0.01	0.00	1.00	1.01
Almond Shells	0.01	0.00	0.00	1.00	1.01
Al Shells - B	0.01	0.00	0.01	0.97	1.00
UWF/Wh Str	0.01	0.01	0.01	1.00	1.03
UWF/Al Shell	0.01	0.00	0.01	1.00	1.02
Olive Pits	0.01	0.00	0.04	1.00	1.06
Rice Straw	0.00	0.01	0.00	1.00	1.01
Rice Straw - B	0.00	0.00	0.00	1.00	1.00
Switch Grass	0.00	0.03	0.01	1.00	1.04
Sw. Grass - B	0.02	0.01	0.00	0.97	1.00
Sw Grass - C1	0.00	0.00	0.00	1.00	1.00
Sw Grass - C2	0.00	0.00	0.00	1.00	1.00
Paper	0.00	0.00	0.01	0.99	1.00
Wheat Straw	0.01	0.02	0.01	1.00	1.05
Wh Straw - B	0.07	0.00	0.00	0.93	1.00

Aluminum

Table 67 Chemical fractionation results for aluminum for selected biomass fuels.

Sample Name	*Water Soluble*	*Ion Exchangeable*	*Acid Soluble*	*Residual*	***Sum***
Almond Hulls	0.00	0.00	0.00	1.14	1.14
Almond Shells	0.03	0.00	0.03	0.67	0.73
Al Shells - B	0.00	0.00	0.23	0.77	1.00
UWF/Wh Str	0.00	0.00	0.06	0.88	0.94
UWF/Al Shell	0.01	0.00	0.03	0.77	0.81
Olive Pits	0.00	0.00	0.15	0.48	0.63
Rice Straw	0.01	0.00	0.02	0.40	0.43
Rice Straw - B	0.02	0.00	0.07	0.91	1.00
Switch Grass	0.01	0.00	0.03	0.43	0.47
Sw. Grass - B	0.00	0.00	0.09	0.91	1.00
Sw Grass - C1	0.00	0.00	0.00	1.00	1.00
Sw Grass - C2	0.00	0.00	0.00	1.00	1.00
Paper	0.00	0.00	0.27	0.73	1.00
Wheat Straw	0.00	0.00	0.01	0.49	0.51
Wh Straw - B	0.08	0.00	0.00	0.92	1.00

Iron

Table 68 Chemical fractionation results for iron for selected biomass fuels.

Sample Name	*Water Soluble*	*Ion Exchangeable*	*Acid Soluble*	*Residual*	***Sum***
Almond Hulls	0.00	0.00	0.08	0.49	0.57
Almond Shells	0.05	0.00	0.25	0.48	0.77
Al Shells - B	0.00	0.00	0.49	0.51	1.00
UWF/Wh Str	0.01	0.00	0.19	0.57	0.77
UWF/Al Shell	0.01	0.00	0.21	0.39	0.60
Olive Pits	0.03	0.00	0.46	0.33	0.81
Rice Straw	0.08	0.03	0.14	0.42	0.67
Rice Straw - B	0.28	0.00	0.34	0.38	1.00
Switch Grass	0.04	0.00	0.11	0.48	0.62
Sw. Grass - B	0.02	0.00	0.18	0.80	1.00
Sw Grass - C1	0.00	0.00	0.39	0.61	1.00
Sw Grass - C2	0.06	0.00	0.28	0.66	1.00
Paper	0.00	0.00	0.23	0.77	1.00
Wheat Straw	0.00	0.00	0.10	14.37	14.48
Wh Straw - B	0.17	0.00	0.09	0.74	1.00

Titanium

Table 69 Chemical fractionation results for titanium for selected biomass fuels.

Sample Name	*Water Soluble*	*Ion Exchangeable*	*Acid Soluble*	*Residual*	***Sum***
Almond Hulls	0.00	0.00	0.00	0.55	0.55
Almond Shells	0.00	0.00	0.00	0.21	0.21
Al Shells - B	0.00	0.00	0.00	1.00	1.00
UWF/Wh Str	0.00	0.00	0.00	0.72	0.72
UWF/Al Shell	0.00	0.00	0.00	0.63	0.63
Olive Pits	0.00	0.00	0.00	0.60	0.60
Rice Straw	0.00	0.00	0.00	0.03	0.03
Rice Straw - B	1.00	0.00	0.00	0.00	1.00
Switch Grass	0.00	0.00	0.00	0.43	0.43
Sw. Grass - B	0.00	0.00	0.00	1.00	1.00
Sw Grass - C1	0.00	0.00	0.00	1.00	1.00
Sw Grass - C2	0.00	0.00	0.00	1.00	1.00
Paper	0.00	0.00	0.00	1.00	1.00
Wheat Straw	0.00	0.00	0.00	0.03	0.03
Wh Straw - B	0.00	0.00	0.00	1.00	1.00

Calcium

Table 70 Chemical fractionation results for calcium for selected biomass fuels.

Sample Name	*Water Soluble*	*Ion Exchangeable*	*Acid Soluble*	*Residual*	***Sum***
Almond Hulls	0.32	0.22	0.20	0.18	0.93
Almond Shells	0.20	0.30	0.37	0.14	1.02
Al Shells - B	0.04	0.22	0.74	0.00	1.00
UWF/Wh Str	0.08	0.22	0.38	0.22	0.90
UWF/Al Shell	0.03	0.13	0.34	0.20	0.71
Olive Pits	0.02	0.35	0.53	0.07	0.97
Rice Straw	0.01	0.00	0.52	0.31	0.84
Rice Straw - B	0.01	0.00	0.32	0.66	1.00
Switch Grass	0.06	0.16	0.35	0.29	0.86
Sw. Grass - B	0.06	0.24	0.31	0.40	1.00
Sw Grass - C1	0.02	0.82	0.07	0.09	1.00
Sw Grass - C2	0.06	0.65	0.22	0.08	1.00
Paper	0.04	0.42	0.54	0.00	1.00
Wheat Straw	0.10	0.21	0.31	0.21	0.82
Wh Straw - B	0.25	0.14	0.17	0.45	1.00

Magnesium

Table 71 Chemical fractionation results for magnesium for selected biomass fuels.

Sample Name	*Water Soluble*	*Ion Exchangeable*	*Acid Soluble*	*Residual*	***Sum***
Almond Hulls	0.55	0.34	0.07	0.00	0.96
Almond Shells	0.52	0.39	0.09	0.00	1.00
Al Shells - B	0.07	0.30	0.09	0.55	1.00
UWF/Wh Str	0.14	0.23	0.17	0.35	0.89
UWF/Al Shell	0.16	0.30	0.14	0.21	0.81
Olive Pits	0.09	0.80	0.11	0.00	1.00
Rice Straw	0.37	0.47	0.16	0.00	1.00
Rice Straw - B	0.61	0.21	0.00	0.18	1.00
Switch Grass	0.25	0.36	0.14	0.07	0.82
Sw. Grass - B	0.19	0.40	0.03	0.39	1.00
Sw Grass - C1	0.32	0.49	0.06	0.13	1.00
Sw Grass - C2	0.31	0.48	0.08	0.13	1.00
Paper	0.02	0.21	0.21	0.56	1.00
Wheat Straw	0.23	0.30	0.15	0.18	0.87
Wh Straw - B	0.56	0.14	0.05	0.25	1.00

Sodium

Table 72 Chemical fractionation results for sodium for selected biomass fuels.

Sample Name	*Water Soluble*	*Ion Exchangeable*	*Acid Soluble*	*Residual*	***Sum***
Almond Hulls	0.53	0.05	0.00	0.40	0.98
Almond Shells	0.35	0.06	0.00	0.30	0.71
Al Shells - B	0.10	0.03	0.03	0.84	1.00
UWF/Wh Str	0.37	0.17	0.00	0.28	0.82
UWF/Al Shell	0.10	0.05	0.00	0.54	0.69
Olive Pits	0.65	0.35	0.00	0.02	1.02
Rice Straw	0.47	0.26	0.00	0.14	0.87
Rice Straw - B	0.93	0.07	0.00	0.00	1.00
Switch Grass	0.06	0.00	0.00	0.42	0.48
Sw. Grass - B	0.05	0.00	0.00	0.95	1.00
Sw Grass - C1	0.56	0.00	0.00	0.44	1.00
Sw Grass - C2	0.59	0.00	0.00	0.41	1.00
Paper	0.34	0.66	0.00	0.00	1.00
Wheat Straw	0.24	0.22	0.10	0.11	0.67
Wh Straw - B	0.43	0.09	0.00	0.48	1.00

Potassium

Table 73 Chemical fractionation results for potassium for selected biomass fuels.

Sample Name	*Water Soluble*	*Ion Exchangeable*	*Acid Soluble*	*Residual*	***Sum***
Almond Hulls	0.81	0.16	0.03	0.01	1.01
Almond Shells	0.72	0.24	0.04	0.01	1.01
Al Shells - B	0.55	0.25	0.02	0.18	1.00
UWF/Wh Str	0.42	0.25	0.06	0.15	0.88
UWF/Al Shell	0.40	0.24	0.04	0.19	0.87
Olive Pits	0.56	0.38	0.05	0.08	1.08
Rice Straw	0.58	0.34	0.08	0.02	1.02
Rice Straw - B	0.87	0.13	0.01	0.00	1.00
Switch Grass	0.51	0.32	0.08	0.04	0.94
Sw. Grass - B	0.68	0.24	0.00	0.08	1.00
Sw Grass - C1	0.70	0.19	0.00	0.10	1.00
Sw Grass - C2	0.71	0.17	0.01	0.10	1.00
Paper	0.33	0.50	0.17	0.00	1.00
Wheat Straw	0.41	0.41	0.18	0.05	1.05
Wh Straw - B	0.89	0.07	0.00	0.04	1.00

Sulfur

Table 74 Chemical fractionation results for sulfur for selected biomass fuels.

Sample Name	*Water Soluble*	*Ion Exchangeable*	*Acid Soluble*	*Residual*	***Sum***
Almond Hulls	1.00	0.00	0.00	0.11	1.11
Almond Shells	1.00	0.00	0.00	0.05	1.05
Al Shells - B	0.39	0.12	0.50	0.00	1.00
UWF/Wh Str	0.23	0.00	0.00	0.17	0.40
UWF/Al Shell	0.00	0.00	0.00	0.32	0.32
Olive Pits	0.00	0.00	0.00	0.00	0.00
Rice Straw	1.00	0.00	0.00	0.06	1.06
Rice Straw - B	0.16	0.00	0.00	0.84	1.00
Switch Grass	0.00	0.00	0.00	0.07	0.07
Sw. Grass - B	0.21	0.31	0.00	0.48	1.00
Sw Grass - C1	0.25	0.69	0.06	0.00	1.00
Sw Grass - C2	0.15	0.55	0.30	0.00	1.00
Paper	0.00	0.00	0.00	1.00	1.00
Wheat Straw	1.00	0.00	0.00	0.04	1.04
Wh Straw - B	0.54	0.03	0.00	0.42	1.00

Phosphorus

Table 75 Chemical fractionation results for phosphorus for selected biomass fuels.

Sample Name	*Water Soluble*	*Ion Exchangeable*	*Acid Soluble*	*Residual*	***Sum***
Almond Hulls	0.49	0.10	0.01	0.19	0.79
Almond Shells	0.66	0.13	0.04	0.21	1.04
Al Shells - B	0.08	0.15	0.52	0.26	1.00
UWF/Wh Str	0.15	0.10	0.24	0.26	0.75
UWF/Al Shell	0.20	0.08	0.12	0.39	0.79
Olive Pits	0.58	0.05	0.11	0.15	0.88
Rice Straw	0.25	0.13	0.05	0.07	0.49
Rice Straw - B	0.77	0.13	0.02	0.08	1.00
Switch Grass	0.35	0.18	0.06	0.12	0.72
Sw. Grass - B	0.54	0.00	0.14	0.32	1.00
Sw Grass - C1	0.69	0.08	0.16	0.07	1.00
Sw Grass - C2	0.68	0.13	0.13	0.06	1.00
Paper	0.11	0.00	0.22	0.67	1.00
Wheat Straw	0.04	0.09	0.06	0.12	0.31
Wh Straw - B	0.76	0.24	0.00	0.00	1.00

Chlorine

Table 76 Chemical fractionation results for chlorine for selected biomass fuels.

Sample Name	*Water Soluble*	*Ion Exchangeable*	*Acid Soluble*	*Residual*	***Sum***
Almond Hulls	0.67	0.00	0.00	0.00	0.67
Almond Shells	1.00	0.00	0.00	0.00	1.00
Al Shells - B	0.05	0.00	0.00	0.95	1.00
UWF/Wh Str	0.69	0.23	0.00	0.00	0.92
UWF/Al Shell	0.67	0.33	0.00	0.00	1.00
Olive Pits	1.00	0.00	0.00	0.00	1.00
Rice Straw	0.19	0.30	0.00	0.00	0.49
Rice Straw - B	1.00	0.00	0.00	0.00	1.00
Switch Grass	0.11	0.33	0.00	0.00	0.44
Sw. Grass - B	0.81	0.19	0.00	0.00	1.00
Sw Grass - C1	0.00	0.00	0.00	0.00	0.00
Sw Grass - C2	0.00	0.00	0.00	0.00	0.00
Paper	0.33	0.33	0.00	0.33	1.00
Wheat Straw	0.59	0.41	0.00	0.00	1.00
Wh Straw - B	1.00	0.00	0.00	0.00	1.00

These pages intentionally left blank

APPENDIX 2

Optical Microscopy, X-Ray Diffraction, and SEM Analyses of Deposits

Material in this appendix has been reproduced from the best available originals

March 16, 1994

Report on Optical Microscopy, X-Ray Diffraction, and SEM Analysis of Biomass Deposits

Compiled by L. Oden, US Bureau of Mines.

Samples analyzed:
Delano 10, 13, 14, 15, 17, and 21,
Woodland 1, 8, 10, and 14,
Marysville 1 and 4.

All photographs taken with polarized light unless indicated.

Delano 10: Sharks tooth deposit on superheater tube.

XRD Fire side:
Secondary phases: $Ca_{10}(SiO_4)_3(SO_4)_3(OH)_2$ (hydroxyl-ellestadite) and $K_2Ca_2(SO_4)_3$
Trace: Calcite ($CaCO_3$) and unidentified compound(s).
No amorphous halos were observed.

Tube side:
Identical analysis

Photograph: Number	Magnification	
		Delano 10 polished in water.
1.	50	Tube side
2.	50	Tube side, duplicate
3.	50	Midway interior
4.	50	Fireside
5.	200	Tube side, fine grained material
6.	200	Tube side, coarse material
7.	200	Interior
8.	100	Fire side
		Delano 10, repolished in oil.
22.	100	Fire side
23.	200	Interior
24.	200	Interior
25.	200	Tube side
26.	200	Interior

SEM Analysis:

Analytical reports provided to T. R. Miles.

Delano 13: Cross section of deposit. Rust on tube side deliberately omitted.

XRD Primary phase: KCl (Silvite)
Minor phase: $K_2Ca_2(SO_4)_3$
Trace: NaCl (Halite), $CaCO_3$, SiO_2, $Ca_{10}(SiO_4)_3(SO_4)_3(OH)_2$, and unidentified compound(s)
No amorphous halos were observed.

Delano 14: Cross section of deposit.

XRD Secondary phases: KCl and $CaCO_3$
Minor phases: $K_2Ca_2(SO_4)_3$ and NaCl
Trace: SiO_2 and unidentified compound(s)
No amorphous halos were observed.

Delano 15: Dust deposit.

XRD Primary phase: $CaCO_3$
Minor phases: SiO_2
Trace: KCl, $CaSO_4$ (Anhydrite) and NaCl
No amorphous halos were observed.

Delano 17: Cross section of friable agglomerate, furnace wall deposit.

XRD Secondary phases: $KAlSi_2O_6$ (Leucite), SiO_2, and Anorthite
Trace: Unidentified compound(s)
No amorphous halos observed

Delano 21: Dust deposit.

XRD Primary phase: $CaCO_3$
Minor phase: $CaSO_4$
Trace: SiO_2, KCl, $Ca(OH)_2$, $Ca_5(PO_4)_3(OH)$ (Hydroxylapatite), and unidentified compound(s)
No amorphous halos observed

Woodland 1: Sharks tooth deposit, hard dense purple-brown outer surface with lighter brown inner layers.

XRD Outer surface layer:
Primary phase: $K_2Ca_2(SiO_4)_3$,
Secondary phase: $CaMgSiO_4$ (Monticellite),
Minor phases: $Ca_5(PO_4)_3(OH)$ and possibly Fe_3O_4,
Trace: Unidentified compound(s),
No amorphous halos observed.

Lighter brown inner layers:
Primary phase: $Ca_2Mg\ Si_2O_7$ and/or $Ca_2Al_2SiO_7$,
Minor phases: $Ca_5(PO_4)_3OH$, $Ca_3Fe_2Si_3O_{12}$ (Andradite), $CaMgSiO_4$,

$K_2Ca_2(SO_4)_3$, and unidentified compound(s).
No amorphous halos observed.

Photographs:
Four locations are displayed beginning at the fire side of the deposit and continuing to the tube side. All photographs are 100 magnification. Photographs have no numbers.

SEM Analysis:

The deposit is a multi-phase, fine-grained material typical of deposits formed by competing forces: deposition by inertial impaction, condensation, and chemical reaction; and erosion by particles that collide but do not stick. SEM figures 1, 2, and 3 are backscattered electron images (BSE) of the fire side of the deposit at increasing magnification: 50, 500, and 2,000. The analysis of the fire side deposit matrix, grey particles, and bright particles by SEM provided on pages 1, 2, and 3, respectively, list the composition normalized to 100 pct in terms of the elements requested by the operator. Oxygen, a major component, is omitted; therefore, the analyses are useful only to the extent that the ratios of elements are correct. From these ratios it is apparent that the fire side matrix material is mostly sulfate, probably a complex mixture of potassium and calcium sulfates. The grey sharply defined particles are obviously silica. Bright particles in the BSE photographs (large atomic number) are either iron or iron oxide particles. The latter analysis is compromised by the small size of the particles which results in excitation of surrounding material, hence the indication of other elements. SEM analyses on pages 4 and 5 are provided in terms of oxide content, and confirm X-ray identification of potassium and calcium sulfates and silicates. Analysis of the bright phase on the tube side indicates that the iron has reacted with its surroundings to form a compound containing magnesium.

Woodland 10: Dense brown case over friable greenish cemented particles.

XRD Dense brown outer case:
Secondary phase: Augite
Minor phases: Wollastonite, Leucite, and Unidentified compound(s)

Cross section of deposit:
Primary phase: Quartz
Minor phases: Augite and Leucite
Trace: Unidentified compound(s),

Woodland 14: Layered deposit with glass wool interior. Deposit comprises greenish cemented particles blending to a semi-hard brown outer surface layer.

XRD Brown outer surface layer:
Secondary phases: $Ca(Mg,Fe)Si_2O_6$ (Augite) and $CaSiO_3$ (Wollastonite)
Minor phases: $KAlSi_3O_8$ (Sanidine) and $KAlSi_2O_6$ (Leucite)
Trace: Unidentified compound(s).

Cross section containing cemented layer of particles and brown surface layer:
Secondary phase: Quartz
Minor phases: Augite, Anorthite, and Leucite
Trace: Unidentified compound(s).

Photograph:

Number	Magnification		**Woodland 14, polished in water.**
14.	50	Fire side	
15.	50	Interior	
16.	50?	Interior	
17.	200	Interior,	bright field illumination
18.	200	Interior	
			Woodland 14, repolished in oil.
32.	200	Fire side	
33.	100	Fire side	
34.	50	Fire side	
35.	50	Interior	
36.	100	Interior	
37.	50	Tube side	

SEM Analysis:

Analytical reports provided to T. R. Miles.

Marysville 1: Light brown layered deposit.

XRD Secondary phases: Leucite and Diopside
Minor phase: Wollastonite
Trace: Unidentified compound(s).

Marysville 4: Secondary superheater tube deposit.

XRD Cross section of deposit:
Primary: $CaSO_4$, (anhydrite)
Minor phase: $K_2Ca_2(SO_4)_3$
Trace: $Ca_5(PO_4)_3OH$ (hydroxylapatite)
$CaMgSiO_4$ (monticellite) and unidentified compound(s).
No amorphous halos were observed.

Photograph: Number	Magnification	
		Marysville 4, polished in water.
9.	50	Fire side, point of sharks tooth
10.	50	Midway
11.	50	Tube side
12.	200	Near tube side
13.	200	Near end of sharks tooth
		Marysville 4, repolished in oil.
27.	200	Fire side
28.	200	Fire side interior
29.	200	Interior, bright field illumination
30.	200	Interior, Polarized light, same area as 29
31.	200	Tube side

SEM Analysis:

Analytical reports provided to T. R. Miles.

02-Mar-1994 09:29:15 FIRE SIDE MATRIX

Accelerating voltage 20.0 KeV

Beam - sample incidence angle 70.0 degrees

Xray emergence angle 21.2 degrees

Xray - window incidence angle 4.8 degrees

QUANTITATIVE EDS RESULTS
(ZAF CORRECTIONS VIA MAGIC V)

ELEMENT & LINE	WEIGHT PERCENT	ATOMIC PERCENT*	PRECISION 2 SIGMA	K-RATIO**	ITER
Na KA	2.19	3.23	0.09	0.0240	
Mg KA	2.25	3.15	0.06	0.0072	
Al KA	4.43	5.58	0.08	0.0173	
Si KA	8.21	9.94	0.06	0.0373	
P KA	4.71	5.17	0.05	0.1596	
S KA	31.26	33.14	0.15	0.3772	
K KA	11.96	10.39	0.07	0.1671	
Ca KA	33.78	28.65	0.13	0.3365	
Mn KA	0.16	0.10	0.03	0.0009	
Fe KA	1.06	0.64	0.05	0.0060	4
TOTAL	100.01				

*NOTE: ATOMIC PERCENT is normalized to 100

**NOTE: K-RATIO = K-RATIO x R
where R = reference(standard)/reference(sample)

NORMALIZATION FACTOR: 1.490

02-Mar-1994 09:48:25 FIRE SIDE GRAY

Accelerating voltage	20.0 KeV
Beam - sample incidence angle	70.0 degrees
Xray emergence angle	21.2 degrees
Xray - window incidence angle	4.8 degrees

QUANTITATIVE EDS RESULTS
(ZAF CORRECTIONS VIA MAGIC V)

ELEMENT & LINE	WEIGHT PERCENT	ATOMIC PERCENT*	PRECISION 2 SIGMA	K-RATIO**	ITER
Si KA	97.85	98.47	0.23	0.3396	
K KA	0.70	0.51	0.05	0.0043	
Ca KA	1.45	1.02	0.06	0.0073	2
TOTAL	100.00				

*NOTE: ATOMIC PERCENT is normalized to 100

**NOTE: K-RATIO = K-RATIO x R
where R = reference(standard)/reference(sample)

NORMALIZATION FACTOR: 2.890

02-Mar-1994 09:40:00 FIRE SIDE BRIGHT

Accelerating voltage	20.0 KeV
Beam - sample incidence angle	70.0 degrees
Xray emergence angle	21.2 degrees
Xray - window incidence angle	4.8 degrees

QUANTITATIVE EDS RESULTS
(ZAF CORRECTIONS VIA MAGIC V)

ELEMENT & LINE	WEIGHT PERCENT	ATOMIC PERCENT*	PRECISION 2 SIGMA	K-RATIO**	ITER
Na KA	3.73	6.26	0.15	0.0201	
Mg KA	9.33	14.80	0.13	0.0166	
Al KA	7.26	10.38	0.13	0.0163	
Si KA	11.96	16.42	0.10	0.0345	
P KA	1.10	1.36	0.04	0.0256	
S KA	3.44	4.14	0.07	0.0333	
K KA	1.03	1.01	0.03	0.0161	
Ca KA	9.88	9.51	0.07	0.1212	
Mn KA	3.03	2.13	0.07	0.0195	
Fe KA	49.24	34.00	0.20	0.3246	4
TOTAL	100.00				

*NOTE: ATOMIC PERCENT is normalized to 100

**NOTE: K-RATIO = K-RATIO x R
where R = reference(standard)/reference(sample)

NORMALIZATION FACTOR: 1.452

02-Mar-1994 09:00:47 TUBE SIDE MATRIX

Accelerating voltage 20.0 KeV

Beam - sample incidence angle 70.0 degrees

Xray emergence angle 21.2 degrees

Xray - window incidence angle 4.8 degrees

QUANTITATIVE EDS RESULTS
(ZAF CORRECTIONS VIA MAGIC V)

ELEMENT & LINE	K-RATIO**	WEIGHT PERCENT	PRECISION 2 SIGMA	FORMULA	OXIDE PERCENT
Na KA	0.0332	2.15	0.07	Na2O	2.89
Mg KA	0.0122	2.60	0.05	MgO	4.32
Al KA	0.0392	6.69	0.07	Al2O3	12.63
Si KA	0.0480	7.27	0.05	SiO2	15.54
P KA	0.1127	2.22	0.03	P2O5	5.08
S KA	0.2016	10.41	0.07	SO3	25.99
Cl KA	0.0042	0.26	0.02	Cl	0.26
K KA	0.0777	2.97	0.03	K2O	3.58
Ca KA	0.3281	16.82	0.06	CaO	23.53
Mn KA	0.0041	0.42	0.02	MnO	0.54
Fe KA	0.0448	4.37	0.05	FeO	5.62
O *		43.83			
TOTAL					100.01

* DETERMINED BY STOICHIOMETRY

**NOTE: K-RATIO = K-RATIO x R
where R = reference(standard)/reference(sample)

NORMALIZATION FACTOR: 1.159

02-Mar-1994 09:40:00 FIRE SIDE BRIGHT

Accelerating voltage 20.0 KeV

Beam - sample incidence angle 70.0 degrees

Xray emergence angle 21.2 degrees

Xray - window incidence angle 4.8 degrees

QUANTITATIVE EDS RESULTS
(ZAF CORRECTIONS VIA MAGIC V)

ELEMENT & LINE	WEIGHT PERCENT	ATOMIC PERCENT*	PRECISION 2 SIGMA	K-RATIO**	ITER
Na KA	3.73	6.26	0.15	0.0201	
Mg KA	9.33	14.80	0.13	0.0166	
Al KA	7.26	10.38	0.13	0.0163	
Si KA	11.96	16.42	0.10	0.0345	
P KA	1.10	1.36	0.04	0.0256	
S KA	3.44	4.14	0.07	0.0333	
K KA	1.03	1.01	0.03	0.0161	
Ca KA	9.88	9.51	0.07	0.1212	
Mn KA	3.03	2.13	0.07	0.0195	
Fe KA	49.24	34.00	0.20	0.3246	4
TOTAL	100.00				

*NOTE: ATOMIC PERCENT is normalized to 100

**NOTE: K-RATIO = K-RATIO x R
where R = reference(standard)/reference(sample)

NORMALIZATION FACTOR: 1.452

02-Mar-1994 09:00:47 TUBE SIDE MATRIX

Accelerating voltage 20.0 KeV

Beam - sample incidence angle 70.0 degrees

Xray emergence angle 21.2 degrees

Xray - window incidence angle 4.8 degrees

QUANTITATIVE EDS RESULTS
(ZAF CORRECTIONS VIA MAGIC V)

ELEMENT & LINE	K-RATIO**	WEIGHT PERCENT	PRECISION 2 SIGMA	FORMULA	OXIDE PERCENT
Na KA	0.0332	2.15	0.07	Na2O	2.89
Mg KA	0.0122	2.60	0.05	MgO	4.32
Al KA	0.0392	6.69	0.07	Al2O3	12.63
Si KA	0.0480	7.27	0.05	SiO2	15.54
P KA	0.1127	2.22	0.03	P2O5	5.08
S KA	0.2016	10.41	0.07	SO3	25.99
Cl KA	0.0042	0.26	0.02	Cl	0.26
K KA	0.0777	2.97	0.03	K2O	3.58
Ca KA	0.3281	16.82	0.06	CaO	23.53
Mn KA	0.0041	0.42	0.02	MnO	0.54
Fe KA	0.0448	4.37	0.05	FeO	5.62
O *		43.83			
TOTAL					100.01

* DETERMINED BY STOICHIOMETRY

**NOTE: K-RATIO = K-RATIO x R
where R = reference(standard)/reference(sample)

NORMALIZATION FACTOR: 1.159

02-Mar-1994 09:07:21 TUBE SIDE FE

Accelerating voltage 20.0 KeV

Beam - sample incidence angle 70.0 degrees

Xray emergence angle 21.2 degrees

Xray - window incidence angle 4.8 degrees

QUANTITATIVE EDS RESULTS
(ZAF CORRECTIONS VIA MAGIC V)

ELEMENT & LINE	K-RATIO**	WEIGHT PERCENT	PRECISION 2 SIGMA	FORMULA	OXIDE PERCENT
Na KA	0.0170	2.33	0.11	Na2O	3.14
Mg KA	0.0302	12.15	0.12	MgO	20.14
Al KA	0.0110	3.64	0.08	Al2O3	6.87
Si KA	0.0049	1.19	0.03	SiO2	2.54
P KA	0.0076	0.20	0.02	P2O5	0.46
S KA	0.0257	1.65	0.04	SO3	4.12
Cl KA	0.0000	0.00	0.00	Cl	0.00
K KA	0.0125	0.52	0.02	K2O	0.63
Ca KA	0.0293	1.58	0.03	CaO	2.21
Mn KA	0.0374	3.92	0.05	MnO	5.06
Fe KA	0.4064	42.17	0.15	FeO	54.26
Cu KA	0.0041	0.47	0.03	CuO	0.59
O *		30.19			
TOTAL					100.01

* DETERMINED BY STOICHIOMETRY

**NOTE: K-RATIO = K-RATIO x R
where R = reference(standard)/reference(sample)

NORMALIZATION FACTOR: 1.345

Fuel Mix: 60% UWW, 37% Ag Wood, 3% Almond Shell

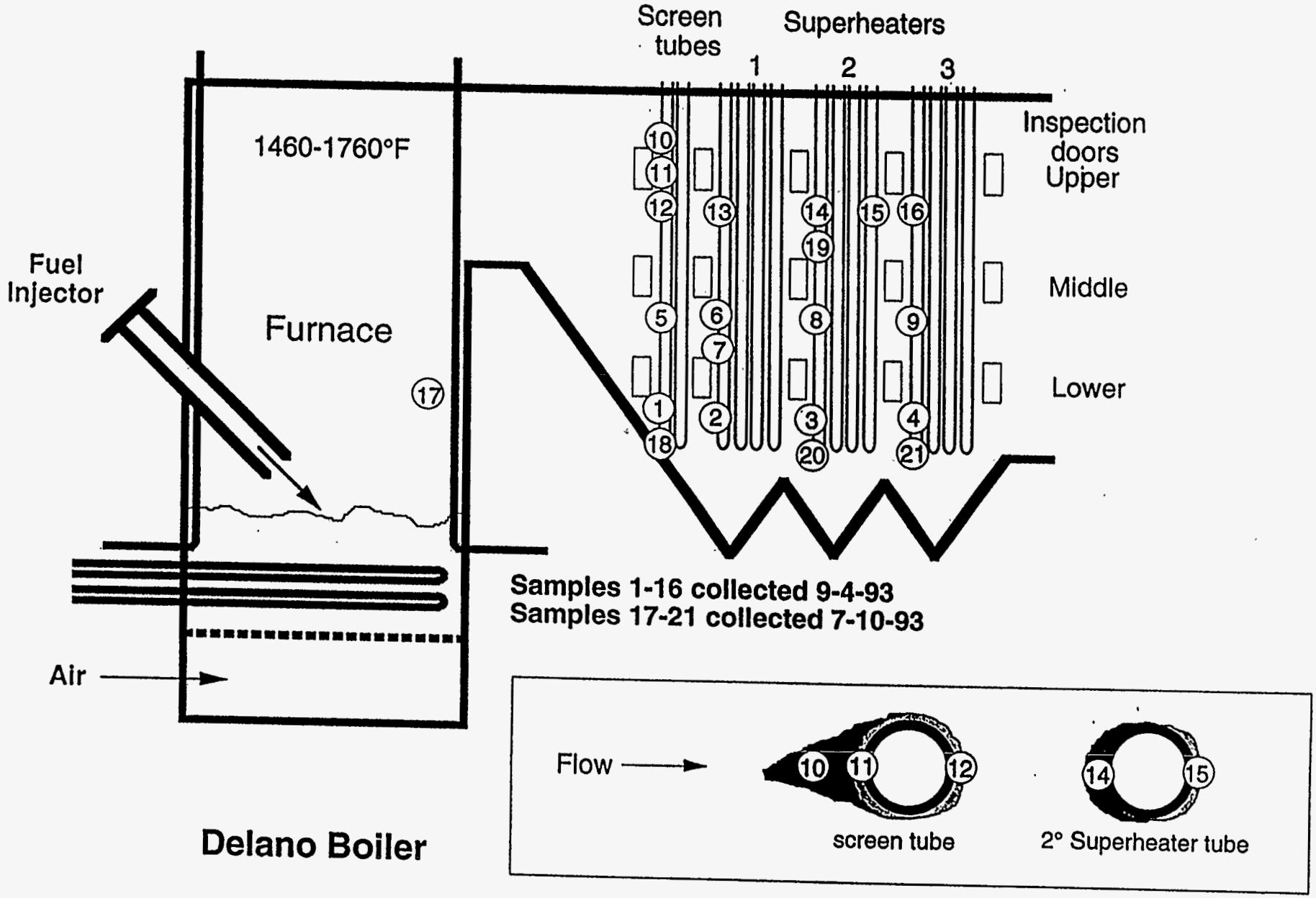

Delano Boiler

TYPE	Location/Form TIME	DATE	ELEMENTAL ANALYSES SiO2	Al2O3	TiO2	Fe2O3	CaO	MgO	Na2O	K2O	P2O5	SO3	Cl	CO2	UDT	Na2O+ K2O
FUELS																
DEL-FUEL-716	7-16 to 7-22	11/12/93	27.72	8.08	0.84	3.38	29.99	4.53	2.43	10.30	3.32	2.27	0.05	4.89	2.20	12.73
DEL-FUEL-824	8-24 to 9-3	11/12/93	28.81	8.47	0.83	3.28	27.99	4.49	3.18	8.86	2.57	2.00	0.72	5.07	3.73	12.04
BOTTOM ASH, FLY ASH																
DEL-BOT-716	7-16 to 7-22	11/12/93	70.09	11.99	0.24	1.40	7.95	0.62	2.05	5.11	0.42	0.11	0.01		0.01	7.16
DEL-BOT-824	8-24 to 9-3	11/12/93	61.34	10.96	0.33	2.46	11.70	1.25	2.49	8.28	0.66	0.10	0.06		0.37	10.77
DEL-FLY-716	7-16 to 7-22	11/12/93	52.51	11.72	0.78	3.68	19.17	0.63	2.63	4.51	1.12	0.97	0.30		1.98	7.14
DEL-FLY-824	8-24 to 9-3	11/12/93	47.18	12.76	0.90	3.99	17.83	0.62	2.71	4.93	1.45	1.51	0.70		5.42	7.64
DEPOSITS, ASH																
DEL-DEP-1	Screen tubes, lower door	9/4/93	9.80	4.07	0.36	1.57	28.61	4.21	2.00	15.30	2.32	28.60	5.50	1.57	-3.91	17.30
DEL-DEP-5	Screen tubes, mid door		10.27	4.62	0.40	1.69	27.71	6.64	2.04	13.40	2.48	26.70	3.26	1.58	-0.79	15.44
DEL-DEP-10	Screen tube upper sharks teeth upstream		9.43	4.57	0.32	1.48	31.74	3.44	1.83	13.20	2.35	28.70	2.99	1.38	-1.43	15.03
DEL-DEP-11	Screen tube upper tube surf layer		16.90	4.09	0.30	1.33	24.63	2.98	2.66	19.60	2.09	17.80	9.98	5.26	-7.62	22.26
DEL-DEP-12	Screen tube upper tube backside		19.52	6.67	0.67	2.80	33.19	4.65	2.12	7.85	2.62	6.30	3.15	8.67	1.79	9.97
DEL-DEP-2	#1 Superheater, lower door	9/4/93	9.82	4.22	0.36	1.52	22.46	2.33	3.03	22.40	1.89	17.11	14.00	2.26	-1.40	25.43
DEL-DEP-6	#1 superheater,mid door		11.01	5.86	0.41	3.20	22.13	2.81	2.84	21.20	1.82	17.46	10.20	2.17	-1.11	24.04
DEL-DEP-13	#1 Superheater, upper dr		8.97	3.16	0.27	4.29	19.34	2.03	3.14	25.90	1.40	17.90	14.20	2.33	-2.93	29.04
DEL-DEP-3	#2 Superheater, lower door		13.49	4.70	0.50	2.96	23.36	3.27	3.07	19.50	2.13	16.83	9.63	2.14	-1.58	22.57
DEL-DEP-8	#2 superheater, mid door		16.78	5.53	0.59	2.48	27.95	3.27	2.68	13.90	2.40	13.10	7.37	4.10	-0.15	16.58
DEL-DEP-14	#2 superheater upper front, hard		14.53	3.76	0.54	2.18	25.78	3.27	2.91	17.20	2.33	13.00	9.74	4.91	-0.15	20.11
DEL-DEP-15	#2 superheater upper backside powder		23.79	5.85	0.72	3.01	31.58	3.89	2.07	5.78	2.41	2.88	1.76	14.00	2.26	7.85
DEL-DEP-17	Combustor S wall, sand gray	7/10/93	62.76	11.49	0.53	2.94	10.15	1.40	2.26	4.72	0.74	0.36	0.13	0.26	2.26	6.98
DEL-DEP-18	Lwr screen tubes hard thin	7/10/93	8.73	5.23	0.26	1.47	22.49	2.95	2.64	17.20	1.80	21.80	9.68	2.74	3.01	19.84
DEL-DEP-19	#2 str upper, hard thin	7/10/93	8.12	4.38	0.26	1.20	27.38	4.19	1.88	14.80	2.26	26.60	5.87	7.88	-4.82	16.68
DEL-DEP-20	#2 str, lower brittel dep	7/10/93	13.46	5.33	0.22	1.74	26.59	4.66	1.86	11.30	2.36	17.50	4.00	14.61	-3.63	13.16
DEL-DEP-21	#3 lower, loose powder	7/10/93	18.34	7.51	0.66	2.61	36.78	4.04	1.59	3.94	2.44	3.13	2.30	23.08	-6.42	5.53

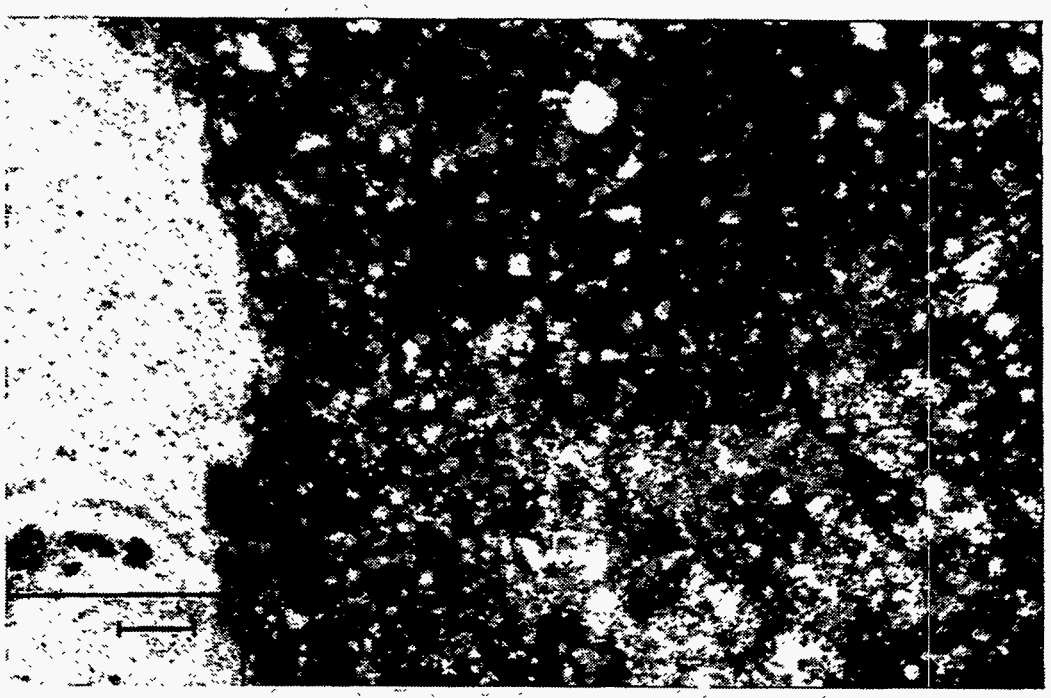

1. DELANO 10 X 50 TUBE SIDE POLISHED IN WATER

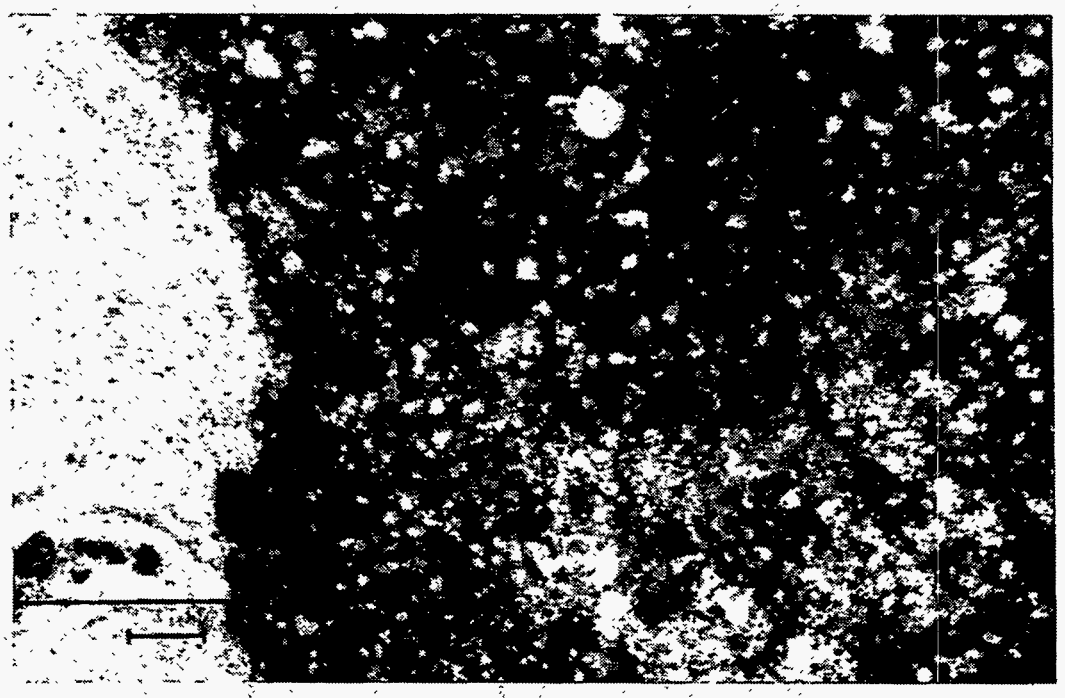

2. DELANO 10 X 50 TUBE SIDE, DUPLICATE, POLISHED IN WATER

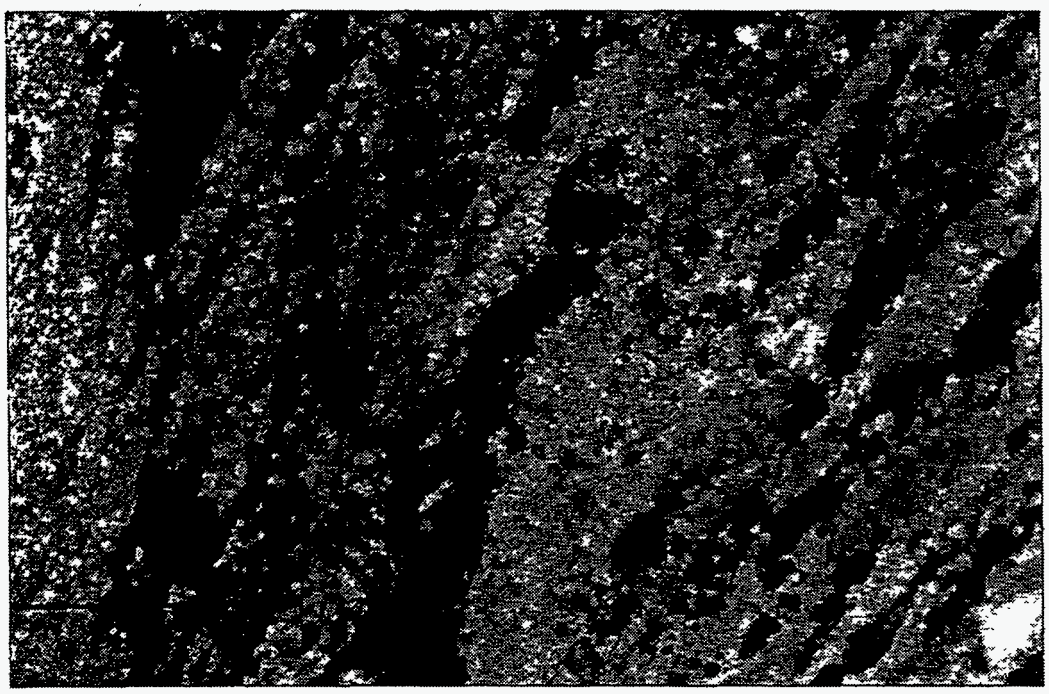

3. DELANO 10 X 50 MIDWAY, INTERIOR POLISHED IN WATER

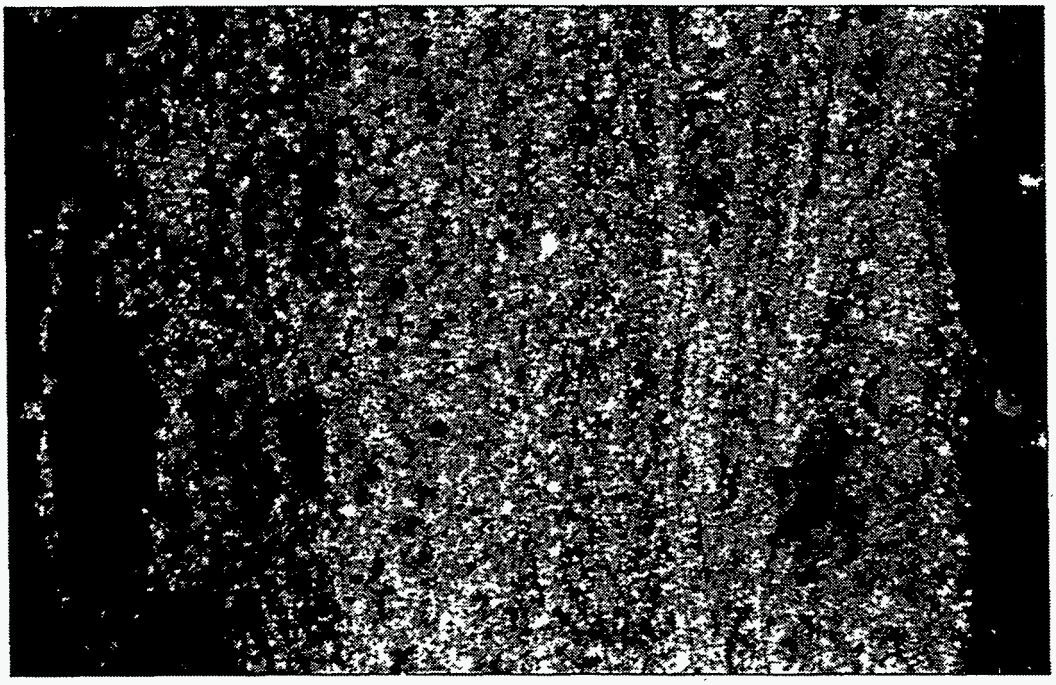

4. DELANO 10 X 50 FIRESIDE, POLISHED IN WATER

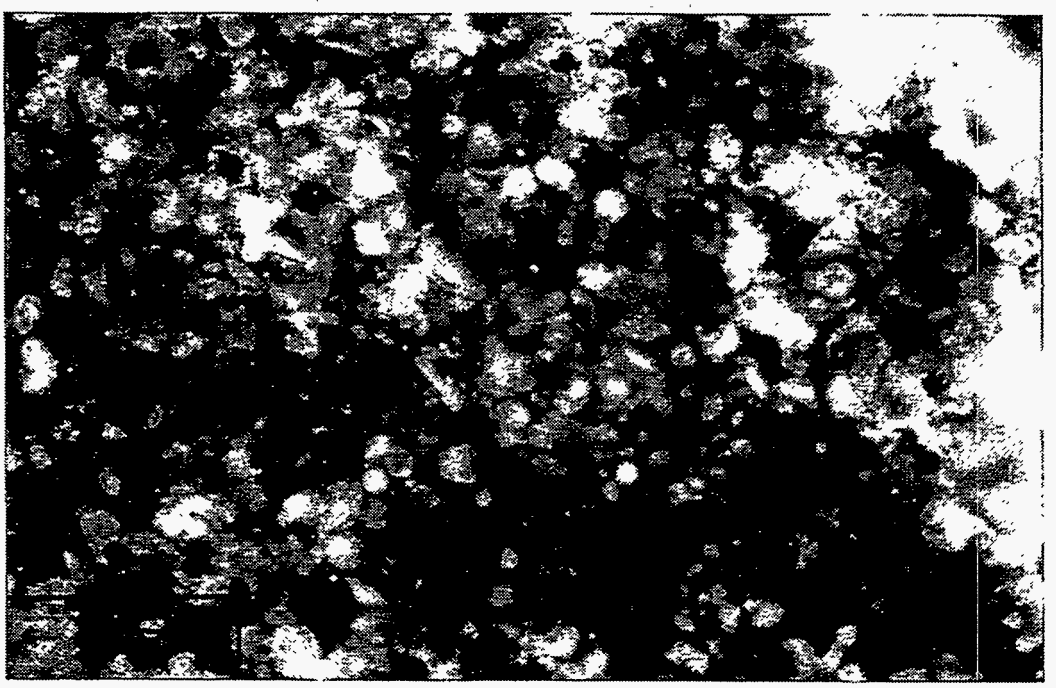

5. DELANO 10 X 200 TUBE SIDE, FINE GRAINED MATERIAL, POLISHED IN WATER

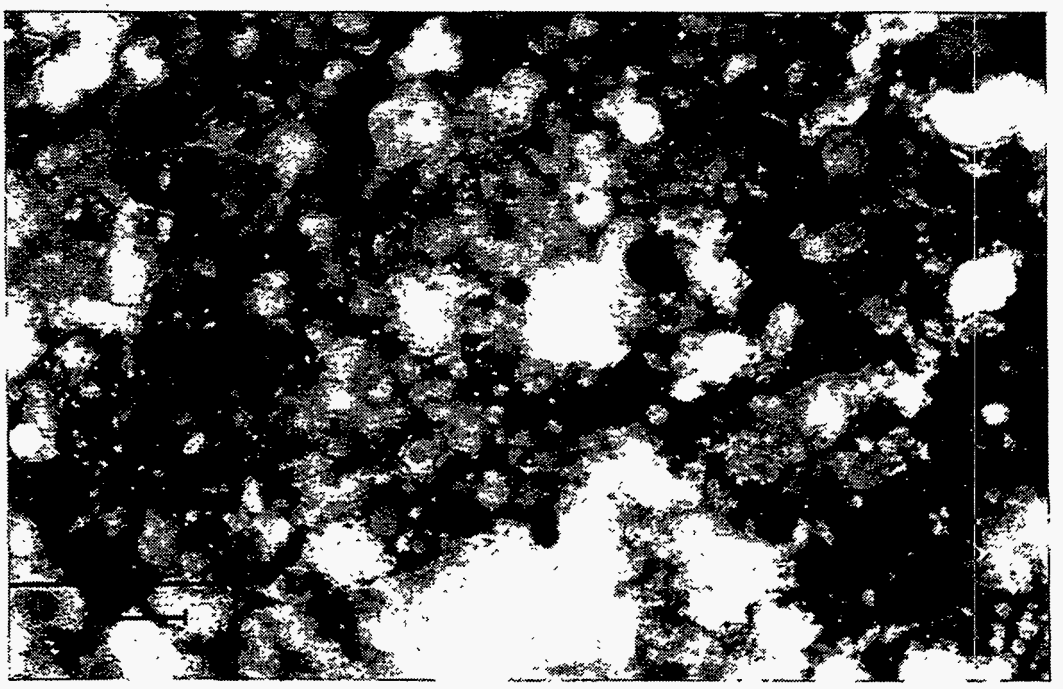

6. DELANO 10 X 200 TUBE SIDE, COARSE GRAINED MATERIAL, POLISHED IN WATE

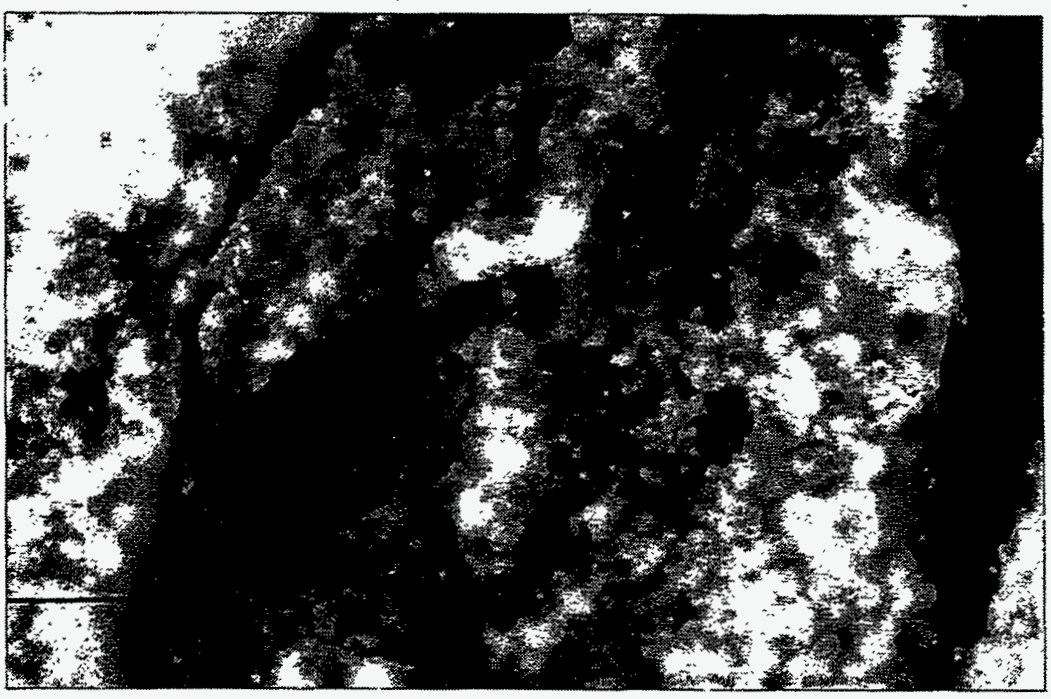

7. DELANO 10 X 200 INTERIOR, POLISHED IN WATER

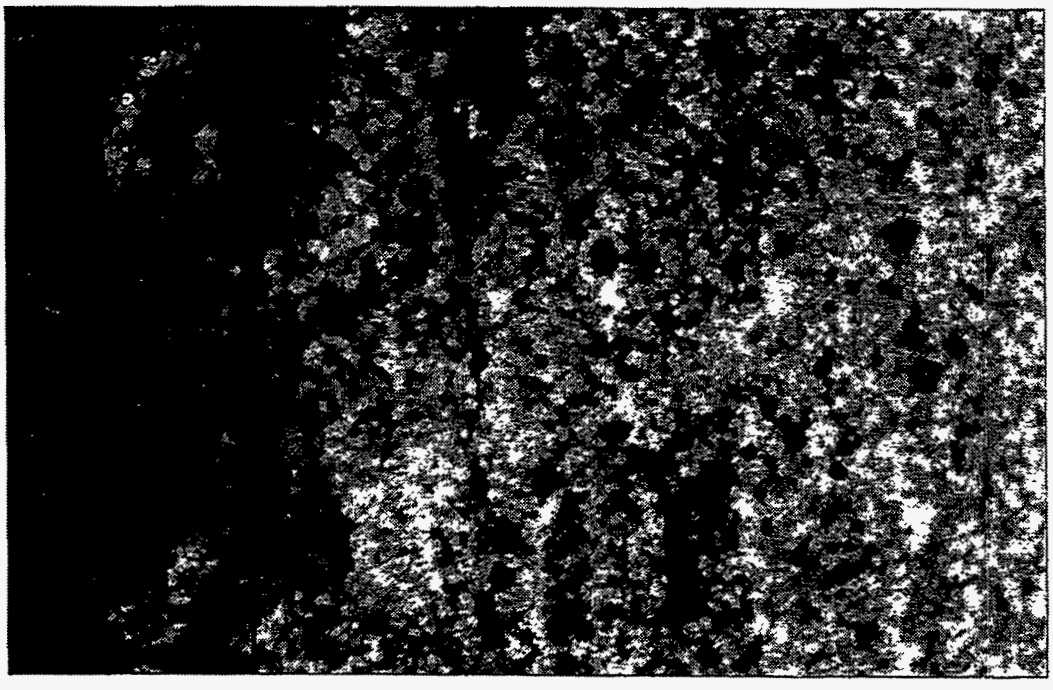

8. DELANO 10 X 100 FIRESIDE, POLISHED IN WATER

22. DELANO 10 X 100 FIRESIDE, REPOLISHED IN OIL

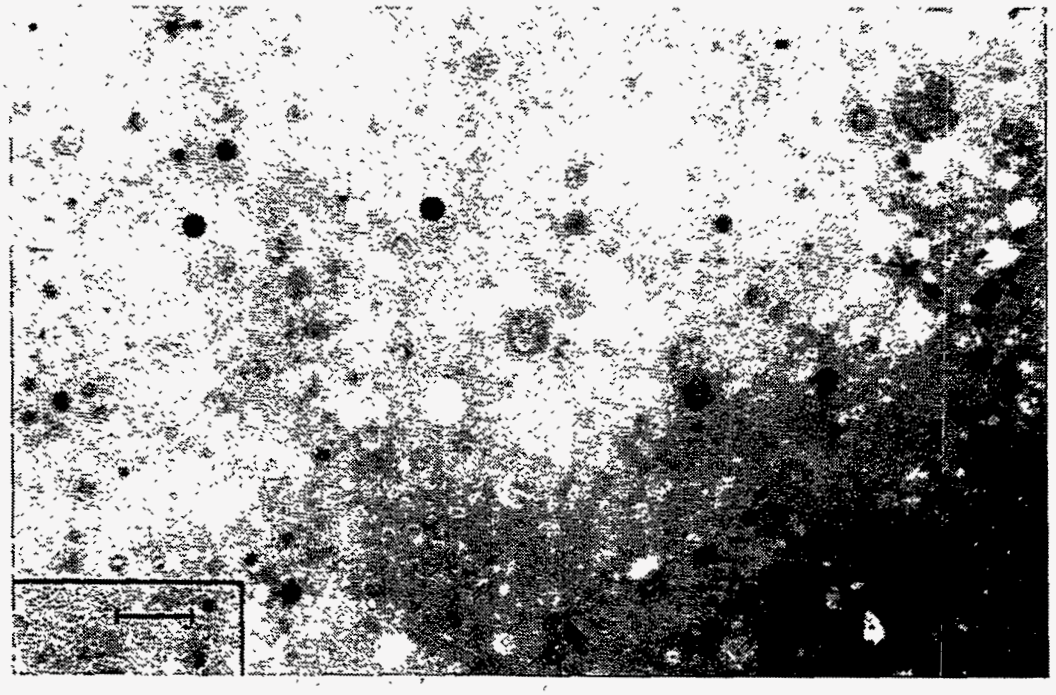

23. DELANO 10 X 200 INTERIOR, REPOLISHED IN OIL

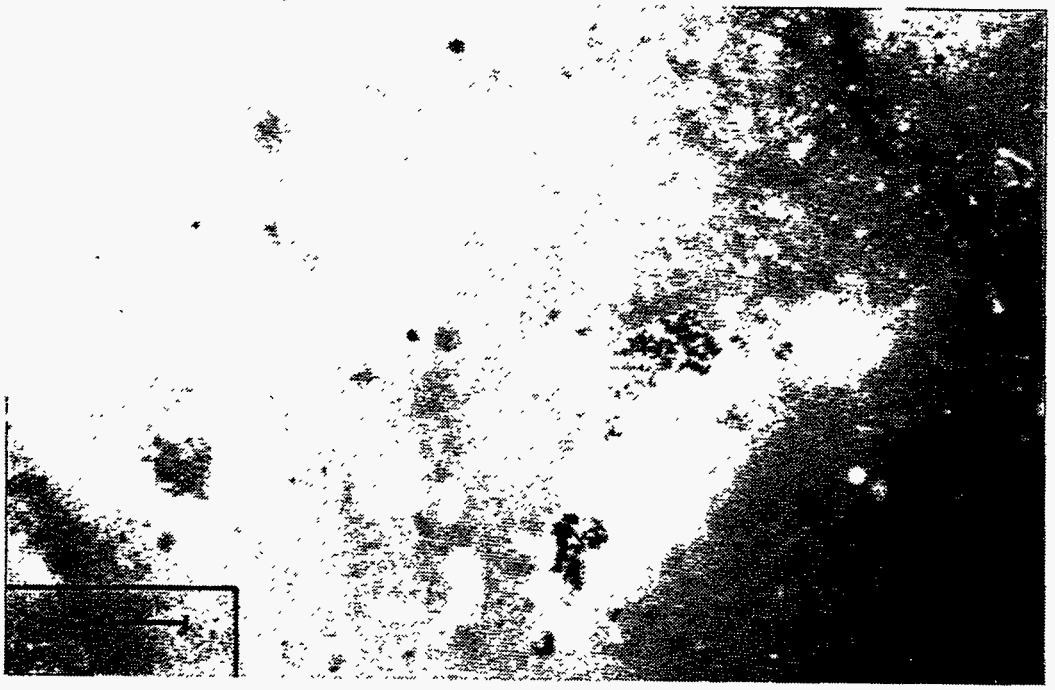

24. DELANO 10 X 200 INTERIOR, REPOLISHED IN OIL

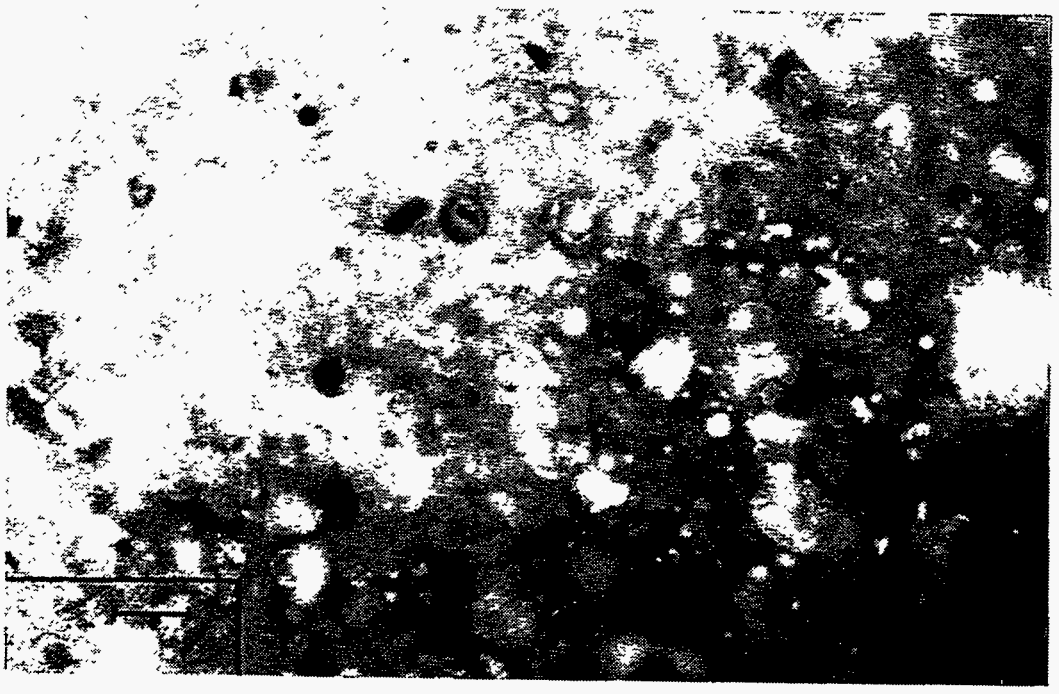

25. DELANO 10 X 200 TUBE SIDE, REPOLISHED IN OIL

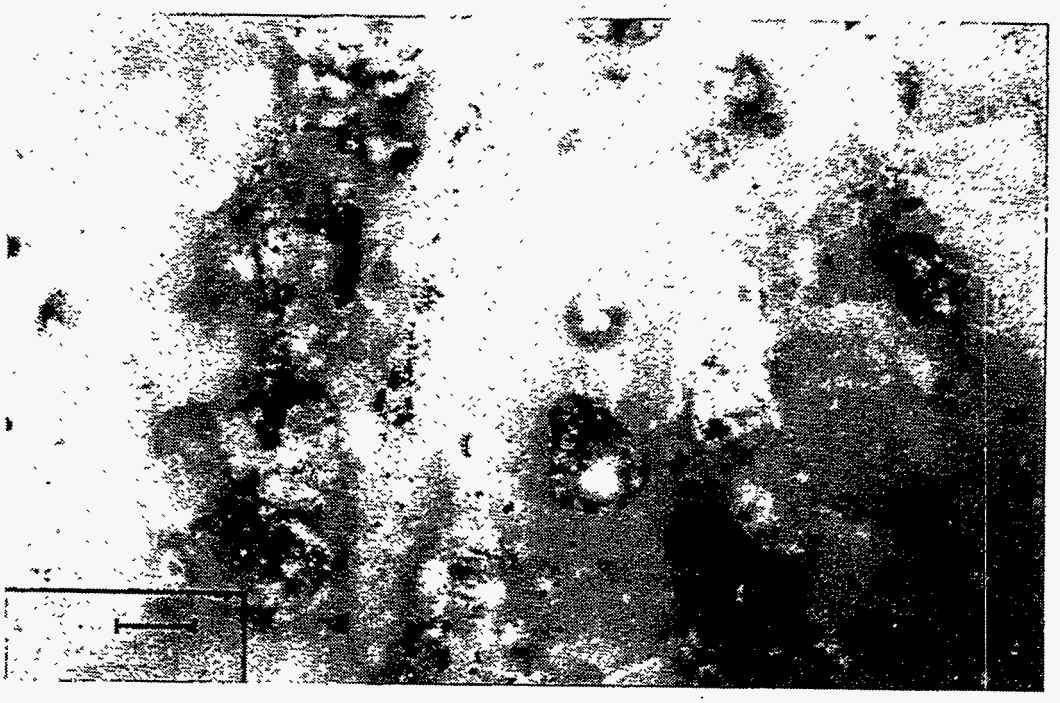

26. DELANO 10 X 200 INTERIOR REPOLISHED IN OIL

DELANO 10 FIRESIDE

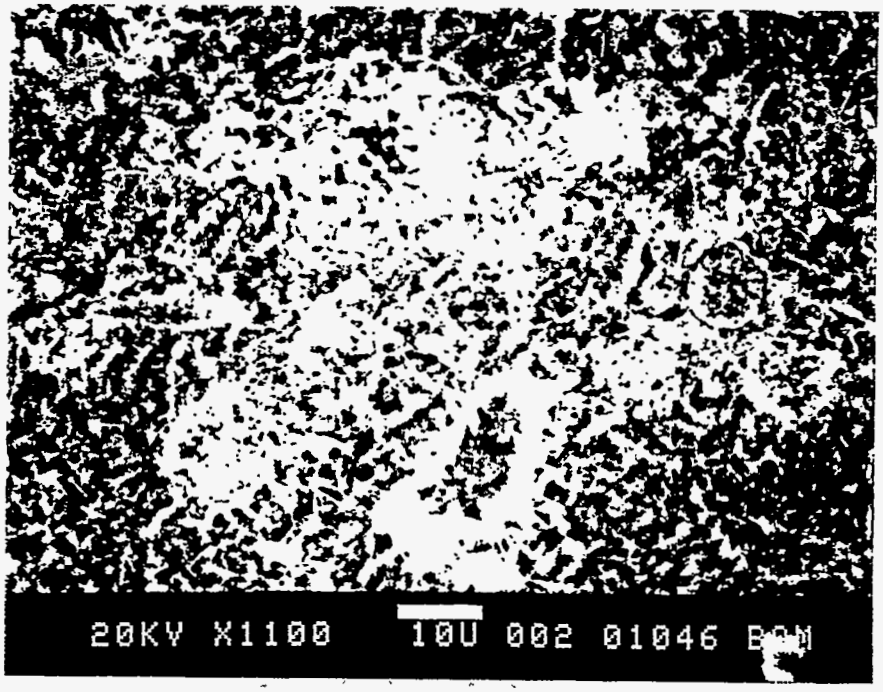

DELANO 10 FIRESIDE X 1100

DELANO 10 TUBESIDE X 20

16-Feb-1994 14:46:43 DELANO 10 GRAY

Accelerating voltage	20.0 KeV
Beam - sample incidence angle	90.0 degrees
Xray emergence angle	5.8 degrees
Xray - window incidence angle	5.8 degrees

QUANTITATIVE EDS RESULTS
(ZAF CORRECTIONS VIA MAGIC V)

ELEMENT & LINE	WEIGHT PERCENT	ATOMIC PERCENT*	PRECISION 2 SIGMA	K-RATIO**	ITER
Mg KA	4.86	6.90	0.28	0.0111	
Si KA	3.28	4.04	0.14	0.0156	
P KA	2.81	3.13	0.11	0.1196	
S KA	40.76	43.92	0.46	0.6852	
K KA	18.12	16.01	0.25	0.2948	
Ca KA	30.17	26.00	0.37	0.3308	10
TOTAL	100.00				

*NOTE: ATOMIC PERCENT is normalized to 100

**NOTE: K-RATIO = K-RATIO x R
where R = reference(standard)/reference(sample)

NORMALIZATION FACTOR: 0.585

16-Feb-1994 14:58:03 DELANO 10 DK GRAY

Accelerating voltage	20.0 KeV
Beam - sample incidence angle	90.0 degrees
Xray emergence angle	5.8 degrees
Xray - window incidence angle	5.8 degrees

QUANTITATIVE EDS RESULTS
(ZAF CORRECTIONS VIA MAGIC V)

ELEMENT & LINE	K-RATIO**	WEIGHT PERCENT	PRECISION 2 SIGMA	FORMULA	OXIDE PERCENT
Al KA	0.4705	36.26	0.09	Al2O3	68.50
Si KA	0.0182	14.41	0.14	SiO2	30.83
Cu KA	0.0065	0.30	0.01	CuO	0.37
Zn KA	0.0052	0.23	0.01	ZnO	0.29
O *		48.80			
TOTAL					100.00

* DETERMINED BY STOICHIOMETRY

**NOTE: K-RATIO = K-RATIO x R
where R = reference(standard)/reference(sample)

NORMALIZATION FACTOR: 0.685

16-Feb-1994 14:47:27 DELANO 10 GRAY

Accelerating voltage 20.0 KeV

Beam - sample incidence angle 90.0 degrees

Xray emergence angle 5.8 degrees

Xray - window incidence angle 5.8 degrees

QUANTITATIVE EDS RESULTS
(ZAF CORRECTIONS VIA MAGIC V)

ELEMENT & LINE	K-RATIO**	WEIGHT PERCENT	PRECISION 2 SIGMA	FORMULA	OXIDE PERCENT
Mg KA	0.0111	4.31	0.25	MgO	7.15
Si KA	0.0156	2.88	0.12	SiO2	6.16
P KA	0.1196	2.47	0.10	P2O5	5.67
S KA	0.6852	17.18	0.19	SO3	42.89
K KA	0.2948	11.74	0.16	K2O	14.14
Ca KA	0.3308	17.15	0.21	CaO	23.99
O *		44.27			
TOTAL					100.00

* DETERMINED BY STOICHIOMETRY

**NOTE: K-RATIO = K-RATIO x R
where R = reference(standard)/reference(sample)

NORMALIZATION FACTOR: 0.285

16-Feb-1994 15:12:54 DELANO 10 FS GRAY

Accelerating voltage	20.0 KeV
Beam - sample incidence angle	90.0 degrees
Xray emergence angle	5.8 degrees
Xray - window incidence angle	5.8 degrees

QUANTITATIVE EDS RESULTS
(ZAF CORRECTIONS VIA MAGIC V)

ELEMENT & LINE	K-RATIO**	WEIGHT PERCENT	PRECISION 2 SIGMA	FORMULA	OXIDE PERCENT
Mg KA	0.0087	3.05	0.06	MgO	5.06
Al KA	0.0131	3.47	0.07	Al2O3	6.56
Si KA	0.0253	5.20	0.05	SiO2	11.13
P KA	0.1146	3.00	0.04	P2O5	6.87
S KA	0.5383	15.25	0.06	SO3	38.07
K KA	0.2168	8.85	0.04	K2O	10.66
Ca KA	0.4120	15.25	0.05	CaO	21.33
Fe KA	0.0053	0.25	0.01	FeO	0.33
O *		45.68			
TOTAL					100.00

* DETERMINED BY STOICHIOMETRY

**NOTE: K-RATIO = K-RATIO x R
where R = reference(standard)/reference(sample)

NORMALIZATION FACTOR: 0.253

16-Feb-1994 15:33:26 DELANO 10 FS DK GRAY

Accelerating voltage	20.0 KeV
Beam - sample incidence angle	90.0 degrees
Xray emergence angle	5.8 degrees
Xray - window incidence angle	5.8 degrees

QUANTITATIVE EDS RESULTS
(ZAF CORRECTIONS VIA MAGIC V)

ELEMENT & LINE	K-RATIO**	WEIGHT PERCENT	PRECISION 2 SIGMA	FORMULA	OXIDE PERCENT
Mg KA	0.0041	2.30	0.07	MgO	3.81
Al KA	0.0185	7.29	0.11	Al2O3	13.77
Si KA	0.0186	6.77	0.07	SiO2	14.48
P KA	0.0586	2.67	0.05	P2O5	6.13
S KA	0.0986	10.55	0.11	SO3	26.33
Cl KA	0.0267	3.62	0.05	Cl	3.62
K KA	0.0204	1.36	0.03	K2O	1.64
Ca KA	0.2693	21.07	0.08	CaO	29.48
Fe KA	0.0053	0.58	0.03	FeO	0.74
O *		43.80			
TOTAL					100.01

* DETERMINED BY STOICHIOMETRY

**NOTE: K-RATIO = K-RATIO x R
where R = reference(standard)/reference(sample)

NORMALIZATION FACTOR: 1.165

Woodland CFB

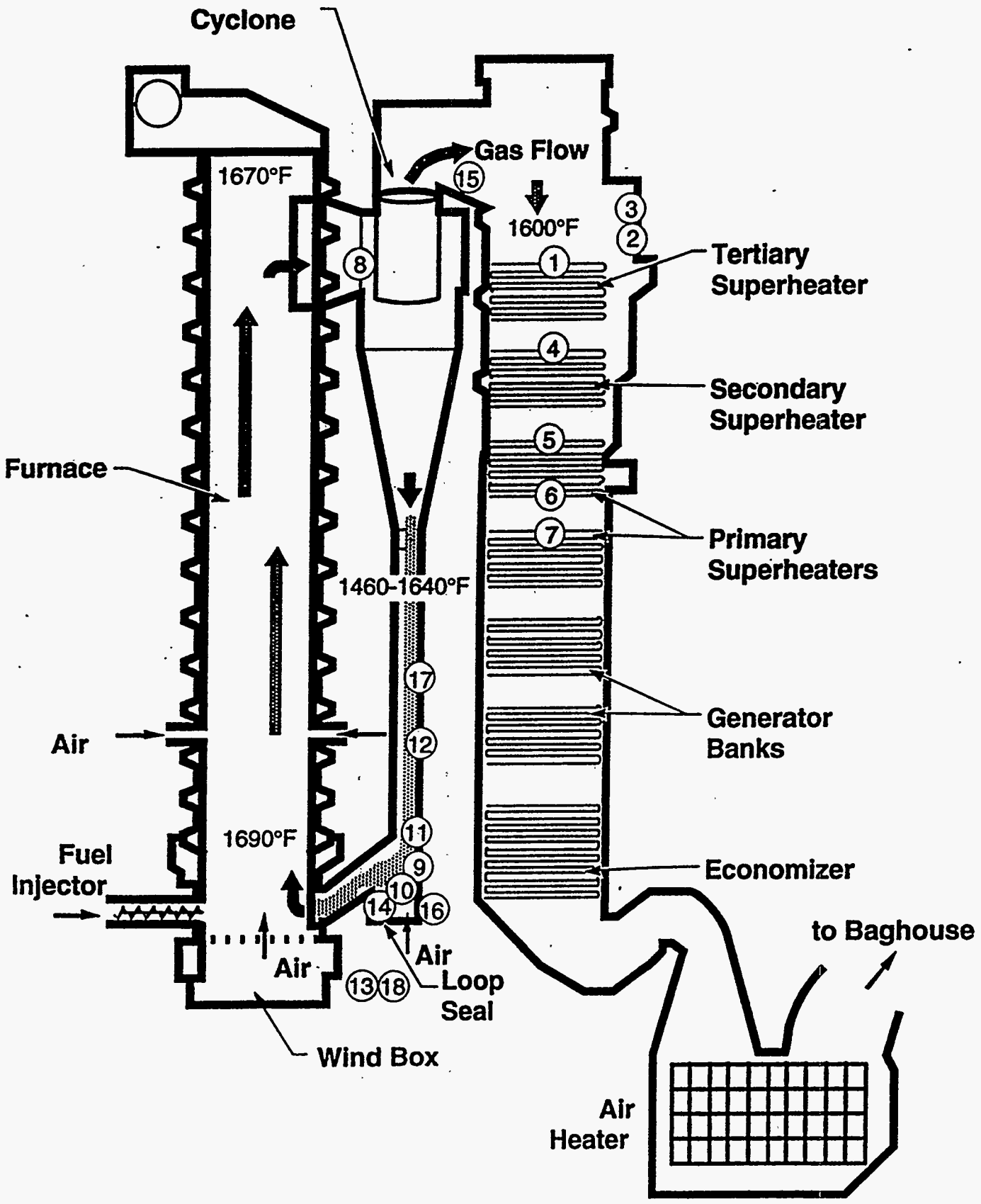

SUMMARY DEPOSITS: Woodland September 1993 REVISED DEC 6, 1993

TYPE	Location/Form TIME	ELEMENTAL ANALYSES SiO2	Al2O3	TiO2	Fe2O3	CaO	MgO	Na2O	K2O	P2O5	SO3	Cl	CO2	UNDT	Na2O+K2O
DEPOSITS															
WLD-DEP-1	Tertiary Superheater (top) , Door 2	12.80	6.15	0.56	3.89	25.50	5.96	3.32	9.41	2.65	29.70	0.01	0.15	-0.10	12.73
WLD-DEP-2	Tertiary Superheater shelf, hard	13.30	6.60	0.62	4.19	28.18	6.86	2.86	7.76	3.09	26.30	0.01	0.09	0.14	10.62
WLD-DEP-3	Tertiary Superheater wall. hard, brittle	13.63	5.06	0.46	3.40	15.37	3.74	7.36	13.40	1.81	34.40	0.01	0.06	1.30	20.76
WLD-DEP-4	Secondary str tubes, teeth, hard D2	11.78	6.52	0.51	1.14	23.28	6.66	4.53	9.99	2.76	28.10	0.21	0.11	4.41	14.52
WLD-DEP-5	Primary superheater, tubes, teeth, hard D3	13.88	6.63	0.58	4.29	22.84	6.10	4.44	9.31	2.78	26.40	0.47	0.17	2.11	13.75
WLD-DEP-6	Tubes above door, bottom, primary str D4	12.47	4.92	0.46	3.80	18.17	4.82	5.05	13.40	2.40	30.90	1.11	0.23	2.27	18.45
WLD-DEP-8	Cycone top cross-over duct, sandy/stone	56.23	13.37	0.80	5.60	6.74	2.50	2.91	4.57	0.83	0.72	0.01	0.01	5.71	7.48
WLD-DEP-9	Loop seal, E cyclone green dep from wall	51.44	10.49	0.48	4.11	9.95	2.33	2.63	6.16	1.38	0.63	0.01	0.04	10.35	8.79
WLD-DEP-10	Loop seal, E cyclone, inside wall, below doo	65.97	9.81	0.51	3.98	7.81	1.40	2.56	5.11	1.00	0.11	0.01	0.02	1.71	7.67
WLD-DEP-11	Loop seal, E cycl hard brn sandstone	58.20	9.54	0.79	4.53	13.03	3.75	2.00	5.44	1.64	1.67	0.01	0.03	-0.63	7.44
WLD-DEP-12	Loop seal, E cyclonesand brn, wall	69.22	10.24	0.46	3.17	5.86	2.81	2.47	5.92	0.80	0.01	0.01	0.02	-0.99	8.39
WLD-DEP-13	E cyclone sand from windbox, loop seal	77.93	9.54	0.28	1.85	1.95	0.93	1.98	2.48	0.14	0.03	0.01	0.02	2.86	4.46
WLD-DEP-14	E cyclone, large hard agglomerage near nozz	61.53	8.69	0.92	5.38	9.01	2.65	2.53	5.64	1.23	0.14	0.01	0.02	2.25	8.17
WLD-DEP-15	West cyclone, top cross over duct	39.47	32.81	1.29	2.64	15.72	1.39	1.32	1.81	1.33	0.25	0.01	0.01	1.95	3.13
WLD-DEP-16A	Loop seal, W cyclone large sandy green	61.22	10.22	0.51	3.61	6.51	1.87	2.92	4.25	0.77	0.86	0.01	0.01	7.24	7.17
WLD-DEP-16B	Loop seal, W cyclone large sandy brown	16.70	13.36	1.20	5.17	2.82	0.47	0.60	1.27	0.37	1.33	0.01	0.01	56.69	1.87
WLD-DEP-17	Loop seal W cyclone sandy/hard dep from w	59.43	10.38	0.78	5.12	9.50	0.16	2.26	6.81	1.15	0.32	0.01	0.02	4.06	9.07
WLD-DEP-18	W cyclone, sand drained from loop seal	78.59	11.16	0.23	1.42	3.25	1.40	1.73	3.49	0.44	0.01	0.20	0.01	-1.93	5.22

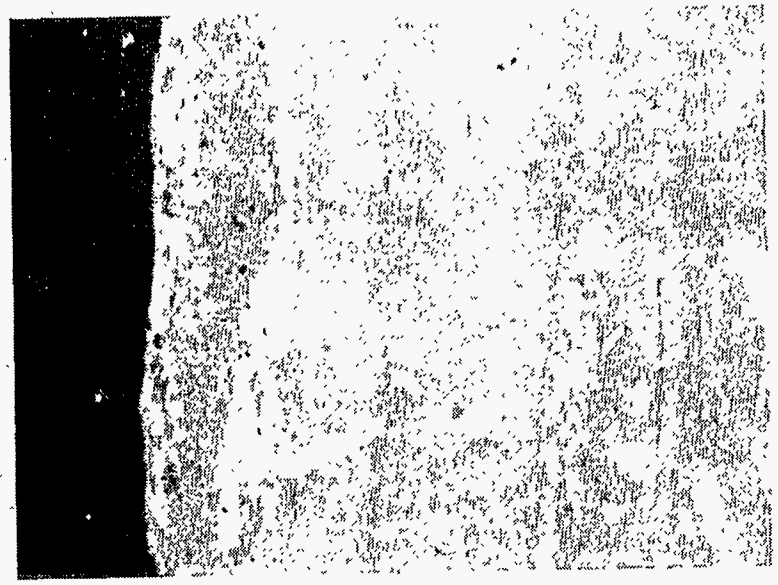

Woodland 1; Fire Side
X100

Woodland 1; Midway
X100

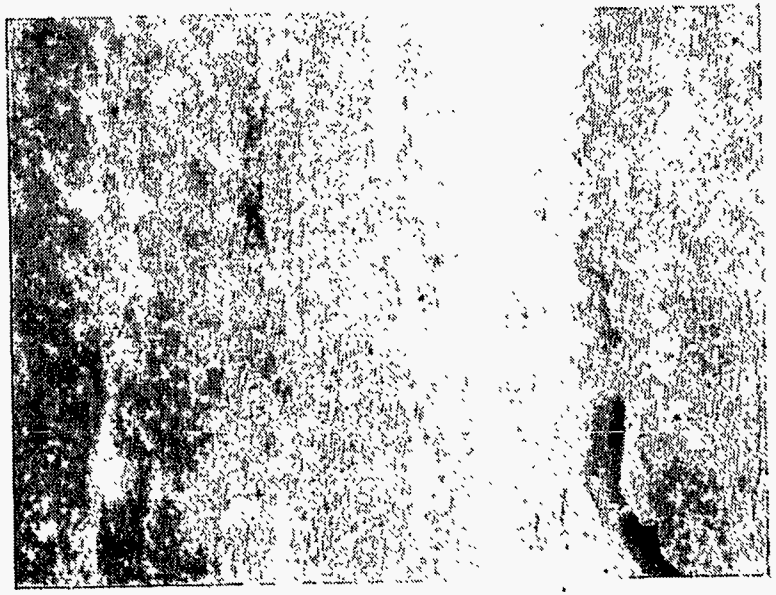

Woodland 1; Midway 2
X100

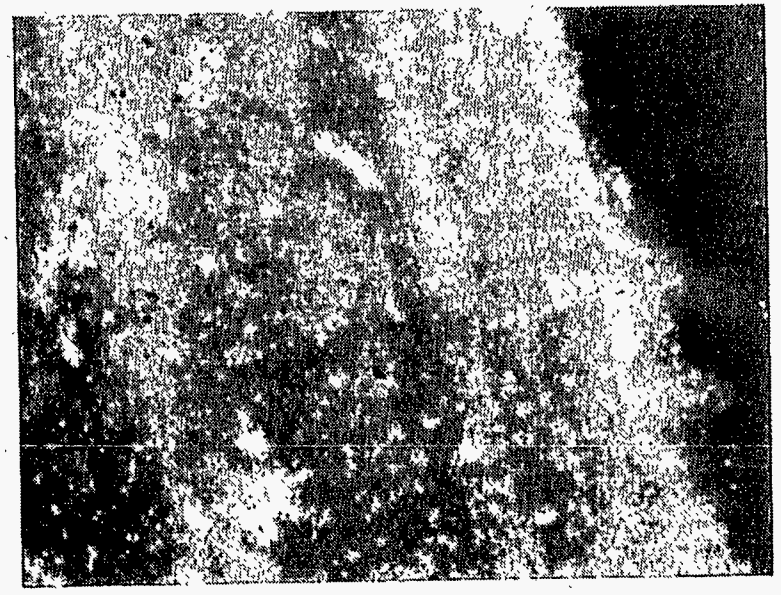

Woodland 1; Tube Side
X100

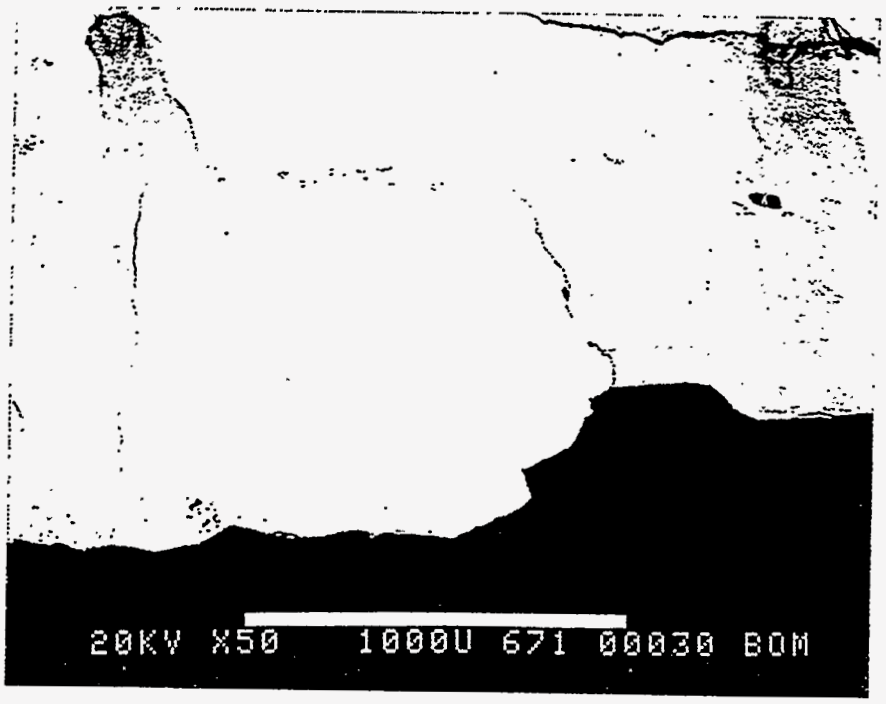

WOODLAND 1 FIRESIDE X 50

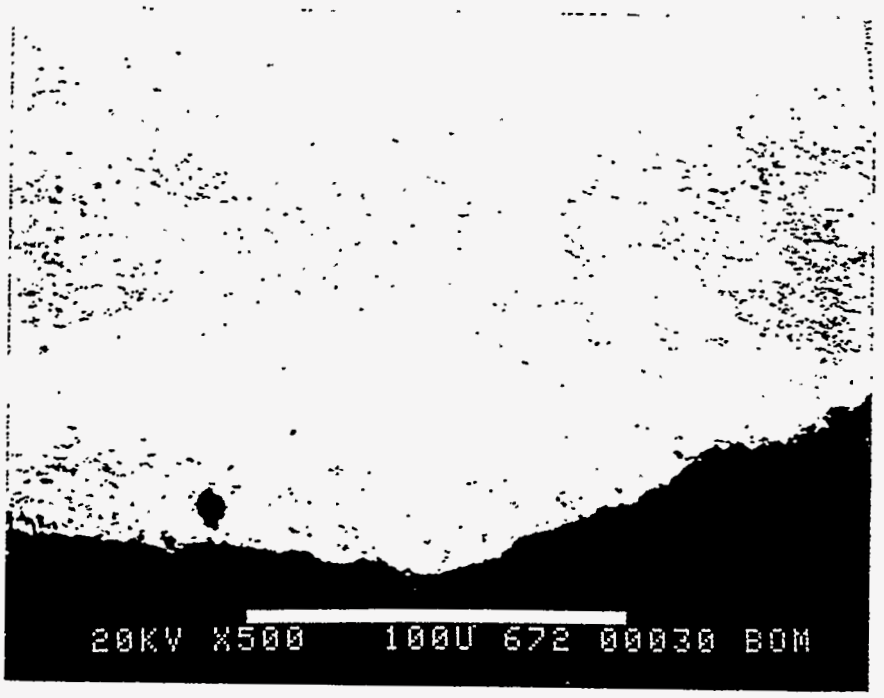

WOODLAND 1 FIRESIDE X 500

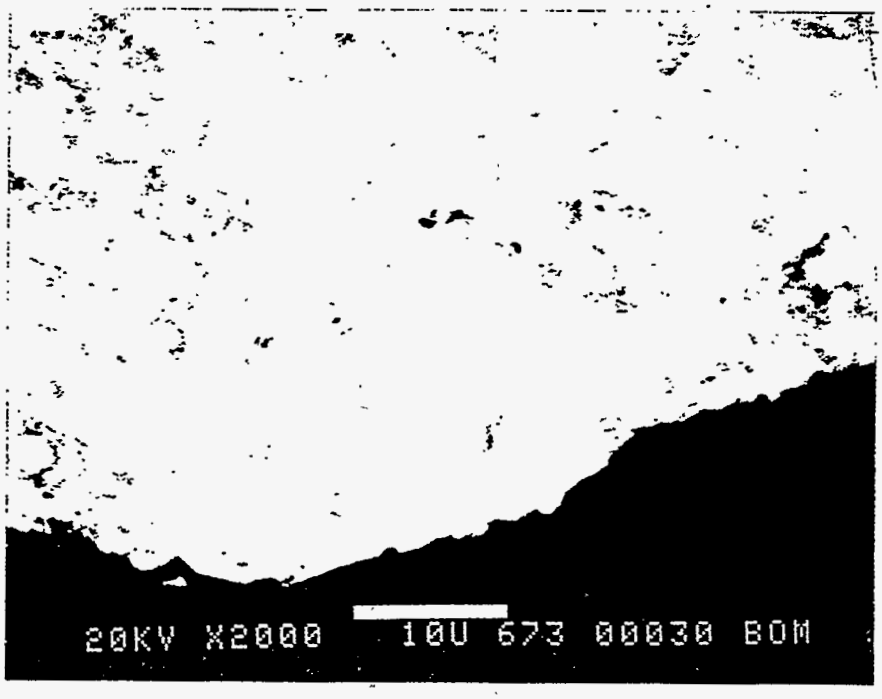

WOODLAND 1 FIRESIDE X 2000

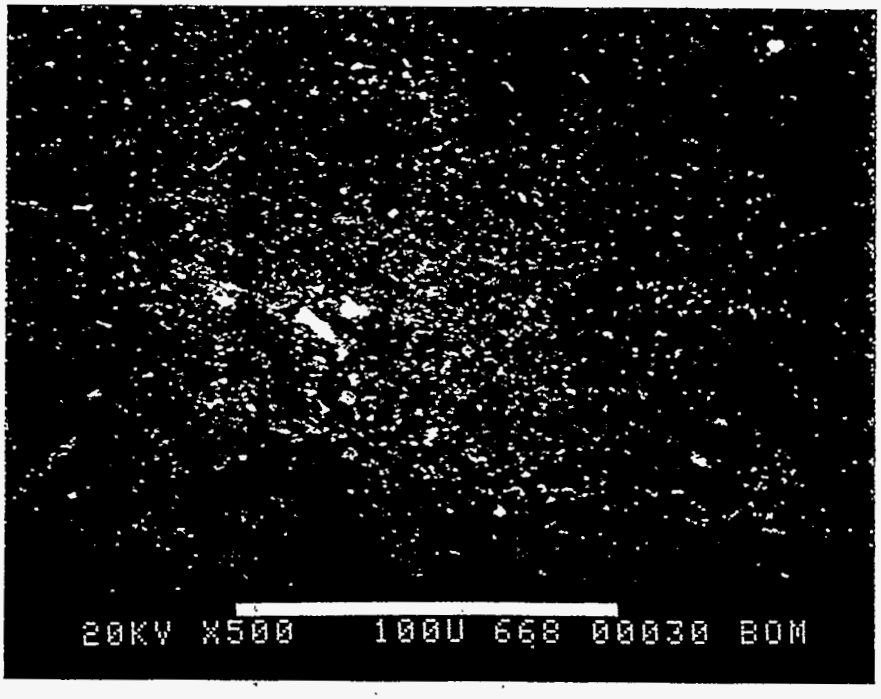

WOODLAND 1 INTERIOR X 500

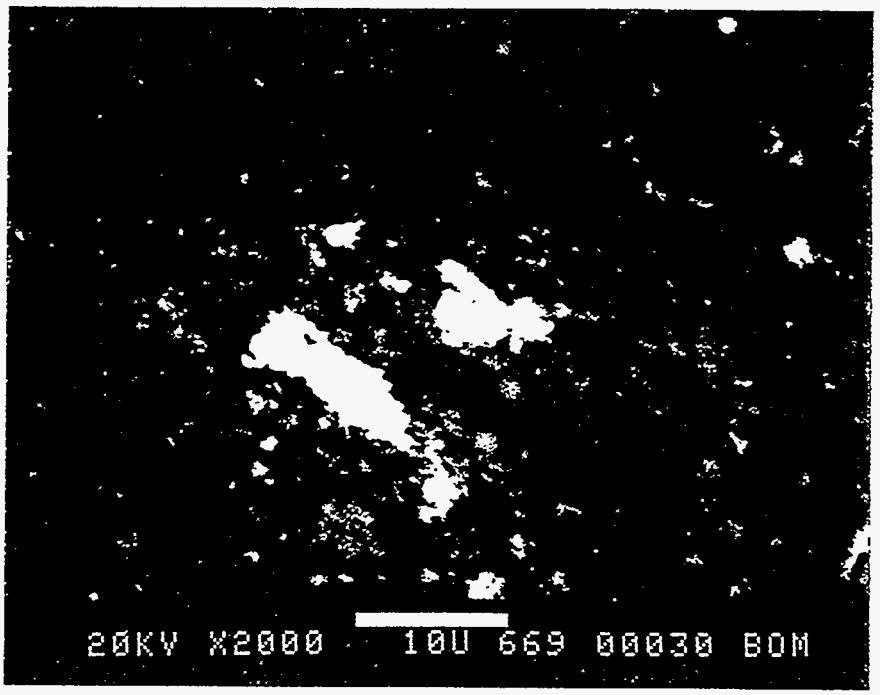

WOODLAND 1 INTERIOR X 2000

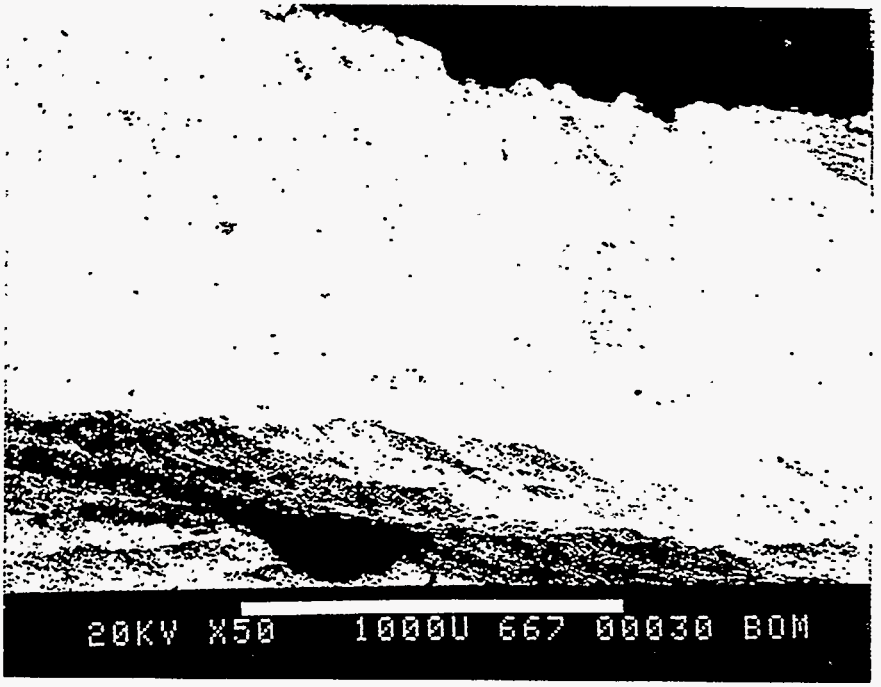

WOODLAND 1 X 50 CENTER (BOTTOM) TO TUBESIDE (TOP)

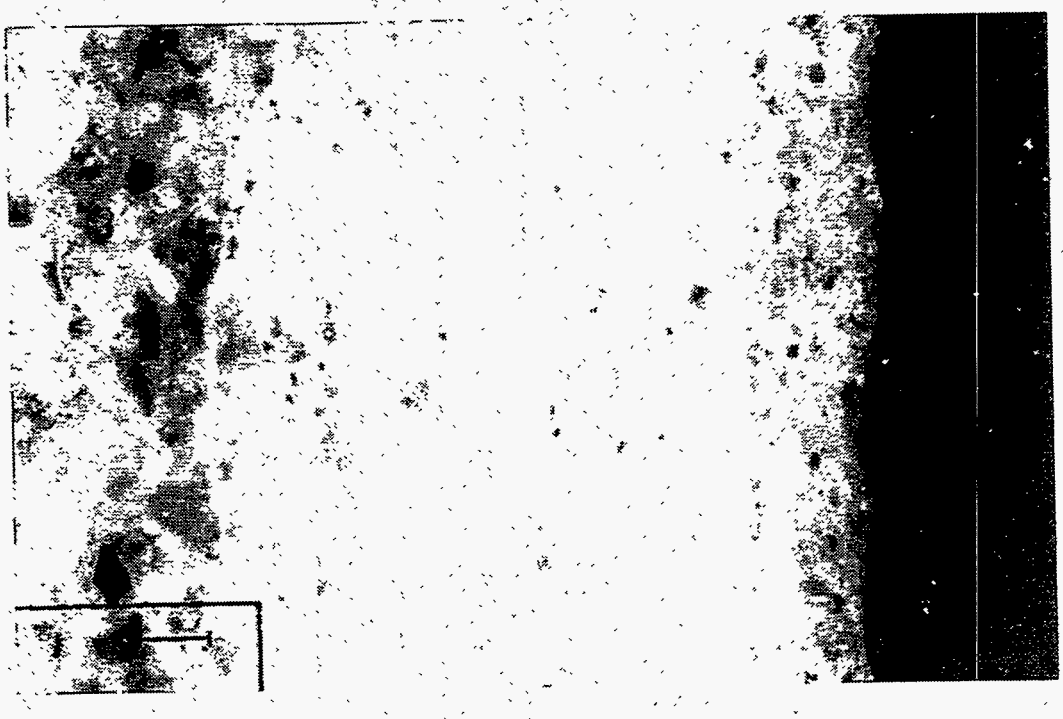

14. WOODLAND 14 X 50 FIRE SIDE, POLISHED IN WATER

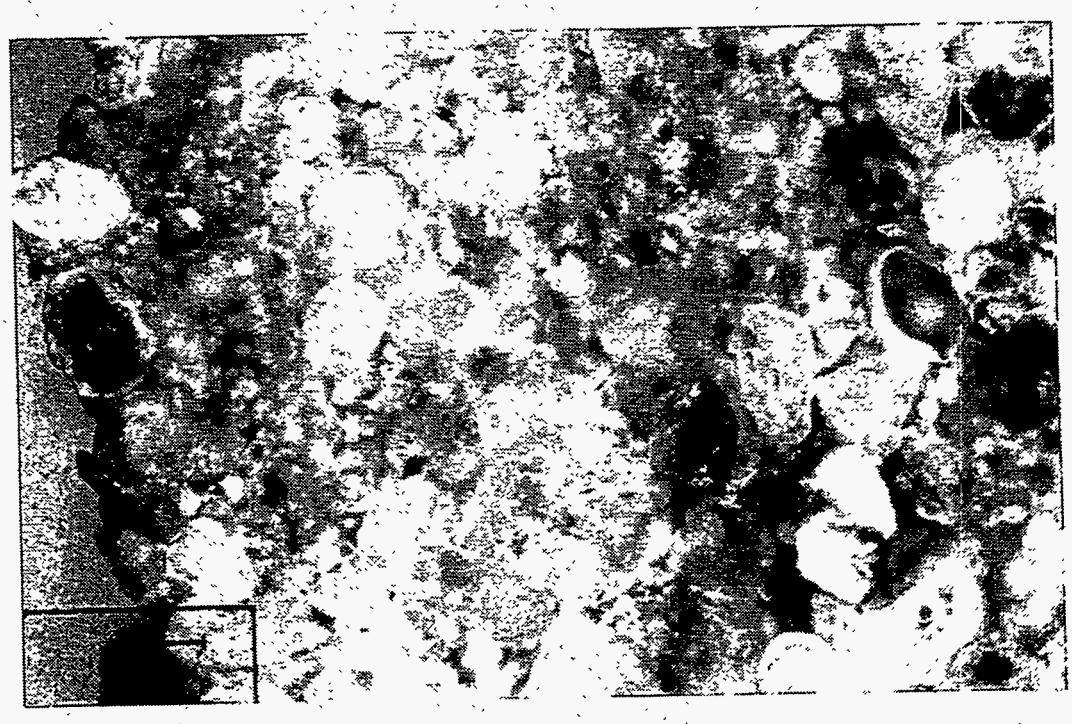

15. WOODLAND 14 X 50 INTERIOR, POLISHED IN WATER

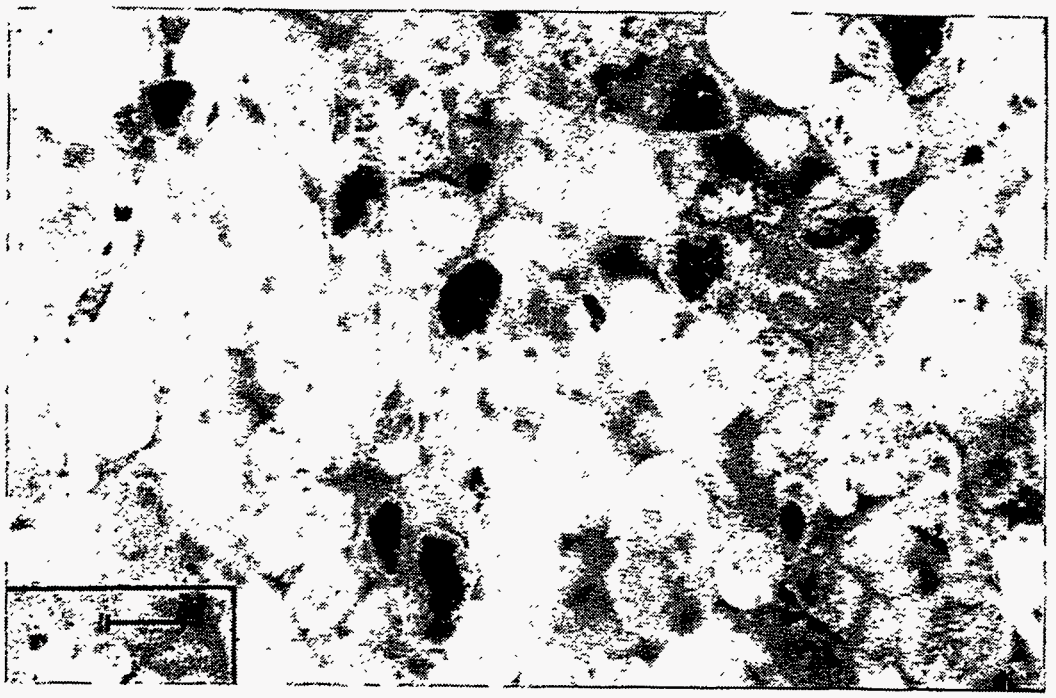

16. WOODLAND 14 X 50? INTERIOR, POLISHED IN WATER

17. WOODLAND 14 X 200 INTERIOR, BRIGHT FIELD ILUMINATION

18. WOODLAND 14 X 200 INTERIOR, POLISHED IN WATER

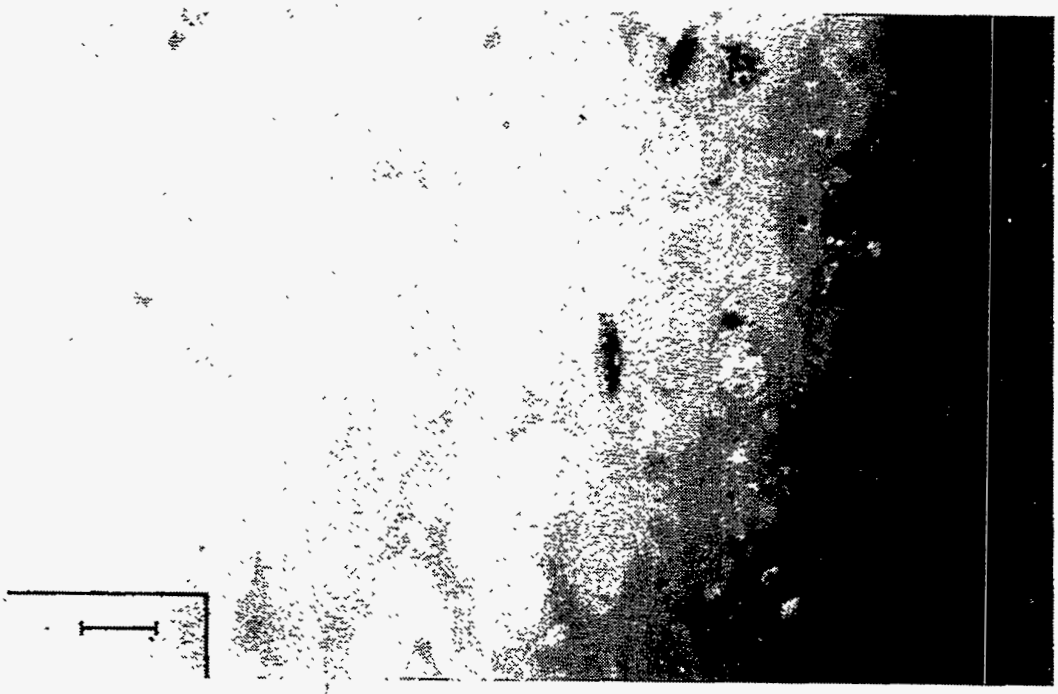

32. WOODLAND 14 X 200 FIRE SIDE, REPOLISHED IN OIL

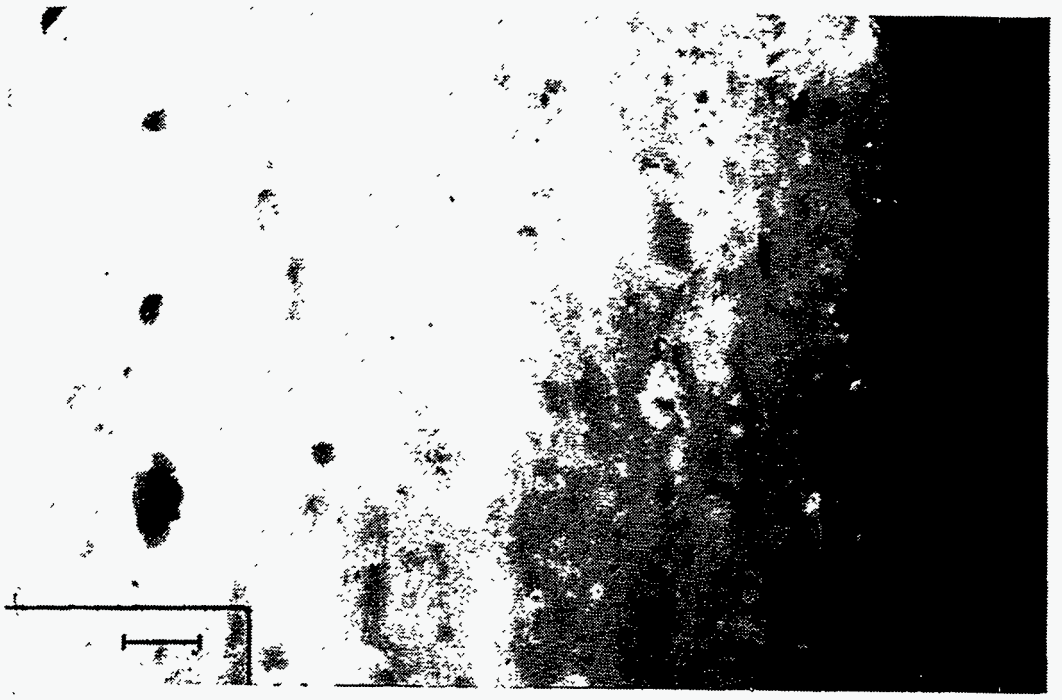

33. WOODLAND X 100 FIRE SIDE, REPOLISHED IN OIL

34. WOODLAND 14 X 50 FIRE SIDE, REPOLISHED IN OIL

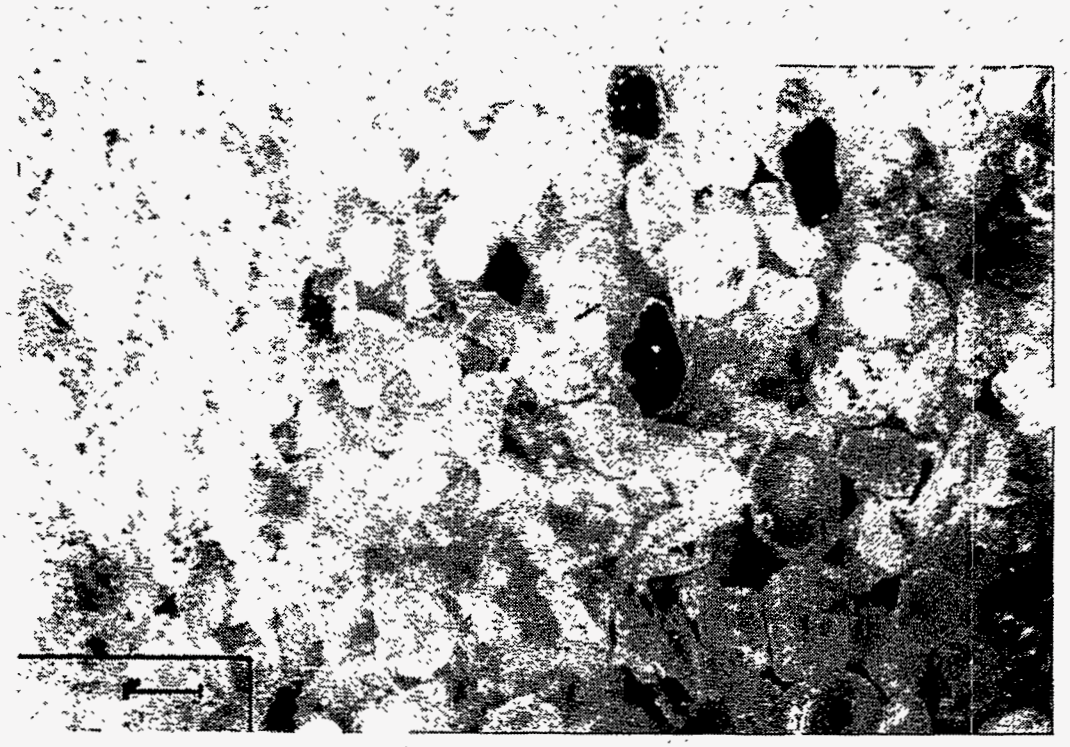

35. WOODLAND 14 X 50 FIRESIDE, REPOLISHED IN OIL

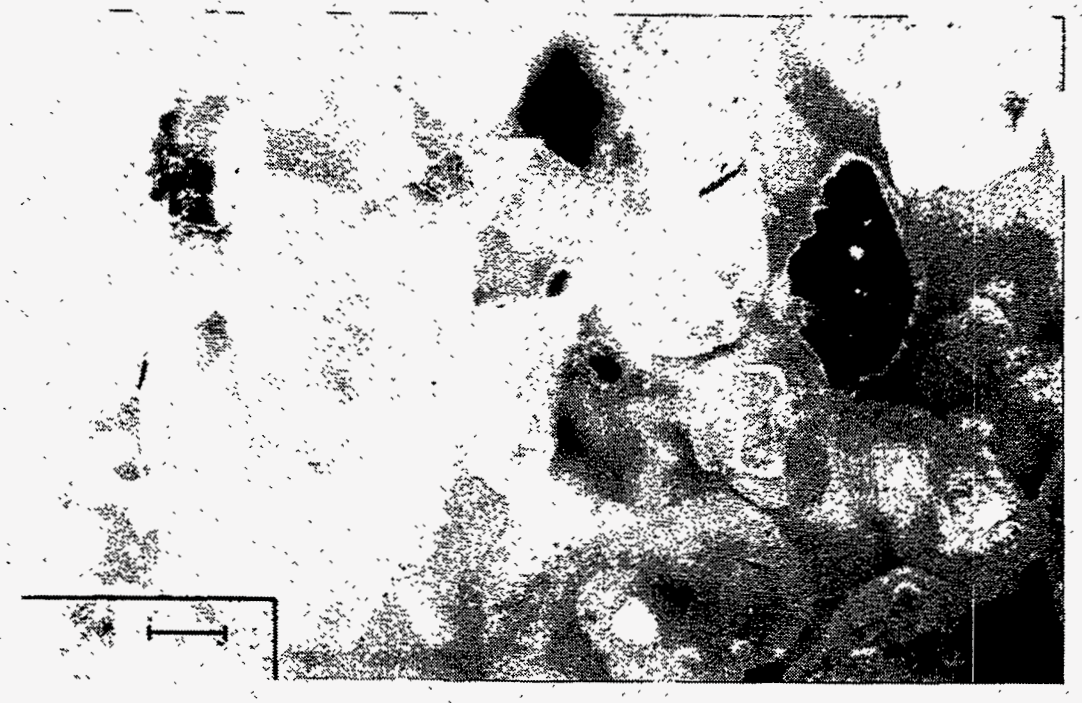

36. WOODLAND 14 X 100 INTERIOR, REPOLISHED IN OIL

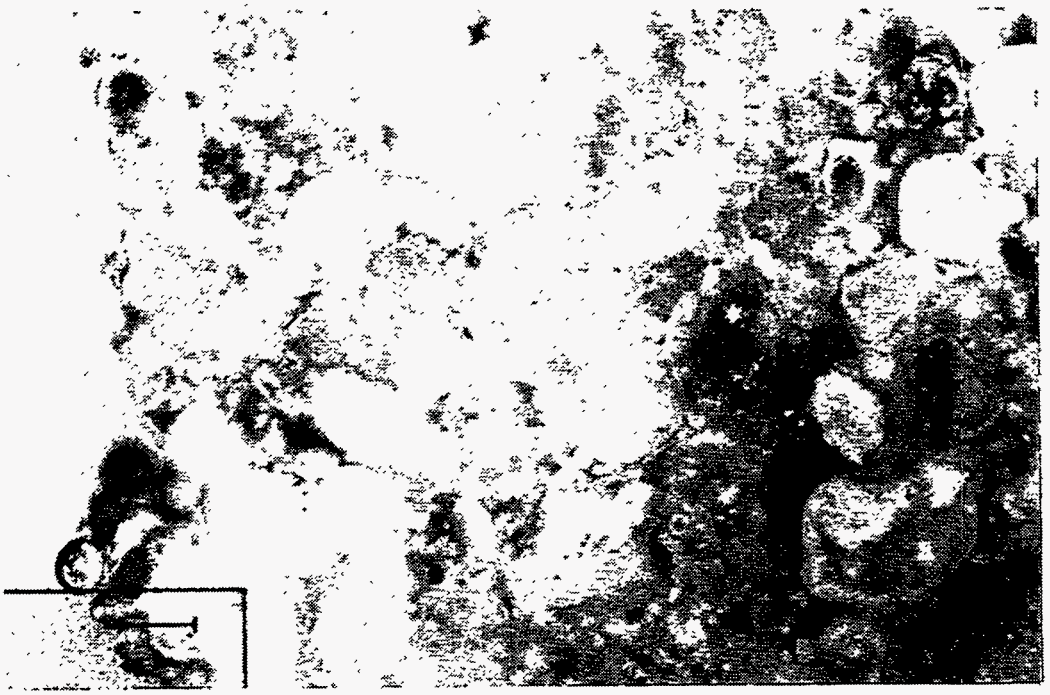

37. WOODLAND 14 X 50 TUBE SIDE, REPOLISHED IN OIL

WOODLAND 14 FIRESIDE X 20

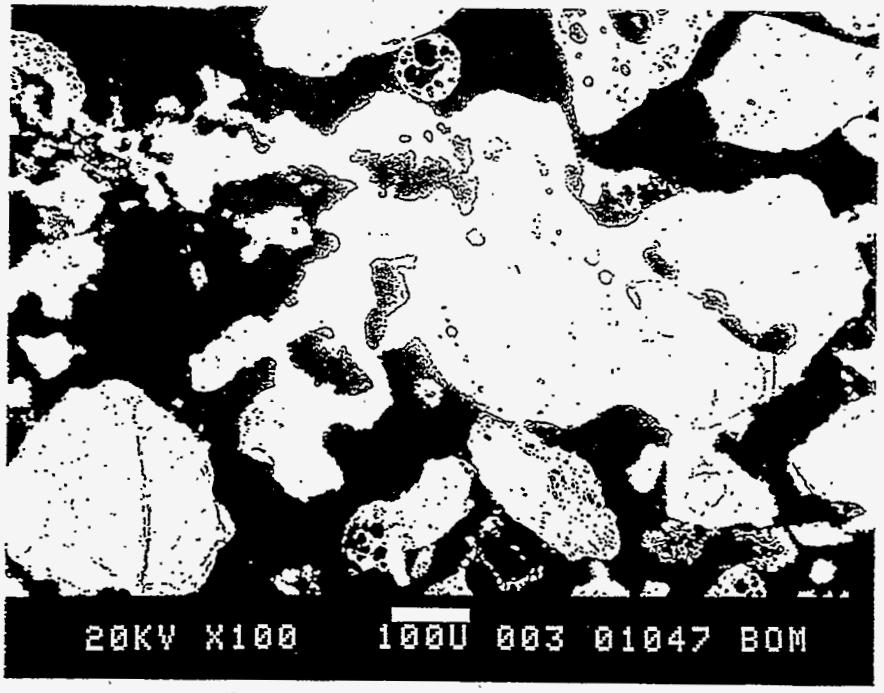

WOODLAND 14 TUBESIDE X 100

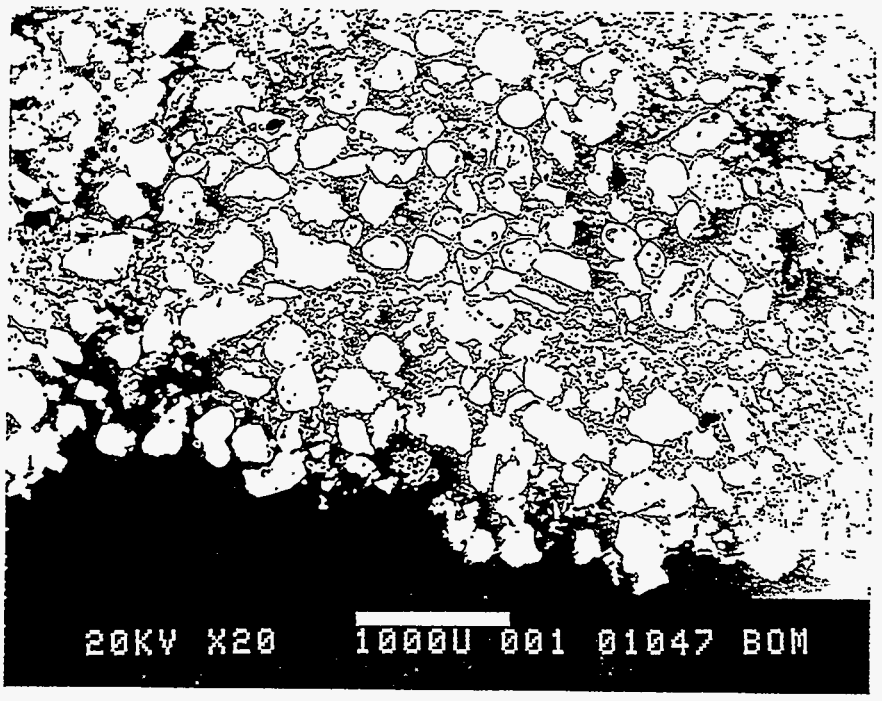

WOODLAND 14 TUBESIDE X 20

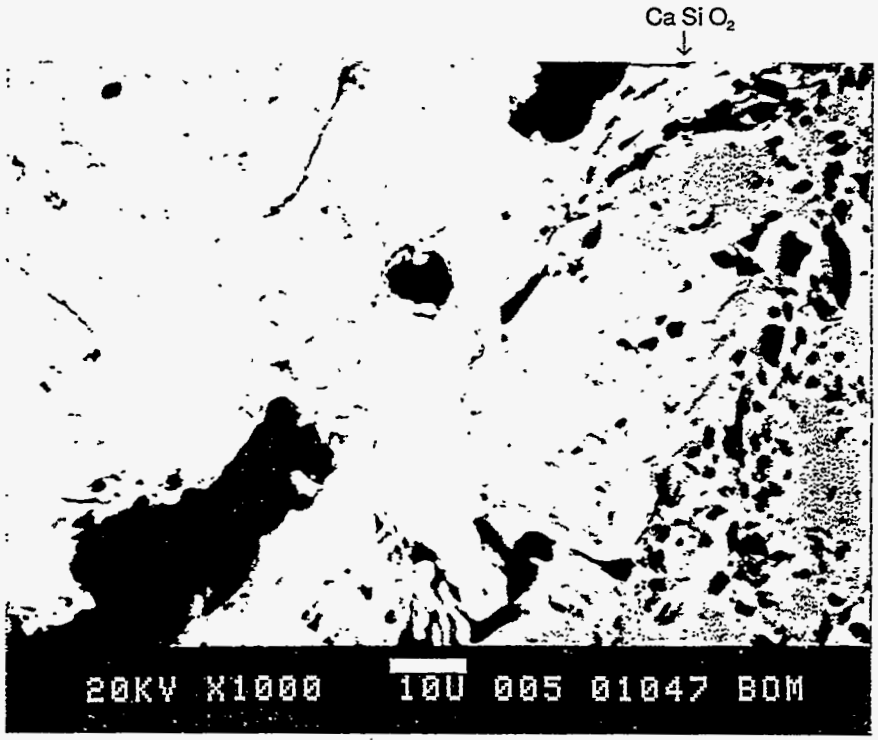

WOODLAND 14 x 1000 CaSiO3 INTERFACE BETWEEN PARTICLES

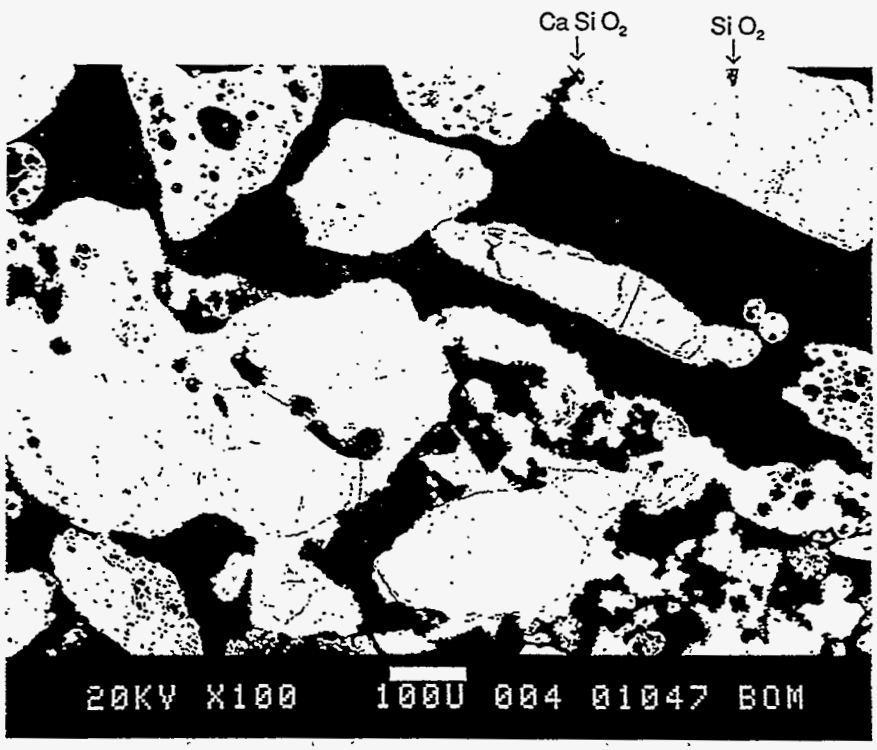

WOODLAND 14 X 100 TUBESIDE: CASiO3, SiO2 TOP RIGHT

16-Feb-1994 16:24:01 WOODLAND TS REAC ZON

Accelerating voltage	20.0 KeV
Beam - sample incidence angle	90.0 degrees
Xray emergence angle	5.8 degrees
Xray - window incidence angle	5.8 degrees

QUANTITATIVE EDS RESULTS
(ZAF CORRECTIONS VIA MAGIC V)

ELEMENT & LINE	K-RATIO**	WEIGHT PERCENT	PRECISION 2 SIGMA	FORMULA	OXIDE PERCENT
Si KA	0.1585	28.03	0.09	SiO2	59.97
Ca KA	0.4946	27.29	0.08	CaO	38.19
Mn KA	0.0026	0.27	0.02	MnO	0.35
Fe KA	0.0129	1.16	0.03	FeO	1.49
O *		43.24			
TOTAL					99.99

* DETERMINED BY STOICHIOMETRY

**NOTE: K-RATIO = K-RATIO x R
where R = reference(standard)/reference(sample)

NORMALIZATION FACTOR: 1.129

16-Feb-1994 16:43:39 WOODLAND TS REAC ZON

Accelerating voltage	20.0 KeV
Beam - sample incidence angle	90.0 degrees
Xray emergence angle	5.8 degrees
Xray - window incidence angle	5.8 degrees

QUANTITATIVE EDS RESULTS
(ZAF CORRECTIONS VIA MAGIC V)

ELEMENT & LINE	K-RATIO**	WEIGHT PERCENT	PRECISION 2 SIGMA	FORMULA	OXIDE PERCENT
Na KA	0.0145	1.45	0.33	Na2O	1.95
Mg KA	0.0076	2.30	0.05	MgO	3.82
Al KA	0.0463	10.54	0.09	Al2O3	19.92
Si KA	0.2165	26.69	0.07	SiO2	57.09
K KA	0.1667	7.84	0.04	K2O	9.44
Ca KA	0.0334	2.19	0.03	CaO	3.07
Ti KA	0.0123	1.14	0.02	TiO2	1.91
Mn KA	0.0035	0.20	0.01	MnO	0.26
Fe KA	0.0345	1.72	0.02	FeO	2.21
Zn KA	0.0072	0.27	0.01	ZnO	0.34
O *		45.66			
TOTAL					100.00

* DETERMINED BY STOICHIOMETRY

**NOTE: K-RATIO = K-RATIO x R
where R = reference(standard)/reference(sample)

NORMALIZATION FACTOR: 0.360

16-Feb-1994 16:12:15 WOODLAND TS GRAY

Accelerating voltage	20.0 KeV
Beam - sample incidence angle	90.0 degrees
Xray emergence angle	5.8 degrees
Xray - window incidence angle	5.8 degrees

QUANTITATIVE EDS RESULTS
(ZAF CORRECTIONS VIA MAGIC V)

ELEMENT & LINE	K-RATIO**	WEIGHT PERCENT	PRECISION 2 SIGMA	FORMULA	OXIDE PERCENT
Si KA	0.5335	46.74	0.08	SiO2	100.00
O *		53.26			
TOTAL					100.00

* DETERMINED BY STOICHIOMETRY

**NOTE: K-RATIO = K-RATIO x R
where R = reference(standard)/reference(sample)

NORMALIZATION FACTOR: 1.040

Marysville CFB

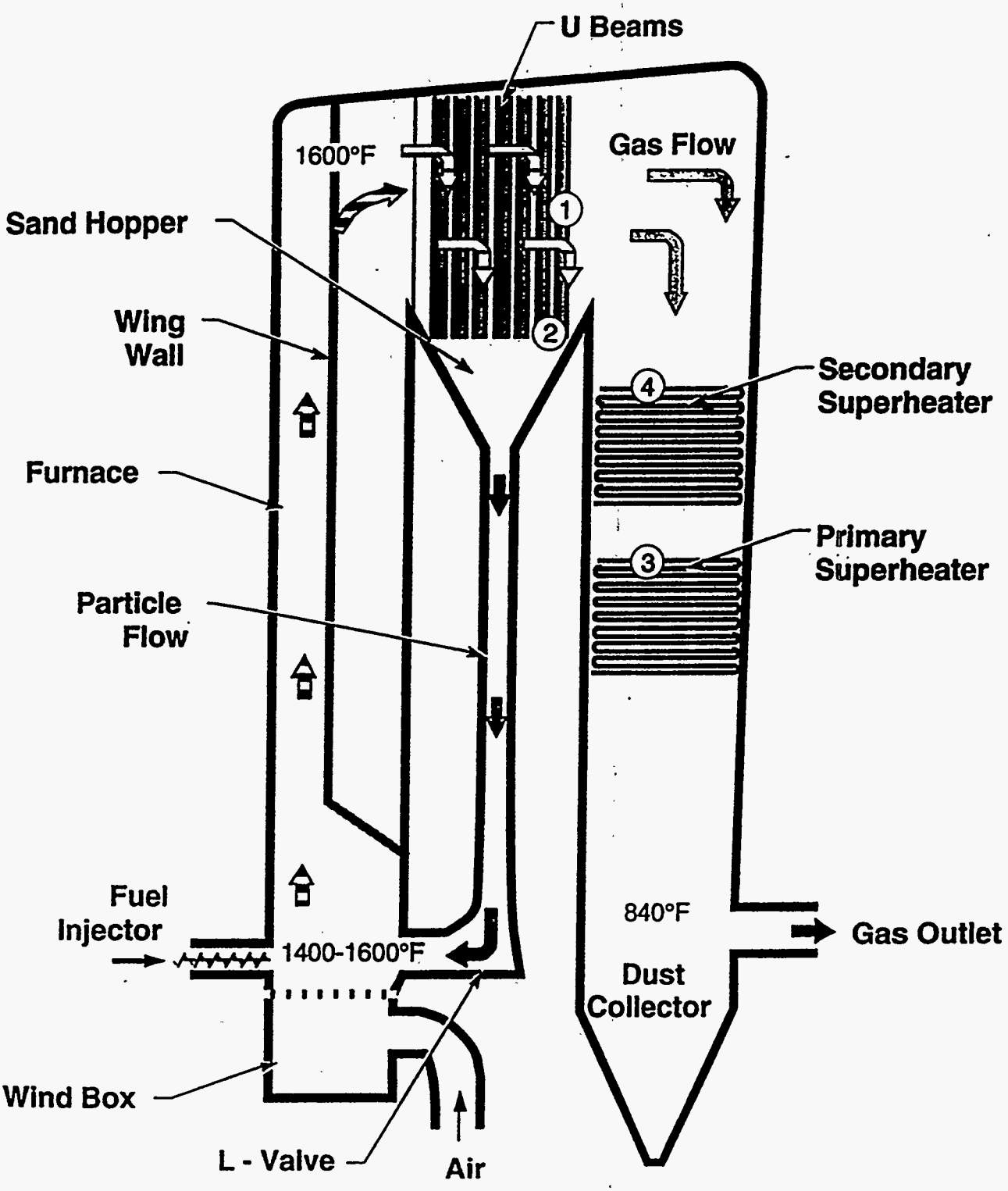

Fuel Mix: Sawdust/Chips (80%), Pits, Almond Shell/Hulls, Sander Dust (Varies)

SUMMARY OF FUEL AND DEPOSITS: SITHE 1992-1993 REVISED DEC 6, 1993

ELEMENTAL ANALYSES

TYPE	Location/Form	DATE	SiO2	Al2O3	TiO2	Fe2O3	CaO	MgO	Na2O	K2O	P2O5	SO3	Cl	UNDT	Na2O K2O	Alkali lb/MMBtu
Fuel Mix		8/6/92	52.55	13.15	0.43	8.18	10.06	3.27	5.90	5.04	1.90	2.10		-2.58	10.94	0.66
Fuel Mix	#6 Conveyor	3/5/92	57.34	13.07	0.53	6.08	10.24	3.19	3.12	4.28	0.94	1.17		0.04	7.40	1.06
Fuel	Sintering	7/1/92	57.35	14.88	1.03	6.09	7.43	1.98	4.04	3.15	0.93	0.53		2.59	7.19	0.78
Fuel	pile	7/7/92	57.01	13.92	0.72	7.33	8.25	2.79	2.80	3.12	0.68	1.35		2.03	5.92	0.49
Fuel Mix	#6 Conveyor	7/7/92	55.84	13.24	0.71	6.25	9.40	3.00	4.81	3.43	0.89	0.92		1.51	8.24	0.70
Fuel Mix	#6 Conveyor	7/30/92	56.48	12.32	0.49	5.31	8.57	2.94	5.42	4.33	1.67	0.72		1.75	9.75	0.45
Sintered Sand		8/4/92	82.19	10.16	0.20	1.80	2.53	0.63	2.53	3.14	0.26	0.02		-3.46	5.67	
Sand	Receiving Bin	8/6/92	82.24	9.99	0.21	1.56	2.33	0.40	2.23	3.10	0.22	0.01		-2.29	5.33	
Bed Drain Sand		8/6/92	91.01	2.49	0.08	0.81	1.44	0.01	0.61	0.66	0.12	0.03		2.74	1.27	
Dust Collector	Sand	8/4/92	75.45	11.31	0.52	2.54	4.03	0.80	3.25	3.77	0.62	0.45		-2.74	7.02	
Whitish sandstone	U-Beam	5/30/93	50.27	15.05	0.62	3.78	13.21	2.49	3.21	10.00	1.23	0.02	0.03	0.09	13.21	
Dark brown sand	U-Beam doorwa	5/30/93	70.58	14.67	0.64	4.93	4.31	1.24	1.62	1.56	0.22	0.03	0.01	0.19	3.18	
Fine powder dk brn	First Secondary	5/30/93	65.06	16.28	0.88	6.46	5.38	1.70	2.00	1.80	0.36	0.74	0.01	-0.67	3.80	
Hard, undev shark	Finishing secon	5/30/93	20.17	9.02	0.55	6.45	26.29	4.65	2.47	6.31	2.16	20.30	0.05	1.58	8.78	

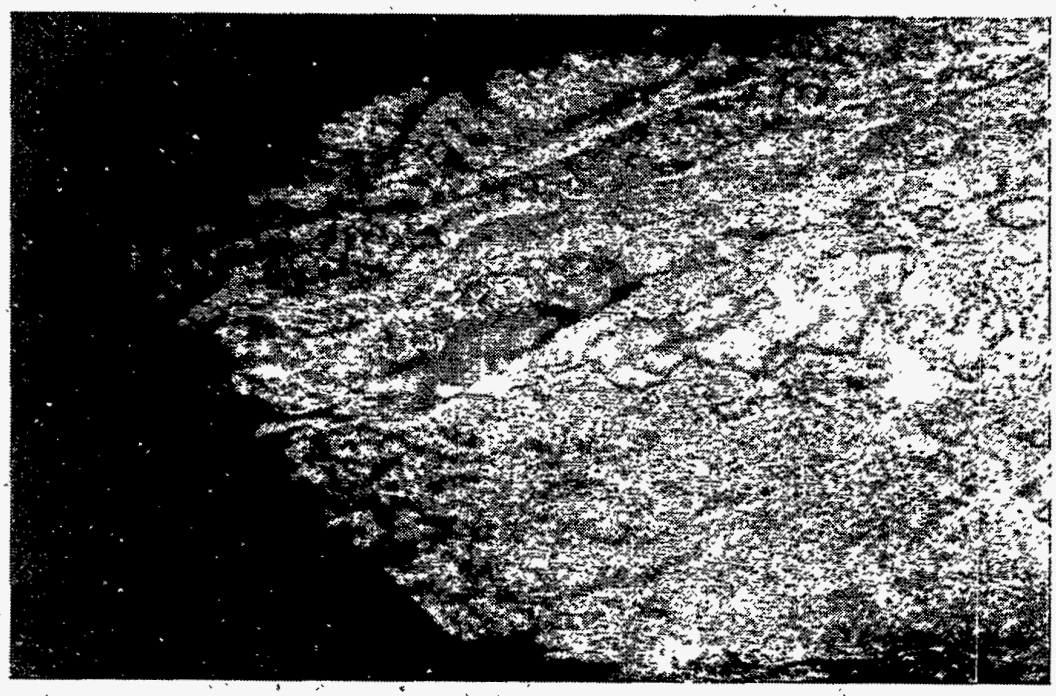

9. MARYSVILLE 4 X 50 FIRE SIDE, POINT OF SHARKS TOOTH, POLISHED IN WATER

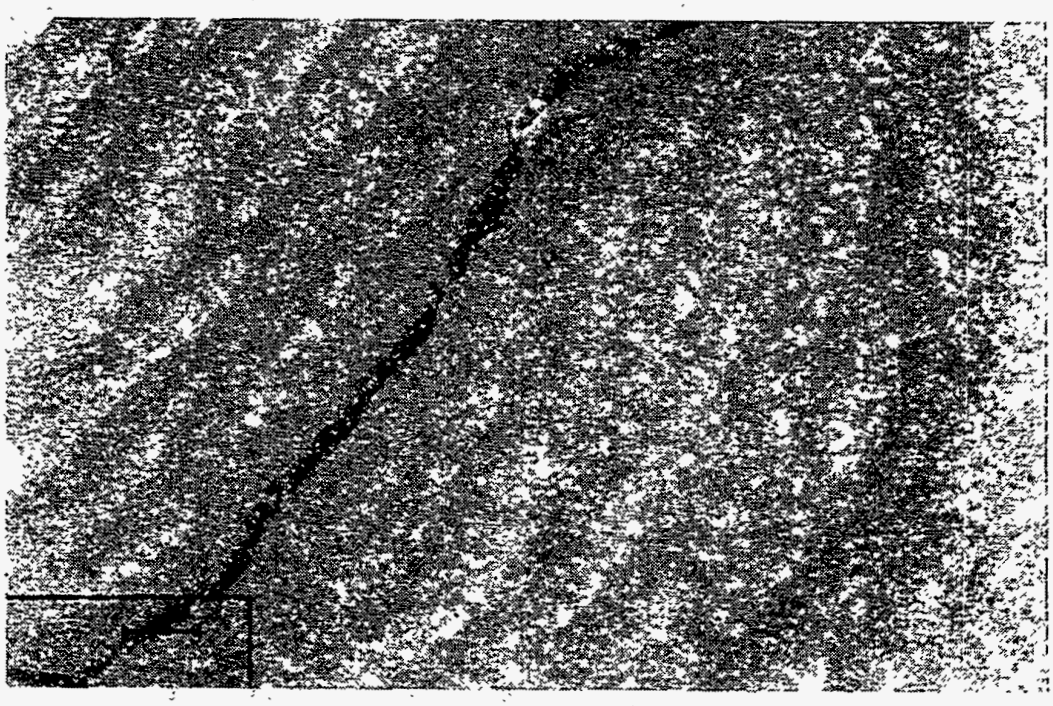

10. MARYSVILLE 4 X 50 MIDWAY, POLISHED IN WATER

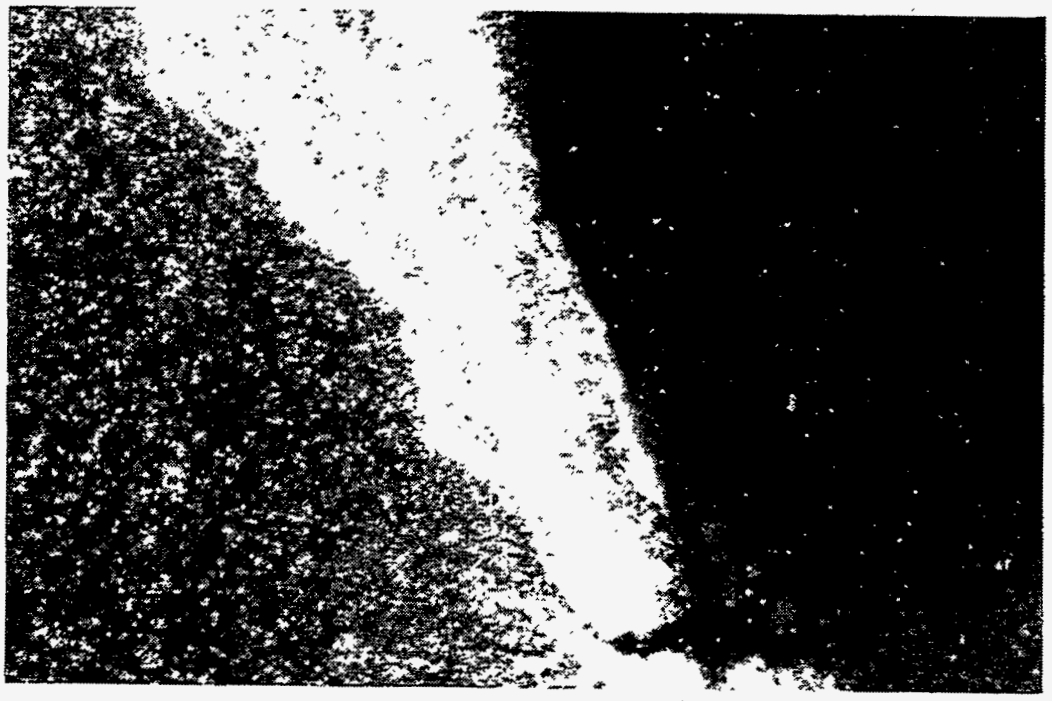

11. MARYSVILLE 4 X 50 TUBE SIDE, POLISHED IN WATER

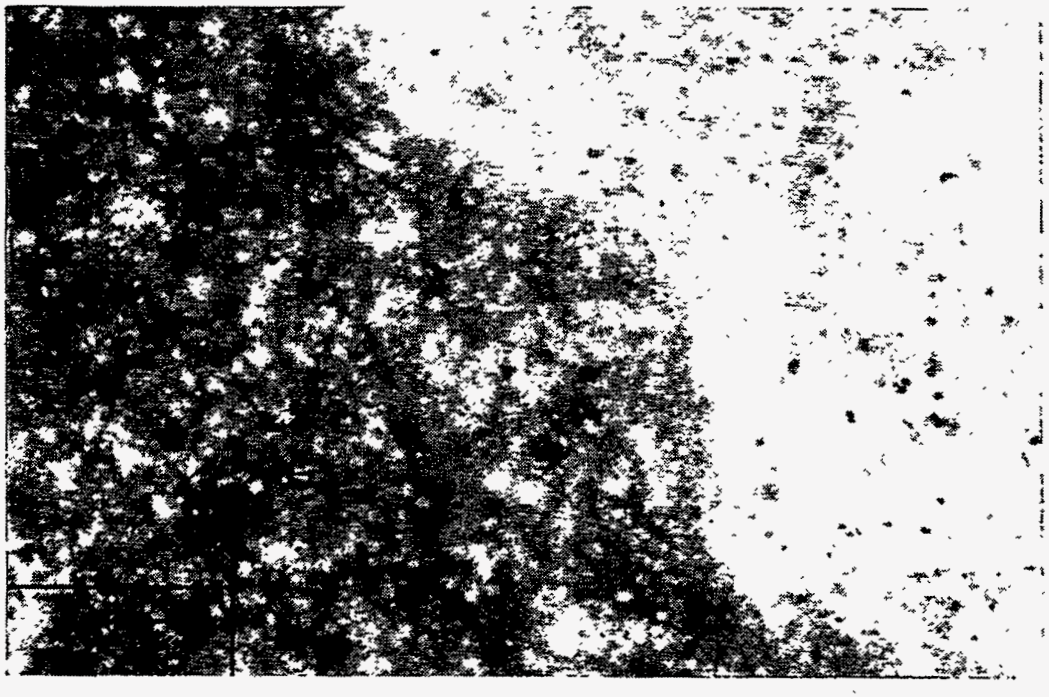

12. MARYSVILLE 4 X 200 NEAR TUBE SIDE, POLISHED IN WATER

13. MARYSVILLE 4 X 200 NEAR END OF SHARKS TOOTH, POLISHED IN WATER

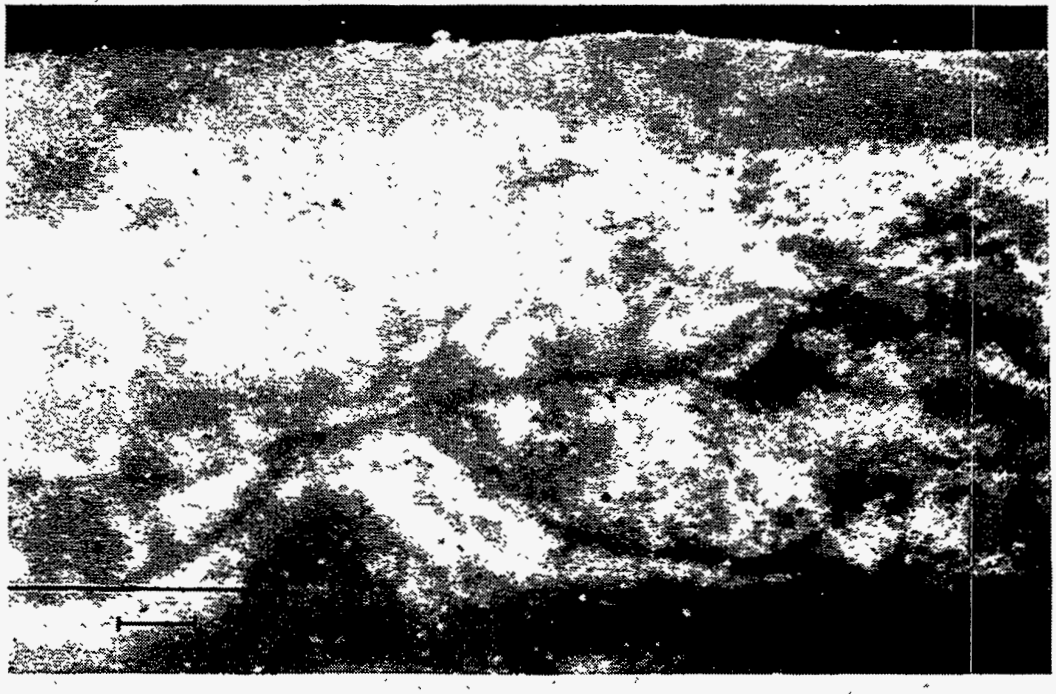

27. MARYSVILLE 4 X 200 FIRE SIDE, REPOLISHED IN OIL

28. MARYSVILLE 4 X 200 FIRE SIDE INTERIOR, REPOLISHED IN OIL

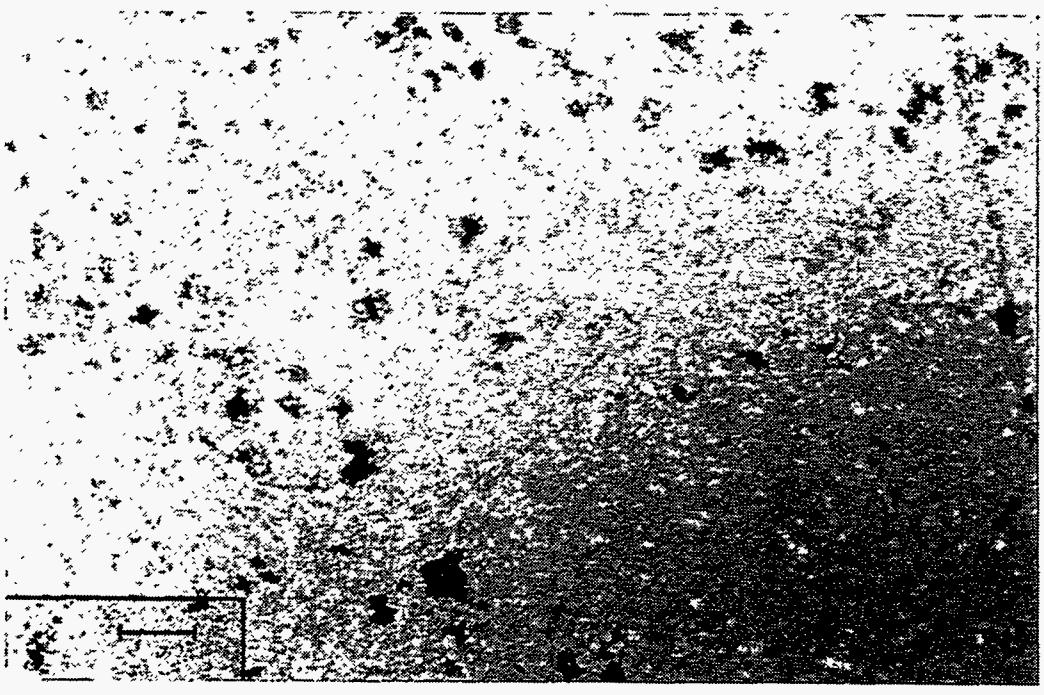

29. MARYSVILLE 4 X 200 INTERIOR, BRIGHT FIELD ILLUMINATION, REPOLISHED IN OIL

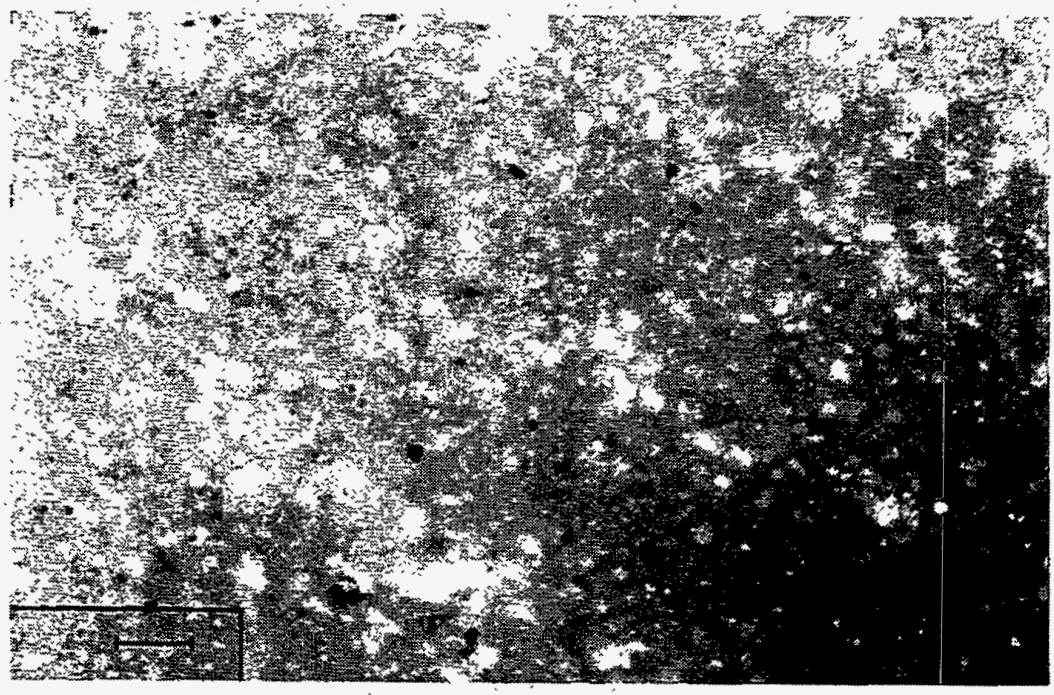

30. MARYSVILLE 4 X 200 INTERIOR, POLARIZED LIGHT, SAME AS 29

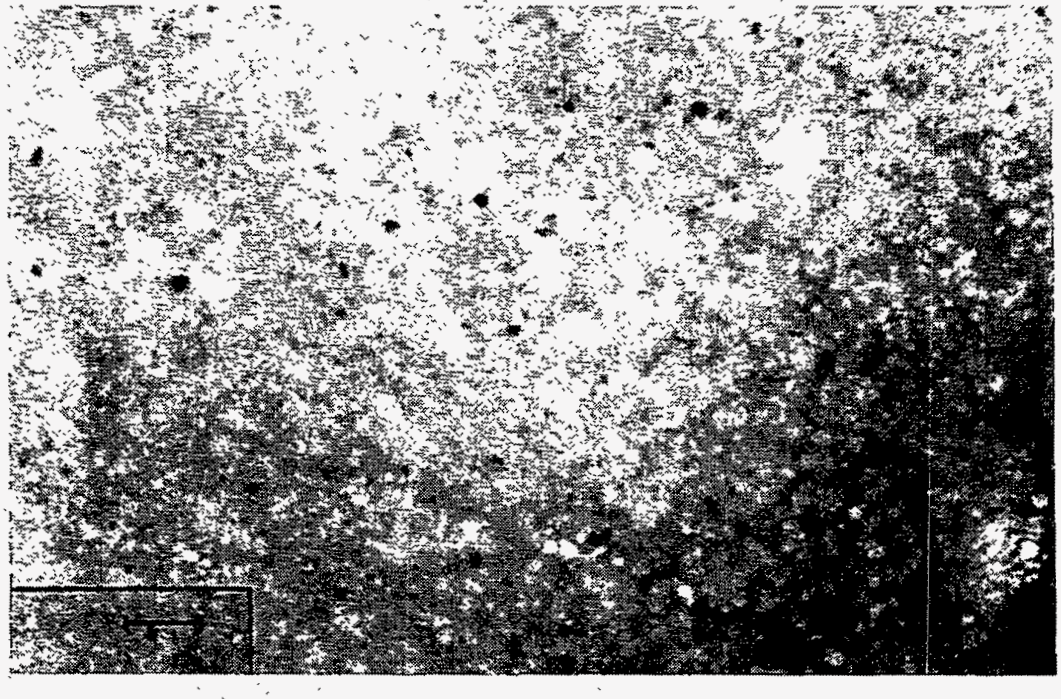

31. MARYSVILLE 4 X 200 TUBE SIDE, POLISHED IN WATER

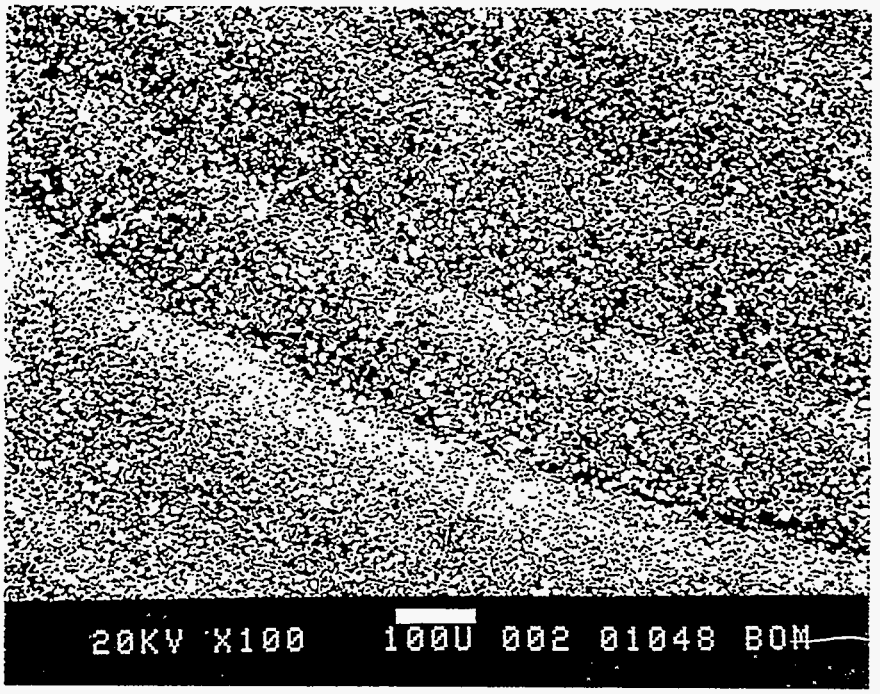

MARYSVILLE 4 X 100 INTERIOR

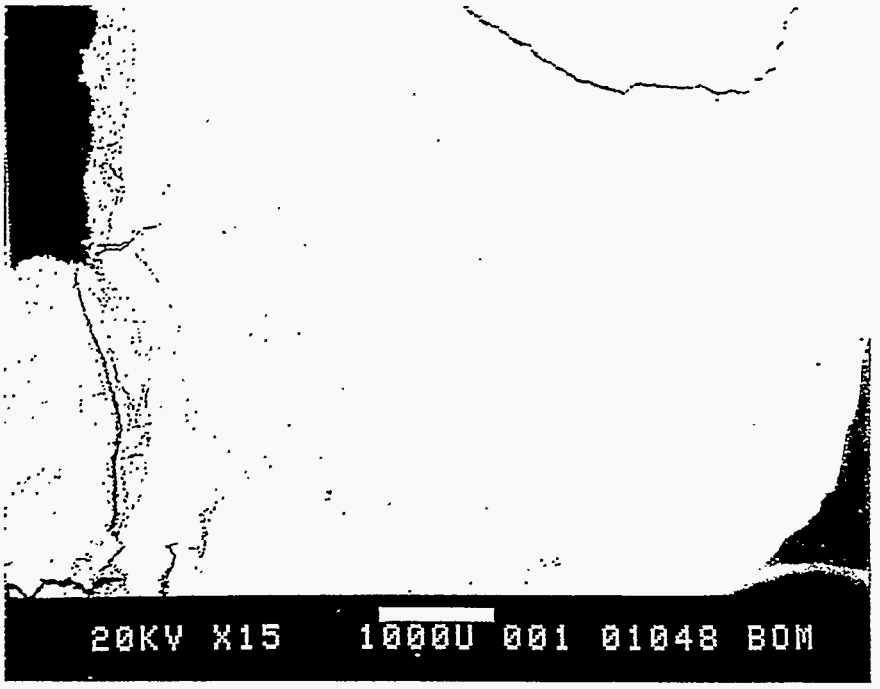

MARYSVILLE 4 X 15

16-Feb-1994 17:26:52 MARYSVILLE CENTER

Accelerating voltage 19.5 KeV

Beam - sample incidence angle 90.0 degrees

Xray emergence angle 5.8 degrees

Xray - window incidence angle 5.8 degrees

QUANTITATIVE EDS RESULTS
(ZAF CORRECTIONS VIA MAGIC V)

ELEMENT & LINE	K-RATIO**	WEIGHT PERCENT	PRECISION 2 SIGMA	FORMULA	OXIDE PERCENT
Na KA	0.0287	2.95	0.07	Na2O	3.97
Mg KA	0.0133	4.39	0.06	MgO	7.28
Al KA	0.0407	10.64	0.09	Al2O3	20.10
Si KA	0.0530	12.01	0.07	SiO2	25.69
P KA	0.0494	2.55	0.04	P2O5	5.84
S KA	0.0642	6.85	0.08	SO3	17.11
K KA	0.0235	0.96	0.02	K2O	1.15
Ca KA	0.3253	11.82	0.04	CaO	16.54
Ti KA	0.0045	0.39	0.01	TiO2	0.65
Mn KA	0.0022	0.10	0.01	MnO	0.13
Fe KA	0.0314	1.19	0.02	FeO	1.53
O *		46.16			
TOTAL					100.01

* DETERMINED BY STOICHIOMETRY

**NOTE: K-RATIO = K-RATIO x R
where R = reference(standard)/reference(sample)

NORMALIZATION FACTOR: 0.162

16-Feb-1994 17:18:10 MARYSVILLE TS

Accelerating voltage	19.5 KeV
Beam - sample incidence angle	90.0 degrees
Xray emergence angle	5.8 degrees
Xray - window incidence angle	5.8 degrees

QUANTITATIVE EDS RESULTS
(ZAF CORRECTIONS VIA MAGIC V)

ELEMENT & LINE	K-RATIO**	WEIGHT PERCENT	PRECISION 2 SIGMA	FORMULA	OXIDE PERCENT
Na KA	0.0425	4.15	0.09	Na2O	5.60
Mg KA	0.0270	8.12	0.08	MgO	13.46
Al KA	0.0434	8.24	0.07	Al2O3	15.56
Si KA	0.0567	8.24	0.04	SiO2	17.62
P KA	0.0914	4.14	0.05	P2O5	9.49
S KA	0.2072	8.24	0.05	SO3	20.57
K KA	0.0679	2.77	0.03	K2O	3.33
Ca KA	0.3710	8.24	0.03	CaO	11.53
Ti KA	0.0072	0.57	0.02	TiO2	0.94
Mn KA	0.0036	0.14	0.01	MnO	0.19
Fe KA	0.0410	1.33	0.02	FeO	1.71
O *		45.83			
TOTAL					100.01

* DETERMINED BY STOICHIOMETRY

**NOTE: K-RATIO = K-RATIO x R
where R = reference(standard)/reference(sample)

NORMALIZATION FACTOR: 0.111

16-Feb-1994 17:01:00 MARYSVILLE FS

Accelerating voltage 19.5 KeV

Beam - sample incidence angle 90.0 degrees

Xray emergence angle 5.8 degrees

Xray - window incidence angle 5.8 degrees

QUANTITATIVE EDS RESULTS
(ZAF CORRECTIONS VIA MAGIC V)

ELEMENT & LINE	K-RATIO**	WEIGHT PERCENT	PRECISION 2 SIGMA	FORMULA	OXIDE PERCENT
Na KA	0.0478	4.86	0.10	Na2O	6.55
Mg KA	0.0167	6.32	0.08	MgO	10.48
Al KA	0.0506	8.27	0.07	Al2O3	15.63
Si KA	0.0633	8.27	0.04	SiO2	17.70
P KA	0.0995	4.37	0.05	P2O5	10.00
S KA	0.2295	8.27	0.05	SO3	20.66
K KA	0.0921	3.72	0.03	K2O	4.48
Ca KA	0.3561	8.27	0.03	CaO	11.58
Ti KA	0.0070	0.56	0.02	TiO2	0.94
Mn KA	0.0039	0.16	0.01	MnO	0.21
Fe KA	0.0414	1.37	0.02	FeO	1.76
O *		45.54			
TOTAL					99.98

* DETERMINED BY STOICHIOMETRY

**NOTE: K-RATIO = K-RATIO x R
where R = reference(standard)/reference(sample)

NORMALIZATION FACTOR: 0.112

APPENDIX 3

Thermogravimetric Analyses of Biomass Fuels

Material in this appendix has been reproduced from the best available originals.

FWC/FWDC/TR-94/03

Analysis of a Suite of Biomass Samples

Prepared by

Richard W. Bryers
Senior Research Associate

May 6, 1994

FOSTER WHEELER DEVELOPMENT CORPORATION
12 Peach Tree Hill Road, Livingston, New Jersey 07039

Analysis of a Suite of Biomass Samples

List of Figures

List of Figures

List of Tables

Analysis of a Suite of Biomass Samples

INTRODUCTION

Certain forms of biomass contain minerals that melt at temperatures below traditional ashing temperatures, precluding the use of standard ASTM ash fusion techniques. Applying differential analysis to low-temperature ashed biomass (i.e., <250°C under an oxygen plasma) appeared to offer an opportunity to identify the precise melting temperature of these minerals as well as the compounds responsible. A suite of eight biomass samples was acquired for experimentation. The samples were selected to a complete fuel and ash characterization according to industrial standards along with low-temperature ashing, thermal analysis, and X-ray diffraction.

FUEL CHARACTERIZATION

Dr. Bryan Jenkins of the University of California provided the following samples prepared for analysis:

Waste Paper	Almond Hulls
Wheat Straw	Almond Shells
80% Wood/20% Wheat Straw	Olive Pits
Rice	Wood Waste/Almond Shells

To this list was added aspen from Canada and a blend of wood and manure for further comparison.

The eight samples provided by Dr. Jenkins were analyzed for complete proximate and ultimate analysis, ash chemistry, and ash fusion temperatures using traditional procedures as applied in the coal industry. In addition, the samples were low-temperature ashed using an oxygen plasma over a period of 70 to 80 hours and then subjected to Differential Thermal Analysis (DTA) as well as Differential Scanning Calorimetry (DSC) to determine low-temperature melts—the thrust of the characterization. The low-temperature ash was also subjected to Thermogravimetric Analysis (TGA) to determine low-temperature losses caused by volatilization of the alkalies. Combustion profiles were also generated using TGA to make a direct comparison with known profiles of various coal ranks. Chemical fractionation was performed on select

samples to determine the quantity and elemental composition of the water-soluble and organically-bound mineral matter. X-ray diffraction was performed on the low-temperature ash by two different laboratories to determine mineral composition.

PRESENTATION OF RESULTS

The proximate and ultimate analyses are summarized in Table 1. The ash content varies from 1.50 to approximately 10% for the agricultural wastes, except for the rice straw which is almost 20%. Percent ash determined by low-temperature ashing ran from 3 to 85% higher than that determined by ashing at 950°C, as shown in Table 3. Ashing for quantitative elemental analysis was performed at 500°C. The percent unaccounted for ran from a few percent to 30% and appears to depend on the level of concentration of alkalies, nitrogen and chlorine present. The fuel and ash analyses presented in Tables 1 and 2 appear, from left to right, in order of increasing potassium concentration.

TGA performed on LTA, appearing in Figure 1 , indicates volatilization began as low as 200°C (392°F) and increased linearly with temperatures to 1000°C (1832°F). The loss in ash at 500°C (932°F) was roughly in proportion to the ash loss predicted by TGA on LTA at 500°C (932°F). The total ash determined by TGA on LTA at 1000°C agrees favorably with ash determined by TGA on raw biomass and ash determined for proximate analysis--see Table 3. The total loss in ash by TGA on LTA correlates reasonably well with the total alkalies present. Waste paper containing 1.3% ($K_2O + Na_2O$) in the ash showed the least difference in quantity of ash when ashed by LTA and high-temperature ashing, while almond hulls and almond shells at ≈50% ($Na_2O + K_2O$) in the ash revealed a 23 to 26% loss in ash when heating to 500°C (932°F), and almost a 50% loss when heated to 1000°C (1832°F). The losses, or unaccounted for, are directly related to potassium and/or nitrogen in the fuel.

CHEMICAL FRACTIONATION

Chemical fractionation was performed on select samples because it is time consuming and expensive. Four samples were selected: olive pits, wheat straw, almond hulls, and almond shells. The latter two were only analyzed for leachate, leaving some speculation as to the composition of the residual, while the olive pits and wheat straw were analyzed for leachate and residuals. The results appear in Tables 4, 5, 6, and 7. Except for the olive pits, the alkalies, of which potassium is a dominant specie, are soluble in water or ammonium acetate and thus volatile during combustion. The sodium found in the olive pits is the dominant form of alkali in this biomass specie

Table 1 Summary of Biomass Fuel Analysis

Fuel	Waste Paper		80% Wood/ 20% Wheat Straw		Wood Waste/ Almond Shells		Rice Straw		Wheat Straw	
Air Dry Loss	0.00		6.00		0.00		0.00		0.00	
	As Rec'd	Dry	As Rec'd	Dry	As Rec'd	Dry	As Rec'd	Dry	As Rec'd	Dry
Proximate Analysis										
Fixed Carbon	9.09	9.74	16.74	18.52	18.69	20.64	16.41	18.73	19.03	20.96
Volatile Matter	76.20	81.70	66.72	73.81	66.23	73.13	54.49	62.18	65.09	71.69
Ash	7.98	8.56	6.93	7.67	5.64	6.23	16.73	19.09	6.67	7.35
Moisture	6.73	--	9.61	--	9.44	--	12.37	--	9.21	--
TOTAL	100.00	100.00	100.00	100.00	100.00	100.00	100.00	100.00	100.00	100.00
Ultimate Analysis										
Carbon	45.74	49.04	43.15	47.74	42.11	46.50	34.10	38.91	41.08	45.25
Hydrogen	6.40	6.86	5.19	5.75	4.93	5.45	4.16	4.74	4.90	5.40
Oxygen	32.66	35.01	34.51	38.16	37.21	41.08	31.34	35.78	37.16	40.92
Nitrogen	0.42	0.45	0.54	0.60	0.64	0.71	1.2	1.37	0.81	0.89
Sulfur	0.07	0.08	0.07	0.08	0.03	0.03	0.10	0.11	0.17	0.19
Ash	7.98	8.56	6.93	7.67	5.64	6.23	16.73	19.09	6.67	7.35
Moisture	6.73	--	9.61	--	9.44	--	12.37	--	9.21	--
TOTAL	100.00	100.00	100.00	100.00	100.00	100.00	100.00	100.00	100.00	100.00
HHV, Btu/lb	8892	9534	7430	8220	7292	8052	5829	6652	7055	7771
Chloride, ppm	420		1240		480		4670		2330	
Percent Ash Determined by LTA (Low-Temperature Ashing)	8.70		9.20		8.32		22.58		9.44	

Table 1 Summary of Biomass Fuel Analysis (Cont)

Fuel	Olive Pits		Almond Shells		Almond Hulls		Aspen		Chicken Litter	
Air Dry Loss	0.00		0.00		0.00		40.41		0.00	
	As Rec'd	Dry	As Rec'd	Dry	As Rec'd	Dry	As Rec'd	Dry	As Rec'd	Dry
Proximate Analysis										
Fixed Carbon	19.73	4.64	19.06	20.81	21.49	23.98	9.72	17.42	--	--
Volatile Matter	69.37	76.11	71.11	77.66	63.76	71.15	44.25	79.37	--	--
Ash	2.05	2.25	1.40	1.53	4.36	4.87	1.79	3.21	--	--
Moisture	8.85	--	8.43	--	10.39	--	44.24	---	--	--
TOTAL	100.00	100.00	100.00	100.00	100.00	100.00	100.00	100.00	100.00	100.00
Ultimate Analysis										
Carbon	44.32	48.62	34.63	37.82	42.75	47.71	29.09	52.17	--	42.80
Hydrogen	5.31	5.83	5.71	6.23	5.26	5.87	3.52	6.32	--	5.60
Oxygen	38.59	42.34	49.15	53.68	35.88	40.03	21.18	37.94	--	30.20
Nitrogen	0.86	0.94	0.65	0.71	1.30	1.45	0.18	0.33	--	5.20
Sulfur	0.02	0.02	0.03	0.03	0.06	0.07	0.02	0.03	--	0.50
Ash	2.05	2.25	1.40	1.53	4.36	4.87	1.79	3.21	--	15.20
Moisture	8.85	--	8.43	--	10.39	--	44.24	--	--	--
TOTAL	100.00	100.00	100.00	100.00	100.00	100.00	100.00	100.00	100.00	100.00
HHV, Btu/lb	7631	8372	8623	9417	7392	8249	4840	8680	--	--
Chloride, ppm	370		680		650		----		5000	
Percent Ash Determined by LTA (Low-Temperature Ashing)	2.26		3.57		9.03		----		----	

Table 2 Summary of Biomass Ash Chemistry

	Waste Paper	80% Wood 20% Wheat Straw	Wood Waste/ Almond Shells	Rice Straw	Wheat Straw	Olive Pits	Almond Shells	Almond Hulls	Aspen	Wood/ Manure
	1	2	3	4	5	6	7	8	9	10
Elemental Composition										
SiO_2	20.5	56.8	49.6	73.0	55.7	23.1	4.9	4.0	14.9	10.7
Al_2O_3	54.0	10.9	11.0	1.4	1.8	5.3	1.5	1.3	1.2	5.8
TiO_2	1.5	0.5	0.4	*	*	0.1	*	*	*	*
Fe_2O_3	0.1	4.9	4.6	0.6	0.7	5.1	1.3	0.4	1.2	0.8
CaO	10.2	10.2	14.4	1.9	2.6	10.9	6.9	5.0	65.2	21.4
MgO	1.9	2.4	2.7	1.8	2.4	3.0	2.6	2.9	4.3	6.2
Na_2O	1.1	3.8	2.4	0.4	0.9	29.9	0.5	0.2	0.4	3.8
K_2O	0.2	6.7	7.4	13.5	22.8	5.2	49.6	50.9	6.5	15.1
SO_3	2.3	1.9	1.4	0.7	1.7	2.4	1.6	1.2	1.8	7.0
P_2O_5	*	1.1	1.5	1.4	1.2	2.7	5.0	5.5	2.0	30.2
Total Percentage	91.8	99.2	95.4	94.7	89.8	87.7	73.9	71.4	97.5	100.0
TGA Loss on LTA, 500°C %	8	9	11	15	10	20	23	26	--	--
Ash Fusion Temperatures										
Reducing										
I.T.	2694	2065	2084	2023	2464	2340	1960	2359	----	----
S.T. (Sph.)	2910	2096	2130	2246	2466	2372	1981	2401	----	----
S.T.(Hem.)	2910	2288	2178	2258	2467	2495	2010	2408	----	----
F.T.	2910	2384	2239	2641	2474	2497	2071	2410	----	----
Oxidizing										
I.T.	2619	2084	2072	1965	1911	2448	1897	2558	----	----
S.T. (Sph.)	2632	2105	2096	2158	1913	2449	1899	2801	----	----
S.T.(Hem.)	2910	2322	2175	2496	2238	2487	1911	2818	----	----
F.T.	2910	2499	2262	2582	2316	2704	2348	2820	----	----

* = Nil

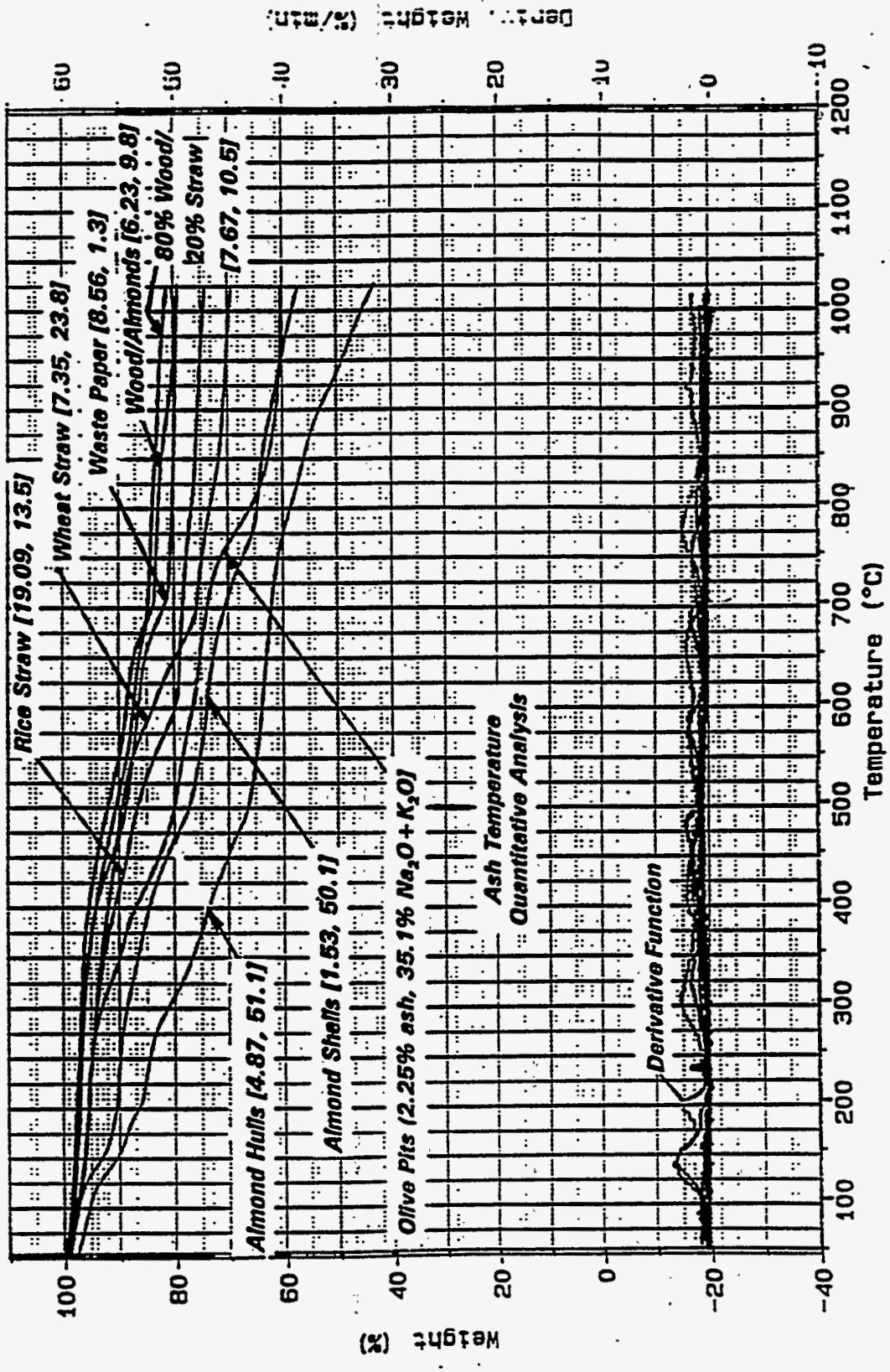

Figure 1 TGA on Low-Temperature Ashed Biomass — Samples

Table 3 Summary of Percent Ash Determined by Various Techniques

	Low-Temp. Ash <250°C	TGA on LTA 1000°C	Proximate Ash ~950°C	TGA on Biomass 1000°C
80% Wood/20% Wheat Straw	9.20	7.6	7.67	4.0
Almond Hulls	9.03	3.79	4.87	5.0
Almond Shells	3.57	2.07	2.25	2.0
Rice Straw	22.58	17.1	19.09	17.5
Wheat Straw	9.44	6.6	7.35	5.0
Olive Pits	2.26	1.28	1.53	1.0
Wood Waste/Almond Shells	8.32	6.6	6.23	2.5
Waste Paper	8.70	6.96	8.56	7.0

Table 4 Chemical Fractionation — Olive Pits

Chemical Fraction	Water	1M Ammonium Acetate µg/g	1M Hydrochloric Acid µg/g	Remaining Residue
Sodium	650	240	420	2400
Potassium	610	1400	150	245
Calcium	170	910	197	940
Magnesium	70	450	66	400
Iron	10	<10	750	112
Alunimum	40	10	400	270

Table 5 Chemical Fractionation — Wheat Straw

Chemical Fraction	Water	1M Ammonium Acetate µg/g	1M Hydrochloic Acid µg/g	Remaining Residue
Sodium	500	810	260	2
Potassium	14,000	220	270	200
Calcium	1770	20,650	185	206
Magnesium	680	370	143	93
Iron	50	<10	790	139
Alunimum	20	60	370	800

Table 6 Chemical Fractionation — Almond Shells

Chemical Fraction	Water	1M Ammonium Acetate µg/g	1M Hydrochloic Acid µg/g
Sodium	310	320	130
Potassium	9800	980	40
Calcium	1750	840	330
Magnesium	220	220	40

Table 7 Chemical Fractionation — Almond Hulls

Chemical Fraction	Water	1M Ammonium Acetate µg/g	1M Hydrochloic Acid µg/g
Sodium	485	438	162
Potassium	18,571	2095	57
Calcium	3048	1305	324
Magnesium	752	390	48

and is concentrated in the residual, probably as a silicate. Hence, it is stable during combustion except in the presence of Cl. These results appear to agree with L. Baxter's report of the occurrence of minerals in biomass.[1] Baxter indices that potassium—an essential element in the growth process—occurs as a univalent ion dispersed throughout the organic phase, whereas sodium is not commonly found in biomass and in most cases, is considered toxic. One might expect to find sodium as a chloride or silicate.

Livingston reported earlier that substantial loss in alkalies began at 800°C—temperatures somewhat higher than projected by TGAs on LTA for the eight specimens tested--see Figure 2. If the results were to agree, it would seem that a substance other than alkalies was being lost.

THERMAL ANALYSIS

DTAs were performed on the LTA to identify low-temperature melts and decomposition in the temperature range of 100-1000°C (212-1832°F). Figure 3 is a typical DTA profile for olive pits performed on low-temperature ash under air. There are three major endotherms occurring at about 350-425°C and beginning at 950°C. The high-temperature endotherm could easily be related to sodium silicates based on the known elemental composition and mineral form as predicted by chemical fractionation. Differential thermal analysis of the remaining seven biomass, reported at the end of the paper, also revealed an array of endotherms occurring below 700°C (1292°F). TGAs superimposed on the DTA thermograms, along with a magnified derivative function, indicate some of the endotherms are directly related to decomposition of specific compounds.

A search of the literature revealed eight potential categories of elements commonly found in the chemical fractionated leachate, which may be responsible for low-temperature decomposition or melts. They include chlorides, carbonates, chlorates, sulfates, hydroxides, sulfides, phosphates, and nitrates of sodium, potassium, calcium, magnesium and iron. The results appear in Table 8. Graphically, they appear in Figure 4 along with eutectics of various combinations that may be responsible for low-melting phases. Chlorides, chlorates, hydroxides and nitrates appear to be likely candidates responsible for the low-melting phases.

To separate endotherms due to melts from endotherms due to decomposition and vaporization, the LTA samples were heated to 1000°C (1832°F), cooled to room temperature, and reheated to 1000°C (1832°F), as shown in Figure 5. It is quite evident that the endotherms disappeared and there was no further sign of a melt. It

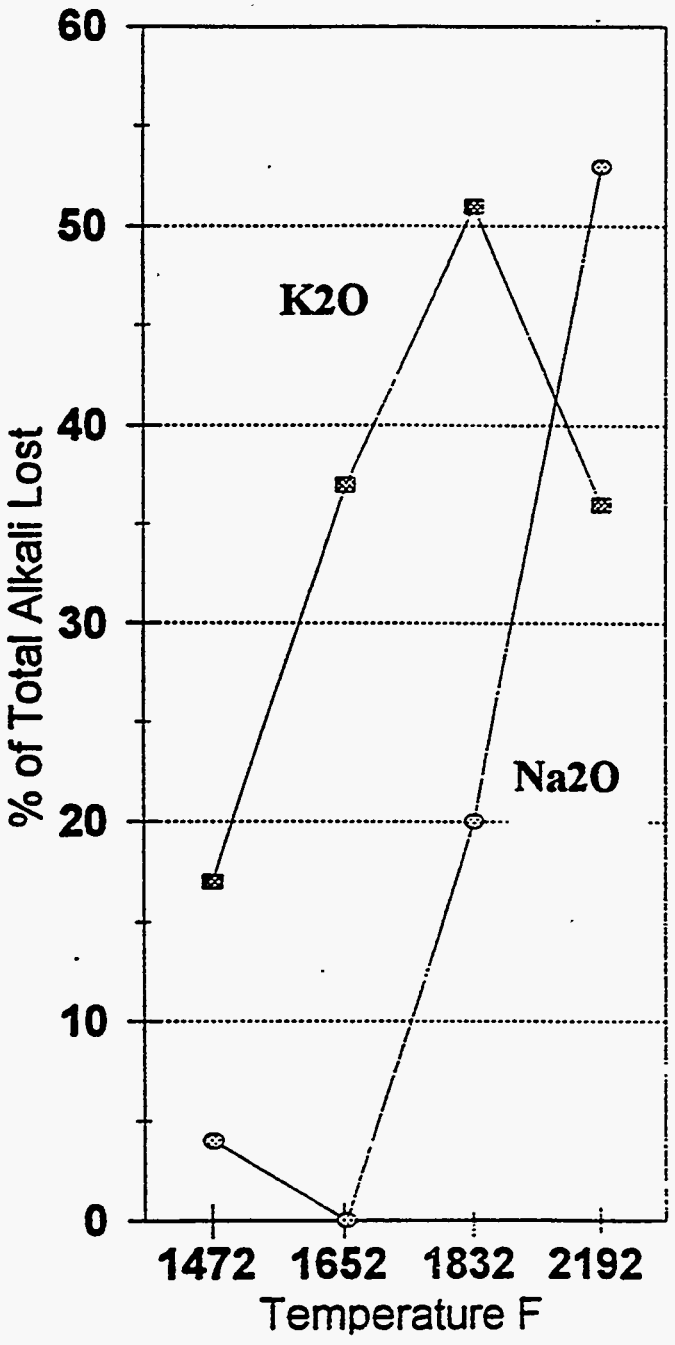

Figure 2 Sodium and Potassium Volatilization from Wheat Straw (Livingston 1991)

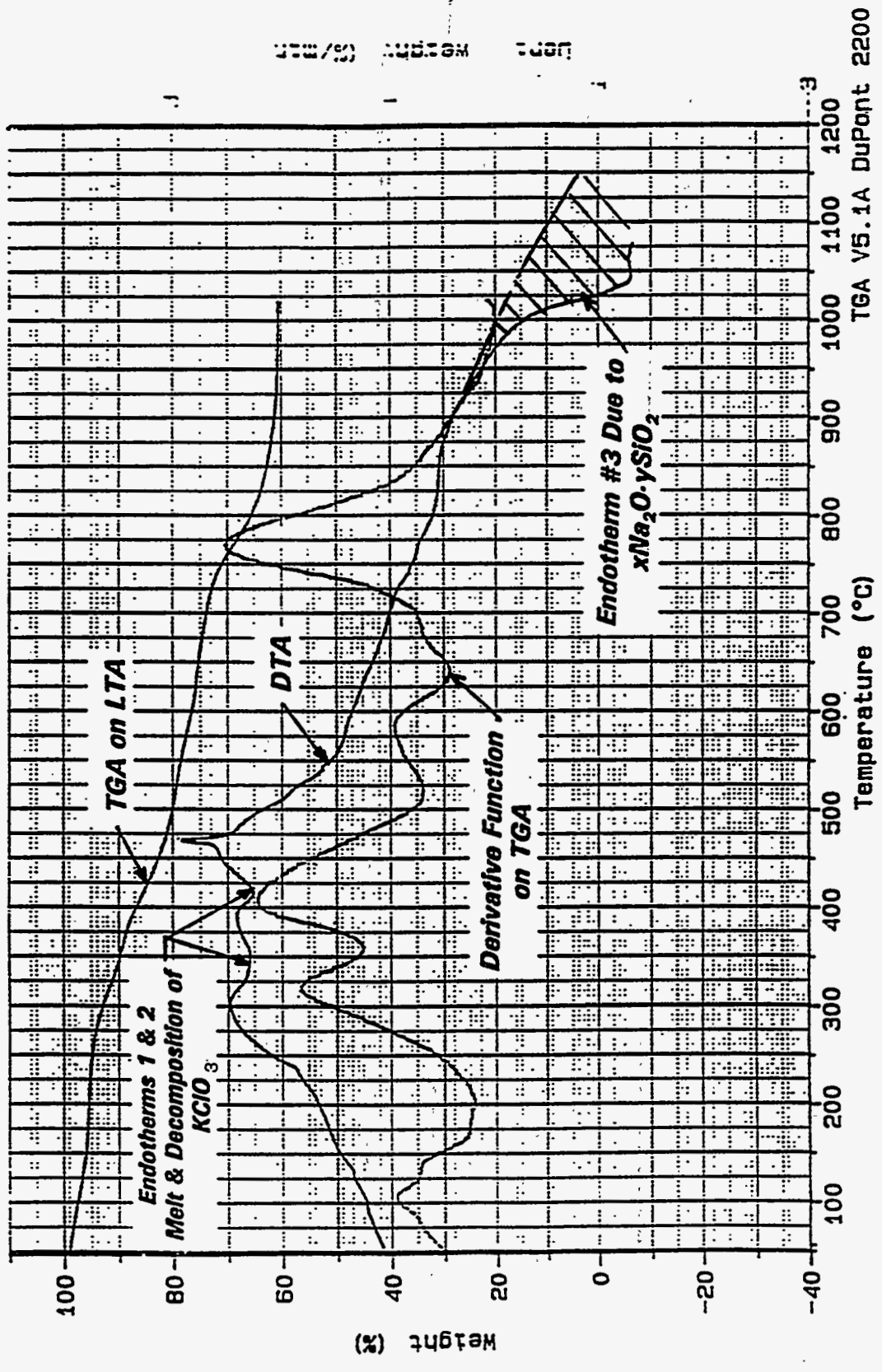

Figure 3 DTA and TGA on Olive Pits — Low-Temperature Ash under Nitrogen

Table 8 Melting Temperature of Potential Low-Melting Minerals Found in Biomass

Group	*Mineral*	*Melting Temperature, °C*
Chlorides	NaCl	801
	$CaCl_2$	782
	KCl	770
	$MgCl_2$	714
	$FeCl_3$	306
Carbonates	Na_2CO_3	851
	$CaCO_3$	1339
	K_2CO_3	891
	$MgCO_3$	Decomp. 350
	$FeCO_3$	Decomp.
Chlorates	$NaClO_3$	248-261
	$Ca(ClO_3)_2$	340
	$KClO_3$	356, decomp. 400
	$MgClO_3 \cdot 6H_2O$	35
	Iron $Fe(ClO_4)_2$	Decomp. >400
Sulfates	Na_2SO_4	
	$CaSO_4$	750-950 (pres. of silicates)
	K_2SO_4	1069 Tr. 558
	$MgSO_4$	1124 Decomp.
	$Fe(SO_4)_3$	480 Decomp.
Hydroxides	Na(OH)	318
	$Ca(OH)_2$	580 — H_2O
	KOH	360
	Mg(OH)	350 — H_2O
	$Fe(OH)_2$	---
Sulfides	Na_2S	1180
	CaS	---
	K_2S	470
	MgS	---
	FeS_2	1171
Phosphates	$Ca_2P_2O_7$	1230
	K_3PO_4	1340
	$Mg_3(PH_4)_2$	1184

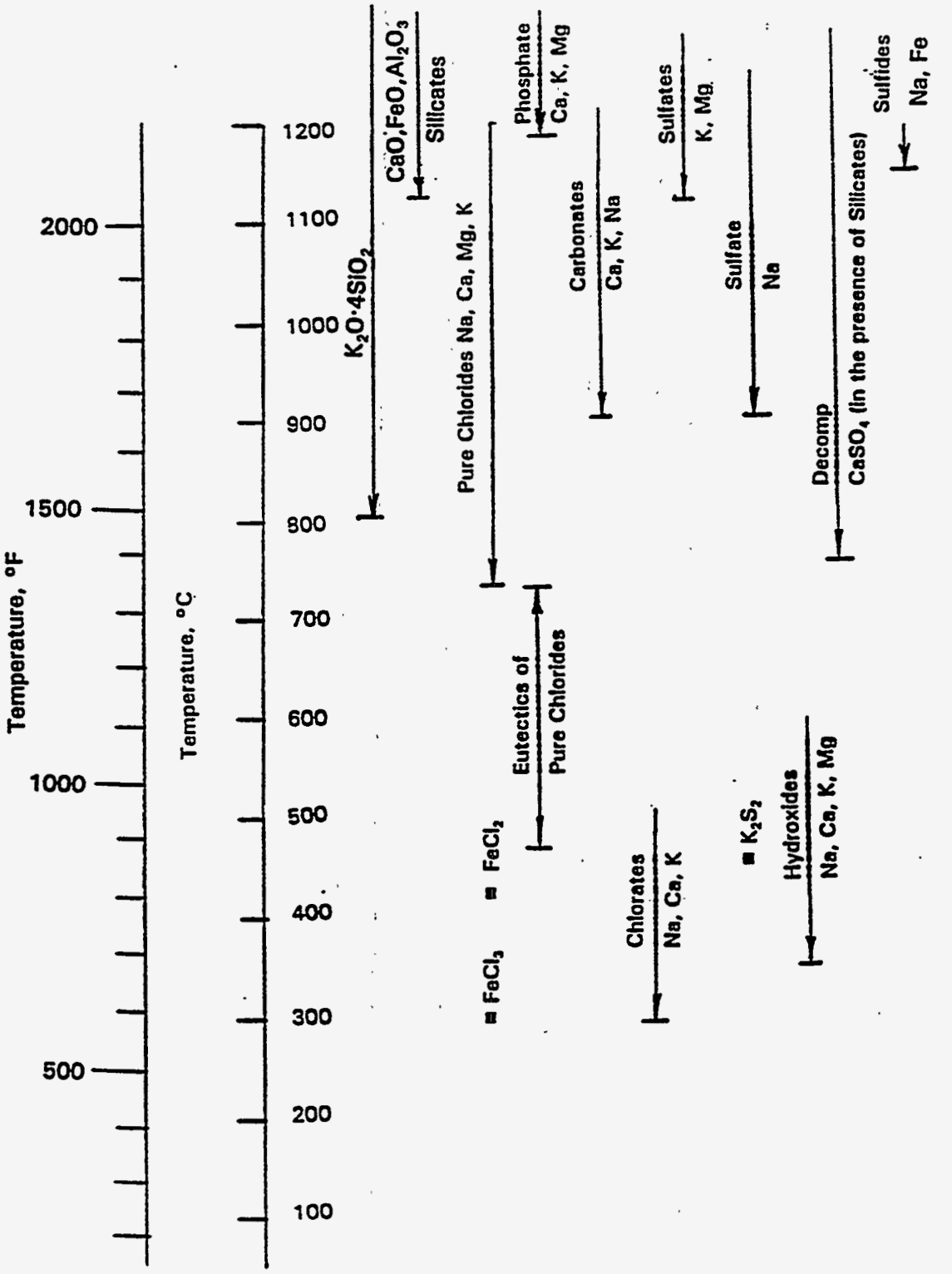

Figure 4 Melting Temperatures of Low-Melting Minerals Which May Occur in Biomass

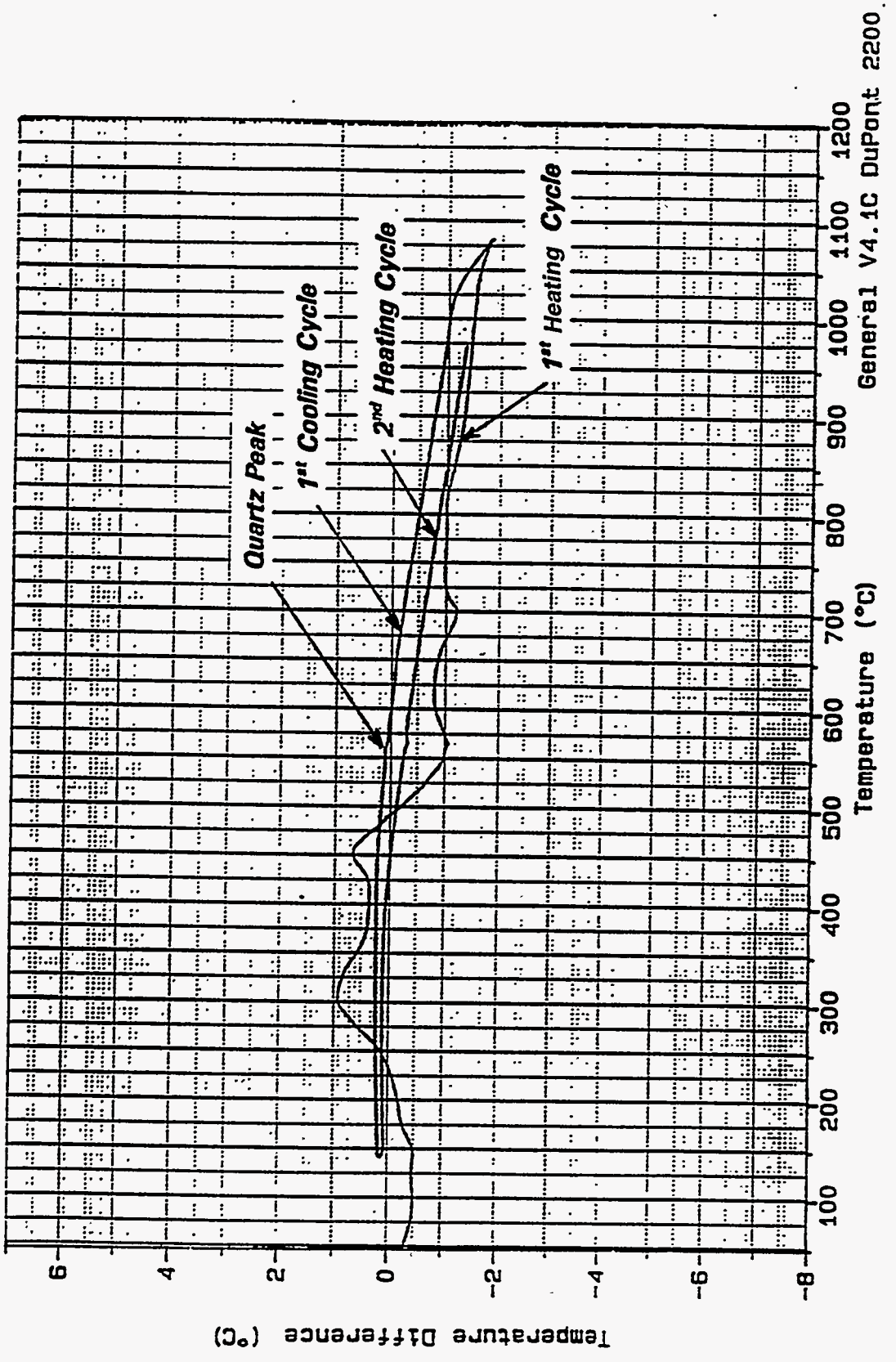

Figure 5 DTA Profiles on Low-Temperature 80% Wood/20% Straw Recycled Through Two Heating Cycles

was quite evident that if a melt formed, it was peculiar to a volatile specie and disappeared once the specie vaporized. Figures 6 and 7 are examples of DTAs/TGAs for potassium chlorates and nitrates. The thermograms identify low-temperature melts and decompositions similar to that found in the LTA. The chlorates reveal a second melt forms at higher temperatures as the result of the formation of chlorides upon completion of the decomposition. Figure 8 summarizes DTAs for potassium, sodium and calcium chloride. DTAs performed on a blend of chlorides in Figure 9 generates two peaks which correspond to the solidus line (initial formation of a melt) and the liquidous line of a mixture, as shown in the ternary phase diagram.

This exercise confirms the accuracy of DTA and also reveals the complexity of interpreting results from a multicomponent system. The chloride mixture was recycled through two heating cycles, as shown in Figure 10. It would appear that some of the minor constituents may have been vaporized as the solidus line was altered while the liquidous line remained unchanged. In addition to chlorates and nitrates, mixtures of chlorides may be responsible for the low-melting phase.

X-RAY DIFFRACTION

Although we had some idea as to what compounds were present, there appeared to be a need for positive identification of the minerals present. Two low-temperature-ashed samples generated in different laboratories from the same raw biomass sample were analyzed by x-ray diffraction by two different laboratories. The results are summarized in Table 9. The biomass samples are presented in descending order according to their increase in potassium concentration. There is reasonably good agreement between laboratories. In some cases there is a reversal in major and minor concentrations of an identifiable constituent. The general trends appear to be the same. Both labs identify quartz as a major constituent and clays as alkali aluminosilicates as minor species. It is important to note that sodium is always identified as being associated with a silicate, while potassium always appears as a compound other than a silicate. Thus each has a different role in fouling and slagging and they should not be lumped together in a common index. As the concentration of potassium increases, so does the concentration of potassium, nitrate, potassium chlorate, and potassium hydroxide. Chlorine appears to be tied up exclusively by the potassium, not an unreasonable expectation if one recognizes it appears ionically bound to some organic compound in the biomass. Sodium is only formed as a silicate or a sulfate.

The x-ray analysis indicates the potassium compounds occur in the LTA as artifacts of the low-temperature ashing process (i.e., potassium nitrate, potassium chlorate, and potassium hydroxide) as the oxygen plasma increases, the oxidation state of chlorine, nitrogen and sulfur. These compounds do not exist in biomass.

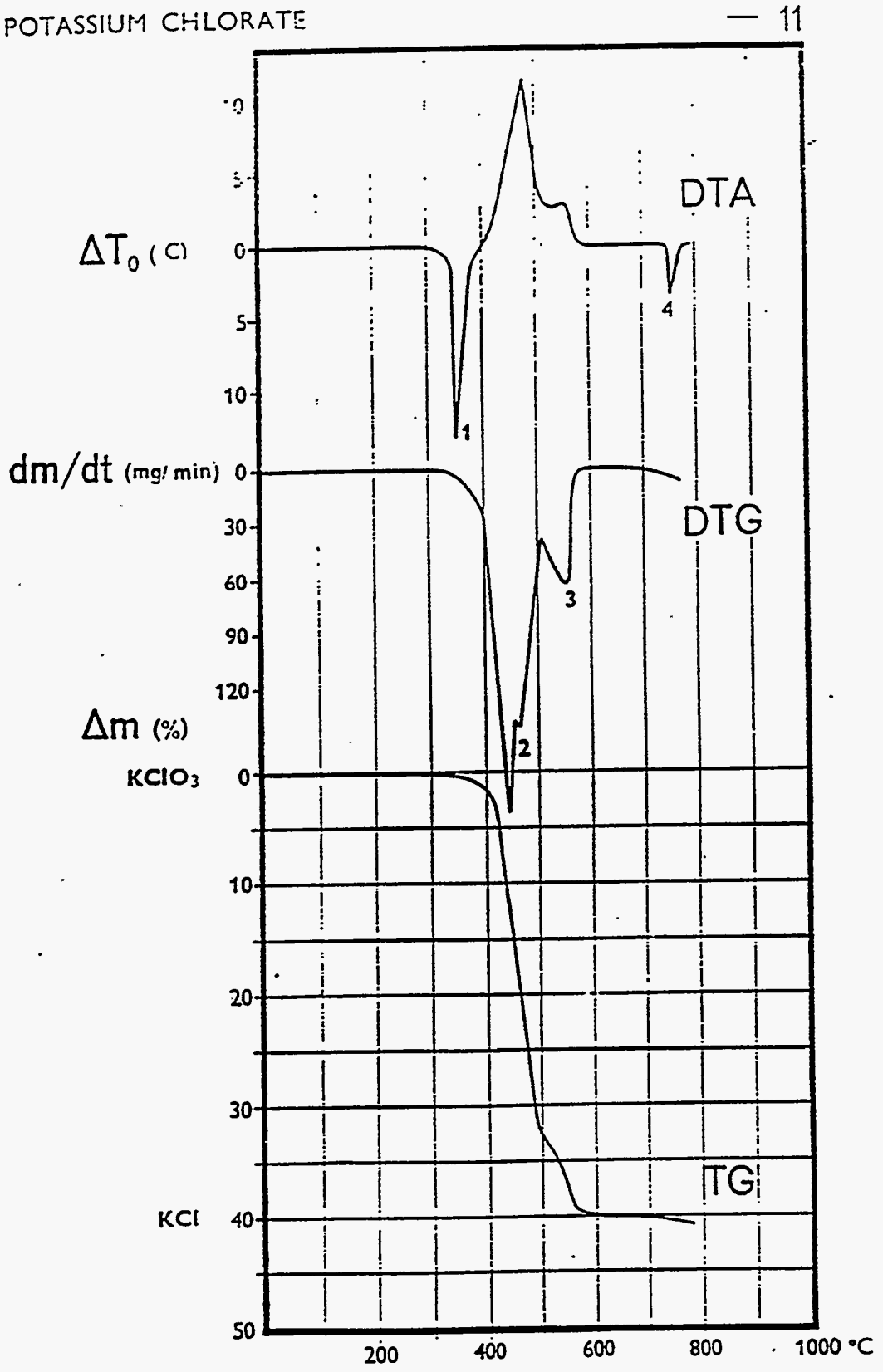

Figure 6 TGA/DTA — Potassium Chlorate

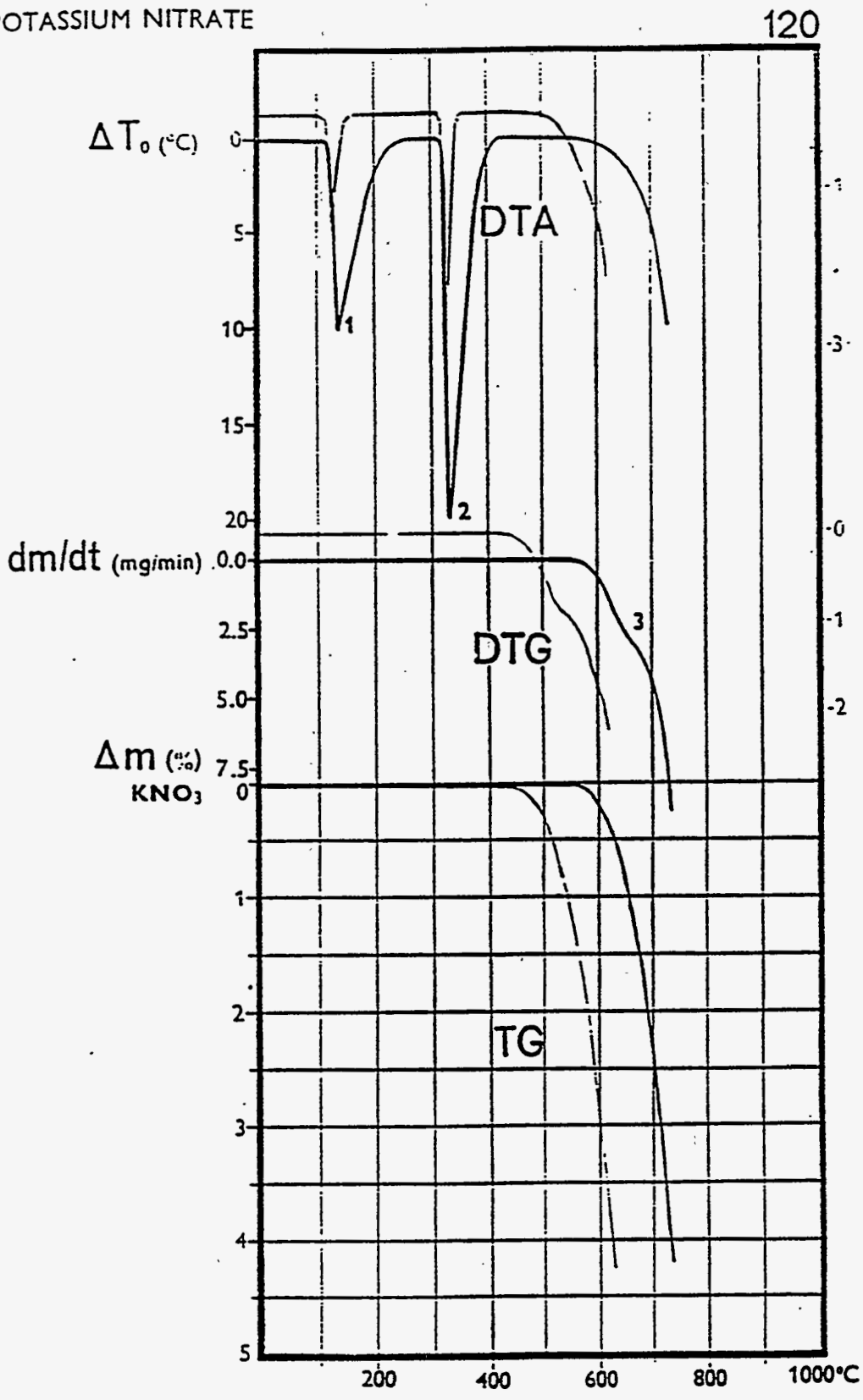

Figure 7 TGA/DTA — Potassium Nitrate

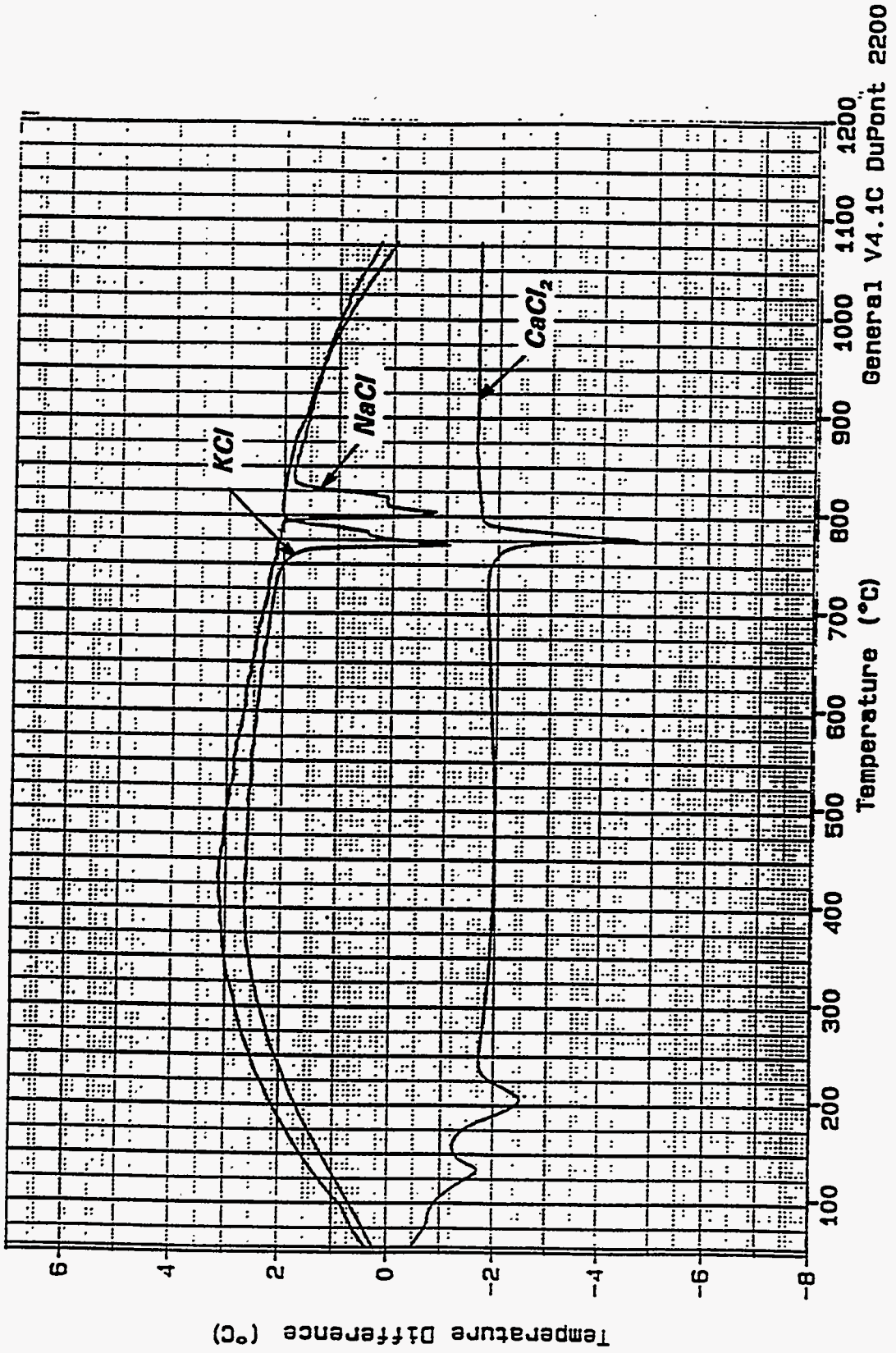

Figure 8 DTA Melting Temperatures for Pure Compounds of KCl, CaCl, and NaCl

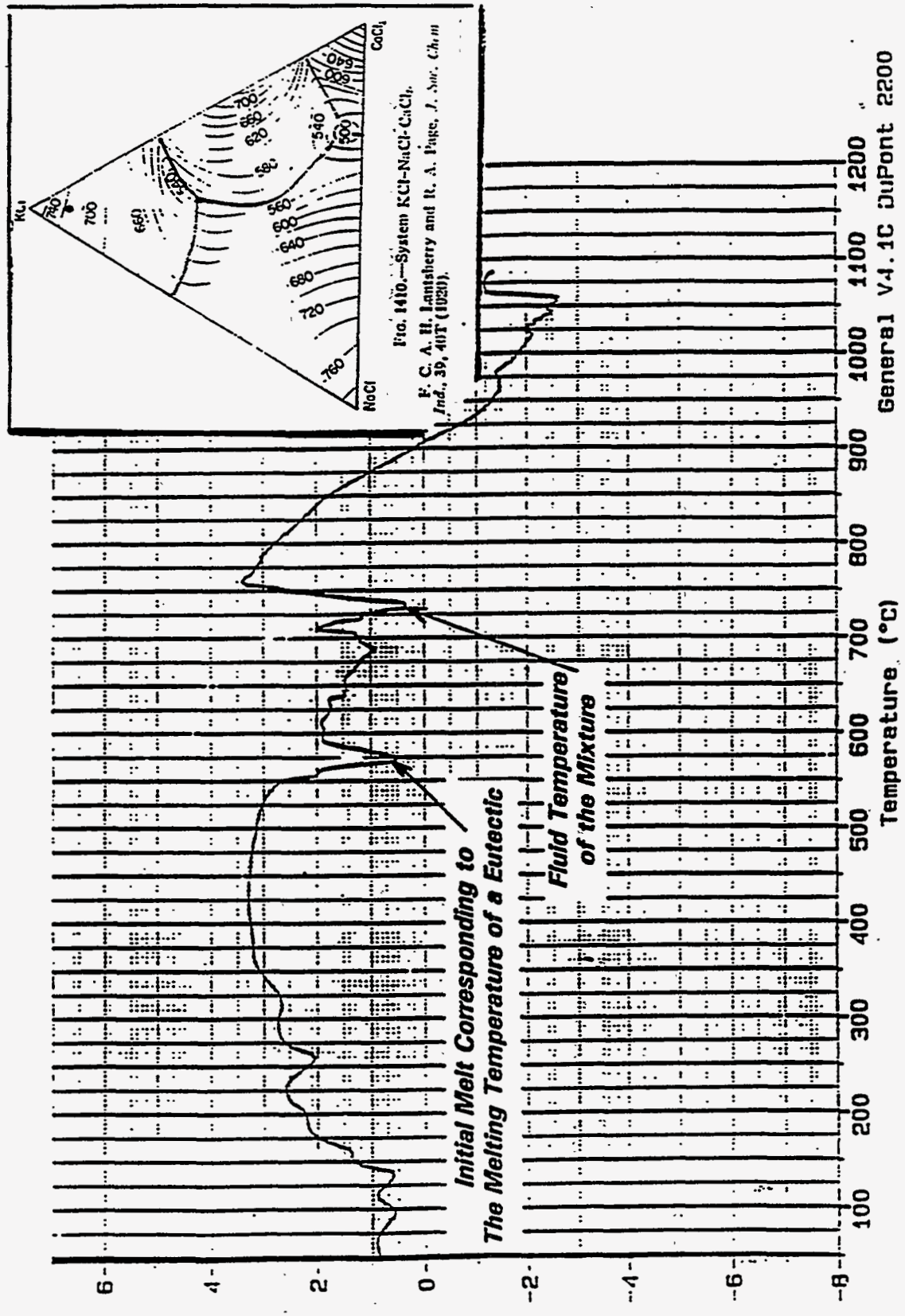

Figure 9 DTA of an 82% KCl/9% $CaCl_2$/9% NaCl Mixture

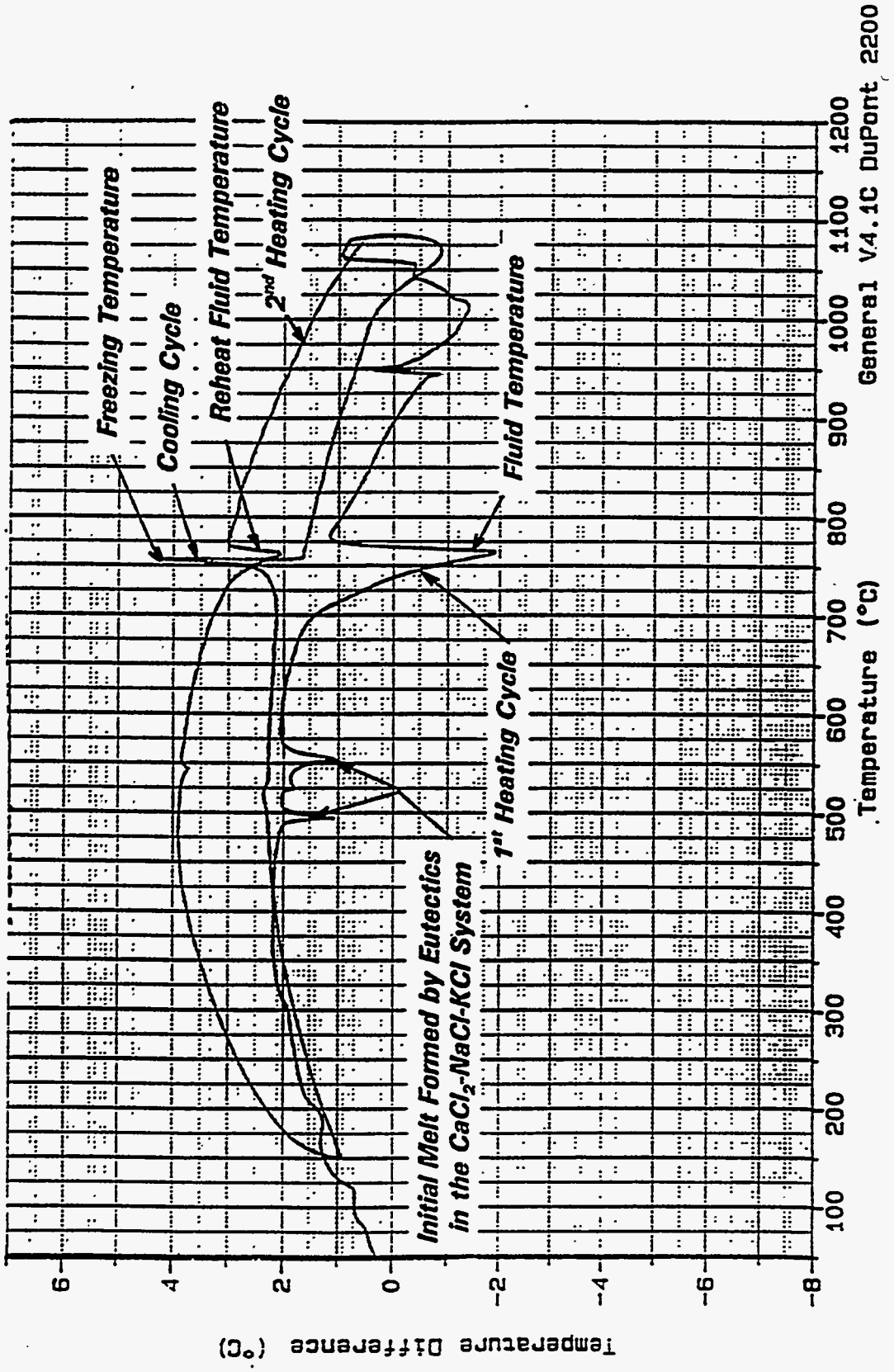

Figure 10 DTA of an 82% KCl/9% $CaCl_2$/9% NaCl Mixture Heated, Cooled and Reheated

Table 9 X-Ray Diffraction of Low-Temperature Ash

Biomass Sample		*Microbeam Technology*		*U.S. Bureau of Mines*
Waste Paper		**Major**	Aluminum — Al	Aluminum — Al
$\%K_{ash}$	0.2			
K_{ppm}	171	**Minor**	Calcite — $CaCO_3$	Calcite — $CaCO_3$
% LTA Loss @ 500°C	8		Rutile — TiO_2	Rutile — TiO_2
			Brindleyite — $(Ni_2Al)(Al,Si)O_5(OH)_4$	
		Trace		Clinochlore — $Mg_3{\cdot}13Fe_2O{\cdot}Al_{.87}Si_{3.3}Al_{.7}O_{10}(OH)_8$
80% Wood/20% Straw		**Major**	Quartz — SiO_2	Quartz — SiO_2
$\%K_{ash}$	6.7			
K_{ppm}	5138	**Minor**	Plagiocase — $(Ca,Na)(Al,Si)_4O_8$	Albite — $(Ca,Na)(AlSi)_4O_8$
% LTA Loss @ 500°C	9		Calcite — $CaCO_3$	
			Clinopyroxene — $Ca(Fe,Mg,Al)Si_2O_6$	
		Trace		*Niter — KNO_3*
				Potassium Chlorate — $KClO_4$
Wood/Almond		**Major**	Quartz — SiO_2	Quartz — SiO_2
$\%K_{ash}$	7.4			
K_{ppm}	4610	**Minor**	*Niter — KNO_3*	Albite $(CaNa)(Al,Si)_4O_8$
% LTA Loss @ 500°C	11		Plagioclase $(Ca,Na)(Al,Si)_4O_8$	
		Trace		Magnesioriebeckite — $(Na,Ca)(MgFe)_5Si_8O_{22}(OH)_2$
Rice Straw		**Major**	Quartz — SiO_2	*Niter — KNO_3*
$\%K_{ash}$	13.5			Potassium Chlorate — $KClO_4$
K_{ppm}	25,771	**Minor**	*Niter — KNO_3*	Quartz — SiO_3
% LTA Loss @ 500°C	15		Potassium Chlorate — $KClO_4$	Anorthite — $(Na,Ca)(AlSi)_4O_8$
			Potassium Hydroxide — K(OH)	

Table 9 X-Ray Diffraction of Low-Temperature Ash (Cont)

Biomass Sample		*Microbeam Technology*	*U.S. Bureau of Mines*
Wheat Straw $\%K_{ash}$ 22.8 K_{ppm} 16,758 % LTA Loss 10 @ 500°C Chem Frac K_{ppm} 14,690	**Major**	Quartz — SiO_2	Arcanite — K_2SO_4
	Minor	***Niter — KNO_3*** Sylvite — KCl ***Potassium Chlorate — $KClO_4$***	Quartz — SiO_2 Sylvite — KCl
Olive Pits $\%K_{ash}$ 5.2 K_{ppm} 1170 % LTA Loss 20 @ 500°C Chem Frac K_{ppm} 2405	**Major**	Quartz — SiO_2	Quartz — SiO_2
	Minor	Plagiocase — $(Ca,Na)(AlSi)_4O_8$ Calcite — $CaCO_3$ ***Potassium Chlorate — $KClO_4$*** Sodium Sulfate — Na_2SO_4	***Niter — KNO_3*** ***Potassium Chlorate — $KClO_4$***
	Trace		Rustomite — $Ca_4Si_2O_7(OH)_2$
Almond Shells $\%K_{ash}$ 49.6 K_{ppm} 7588 % LTA Loss 23 @ 500°C	**Major**	***Niter — KNO_3***	***Niter — KNO_3***
	Minor	Potassium Hydroxide — KOH ***Potassium Chlorate — $KClO_4$*** Langbeinite — $K_2Mg_2(SO_4)_3$	Quartz — SiO_2 ***Potassium Chlorate — $KClO_4$***
Almond Hulls $\%K_{ash}$ 50.9 K_{ppm} 24,788 % LTA Loss 26 @ 500°C Chem Frac K_{ppm} 20,723	**Major**	***Niter — KNO_3***	***Niter — KNO_3***
	Minor	Potassium Hydroxide — K(OH) Langbeinite — $K_2Mg_2(SO_4)_3$ Potassium Oxide — KO_2 ***Potassium Chlorate — $KClO_4$***	***Kalicinite — $KHCO_3$***
	Trace		Quartz — SiO_2 Potassium Chlorate — $KClO_4$

Consequently, endotherms below 750°C (1383°F) are questionable unless they can be isolated and directly associated with a specific mineral. Although x-ray diffraction and thermal analysis has discounted low-temperature ashing as a viable test for commercial characterization of biomass, the analysis has confirmed the partitioning of the alkalies into volatile species associated with potassium and non-volatile stable silicates associated with sodium. It has also identified low-melting species due to sodium silicates and a loss of ash at very low temperatures. Between 100-1000°C (212-1832°F) any loss in ash is primarily due to decomposition of the nitrates and chlorates, and hence in nitrogen and chlorine. Below 500°C (932°F), the potassium nitrates and chlorates are stable and the potassium levels reported by chemical fractionation and conventional ashing techniques apparently agree. Between 500°C (932°F) and 1000°C (1832°F), there is some uncertainty about the disposition of the potassium. This should be investigated by a mass spectrometer, or FT-IR, in conjunction with TGA. Care should be taken in selecting a procedure that will not require further heating of the ash during elemental analysis, such as formation of a bead, to avoid loss of the potassium.

GENERAL COMMENTS ON FUEL CHARACTERIZATION

The fuel analysis appearing in Tables 1 and 2 indicate the biomass fuels examined are low in sulfur, contain modest to large concentrations of chlorine, and very large concentrations of potassium. Calcium is also generally high and silicate may be very high or low depending upon the biomass specie. Agriculture residues may contain high phosphorous. There appears to be three groups of biomass (i.e., high silica, potassium and calcium; low silica, high potassium and calcium; and low silica, high potassium, calcium and phosphorous). Consequently, the nature of slagging and fouling may vary substantially according to type.

In the absence of sulfur, the low-silica/high-calcium/high-potassium wood-type biomass should cause little to no problem as the potassium forms oxides and hydroxides with very high vapor pressures and thus remain in a volatile state to very low temperatures, as shown in Figure 11. The use of a supplemental fuel such as oil, or disposing of waste gases or solids containing sulfur causes the formation of SO_2 and SO_3 at the tube surface, which in turn promotes the deposition of low-melting sulfates. Fouling will certainly be encountered.

The high-silica fuels containing substantial concentrations of potassium are subject to slagging as they form potassium silicates with potentially low-melting eutectics--see Figures 12 and 13.[2] The potassium is absorbed on the surface and diffuses into the core of the particle, as illustrated by Jackson in Figure 14.[3] This generates a particle with a wet, viscous surface at temperatures much below that

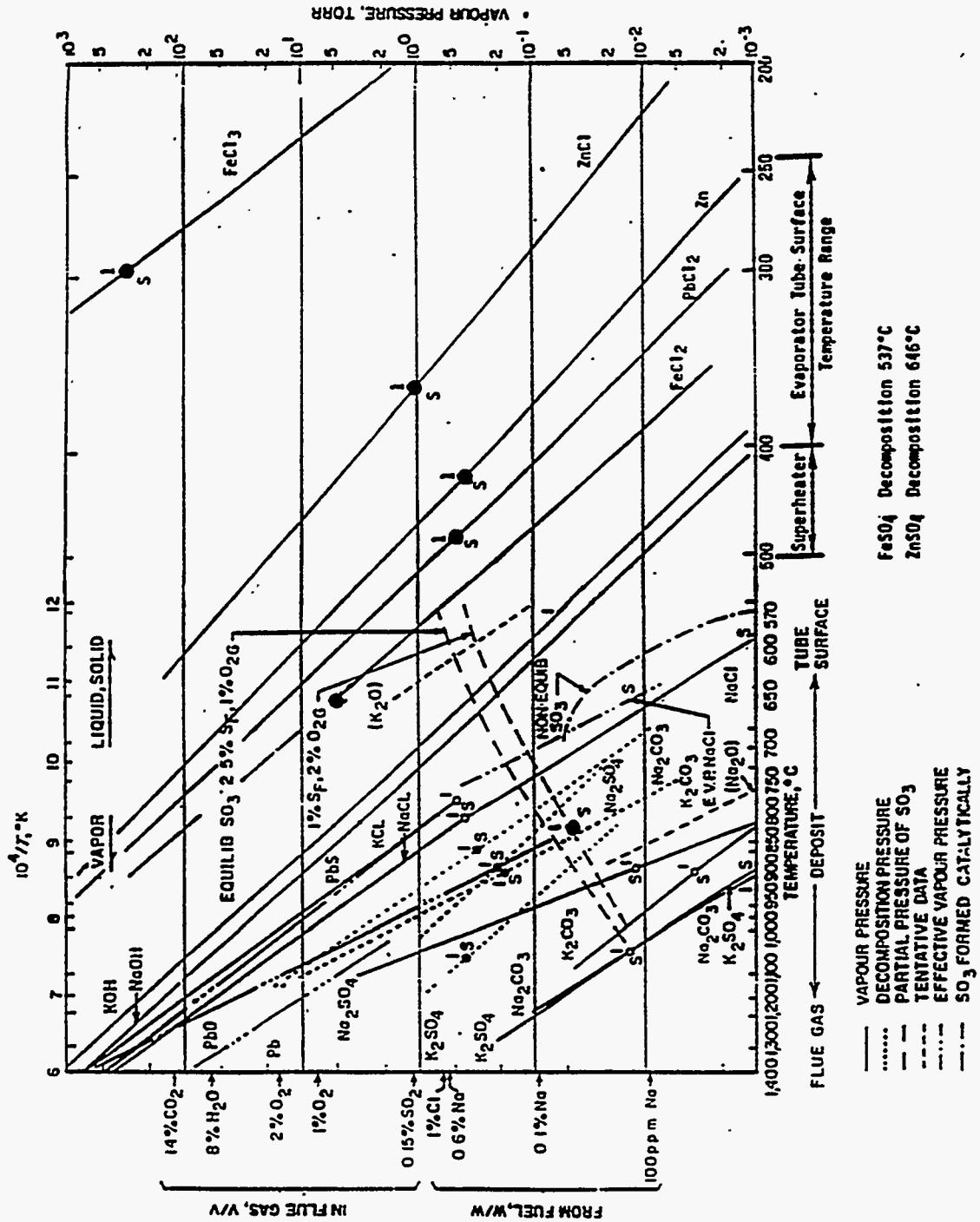

Figure 11 Vapor and Decomposition Pressures of Sodium and Potassium Compounds, and Partial Pressues of Sulfur Trioxide

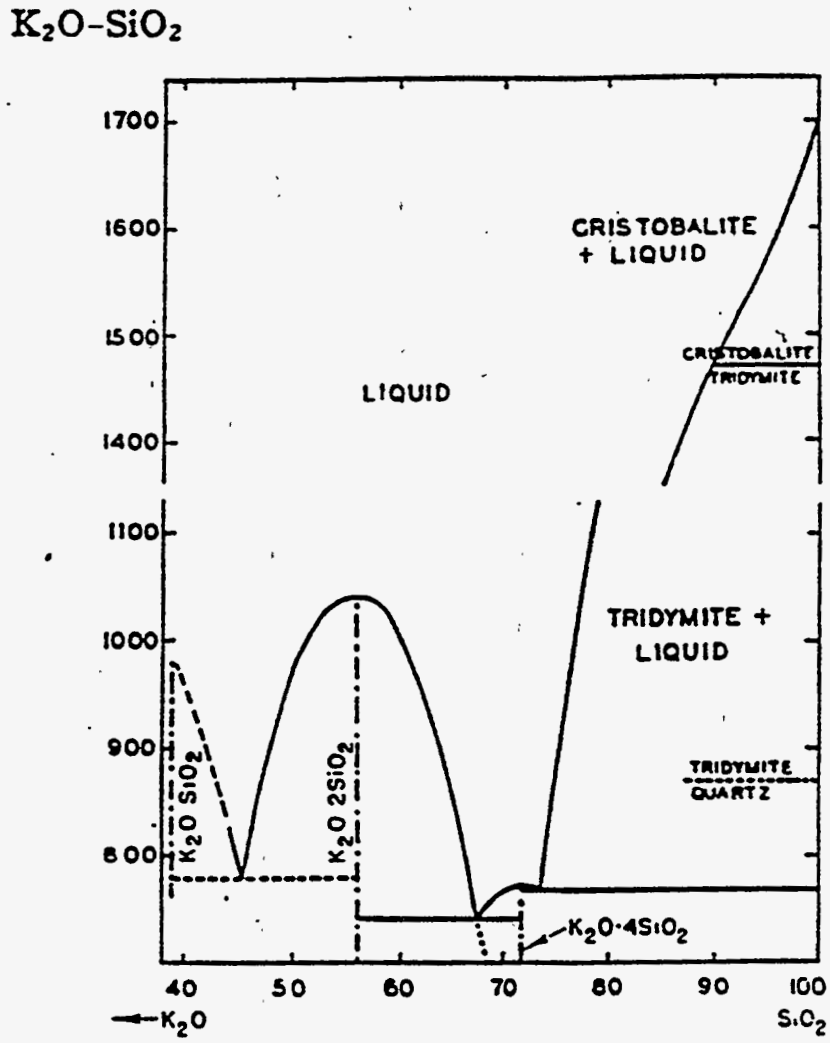

Figure 12 System SiO_2-J_2O·SiO_2
[F C. Kracek, N. L. Bowen, and G. W. Morey, J. Phys. Chem., 41, 118 (1937)]

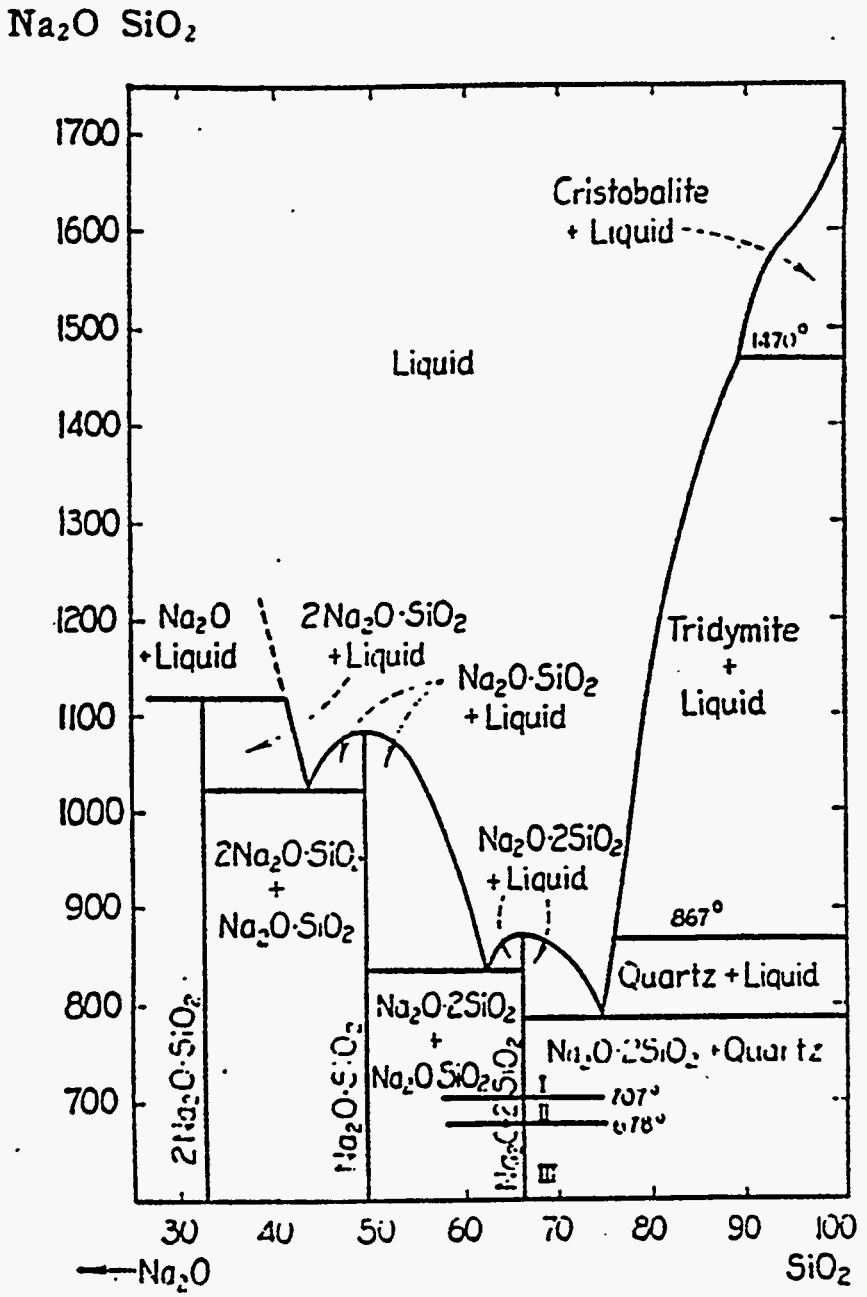

Figure 13 System SiO_2-$2Na_2O \cdot SiO_2$
[F. C. Kracek, J. Phys. Chem., 34, 1588 (1930); J. Am. Chem. Soc., 61, 2869 (1939)]

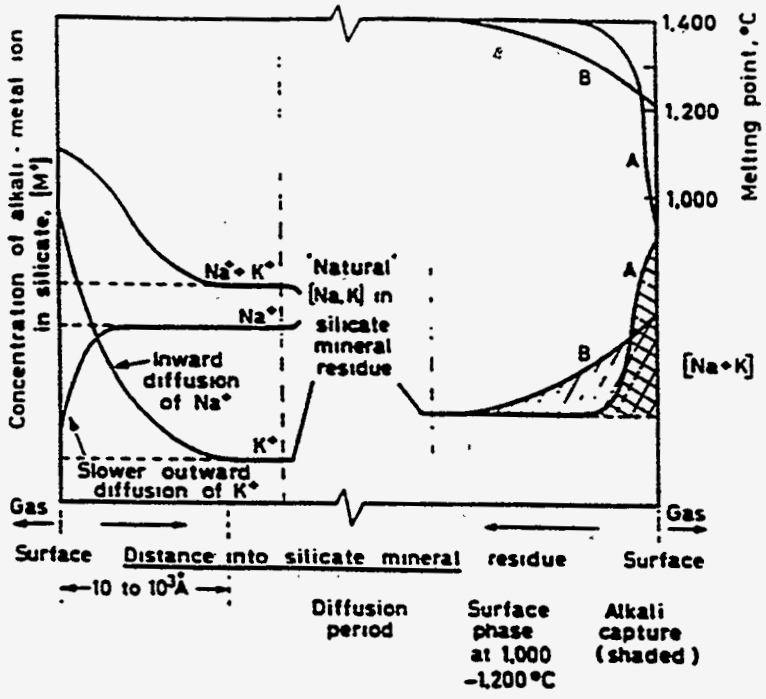

Figure 14 Reaction of Alkali Metals at Surface of Fused Silica Particles

predicted by ASTM ash fusion temperatures. Deposition in the form of a slag or sintered ash results. Slagging will be accompanied by fouling at gas temperatures as low as 676°C (1250°F). If sulfur is introduced with a secondary fuel, at least one fuel in this group was enriched with a sodium-bearing silicate. The latter has a propensity for forming low-melting species, but possibly not as low as one created by the absorption of an alkali on the surface. In the presence of high levels of Cl, an ion-exchange will occur with the liberation of the alkali, free to form a silicate at the tube surface. Hence, a situation is created for forming the corrosive alkali trisulfates.

High phosphorous is somewhat of an unknown. Formation of phosphoric acid during combustion can result in the formation of calcium phosphates, which have a substantial array of eutectics and intermediate compounds depending upon the concentration of P_2O_5.

Chlorine in the fuel may also be responsible for corrosion. At levels exceeding 3000 ppm, Cl will be responsible for tube wastage under reducing conditions or cycling, oxidizing reducing conditions. The mechanism is not clearly understood. Figure 15 [4,9] shows the linear dependency of corrosion rate on Cl, while Figure 16

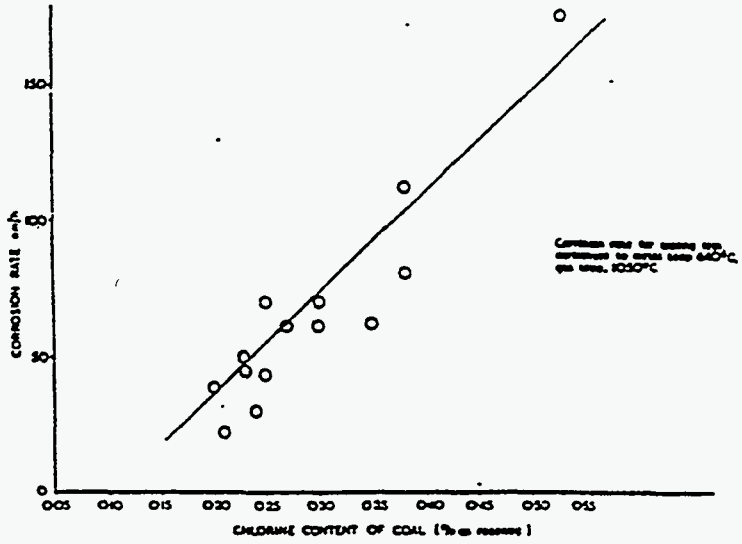

Figure 15 The linear Dependence of Corrosion Rate on Coal Chloride Content for Austenitic Steels [4,9]

demonstrates its dependency on CO.[4,9] Krause, Grabke, and Mayer report disruption of a protective oxide layer by HCl.[4-9] The porosity increases with an increase in HCl concentration.[6] At 2 volume percent, the layers are completely destroyed. Since $FeCl_2$ is found in the corrosion product at lower temperatures, one must conclude that Cl, which forms preferentially over HCl under reducing conditions, was present at some point in time. Brown clearly shows that Cl corrodes steel rapidly at the lower temperature--see Figure 17.[8] Krause indicates cyclic reaction can occur beneath the deposit with the chlorine attacking the tube metal to form more FeCl.[5]

$$2/3\ FeCl_2 + 1/2\ O_2 \rightarrow 1/3\ Fe_2O_3 + Cl_2$$
$$\uparrow \qquad\qquad\qquad\qquad\qquad\qquad \downarrow$$
$$\leftarrow\ Fe\ \leftarrow$$

Under reducing conditions, Brooks and Meadowcroft have shown that the corrosion rate due to CO is enhanced by the presence of Cl. At concentrations of HCl exceeding 200 ppm, there is a transition from parabolic to linear kinetics, with little further increase in rate for higher concentrations of HCl--see Figure 18.[9] The increase in corrosion resulting from the presence of HCl in the reducing atmosphere was attributed to oxidation/sulfidation promoted by scale disruption through $FeCl_2$ formation and volatilization.

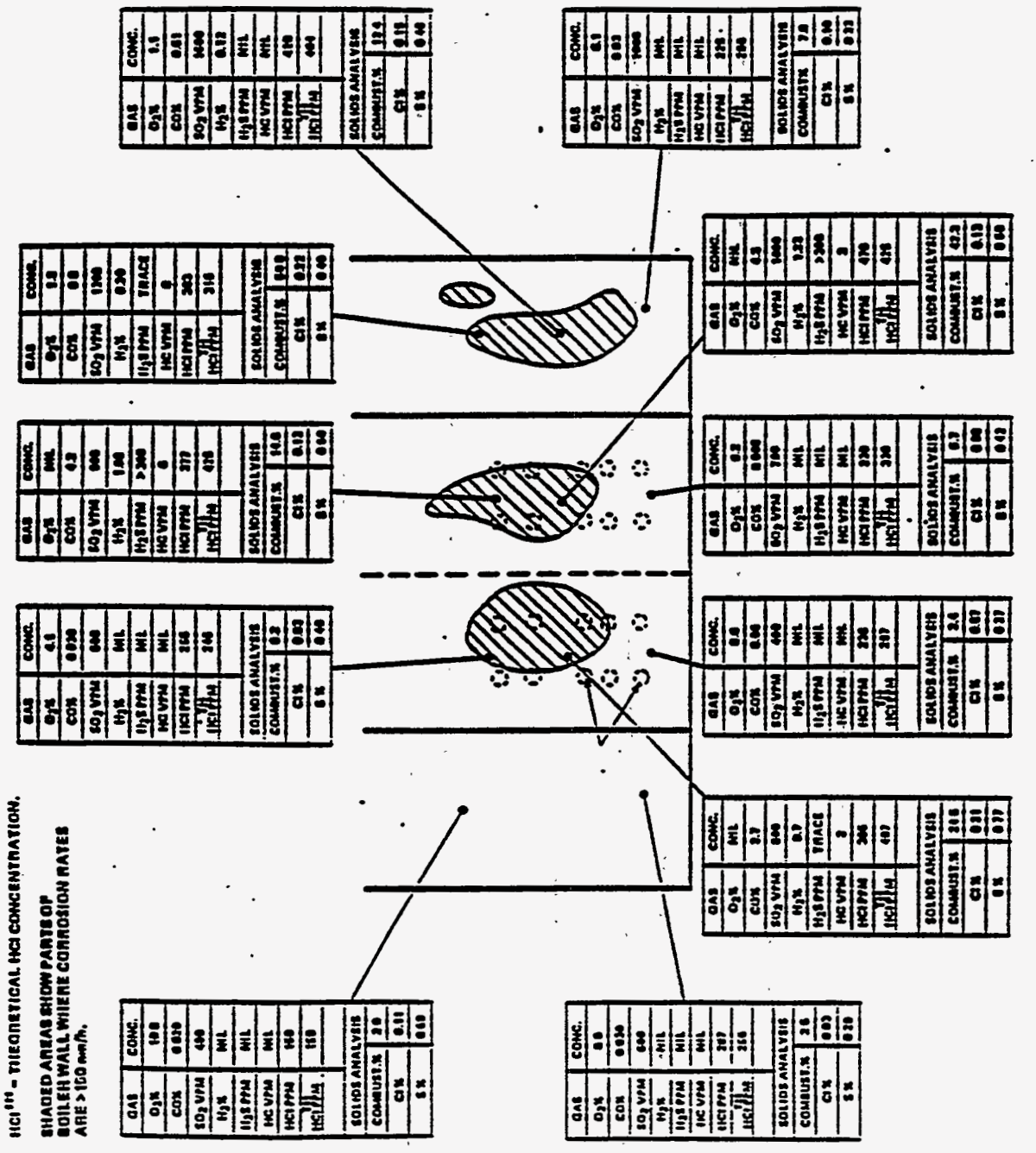

Figure 16 Field Evidence of Occurrence of Chloride Attack under Localized Reducing Conditions (Lees and Whitehead [10])

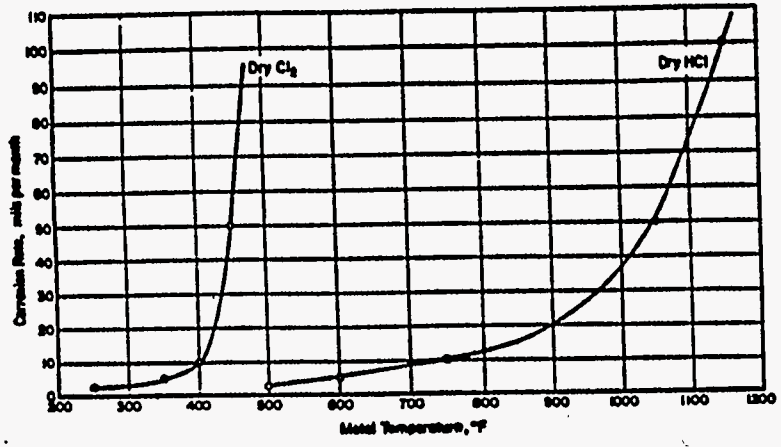

Figure 17 Corrosion Rates of Carbon Steel in Chlorine and HCL as a Function of Temperature[7]

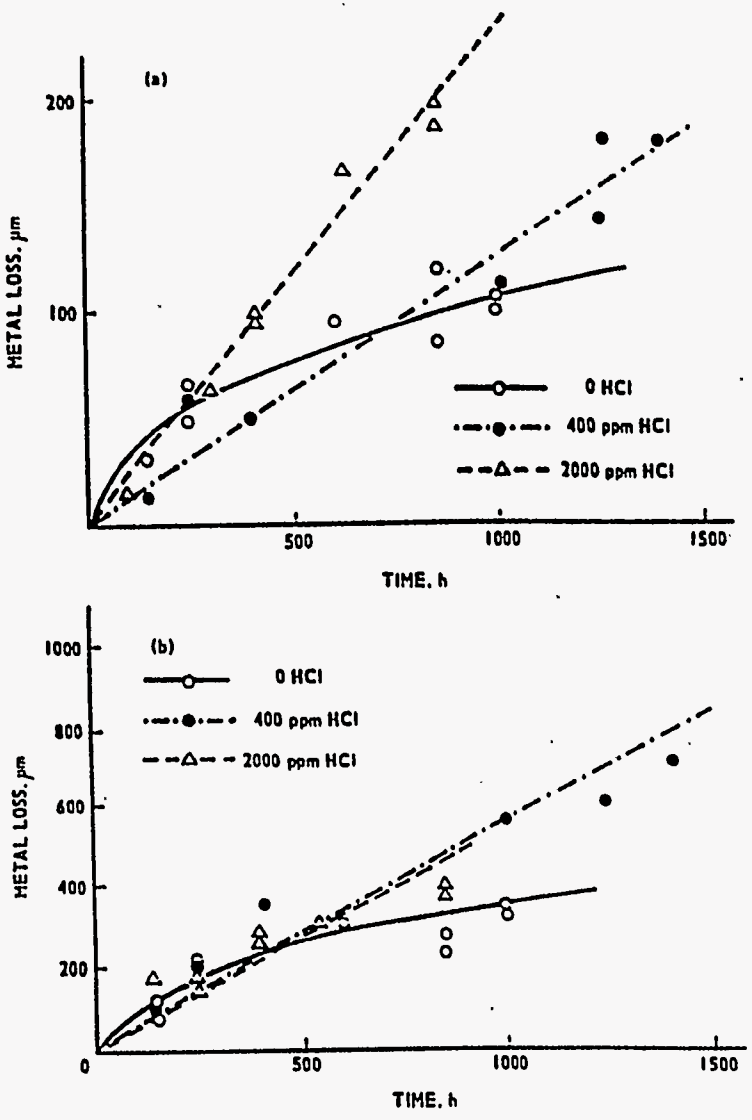

Figure 18 Metal Loss Data for Mild Steel in N_2-10%CO-10%N_2O-0.5%SO_2 Concentration as Shown [(a) 400°C, (b) 500°C] [4,9]

Chlorine may also cause high-temperature corrosion due to the fluxing action of molten salts of heavy metals. Chlorine can also contribute to alkali trisulfate attack by release of potassium and sodium from silicates in the presence of SO_2/SO_3.

The specific mechanism of corrosion in biomass plants should be defined as well as the associated operating and design conditions. At times, corrosion can be avoided by good operating practice and exotic alloys need not be used.

Ash fusion temperatures have been used since the turn of the century to predict the stickiness of fly ash and hence it potential to cause slagging. Furnace exist temperatures are generally based on these temperatures. As shown in Figure 19, numerous correlations have been developed to expressed these fusion temperatures in terms of the ash chemistry and thus aid in the selection or altering of fuels. A plot of Osman's data, illustrated in Table 10 for 26 different biomass species, indicates biomass behaves quite differently from coal.[11,12] There are three different categories of biomass as previously discussed, and the samples chosen represent several different types of biomass. The ash fusion temperatures are subject to considerable error due to the loss of alkali during ashing. Those ashes high in alkali have meaningless fusion temperatures as the alkalies are lost during combustion, leaving a fly ash with a high melting temperature. This temperature may be altered subsequent with the re-absorption of a portion of the alkalies during quenching associated with heat recovery.

TRANSFORMATION OF MINERAL MATTER AND FIRESIDE DEPOSITION

An understanding of the fireside behavior of biomass ash requires an understanding of the mineral matter and impurities in biomass as well as the transformations they undergo during combustion and the mechanism by which they deposit.

Mineral Matter

Marschner, as reported by Baxter, has indicated that sulfur, chlorine, phosphorous, and potassium are associated with the organic portion of the biomass.[13]

- Sulfur occurs as sulfate and organic sulfur. The former increases with increasing sulfate in the nutrient supply.
- Chlorine occurs dominantly in the form of the chloride ion and serves the primary role of balancing charge. Its concentration is closely related to the nutrient composition of the soils. The levels of chlorine required for optimal plant growth are usually far less than the levels available in the nutrients. Therefore, chlorine levels observed in these and other data are likely to be more indicative of local soil conditions than plant physiology.

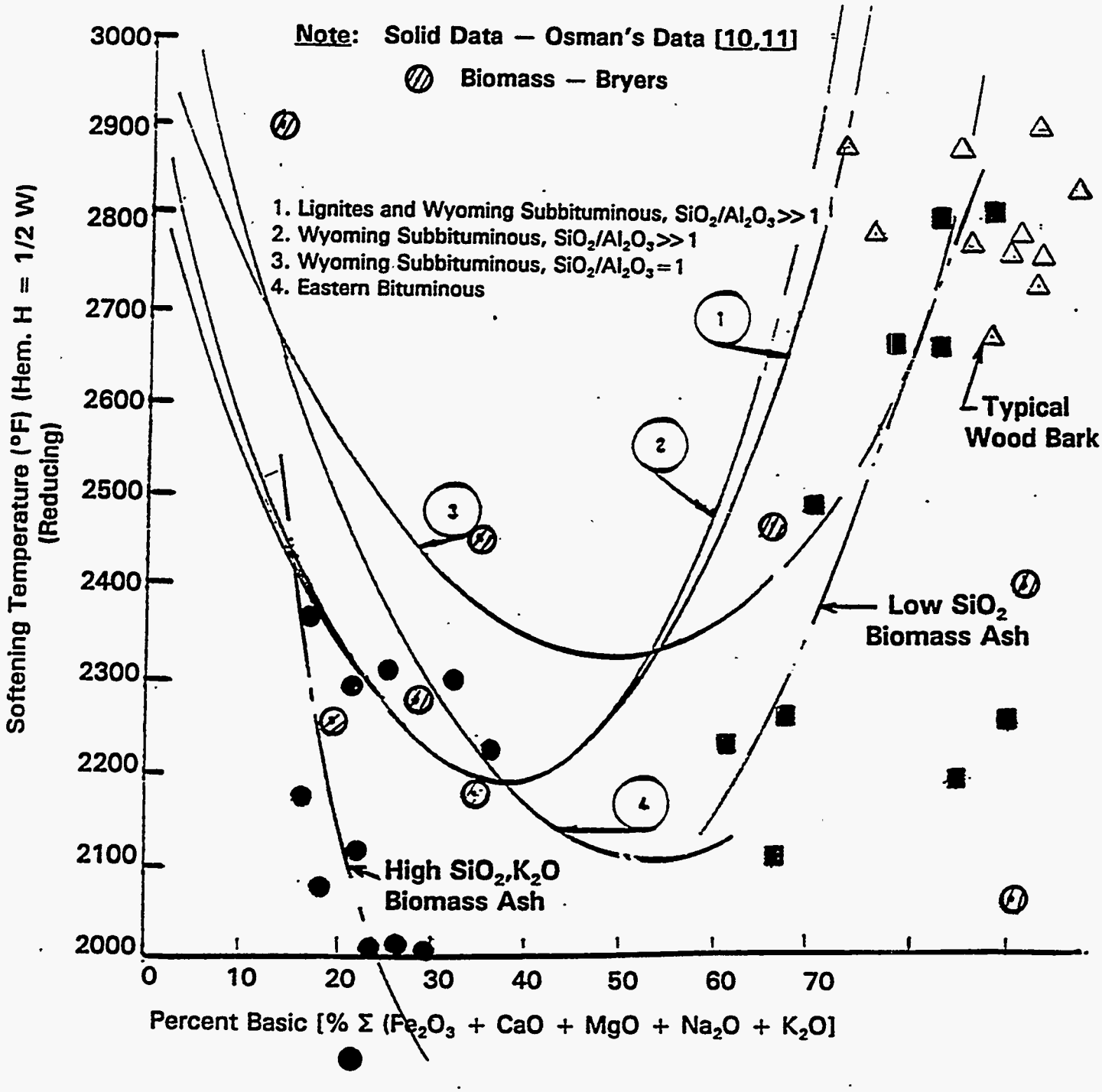

Figure 19 Influence of Percentage of Basic Constituents in Ash on Ash Softening Temperatures under Reducing Conditions for Different Ranks of Coal

Table 10 Computer Oxide Form of Test Sampels (wt%)
By E. A. Osman[10,11]

	SiO_2	Fe_2O_3	MgO	CaO	ZnO	K_2O	Na_2O	SO_3	P_2O_5	Total
Bean straw (I)	29.9	2.7	0.9	4.67	0.03	22.34	0.52	4.7	2.29	68.05
Safflower	20.46	1.2	6.1	10.84	0.03	30.01	0.91	8.36	3.64	81.65
Rice hulls	94.6	0.03	0.02	0.25	0.00	2.4	0.135	2.24	0.46	100.12
Alfalfa	7.96	0.51	2.87	11.2	0.125	33.97	3.64	4.64	10.46	75.46
Cotton gin trash	23.2	1.93	2.87	7.18	0.187	13.00	1.59	4.24	10.00	64.20
Barley straw	44.7	2.6	4.84	3.22	0.125	8.01	5.25	1.8	11.56	81.11
Corn stalks	50.7	3.14	3.08	3.9	0.95	10.3	0.53	11.08	10.00	93.68
Rice straw	75.2	0.58	0.83	0.72	0.00	11.9	0.28	1.51	8.87	99.89
Bean straw (II)	32.7	3.93	3.65	6.3	0.15	25.3	0.82	2.28	7.3	82.43
Wood chips	8.3	10.0	6.22	18.61	0.193	11.8	1.32	9.0	6.87	71.61
Corn fodder	55.3	2.4	3.32	1.05	0.087	9.59	0.73	3.48	2.98	78.95
Paper pellets	57.2	4.29	0.83	0.15	0.31	1.85	5.09	4.0	4.46	78.19
Corn stalks (ex.)	63.3	4.72	4.78	0.56	0.00	8.37	0.47	7.2	2.06	91.46
Almond shell	22.6	3.77	2.49	12.27	0.05	14.14	5.08	8.0	5.5	73.90
Corn cobs	40.3	4.06	2.49	1.27	0.22	2.04	1.19	8.74	6.87	86.53
Manzanita chips	5.97	2.86	4.94	24.49	0.25	10.96	2.85	6.74	8.2	67.16
Tree pruning	9.95	1.94	8.29	19.87	0.06	12.66	1.48	19.72	4.96	85.93
Walnut shell	13.6	2.44	3.65	7.0	0.44	21.50	1.08	8.48	4.58	62.92
Olive pits	10.5	2.2	3.48	25.89	0.12	3.13	7.60	17.2	7.56	77.74
Almond shells	18.6	3.83	1.99	16.0	0.23	14.7	5.86	17.48	7.79	86.48
Corn stalks	71.7	7.1	2.7	0.46	0.02	10.28	0.33	2.2	0.66	95.45
Cotton stalks	33.0	2.8	6.05	3.56	0.07	21.40	1.374	6.55	6.4	83.57
Rice mix	75.0	0.47	2.5	1.1	0.00	15.85	0.54	1.0	1.1	97.56
Wheat + corn (1:3)	71.7	3.3	8.3	0.95	0.619	14.76	0.54	2.96	1.1	103.64
Rice straw (good bales)	78.3	0.36	2.0	0.7	0.00	13.0	0.43	1.69	0.8	97.78
Rice straw (decayed bales)	78.6	0.44	2.0	0.88	0.00	14.50	0.44	1.83	0.9	99.59

- Phosphorous exists in its most oxidized form. It is primarily introduced in the form of dihydrogen phosphates ions ($H_2PO_4^-$) and either remains in inorganic form or is incorporated into organic structures by forming esters or pyrophosphates.
- Potassium occurs as a univalent ion (K^+) that is highly mobile, with little structural function. Potassium correlates with plant metabolic activity. It regulates osmotic and ionic potential in the cytoplasm and plays an active roles in enzyme activation, membrane transport, and stomatal regulation. Because of these roles, they are most often found in regions of most vigorous plant growth.
- Sodium is not considered essential for plant growth. It may substitute for potassium in certain roles. It is usually considered toxic in high concentrations and rarely exceeds 2% in the plant.
- Calcium occurs in the axoplasm where it forms exchangeable bonds with the cell wall, permitting cell wall stiffening.
- Iron forms cleats that are active in transport and a reversible oxidation-reduction reaction. Iron is concentrated in the leaves in the chloroplast.
- Alumina is toxic to most plants and occurs in small quantities.[13]

Minerals

Silicon is the most prevalent inorganic mineral species. Silicon is incorporated in plants by absorption of silicic acid from soil solution. It occurs in plants are macronutrient levels (0.1-10% dry basis). The silicon is deposited as a hydrated oxide, $SiO_2 \cdot nH_2O$, usually in amorphous, but occasionally in crystalline, forms. Other minerals may be introduced with the biomass as extraneous species acquired from the soil or other sources during handling. These minerals frequently include clays peculiar to the area in which they are harvested or brine, NaCl, intrusions encountered during transportation. The sodium sulfate in the almond hulls would appear to have been introduced during processing. Compared to grasses, wood appears to be free of silicon and the total ash level is very small.

During combustion, the mineral matter generally referred to as ionically or organically-bound inorganic species (i.e., K, Ca, P, Fe, S and Cl) are released as a vapor phase. Depending upon how they are released and during which phase of combustion (i.e., devolatilization or char), a portion may be absorbed by the minerals present [i.e., SiO_2 or included extraneous clay (dirt)]. TGAs of the biomass appearing in Figure 19 indicate less than ~15% char is generated, except for biomass such as olive pits or waste paper. As shown in Figure 20, the K, P, Ca and Cl are oxidized,

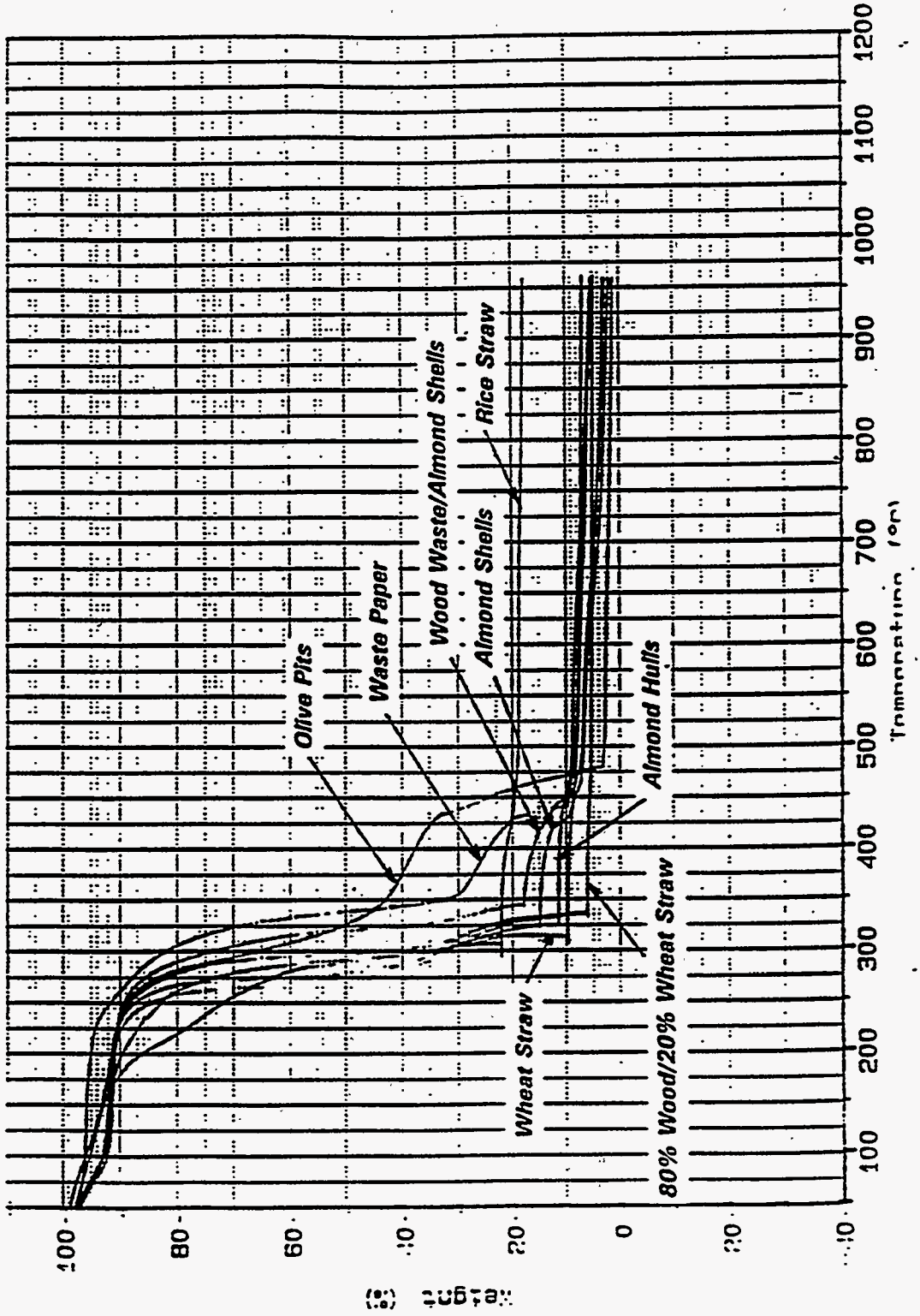

Figure 20 TGA Composition Profiles on Various Types of Biomass under Air at 20°C/Min

chlorated or sulfated, as the case may be, to form oxides, hydroxides and chlorides. As shown in Figure 21, these compounds all have high vapor pressures and remain in a gaseous state until cooled to very low temperatures. Equilibria in the presence of silica, chlorine and sulfur dioxide favors the formation of chlorides at high temperatures, silicates at intermediate temperatures, and sulfates at the lower temperatures, say 1000°C (1832°F) and lower.

The compounds formed and their level of concentration depends on the level of concentration of Cl, S, and O_2 in the gas stream. Being that Cl concentration is generally low, potassium will be absorbed by the silicates, creating a particle encapsulated by a viscous potassium silicate enriched with potassium. The level at the surface and hence its melting temperature and viscosity depend on the rate of absorption of potassium and counter-diffusion of potassium and silica to and from the core--see Figure 24. Potassium may also be absorbed on high-temperature surfaces of well-developed deposits or it may homogeneous condense in the present of SO_3 or SO_3 at lower temperatures as potassium sulfate. If this occurs in the gas stream, nucleation produces submicron particles that are subsequently agglomerates or scavenged by larger fly ash, deposited on cooler tube surfaces by thermophoresis, or leaves the boiler as a fume. Depending upon time and temperature, the potassium sulfate may also deposit directly on a tube surface, creating a low-melting sticky surface. Such a deposit will continue to grow until it reaches its dewpoint, at which time equilibria is reached and growth ceases. If, during the course of the formation of the deposits, discrete particles impinge upon the surface, they may become entrapped, permitting interaction of the potassium sulfate with the aggregate and allowing it to grow thicker.

Chlorides may form in a similar manner. However, their high vapor pressures, lower concentrations, and equilibria with other contaminants present produce a very narrow window for their deposition and collection. They may be confined to the external surfaces of low-temperature deposits [i.e., in the temperature range of 750-800°C (1382-1472°F)].

The minerals in the biomass (i.e., SiO_2 and $SiO_7(NaCa)(AlSi)_4O_8$ melt and agglomerate during combustion. They may be subject to some fragmentation of the mineral or biomass char. Upon cooling, they solidify. Some SiO vapor may be released during reducing conditions at high temperatures. The dry, pure species impact on heat-transfer surfaces and reentrain unless captured mechanically or in a viscous layer. At very high temperatures, some of the silicates may absorb potassium, forming a low-melting compounds described by the phase diagram in Figure 25. Whether or not the low-melting fly ash sticks and forms a deposit depends on the surface temperature, local temperature gradient, the level of local kinetic energy, and degree of supercooling of the depositing fly ash. Surface temperatures in excess of ~850°C (1600°F), such as exposed refractory, will certainly be good collectors of

Figure 21 Transformation of Mineral Matter in Biomass

impacting fly ash, particularly if exposed to gases with a low level of turbulence. Deposits may grow to great thicknesses on such surfaces due to low heat flux and flat temperature profiles, particularly if the deposit is viscous or in a semi-crystalline state over a wide temperature range.

Molten and supercooled fly ash depositing on cool surfaces stick and form either a frozen fused layer or sintered deposit. At high absorption rates (i.e., high flame temperatures), the ash experiences a steep temperature gradient due to the low thermal conductivity of dry sintered ash. Once the surface temperature reaches the initial deformation temperature of the lowest melting phase or the plastic range of the deposited ash, the thermal conductivity increases and the temperature gradients flattens, allowing the deposit to grow. Growth continues through the plastic range until the fluid temperature is reached. Equilibrium is reached once the fluid temperature is achieved at the surface and the flow away from the surface of molten slag equals the rate of ash deposition, as shown in Figure 22. The initial layer of dry sintered ash is primarily responsible for loss in heat transfer. The thickness of the deposit is primarily governed by the temperature range over which a multicomponent is plastic (i.e., the range over which the crystalline phase melts and goes into solution and the viscosity of the final molten phase).

FIELD EXPERIENCE

The mechanisms of deposition discussed above may be illustrated by deposits formed in the biomass steam generator, illustrated in Figure 23, firing a blend of wood and manure. The ash chemistry of the fuel is different than that of pure wood or grass in that it is rich in calcium, potassium and phosphorous--see table insert in Figure 23. The biomass steam generator is of a "folded furnace" design consisting of a radiant furnace upfired over a grate, followed by a down-fired convective furnace very similar to many low-pressure MSW steam generators. The 75-MW boiler operates at 1000 psi and 850°F superheat. The furnace exit was designed for 1750°F and 1260°F convection bank inlet. Oil-fired burners were installed in the upper furnace to compensate for unexpectedly high moisture. The oil contained 0.5% sulfur. Shortly after operation, gas temperatures to the furnace exit rose to 1850-2000°F, and those to the convection bank to 1650-1750°F due to the location of the oil burners and deposition of a highly refractory layer of K_2SO_4 on the convective furnace walls. By adding surface and relocation of the oil burners, operational problems have been overcome.

Sintered voluminous deposits initially formed on the screen tubes at the furnace exit and on the upper convective furnace walls subject to changes in direction of flow, as illustrated in Figure 24. A thin layer of deposit, 1/8 to 1-1/4" thick, lined

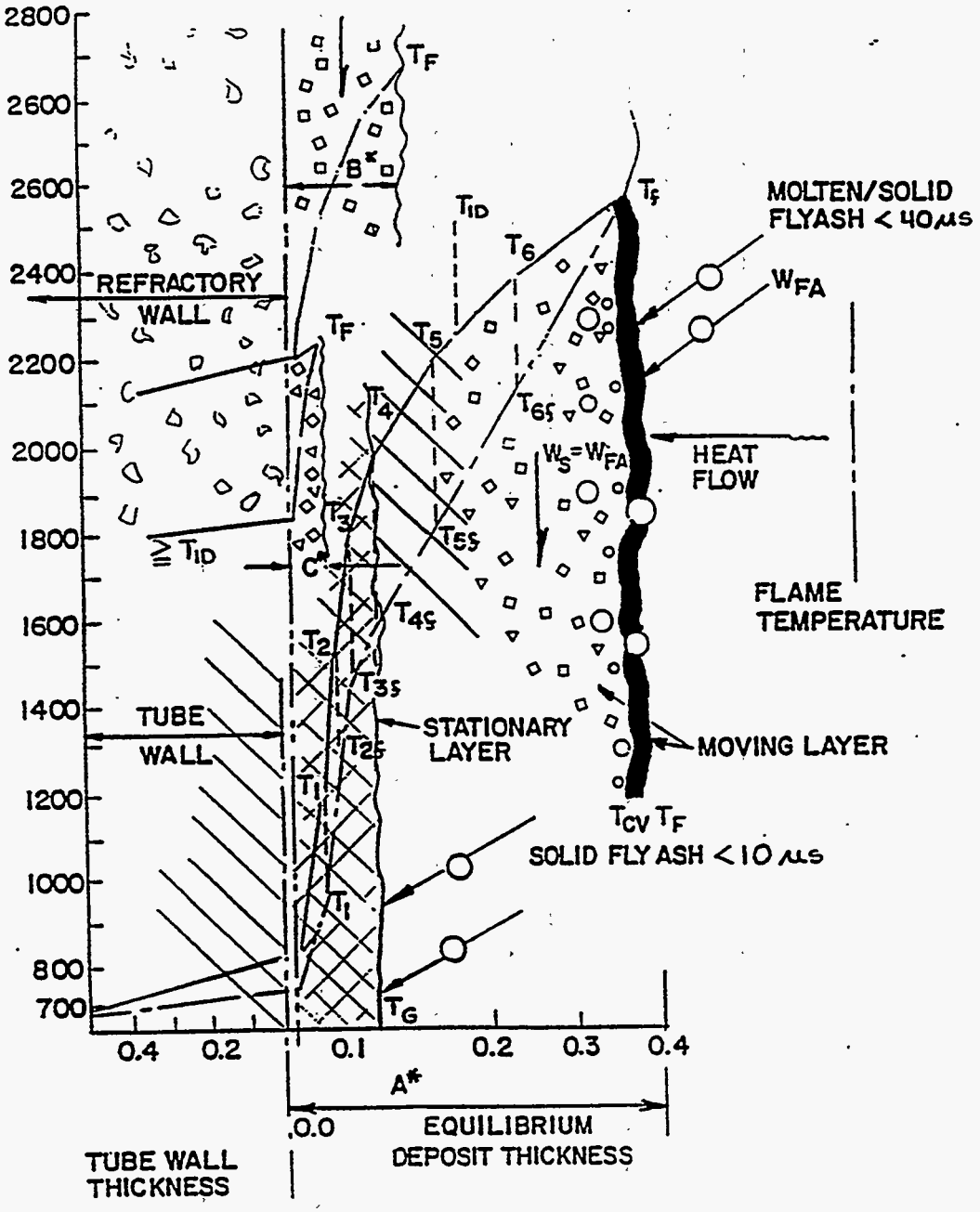

Figure 22 Temperature Profiles Through Slag on Refractory-Lined and Water-Cooled Furnace Walls

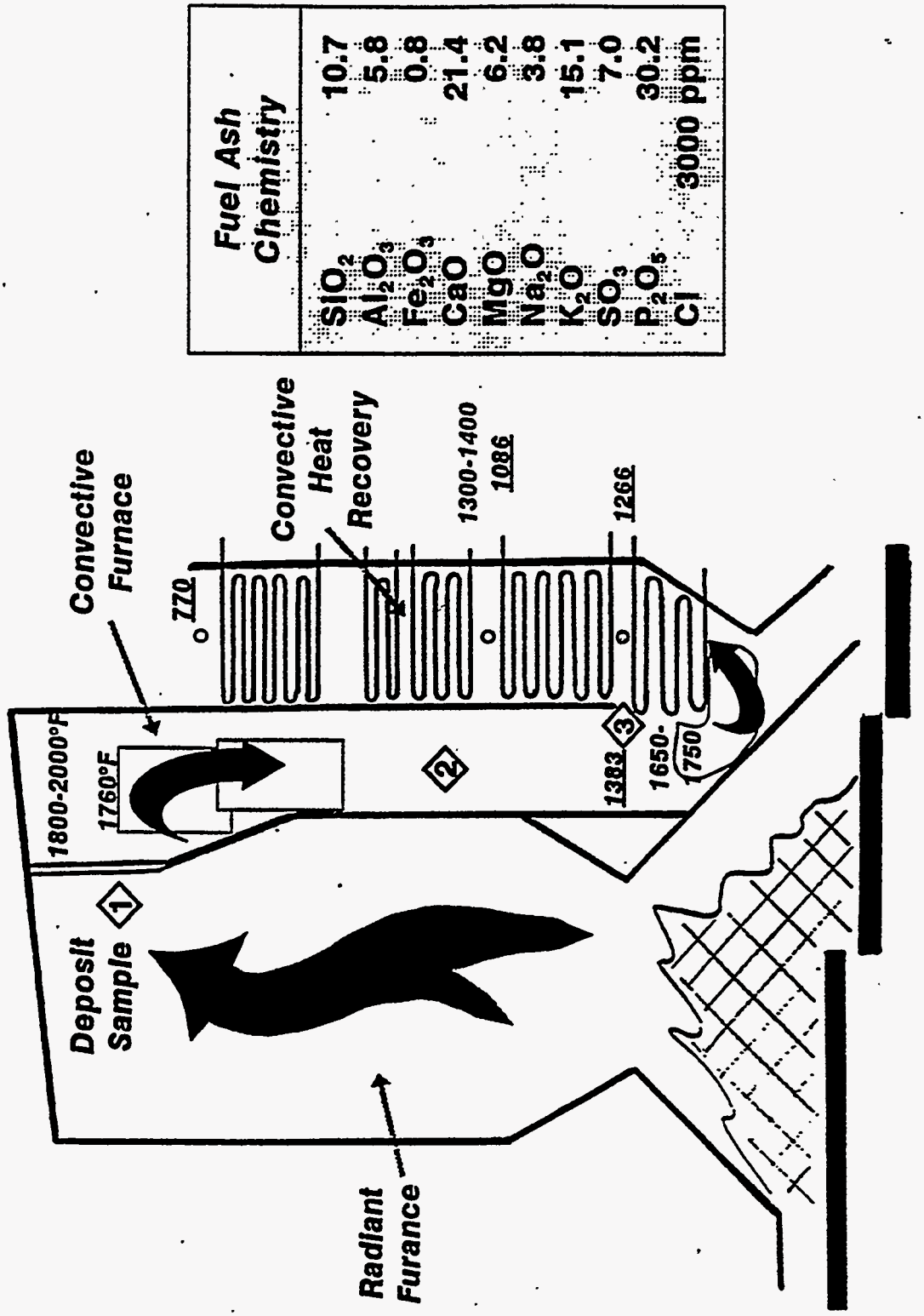

Figure 23 Biomass-Fired Steam Generator

Location 1
Figure 23

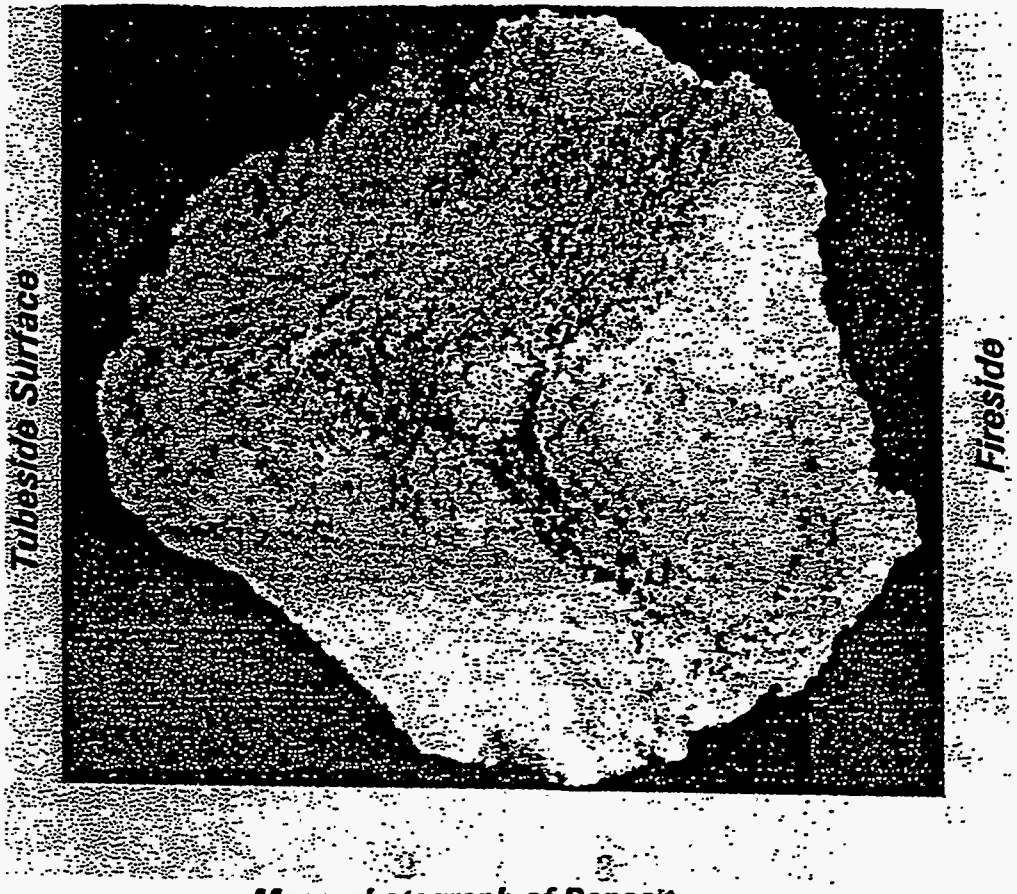

Macrophotograph of Deposit
Radiant Furnace Exit

Location 2

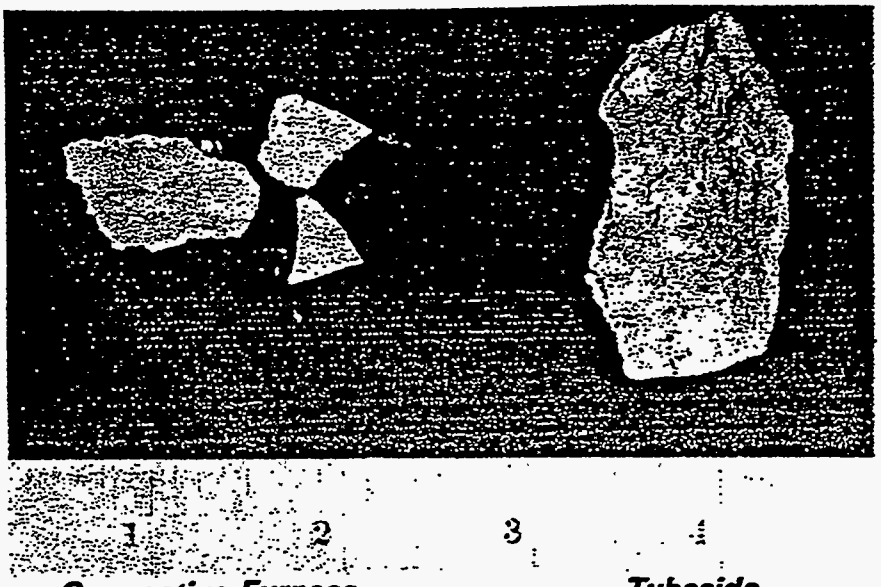

Location 3

Convective Furnace
Side Wall

Tubeside
Economizer Inlet

Figure 24 Macrophotographs of Deposits in Convection Bank

the lower furnace convective wall, also illustrated in Figure 24. Wedge-shaped deposits formed on the leading edge of the convective bank tubes. The bulk ash chemistry of the deposit taken from locations 1, 2 and 3 appear in Table 11, along with the fuel ash analysis and the ash fusion temperatures. The data clearly shows partitioning of the minerals in the biomass mixture. Calcium and potassium phosphates deposited at the highest temperature. Virtually pure potassium sulfate condensed on the convective pass walls and fly ash composed of calcium phosphate coated with potassium sulfate deposited on the tubes at the entrance to the convective heat recovery zone.

An examination of the deposits on a microscopic level using Scanning Electron Microscopy (SEM) and Energy Dispersive X-ray Analysis (EDAX) reveals the morphology of the deposit as well as its chemistry. In so doing, the mechanisms of deposition as discussed earlier, are also revealed. Figure 25 shows the surface morphology of the deposits laid down on the tube surface as well as the hotter fireside layer. The tubeside of the deposit is composed of fly ash spheres of calcium phosphate upon which has deposited submicron particles of potassium sulfate. Since there is no evidence of crystals, one might suspect the potassium sulfate has undergone homogeneous nucleation in the close proximity of the tube surface and the resulting particulate has been scavenged by particles of calcium sulfate. Once the deposit developed, the surface temperature increased and a continuous layer of molten K_2SO_4 was laid down over the deposited surface. Heat-transfer surfaces at this location were immersed in the flue gas perpendicular to the direction of flow. Deposition was by inertial impact of particles, 10-30μ in size.

Deposits formed on the convective furnace wall parallel to the flow of the flue gas in the temperature range of 871-982°C (1600-1800°F) were about 1/8 - 1/4" thick and composed of semi-molten particles about 1μ in diameter. Figure 26 shows the tubeside surface is sintered, pure potassium sulfate. This observation is confirmed by DTA analysis in Figure 27. The fireside surface is essentially the same except for a random inclusion of calcium phosphate. Deposits with a porous sintered morphology generally have a thermal conductive as much as one-fourth that of the fused material. The deposit was formed by a diffusion mechanism such as thermophoresis of homogeneously condensed and nucleate potassium sulfate.

At about 704°C (1300°F), the flue gases change direction and enter an economizer bank of convective heat-transfer surfaces immersed perpendicular to the direction of flow. The tubeside layer is composed of calcium phosphate particles, 10-50μ in size, encrusted with potassium sulfate heterogenically condensed on the surface, as shown in Figure 28. Figure 29 reveals the condensation of submicron particles $<1\mu$ in size as well as fully-developed crystals, suggesting condensation is taking place after deposition occurred. Figure 29 also shows the formation of potassium

Table 11 Comparison of Ash Deposit Analyses for Deposits Formed at Different Gas Temperatures

	Fuel Analysis	Radiant Furnace Exit	Lower Convective Furnace	Exporator
SiO_2	8.4	10.6	0.4	1.3
Al_2O_3	0.7	2.5	3.0	2.0
TiO_2	0.1	Nil	Nil	Nil
Fe_2O_3	1.2	1.2	0.1	0.3
CaO	32.3	24.7	4.3	10.3
MgO	4.9	8.5	1.4	2.6
Na_2O	3.0	2.8	2.0	1.4
K_2O	14.3	15.9	41.4	34.7
SO_3	6.4	1.8	40.0	31.9
P_2O_5	28.7	32.5	7.6	16.4
ASTM Ash Fusion Temperatures				
Initial Deformation		2187	2369	2554
Softening (Hem.)		2263	2372	2642
Softening (Sph.)		2319	2455	2900
Fluid		2460	2659	2900
Initial Deformation		2186	2378	2494
Softening (Hem.)		2231	2384	2522
Softening (Sph.)		2274	2394	2677
Fluid		2327	2500	2900

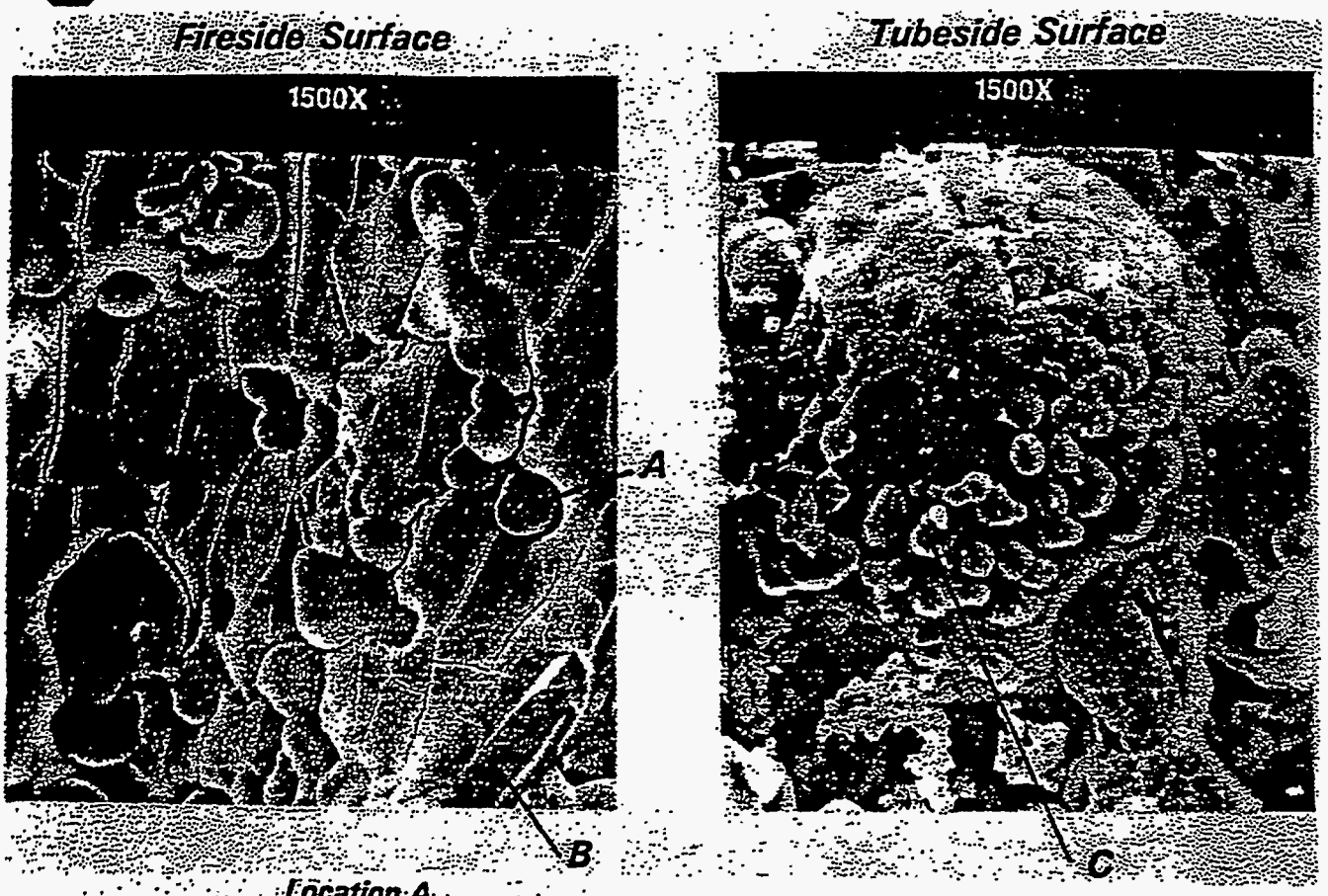

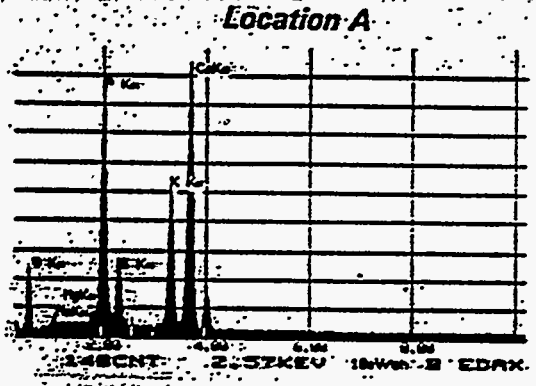

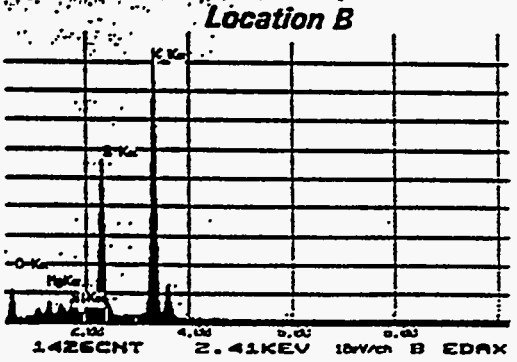

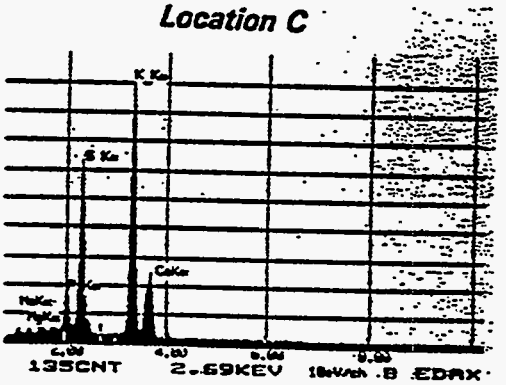

Figure 25 SEM Photomicrographs and EDAX Scans of Deposits Formed in the Screen Section at the Exit of the Radiant Furnace

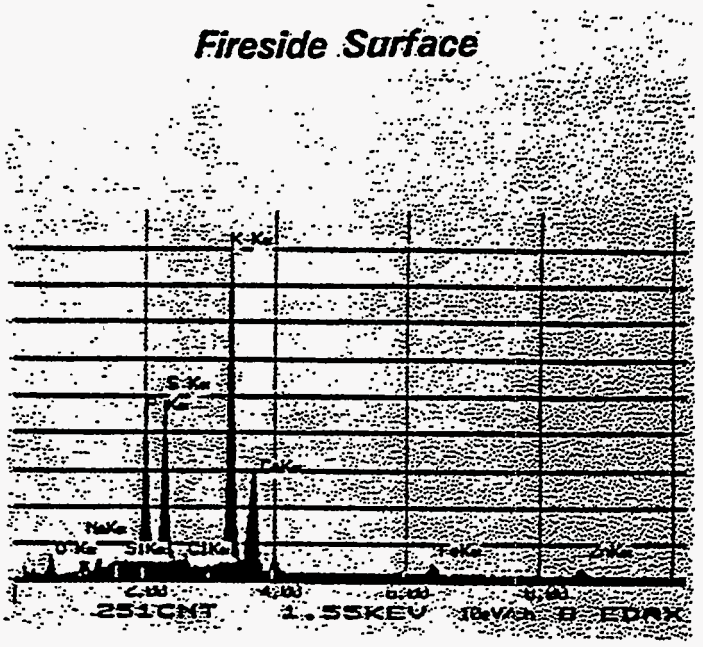

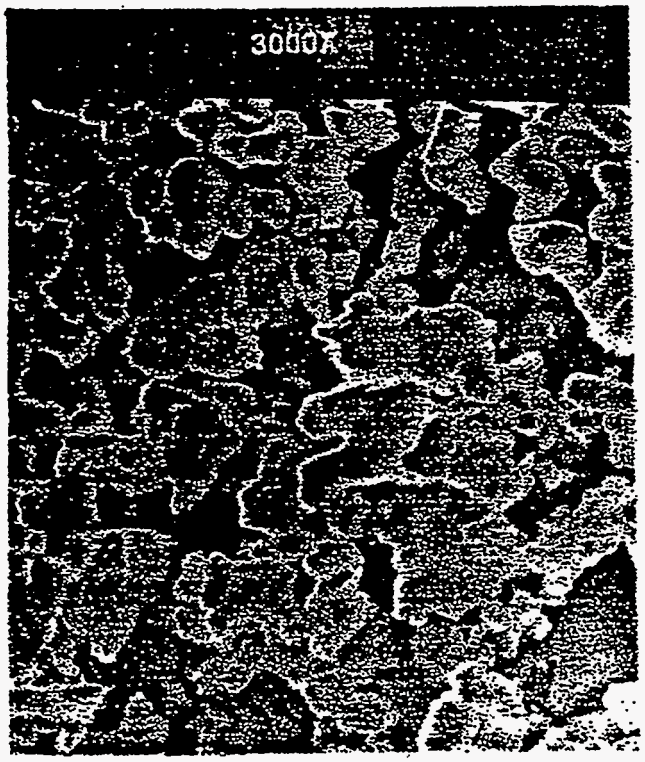

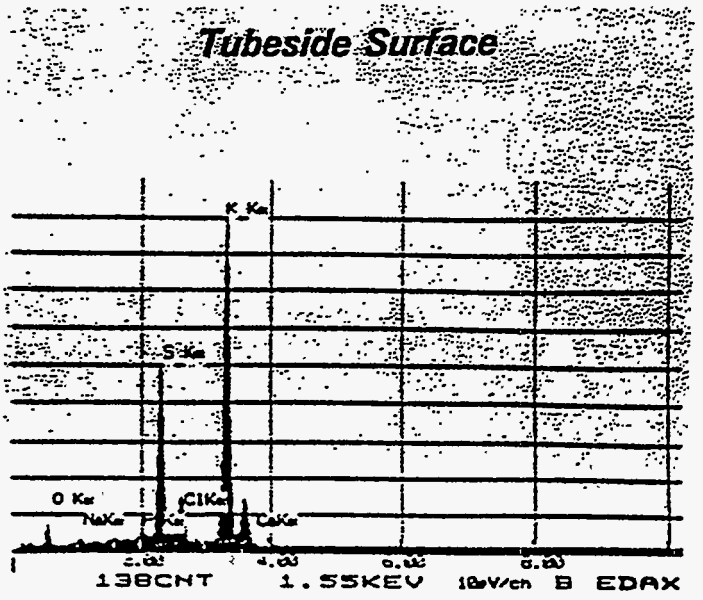

Figure 26 Deposits from Convective Furnace Wall

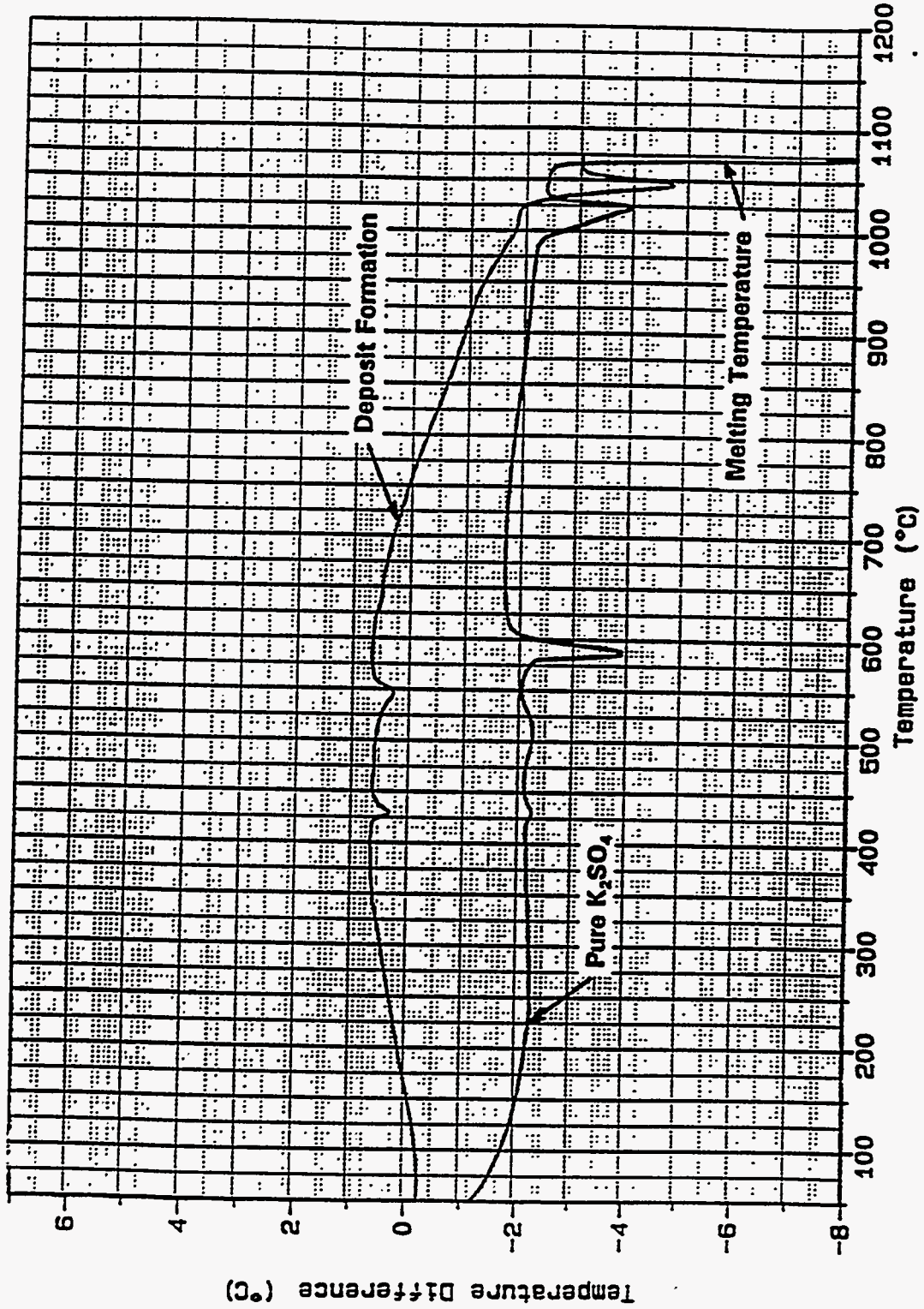

Figure 27 A Comparison of Differential Thermal Analysis Thermograms for a Biomass Deposit Formed in a Convective Heat-Transfer Zone with That of Pure K_2SO_4

Figure 28 SEM Photomicrographs and EDAX Scans of Deposits Formed on the Inlet Tubes of the Economizer at 1300-1600°F

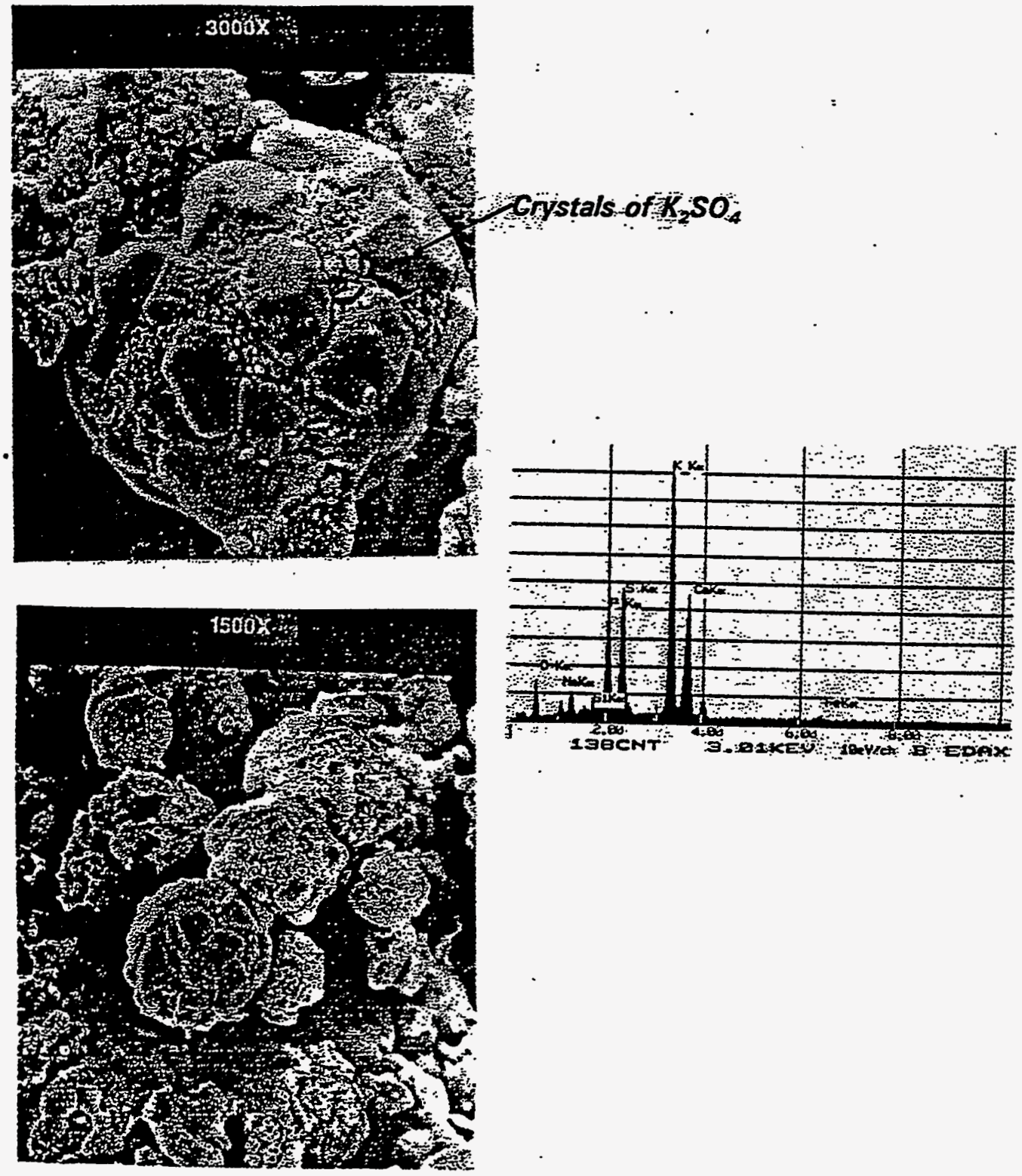

Figure 29 Deposits on Economizer Illustrating Heterogeneous Condensation of K_2SO_4

chlorides on the fireside surface of the fully-developed deposit. This is the only location in which chloride appeared in the deposit. Generally equilibria favors chloride formation at higher temperatures than sulfates. The window for deposition of chlorides is very narrow due to their high vapor pressures--see Figure 30.

Deposition, in the case of this biomass fuel, is primarily associated with the sulfidation and condensation of volatile potassium. Therefore, fouling is sensitive to the levels of concentration of potassium and sulfur in the fuel and the melting temperature of potassium sulfate. Characterization of the fireside behavior of impurities in the fuel depends more on understanding the nature of the behavior of the impurities in the fuel than an empirical index.

SUMMARY AND CONCLUSIONS

There are at least three different types of biomass, characterized on the basis of the impurities in the fuel: one rich in silica and potassium; one rich in calcium and potassium; and the third, rich in phosphorous, calcium and potassium. Sulfur is generally very low to nil but may be introduced via a secondary fuel. Chlorine is variable and may also be introduced during handling.

The bulk of the mineral matter is volatile during combustion. Except for extraneous clays, silica appears to be the sole mineral species. The dominant mechanism for deposition is condensation directly or indirectly via heterogeneous condensation on quartz particles. Therefore, ash fusion temperatures generated in the laboratory are meaningless. Concentration of the various volatile constituents is the single most important characterization of the ash. Sodium, unlike potassium, occurs as a clay and thus should not be lumped together with potassium when characterizing alkalies. Univalent compounds such as potassium may volatilize during ashing or form temporary artifacts with oxygen, nitrogen, chlorine or sulfur subsequently decomposing and volatilizing at elevated temperature. Accurate determination of the concentration of the mineral matter requires ashing at temperatures below 500°C and selecting analytical techniques that do not require further heating during preparation. Low-temperature ashing is not a viable technique for fuels rich in mineral matter. It may be successfully applied where the impurities consist primarily of inorganic minerals (i.e., bituminous anthracite, etc.).

Predicting the fireside behavior of minerals and mineral matter in the biomass requires at least a conceptual understanding of how the mineral matter present will behave thermally and some insight into the thermophysical properties of the compounds they will form. Laboratory characterization, short of testing in a combustor of one sort or another, would appear to be inappropriate.

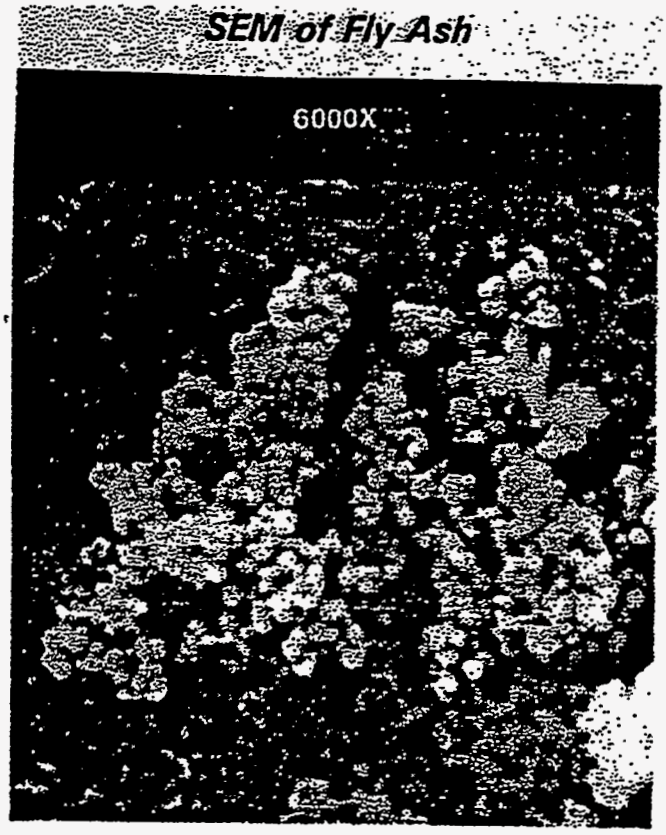

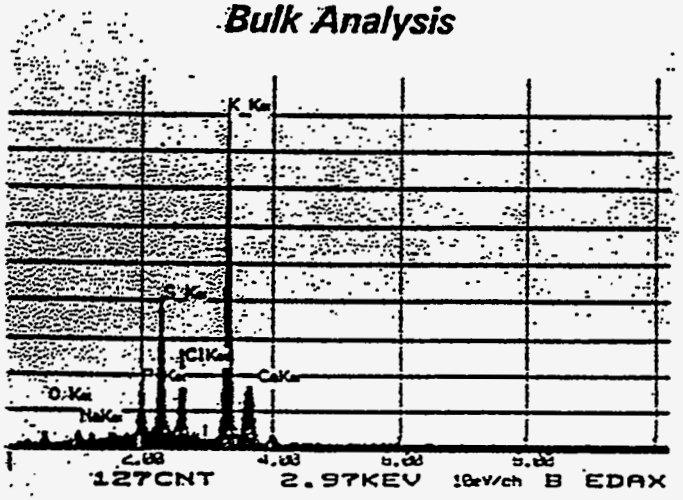

Figure 30 SEM Photomicrograph of Fly Ash

The biomass fuels may be the source of corrosion by Cl-enhanced CO attack or alkali trisulfates depending upon local environmental conditions or sulfur levels of supplemental fuels respectively. The subject of corrosion should be carefully monitored to be certain of the cause.

REFERENCES

[1] Baxter, L.L., "Pollutant Emission and Deposit Formation Durign Combustion of Biomass Fuels," Third Contractors Meeting 'Alkali Deposits Found in Biomass Power Plants,' Sandia, Livermore, California, November 30, 1993.

[2] Levin, E.M., Robbins, C.R., and McMurdie, H.F., "Phase Diagrams for Ceramists," Columbus, Ohio American Ceramic Society, 1964.

[3] Jackson, J.P., "The Physicochemical Behavior of Alkali-Metal Compound in Fireside Boiler Deposits," The Mechanism of Corrosion by Fuel Impurities, H.R. Johnson and D.J. Littler (eds.), Butterworths, London, 1963.

[4] Bryers, R.W., "Incinerating Municipal and Industrial Waste—Fireside Problems and Prospects for Improvements," Proceedings of the Engineering Foundation Conference on Fireside Problems While Incinerating Municipal and Industrial Waste, Hemisphere Publishing Corporation, New York, 1989.

[5] Krause, H.H., "Corrosion by Chlorine in Waste-Fueled Boilers," Proceedings of the Engineering Foundation Conference on Fireside Problems While Incinerating Municipal and Industrial Waste, Hemisphere Publishing Corporation, New York, 1989.

[6] Grabke, H.J., "Fundamental Mechanisms of the Attack of Chlorine, HC and Chlorides on Steel and High-Temperature Alloys in the Temperature Range of 500°C to 900°C," Proceedings of the Engineering Foundation Conference on Fireside Problems While Incinerating Municipal and Industrial Waste, Hemisphere Publishing Corporation, New York, 1989.

[7] Mayer, P., and Manolescu, A.V., "Influence of Hydrogen Chloride on Corrosion of Boiler Steels in Synthetic Flue Gases," Corrosion 36(7), 1980.

[8] Brown, M.H., DeLong, W.B., and Auld, J.R., "Corrosion by Chlorine Hydrogen Chloride at High Temperatures," Ind. Eng. Chem., Vol. 39, No. 7, 834-844, 1947.

[9] Latham, E., Meadowcroft, D.B., and Pinder, L., "The Effects of Coal Chlorine on Fireside Corrosion," Proceedings of the Engineering Foundation Conference on Fireside Problems While Incinerating Municipal and Industrial Waste, Hemisphere Publishing Corporation, New York, 1989.

[10] Lees, D.J., and Whitehead, M.E., "The Influence of Gas and Deposit Chemistry on the Fireside Corrosion of Furnace Wall Tubes in Coal-Fired Boilers," Proceedings of the Engineering Foundation Conference on 'Fouling of Heat Exchanger Surfaces,' R.W. Bryers (ed.), Hersey Pocono Resort, White Haven, PA, October 1982.

[11] Osman, E.A., and Gross, J.R., "Ash Chemical Composition, Deformation and Fusion Temperatures for Wood and Agriculture Residues," American Society of Agriculture Engineers, Paper No. 83-3549, Chicago, Illinois, 1983.

[12] Osman, E.A., and Gross, J.R., "Ash Deformation and Fusion Temperature Models for Wood and Agriculture Residues," American Society of Agriculture Engineers, Paper No. 83-3550, Chicago, Illinois, 1983.

[13] Marschner, H., "Mineral Nutrition of Higher Plants," London Harcourt Brace Jovanovich, 1986.

APPENDIX 4

Heating Valves, Total Ash and Total Alkali Range for Power Plant Fuels

Material in this appendix has been reproduced from the best available originals

Table 1. Fuels Reported By All Plants

Fuel Type	Heating Value Btu/lb, dry basis		Total Ash % Dry		Total Alkali % Na2O + % K2O		Total Alkali Lb/MMBtu	
	Low	Hi	Low	Hi	Low	Hi	Low	Hi
FUEL MIX	5,954 --	8,818	1.6 --	11.0	2.8 --	16.4	0.45 --	1.06
Fines, trommel/shaker screen		3,900	39.8 --	48.0	2.6 --	6.4	3.10 --	1.94
WOOD								
a) Bark		9,784	1.0 --	8.9				
b) Shavings, sawdust, chips	8,581 --	8,889	0.7 --	2.5				
c) Hog fuel	9,077 --	9,474	1.8 --	3.8				
d) Salt water hog fuel		9,437		5.8		8.5		0.52
URBAN WOOD WASTE	7,400 --	9,340	1.0 --	17.9	3.0 --	11.6	0.15 --	1.61
a) Clean, construction	8,359 --	8,508	1.0 --	3.4	10.3 --			0.41
b) Demolition								0.37
FRUIT AND NUT CHIPS STUMPS PRUNINGS								
Almond Prunings	7,780 --	8,520	1.7 --	5.7				
Citrus prunings		8,160		2.8		6.2		
Fig chips		6,740		15.8				
Grape Prunings, vines	7,260 --	7,950	5.5 --	7.3		2.8		0.26
Olive prunings		9,270		4.7		13.7		0.70
Peach Stumps		7,390		12.8				
Walnut chips				18.2				
NUTS, SHELLS, HULLS AND PITS								
Almond shells	7,560 --	8,080	3.4 --	5.5				
Capified figs		7,090		6.9		20.3		1.98
Cocoa beans		8,690		7.2				
Grape pits		9,000		3.6				
Olive pits	7,630 --	8,820	2.0 --	3.9				
Peach pits			3.2 --	23.1		6.6		
Prune pits				2.3				
FIELD CROPS, STRAWS AND STALKS								
Alfalfa, cleanings		7,602		16.2				
Bermuda Grass straw	7,534 --	7,553	5.5 --	9.9				
Cotton stalks		7,500		7.2				
Kenaf plot		9,640		4.2				
Straw - fresh	6,360 --	7,040	5.5 --	16.2		34.5		10.20
Straw - bedding	6,170 --	7,129	6.8 --	22.9		16.8	3.35 --	4.85
Wheat straw	5,082 --	7,944	4.4 --	11.8	2.6 --	31.4	0.15 --	4.15
MANURE		5,571		34.9		17.1		10.70
Bedding - shavings					9.6 --	13.4		

TRM 2/10/93

Table 2. Fuels Reported in References

Fuel Type	Heating Value Btu/lb, dry basis		Total Ash % Dry		Total Alkali %Na2O + %K2O		Total Alkali Lb/MMBtu		
	Low	Hi	Low	Hi	Low	Hi	Low	Hi	Estimated
WOOD									
a) Bark	7,593 --	9,456	0.5 --	11.2	5.4 --	10.4		0.46	
b) Shavings, sawdust, chips	7,644 --	9,130	0.1 --	1.1	1.3 --	43.6	0.03 --	0.44	
c) Hog fuel									
Urban Wood Waste	7,927 --	9,047	1.0 --	4.4					
a) Clean, construction									
b) Demolition									
c) Tree Trimmings									
FRUIT AND NUT CHIPS STUMPS PRUNINGS									
Almond Prunings	7,989 --	8,609	1.6 --	4.1		10.3		0.42	
Citrus prunings									
Cherry chips		8,408		1.4					
Grape Prunings, vines	7,080 --	8,325	2.2 --	8.8					
Olive prunings									
Peach Stumps									
Walnut chips	8,445 --	8,531	0.8 --	1.1					
NUTS, SHELLS, HULLS AND PITS									
Almond shells	7,009 --	7,580	3.5 --	18.2	19.2 --	35.0	1.60		8.38
Almond hulls		7,838		5.8					
Almond shells and hulls		7,930		4.7		6.2		0.36	
Cherry pits		9,357		1.0					
Cocoa hulls		8,191		8.3					
Coconut shell		8,845		0.5					
Coconut fiber	8,277 --	8,626	3.7 --	5.1					
Grape pomace		8,750		9.5					
Macadamia shells		9,039		0.4					
Olive pits	8,531 --	9,202	3.2 --	4.5	10.7 --	46.1		1.78	
Peach pits	7,420 --	8,957	1.0 --	8.2		27.0		0.35	
Peanut hulls		8,019		5.9					
Pistachio shells		8,286	0.4 --	1.1					
Plum pits		9,094		0.1					
Prune pits				0.5					
Sunflower seed husks	8,594 --	8,713	3.8 --	4.2		39.7		1.76	
Tomato pomace		10,226		4.1					

TRM 2/10/93

Table 3. Fuels Reported in References

Fuel Type	Heating Value Btu/lb, dry basis		Total Ash % Dry		Total Alkali %Na2O + %K2O		Total Alkali Lb/MMBtu		
	Low	Hi	Low	Hi	Low	Hi	Low	Hi	Estimated
FIELD CROPS, STRAWS AND STALKS									
Alfalfa, seed, straw		7,937		7.3		37.6			3.44
Barley, straw	7,447 --	7,600	4.0 --	10.3	0.3 --	41.4			5.62
Bean straw		7,511		5.9	22.9 --	26.1			2.06
Bermuda Grass straw		8,000							
Corn cobs		8,075		1.4		3.2			0.05
Corn stalks		7,593		5.6	4.4 --	10.3			0.76
Cotton stalks		7,500		7.2					
Cotton gin trash	7,064 --	7,720	8.4 --	17.6		11.3		1.23	2.58
Cotton stalks	6,810 --	8,219	3.8 --	17.3	22.7 --	32.0		1.48	6.74
Grass seed straw, bentgrass	7,960 --	8,420	2.8 --	3.0					
bluegrass	7,960 --	8,060	4.2 --	5.5					
fescue	7,760 --	7,800	3.5 --	5.9					
orchardgrass	7,810 --	8,150	4.6 --	5.3					
ryegrass		8,312			10.7 --	18.1			
Grass clippings		8,312		1.6					
Kenaf plot									
Oats, straw			1.8 --	5.1	3.3 --	41.7			
Rice, hulls	6,334 --	7,470	13.6 --	24.0	1.3 --	4.8	0.37 --	0.50	
Rice, straw	6,840 --	7,004	13.4 --	24.4	12.2 --	14.9			5.20
Rye, straw	7,560 --	7,590	2.0 --	6.9	14.9 --	19.9			1.81
Safflower straw		8,273		4.7		30.9			1.74
Sorghum stalks, leaves		7,461		13.2		11.6		2.05	
Sorghum Sweet bagasse, heads		7,285		10.3		2.9		0.41	
Sudan grass straw		7,481		8.7					
Sugar cane bagasse	7,456 --	8,236	1.7 --	11.3	5.7 --	7.1	0.12 --	0.15	
Switch grass, stems				5.4		13.1			0.94
Wheat straw	7,533 --	8,787	3.1 --	8.9	9.4 --	52.1			6.18
MANURE									
Manure, cattle		3,738							
Manure, feedlot	2,520 --	7,810	13.7 --	34.9	1.3 --	17.1			
Manure, dairy		6,500				1.7			
Manure, horse					1.8				
Manure, chicken broiler		6,800							
Manure, chick, composted		6,502		41.6		7.7		4.95	

TRM 2/10/93

Table 4. Wood Fuels Reported in References

Fuel Type	Heating Value Btu/lb, dry basis		Total Ash % Dry		Total Alkali %Na2O + %K2O		Total Alkali Lb/MMBtu		
	Low	Hi	Low	Hi	Low	Hi	Low	Hi	Estimated
Alder, red				0.4					
Ash, white		8,507		0.4		35.6			0.18
Aspen	8,189 --	8,674	0.8 --	3.5	6.0 --	7.8	0.07 --	0.31	
Aspen Bark	8,590 --	8,706	4.3 --	5.0	5.4 --	6.6	0.27 --	0.38	
Balsam bark		4,100		1.2		12.6		0.37	
Beech		7,644		3.6		2.7		0.28	
Birch	8,458 --	8,870		2.0	1.3 --	6.6	0.03		0.15
Black locust		8,479		0.8					
Cedar		8,845		0.3					
Cedar bark		8,965		1.2					
Cherry		8,408		1.3					
Cottonwood	8,423 --	8,583	1.1 --	1.4	16.3 --	19.2	0.21 --	0.30	
Cottonwood bark		9,324		5.0					
Elm	8,167 --	8,228	1.0 --	1.1		37.7		0.44	
Eucalyptus	8,273 --	8,355	0.5 --	1.1					
Eucalyptus leaves		8,737		4.8					
Fir, Douglas		8,490	0.1 --	0.8					
Fir, Douglas, bark	9,324 --	9,500	0.5 --	3.2					
Fir, white		8,583		0.3					
Gum	8,380 --	8,475	1.3 --	2.2					
Hardwood, bark	7,593 --	8,404	4.0 --	11.2					
Hardwood, chips	7,827 --	8,469	0.4 --	1.7					
Hemlock, western	8,556 --	8,700	0.3 --	2.2					
Hemlock, western, bark		9,456		0.8					
Hemlock, eastern		8,885		2.5		4.6		0.13	0.13
Hickory		8,670							
Larch, Tamarack		8,514		0.3					
Larch, Tamarack, bark		8,838		2.5					
Locust, black		8,479		0.8					
Madrone		8,350		0.6					
Manzanita		7,783		0.8		13.8			
Maple	8,113 --	8,580	0.3 --	4.3	5.8 --	20.0		0.30	
Oak	8,144 --	8,561	0.4 --	5.3	31.8 --	43.6			2.70
Pine	8,551 --	9,130	0.2 --	1.0	2.6 --	4.1			0.05
Pine, Jack				3.1		18.4			
Pine bark	8,630 --	9,302	0.5 --	2.7	7.2 --	7.3	0.12 --	0.18	
Poplar	8,337 --	8,920		1.3		20.2			0.30
Redwood	8,350 --	9,040	0.4 --	1.6					
Softwood, bark				3.1		7.2			
Softwood									
Spruce		9,547							
Spruce, bark		8,622	1.5 --	3.8	7.3 --	10.4	0.12		0.46
Tamarack				0.2		32.7			
Walnut		8,445		1.1					

TRM 2/10/93

REPRESENTATIVE FUEL ANALYSES: All Plants

TYPE	FUEL CHARACTERISTICS AS FIRED, %								Heating Value		ELEMENTAL ANALYSES										
	Moisture	C	H	N	S	O	Cl	Ash	As Fired Btu/lb	Dry Btu/lb	SiO2	Al2O3	TiO2	Fe2O3	CaO	MgO	Na2O	K2O	P2O5	SO3	Alkali lb/MMBtu
FUEL MIX																					
Fines, shaker											85.00	3.20		3.00	4.40	1.80	0.65	1.90			
Fines, trommel	25.72	23.07	2.62	0.25	0.15	18.60	0.41	29.59	3,860	5,196	62.38	13.14	0.46	4.70	8.01	2.54	2.86	3.58	0.63	0.73	4.94
Fuel Mix	35.11	32.24	3.81	0.24	0.04	25.99	0.02	2.57	5,539	8,535	56.48	12.32	0.49	5.31	8.57	2.94	5.42	4.33	1.67	0.72	0.45
Fuel Mix	36.23	31.00	3.68	0.42	0.04	25.36	0.02	3.27	5,388	8,450	52.55	13.15	0.43	8.18	10.06	3.27	5.90	5.04	1.90	2.10	0.66
Fuel Mix	15.32	41.09	4.88	0.50	0.05	34.72	0.02	3.44	6,929	8,182	41.04	9.89	0.44	3.90	22.44	4.47	2.93	8.22	2.22	1.79	0.55
Fuel Mix	15.76	40.24	4.63	0.46	0.06	34.19	0.02	4.66	6,864	8,148	48.98	11.04	0.46	4.42	18.69	3.66	2.23	6.97	1.53	1.35	0.62
Fuel Mix	22.66	36.70	4.28	0.45	0.06	30.60	0.02	5.25	5,281	6,829	45.60	10.75	0.54	4.06	18.96	4.22	3.08	6.26	1.47	2.06	0.93
Fuel Mix	46.21	24.70	2.85	0.44	0.05	19.64	0.02	6.11	4,246	7,894	57.34	13.07	0.53	6.08	10.24	3.19	3.12	4.28	0.94	1.17	1.06
Fuel Mix	19.20	37.00	4.31	0.51	0.06	31.13	0.02	7.79	6,309	7,809	54.11	11.60	0.42	4.07	13.85	3.11	2.15	5.79	1.16	1.13	0.98
Fuel Mix	20.97	35.28	4.13	0.51	0.07	29.78	0.02	9.26	6,123	7,748	53.60	10.75	0.54	4.14	14.74	3.03	2.34	5.74	1.01	0.77	1.22
Fuel Mix	15.69	37.76	4.48	0.55	0.08	31.44	0.03	10.00	6,361	7,544	52.74	13.08	0.49	4.33	14.29	3.11	2.60	5.60	1.12	1.05	1.29
Fuel	18.15	34.44	4.06	1.10	0.16	28.23	0.11	13.86	5,904	7,213	42.61	9.48	2.03	5.94	19.93	3.90	2.34	2.14	1.50	4.91	1.05
Fuel	29.93	27.23	3.23	0.40	0.09	22.66	0.04	16.46	4,629	6,607	55.49	13.87	0.62	5.61	10.58	2.99	2.27	3.37	0.94	0.85	2.01
WOOD AND URBAN WOOD																					
Urban	10.61	45.90	5.31	0.15	0.02	37.39	0.01	0.62	7,795	8,720	29.50	7.93	3.00	5.07	22.16	5.72	3.56	6.89	1.73	7.94	0.08
Urban	22.17	39.89	4.61	0.28	0.04	32.01	0.01	1.00	6,667	8,566	34.65	8.98	1.00	4.37	24.58	10.76	3.30	6.89	2.56	4.28	0.15
Urban	14.17	42.97	5.20	0.10	0.04	35.94	0.01	1.58	7,364	8,580	41.81	8.17	1.02	6.58	16.90	5.08	6.05	4.35	1.15	3.61	0.22
Urban	23.36	38.52	4.51	0.20	0.07	31.19	0.03	2.15	6,525	8,514	29.43	7.45	0.96	3.61	27.80	5.26	3.68	7.10	2.80	8.34	0.36
Wood	17.96	41.06	4.65	0.45	0.08	33.55	0.14	2.25	6,798	8,286	50.31	11.66	0.82	5.08	13.00	1.56	5.85	8.64	0.52	2.63	0.48
Urban	30.76	34.37	4.17	0.25	0.03	27.81	0.03	2.61	5,839	8,432	43.77	11.26	0.43	5.21	18.44	4.44	3.59	7.10	2.16	2.05	0.48
Urban Wood	15.98	41.37	4.87	0.28	0.04	34.42	0.03	3.04	6,978	8,305	34.30	9.05	0.85	3.78	22.29	5.04	3.92	7.69	2.74	4.51	0.51
Wood Fuel	12.07	43.85	5.20	0.25	0.03	35.42	0.01	3.18	7,613	8,658	57.62	12.23	0.50	5.63	13.89	3.28	2.36	3.77	0.50	1.00	0.26
Urban	34.19	31.97	3.79	0.24	0.03	26.12	0.03	3.66	5,470	8,312	52.00	8.37	0.80	4.15	16.01	4.10	2.92	5.58	2.98	2.21	0.57
Urban	38.18	29.71	3.48	0.25	0.04	24.27	0.03	4.07	5,029	8,135	51.76	11.28	0.61	5.20	16.11	3.06	1.97	4.88	2.03	1.57	0.55
Wood Fuel	16.67	40.64	4.80	0.22	0.06	32.99	0.05	4.62	6,967	8,361	55.12	12.49	0.72	4.51	13.53	2.93	3.19	4.78	0.88	1.92	0.53
Urban	31.88	32.42	3.90	0.08	0.04	26.66	0.01	5.02	5,549	8,146	58.62	16.29	1.23	7.42	7.03	2.56	2.84	2.82	0.53	2.26	0.51
Urban	17.06	39.07	4.64	0.28	0.06	32.44	0.05	6.45	6,729	8,113	54.18	10.36	1.06	4.64	12.82	3.82	2.55	3.90	1.73	1.52	0.62
Wood Fuel	27.53	32.76	3.93	0.17	0.05	27.73	0.07	7.83	5,660	7,811	62.12	11.37	0.49	4.49	11.91	2.23	2.49	4.28	0.77	0.96	0.94
Wood	18.00	39.05	4.12	0.48	0.26	29.51	0.12	8.58	6,413	7,821	51.90	15.70	1.20	6.53	8.79	0.40	3.93	8.10	0.45	4.08	1.61
Wood	7.54	43.39	5.05	0.61	0.10	33.72	0.25	9.59	7,315	7,911	58.46	12.77	0.68	4.43	8.40	2.83	3.51	5.65	1.03	1.62	1.20
Wood	6.18	44.46	4.47	0.33	0.11	32.50	0.24	11.95	7,492	7,986	63.23	12.98	0.92	6.11	4.20	2.02	3.54	4.07	0.29	3.54	1.21
Urban	22.54	33.35	3.92	0.60	0.10	26.43	0.07	13.06	5,732	7,400	60.42	12.42	0.94	5.98	9.04	3.03	0.45	2.59	0.66	1.00	0.69

ASH VISCOSITY CALCULATIONS AND DEPOSIT CHARACTERISTICS

(For Lignite Type Fuel From Hazen Research Laboratory Reports)

TYPE	Alkali lb/MMBtu	% Base Content	% Acid Content	Dolomite Ratio %	Base/Acid Ratio	Silica/Al Ratio	T (CV) (DEG F)	T250 (Deg F)	Equiv Silica %	Viscosity from SiO2	Slagging Type*	Fouling Type**
FUEL MIX												
Fines, shaker												
Fines, trommel	4.94	22.21	77.79	48.64	0.29	4.75			80.36	887.18		LOW
Fuel Mix	0.45	27.04	70.52	43.32	0.38	4.58						
Fuel Mix	0.66	32.92	67.08	41.08	0.49	4.00	2259	2317	70.96	175.71	HIGH	HIGH
Fuel Mix	0.55	44.96	55.04	64.13	0.82	4.15		2093	57.12	21.89	SEVERE	LOW
Fuel Mix	0.62	37.29	62.71	62.14	0.59	4.44		2253	64.66	66.07	HIGH	LOW
Fuel Mix	0.93	39.14	60.86	63.37	0.64	4.24		2232	62.60	48.83	HIGH	MEDIUM
Fuel Mix	1.06	26.92	70.97	49.91	0.38	4.39						
Fuel Mix	0.98	30.46	69.54	58.54	0.44	4.66		2363	72.01	208.74	MEDIUM	LOW
Fuel Mix	1.22	31.61	68.39	59.25	0.46	4.99		2340	70.98	176.51	HIGH	LOW
Fuel Mix	1.29	31.10	68.90	58.14	0.45	4.03		2348	70.82	171.87	HIGH	LOW
Fuel	1.05	36.14	57.10	69.58	0.63	4.49						
Fuel	2.01	25.70	72.45	54.67	0.35	4.00						
WOOD AND URBAN WOOD												
Urban	0.08	46.42	43.24	64.24	1.07	3.72						
Urban	0.15	49.23	44.03	70.82	1.12	3.86						
Urban	0.22	41.13	53.84	56.42	0.76	5.12						
Urban	0.36	49.21	39.24	69.67	1.25	3.95						
Wood	0.48	34.11	62.75	42.66	0.54	4.31						
Urban	0.48	39.39	56.33	59.00	0.70	3.89						
Urban Wood	0.51	45.36	46.94	63.97	0.97	3.79						
Wood Fuel	0.26	29.14	70.86	59.35	0.41	4.71	2367	2392	71.65	196.73	MEDIUM	LOW
Urban	0.57	33.05	61.71	61.39	0.54	6.21						
Urban	0.55	31.71	64.64	61.40	0.49	4.59						
Wood Fuel	0.53	29.75	70.25	56.88	0.42	4.41		2379	72.44	223.84	MEDIUM	MEDIUM
Urban	0.51	22.31	74.94	42.30	0.30	3.60						
Urban	0.62	28.71	67.92	60.01	0.42	5.23						
Wood Fuel	0.94	25.56	74.44	55.67	0.34		2502	2481	76.93	472.88	MEDIUM	LOW
Wood	1.61	27.45	68.06	33.12	0.40	3.31						
Wood	1.20	24.97	72.36	45.25	0.35	4.58						
Wood	1.21	19.76	76.44	31.19	0.26	4.87						
Urban	0.69	21.85	76.43	57.23	0.29	4.86						

* From Slag Temperature at 250 Poise Viscosity. Blank = not determined or off lignite table limits.

** Based on Na2O only. Other alkali (K2O) not considered.

REPRESENTATIVE FUEL ANALYSES: All Plants

TYPE	FUEL CHARACTERISTICS AS FIRED, %								Heating Value		ELEMENTAL ANALYSES										
									As Fired	Dry	SiO2	Al2O3	TiO2	Fe2O3	CaO	MgO	Na2O	K2O	P2O5	SO3	Alkali
	Moisture	C	H	N	S	O	Cl	Ash	Btu/lb	Btu/lb											lb/MMBtu
WOOD																					
Christmas Tree	37.81	32.09	3.47	0.32	0.25	22.82		3.24	5,603	9,009	38.89	14.74	0.36	9.30	9.50	2.52	0.53	7.86	2.40	11.36	0.49
Hog Fuel	59.99	21.70	2.26	0.11	0.02	14.60		1.32	3,719	9,296											
Hog Fuel	45.64	27.27	2.99	0.13	0.06	20.66	0.12	3.25	4,587	9,437	43.94	12.32	0.56	5.86	18.38	4.18	5.22	3.26	1.32	2.21	0.60
Redwood	57.99	21.97	2.50	0.07	0.01	16.92		0.54	3,700	8,807											
Shavings	17.00	38.35	5.77	0.24		37.13		1.36	6,800	8,210		7.60	0.39	4.40	17.00	4.40	2.90	6.00			0.18
Sawdust, Chips									6,714	8,581											
FRUIT AND NUT CHIPS STUMPS PRUNINGS																					
Almond Pruning									3,900	8,520											
Citrus	8.77	43.78	5.21	0.53	0.07	39.10		2.54	7,444	8,160											
Fig Chips									3,780	6,740											
Grape Prunings	30.00	28.64	4.42	0.39		31.26		5.09	5,550	7,950	77.00	3.40	0.17	2.90	9.50	1.50	0.95	1.90			0.26
Grape Vine									3,780	7,370											
Olive Tree	37.61	31.97	3.90	0.69	0.11	22.76		2.96	5,783	9,270	6.90	0.89	0.14	1.14	33.60	8.60	0.61	13.10	5.80	4.82	0.70
Peach Stumps									6,220	7,390											
Walnut Chips	8.60	40.41	5.46	1.08	0.07	28.55		15.79													
Walnut Trim	27.88	37.21	4.03	0.75	0.06	27.41		2.66	6,316	8,758	15.25	5.84	0.28	2.28	50.27	6.82	0.85	7.86	4.28	4.23	0.37
NUTS, SHELLS, HULLS AND PITS																					
Almond Shells	35.00	30.07	3.07			26.07		3.57													
Almond Shells									6,780	7,560											
Cocoa Beans	4.30	46.56	6.66	2.99	0.20	32.37		7.00	8,320	8,690											
Capified Figs	7.50	41.28	6.55	1.05	0.08	36.96		6.40	6,560	7,090	15.00	1.10		0.65	40.00	9.60	1.30	19.00			1.98
Grape Pits									8,194	9,000											
Olive Mash	90.94	5.60	0.81	0.13	0.01	2.05	0.09	0.46	1,170	12,911	11.43	1.25	0.29	6.51	26.52	8.05	22.10	1.64	3.76	1.24	0.93
Olive Pits	50.00	27.28	3.65	0.80		17.18		1.00													
Olive Pits	14.44	44.85	5.39	0.33	0.79	25.64	0.14	8.56	8,044	9,401	30.03	8.98	0.45	6.40	12.51	7.18	22.50	1.13	5.58	3.33	2.51
Peach Pits	13.00	46.11	6.25	0.48		31.09		2.80			66.00	4.70	0.14	3.80	3.70	4.00	0.93	5.70			
Prune Pits	33.59	32.71	4.38	0.56	0.05	27.77	0.01	0.94	5,737	8,638	3.00	0.09	0.02	0.57	12.25	9.72	0.39	37.50	16.80	2.07	0.62
Walnut	47.85	27.90	3.40	0.80	0.06	18.45	0.01	1.54	4,976	9,541	6.88	2.42	0.09	1.14	16.62	13.45	0.99	32.90	6.24	2.25	1.05
Walnut	65.21	16.52	1.87	0.62	0.05	11.99	0.01	3.74	2,890	8,307	20.26	6.23	0.17	3.09	17.19	6.70	1.30	28.30	3.39	1.18	3.83
Walnut Blows	23.49	41.05	4.97	1.02	0.08	27.58	0.02	1.81	7,345	9,600	5.18	1.82	0.09	0.85	22.32	11.58	0.74	28.00	8.30	1.88	0.71
Walnut Hulls	65.21	16.52	1.87	0.62	0.05	11.99	0.01	3.74	2,890	8,307	20.26	6.23	0.17	3.09	17.19	6.70	1.30	28.60	3.39	1.18	3.87
Walnut Shells	6.24	48.51	5.96	1.13	0.08	37.40		0.68	8,469	9,033	7.86	10.11	0.08	1.41	42.90	0.76	6.75	17.30	8.40	2.19	0.19
Walnut Shells	33.69	14.04	1.67	1.09	0.09	11.07	0.01	38.35	2,254	3,399	50.96	19.84	0.91	9.91	8.15	4.77	1.77	1.21	0.67	0.24	5.07

ASH VISCOSITY CALCULATIONS AND DEPOSIT CHARACTERISTICS

(For Lignite Type Fuel From Hazen Research Laboratory Reports)

TYPE	Alkali lb/MMBtu	% Base Content	% Acid Content	Dolomite Ratio %	Base/Acid Ratio	Silica/Al Ratio	T (CV) (DEG F)	T250 (Deg F)	Equiv Silica %	Viscosity from SiO2	Slagging Type*	Fouling Type**
WOOD												
Christmas Tree	0.49	35.50	64.50	40.46	0.55	2.64	2577	2279	64.59	65.40	HIGH	LOW
Hog Fuel												
Hog Fuel	0.60	37.94	58.43	61.14	0.65	3.57						
Redwood												
Urban	0.18	81.28	18.72	61.67	4.34							
Sawdust, Chips												
FRUIT AND NUT CHIPS STUMPS PRUNINGS												
Almond Pruning												
Orchard												
Fig Chips												
Grape Prunings	0.26	17.21	82.79	65.67	0.21	22.65						
Grape Vine												
Olive Tree	0.70	87.80	12.20	73.97	7.19	7.75			13.73	1.00		LOW
Peach Stumps												
Walnut Chips												
Walnut Trim	0.37	76.11	23.89	83.86	3.19	2.61	2855		20.44	1.00		LOW
NUTS, SHELLS, HULLS AND PITS												
Almond Shells												
Almond Shells												
Cocoa Beans												
Capified Figs	1.98	81.42	18.58	70.30	4.38	13.64						
Grape Pits												
Olive Mash	0.93	83.33	16.67	53.33	5.00	9.14	2600		21.77	1.00		SEVERE
Olive Pits												
Olive Pits	2.51	55.75	44.25	39.60	1.26	3.34			53.51	13.48		SEVERE
Peach Pits		20.38	79.62	42.47	0.26							
Prune Pits	0.62	95.11	4.89	36.36	19.43	33.33			11.75	1.00		LOW
Walnut	1.05	87.39	12.61	46.19	6.93	2.84			18.06	1.00		LOW
Walnut	3.83	64.43	30.36	42.22	2.12	3.25						
Walnut Blows	0.71	89.95	10.05	53.39	8.95	2.85			12.97	1.00		LOW
Walnut Hulls	3.87	68.07	31.91	42.00	2.13	3.25	2527		42.89	3.75		LOW
Walnut Shells	0.19	79.29	20.71	63.17	3.83	0.78			14.85	1.00		HIGH
Walnut Shells	5.07	26.47	73.53	50.06	0.36	2.57	2383	2457	69.06	128.99	MEDIUM	LOW

* From Slag Temperature at 250 Poise Viscosity. Blank = not determined or off lignite table limits.

** Based on Na2O only. Other alkali (K2O) not considered.

REPRESENTATIVE FUEL ANALYSES: All Plants

TYPE	FUEL CHARACTERISTICS AS FIRED, %								Heating Value		ELEMENTAL ANALYSES										
	Moisture	C	H	N	S	O	Cl	Ash	As Fired Btu/lb	Dry Btu/lb	SiO2	Al2O3	TiO2	Fe2O3	CaO	MgO	Na2O	K2O	P2O5	SO3	Alkali lb/MMBtu
FIELD CROPS, STRAWS AND STALKS																					
Ag Waste	29.00	31.99	4.88	0.56		32.77		1.12	5,360	7,520		1.10		1.00	42.00	4.70	2.10	8.00			0.21
Ag Waste	35.00	30.26	4.59	0.45		27.86		2.22	5,030	7,690		1.40	0.12	0.85	55.00	6.10	1.30	8.40			0.43
Alfalfa Straw	6.43	43.82	5.46	0.98	0.11	39.78	0.49	3.42	7,433	7,944	5.87	1.32	0.04	0.43	24.06	7.06	8.86	25.30	7.56	1.97	1.57
Alfalfa Straw	6.59	43.01	5.46	1.06	0.17	39.15	1.04	4.56	7,293	7,808	7.04	1.12	0.05	0.41	21.37	5.83	11.20	22.90	6.32	4.27	2.13
Bermuda Grass	6.67	41.49	5.25	0.79	0.64	37.95	0.84	7.21	7,137	7,647	29.81	0.91	0.02	0.35	11.61	4.39	3.19	25.70	3.76	12.50	2.92
Fescue Straw	13.30	39.62	4.82	0.52	0.10	36.79	0.63	4.85	6,717	7,747	33.66	0.88	0.05	0.62	6.45	3.02	7.77	29.40	3.44	2.77	2.68
Kanaf									3,740	9,640											
Rice Straw	7.93	35.20	4.79	0.80	0.17	33.92	0.54	17.19	5,971	6,486	74.67	1.04	0.09	0.85	3.01	1.75	0.96	12.30	1.41	1.24	3.82
Ryegrass	12.69	40.81	5.09	0.87	0.16	36.55	0.08	3.83	6,963	7,975	39.88	0.40	0.05	1.10	14.69	4.53	10.08	13.10	6.16	8.11	1.28
Safflower										8,273											
Wheat OR	9.89	42.32	5.12	0.39	0.17	38.22	0.13	3.89	7,152	7,937	46.07	1.69	0.09	1.85	9.95	2.45	1.18	25.20	3.32	4.92	1.43
Wheat OR	10.81	41.97	4.75	0.39	0.16	37.39	0.29	4.53	7,116	7,978	46.59	2.51	0.14	1.76	8.28	1.73	1.15	30.30	2.17	2.79	2.00
Wheat Straw	11.68	40.62	5.00	0.48	0.19	36.28	0.07	5.75	6,942	7,860	48.94	0.28	0.05	2.47	4.92	1.52	2.11	35.40	1.49	5.64	3.11
Wheat Straw	7.04	41.75	5.07	0.40	0.14	39.08	0.21	6.52	7,171	7,714	55.32	1.88	0.08	0.73	6.14	1.06	1.71	25.60	1.26	4.40	2.48
Wheat Straw	29.07	30.78	3.96	0.23	0.16	28.47	1.20	7.33	5,213	7,350	56.41	0.38	0.05	0.42	3.43	1.74	1.45	23.20	1.20	2.40	3.47
Wheat Straw	13.29	37.70	4.79	0.71	0.15	34.61	0.49	8.75	6,351	7,325	50.76	0.84	0.09	0.96	4.12	2.15	1.32	32.50	3.60	1.25	4.66
Wheat Straw	4.09	40.91	5.17	0.64	0.29	38.34	1.90	10.56	6,874	7,167	38.81	0.57	0.02	0.17	4.78	1.03	11.70	24.70	1.31	2.54	5.59
Wheat	5.83	29.03	3.98	0.41	0.11	22.37	0.55	38.27	4,908	5,212	72.31	5.56	1.16	2.18	6.02	0.61	1.37	3.58	0.56	0.03	3.86
MANURE, BEDDING																					
Manure	34.07	21.91	2.82	1.46	0.64	14.85	1.23	23.02	3,673	5,571	41.99	6.06	0.25	1.88	13.05	4.45	4.85	12.29	5.52	5.10	10.74
Manure											57.51	7.63	0.42	3.58	7.48	3.67	3.32	6.29	2.23	2.20	
Bedding											49.12	10.91	0.42	3.64	14.24	3.18	4.26	6.40	3.12	2.06	
Bedding											43.87	9.05	0.25	3.11	12.99	7.62	4.12	8.38	9.96	2.08	

ASH VISCOSITY CALCULATIONS AND DEPOSIT CHARACTERISTICS

(For Lignite Type Fuel From Hazen Research Laboratory Reports)

TYPE	Alkali lb/MMBtu	% Base Content	% Acid Content	Dolomite Ratio %	Base/Acid Ratio	Silica/Al Ratio	T (CV) (DEG F)	T250 (Deg F)	Equiv Silica %	Viscosity from SiO2	Slagging Type*	Fouling Type**
FIELD CROPS, STRAWS AND STALKS												
Ag Waste	0.21	98.13	1.87	80.80	52.55							
Ag Waste	0.43	97.92	2.08	85.28	47.14							
Alfalfa Straw	1.57	90.09	9.91	47.36	9.09	4.45			15.69	1.00		SEVERE
Alfalfa Straw	2.13	88.26	11.74	44.08	7.52	6.29			20.32	1.00		SEVERE
Bermuda Straw	2.92	59.54	40.46	35.37	1.47	32.76			32.76	65.30		MEDIUM
Fescue StrawOR	2.68	57.74	42.26	20.04	1.37	38.25			76.94	473.59		SEVERE
Kanaf												
Rice Straw	3.82	19.93	80.07	25.23	0.25	71.80	2479		93.01	999.99		LOW
Ryegrass Straw	1.28	51.89	48.11	44.18	1.08	99.70			66.25	83.27		SEVERE
Safflower												
Wheat Straw OR	1.43	45.92	54.08	30.52	0.85	27.26	2173	2175	76.38	428.04	SEVERE	LOW
Wheat Straw OR	2.00	46.74	53.26	23.16	0.88	18.56		2169	79.83	804.97	SEVERE	LOW
Wheat Straw	3.11	48.51	51.49	13.87	0.94	174.79		2160	84.60	999.99	SEVERE	LOW
Wheat Straw	2.48	38.09	61.91	20.43	0.62	29.43		2243	87.46	999.99	HIGH	LOW
Wheat Straw	3.47	34.73	65.27	17.10	0.53	148.45	2600	2290	90.98	999.99	HIGH	LOW
Wheat Straw	4.66	44.26	55.74	15.27	0.79	60.43	2185	2186	87.53	999.99	SEVERE	LOW
Wheat Straw	5.59	51.82	48.18	13.71	1.08	68.09			86.65	999.99		SEVERE
Wheat	3.86	14.74	84.63	48.18	0.17	13.01						
MANURE, BEDDING												
Manure	10.74	38.26	50.61	47.92	0.76	6.93						
Manure												
Bedding												
Bedding												

* From Slag Temperature at 250 Poise Viscosity. Blank = not determined or off lignite table limits.

** Based on Na2O only. Other alkali (K2O) not considered.

APPENDIX 5

Fuel Characterization of Biomass Samples

Material in this appendix has been reproduced from the best available originals

FWC/FWDC/TR-93/08

Fuel Characterization of Biomass Samples

Prepared by

Richard W. Bryers
Senior Research Associate

November 1993

FOSTER WHEELER DEVELOPMENT CORPORATION
12 Peach Tree Hill Road, Livingston, New Jersey 07039

Fuel Characterization of Biomass Samples

Table of Contents

List of Figures

List of Figures (Cont)

List of Tables

Fuel Characterization of Biomass Samples

INTRODUCTION

The genesis of the biomass power industry is in the paper and wood products industry, where wood is used to cogenerate heat and power for process uses. Foster Wheeler has been a leader in this field for over 40 years. By 1989 approximately 6 GWe of biomass energy-based generating capacity was available in the United Sates—primarily owned and operated by industrial entities. Disposal of wood waste and availability of a cheaper source of fuel were the main reasons for using biomass as a source of energy. In the United States, biomass electric power generation experienced dramatic growth after the Public Utilities Regulatory Policies Act (PURPA) of 1977, which guaranteed small electric producers that utilities would purchase their surplus electricity at a price based on the cost of producing electricity that was avoided by the utilities. From less than 200 MWe in 1979, biomass energy-based generating capacity in the U.S. grew to approximately 66 GWe by 1989. It is estimated that there are 1000 wood-fired plants in the United States, typically in the range of 10 to 25 MW.[1]

Wood represents about 80% of the biomass consumed for raising steam. Agricultural waste (i.e., straw, manure, shells, etc.) constitute the remaining 20%. Wood presents very little fireside problems when burned in a steam generator by itself, despite the fact that 5 to 10% of the ash is composed of potassium. The bulk of the ash is composed of calcium, and silica appears to constitutes less than 10%. The ash is highly basic with high melting temperatures. Although potassium appears to be present as an organically-bound constituent which is highly volatile

during combustion, in the absence of sulfur, it presents little trouble as it remains suspended in the gas stream as K_2O or K(OH) to very low temperatures.

Agricultural wastes, on the other hand, are rich in silica and high in potassium. Occasionally sodium occurs in substantial amounts. Calcium occurs in modest concentrations. The solid ash has very high melting temperatures; however, once the silica absorbs the alkalies present, the fly ash particulate surface becomes molten to very low temperatures. Thomas Miles Associates, along with Sandia National Laboratory and the University of California, have a DOE/NREL contract to investigate the fireside behavior of these high-alkali species in various combustors. It was found that some of the agricultural residues have melting temperatures below the ashing temperature range for ASTM ash fusion temperatures—a standard technique extrapolated from the coal industry. To gain a better understanding of these fuels, a request was made for eight samples of biomass, presently under study by DOE/ENREL, to be evaluated in the FWDC laboratories.

FUEL CHARACTERIZATION

Dr. Bryan Jenkins of the University of California provided the following samples, prepared for analysis:

Waste Paper	Almond Hulls
Wheat Straw	Almond Shells
80% Wood/20% Wheat Straw	Olive Pits
Rice Straw	Wood Waste/Almond Shells

To this list were added Aspen from Daishowa, Canada and chicken litter from the U.K. for further comparison.

The eight samples provided by Dr. Jenkins were analyzed for complete proximate and ultimate analysis, ash chemistry and ash fusion temperatures using traditional procedures as applied in the coal industry. In addition, the samples were low-temperature ashed using an oxygen plasma over a period of 70 to 80 hours and then subjected to Differential Thermal Analysis (DTA) as well as Differential Scanning Calorimetry (DSC) to determine low-temperature melts—the thrust of the characterization. The low-temperature ash was also subjected to Thermogravimetric Analysis (TGA) to determine low-temperature losses caused by volatilization of the alkalies. Combustion profiles were also generated using TGA to make a direct comparison with known profiles of various coal ranks. Chemical fractionation was performed on select samples to determine the quantity and elemental composition of the water-soluble and organically-bound mineral matter.

PRESENTATION OF RESULTS

The proximate and ultimate analyses are summarized in Table 1, with the individual analyses appearing in Appendix A. The ash content varies from 1.50 to approximately 10% for the agricultural wastes, except for the rice straw which is almost 20%. Percent ash determined by low-temperature ashing ran from 3 to 85% higher than that determined by ashing at 950°C, as shown in Table 2. The ashing for quantitative analysis was performed at 500°C, and the percent unaccounted for ran from a few percent to 30% and appeared to be a function of the combined alkalies present. TGA performed on LTA and appearing in Figure 1 indicates volatilization began as low as 200°C (392°F) and increased roughly

Table 1 Summary of Biomass Fuel Analysis

Fuel	Waste Paper		Wheat Straw		80% Wood/ 20% Wheat Straw		Rice Straw		Almond Hulls	
Air Dry Loss	0.00		0.00		6.00		0.00		0.00	
	As Rec'd	Dry	As Rec'd	Dry	As Rec'd	Dry	As Rec'd	Dry	As Rec'd	Dry
Proximate Analysis										
Fixed Carbon	9.09	9.74	19.03	20.96	16.74	18.52	16.41	18.73	21.49	23.98
Volatile Matter	76.20	81.70	65.09	71.69	66.72	73.81	54.49	62.18	63.76	71.15
Ash	7.98	8.56	6.67	7.35	6.93	7.67	16.73	19.09	4.36	4.87
Moisture	6.73	--	9.21	--	9.61	--	12.37	--	10.39	--
TOTAL	100.00	100.00	100.00	100.00	100.00	100.00	100.00	100.00	100.00	100.00
Ultimate Analysis										
Carbon	45.74	49.04	41.08	45.25	43.15	47.74	34.10	38.91	42.75	47.71
Hydrogen	6.40	6.86	4.90	5.40	5.19	5.75	4.16	4.74	5.26	5.87
Oxygen	32.66	35.01	37.16	40.92	34.51	38.16	31.34	35.78	35.88	40.03
Nitrogen	0.42	0.45	0.81	0.89	0.54	0.60	1.2	1.37	1.30	1.45
Sulfur	0.07	0.08	0.17	0.19	0.07	0.08	0.10	0.11	0.06	0.07
Ash	7.98	8.56	6.67	7.35	6.93	7.67	16.73	19.09	4.36	4.87
Moisture	6.73	--	9.21	--	9.61	--	12.37	--	10.39	--
TOTAL	100.00	100.00	100.00	100.00	100.00	100.00	100.00	100.00	100.00	100.00
HHV, Btu/lb	8892	9534	7055	7771	7430	8220	5829	6652	7392	8249
Chloride, ppm	420		2330		1240		4670		650	
Percent Ash Determined by LTA (Low-Temperature Ashing)	8.70		9.44		9.20		22.58		9.03	

Table 1 Summary of Biomass Fuel Analysis (Cont)

Fuel	Almund Shells		Olive Pits		Wood Waste/ Almond Shells		Aspen		Chicken Litter	
Air Dry Loss	0.00		0.00		0.00		40.41		0.00	
	As Rec'd	Dry	As Rec'd	Dry	As Rec'd	Dry	As Rec'd	Dry	As Rec'd	Dry
Proximate Analysis										
Fixed Carbon	19.06	20.81	19.73	4.64	18.69	20.64	9.72	17.42	--	--
Volatile Matter	71.11	77.66	69.37	76.11	66.23	73.13	44.25	79.37	--	--
Ash	1.40	1.53	2.05	2.25	5.64	6.23	1.79	3.21	--	--
Moisture	8.43	--	8.85	--	9.44	--	44.24	---	--	--
TOTAL	100.00	100.00	100.00	100.00	100.00	100.00	100.00	100.00	100.00	100.00
Ultimate Analysis										
Carbon	34.63	37.82	44.32	48.62	42.11	46.50	29.09	52.17	--	42.80
Hydrogen	5.71	6.23	5.31	5.83	4.93	5.45	3.52	6.32	--	5.60
Oxygen	49.15	53.68	38.59	42.34	37.21	41.08	21.18	37.94	--	30.20
Nitrogen	0.65	0.71	0.86	0.94	0.64	0.71	0.18	0.33	--	5.20
Sulfur	0.03	0.03	0.02	0.02	0.03	0.03	0.02	0.03	--	0.50
Ash	1.40	1.53	2.05	2.25	5.64	6.23	1.79	3.21	--	15.20
Moisture	8.43	--	8.85	--	9.44	--	44.24	--	--	--
TOTAL	100.00	100.00	100.00	100.00	100.00	100.00	100.00	100.00	100.00	100.00
HHV, Btu/lb	8623	9417	7631	8372	7292	8052	4840	8680	--	--
Chloride, ppm	680		370		480		----		5000	
Percent Ash Determined by LTA (Low-Temperature Ashing)	3.57		2.26		8.32		----		----	

Table 2 Summary of Percent Ash Determined by Various Techniques

	Low-Temp. Ash <250°C	TGA on LTA 1000°C	Proximate Ash ≈950°C	TGA on Biomass 1000°C
80% Wood/20% Wheat Straw	9.20	7.6	7.67	4.0
Almond Hulls	9.03	3.79	4.87	5.0
Almond Shells	3.57	2.07	2.25	2.0
Rice Straw	22.58	17.1	19.09	17.5
Wheat Straw	9.44	6.6	7.35	5.0
Olive Pits	2.26	1.28	1.53	1.0
Wood Waste/Almond Shells	8.32	6.6	6.23	2.5
Waste Paper	8.70	6.96	8.56	7.0

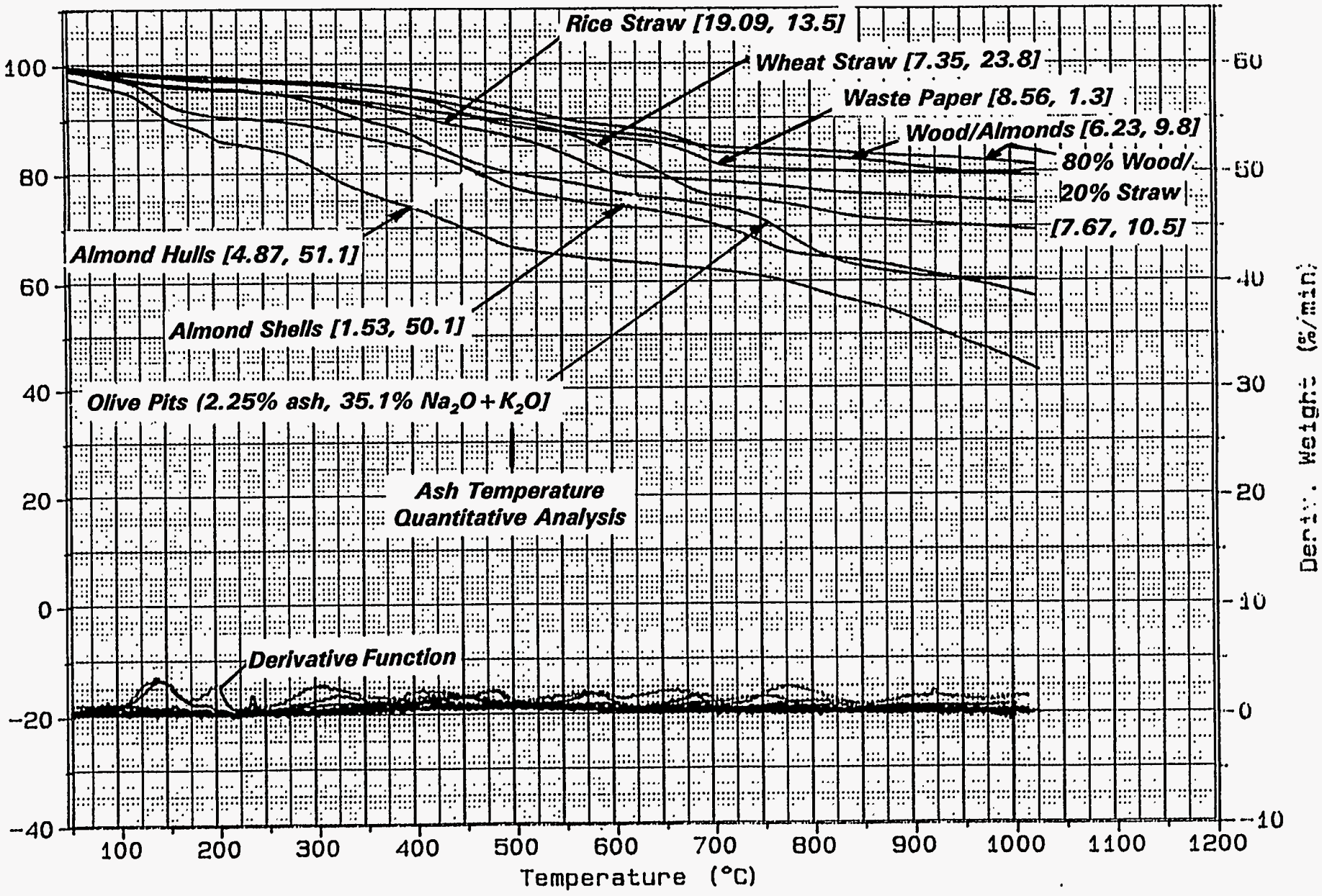
Rice Straw [19.09, 13.5]
Wheat Straw [7.35, 23.8]
Waste Paper [8.56, 1.3]
Wood/Almonds [6.23, 9.8]
80% Wood/
20% Straw
[7.67, 10.5]
Almond Hulls [4.87, 51.1]
Almond Shells [1.53, 50.1]
Olive Pits (2.25% ash, 35.1% Na_2O+K_2O]
Ash Temperature
Quantitative Analysis
Derivative Function
Weight (%)
Temperature (°C)
100
80
60
40
20
0
-20
-40
100
200
300
400
500
600
700
800
900
1000
1100
1200
60
50
40
30
20
10
0
-10

linearly with temperatures to 1000°C (1832°F). The loss at 500°C (932°F) was roughly in proportion to the difference in total ash predicted by LTA and ashing at 500°C (932°F). Below 200°C (392°F), the losses are believed to be caused primarily by moisture. The total loss appears to correlate reasonably well with total alkalies present. Waste paper containing 35.1 (K_2O+Na_2O) in the ash showed the least difference in quantity of ash when ashed by LTA and high-temperature ashing, while almond hulls and almond shells at ≈50% (Na_2O+K_2O) in the ash revealed a 23 to 26% loss in ash when heating to 500°C (932°F), and almost a 50% loss when heated to 1000°C (1832°F). Although the composition of the losses was not positively identified, it seems very reasonable to assume the material volatilized was alkali plus water of hydration. Chemical fractionation of the two almond samples summarized in Tables 3 and 4 indicate Na, K, Ca, and Mg occurring as water-soluble and organically-bound species account for 40 to 50% of the minerals found in the biomass samples.

Ash chemistry of agricultural waste cannot be evaluated using the quicker, cheaper, high-temperature analysis normally applied to fossil fuels. Analyses must be performed at low temperatures by chemical fractionation or other wet analytical techniques. Trend-wise, the loss of alkali with ashing temperature appears to agree with Livingston's data reported by Miles Associates [2,3] and illustrated in Figure 2. The percent loss, however, appears to depend on concentration level as well as temperature, suggesting either low-temperature absorption or a transport barrier to release imposed by other less volatile ash species may be altering the percent of alkali being release. The impact of time was not evaluated. It is also possible that a portion of the alkalies occur naturally as silicates. X-ray diffraction should be performed on the LTA.

Table 3 Chemical Fractionation — Almond Hulls

	Total[2] Concentration	Removed by H_2O	Removed by NH_4OAc	Removed by HCl	Remaining[1]
Na	994	485	438	162	72
K	41,237	18,571	2,095	57	20,571
Mg	1,993	752	390	48	851
Ca	6,093	3,048	1,305	324	1,740

Distribution of Elements

	% Removed by H_2O	% Removed by HN_4OAc	% Removed by HCl	% Remaining
Na	48.7	44.0	7.2	0.0
K	45.0	5.0	0.1	49.8
Mg	37.7	19.5	0.1	47.6
Ca	50.0	21.4	5.3	23.1

Notes: (1) Based on high-temperature ashing.

(2) Combined Analysis: Chemical fractionation and high-temperature ashing assuming those concentrations removed by H_2O, NH_4OAc, and HCl were lost during ashing. This may not be a valid assumption since the residue from the chemical fractionation process was not analyzed.

Table 4 Chemical Fractionation — Almond Shells

	Total[2] Concentration	Removed by H_2O	Removed by NH_4OAc	Removed by HCl	Remaining[1]
Na	713	310	320	130	83
K	20,041	9,800	980	40	9,261
Mg	792	220	220	40	352
Ca	3,699	1,750	840	330	1,109

Distribution of Elements

	% Removed by H_2O	% Removed by HN_4OAc	% Removed by HCl	% Remaining
Na	43.5	44.8	11.6	0.0
K	48.9	4.8	0.2	46.2
Mg	27.7	27.7	0.1	44.4
Ca	47.3	27.7	8.9	21.9

Notes: (1) Based on high-temperature ashing.

(2) Combined Analysis: Chemical fractionation and high-temperature ashing assuming those concentrations removed by H_2O, NH_4OAc, and HCl were lost during ashing.

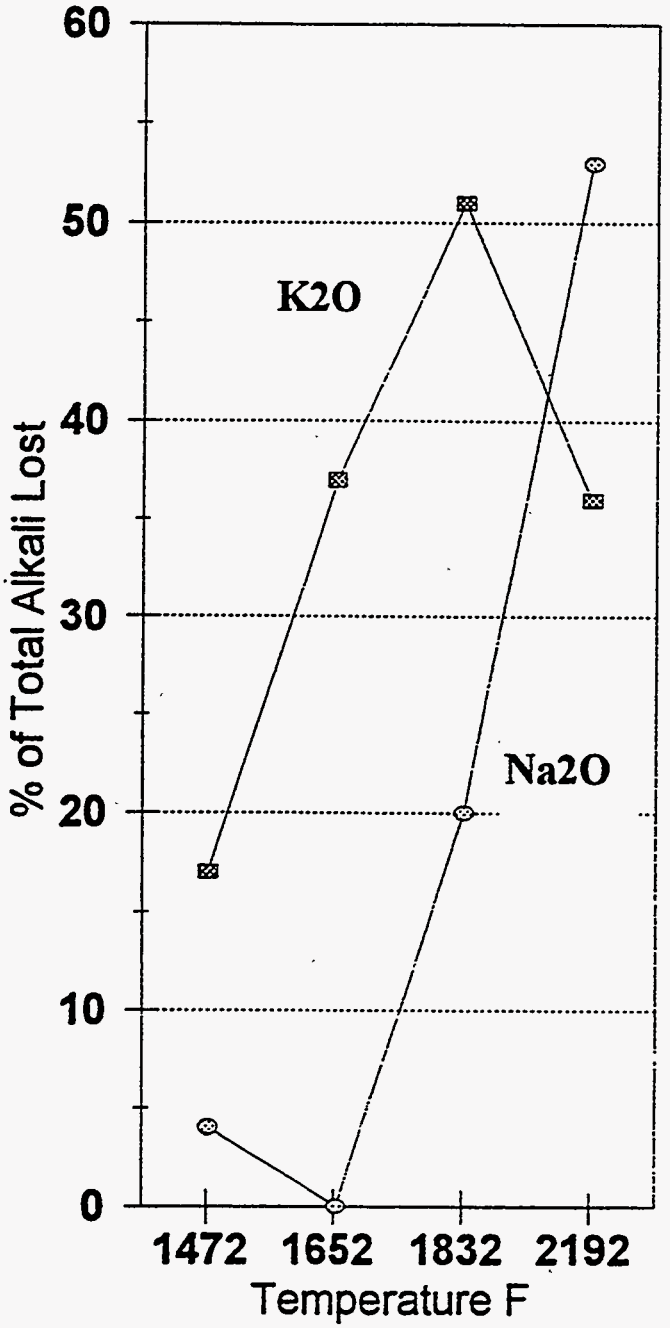

Figure 2 *Sodium and Potassium Volatilization from Wheat Straw (Livingston, 1993) [2,3]*

The ash chemistry of the agricultural waste is summarized in Table 5. Table 6 is a summary of ash chemistry of different species of wood included for comparison. Except for the almond hulls and almond shells, the agricultural wastes are rich in silica as free quartz and potassium, and contain relatively low concentrations of calcium. It has already been established that the potassium reported in the table, although high, is lower than the total potassium actually present by virtue of losses during ashing. The olive pits are enriched with sodium rather than potassium, and the almond residues are surprisingly low in silica. The agricultural products differ from wood waste primarily by the concentration of silica present. Wood generally contains only a few percent of quartz. The wood agricultural blends analyzed are unusually higher in quartz, suggesting they may have picked up some sand during handling. The waste paper contains a substantial quantity of alumina and is low in potassium. The agricultural products tend to be acidic in nature, whereas the wood residue tends to be basic. Blending of the two could create some low-melting species as suggested by a plot of ash fusion temperatures vs. percent basic constituents in Figure 3 on a regression analysis for coal. The data suggest coal technology can not be extrapolated to biomass for interpretation of the fireside behavior of the contained mineral analysis.

The regression analysis works well for coals in which the ash is essentially part of the SiO_2-Al_2O_3-Fe_2O_3 system or SiO_2-Al_2O_3-CaO system. Once the alkali content exceeds 3 to 4%, the curves become altered. Biomass data appears to fall into either a SiO_2-K_2O or K_2OCaO (low SiO_2) system and thus do not fit well on the pseudo-phase diagrams for coal ash. Phase diagrams for the two systems appear in Figures 4 and 5. Excursions in K_2O, CaO, or the addition of alumina skew the data. The scatter is also caused by discrepancies in actual ash composition of the samples on which the melting temperatures are determined and the composition of the samples reported in the analysis. Like Foster Wheeler, Osman ashed his

Table 5 Summary of Biomass Ash Chemistry

	Waste Paper	Wheat Straw	80% Wood 20% Wheat Straw	Rice Straw	Almond Hulls	Almond Shells	Olive Pits	Wood Waste/ Almond Shells	Aspen	Chicken Litter
	1	2	3	4	5	6	7	8	9	10
Elemental Composition										
SiO_2	20.5	55.7	56.8	73.0	4.0	4.9	23.1	49.6	14.9	10.7
Al_2O_3	54.0	1.8	10.9	1.4	1.3	1.5	5.3	11.0	1.2	5.8
TiO_2	1.5	•	0.5	•	•	•	0.1	0.4	•	•
Fe_2O_3	0.1	0.7	4.9	0.6	0.4	1.3	5.1	4.6	1.2	0.8
CaO	10.2	2.6	10.2	1.9	5.0	6.9	10.9	14.4	65.2	21.4
MgO	1.9	2.4	2.4	1.8	2.9	2.6	3.0	2.7	4.3	6.2
Na_2O	1.1	0.9	3.8	0.4	0.2	0.5	29.9	2.4	0.4	3.8
K_2O	0.2	22.8	6.7	13.5	50.9	49.6	5.2	7.4	6.5	15.1
SO_3	2.3	1.7	1.9	0.7	1.2	1.6	2.4	1.4	1.8	7.0
P_2O_5	•	1.2	1.1	1.4	5.5	5.0	2.7	1.5	2.0	30.2
Total Percentage	91.8	89.8	99.2	94.7	71.4	73.9	87.7	95.4	97.5	100.0
TGA Loss on LTA, 500°C %	8	10	9	15	26	23	20	11	--	--
Ash Fusion Temperatures										
Reducing										
I.T.	2694	2464	2065	2023	2359	1960	2340	2084	----	----
S.T. (Sph.)	2910	2466	2096	2246	2401	1981	2372	2130	----	----
S.T.(Hem.)	2910	2467	2288	2258	2408	2010	2495	2178	----	----
F.T.	2910	2474	2384	2641	2410	2071	2497	2239	----	----
Oxidizing										
I.T.	2619	1911	2084	1965	2558	1897	2448	2072	----	----
S.T. (Sph.)	2632	1913	2105	2158	2801	1899	2449	2096	----	----
S.T.(Hem.)	2910	2238	2322	2496	2818	1911	2487	2175	----	----
F.T.	2910	2316	2499	2582	2820	2348	2704	2262	----	----

• = Nil

Table 6 Fuel Properties of Eastern Canadian Bark

	Spruce				Jack Pine	Poplar	Birch		Maple		Elm	Beech	Tama-rack	Hem-lock
	Balsam	Black	White	Red			White	Yellow	Hard	Soft				
Proximate Analysis, wt%														
Volatile	77.4	74.7	72.5	72.9	74.3	78.9	80.3	76.5	75.1	78.1	73.1	75.2	69.5	72.0
Fixed Carbon	20.0	22.5	24.0	23.7	23.6	17.2	18.0	21.0	19.9	18.9	18.8	18.9	26.3	25.5
Ash	2.6	2.8	3.5	3.3	2.1	2.2	1.7	2.5	5.0	3.0	0.1	7.9	4.2	2.5
Ultimate Analysis, wt%														
Carbon	52.8	52.0	52.4	52.1	53.4	51.8	57.4	54.5	50.4	50.1	46.9	47.5	55.2	53.6
Hydrogen	6.1	5.8	6.4	5.9	5.9	6.5	6.7	6.4	5.9	5.9	5.3	5.5	9.9	5.8
Sulfur	0.0	0.0	0.0	0.0	0.0	0.0	0.0	0.0	0.0	0.0	0.0	0.0	0.0	0.0
Nitrogen	0.2	0.1	0.1	0.1	0.2	0.3	0.3	0.6	0.5	0.3	0.6	0.6	0.7	0.2
Oxygen	38.6	39.7	38.4	38.6	38.9	38.0	33.8	26.2	39.1	40.7	39.1	38.5	31.0	37.9
Ash	2.3	2.4	3.0	2.0	3.1	3.4	1.8	2.3	4.1	3.0	8.1	7.9	4.2	2.5
Ash Analysis, wt%														
SiO_2	24.6	6.4	2.0	7.6	16.0	1.5	3.0	4.1	39.5	6.1	3.6	12.4	7.3	10.0
Al_2O_3	1.8	1.1	0.6	0.0	6.3	0.5	0.6	0.3	3.8	3.1	0.0	0.0	8.4	2.1
TiO_2	0.2	*	*	0.1	0.2	*	*	*	*	0.1	0.1	*	0.1	*
Fe_2O_3	2.5	1.1	0.7	3.1	5.0	0.6	2.9	0.8	1.7	0.8	0.3	1.1	3.6	1.3
CaO	43.2	67.6	62.9	58.4	51.6	62.3	58.2	54.2	55.5	60.4	67.1	68.3	50.3	53.6
$CaCO_3$	7.8	11.2	13.6	11.3	4.9	14.6	13.0	17.8	1.4	16.7	16.3	2.2	4.1	9.7
MgO	2.2	1.7	6.4	4.7	5.5	1.9	4.2	5.4	19.4	2.3	2.0	11.5	8.5	13.1
MnO	2.6	2.2	1.2	2.0	1.6	0.3	4.6	1.3	1.0	0.4	0.1	0.4	3.4	1.2
P_2O_5	4.6	2.2	2.6	2.2	2.8	2.0	2.9	3.8	1.1	0.3	1.3	2.3	4.7	2.1
K_2O	10.1	6.2	7.3	5.3	4.1	7.2	6.6	8.0	5.8	6.3	4.4	2.6	5.3	4.6
Na_2O	2.5	2.5	0.8	2.0	3.1	3.9	1.3	1.7	2.2	0.9	0.7	0.9	3.2	1.1
SO_3	2.7	1.4	2.2	1.3	2.6	0.6	3.2	1.3	1.4	2.0	0.8	0.8	2.6	1.9
Fusion Temperatures, K														
Initial	1838	1760	1755	1627	1616	1744	1760	---	1727	1660	---	1633	1505	1788
Softening	1844	1784	1755	1821	1783	1810	1766	1777	1821	1738	---	1811	1533	1744
Fluid	1849	---	1760	1827	1805	1816	1771	1777	1827	1744	---	1816	1560	1799

*Trace.

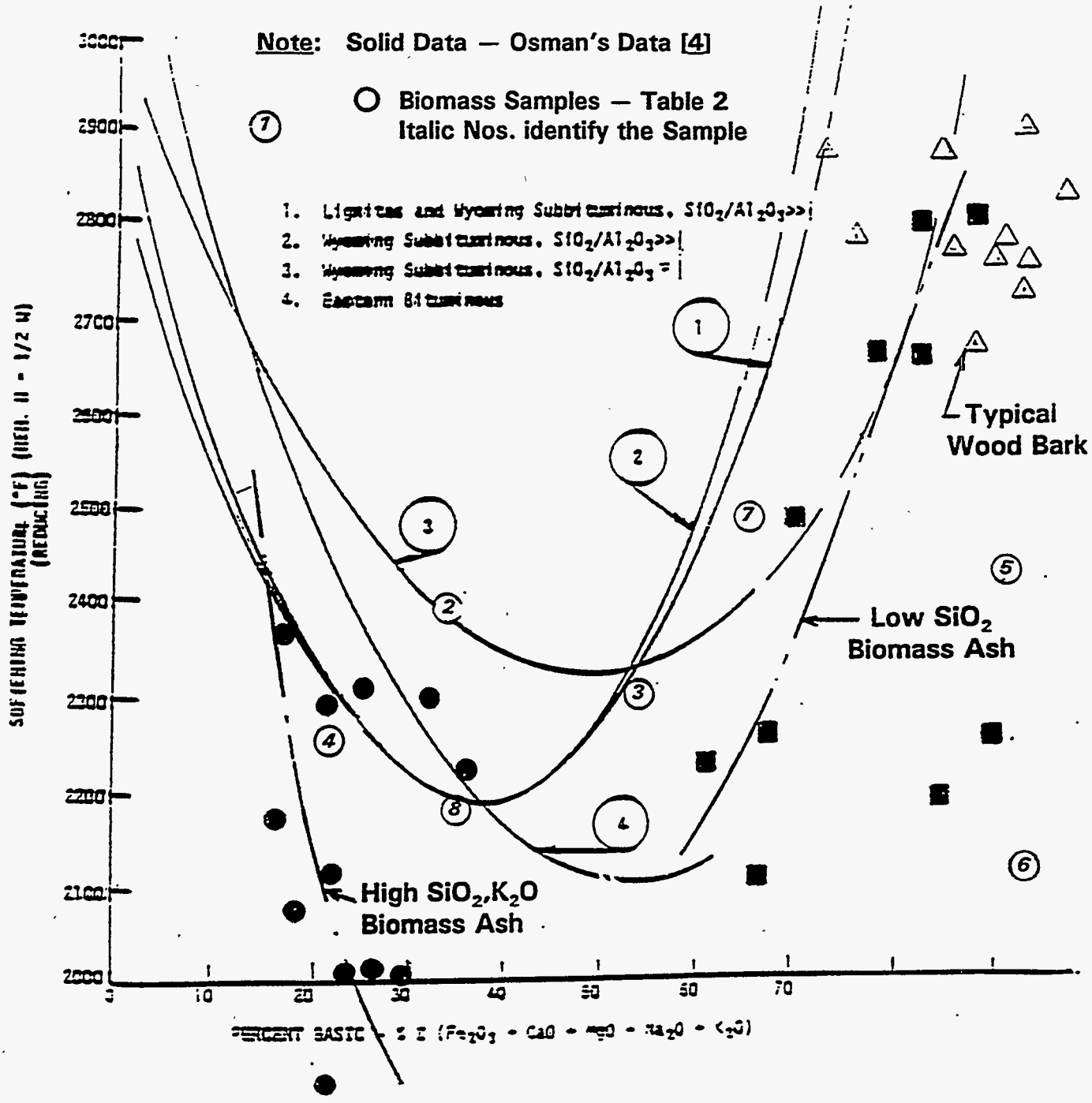

Figure 3 ***Biomass Data Superimposed on a Regression Analysis Illustrating the Influence of Percentage of Basic Constituents in Ash on Ash Softening Temperatures Under Reducing Conditions for Different Ranks of Coal (Regression analysis performed on many coal ash and slag deposits)***

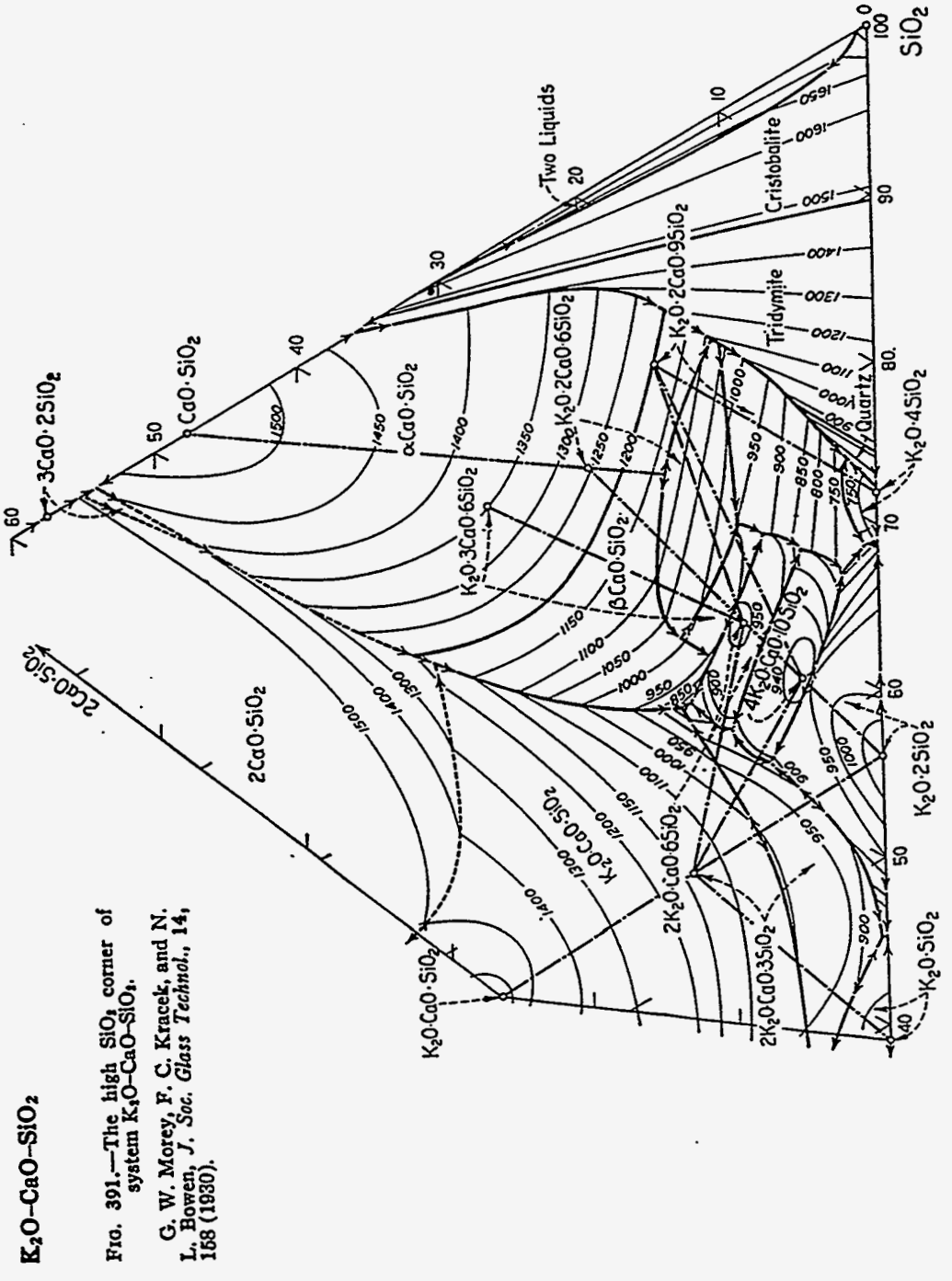

FIG. 391.—The high SiO_2 corner of system K_2O–CaO–SiO_2.

G. W. Morey, F. C. Kracek, and N. L. Bowen, *J. Soc. Glass Technol.*, 14, 158 (1930).

Figure 4 K_2O-CaO-SiO_2 System

K_2O–SiO_2

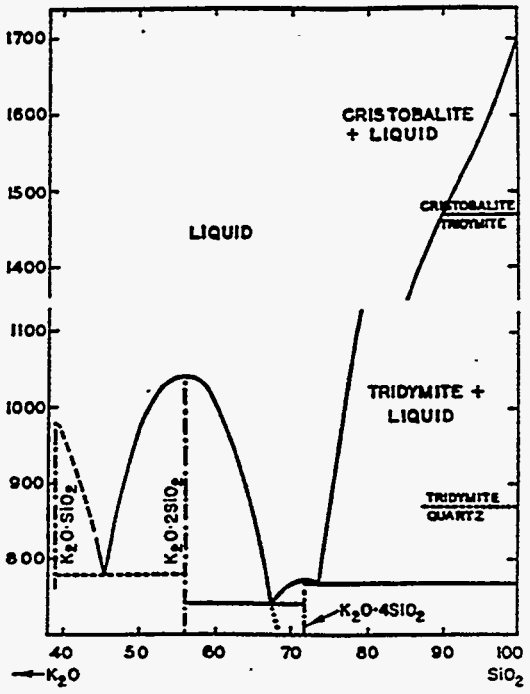

FIG. 167.—System SiO_2–$K_2O \cdot SiO_2$.

F. C. Kracek, N. L. Bowen, and G. W. Morey, *J. Phys. Chem.*, 41, 1188 (1937).

Figure 5 K_2O-SiO_2 System

samples at 575°C. In so doing, he lost some alkalies. In the process of analysis, he may have lost some more. This is quite evident in Table 7 in which Osman reports the analysis and fails to meet closure.

As already discussed, the potassium is a volatile species whose concentration is dependent upon ashing temperature. The quantitative analysis only applies to the temperature at which the fuel was ashed and therefore cannot be used as means for predicting melting temperatures. Furthermore, during combustion the alkalies are completely partitioned, leaving a high melting silicate and a volatile gaseous alkali, probably occurring as an oxide or hydroxide, as shown in Figure 6. The alkali, when united with the silicates via condensation and absorption will only be a portion of the total alkali present and its concentration will vary across the width of the silicate fly ash particle as condensation is a surface effect--see illustration in Figure 7. The concentration of the alkalies in the bulk deposited ash is time dependent and will be quite different from that determined by laboratory ashing, even at room temperature. The concentration of alkalies will vary over the deposit as the surface layer changes temperature. Furthermore, some potassium will deposit directly on the heat-transfer surface and its melting temperature will depend upon the availability of Cl or SO_2. The melting temperatures of KCl_2 and K_2SO_4 are 770°C (1418°F) and 1969°C (1956°F) respectively. Table 8 summarizes low-melting species which may be present in the deposited ash as well as the low-temperature ash.

Despite their questionable meaning, ash fusion temperatures were determined according to ASTM procedures with one exception—the ash was generated at 500°C (932°F). Even at the lower temperatures, the data is meaningless unless one is concerned about the ash fusion temperatures of ash normalized to a low level of alkali. This procedure may, however, provide some insight into the impact

Table 7 Computed Oxide Form of Test Samples (wt%)
By E. A. Osman [4,5]

	SiO_2	Fe_2O_3	MgO	CaO	ZnO	K_2O	Na_2O	SO_3	P_2O_5	Total
Bean straw (I)	29.9	2.7	0.9	4.67	0.03	22.34	0.52	4.7	2.29	68.05
Safflower	20.46	1.2	6.1	10.84	0.03	30.01	0.91	8.36	3.64	81.65
Rice hulls	94.6	0.03	0.02	0.25	0.00	2.4	0.135	2.24	0.46	100.12
Alfalfa	7.96	0.51	2.87	11.2	0.125	33.97	3.64	4.64	10.46	75.46
Cotton gin trash	23.2	1.93	2.87	7.18	0.187	13.00	1.59	4.24	10.00	64.20
Barley straw	44.7	2.6	4.84	3.22	0.125	8.01	5.25	1.8	11.56	81.11
Corn stalks	50.7	3.14	3.08	3.9	0.95	10.3	0.53	11.08	10.00	93.68
Rice straw	75.2	0.58	0.83	0.72	0.00	11.9	0.28	1.51	8.87	99.89
Bean straw (II)	32.7	3.93	3.65	6.3	0.15	25.3	0.82	2.28	7.3	82.43
Wood chips	8.3	10.0	6.22	18.61	0.193	11.8	1.32	9.0	6.87	71.61
Corn fodder	55.3	2.4	3.32	1.05	0.087	9.59	0.73	3.48	2.98	78.95
Paper pellets	57.2	4.29	0.83	0.15	0.31	1.85	5.09	4.0	4.46	78.19
Corn stalks (ex.)	63.3	4.72	4.78	0.56	0.00	8.37	0.47	7.2	2.06	91.46
Almond shell	22.6	3.77	2.49	12.27	0.05	14.14	5.08	8.0	5.5	73.90
Corn cobs	40.3	4.06	2.49	1.27	0.22	2.04	1.19	8.74	6.87	85.53
Manzanita chips	5.97	2.86	4.94	24.49	0.25	10.96	2.85	6.74	8.2	67.16
Tree pruning	9.95	1.94	8.29	19.87	0.06	12.66	1.48	19.72	4.96	85.93
Walnut shell	13.6	2.44	3.65	7.0	0.44	21.50	1.08	8.48	4.58	62.92
Olive pits	10.5	2.2	3.48	25.89	0.12	3.13	7.60	17.2	7.56	77.74
Almond shells	18.6	3.83	1.99	16.0	0.23	14.7	5.86	17.48	7.79	86.48
Corn stalks	71.7	7.1	2.7	0.46	0.02	10.28	0.33	2.2	0.66	95.45
Cotton stalks	33.0	2.8	6.05	3.56	0.07	21.40	1.374	6.55	6.4	83.57
Rice mix	75.0	0.47	2.5	1.1	0.00	15.85	0.54	1.0	1.1	97.56
Wheat + corn (1:3)	71.7	3.3	8.3	0.95	0.619	14.76	0.54	2.96	1.1	103.64
Rice straw (good bales)	78.3	0.36	2.0	0.7	0.00	13.0	0.43	1.69	0.8	97.78
Rice straw (decayed bales)	78.6	0.44	2.0	0.88	0.00	14.50	0.44	1.83	0.9	99.59

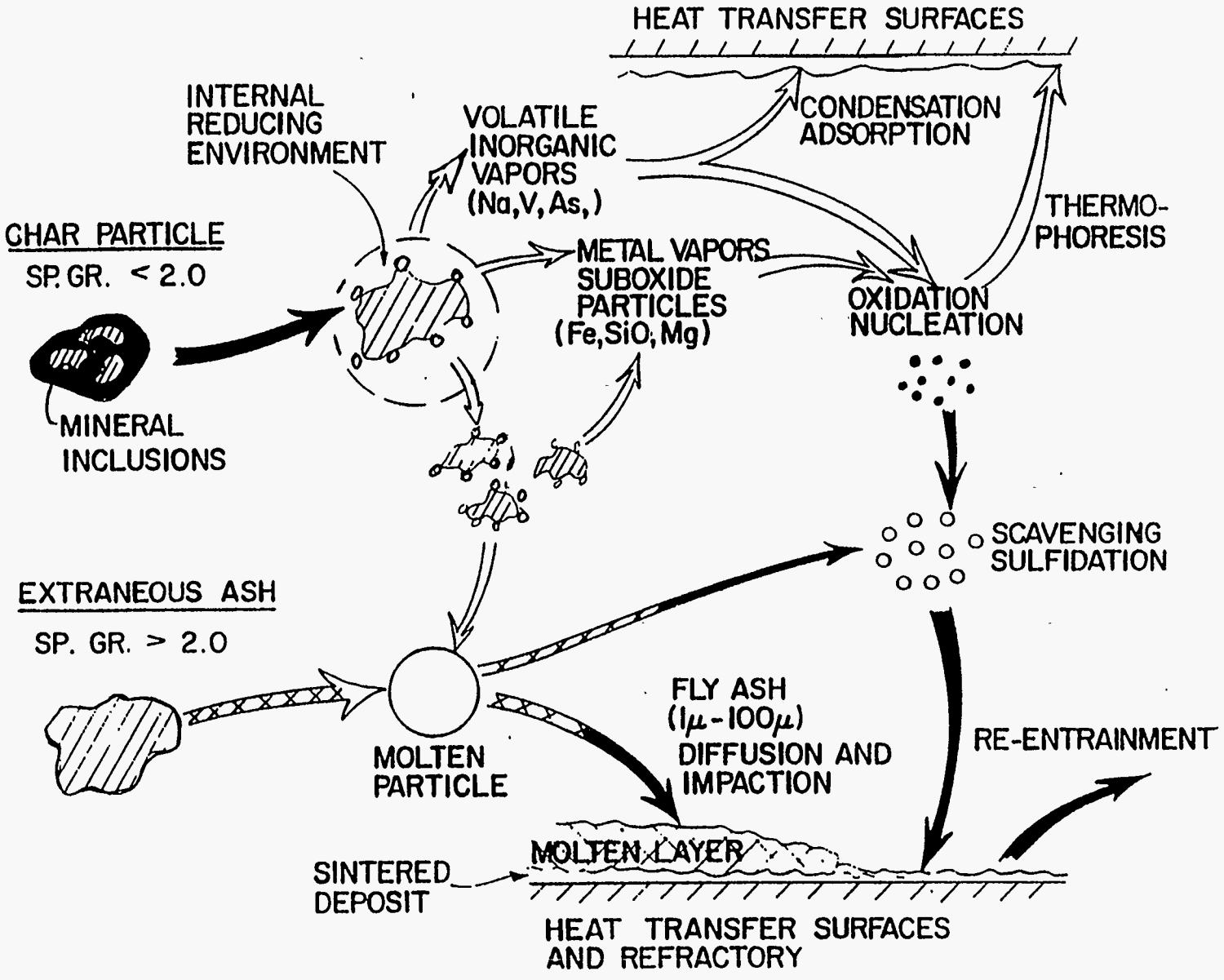

Figure 6 Phase Transformation of Minerals in Fuels

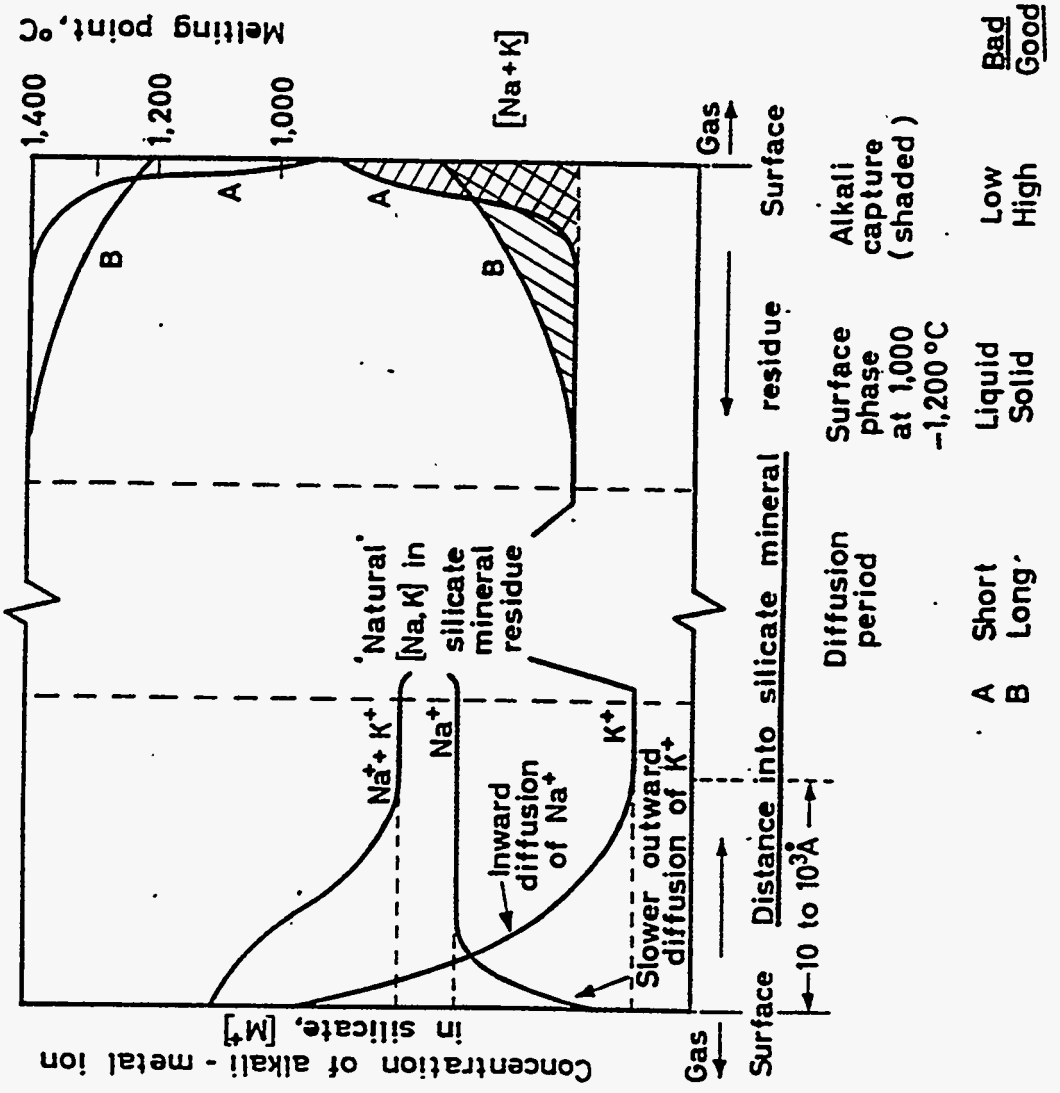

Figure 7 Reaction of Alkali Metals at Surface of Fused Silicate Particles [6]

Table 8 Melting Temperature of Potential Low-Melting Minerals Found in Biomass

Group	*Mineral*	*Melting Temperature, °C*
Chlorides	$NaCl$ $CaCl_2$ KCl $MgCl_2$ $FeCl_3$	801 782 770 714 306
Carbonates	Na_2CO_3 $CaCO_3$ K_2CO_3 $MgCO_3$ $FeCO_3$	851 1339 891 Decomp. 350 Decomp.
Chlorates	$NaClO_3$ $Ca(ClO_3)_2$ $KClO_3$ $MgClO_3 \cdot 6H_2O$ Iron $Fe(ClO_4)_2$	248-261 340 356, decomp. 400 35 Decomp. >400
Sulfates	Na_2SO_4 $CaSO_4$ K_2SO_4 $MgSO_4$ $Fe(SO_4)_3$	 750-950 (pres. of silicates) 1069 Tr. 558 1124 Decomp. 480 Decomp.
Hydroxides	$Na(OH)$ $Ca(OH)_2$ KOH $Mg(OH)$ $Fe(OH)_2$	318 580 – H_2O 360 350 – H_2O ---
Sulfides	Na_2S CaS K_2S MgS FeS_2	1180 --- 470 --- 1171
Phosphates	$Ca_2P_2O_7$ K_3PO_4 $Mg_3(PH_4)_2$	1230 1340 1184

of other elements such as calcium on the high-temperature melting of free quartz, but it will tell nothing about the role of the alkalies. To evaluate the impact of potassium on the other mineral species at low temperature, the biomass was low-temperature ashed and subjected to differential thermal analysis (TGA). The results appear in Figures 8 through 15. It was hoped that since there were only a few major elements present in the low-temperature ashed, DTA would reveal a few clear, decisive endotherms corresponding to the low-temperature constituents present. The thermograms in Figures 8 through 15 indicate the endotherms present may vary from only one or two, to many of different intensity, thus representing different concentrations and compounds, and possible decompositions rather than melts. The problem is compounded by the presence of exotherms, endotherms and transformations, some of which overlap. To overcome some of these problems, a TGA and its derivative were included to help distinguish between melts and decompositions.

Thermal analysis of the blend of 80% wood and 20% straw, shown in Figure 8, revealed three minor endotherms at about 400 to 425°C (752 to 797°F), 550 to 575°C (1022 to 1067°F), and 650°C (1202°F). The thermogravimetric analysis indicated the latter two occur simultaneously with a significant weight loss, implying a decomposition. The first or lowest endotherm is believed to be caused by a melting that could be due to a complex system of chlorides of Ca, Mg, Na and potassium. It should be noted that all three compounds may be artifacts of low-temperature ashing depending upon the actual occurrence of Cl in the wood and/or straw.

Thermal analysis of the olive pits, shown in Figure 9, reveals two minor endotherms at 325°C (617°F) and 425°C (797°F) which correspond to sudden losses in weight, suggesting they are caused by decomposition. If melts are also

Figure 8 DTA Thermogram under Air of Low-Temperaure Ashed 80% Wood/20% Straw

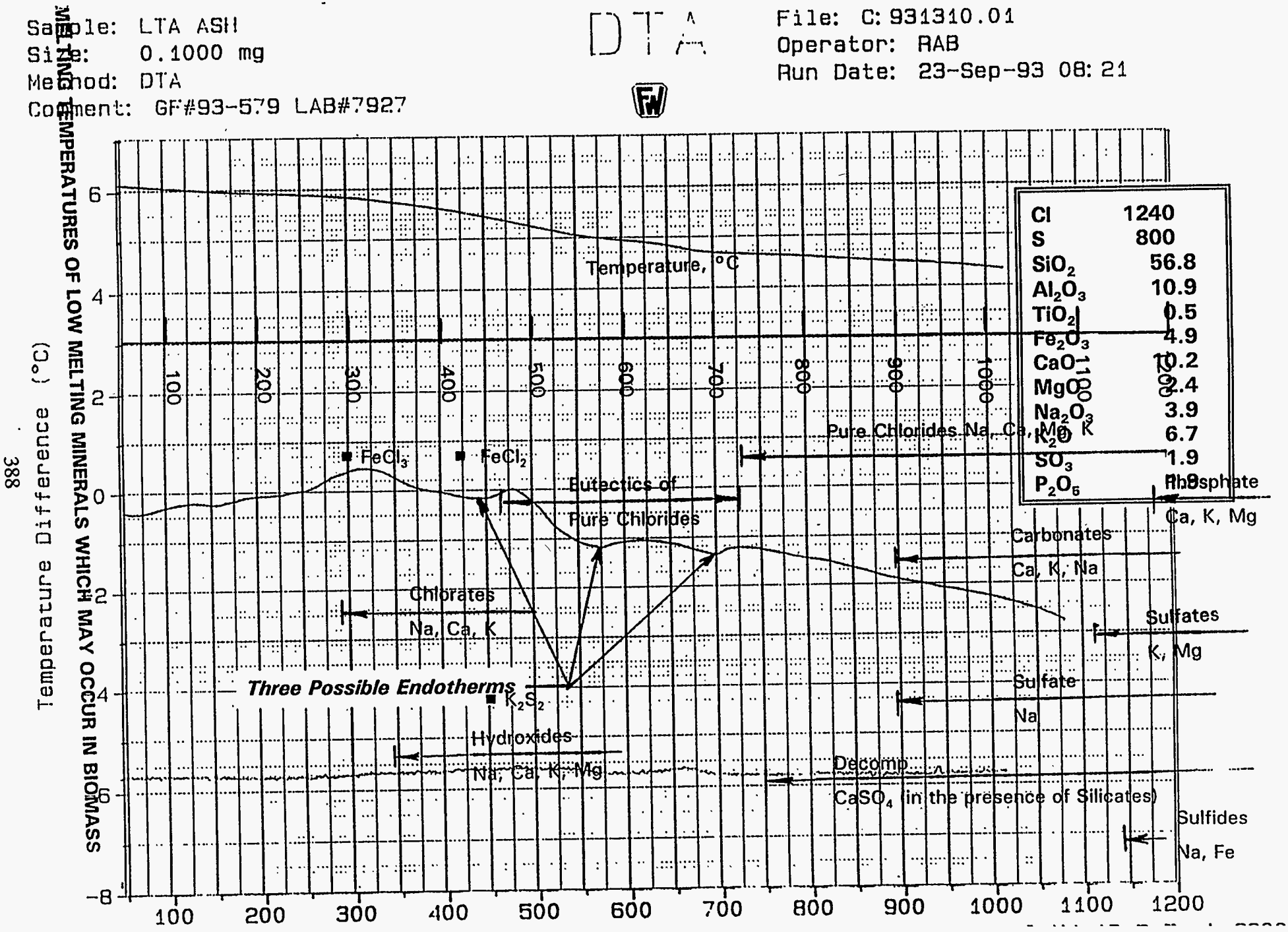

Sample: LTA ASH OLIVE PITS
Size: 0.1000 mg
Method: DTA
Comment: GF#93-580 LAB#7928

DTA

File: C:931311.01
Operator: RAB
Run Date: 23-Sep-93 10:45

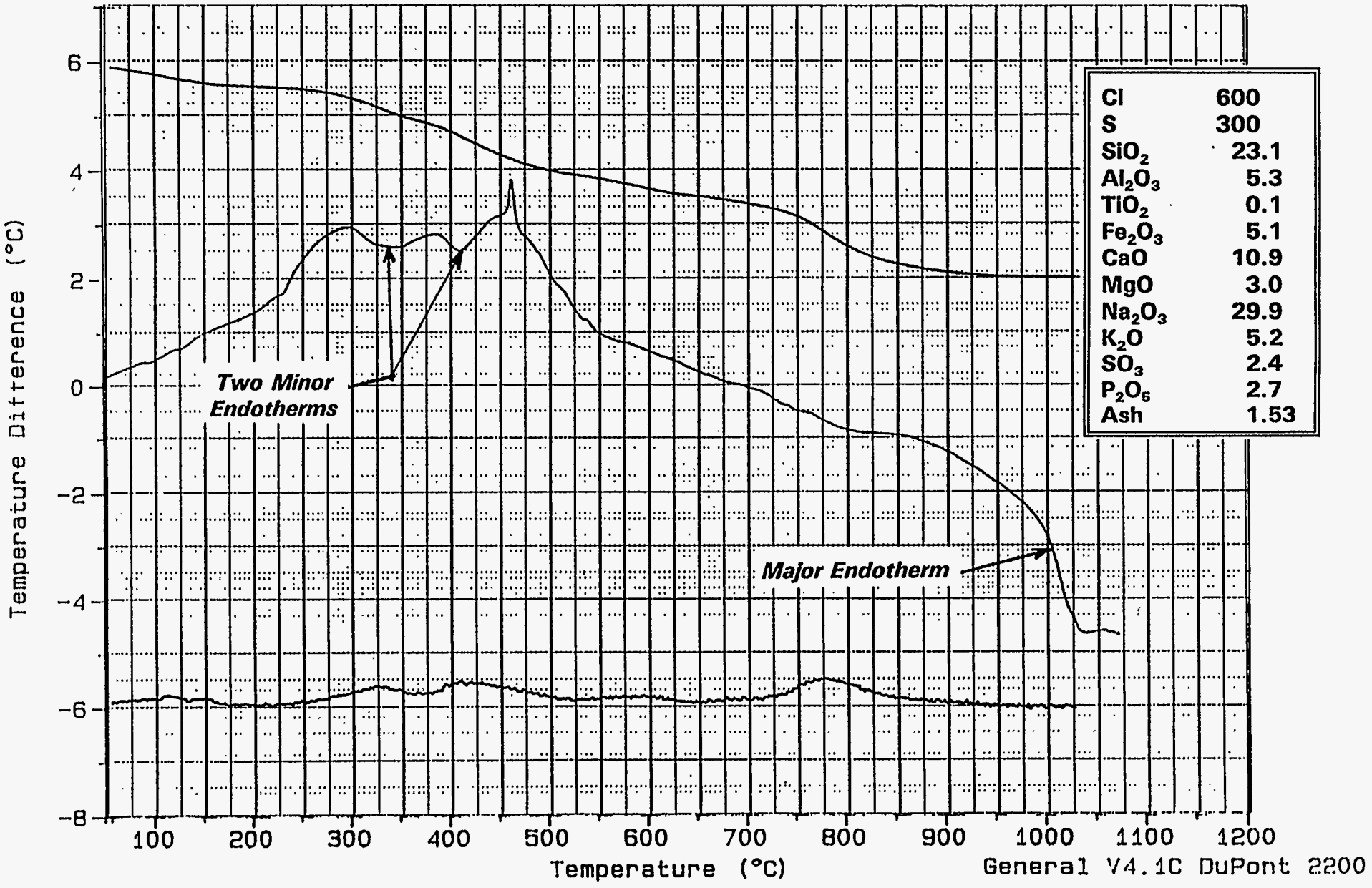

389

General V4.1C DuPont 2200

Sample: LTA ASH WASTE PAPER
Size: 0.1000 mg
Method: DTA
Comment: GF#93-581 LAB#7929

DTA

File: C:931312.01
Operator: RAB
Run Date: 23-Sep-93 13:35

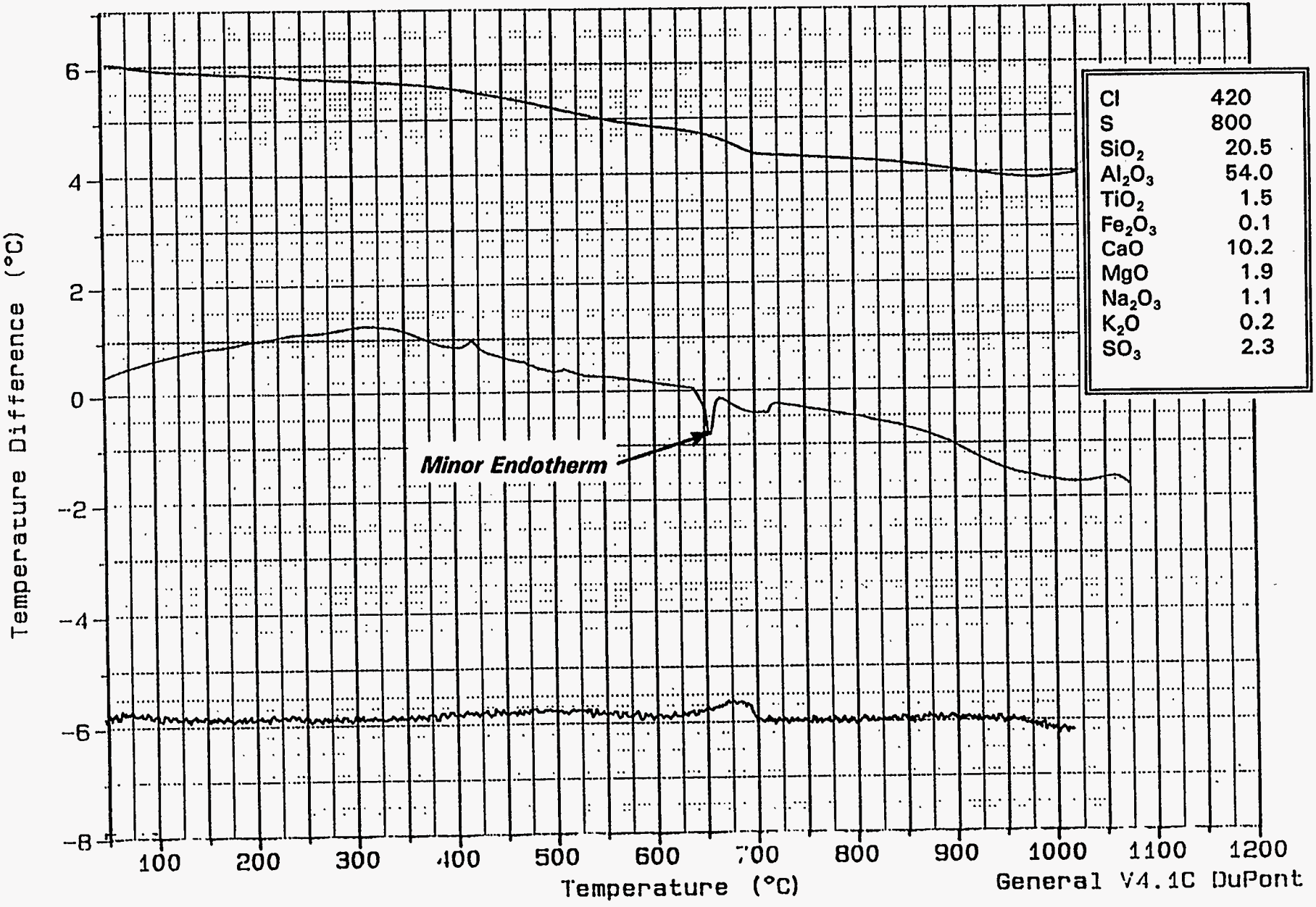

General V4.1C DuPont 2200

Sample: LTA ASH ALMOND HULLS
Size: 0.1000 mg
Method: DTA
Comment: GF#93-582 LAB#7930

DTA

File: C:931313.01
Operator: RAB
Run Date: 24-Sep-93 07:46

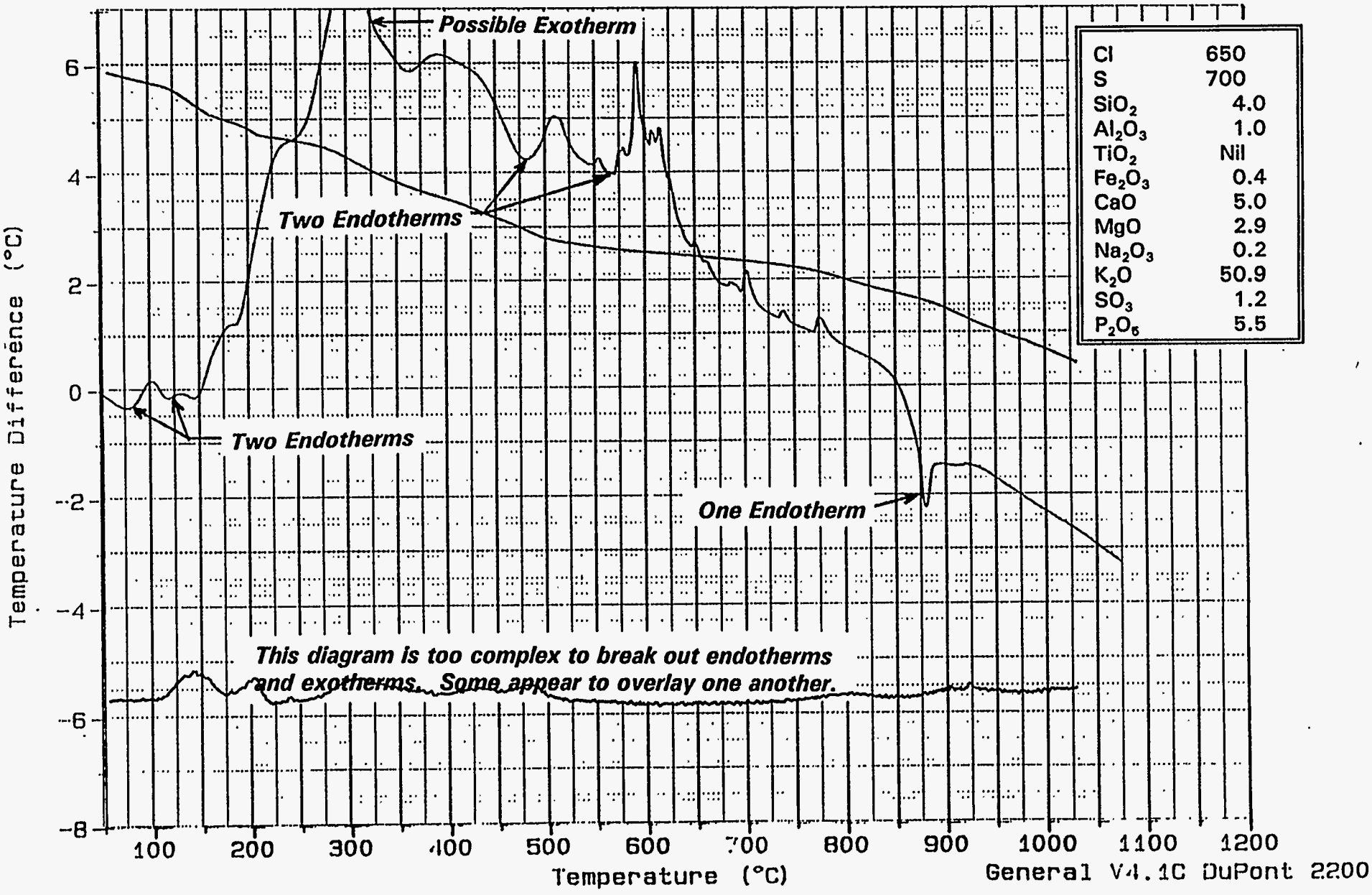

General V4.1C DuPont 2200

Sample: LTA ASH ALMOND SHELLS
Size: 0.1000 mg
Method: DTA
Comment: GF#93-583 LAB#7931

DTA

File: C:931314.01
Operator: RAB
Run Date: 24-Sep-93 10:43

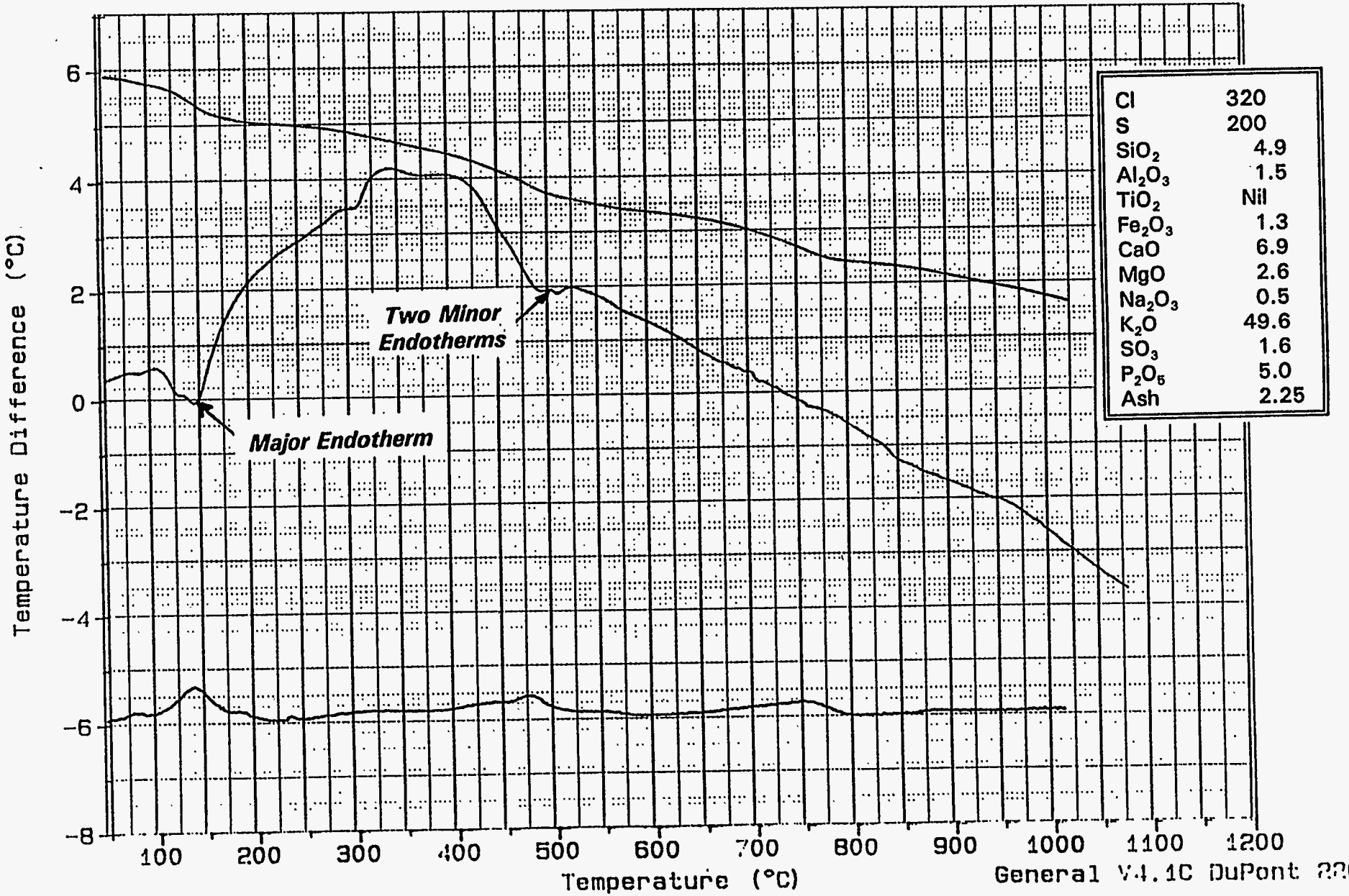

Cl	320
S	200
SiO_2	4.9
Al_2O_3	1.5
TiO_2	Nil
Fe_2O_3	1.3
CaO	6.9
MgO	2.6
Na_2O_3	0.5
K_2O	49.6
SO_3	1.6
P_2O_5	5.0
Ash	2.25

392

General V4.1C DuPont 2200

Sample: LTA ASH RICE STRAW
Size: 0.1000 mg
Method: DTA
Comment: GF#93-585 LAB#7933

DTA

File: C:931316.01
Operator: RAB
Run Date: 27-Sep-93 11:08

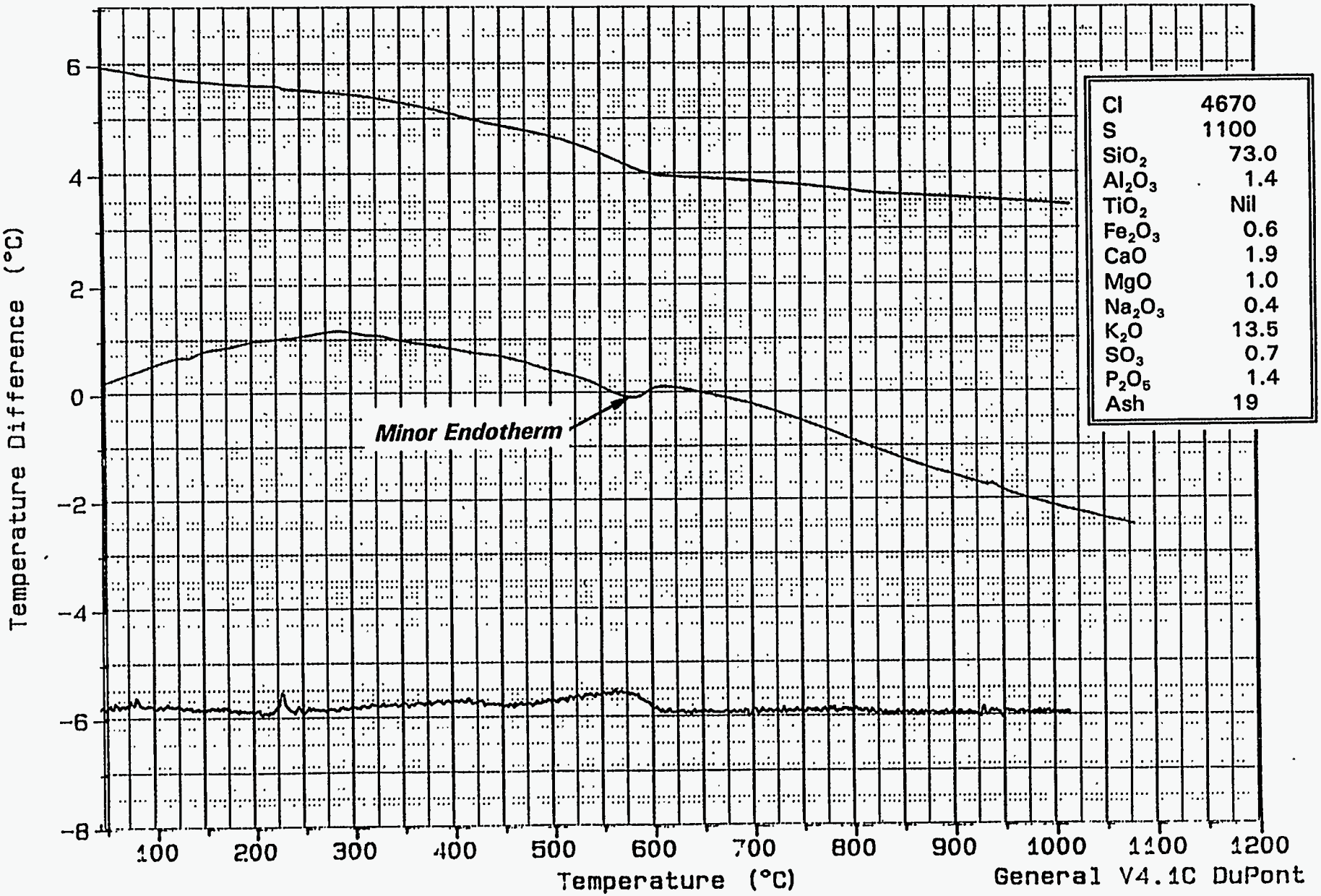

General V4.1C DuPont 2200

Sample: LTA ASH WOOD ALMOND
Size: 0.1000 mg
Method: DTA
Comment: GF#93-586 LAB#7934

DTA

File: C:931317.01
Operator: RAB
Run Date: 27-Sep-93 13:43

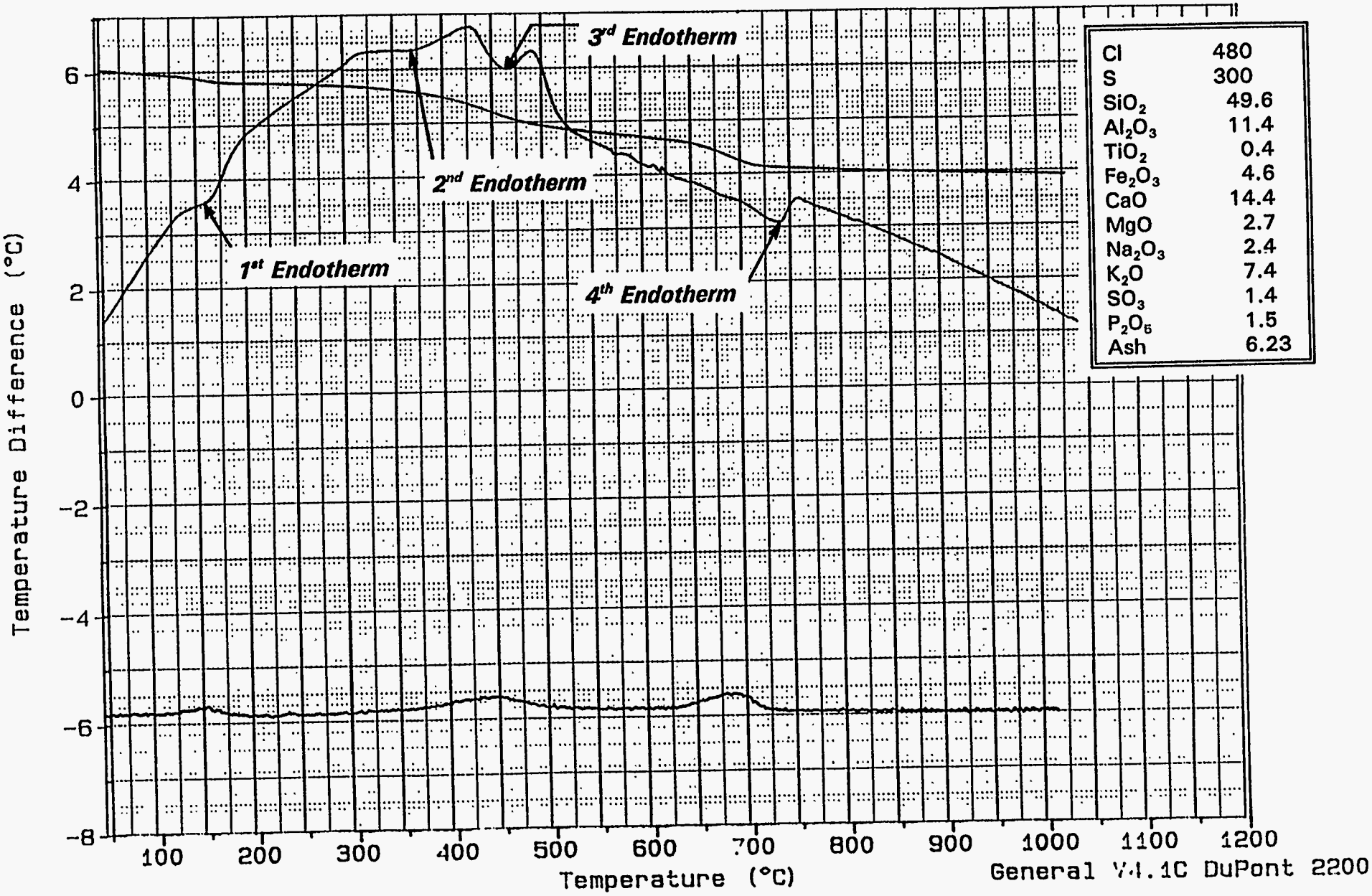

Figure 15 DTA Thermogram under Air of Low-Temperature Ashed Wheat Straw

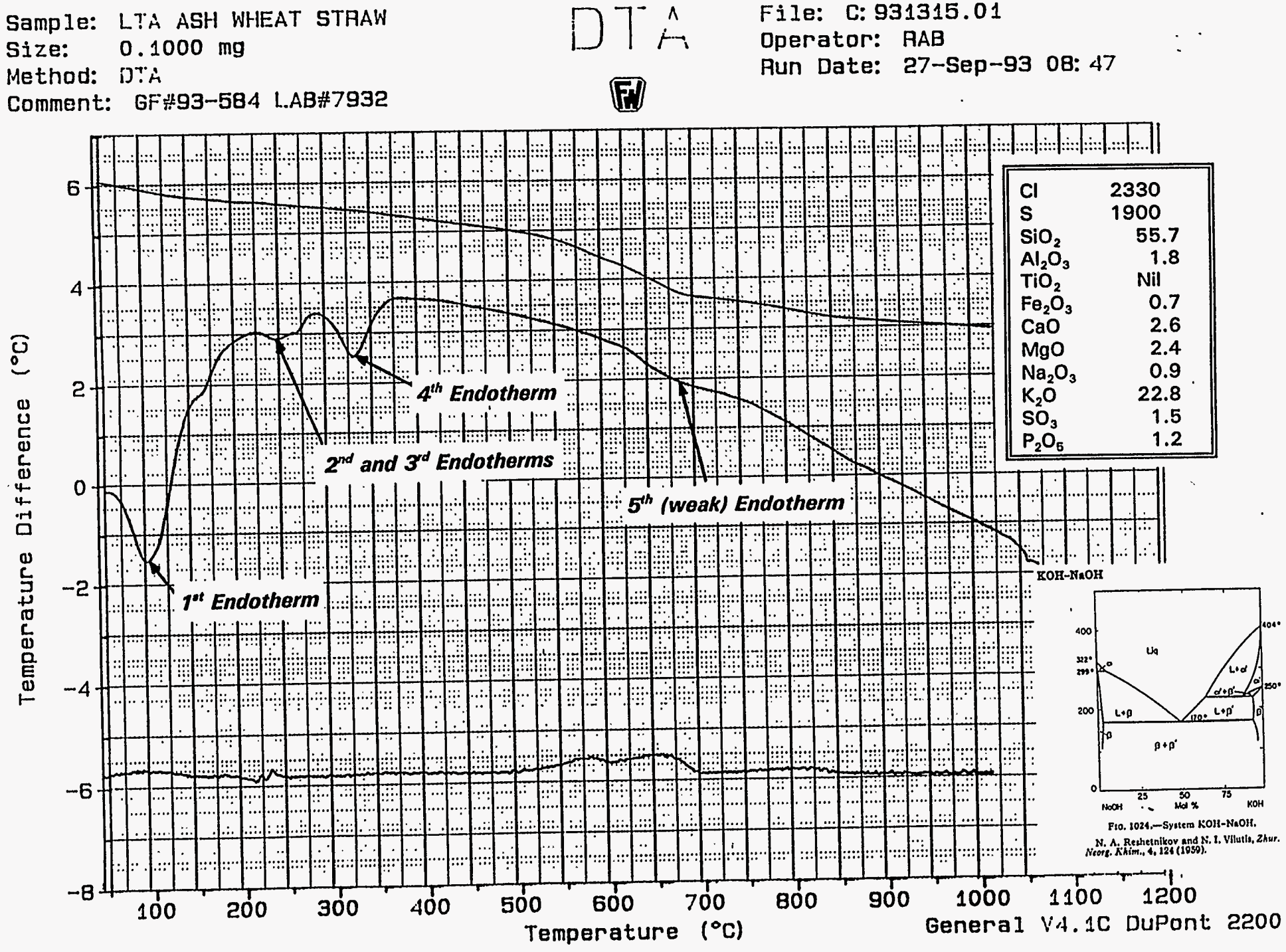

occurring, they are possibly associated with chlorates of potassium and sodium, as suggested by the overlay based on the CRC tables and the American Ceramic Society collection of phase diagrams. A major endotherm occurs at about 815°C (1602°F), during which no loss in weight is experienced. This endotherm is believed to be part of the sodium-silicate system illustrated in Figure 5.

The thermogram for waste paper, shown in Figure 10, reveals only one endotherm of any consequence, coincidental with a sudden weight loss at 675°C (1247°F). There is a degree of uncertainty.

The thermal analysis of almond hulls in Figure 11 is extremely complex despite the simple apparent chemical analysis. The ash analyzed at 500°C (932°F) and included in the diagram is primarily potassium with trace amounts of other elements. Thirty percent of the mineral matter released during the ashing process is composed of calcium, magnesium and sodium, as determined by chemical fractionation. Two endotherms occur at 50°C (122°F) and 125 to 150°C (257 to 300°F). The latter is associated with a decomposition, possibly associated with hydration. The next endotherm occurs at about 195°C (383°F) which is also coexistent with a weight loss. An apparent exotherm occurs at 300°C (572°F), coincident with a weight loss which remains unexplained. The next two endotherms occur at 475 and 575°C (887 and 1067°F). The latter could be caused by the dehydration of calcium hydroxide. The final endotherm occurs at 875°C (1607°F), which is also associated with a weight loss.

Thermal analysis of almond shells, appearing in Figure 12, reveals a lot less activity than almond hulls. Two out of three endotherms are associated with weight losses. Two of them occur at the same temperature levels as found in almond hulls [i.e., 150°C (302°F) and 475°F (887°F)]. One small endotherm

occurs at 300°C (572°F). At this point in time, it is difficult to identify it with any specific compound.

The rice straw thermal analysis in Figure 13 revealed only one endotherm coincident with a weight loss at 575°C (1067°F). This could be caused by dehydration of calcium hydroxide; however, there is little calcium in the system.

The wood/almond mixture thermal analysis appearing in Figure 14 revealed four endotherms at 150°C (302°F), 425°C (797°F), 455°C (851°F), and 675°C (1247°F). Three of these are associated with weight losses—one is associated with a melt. The endotherms at 150°C (302°F), 450°C (842°F), and 650°C (1202°F) were also found in the straight almond shells.

The last biomass sample examined was wheat straw and its thermal analysis appears in Figure 15. The first four endotherms occur at 100°C (212°F), 250°C (482°F), 270°C (518°F), and 325°C (617°F), and are not associated with specific accompanying weight loss. These melts could be associated with Na(OH) and K(OH) melts illustrated in the phase diagram insert. There is also a major endotherm beginning at about 800°C corresponding to zero weight loss. This endotherm is frequently associated with the decomposition of $CaSO_4$ in the presence of silicates. In the absence of a weight loss, it is probably due to a melt in the K_2O-SiO_2 system--see Figure 5.

It appears that most of the endotherms are associated with weight losses and not melts. The systems are too complex to use DTA as a means of identifying compounds present. X-ray diffraction should be applied to the low-temperature ash to identify the specific compounds present. Producing characteristics thermograms of pure compounds of hydroxides and chlorides of Ca, Na, K, Mg and Fe

may be helpful. If, indeed, melts are formed, they must be transitional as most of the low-melting alkalies and alkali earth metals volatilize at low temperatures upon heating.

To examine fouling and slagging, we must examine the thermal behavior of the compounds that will reunite upon quenching during the post-combustion heat recovery stage. Possibly sintering tests could be developed using simulated flue gas containing the correct dose of K(OH), Na(OH), Cl, and S.

Combustibility of the biomass samples was investigated using TGA simply because of the availability of the samples. The TGAs were run at a heating rate of 20°C/min. The results are summarized in Figures 16 and 17. Figure 18 compares the combustibility of a typical TGA profile with other rank coals. The DTA indicates that biomass ground to the same size as other fossil fuels behaves very much like a lignite. The residual char in olive and waste paper is significantly higher than the other fuels. The difference in rates of combustion between the volatiles and char may be the source of some carbon loss.

SUMMARY AND CONCLUSIONS

Fuel characterization of the eight biomass samples indicates:

- Ash analyses must be performed at temperatures below 250°C to avoid loss of alkali during ashing.
- ASTM ash fusion tests are meaningless. A substantial amount of potassium is lost during ashing, numerous low-temperature melts occur below 1000°F, and the stickiness or melting temperature of fly ash is dependent upon the absorption of potassium during the post-combustion process by species partitioned during combustion.

Figure 16 Thermogravimetric Analysis of Biomass Samples Heated at a Rate of 20°C/Min

Figure 18

Combustion Profiles of Various Rank Coals

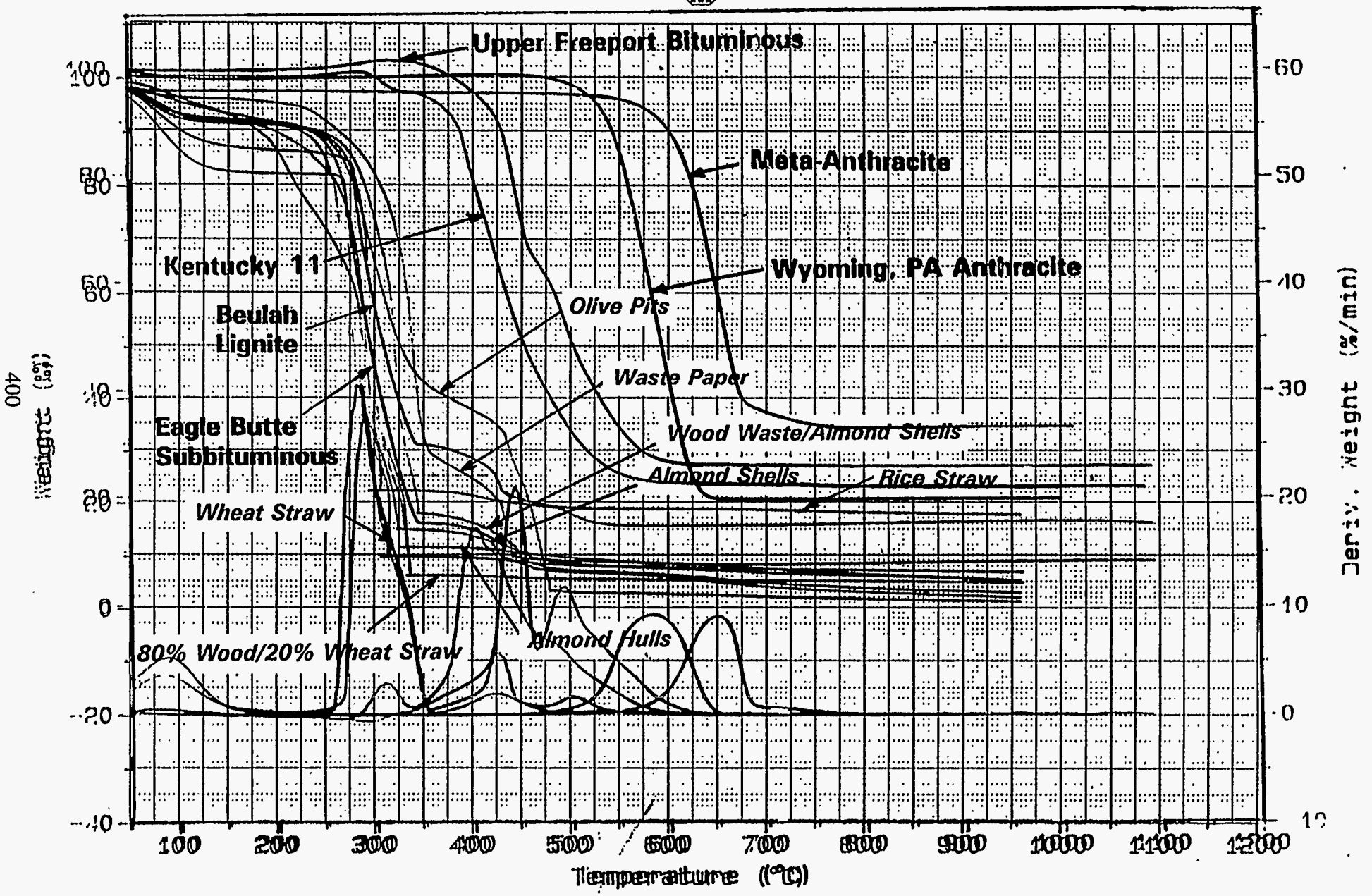

Figure 17 The Derivative Function of TGA Combustion Profiles Illustrated in Figure 12

Figure 18

Combustion Profiles of Various Rank Coals

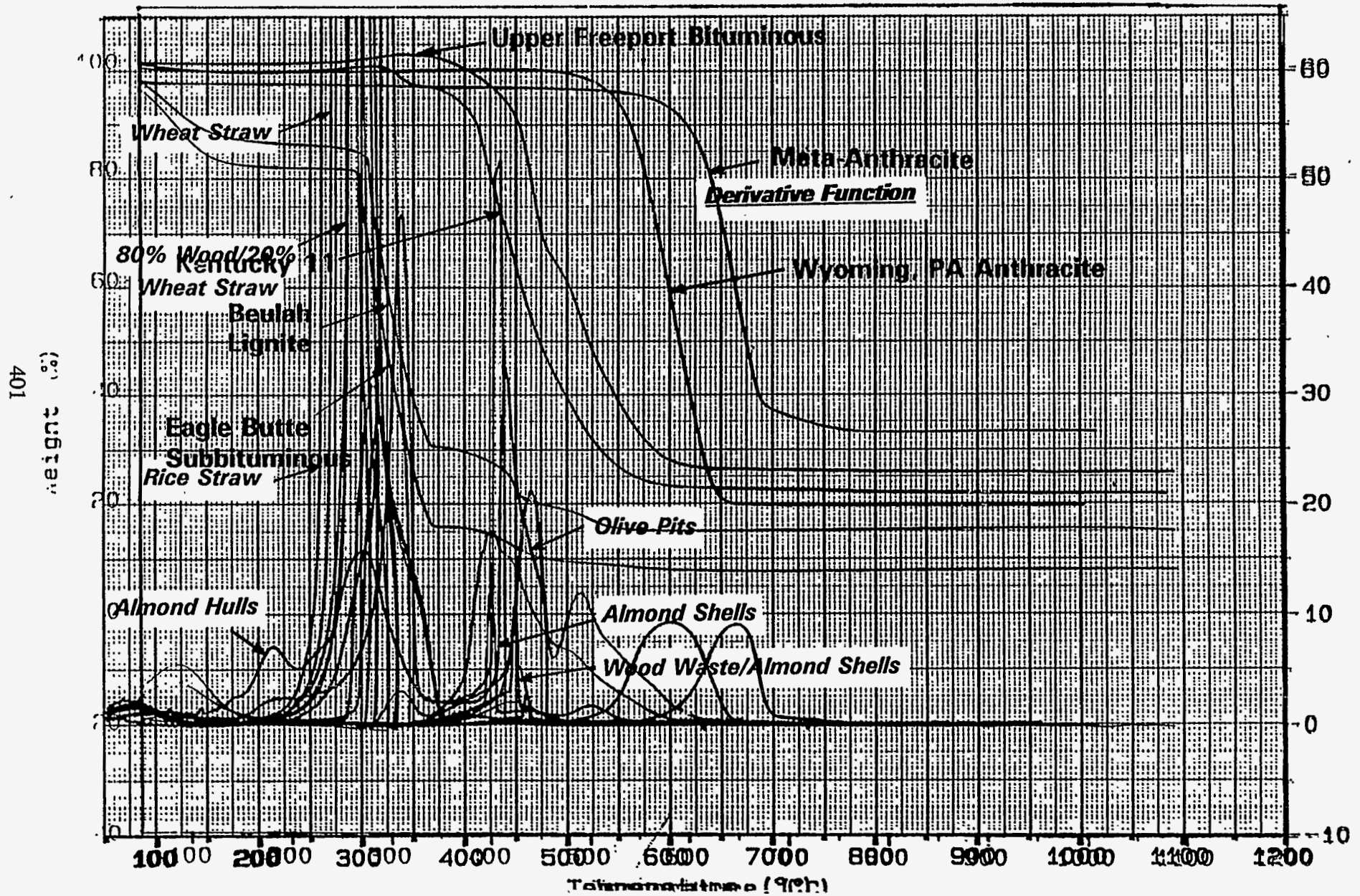

- Approximately 35 to 70% of the potassium is lost at 500°C, and the loss is linear with temperature and somewhat dependent upon the percent potassium in the ash.
- Differential thermal analysis was only partially successful in identifying specific melts as too many endotherms are generated below 1000°F due to melting of complex mixtures of compounds, decomposition, and exothermic reactions.
- X-ray diffraction should be performed on low-temperature ash.
- Fireside behavior may best be evaluated by determining the potassium and sodium concentration at ambient temperature and performing a sintering test on artificial fly ash in an environment simulating flue gas enriched with alkali vapor.
- The combustibility of biomass closely resembles that of subbituminous or lignites.

REFERENCES

[1] "Electricity from Biomass — A Development Strategy," DOE/CH 10093-152, Solar Thermal and Biomass Power Division, U.S. Department of Energy, april 1962.

[2] Miles, T.R. and Davis, U.C., "Alkali Deposits Found in Biomass Power Plants — Straw Boilers in Europe," NREL Subcontract TZ-2-11226-1, August 1993.

[3] Livingston, W.R., "Straw Ash Characteristics," Energy Technology Support Unit (ETSU) Report B1242 by Babcock Energy Ltd., Harwell, U.K., 1991.

[4] Osman, E.A. and Gross, J.R., "Ash Chemical Composition, Deformation, and Fusion Temperatures for Wood and Agriculture Residues," Paper No. 83-3549, American Society of Agriculture Engineers, Chicago, Illinois, 1983.

[5] Osman, E.A. and Gross, J.R., "Ash Deformation and Fusion Temperature Models or Wood and Agriculture Residues," Paper No. 83-3550, American Society of Agriculture Engineers, Chicago, Illinois, 1983.

[6] Jackson, J.P., "The Physicochemical Behavior of Alkali-Metal Compounds in Fireside Boiler Deposits," The Mechanism of Corrosion by Fuel Impurities, ed. H.R. Johnson and D.J. Littler, Butterworths, London, 1963.

Appendix A

INDIVIDUAL FUEL ANALYSIS

Table A-1
FOSTER WHEELER DEVELOPMENT CORPORATION
FUEL ANALYSIS

Sample Description: BIOMASS-Waste Paper					
Charge No. : 9-17-2199		**Date:** 8/5/93		**Lab. Ref. No.:** 931188	
Air Dry Loss (%)	0.00		Equilibrium Moisture (%)		
	As Received	Dry			
Proximate Analysis, wt%			Reactivity Index (°C)		
Fixed Carbon	9.09	9.74	Activation Energy (cal/g-mol)		
Volatile Matter	76.20	81.70	Hardgrove Index		
Ash	7.98	8.56	Free Swelling Index		
Moisture	6.73	---	Specific Gravity		
Total	100.00	100.00	Viscosity		
Ultimate Analysis, wt%			**Ash Fusion Temperature, °F**		
Carbon	45.74	49.04		Red.	Oxid.
Hydrogen	6.40	6.86	Initial Deform.		
Oxygen	32.66	35.01	Soft. Temp. Sph.		
Nitrogen	.42	.45	Soft. Temp. Hem.		
Sulfur	.07	.08	Fluid Temp.		
Ash	7.98	8.56			
Moisture	6.73	---			
Total	100.00	100.00			
			Bulk Density (gr/ml)		
HHV, Btu/lb	8892	9534	Carbonate Carbon		
Sulfate S	---	---	Organic Carbon		
Pyritic S	---	---	Total Carbon		
Organic S	---	---	Chloride	420ppm	
Dulong's =	8676	Btu/lb			
Remarks: Unable to run ash fusion.					

Analyst: _____ Approved: GABRIEL P LANTOS

Table A-2
FOSTER WHEELER DEVELOPMENT CORPORATION
FUEL ANALYSIS

Sample Description: BIOMASS, 80%Wood/20% Wheat Straw					
Charge No. : 9-17-2199		**Date:** 8/5/93		**Lab. Ref. No.:** 931189	
Air Dry Loss (%)	0.00		Equilibrium Moisture (%)		
	As Received	Dry			
Proximate Analysis, wt%			Reactivity Index (°C)		
Fixed Carbon	16.74	18.52	Activation Energy (cal/g-mol)		
Volatile Matter	66.72	73.81	Hardgrove Index		
Ash	6.93	7.67	Free Swelling Index		
Moisture	9.61	---	Specific Gravity		
Total	100.00	100.00	Viscosity		
Ultimate Analysis, wt%			**Ash Fusion Temperature, °F**		
Carbon	43.15	47.74		Red.	Oxid.
Hydrogen	5.19	5.75	Initial Deform.		
Oxygen	34.51	38.16	Soft. Temp. Sph.		
Nitrogen	.54	.60	Soft. Temp. Hem.		
Sulfur	.07	.08	Fluid Temp.		
Ash	6.93	7.67			
Moisture	9.61	---			
Total	100.00	100.00			
			Bulk Density (gr/ml)		
HHV, Btu/lb	7430	8220	Carbonate Carbon		
Sulfate S	---	---	Organic Carbon		
Pyritic S	---	---	Total Carbon		
Organic S	---	---	Chloride	1240ppm	
Dulong's =	7554	Btu/lb			
Remarks: Unable to run ash fusion.					

Analyst: _____ Approved: GABRIEL P LANTOS

Table A-3
FOSTER WHEELER DEVELOPMENT CORPORATION
FUEL ANALYSIS

Sample Description: BIOMASS, Rice Straw					
Charge No. : 9-17-2199		**Date:** 8/5/93		**Lab. Ref. No.:** 931190	
Air Dry Loss (%)	0.00		Equilibrium Moisture (%)		
	As Received	Dry			
Proximate Analysis, wt%			Reactivity Index (°C)		
Fixed Carbon	16.41	18.73	Activation Energy (cal/g-mol)		
Volatile Matter	54.49	62.18	Hardgrove Index		
Ash	16.73	19.09	Free Swelling Index		
Moisture	12.37	---	Specific Gravity		
Total	100.00	100.00	Viscosity		
Ultimate Analysis, wt%			**Ash Fusion Temperature, °F**		
Carbon	34.10	38.91		Red.	Oxid.
Hydrogen	4.16	4.74	Initial Deform.		
Oxygen	31.34	35.78	Soft. Temp. Sph.		
Nitrogen	1.20	1.37	Soft. Temp. Hem.		
Sulfur	.10	.11	Fluid Temp.		
Ash	16.73	19.09			
Moisture	12.37	---			
Total	100.00	100.00			
			Bulk Density (gr/ml)		
HHV, Btu/lb	5829	6652	Carbonate Carbon		
Sulfate S	---	---	Organic Carbon		
Pyritic S	---	---	Total Carbon		
Organic S	---	---	Chloride	4670ppm	
Dulong's =	5829	Btu/lb			
Remarks: Unable to run ash fusion.					

Analyst: _____ Approved: GABRIEL P LANTOS

Table A-4

FOSTER WHEELER DEVELOPMENT CORPORATION
FUEL ANALYSIS

Sample Description: BIOMASS, Almond Hulls					
Charge No. : 9-17-2199		**Date:** 8/5/93		**Lab. Ref. No.:** 931191	
Air Dry Loss (%)	0.00		Equilibrium Moisture (%)		
	As Received	Dry			
Proximate Analysis, wt%			Reactivity Index (°C)		
Fixed Carbon	21.49	23.98	Activation Energy (cal/g-mol)		
Volatile Matter	63.76	71.15	Hardgrove Index		
Ash	4.36	4.87	Free Swelling Index		
Moisture	10.39	---	Specific Gravity		
Total	100.00	100.00	Viscosity		
Ultimate Analysis, wt%			**Ash Fusion Temperature, °F**		
Carbon	42.75	47.71		Red.	Oxid.
Hydrogen	5.26	5.87	Initial Deform.		
Oxygen	35.88	40.03	Soft. Temp. Sph.		
Nitrogen	1.30	1.45	Soft. Temp. Hem.		
Sulfur	.06	.07	Fluid Temp.		
Ash	4.36	4.87			
Moisture	10.39	---			
Total	100.00	100.00			
			Bulk Density (gr/ml)		
HHV, Btu/lb	7392	8249	Carbonate Carbon		
Sulfate S	---	---	Organic Carbon		
Pyritic S	---	---	Total Carbon		
Organic S	---	---	Chloride	650ppm	
Dulong's =	7479	Btu/lb			
Remarks: Unable to run ash fusion.					

Analyst: _____ Approved: GABRIEL P LANTOS

Table A-5

FOSTER WHEELER DEVELOPMENT CORPORATION

FUEL ANALYSIS

Sample Description: BIOMASS, Wheat Straw					
Charge No. : 9-17-2199		**Date:** 8/5/93		**Lab. Ref. No.:** 931192	
Air Dry Loss (%)	0.00		Equilibrium Moisture (%)		
	As Received	Dry			
Proximate Analysis, wt%			Reactivity Index (°C)		
Fixed Carbon	19.03	20.96	Activation Energy (cal/g-mol)		
Volatile Matter	65.09	71.69	Hardgrove Index		
Ash	6.67	7.35	Free Swelling Index		
Moisture	9.21	---	Specific Gravity		
Total	100.00	100.00	Viscosity		
Ultimate Analysis, wt%			**Ash Fusion Temperature, °F**		
Carbon	41.08	45.25		Red.	Oxid.
Hydrogen	4.90	5.40	Initial Deform.		
Oxygen	37.16	40.92	Soft. Temp. Sph.		
Nitrogen	.81	.89	Soft. Temp. Hem.		
Sulfur	.17	.19	Fluid Temp.		
Ash	6.67	7.35			
Moisture	9.21	---			
Total	100.00	100.00			
			Bulk Density (gr/ml)		
HHV, Btu/lb	7055	7771	Carbonate Carbon		
Sulfate S	---	---	Organic Carbon		
Pyritic S	---	---	Total Carbon		
Organic S	---	---	Chloride	2330ppm	
Dulong's =	6766	Btu/lb			
Remarks: Unable to run ash fusion.					

Analyst: _____ Approved: GABRIEL P LANTOS

Table A-6
FOSTER WHEELER DEVELOPMENT CORPORATION
FUEL ANALYSIS

Sample Description: BIOMASS, Olive Pitts					
Charge No. : 9-17-2199		**Date:** 8/5/93		**Lab. Ref. No.:** 931193	
Air Dry Loss (%)	0.00		Equilibrium Moisture (%)		
	As Received	Dry			
Proximate Analysis, wt%			Reactivity Index (°C)		
Fixed Carbon	19.06	20.81	Activation Energy (cal/g-mol)		
Volatile Matter	71.11	77.66	Hardgrove Index		
Ash	1.40	1.53	Free Swelling Index		
Moisture	8.43	---	Specific Gravity		
Total	100.00	100.00	Viscosity		
Ultimate Analysis, wt%			**Ash Fusion Temperature, °F**		
Carbon	34.63	37.82		Red.	Oxid.
Hydrogen	5.71	6.23	Initial Deform.		
Oxygen	49.15	53.68	Soft. Temp. Sph.		
Nitrogen	.65	.71	Soft. Temp. Hem.		
Sulfur	.03	.03	Fluid Temp.		
Ash	1.40	1.53			
Moisture	8.43	---			
Total	100.00	100.00			
			Bulk Density (gr/ml)		
HHV, Btu/lb	8623	9417	Carbonate Carbon		
Sulfate S	---	---	Organic Carbon		
Pyritic S	---	---	Total Carbon		
Organic S	---	---	Chloride	680ppm	
Dulong's =	5204	Btu/lb			
Remarks: Unable to run ash fusion.					

Analyst: _____ Approved: GABRIEL P LANTOS

Table A-7
FOSTER WHEELER DEVELOPMENT CORPORATION
FUEL ANALYSIS

Sample Description: BIOMASS, Almond Shells					
Charge No. : 9-17-2199		**Date:** 8/5/93		**Lab. Ref. No.:** 931194	
Air Dry Loss (%)	0.00		Equilibrium Moisture (%)		
	As Received	Dry			
Proximate Analysis, wt%			Reactivity Index (°C)		
Fixed Carbon	19.73	21.64	Activation Energy (cal/g-mol)		
Volatile Matter	69.37	76.11	Hardgrove Index		
Ash	2.05	2.25	Free Swelling Index		
Moisture	8.85	---	Specific Gravity		
Total	100.00	100.00	Viscosity		
Ultimate Analysis, wt%			**Ash Fusion Temperature, °F**		
Carbon	44.32	48.62		Red.	Oxid.
Hydrogen	5.31	5.83	Initial Deform.		
Oxygen	38.59	42.34	Soft. Temp. Sph.		
Nitrogen	.86	.94	Soft. Temp. Hem.		
Sulfur	.02	.02	Fluid Temp.		
Ash	2.05	2.25			
Moisture	8.85	---			
Total	100.00	100.00			
			Bulk Density (gr/ml)		
HHV, Btu/lb	7631	8372	Carbonate Carbon		
Sulfate S	---	---	Organic Carbon		
Pyritic S	---	---	Total Carbon		
Organic S	---	---	Chloride	370ppm	
Dulong's =	7406	Btu/lb			
Remarks: Unable to run ash fusion.					

Analyst: _____ Approved: GABRIEL P LANTO

Table A-8
FOSTER WHEELER DEVELOPMENT CORPORATION
FUEL ANALYSIS

Sample Description: BIOMASS, Wood Waste/Almond Shells					
Charge No. : 9-17-2199		**Date:** 8/5/93		**Lab. Ref. No.:** 931195	
Air Dry Loss (%)	0.00		Equilibrium Moisture (%)		
	As Received	Dry			
Proximate Analysis, wt%			Reactivity Index (°C)		
Fixed Carbon	18.69	20.64	Activation Energy (cal/g-mol)		
Volatile Matter	66.23	73.13	Hardgrove Index		
Ash	5.64	6.23	Free Swelling Index		
Moisture	9.44	---	Specific Gravity		
Total	100.00	100.00	Viscosity		
Ultimate Analysis, wt%			**Ash Fusion Temperature, °F**		
Carbon	42.11	46.50		Red.	Oxid.
Hydrogen	4.93	5.45	Initial Deform.		
Oxygen	37.21	41.08	Soft. Temp. Sph.		
Nitrogen	.64	.71	Soft. Temp. Hem.		
Sulfur	.03	.03	Fluid Temp.		
Ash	5.64	6.23			
Moisture	9.44	---			
Total	100.00	100.00			
			Bulk Density (gr/ml)		
HHV, Btu/lb	7292	8052	Carbonate Carbon		
Sulfate S	---	---	Organic Carbon		
Pyritic S	---	---	Total Carbon		
Organic S	---	---	Chloride	480ppm	
Dulong's =	6960	Btu/lb			
Remarks: Unable to run ash fusion.					

Analyst: _____ Approved: GABRIEL P LANTOS

Table A-9

FOSTER WHEELER DEVELOPMENT CORPORATION
ASH/DEPOSIT ANALYSIS

Sample Description: BIOMASS-Waste Paper

Charge No. : 9-17-2199 Date: 09-01-1993 Lab. Ref. No. : 931188

Analyte	As Element	Factor		As Oxide	Analyt. Method
Silicon	Si	2.140	Silicon Dioxide	20.5	X-RAY
Aluminum	Al	1.890	Aluminum Oxide	54.0	X-RAY
Titanium	Ti	2.668	Titanium Dioxide	1.5	X-RAY
Iron	Fe	1.430	Ferric Oxide	0.1	X-RAY
Calcium	Ca	1.399	Calcium Oxide	10.2	X-RAY
Magnesium	Mg	1.658	Magnesium Oxide	1.9	AA
Sodium	Na	1.348	Sodium Oxide	1.1	AA
Potassium	K	1.205	Potassium Oxide	0.2	X-RAY
Sulfur	S	2.500	Sulfur Trioxide	2.3	X-RAY
Phosphorus	P	2.291	Phos. Pentoxide	NIL	X-RAY
Nickel	Ni	1.273	Nickel(ic) oxide		
Vanadium	V	1.785	Vand. Pentoxide		
Manganese	Mn	1.583	Mangan. Dioxide		
Chromium	Cr	1.461	Chromic Oxide		
Molybdenum	Mo	1.500	Moly. Trioxide		
Zinc	Zn	1.245	Zinc Oxide		
Lead	Pb	1.077	Lead Oxide		
Tin	Sn	1.270	Stannic Oxide		
Copper	Cu	1.252	Cupric Oxide		
Silver	Ag	1.074	Silver Oxide		
Antimony	Sb	1.197	Antimony Trioxide		
Chlorine	Cl	1.000	Chloride		

Remarks: Total Percentage 91.8

Analyst: _____

Approved: GABRIEL P LANTOS

Table A-10

FOSTER WHEELER DEVELOPMENT CORPORATION
ASH/DEPOSIT ANALYSIS

Sample Description: BIOMASS, Wheat Straw

Charge No. : 9-17-2199 Date: 09-02-1993 Lab. Ref. No. : 931192

Analyte	As Element	Factor		As Oxide	Analyt. Method
Silicon	Si	2.140	Silicon Dioxide	55.7	X-RAY
Aluminum	Al	1.890	Aluminum Oxide	1.8	X-RAY
Titanium	Ti	2.668	Titanium Dioxide	NIL	X-RAY
Iron	Fe	1.430	Ferric Oxide	0.7	X-RAY
Calcium	Ca	1.399	Calcium Oxide	2.6	X-RAY
Magnesium	Mg	1.658	Magnesium Oxide	2.4	AA
Sodium	Na	1.348	Sodium Oxide	0.9	AA
Potassium	K	1.205	Potassium Oxide	22.8	X-RAY
Sulfur	S	2.500	Sulfur Trioxide	1.7	X-RAY
Phosphorus	P	2.291	Phos. Pentoxide	1.2	X-RAY
Nickel	Ni	1.273	Nickel(ic) oxide		
Vanadium	V	1.785	Vand. Pentoxide		
Manganese	Mn	1.583	Mangan. Dioxide		
Chromium	Cr	1.461	Chromic Oxide		
Molybdenum	Mo	1.500	Moly. Trioxide		
Zinc	Zn	1.245	Zinc Oxide		
Lead	Pb	1.077	Lead Oxide		
Tin	Sn	1.270	Stannic Oxide		
Copper	Cu	1.252	Cupric Oxide		
Silver	Ag	1.074	Silver Oxide		
Antimony	Sb	1.197	Antimony Trioxide		
Chlorine	Cl	1.000	Chloride		

Remarks: Total Percentage 89.8

Analyst: _____

Approved: GABRIEL P LANTOS

Table A-12

FOSTER WHEELER DEVELOPMENT CORPORATION
ASH/DEPOSIT ANALYSIS

Sample Description: BIOMASS, Rice Straw

Charge No. : 9-17-2199 Date: 09-02-1993 Lab. Ref. No. : 931190

Analyte	As Element	Factor		As Oxide	Analyt. Method
Silicon	Si	2.140	Silicon Dioxide	73.0	X-RAY
Aluminum	Al	1.890	Aluminum Oxide	1.4	X-RAY
Titanium	Ti	2.668	Titanium Dioxide	NIL	X-RAY
Iron	Fe	1.430	Ferric Oxide	0.6	X-RAY
Calcium	Ca	1.399	Calcium Oxide	1.9	X-RAY
Magnesium	Mg	1.658	Magnesium Oxide	1.8	AA
Sodium	Na	1.348	Sodium Oxide	0.4	AA
Potassium	K	1.205	Potassium Oxide	13.5	X-RAY
Sulfur	S	2.500	Sulfur Trioxide	0.7	X-RAY
Phosphorus	P	2.291	Phos. Pentoxide	1.4	X-RAY
Nickel	Ni	1.273	Nickel(ic) oxide		
Vanadium	V	1.785	Vand. Pentoxide		
Manganese	Mn	1.583	Mangan. Dioxide		
Chromium	Cr	1.461	Chromic Oxide		
Molybdenum	Mo	1.500	Moly. Trioxide		
Zinc	Zn	1.245	Zinc Oxide		
Lead	Pb	1.077	Lead Oxide		
Tin	Sn	1.270	Stannic Oxide		
Copper	Cu	1.252	Cupric Oxide		
Silver	Ag	1.074	Silver Oxide		
Antimony	Sb	1.197	Antimony Trioxide		
Chlorine	Cl	1.000	Chloride		

Remarks: Total Percentage 94.7

Analyst: _____

Approved: GABRIEL P LANTOS

Table A-11

FOSTER WHEELER DEVELOPMENT CORPORATION
ASH/DEPOSIT ANALYSIS

Sample Description: BIOMASS, 80%Wood/20% Wheat Straw

Charge No. : 9-17-2199 Date: 09-02-1993 Lab. Ref. No. : 931189

Analyte	As Element	Factor		As Oxide	Analyt. Method
Silicon	Si	2.140	Silicon Dioxide	56.8	X-RAY
Aluminum	Al	1.890	Aluminum Oxide	10.9	X-RAY
Titanium	Ti	2.668	Titanium Dioxide	0.5	X-RAY
Iron	Fe	1.430	Ferric Oxide	4.9	X-RAY
Calcium	Ca	1.399	Calcium Oxide	10.2	X-RAY
Magnesium	Mg	1.658	Magnesium Oxide	2.4	AA
Sodium	Na	1.348	Sodium Oxide	3.8	AA
Potassium	K	1.205	Potassium Oxide	6.7	X-RAY
Sulfur	S	2.500	Sulfur Trioxide	1.9	X-RAY
Phosphorus	P	2.291	Phos. Pentoxide	1.1	X-RAY
Nickel	Ni	1.273	Nickel(ic) oxide		
Vanadium	V	1.785	Vand. Pentoxide		
Manganese	Mn	1.583	Mangan. Dioxide		
Chromium	Cr	1.461	Chromic Oxide		
Molybdenum	Mo	1.500	Moly. Trioxide		
Zinc	Zn	1.245	Zinc Oxide		
Lead	Pb	1.077	Lead Oxide		
Tin	Sn	1.270	Stannic Oxide		
Copper	Cu	1.252	Cupric Oxide		
Silver	Ag	1.074	Silver Oxide		
Antimony	Sb	1.197	Antimony Trioxide		
Chlorine	Cl	1.000	Chloride		

Remarks: Total Percentage 99.2

Analyst: _____

Approved: GABRIEL P LANTOS

Table A-13

FOSTER WHEELER DEVELOPMENT CORPORATION
ASH/DEPOSIT ANALYSIS

Sample Description: BIOMASS, Almond Hulls

Charge No. : 9-17-2199 Date: 09-02-1993 Lab. Ref. No. : 931191

Analyte	As Element	Factor		As Oxide	Analyt. Method
Silicon	Si	2.140	Silicon Dioxide	4.0	X-RAY
Aluminum	Al	1.890	Aluminum Oxide	1.3	X-RAY
Titanium	Ti	2.668	Titanium Dioxide	NIL	X-RAY
Iron	Fe	1.430	Ferric Oxide	0.4	X-RAY
Calcium	Ca	1.399	Calcium Oxide	5.0	X-RAY
Magnesium	Mg	1.658	Magnesium Oxide	2.9	AA
Sodium	Na	1.348	Sodium Oxide	0.2	AA
Potassium	K	1.205	Potassium Oxide	50.9	X-RAY
Sulfur	S	2.500	Sulfur Trioxide	1.2	X-RAY
Phosphorus	P	2.291	Phos. Pentoxide	5.5	X-RAY
Nickel	Ni	1.273	Nickel(ic) oxide		
Vanadium	V	1.785	Vand. Pentoxide		
Manganese	Mn	1.583	Mangan. Dioxide		
Chromium	Cr	1.461	Chromic Oxide		
Molybdenum	Mo	1.500	Moly. Trioxide		
Zinc	Zn	1.245	Zinc Oxide		
Lead	Pb	1.077	Lead Oxide		
Tin	Sn	1.270	Stannic Oxide		
Copper	Cu	1.252	Cupric Oxide		
Silver	Ag	1.074	Silver Oxide		
Antimony	Sb	1.197	Antimony Trioxide		
Chlorine	Cl	1.000	Chloride		

Remarks: Total Percentage 71.4

Analyst: _____

Approved: GABRIEL P LANTOS

Table A-14

FOSTER WHEELER DEVELOPMENT CORPORATION
ASH/DEPOSIT ANALYSIS

Sample Description: BIOMASS, Almond Shells

Charge No. : 9-17-2199 Date: 09-02-1993 Lab. Ref. No. : 931194

Analyte-	As Element	Factor		As Oxide	Analyt. Method
Silicon	Si	2.140	Silicon Dioxide	4.9	X-RAY
Aluminum	Al	1.890	Aluminum Oxide	1.5	X-RAY
Titanium	Ti	2.668	Titanium Dioxide	NIL	X-RAY
Iron	Fe	1.430	Ferric Oxide	1.3	X-RAY
Calcium	Ca	1.399	Calcium Oxide	6.9	X-RAY
Magnesium	Mg	1.658	Magnesium Oxide	2.6	AA
Sodium	Na	1.348	Sodium Oxide	0.5	AA
Potassium	K	1.205	Potassium Oxide	49.6	X-RAY
Sulfur	S	2.500	Sulfur Trioxide	1.6	X-RAY
Phosphorus	P	2.291	Phos. Pentoxide	5.0	X-RAY
Nickel	Ni	1.273	Nickel(ic) oxide		
Vanadium	V	1.785	Vand. Pentoxide		
Manganese	Mn	1.583	Mangan. Dioxide		
Chromium	Cr	1.461	Chromic Oxide		
Molybdenum	Mo	1.500	Moly. Trioxide		
Zinc	Zn	1.245	Zinc Oxide		
Lead	Pb	1.077	Lead Oxide		
Tin	Sn	1.270	Stannic Oxide		
Copper	Cu	1.252	Cupric Oxide		
Silver	Ag	1.074	Silver Oxide		
Antimony	Sb	1.197	Antimony Trioxide		
Chlorine	Cl	1.000	Chloride		

Remarks: Total Percentage 73.9

Analyst: _____

Approved: GABRIEL P LANTOS

Table A-15

FOSTER WHEELER DEVELOPMENT CORPORATION
ASH/DEPOSIT ANALYSIS

Sample Description: BIOMASS, Olive Pitts

Charge No. : 9-17-2199 Date: 09-02-1993 Lab. Ref. No. : 931193

Analyte	As Element	Factor		As Oxide	Analyt. Method
Silicon	Si	2.140	Silicon Dioxide	23.1	X-RAY
Aluminum	Al	1.890	Aluminum Oxide	5.3	X-RAY
Titanium	Ti	2.668	Titanium Dioxide	0.1	X-RAY
Iron	Fe	1.430	Ferric Oxide	5.1	X-RAY
Calcium	Ca	1.399	Calcium Oxide	10.9	X-RAY
Magnesium	Mg	1.658	Magnesium Oxide	3.0	AA
Sodium	Na	1.348	Sodium Oxide	29.9	AA
Potassium	K	1.205	Potassium Oxide	5.2	X-RAY
Sulfur	S	2.500	Sulfur Trioxide	2.4	X-RAY
Phosphorus	P	2.291	Phos. Pentoxide	2.7	X-RAY
Nickel	Ni	1.273	Nickel(ic) oxide		
Vanadium	V	1.785	Vand. Pentoxide		
Manganese	Mn	1.583	Mangan. Dioxide		
Chromium	Cr	1.461	Chromic Oxide		
Molybdenum	Mo	1.500	Moly. Trioxide		
Zinc	Zn	1.245	Zinc Oxide		
Lead	Pb	1.077	Lead Oxide		
Tin	Sn	1.270	Stannic Oxide		
Copper	Cu	1.252	Cupric Oxide		
Silver	Ag	1.074	Silver Oxide		
Antimony	Sb	1.197	Antimony Trioxide		
Chlorine	Cl	1.000	Chloride		

Remarks: Total Percentage 87.7

Analyst: _____

Approved: GABRIEL P LANTOS

Table A-16

FOSTER WHEELER DEVELOPMENT CORPORATION
ASH/DEPOSIT ANALYSIS

Sample Description: BIOMASS, Wood Waste/Almond Shells

Charge No. : 9-17-2199 Date: 09-02-1993 Lab. Ref. No. : 931195

Analyte	As Element	Factor		As Oxide	Analyt. Method
Silicon	Si	2.140	Silicon Dioxide	49.6	X-RAY
Aluminum	Al	1.890	Aluminum Oxide	11.0	X-RAY
Titanium	Ti	2.668	Titanium Dioxide	0.4	X-RAY
Iron	Fe	1.430	Ferric Oxide	4.6	X-RAY
Calcium	Ca	1.399	Calcium Oxide	14.4	X-RAY
Magnesium	Mg	1.658	Magnesium Oxide	2.7	AA
Sodium	Na	1.348	Sodium Oxide	2.4	AA
Potassium	K	1.205	Potassium Oxide	7.4	X-RAY
Sulfur	S	2.500	Sulfur Trioxide	1.4	X-RAY
Phosphorus	P	2.291	Phos. Pentoxide	1.5	X-RAY
Nickel	Ni	1.273	Nickel(ic) oxide		
Vanadium	V	1.785	Vand. Pentoxide		
Manganese	Mn	1.583	Mangan. Dioxide		
Chromium	Cr	1.461	Chromic Oxide		
Molybdenum	Mo	1.500	Moly. Trioxide		
Zinc	Zn	1.245	Zinc Oxide		
Lead	Pb	1.077	Lead Oxide		
Tin	Sn	1.270	Stannic Oxide		
Copper	Cu	1.252	Cupric Oxide		
Silver	Ag	1.074	Silver Oxide		
Antimony	Sb	1.197	Antimony Trioxide		
Chlorine	Cl	1.000	Chloride		

Remarks: Total Percentage 95.4

Analyst: _____

Approved: GABRIEL P. LANTOS

Appendix B

INDIVIDUAL COMBUSTION PROFILES

Figure B-1

TGA

Sample: BIOMASS
Size: 12.1550 mg
Method: TGA/20
Comment: WHEAT STRAW

File: C:931192.01
Operator: RAB
Run Date: 19-Aug-93 07:28

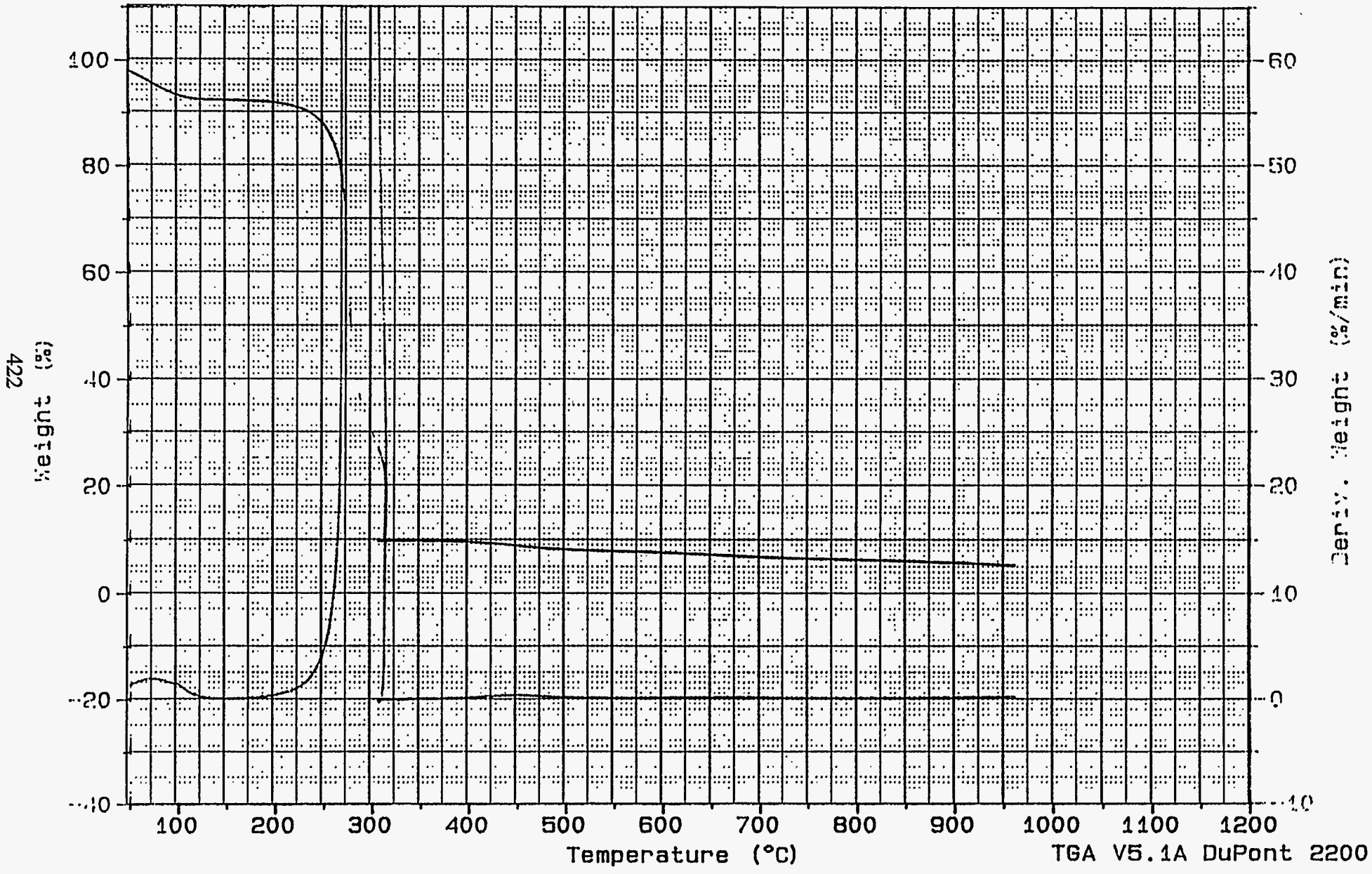

Figure B-2

Sample: BIOMASS
Size: 10.1610 mg
Method: TGA/20
Comment: 80%WOOD, 20%WHEAT STRAW

TGA

File: C:931189.01
Operator: RAB
Run Date: 18-Aug-93 11:12

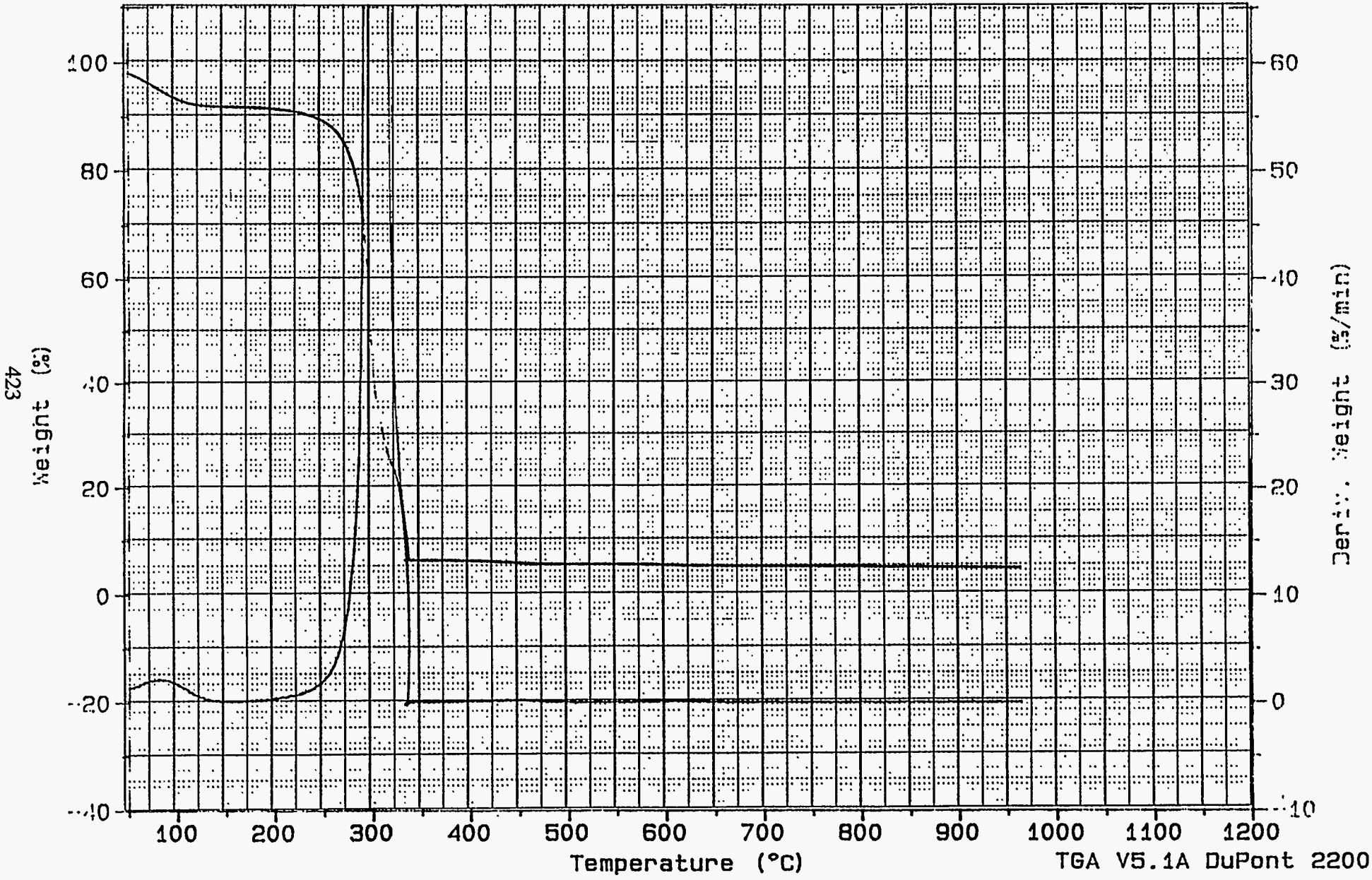

Figure B-3

TGA

Sample: BIOMASS
Size: 12.6460 mg
Method: TGA/20
Comment: RICE STRAW

File: C:931190.01
Operator: RAB
Run Date: 18-Aug-93 12:52

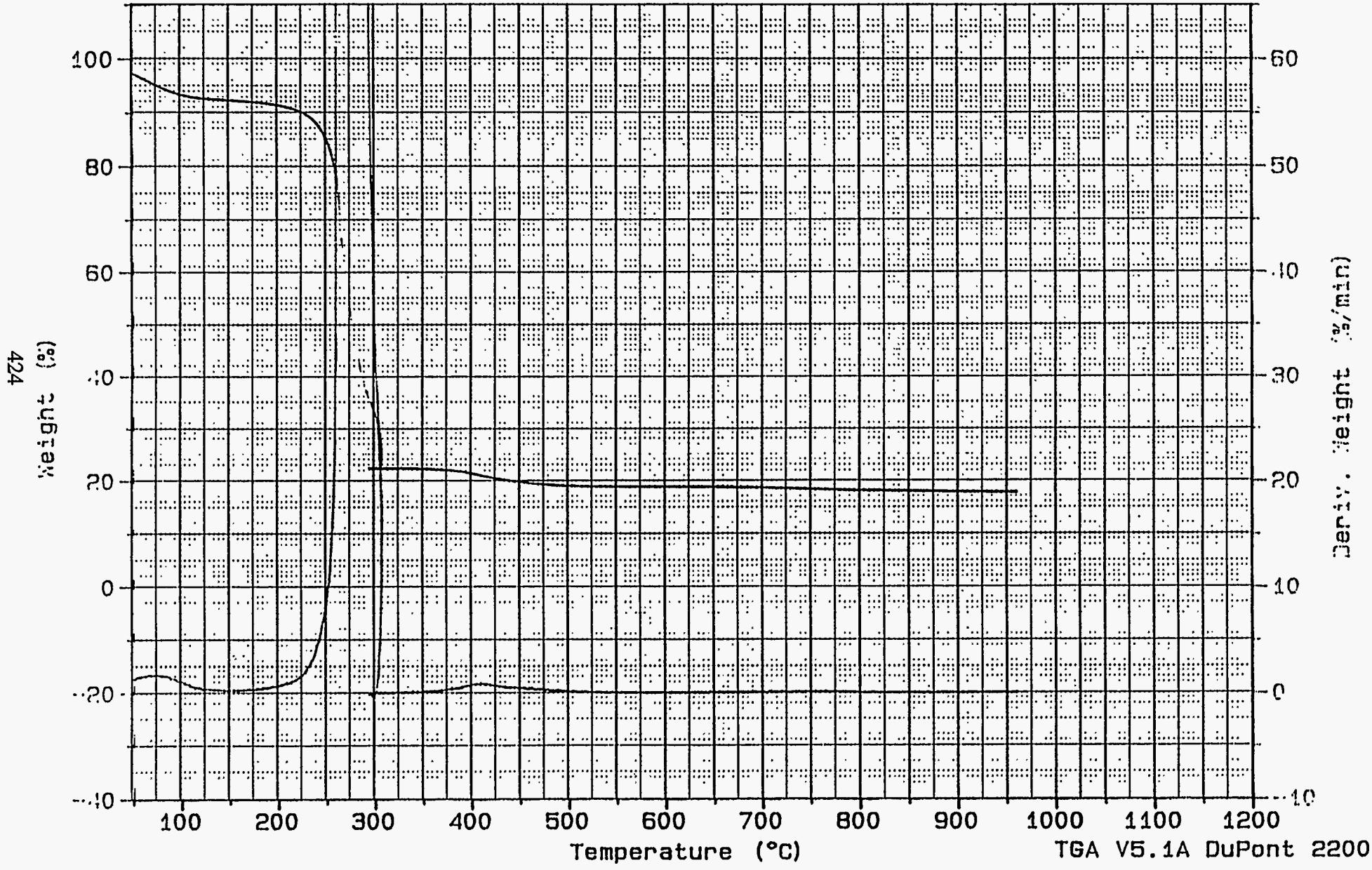

Figure B-4

TGA

Sample: BIOMASS
Size: 15.4800 mg
Method: TGA/20
Comment: ALMOND HULLS

File: C:931191.01
Operator: RAB
Run Date: 18-Aug-93 14:41

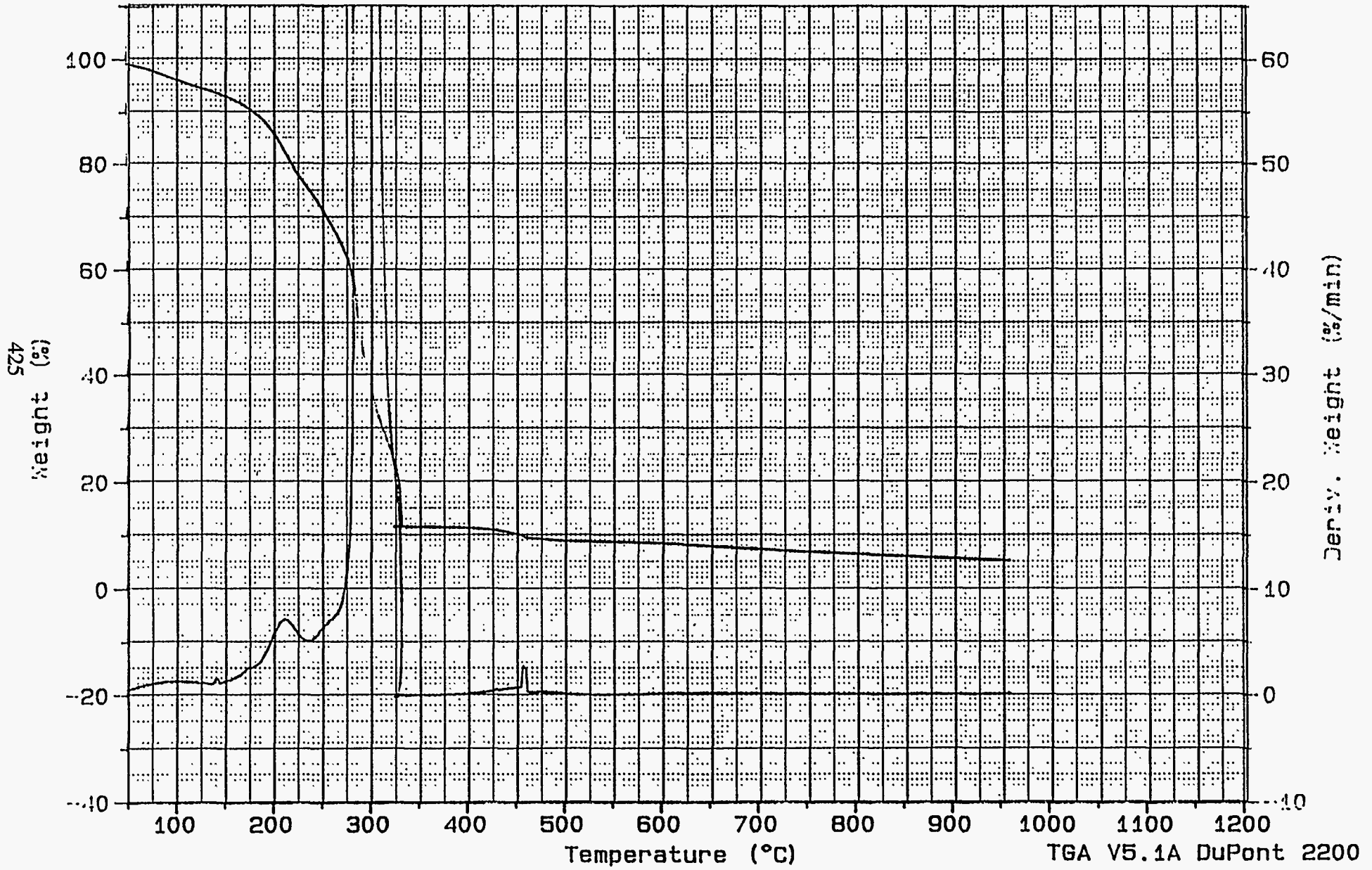

Figure B-5

TGA

Sample: BIOMASS
Size: 10.0050 mg
Method: TGA/20
Comment: ALMOND SHELLS

File: C:931194.01
Operator: RAB
Run Date: 19-Aug-93 10:30

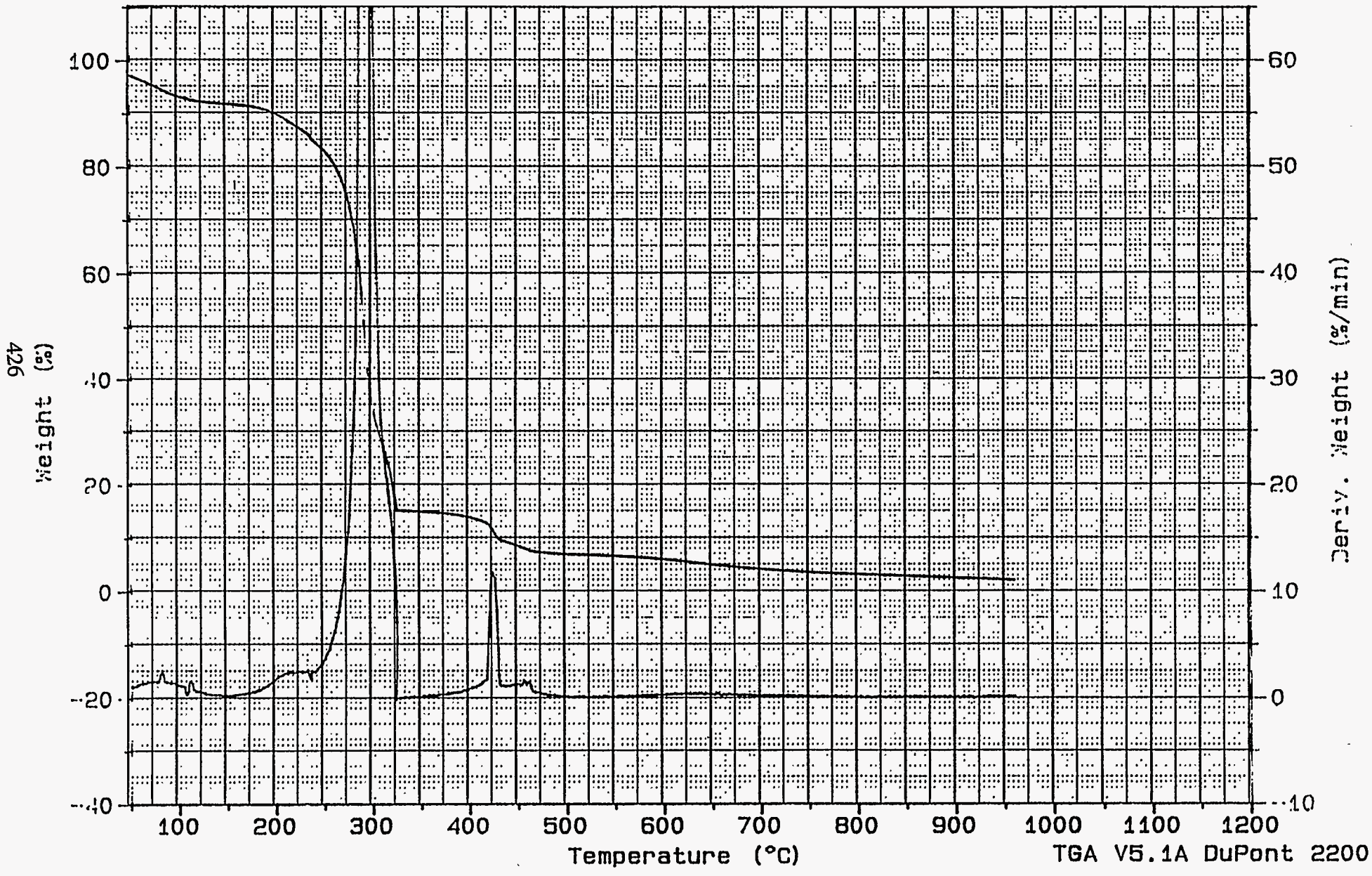

426

Figure B-6

TGA

Sample: BIOMASS
Size: 7.1710 mg
Method: TGA/20
Comment: WOOD WASTE / ALMOND SHELLS

File: C:931195.01
Operator: RAB
Run Date: 20-Aug-93 07:39

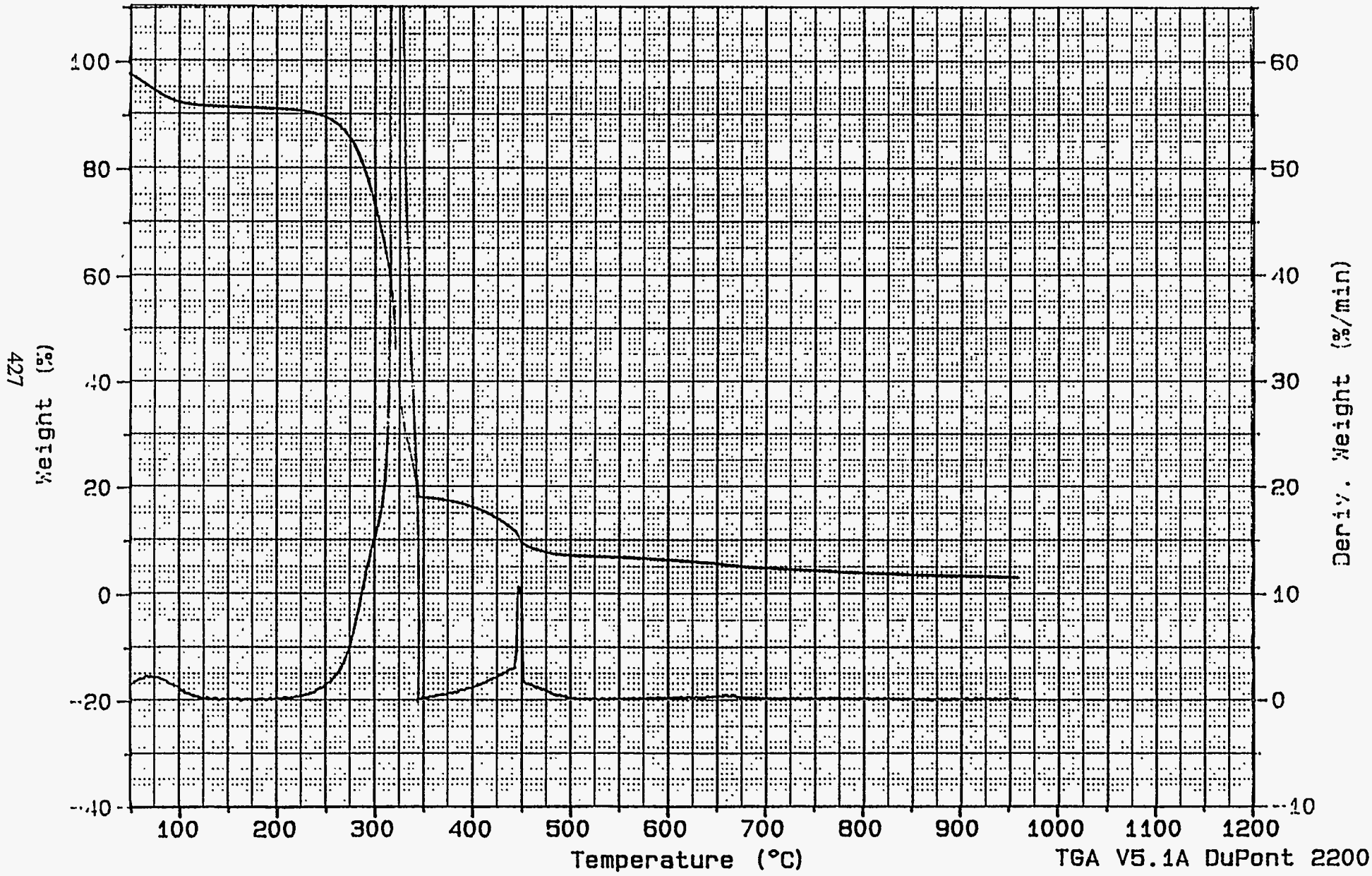

Figure B-7

Sample: OLIVE PITS
Size: 16.6800 mg
Method: TGA/20
Comment: ORIGINAL

TGA

File: C:931193.02
Operator: RAB
Run Date: 27-Aug-93 09:51

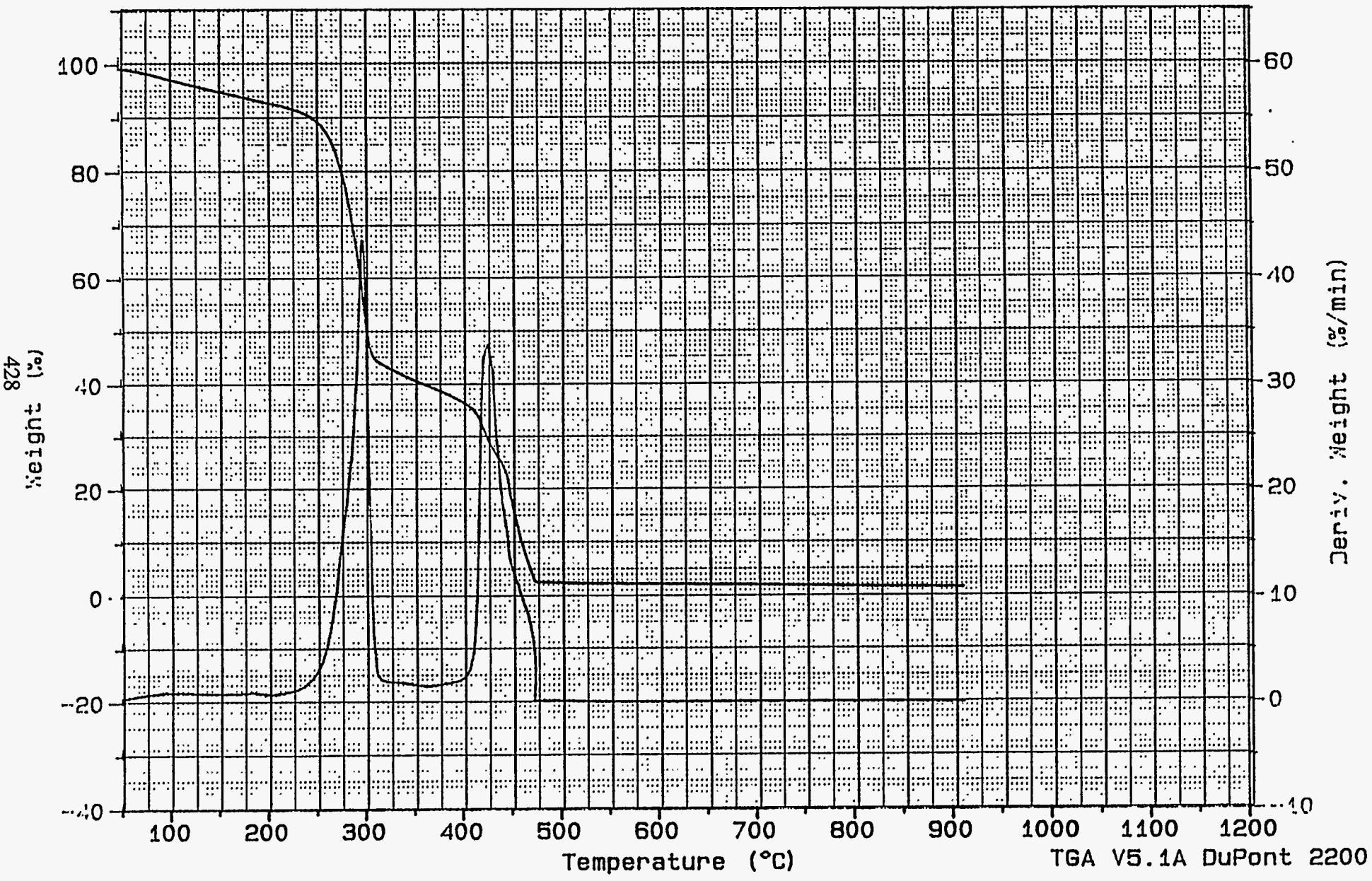

Distribution

J. Briggs (FWL—St. Catharines)

A. Gillespie (FWL—St. Catharines)

J. Tang (FWEC)

S. Gezin (FWEC)

D. H. Pai/W. Wolowodiuk

P. Steiner

APPENDIX 6

Alkali Deposits Found in Biomass-Fueled Power Plants

Material in this appendix has been reproduced from the best available originals

Alkali Deposits Found in Biomass-Fueled Power Plants

Contribution by the Bureau of Mines, Albany Research Center
Albany, Oregon

Compiled by L. Oden, November 27, 1993

Performed mineralogical analyses including x-ray identification of phases and SEM analysis of selected biomass deposits.

THOMAS R. MILES CONSULTING DESIGN ENGINEERS
Phone (503) 292-0107
FAX (503) 292-2919

Alkali Deposits Found in Biomass-Fueled Power Plants

1. Accomplishments:

Provided technical description of "wet ashing technique" to commercial laboratory.

Performed modified chemical fractionation leaching tests for four biomass fuels.

Developed conceptual design and working model for "ash sticky temperature" apparatus.

Performed mineralogical analyses including x-ray identification of phases and SEM analysis of selected biomass deposits.

1.1. Wet ashing technique for biomass analysis.

The major contributor to the uncertainty in biomass analysis is the initial thermal ashing step. The dilemma is that thorough ashing requires high temperature, but high temperature encourages vaporization of some important components, principally the alkali metals. The wet ashing technique as pioneered by the Bureau replaces thermal ashing with wet oxidation. A biomass sample in as-received condition is heated by microwave radiation within a sealed Teflon container along with aqueous solutions of HCl, HNO_3, and HF to effect oxidation of organic material and complete dissolution of all components. The resulting solution then is analyzed by conventional instrumental methods. The biomass compositions reported later in this report were determined by the wet ashing technique. A description of the wet ashing technique was transferred to the Hazen Laboratory and is available upon request from Mr Joe Perry at the Albany Research Center.

Table 1 lists analyses for rice straw, wheat straw, Mendota almond fuel, and switch grass determined by the Bureau. Sulfur, Cl, C, H, N, and total O were determined by independent analysis of samples. All other components were determined by the wet ashing technique. Closure for all components (Total all components) is good for the four biomass samples. Compositions for rice straw and wheat straw, as calculated from the results of thermal ashing by the Hazen Laboratory, are listed for comparison. The analyses strongly suggest that potassium is lost during the thermal ashing treatment.

THOMAS R. MILES CONSULTING DESIGN ENGINEERS
Phone (503) 292-0107
FAX (503) 292-2919

Table 1.- Biomass Analysis; Comparison Between Laboratories.

All compositions wt pct; all materials in as-received condition.

Prepared 8-3-93. Updated 11-26-93.

	Bureau of Mines wet ashing method.				Thermal ashing method: H=Hazen			
					Rice straw, H		Wheat straw, H	
Component	Rice straw	Wheat straw	Hendota (almond)	Switch grass	Ash	straw**	Ash	straw**
Al2O3	0.25	0.10	0.56	0.14	1.04	0.18	1.88	0.12
CaO	1.24	0.35	0.85	0.61	3.01	0.52	6.14	0.40
K2O	2.68	1.97	0.37	0.51	12.30	2.11	25.60	1.67
Na2O	0.12	0.19	0.22	0.08	0.96	0.17	1.71	0.11
MgO	0.36	0.23	0.24	0.23	1.75	0.30	1.06	0.07
P2O5	0.25	0.08	0.08	0.13	1.41	0.24	1.26	0.08
S	0.12	0.22	0.03	0.03	0.50	0.17	1.76	0.14
SiO2	12.30	4.50	1.76	4.12	74.67	12.84	55.32	3.61
TiO2	0.09	0.01	0.04	0.01	0.09	0.02	0.08	0.01
Fe2O3	0.12	0.10	0.45	0.14	0.85	0.15	0.73	0.05
Cl	NA	0.22	0.76	0.03		0.54	-	0.21
Pct ash	17.53	7.97	5.36	6.03	17.19		6.52	
Total oxygen in ash	8.19	3.33	1.90	2.81				
Total metals in ash	9.34	4.64	3.46	3.22				
C	35.73	42.14	43.97	40.58	-	35.20	-	41.75
H	5.02	5.56	6.03	6.17	-	4.79	-	5.07
N	0.89	0.50	0.42	0.27	-	0.80	-	0.40
Nonmetal oxygen***	41.31	46.17	47.70	50.09	-	33.92	-	39.08
Total oxygen	49.50	49.50	49.60	52.90				
Total all components	100.48	102.33	103.48	103.13		91.94	-	92.76

** Calculated from pct ash and ash composition, except C, H, N, S, and O(by difference) from Ultimate analysis.
*** Total oxygen minus oxygen in ash.

THOMAS R. MILES CONSULTING DESIGN ENGINEERS
Phone (503) 292-0107
FAX (503) 292-2919

1.2 Modified chemical fractionation leaching tests.

The ASTM/ISO chemical fractionation test, which was developed for coal characterization, requires that a common sample be leached with three different solutions; water, 1 M ammonium acetate (NH_4OAc), and 1M hydrochloric acid (HCl) to determine, respectively, four classes of inorganic material: water soluble, ion exchangeable, acid soluble, and residual material. The method requires filtering and multiple rinsing of the solid material following each leaching step, determining the remaining moisture in each filter cake, and ash analysis of the filter cakes. The leachates and rinse solutions also must be analyzed to calculate a mass balance. The method is convenient for coal, which has relatively low surface area, filters easily, and rinses readily, but is quite inconvenient for biomass samples which are absorbent with large surface area.

The modified method is a simplification in which separate samples of biomass are leached with water, 1 M NH_4OAc, and 1 M HCl in the ratio 10 gm of biomass to 100 ml of solution. That ratio was arbitrarily chosen for simplicity of measurement (solution volume versus weight) and the 1:10 mixture can be stirred effectively with a magnetic stirring bar. After stirring at room temperature overnight, the insoluble residues are separated from the leachates by filtering, but rinsing is not required. Analysis of the leachates provides the water soluble, ion exchangeable, and acid soluble fractions. Residual material is determined by difference. Analysis of the insoluble residues provides a mass balance if desired. Tables 2-5 list the results of modified chemical fractionation tests for rice straw, wheat straw, Mendota almond fuel, and switch grass. Duplicate samples of wheat straw were analyzed to ascertain the reproducibility of the method. The data, listed in the second column of Table 3, are quite consistent.

It is important to recognize that the solution concentration changes as leaching progresses. The leach solution for rice straw that started as distilled water, for example, became 0.041 molar in alkali when in equilibrium with the undissolved solids. With that view point it is logical to expect some SiO_2 to dissolve. Such was not the case for rice straw, in which the SiO_2 appears to be very strongly bonded. However, nearly 7 pct of the SiO_2 content was dissolved from wheat straw by water. In fact, more SiO_2 was dissolved from wheat straw by water than by 1 M HCl. NH_4OAc was consistently more effective that water at dissolving SiO_2 and the ion exchangeable cations such as calcium and magnesium.

These data are compared on Table 6, which reveals some significant observations. For examples; 1. K_2O, which plays an important biological role in plant physiology, is consistently more leachable than Na_2O, which has no biological function, 2. Water, NH_4OAc, and HCl removed significant proportions of the alkalis from rice straw and wheat straw, but only wheat straw yielded SiO_2 to the solutions, and 3. Calcium and iron oxides are consistently more

ALKALI DEPOSIT INVESTIGATION

THOMAS R. MILES CONSULTING DESIGN ENGINEERS

Phone (503) 292-0107
FAX (503) 292-2919

Table 2.-Correlation of Modified Chemical Fractionation Leaching Tests: 2-17-93 Report updated 8-10-93
Test #3; Milled rice straw '92: Wet ashing technique, except S by LECO.
100 ml leaching agent for each 10 g sample, 10 ml H2O added to leachate to seat filter paper.

Leaching agent:	Volume analyzed, ml:	Corrections for leach solutions. Cl	Na2O
H2O	46.20	0.15	3.50
1M NH4OAc	50.00	2.4	4.30
1M HCl	51.00	NA	8.30

Component	Biomass			Solution Analysis Corrected for Cl and Na2O		Leachate	
	Calculated from ash*	Conc by wet ashing, pct	mg per 10 g biomass	Leaching agent	mg/l solution	mg removed by 100 ml	Pct removed by agent
Al2O3	0.205	0.25	25	H2O	3.80	0.48	1.94
				NH4OAc	4.20	0.53	2.10
				HCl	18.10	2.25	9.01
CaO	0.333	1.24	124	H2O	10.30	1.31	1.06
				NH4OAc	12.20	1.53	1.23
				HCl	334.00	41.55	33.51
K2O	1.67	2.68	268	H2O	1820.00	232.28	86.67
				NH4OAc	2130.00	266.25	99.35
				HCl	2190.00	272.41	101.65
	0.334	0.12	12	H2O	87.80	11.21	93.38
				NH4OAc	127.70	15.96	133.02
				HCl	107.70	13.40	111.64
MgO	0.329	0.36	36	H2O	172.00	21.95	60.98
				NH4OAc	235.00	29.38	81.60
				HCl	207.00	25.75	71.52
P2O5	0.231	0.25	25	H2O	150.00	19.14	76.57
				NH4OAc	179.00	22.38	89.50
				HCl	184.00	22.89	91.55
S	0.079	0.12	12	H2O	14.95	1.91	15.90
				NH4OAc	14.62	1.83	15.23
				HCl	14.95	1.86	15.50
SiO2	13.29	12.3	1230	H2O	< 5.00	< 0.64	< 0.05
				NH4OAc	< 5.00	< 0.63	< 0.05
				HCl	< 5.00	< 0.62	< 0.05
TiO2	0.0085	0.0085*	0.85	H2O	NA	NA	NA
				NH4OAc	NA	NA	NA
				HCl	NA	NA	NA
Fe2O3	0.124	0.124*	12.4	H2O	27.00	3.45	27.79
				NH4OAc	6.90	0.86	6.96
				HCl	61.80	7.69	61.99
Cl	NA	NA	ERR	H2O	394.85	50.39	NA
				NH4OAc	409.60	51.20	NA
				HCl	NA	NA	NA

* By calculation from the ash (1.24 mg ash after 1.5 hr @ 900 C).

THOMAS R. MILES CONSULTING DESIGN ENGINEERS
Phone (503) 292-0107
FAX (503) 292-2919

le 3.- Correlation of Modified Chemical Fractionation Leaching Tests: 1-24-93Report updated 8-10-93
Test #4; Milled wheat straw '92; Sacramento Valley: Wet ashing technique, except S by LECO.
100 ml leaching agent for each 10 g sample, 10 ml H2O added to leachate to seat filter paper.

Leaching agent:	Volume analyzed, ml:	Corrections for leach solutions. Cl	Na2O
H2O	60.50	0.15	3.50
1M NH4OAc	75.00	2.4	4.30
1M HCl	65.00	NA	8.30

Component	Biomass		Solution Analysis Corrected for Cl and Na2O		Leachate	
	Conc by wet ashing, pct	mg per 10 g biomass	Leaching agent	mg/l solution	mg removed by 100 ml	Pct removed by agent
Al2O3	0.10	10	H2O	6.40	0.77	7.67
	dup 0.11		NH4OAc	< 2.00	< 0.23	< 2.31
			HCl	3.80	0.45	4.49
CaO	0.35	35	H2O	71.90	8.61	24.61
	dup 0.34		NH4OAc	116.00	13.38	38.24
			HCl	163.00	19.26	55.04
K2O	1.97	197	H2O	1460.00	174.91	88.79
	dup 1.93		NH4OAc	1640.00	189.23	96.06
			HCl	1590.00	187.91	95.39
)	0.19	19	H2O	68.50	8.21	43.19
	dup 0.18		NH4OAc	86.40	9.97	52.47
			HCl	68.10	8.05	42.36
MgO	0.23	23	H2O	107.00	12.82	55.73
	dup 0.24		NH4OAc	139.00	16.04	69.73
			HCl	146.00	17.25	75.02
P2O5	0.08	8	H2O	51.00	6.11	76.37
	dup 0.084		NH4OAc	79.00	9.12	113.94
			HCl	68.00	8.04	100.45
S	0.22	22	H2O	100.00	11.98	54.46
	dup 0.23		NH4OAc	110.00	12.69	57.69
			HCl	100.00	11.82	53.72
SiO2	4.50	450	H2O	252.00	30.19	6.71
	dup 4.48		NH4OAc	274.00	31.62	7.03
			HCl	116.00	13.71	3.05
TiO2	0.01	1	H2O	< 1.00	< 0.12	< 11.98
	dup 0.0118		NH4OAc	< 1.00	< 0.12	< 11.54
			HCl	< 1.00	< 0.12	< 11.82
Fe2O3	0.10	10	H2O	14.00	1.68	16.77
	dup 0.098		NH4OAc	3.60	0.42	4.15
			HCl	21.70	2.56	25.65
l	0.22	22	H2O	238.85	28.61	130.07
	dup 0.21		NH4OAc	198.60	22.92	104.16
			HCl	NA	NA	NA

THOMAS R. MILES CONSULTING DESIGN ENGINEERS
Phone (503) 292-0107
FAX (503) 292-2919

Table 4.- Correlation of Modified Chemical Fractionation Leaching Tests: 4-29-93Report updated 8-10-93
Test #5; Mendota fuel; almond shells. Wet ashing technique, except S by LECO.
100 ml leaching agent for each 10 g sample, 10 ml H2O added to leachate to seat filter paper.

Leaching agent:	Volume analyzed, ml:	Corrections for leach solutions. Cl	Na2O
H2O	39.40	0.15	3.50
1M NH4OAc	75.20	2.4	4.30
1M HCl	78.00	NA	8.30

Component	Biomass		Solution Analysis Corrected for Cl and Na2O		Leachate	
	Conc by wet ashing, pct	mg per 10 g biomass	Leaching agent	mg/l solution	mg removed by 100 ml	Pct removed by agent
Al2O3	0.56	56	H2O	< 2.00	< 0.27	< 0.48
			NH4OAc	< 2.00	< 0.23	< 0.41
			HCl	111.00	12.73	22.74
CaO	0.85	85	H2O	25.30	3.39	3.99
			NH4OAc	192.00	22.14	26.05
			HCl	838.00	96.12	113.09
K2O	0.37	37	H2O	151.00	20.24	54.69
			NH4OAc	256.00	29.53	79.80
			HCl	264.00	30.28	81.84
O	0.22	22	H2O	17.20	2.31	10.48
			NH4OAc	25.00	2.88	13.11
			HCl	30.30	3.48	15.80
MgO	0.24	24	H2O	12.60	1.69	7.04
			NH4OAc	76.10	8.78	36.57
			HCl	94.70	10.86	45.26
P2O5	0.078	7.8	H2O	4.60	0.62	7.90
			NH4OAc	15.20	1.75	22.48
			HCl	50.50	5.79	74.26
S	0.03	3	H2O	8.70	1.17	38.86
			NH4OAc	13.10	1.51	50.36
			HCl	49.80	5.71	190.41
SiO2	1.76	176	H2O	18.80	2.52	1.43
			NH4OAc	21.10	2.43	1.38
			HCl	44.10	5.06	2.87
TiO2	0.04	4	H2O	< 1.00	< 0.13	< 3.35
			NH4OAc	< 1.00	< 0.12	< 2.88
			HCl	< 1.00	< 0.11	< 2.87
Fe2O3	0.45	45	H2O	1.60	0.21	0.48
			NH4OAc	0.40	0.05	0.10
			HCl	193.00	22.14	49.20
Cl	0.76	76	H2O	25.85	3.46	4.56
			NH4OAc	0.00	0.00	0.00
			HCl	NA	NA	NA

THOMAS R. MILES CONSULTING DESIGN ENGINEERS
Phone (503) 292-0107
FAX (503) 292-2919

ble 5.- Correlation of Modified Chemical Fractionation Leaching Tests: 5-13-93Report updated 8-10-93
Test #6; Switch grass from L. Baxter. Wet ashing technique, except S by LECO.
100 ml leaching agent for each 10 g sample, 10 ml H2O added to leachate to seat filter paper.

Leaching agent:	Volume analyzed, ml:	Corrections for leach solutions. Cl-	Na2O
H2O	45.00	0.15	3.50
1M NH4OAc	60.50	2.4	4.30
1M HCl	92.50	NA	8.30

Component	Biomass		Solution Analysis Corrected for Cl and Na2O		Leachate	
	Conc by wet ashing, pct	mg per 10 g biomass	Leaching agent	mg/l solution	mg removed by 100 ml	Pct removed by agent
Al2O3	0.14	14	H2O	< 1.00	< 0.13	< 0.92
			NH4OAc	< 1.00	< 0.12	< 0.86
			HCl	11.00	1.23	8.81
CaO	0.61	61	H2O	30.00	3.86	6.32
			NH4OAc	152.00	18.21	29.85
			HCl	329.00	36.89	60.47
K2O	0.51	51	H2O	270.00	34.71	68.07
			NH4OAc	393.00	47.08	92.32
			HCl	420.00	47.09	92.34
)	0.079	7.9	H2O	2.90	0.37	4.72
			NH4OAc	2.00	0.24	3.03
			HCl	0.00	0.00	0.00
MgO	0.23	23	H2O	33.60	4.32	18.78
			NH4OAc	112.00	13.42	58.34
			HCl	126.00	14.13	61.42
P2O5	0.13	13	H2O	55.00	7.07	54.40
			NH4OAc	18.00	2.16	16.59
			HCl	79.00	8.86	68.14
S	0.03	3	H2O	4.80	0.62	20.57
			NH4OAc	13.00	1.56	51.91
			HCl	6.70	0.75	25.04
SiO2	4.12	412	H2O	60.70	7.80	1.89
			NH4OAc	101.00	12.10	2.94
			HCl	35.90	4.03	0.98
TiO2	0.01	1	H2O	< 1.00	< 0.13	< 12.86
			NH4OAc	< 1.00	< 0.12	< 11.98
			HCl	< 1.00	< 0.11	< 11.21
Fe2O3	0.14	14	H2O	2.30	0.30	2.11
			NH4OAc	2.00	0.24	1.71
			HCl	25.00	2.80	20.02
I	0.03	3	H2O	18.85	2.42	80.79
			NH4OAc	80.60	9.66	321.87
			HCl	NA	NA	NA

THOMAS R. MILES CONSULTING DESIGN ENGINEERS
Phone (503) 292-0107
FAX (503) 292-2919

Table 6.- Correlation of Modified Chemical Fractionation Tests for Selected Biomass Samples

Date prepared: 8-11-93

Component	Leaching agent	Pct removed by agent Rice Straw	Wheat Straw	Mendota Fuel	Switch Grass
Al2O3	H2O	1.94	7.67	< 0.5	< 1
	1M NH4OAc	2.1	< 2.3	< 0.5	< 1
	1M HCl	9.01	4.49	22.74	8.81
CaO	H2O	1.06	24.61	3.99	6.32
	1M NH4OAc	1.23	38.24	26.05	29.85
	1M HCl	33.51	55.04	100	60.47
K2O	H2O	86.67	88.79	54.69	68.07
	1M NH4OAc	99.35	96.06	79.8	92.32
	1M HCl	100	95.39	81.84	92.34
Na2O	H2O	93.38	43.19	10.48	4.72
	1M NH4OAc	100	52.47	13.11	3.03
	1M HCl	100	42.36	15.8	0
MgO	H2O	60.98	55.73	7.04	18.78
	1M NH4OAc	81.6	69.73	36.57	58.34
	1M HCl	71.52	75.02	45.26	61.42
P2O5	H2O	76.57	76.37	7.9	54.4
	1M NH4OAc	89.5	100	22.48	16.59
	1M HCl	91.55	100	74.26	68.14
S	H2O	15.9	54.46	38.86	20.57
	1M NH4OAc	15.23	57.69	50.36	51.91
	1M HCl	15.5	53.72	100	25.04
SiO2	H2O	0.05	6.71	1.43	1.89
	1M NH4OAc	0.05	7.03	1.38	2.94
	1M HCl	0.05	3.05	2.87	0.98
TiO2	H2O	NA	< 11	< 3	< 12
	1M NH4OAc	NA	< 11	< 3	< 12
	1M HCl	NA	< 11	< 3	< 12
Fe2O3	H2O	27.79	16.77	0.48	2.11
	1M NH4OAc	6.96	4.15	0.1	1.71
	1M HCl	61.99	25.65	49.2	20.02
Cl	H2O	NA	100	4.56	80.79
	1M NH4OAc	NA	100	0	100
	1M HCl	NA	NA	NA	NA

THOMAS R. MILES CONSULTING DESIGN ENGINEERS
Phone (503) 282-0107
FAX (503) 292-2919

leachable in water and HCl than in NH_4OAc, with HCl consistently more effective than water. The data in Tables 2-6 were provided to Larry Baxter, who will provide comparisons with chemical fractionation tests conducted by ASTM/ISO standard methods.

1.3 Sticky temperature apparatus

Sticking of particles at any temperature is largely a function of liquid formation. The fraction of liquid phase leading to sticking of ash particles is usually a very small fraction of the total mass, and therein lies the problem of developing a field test to determine the sticky temperature. A novel approach, conceived by Mr Jack White of the Bureau of Mines, is based upon an apparatus similar to an hour glass. Anyone who has attempted to make an hour glass knows that the slightest moisture causes the sand grains to refuse to pass through the orifice from one lobe to the other. Moisture provides a liquid phase on the surface of sand particles, not unlike the liquid phase leading to sticking of ash particles. The modified hour glass, constructed of fused quartz or Vycor, has a side tube on one lobe for introducing the ash and for inserting a thermocouple, as shown on the drawing below. The apparatus containing the ash sample and a thermocouple is slowly rotated alternately through positive 180 deg and negative 180 deg within a muffle furnace programmed to ramp up at a reasonable rate, say 25 C/min. Visual observation of ash movement correlated with the temperature is expected to provide the sticky temperature. The temperature is indicated unambiguously by the thermocouple embedded within the ash itself. A working model of the apparatus has been constructed, but to date has not been tried.

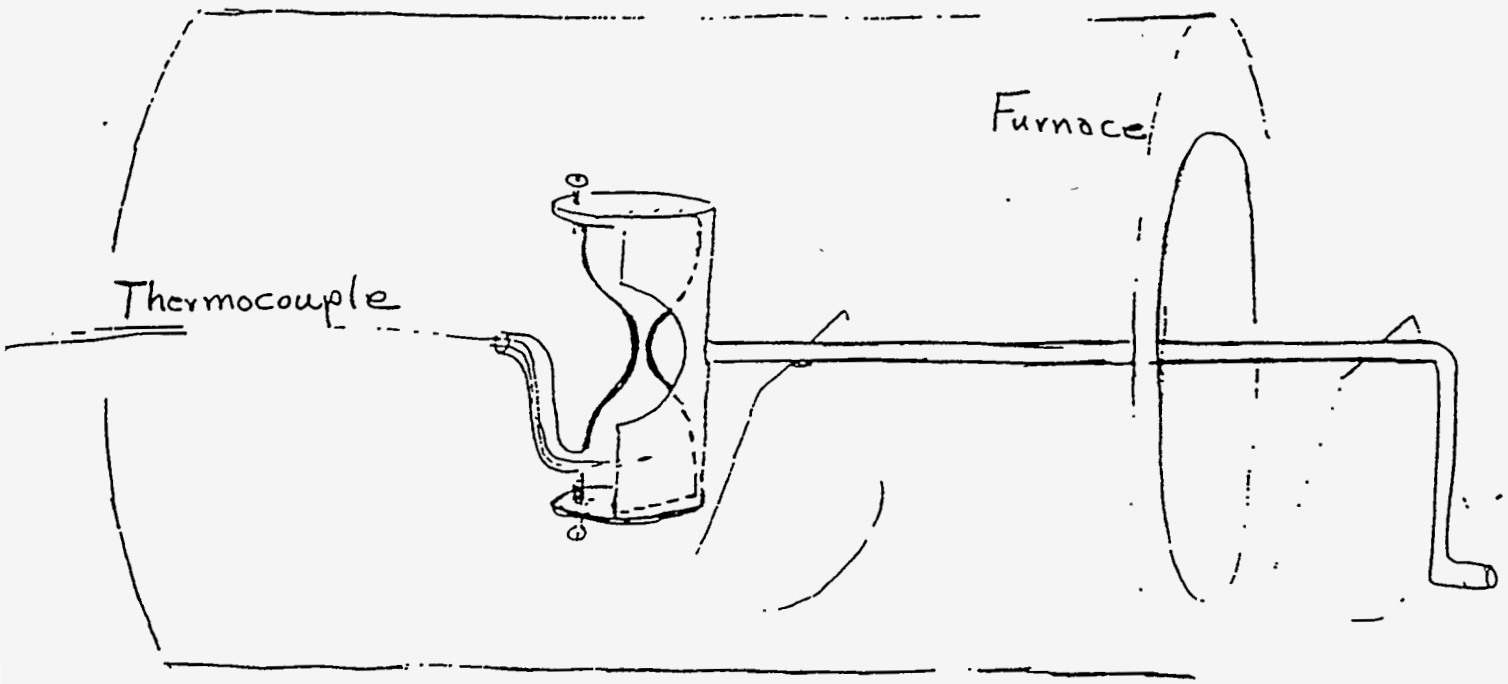

Sticky Temperature Apparatus

1.4. Mineralogical and X-ray Diffraction (XRD) Analysis of Biomass Deposits

XRD is a comparative method of analysis in which the observed X-ray diffraction pattern obtained from a finely ground sample is compared with a catalog of patterns for pure materials. Ambiguities are not uncommon, because different materials can have identical crystal structures and similar if not identical lattice parameters. Therefore samples are often analyzed by EDAX to verify the existence of elemental components. The relative proportion of phases, as estimated from line intensities are indicated as follows:

Primary, 40 to 100 pct of the sample,
Secondary, 20 to 60 pct of the sample,
Minor, 5 to 30 pct of the sample,
Trace, 1 to 10 pct of the sample, and
Barely detectable trace (BDT) less than 1 pct.

In point of fact, an experienced analyst can estimate the proportion of phases much more accurately than indicated by the designations.

1.4.1 Woodland Biomass cyclone deposit:

This deposit, as shown on Figure 1, was obtained from a pile of material removed from the cyclone following a clean-up. Many layers with different colors were apparent across a broken section of the deposit. Eleven individual layers representing many shades of yellow, grey, brown, and green were physically separated for XRD analysis, with the first layer selected to represent material adjacent to the cyclone wall. XRD detected $CaMg(SiO_3)_2$ (Diopside) and $CaSiO_3$ (Wollastonite) as secondary phases and $KAlSiO_3O_8$ as a minor phase in each of the layers. No significant difference in the relative proportion of phases was observed.

A sample of the layered material representing the XRD samples was mounted for analysis by the scanning electron microscope (SCE). Figure 2 is a back scattered electron (BSE) image at 20 X magnification of a series of layers. Atoms scatter electrons in proportion to their atomic number; therefore regions containing proportionately more of the heavy elements will appear lighter in the BSE image. Figures 3 and 4 are characteristic x-ray maps for the major elements present in the image shown on Figure 2. Darkness on Figures 3 and 4 is proportional to the element concentration. The map for Fe is complicated by a change in beam current that is responsible for the change in darkness along the horizontal line. Points of interest in this qualitative presentation are the following:

Al, and Si are nearly constant across individual layers and constant from layer to layer,

K, atomic number 19 is deficient in the bright layers on Figure 2, especially the thick bright layer in the lower left, thereby indicating a larger proportion of Diopside and/or Wollastonite in the light layers.

Ca, K, and to a lesser extent P and Fe appear to be responsible for the layered appearance.

1.4.2 HydraCo grate clinker formed on the moving grate during burning of 95 pct wood chips-5 pct straw:

This sample was a mixture of white, grey, and black phases, which were physically separated for XRD analysis.

The white material was a complex mixture of quartz and $KAlSi_3O_8$ (Microcline) as secondary phases; $CaAl_2Si_2O_8$ (Anorthite) as a minor phase; and $Ca_2Al_2SiO_7$ (Gehlenite) and unidentified compounds as trace phases.

The grey material was primarily quartz, with traces of $KAlSi_3O_8$, $CaAl_2Si_2O_3$, and $Ca_2Al_2SiO_7$.

The black material comprised primarily quartz with traces of $CaAl_2Si_2O_8$ (Anorthite) and $Ca_2Al_2SiO_7$ (Gehlenite).

The white material, by EDAX analysis, contained the primary elemental constituents Si, K, Ca, and Al with lesser amounts of Fe and S. The grey and black materials contained slightly more Fe. To summarize the XRD and EDAX results, the grate clinker was a physical mixture of the rather refractory calcium aluminum silicate minerals quartz, Anorthite, and Gehlenite likely bonded together by the lower melting Microcline, which is rich in potassium.

EDAX raises the warning that sulfur may play a role in the bonding. Color is likely related to the iron content.

Figure 5 is the BSE image at 19 magnification of a polished surface of the grate clinker, and Figures 6 and 7 are characteristic X-ray maps for the same surface. Four phases were analyzed, indicated 1 through 4 on Figure 5, and the results are listed on Table 7.

Table 7. SEM Analysis of HydraCo Grate Clinker

Phase	1	2	3	4
Na_2O	5.92	3.80	ND	1.32
Al_2O_3	31.84	31.05	2.42	17.3
SiO_2	57.52	59.76	97.29	49.47
K_2O	1.34	3.58	0.09	0.88
CaO	2.97	1.68	0.07	22.54
Fe_2O_3	0.40	0.14	0.12	4.39
MgO	ND	ND	ND	2.44
SO_3	ND	ND	ND	1.03
TiO_2	ND	ND	ND	0.63

The phases detected by XRD can be referenced to the BSE image of Figure 5 and the characteristic X-ray maps of Figures 6 and 7.

Phase 1, the porous phase on the bottom right of Figure 5, is likely an amorphous material owing to its silica and alkali content, and was not detected by XRD.

Phase 2, the light grey phase is likely Microcline. This phase contains most of the K and effectively surrounds crystallites of phase 3.

Phase 3, the darker grey internally fractured phase is nearly pure quartz.

Phase 4, the nearly white material, forms the matrix and may very well be composed of more than one phase. This mixture, which may be amorphous, contains most of the Ca and Fe as well as the other remaining impurities S and Ti. This characteristic of phase 4 identifies it as the last phase to solidify on cooling.

1.4.3. Deposit 007 from HydraCo Wood-20 pct Willamette Valley straw test burn:

Deposit 007, which formed as a white chalky coating at superheater level, was analyzed by x-ray diffraction (XRD) to determine the phases present. The primary phase is Aphthitalite, which has the chemical formula $K_3Na(SO_4)_2$. Palmierite ($K_2Pb(SO_4)_2$ was recognized as a minor phase. For practical purposes, the white deposit is potassium sulfate with sodium and lead substituting for some of the potassium. EDAX confirmed the presence of S, K, and Pb in the sample.

1.4.4 Deposit 008 from HydraCo Wood-20 pct Willamette Valley straw test burn:

Deposit 008 formed as a hard brown layered accretion 1/8 to 1/4 in thick on the leading surface of the superheater tubes. The sample was analyzed by XRD in two conditions: as-received and after leaching with acid. Removal of the acid soluble compounds greatly simplified the diffraction pattern of the remaining mixture of materials.

The as-received sample contained $KNaSO_4$ and unidentified compound(s) as secondary phases and quartz (SiO_2) and $K_2Ca_2(SO_4)_3$ as minor phases. The insoluble material comprised quartz, Albite ($NaAlSi_3O_8$), and Angite ($Ca(MgFe)Si_2O_6$). For practical purposes, the deposit consists of silicate minerals bonded together with impure potassium sulfates.

Figure 8 is the BSE image at 19 magnification of a polished surface of the superheater tube accretion showing the layered nature of the deposit. In plane polarized light at 100 magnification the polished surface near the fire side appears as in Figure 9. The tube side deposit is identical. Individual mineral crystallites often very poorly bonded together are clearly visible in the photographs. Figure 10, the BSE image at 200 magnification from the SEM, verifies the composite nature of the deposit. Individual particles indicated on Figure 10 as particles 1, 2, and 3 were analyzed with the following results listed on Table 8.

Table 8. SEM Analysis of HydraCo Superheater Tube Deposit

Particle	1	2*	3**	4***
Na_2O	ND	1.08	ND	11.50
Al_2O_3	ND	15.44	29.94	ND
SiO_2	100	36.96	27.94	4.11
K_2O	ND	12.00	13.40	20.29
CaO	ND	11.16	5.73	3.08
Fe_2O_3	ND	2.19	7.43	ND
MgO	ND	2.68	4.77	ND
SO_3	ND	18.26	6.77	61.01
TiO_2	ND	ND	1.52	ND
Cl	ND	ND	1.75	ND

* Particle 2 is very porous.

** Particle 3 has a well defined core and case which have identical analyses.

*** Phase 4 is the matrix surrounding the individual grains. The matrix is uniform across the sample.

A BSE image of cored particle 3 at 2,000 magnification is shown on Figure 11. A BSE image at 1,000 magnification of the center region of Figure 10 is shown on Figure 12. Figures 13 and 14 are characteristic X-ray maps of the surface on Figure 12. The phases detected by XRD can be referenced to the BSE image of Figure 12 and the characteristic X-ray maps of Figures 13 and 14.

Phase 1 is clearly nearly pure quartz.

Phase 2, although off the field of view, is likely a composite particle comprising sulfates and silicates.

Phase 3, the cored particle which also if off the field of view, is likely a low-melting flux-like material owing to its composition.

Phase 4, the matrix material, is largely alkali sulfate, and is likely the material responsible for accretion formation.

1.4.3 Deposit 016 from HydraCo Wood-20 pct Willamette Valley straw test burn:

Deposit 016 formed as an "eyebrow" over feeder number 2. The deposit was semi-liquid and "dripped" during operation of the boiler. The sample was separated into a blue and mustard colored glassy phase and a granular phase for XRD analysis. The blue and mustard colored material was primarily noncrystalline with minor quartz and Angite ($Ca(MgFe)Si_2O_6$) phases. The crystalline material comprised quartz, Angite, and Leucite ($NaAlSi_3O_8$) as minor phases and Albite as a trace phase.

Figure 15 shows the polished surface at 100 magnification of Deposit 016 under differential interference contrast (DIC) which accentuates surface texture. The surface at 50 magnification of an adjacent region having more porosity appears as Figure 16 under bright field illumination. Surface and subsurface porosity at 100 magnification is clearly illustrated by Figure 17, which is a view under plane polarized light. In some highly noncrystalline regions of the sample shown on Figure 18, polarized light reveals flow patterns and starburst crystallites which exsolved from the liquid during cooling. The crystallites visible in Figure 18 are largely below the polished surface, although some rays extent to the surface giving rise to the texture shown under DIC. The flow pattern, vaguely visible in Figure 18 is vivid in Figure 19, which also indicates the presence of cubic crystals of quartz. The BSE image at 1,000 magnification is shown on Figure 20, and the corresponding X-ray maps for the principal elements are shown on Figures 21 and 22. It is clear from the latter that the starburst crystallites are complex calcium magnesium silicate, likely Angite. SEM analysis of the various phases provided the data in Table 9

Table 9. SEM Analysis of Eyebrow Piece Above Feeder #2

Region	Matrix	Cubic crystals*	Starburst*	Amorphous**
Na_2O	2.11	ND	ND	ND
Al_2O_3	20.34	10.8	7.68	27.63
SiO_2	60.24	54.74	53.92	63.27
K_2O	4.65	0.94	0.24	ND
CaO	9.07	18.43	20.66	ND
Fe_2O_3	2.83	4.93	5.14	ND
MgO	ND	9.78	11.90	ND
SO_3	ND	ND	ND	4.82
TiO_2	0.67	0.38	0.45	ND
Cl	ND	ND	ND	4.29

* Analysis of the small crystallites is complicated by excitation of adjacent material be the electron beam. The cubic and starburst crystallites may the same substance. The cubic crystallites shown in cross section on Figure 20 are not the well defined crystals observed on Figure 19.

** Amorphous material was variable in composition.

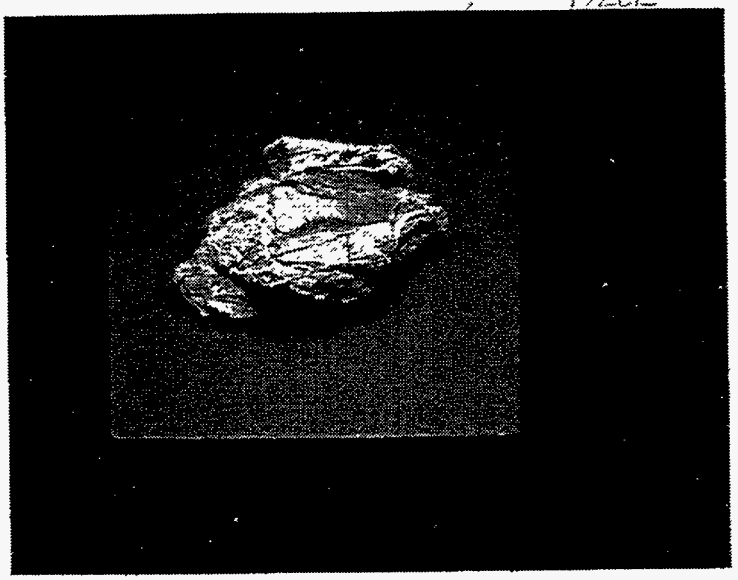

Figure 1.- Woodland Biomass Cyclone Deposit

Figure 2.- Woodland Biomass Cyclone Deposit:
Backscattered Electron Image, X20

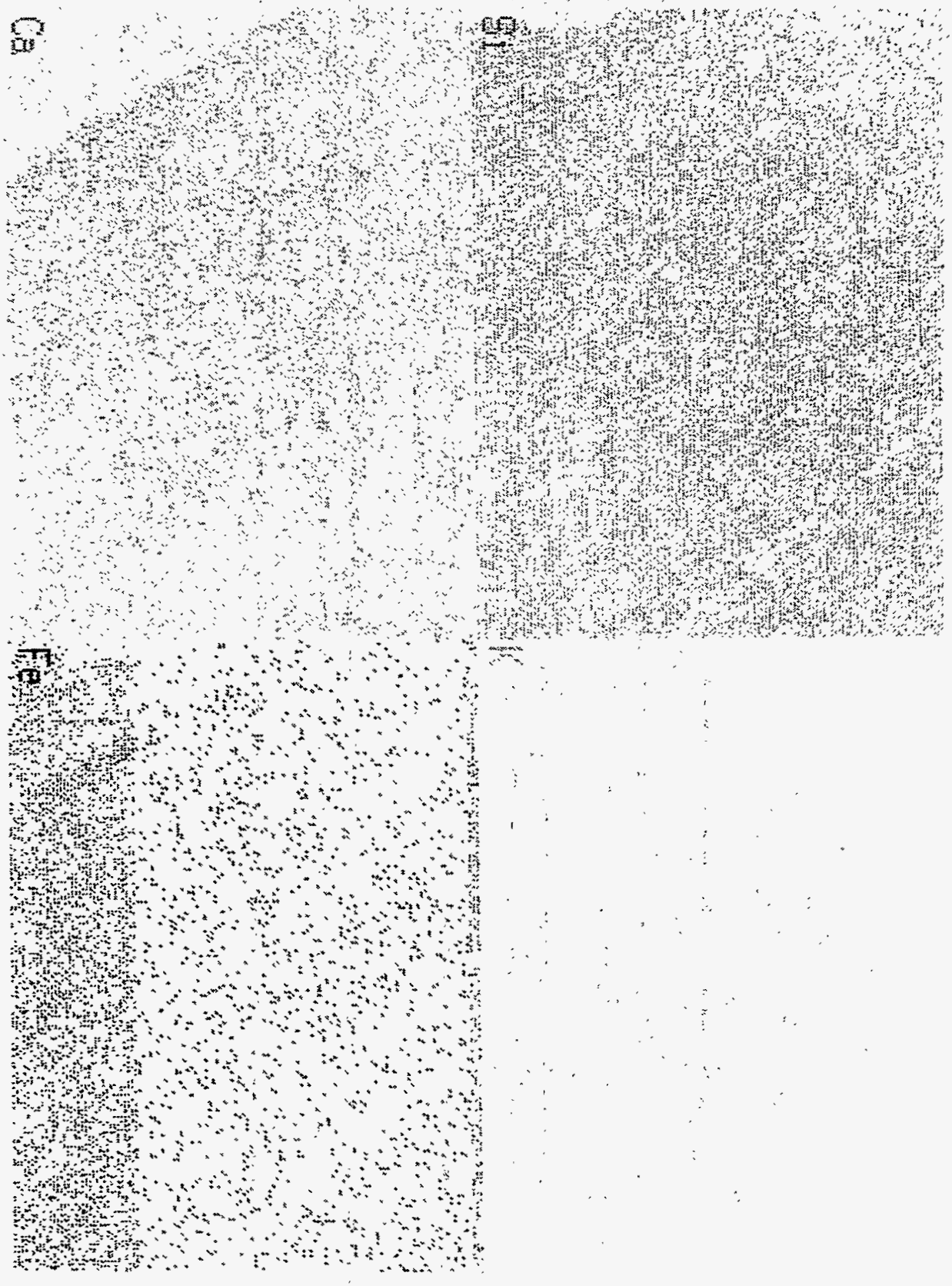

Figure 3.- Woodland Biomass Cyclone Deposit:
Characteristic X-ray Map: Si, Ca, K, and Fe.

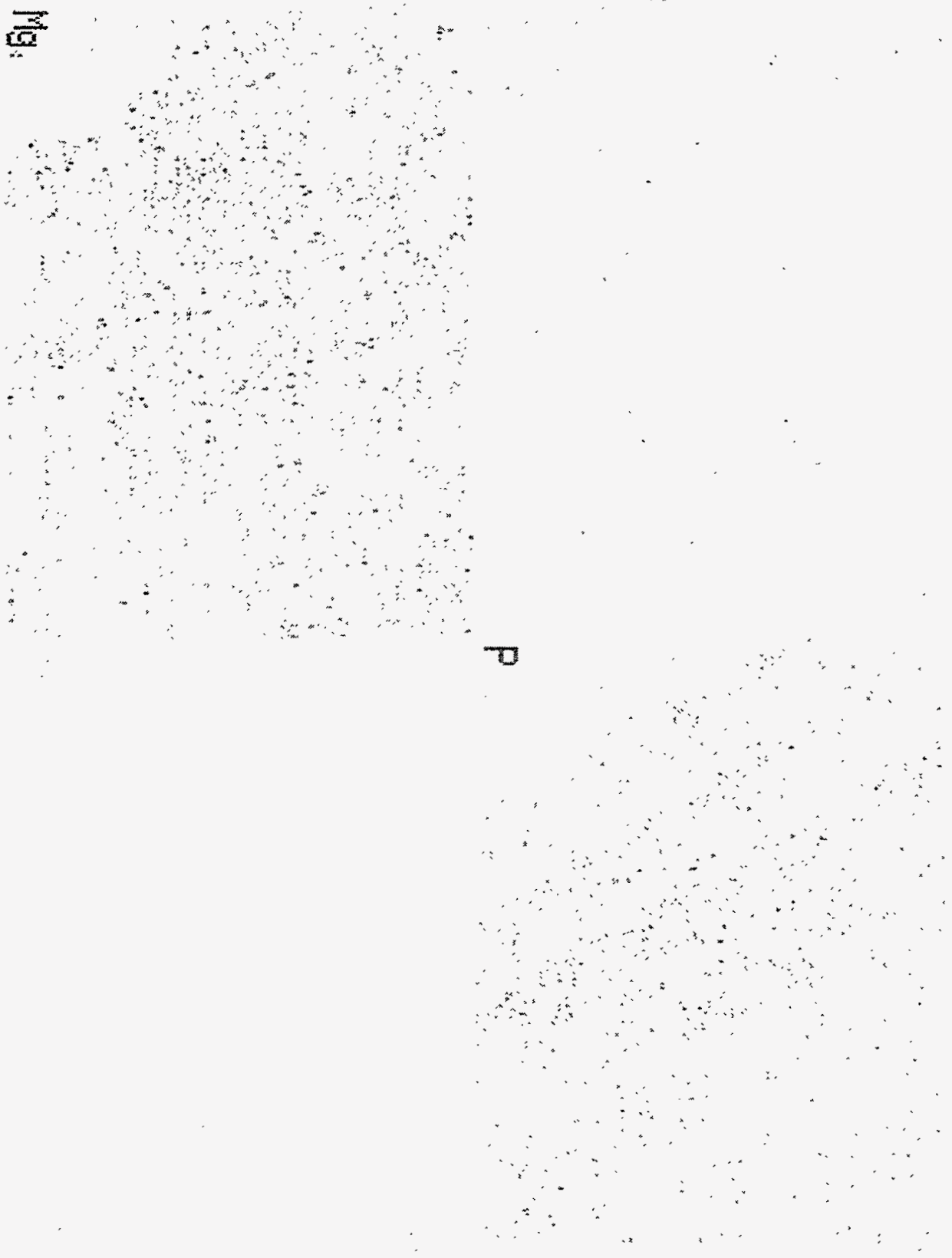

Figure 4.- Woodland Biomass Cyclone Deposit:
Characteristic X-ray Map: Al, Mg, and P.

THOMAS R. MILES CONSULTING DESIGN ENGINEERS
Phone (503) 292-0107
FAX (503) 292-2919

MICROWAVE DISSOLUTION AND ATOMIC ABSORPTION METHOD FOR THE DETERMINATION OF SEVEN ELEMENTS IN BIOMASS

The following is a method developed by the U. S. Bureau of Mines, Albany Research Center, for the determination of Al_2O_3, CaO, K_2O, Na_2O, MgO, SiO_2, and Fe_2O_3 in straws and other biomass:

1. Weigh 100 to 250 mg sample into a 120 mL Teflon vessel.
2. Wet sample with 5 mL con. HF.
3. Seal vessel with cap and relief valve.
4. Digest in microwave oven for 90 sec. at 70% power.
5. Cool vessel to room temperature.
6. Place vessel into microwave oven and digest again for 90 sec. at 70% power.
7. Cool vessel to room temperature.
8. Unseal vessel in a hood, add 5 mL con. HCl and 5 mL con. HNO_3.
9. Repeat steps 3 through 7.
10. Unseal vessel in a hood, wash contents into a 100 mL plastic volumetric flask using distilled water and make to the mark.
11. The solution thus produced is now introduced to an atomic absorption spectrophotometer, using the proper conditions for each element.

The above method assumes the analyst has had experience with microwave dissolution techniques. If the analyst has not had experience with microwave dissolution techniques or experience using apparatus designed for use in microwave ovens, care must be exercised to avoid explosions or other accidents.

The analytical laboratory at the U.S. Bureau of Mines, Albany Research Center used the following special apparatus for the above dissolution method:

- A 1000 watt microwave oven, equipped with a turntable; ours is a Tappan purchased from Sears and Roebuck that has been specially modified.
- 120 mL microwave vessels marketed by CEM Corporation.
- Plastic volumetric ware available from Nalgene labware.

If the analyst has had no experience with microwave sample dissolution, the following is recommended reading: Introduction to Microwave Sample Preparation, edited by H. M. Kingston and Lois B. Jassie published by The American Chemical Society, Washington, D.C. in 1988.

If you have any questions I may be reached by telephone at: (503) 967-5800.

Joseph A. Perry, Supervisory Chemist

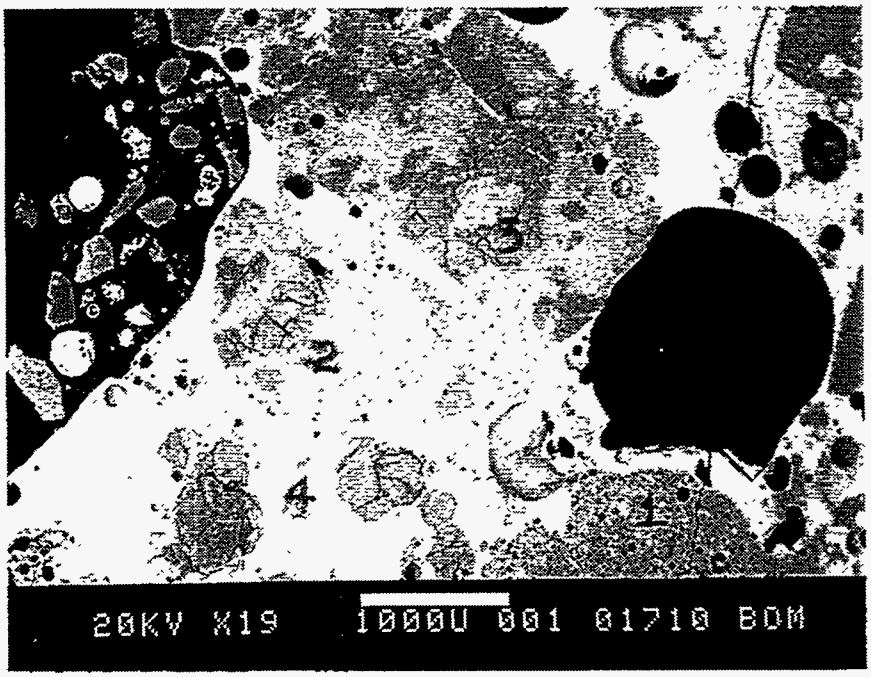

Figure 5.- HydraCo Grate Clinker:
Backscattered Electron Image, X19

Figure 6.- Hydraco Grate Clinker:
Characteristic X-ray Map: Al, Na, and Cl.

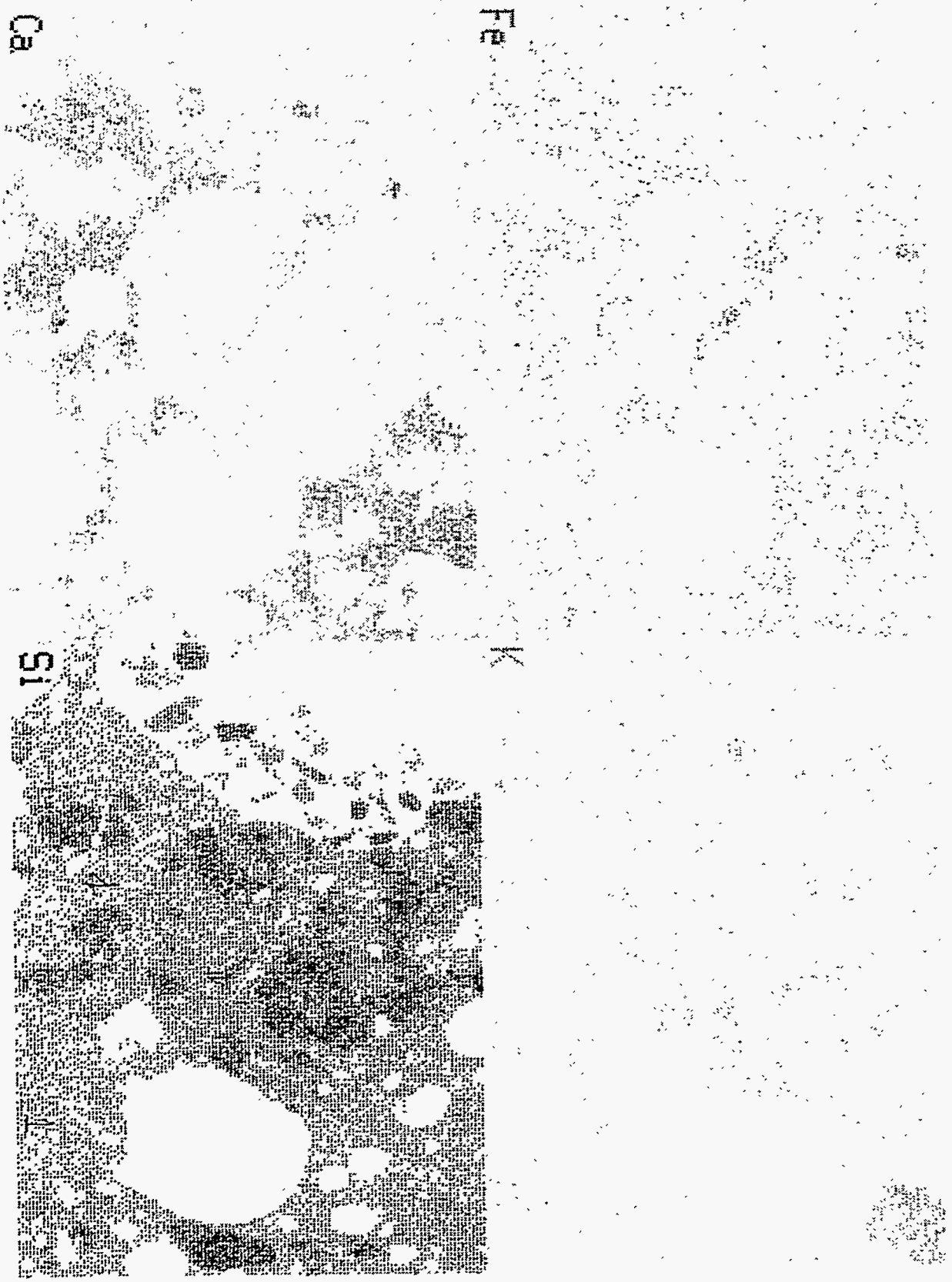

Figure 7.- HydraCo Grate Clinker:
Characteristic X-ray Map: Fe, Ca, K, and Si.

Figure 8.- HydraCo Wood-20 pct Willamette Valley Straw Test Burn: Deposit 008, Backscattered Electron Image, X19.

Figure 9.- HydraCo Wood-20 pct Willamette Valley Straw Test Burn: Deposit 008, Fireside Deposit, Polarized Light, X100.

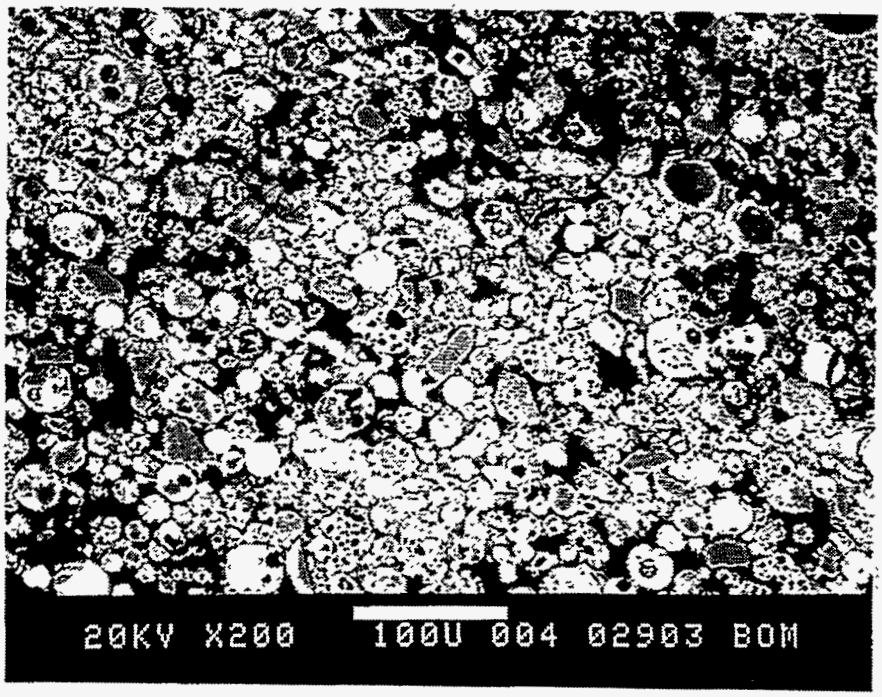

Figure 10.- HydraCo Wood-20 pct Willamette Valley Straw Test Burn: Deposit 008, Backscattered Electron Image, X200.

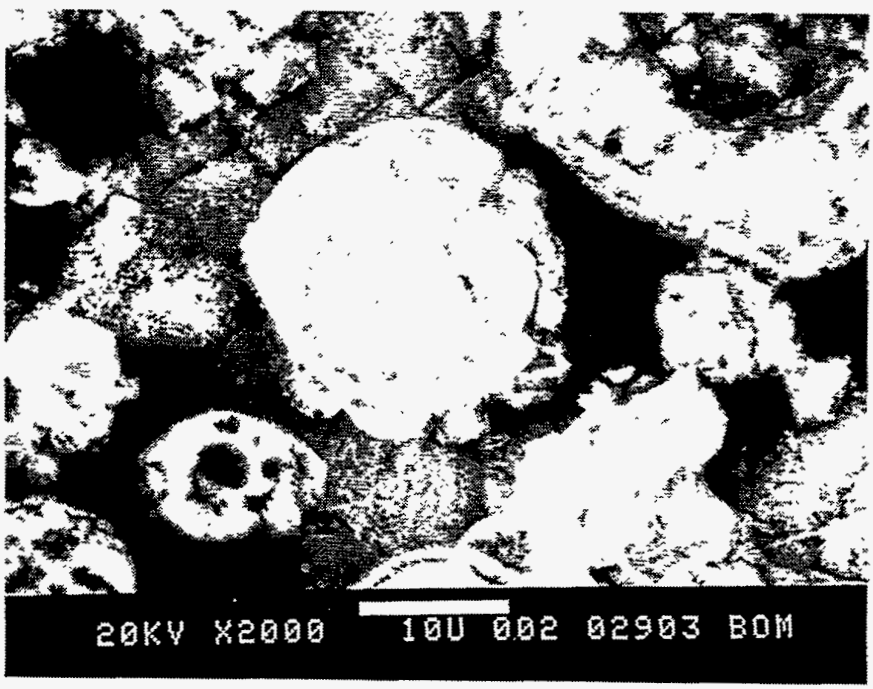

Figure 11.- HydraCo Wood-20 pct Willamette Valley Straw Test Burn: Deposit 008, Backscattered Electron Image of Cored Particle 3, X2000.

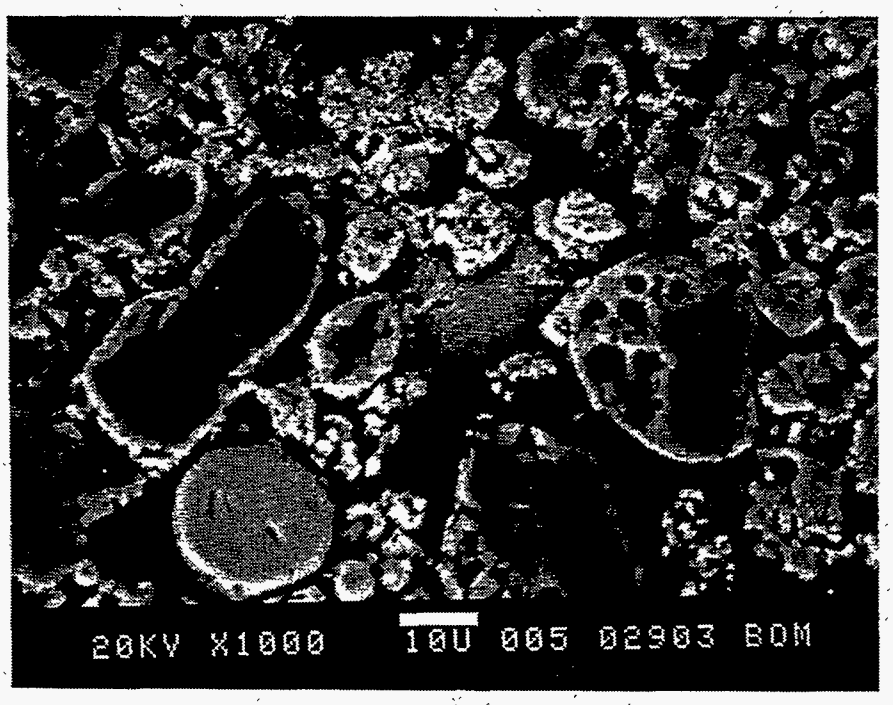

Figure 12.- HydraCo Wood-20 pct Willamette Valley Straw Test Burn: Deposit 008, Backscattered Electron Image of the Center Region of Figure 10, X1,000.

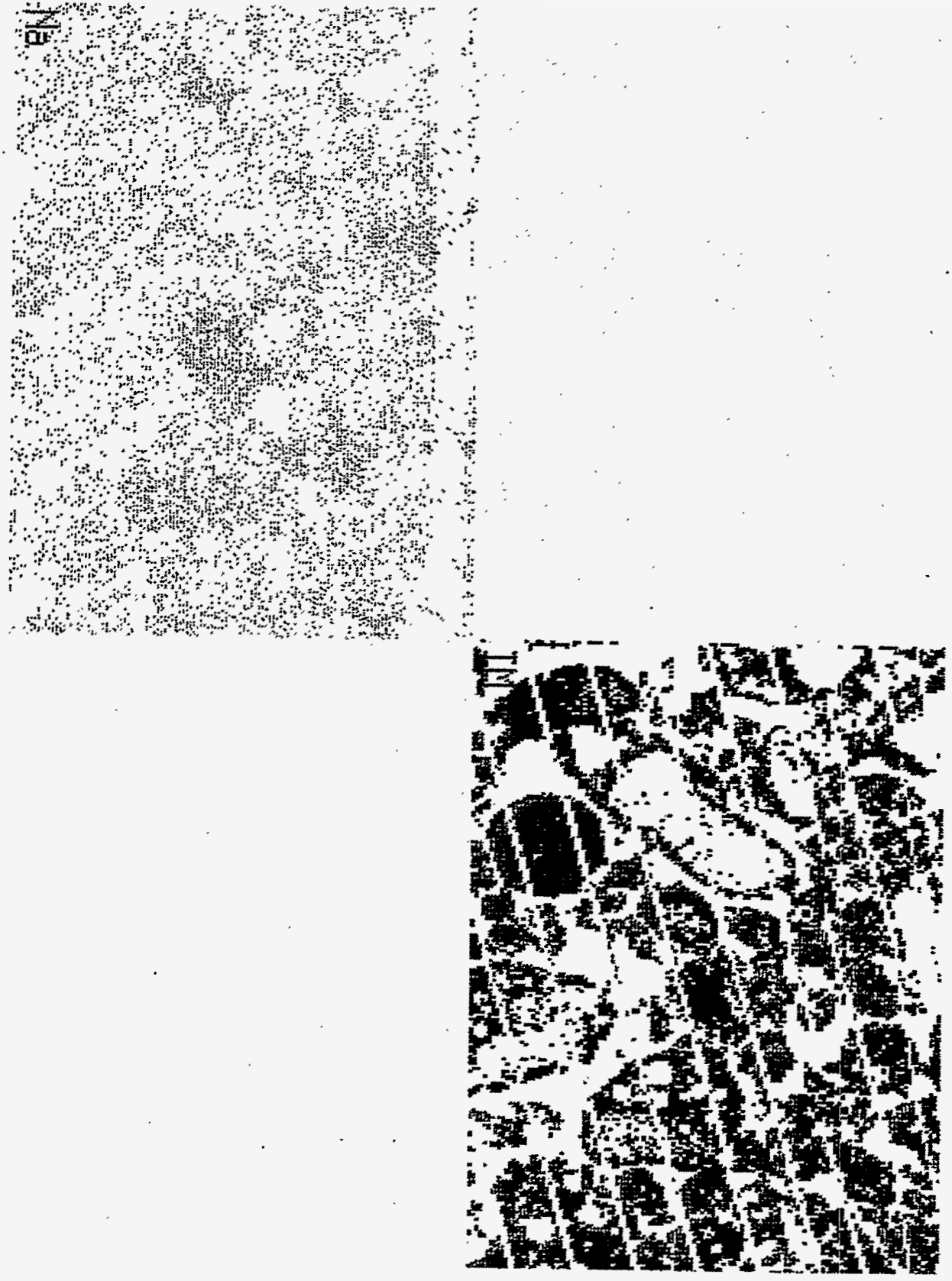

Figure 13.-HydraCo Wood-20 pct Willamette Valley Straw Test Burn: Deposit 008, Characteristic X-ray Map: Na, and Ca.

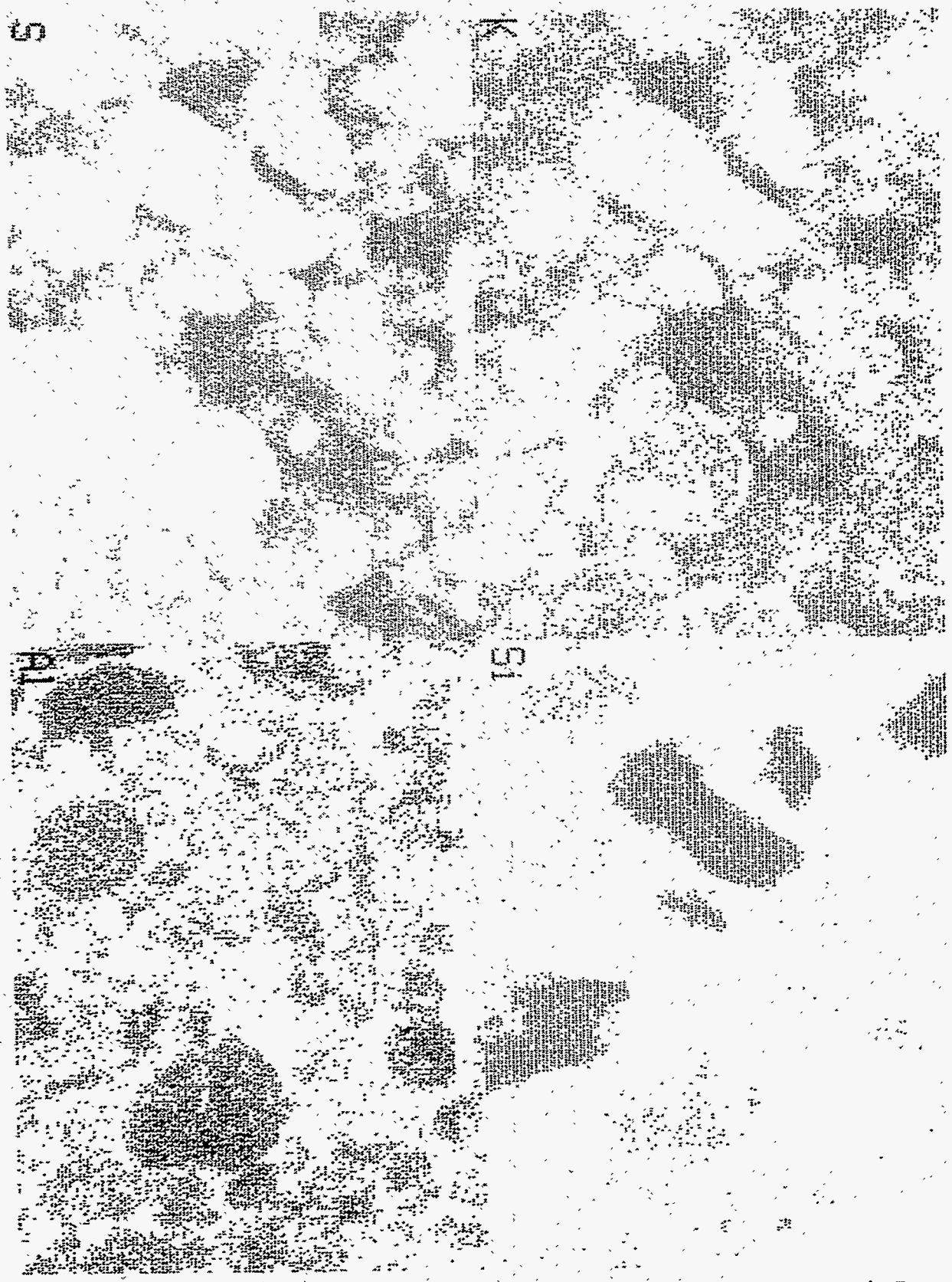

Figure 14.-HydraCo Wood-20 pct Willamette Valley Straw Test Burn: Deposit 008, Characteristic X-ray Map: K, S, Si, and Al.

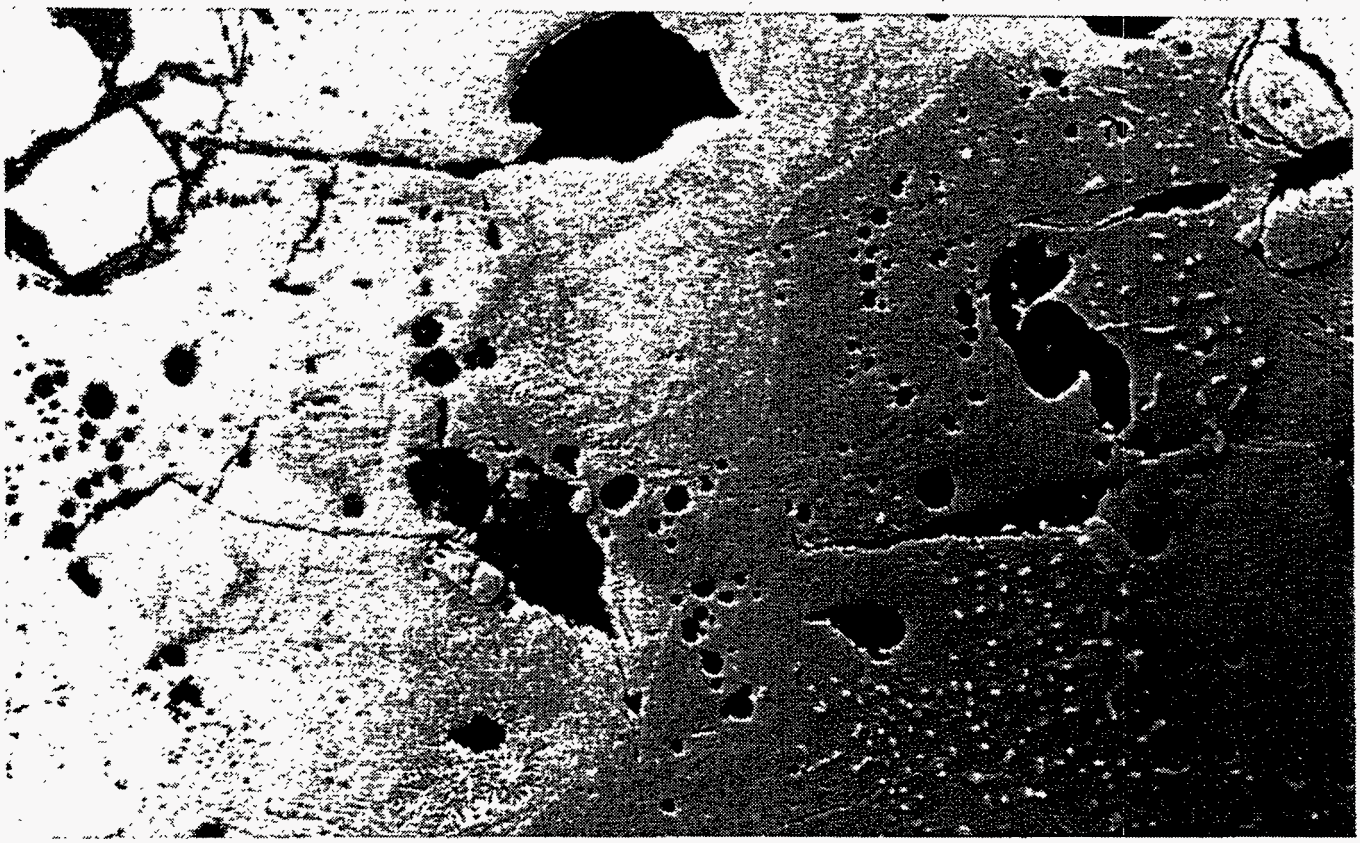

Figure 15.- HydraCo Wood-20 pct Willamette Valley Straw Best Burn: Deposit 016, Differential Interference Contrast, X100.

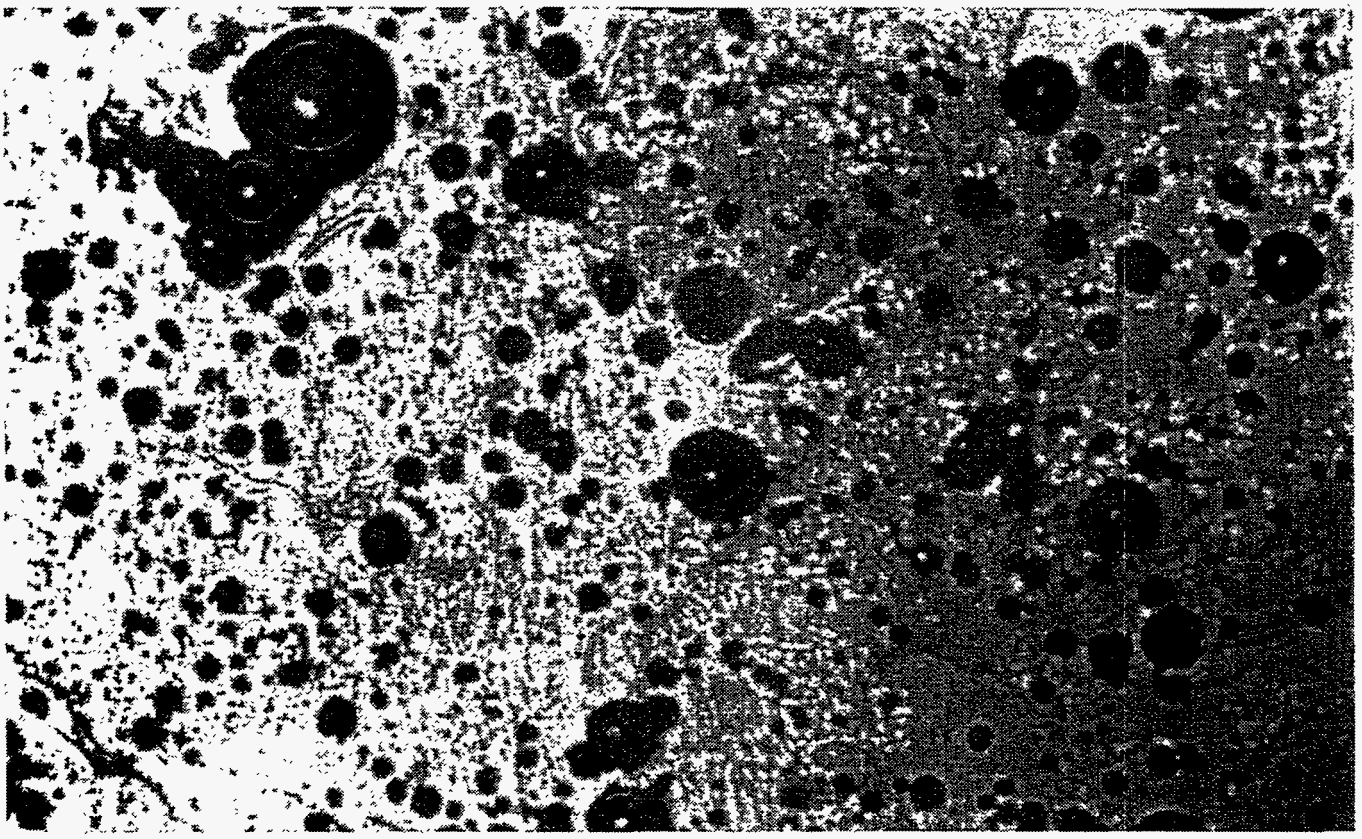

Figure 16.- HydraCo Wood-20 pct Willamette Valley Straw Test Burn: Deposit 016, Bright Field Illumination, X100.

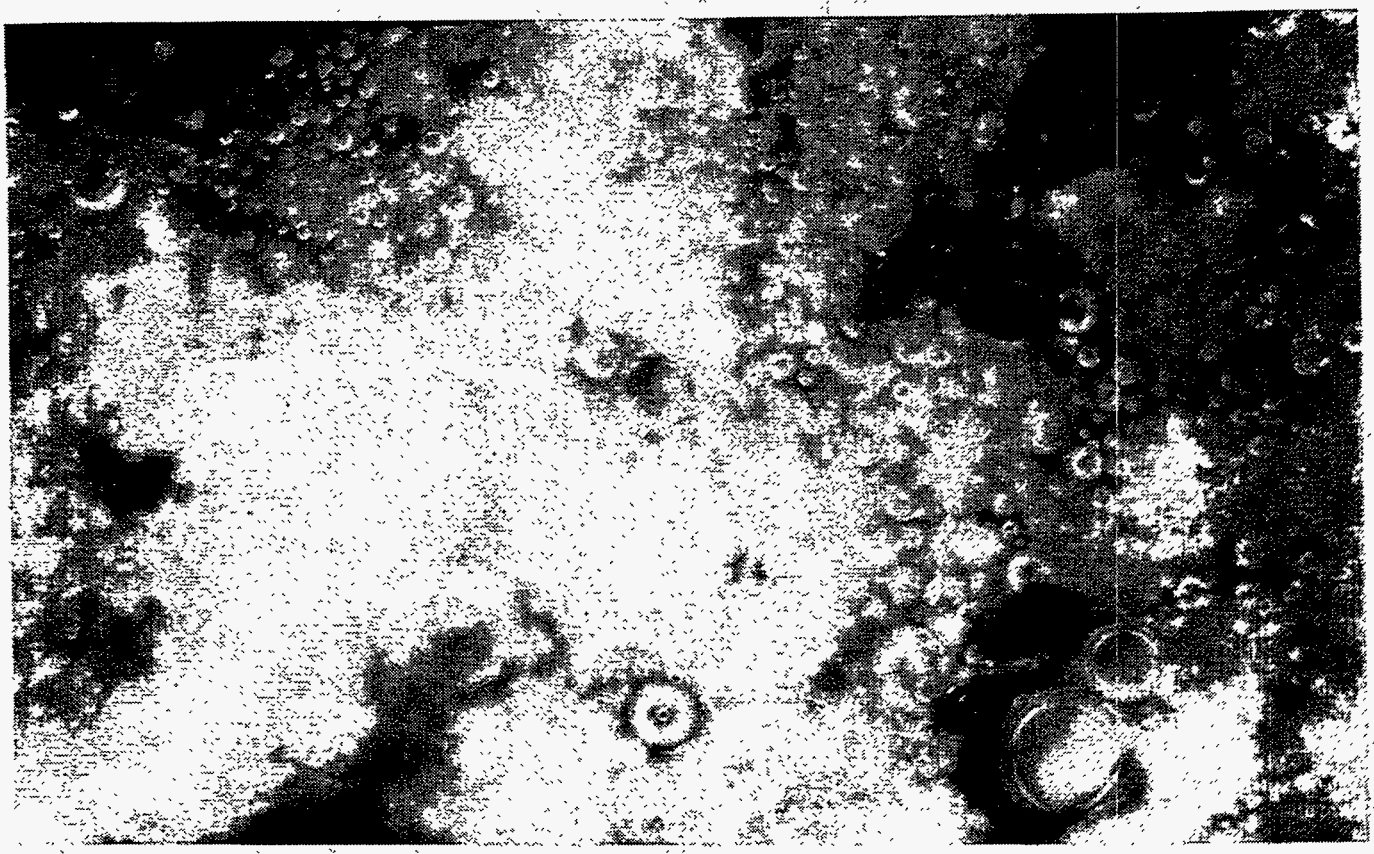

Figure 17.- HydraCo Wood-20 pct Willamette Valley Straw Test Burn: Deposit 016, Porous Region under Polarized Light, X100.

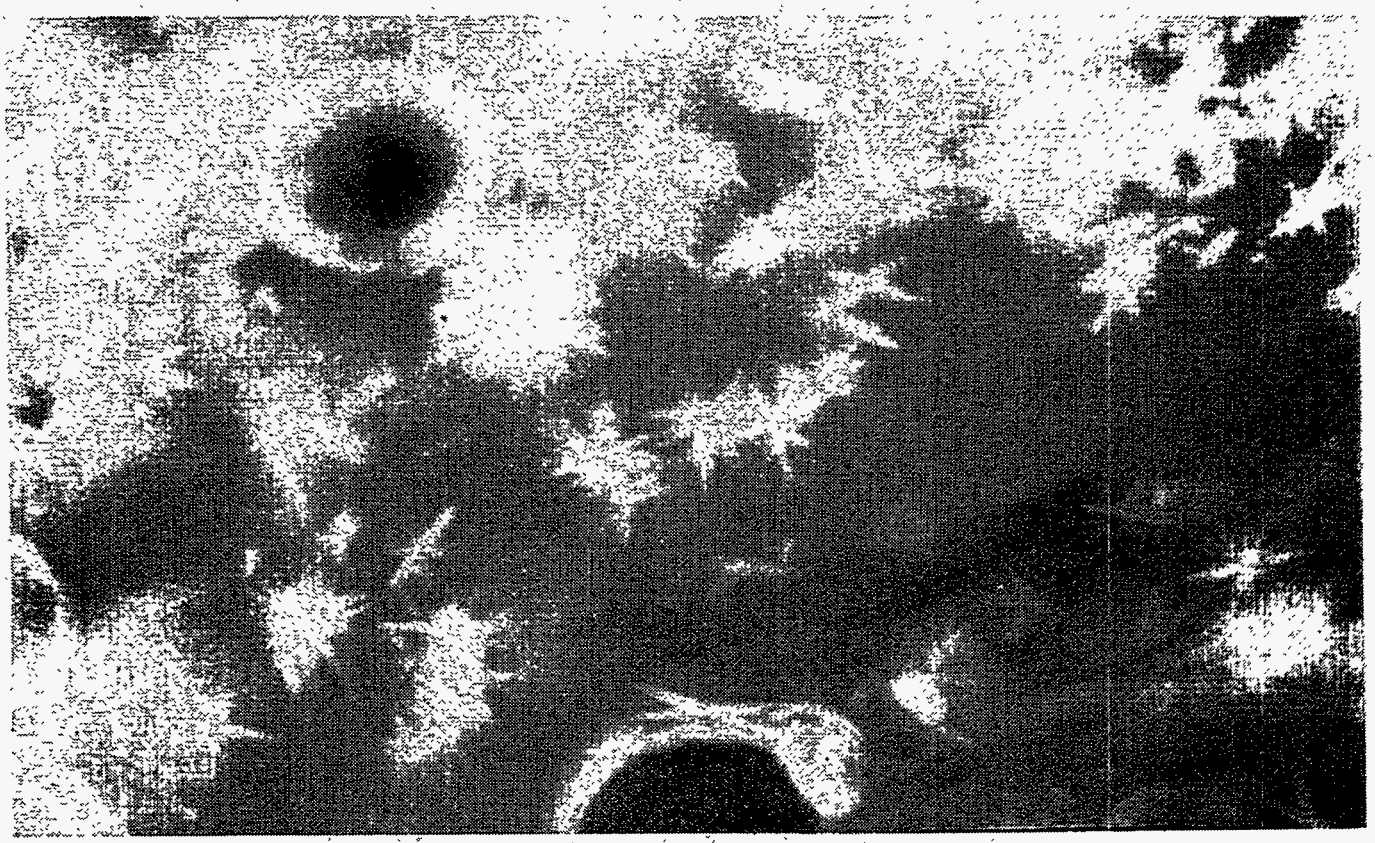

Figure 18.- HydraCo Wood-20 pct Willamette Valley Straw Test burn: Deposit 016, Noncrystalline Region under Polarized Light, X100.

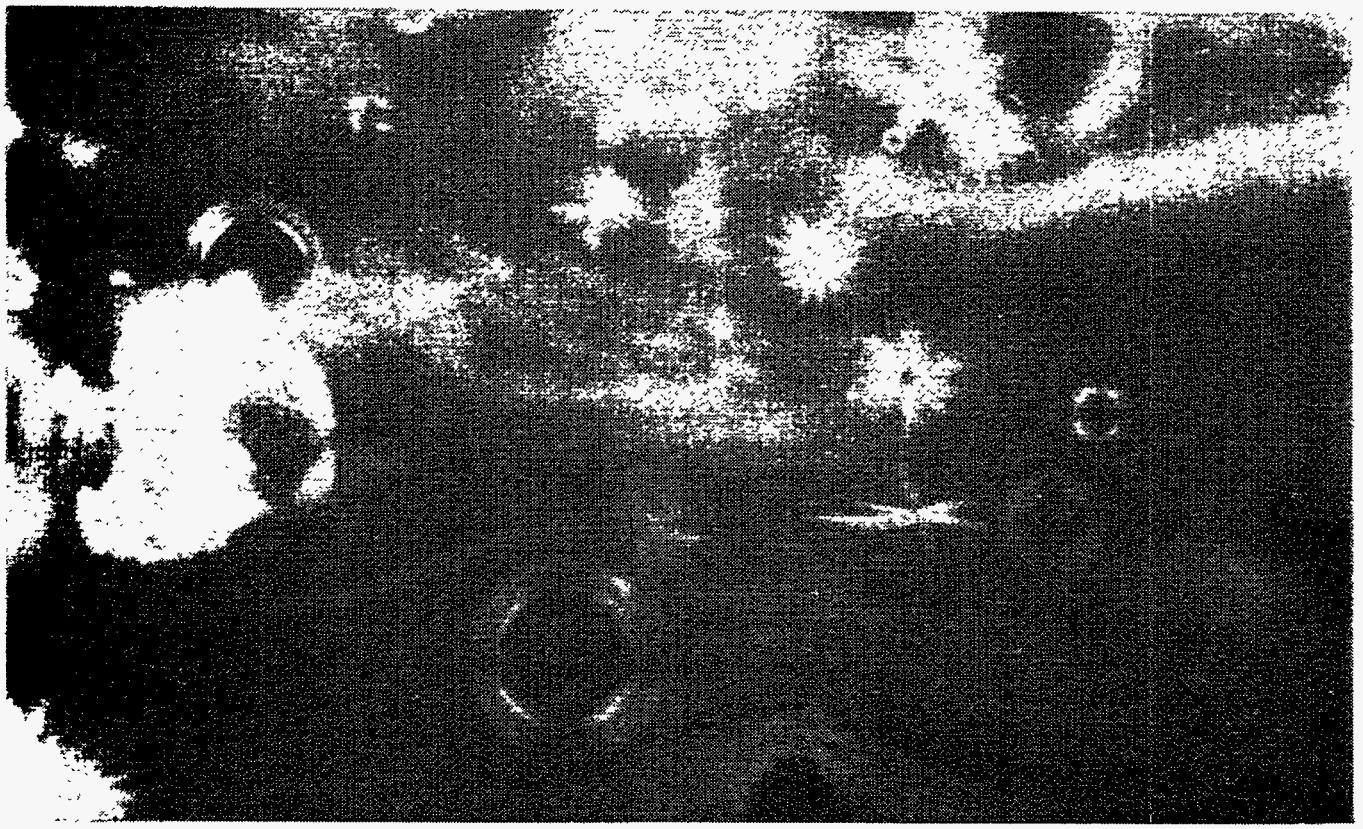

Figure 19.- HydraCo Wood-20 pct Willamette Valley Straw Test Burn: Deposit 016, Noncrystalline Region under Polarized Light Showing Flow Pattern, X100.

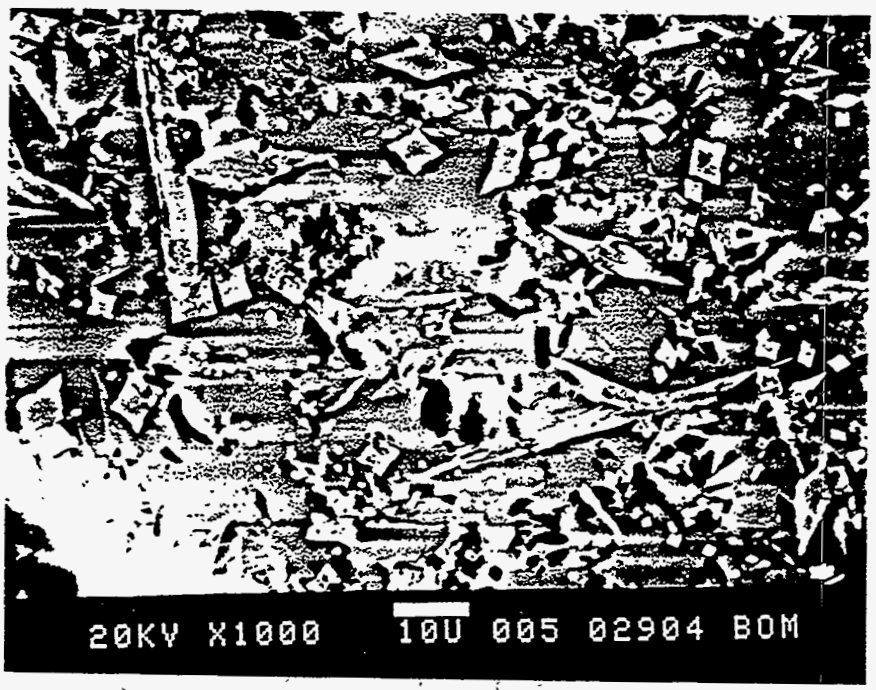

Figure 20.- HydraCo Wood-20 pct Willamette Valley Straw Test Burn: Deposit 016, Backscattered Electron Image, X1,000.

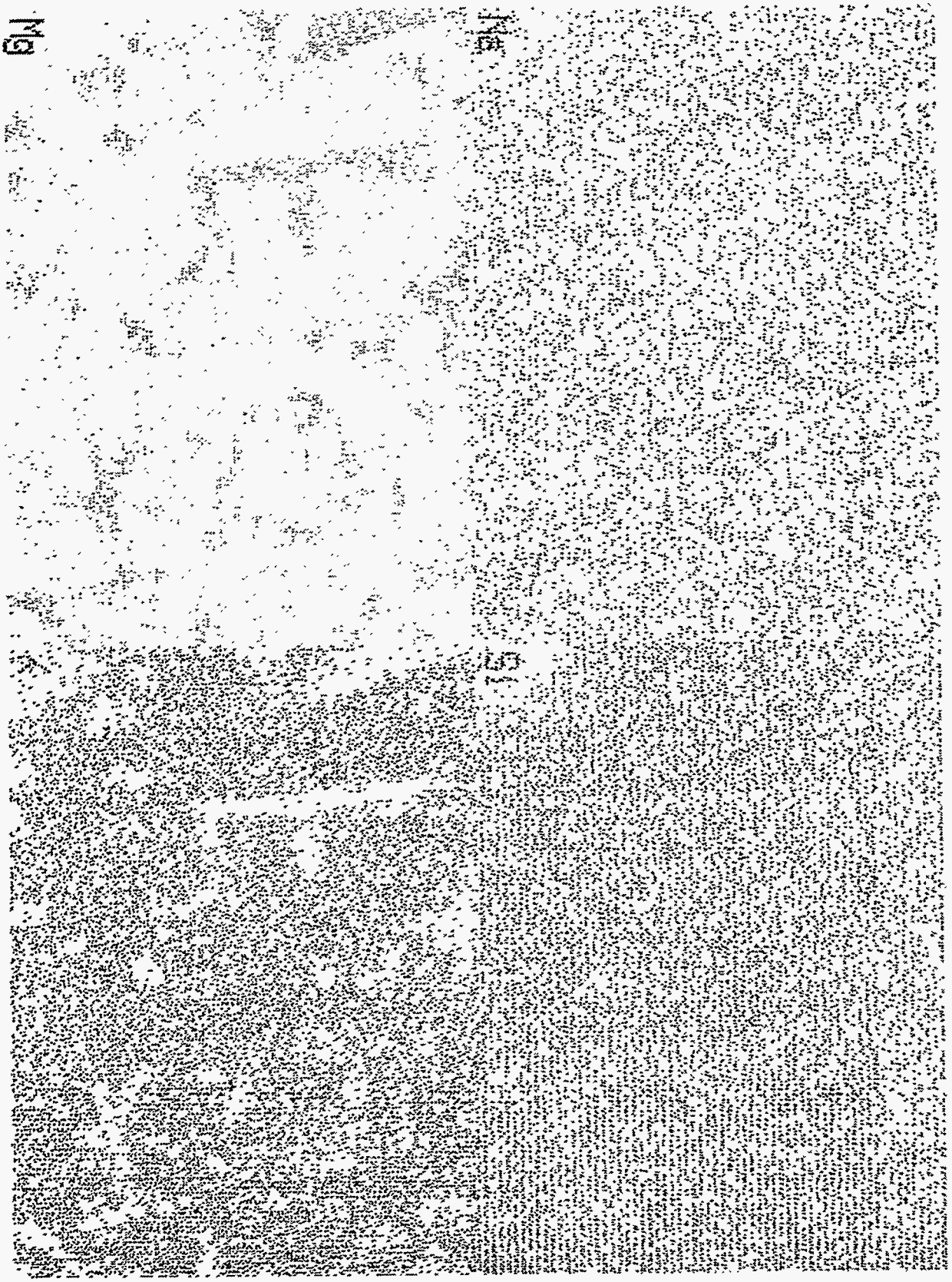

Figure 21.- HydraCo Wood-20 pct Willamette Valley Straw Test Burn: Deposit 016, Characteristic X-ray Map: Mg, Na, Si, and K.

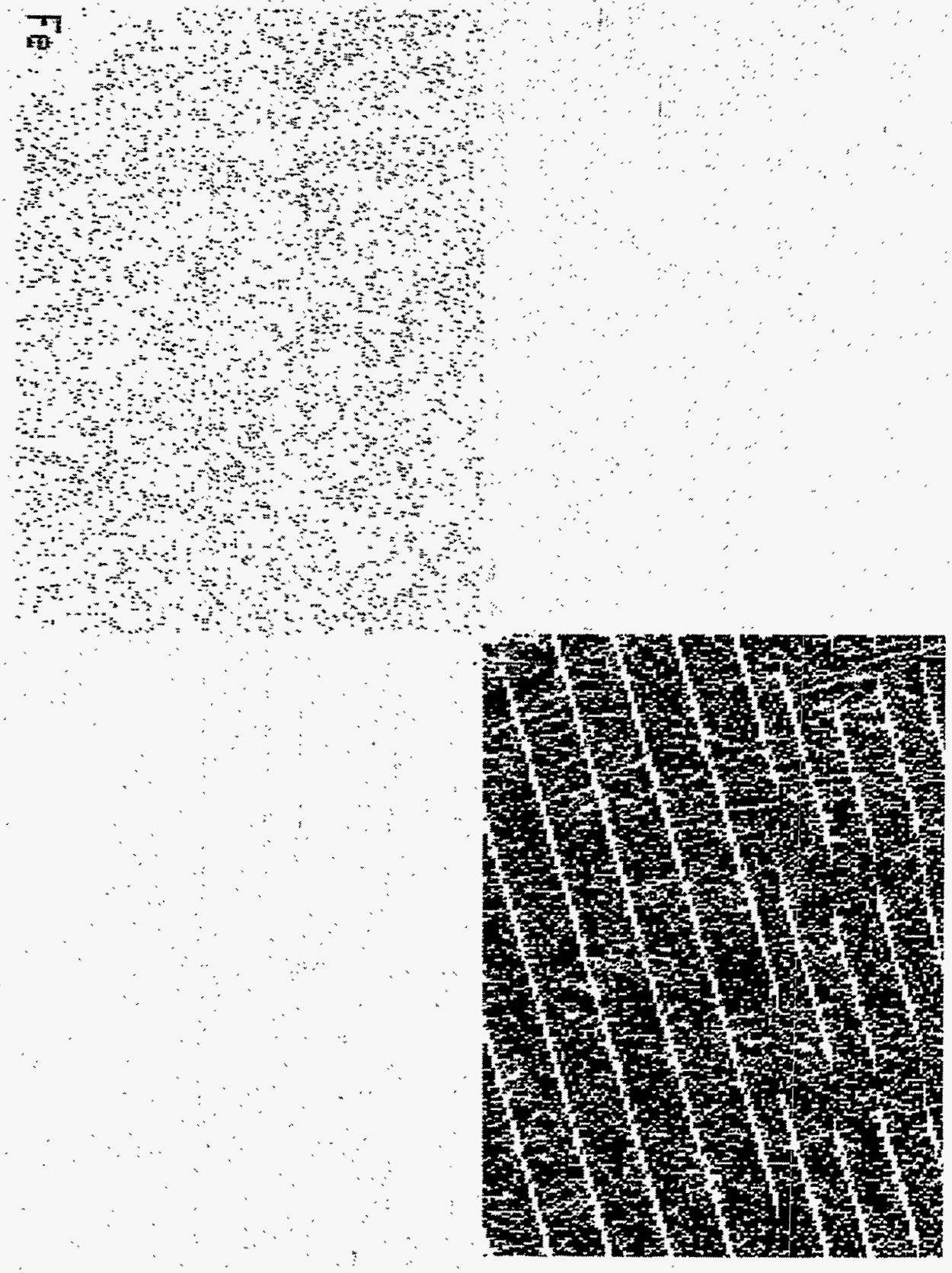

Figure 22.- HydraCo Wood-20 pct Willamette Valley Straw Test Burn: Deposit 016, Characteristic X-ray Map: Ca, and Fe.

THOMAS R. MILES CONSULTING DESIGN ENGINEERS
Phone (503) 292-0107
FAX (503) 292-2919

Hazen Research, Inc. Project 009-381
Alkali Deposit Investigation

SEQUENTIAL LEACH PROCEDURE

Procedural Comments and Notes

See the attached flow chart for an outline of the procedure used to perform the sequential leach.

The largest problem encountered with performing the sequential leach procedure was obtaining adequate phase separations. Initially, a 1:3 ratio of sample to extractant was attempted. Most of the samples absorbed all of the extractant leaving no liquid phase present. A distinct liquid phase was formed when a ratio of approximately 1:6 was used.

The extractions were performed in 500 ml Erlenmeyer flasks, and agitation was supplied by clamping the flasks onto a wrist action type shaking apparatus.

Following extraction, vacuum filtration of the mixture was attempted. The samples immediately plugged the filters, and filtration was not possible. Pressure filtration was then attempted, with similar results.

The use of a large centrifuge permitted a reasonable phase separation. However, the samples retained a fair amount of residual leach liquor, and the several washes that were performed were probably not totally effective in cleaning the samples of leach solution.

The leach solutions were combined with the washes and diluted to a volume of 500 ml. These diluted solutions then were analyzed for the elements of interest.

It is recommended that some sort of mechanical filter press be used for future work. The samples would be filtered under mechanical pressure, permitting residual fluid to be squeezed out.

The Pistachio Shell sample was not treated, due to insufficient sample.

The flask containing the Wheat Straw sample came loose after the water leach, and was lost: Therefore, only the water leach data is available for this sample.

Chloride results are not available on the ammonium acetate leach, because of a very large chloride blank due, apparently, from chloride contained in the ammonium acetate reagent.

THOMAS R. MILES CONSULTING DESIGN ENGINEERS
Phone (503) 282-0107
FAX (503) 282-2919

Hazen Research, Inc. Project 009-381
November 26, 1993

SEQUENTIAL LEACH PROCEDURE

Analysis of Starting Material

50 grams of sample (as received). Sample weight = W1.
Ash entire sample @ 600 deg C.
Analyze ash for 10 elements plus chloride
Calculate results back to starting weight (W1)

Element Solubility Test:

50 grams of sample (as received). Sample Weight = W2.

↓

Leach w/water
wash --------> combine leachate and wash, dilute to volume, analyze for 11 elements

↓

Leach w/NH4OAc
wash --------> combine leachate and wash, dilute to volume, analyze for 10 elements

↓

Leach w/HCl
wash --------> combine leachate and wash, dilute to volume, analyze for 10 elements

↙

Residual Elements:

Ash residue from final leach @ 600 deg C.
Analyze ash for 10 elements.

All analyses on the leachable elements and the residual elements will be calculated back to the original (as received) sample weight (W2).

Analysis Methods:

Leach Liquors:

Ca,Mg,P,Si,Al,Ti,Fe	ICP Emission Spectroscopy
Na,K	Flame Atomic Absorption Spectroscopy
Cl,S	Ion Chromatography

As Received and Residue Samples:
ASTM Method D2795

THOMAS R. MILES
CONSULTING DESIGN ENGINEERS

Phone (503) 292-0107
FAX (503) 292-2919

ALKALI DEPOSIT INVESTIGATION

December 31, 1992

SOME THOUGHTS -

PROBLEMS W/ ASTM D 1857 ON BIOMASS ASH

We have all been somewhat concerned about the ASH FUSION TEMPERATURES being reported by Analytical Labs, consistently in the 2000°-2200° F. range. Our Biomass Deposit data indicates much lower temperatures, with "sticky" temperatures at least as low as 1500° F.

This discrepancy is quite puzzling to the plant personnel. Their question: Who's right? and, If it's not correct why bother to do it?

We have made a run at the problem by getting the ASTM D 1857-87, copy enclosed.

Note that it calls for:

- Ashing @ 1470°-1650° F. (800°-900° C.)
- Grinding to 200 m
- Oxidizing at 1470°-1560° F. in O_2 - for 1½ hours
- Making the cone
- Running the pyrometric test

Given that this standard is for coal, and given that the ashing temperature is really higher than need be for biomass, all the labs are using this method. So if we are in fact possibly losing some K and Na by vaporization during ashing, the method probably loses about the same amount that would be lost burning on the grate or in a fluid bed at approximately the same temperatures and by prolonged exposure of the ash at temperature.

It is also probable that the ashing method does not give a true concentration of these metals in the original fuel. This is somewhat academic because it is the effective furnace temperatures and the residual alkali mixture concentrations that count as far as grate or bed deposits are concerned.

5475 S.W. ARROWWOOD LANE PORTLAND, OREGON 97225

THOMAS R. MILES CONSULTING DESIGN ENGINEERS
Phone (503) 292-0107
FAX (503) 292-2919

The higher alkali concentrations in superheater and convective pass deposits apparently are produced from fine particle aerosols and as vapor during the fairly long residence of the ash at temperature on the grate or in the F.B. The vapors condense on these tube surfaces and capture the fine particles, creating strange shapes on the tubes.

We probably should be using one of the following ashing standards for biomass:

D 1102 - Ash in wood
E 830 - Ash in RDF
E 953 - Fusibility of RDF ash

See the enclosed instructions to Hazen which may shed some light on the situation.

TRM

Ash Concentration (600°C)

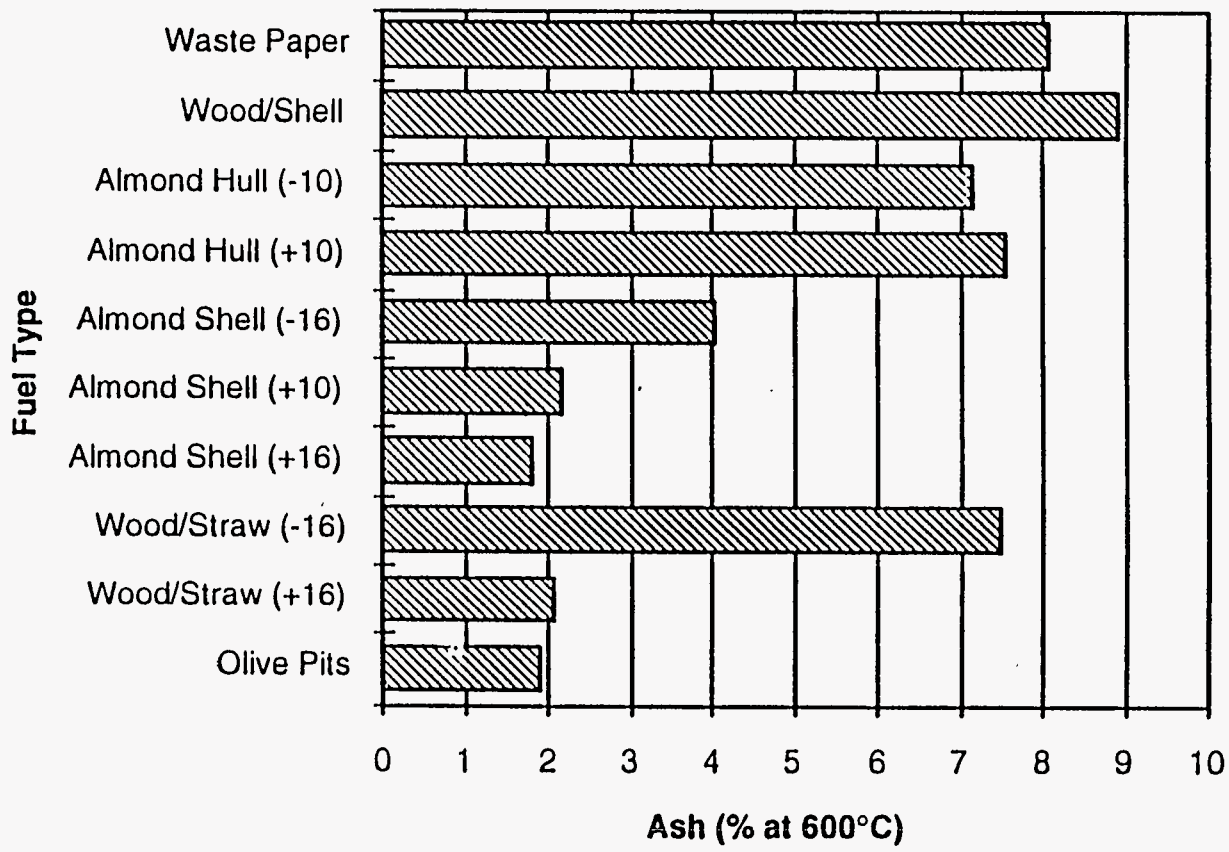

Muffle Furnace: Ashing Results

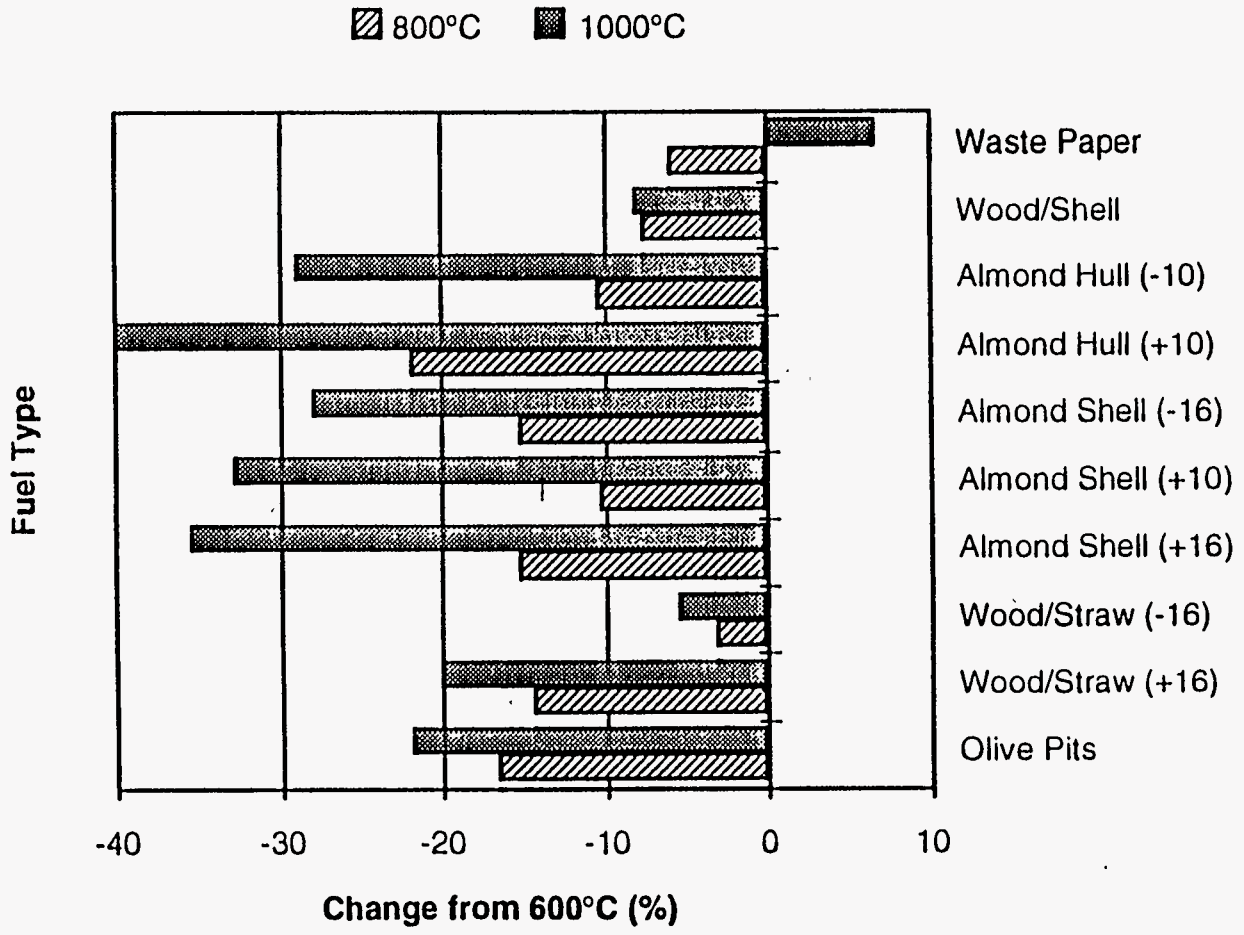

Muffle Furnace: Ash Appearance

	600°C (1110°F)		800°C (1470°F)		1000°C (1830°F)	
Fuel Type	Color	Condition	Color	Condition	Color	Condition
Olive Pits	tan	loose	green	sintered	brown/yellow/green	sintered
Wood/Straw (+16)	brown	loose	tan	loose	light brown	slight sinter
Wood/Straw (-16)	brown	loose	tan	loose	tan	loose
Almond Shell (+10)	white/black	loose	white/gray	loose	brown/white/blue	fused
Almond Shell (+16)	white/black	loose	white/green	loose	brown/white/purple	fused
Almond Shell (-16)	ivory	loose	green	loose	tan/white/green	sintered
Almond Hull (+10)	white/black	loose	white/green	loose	turquoise	fused
Almond Hull (-10)	white/black	loose	white/green	loose	dark turquoise	fused
Wood/Shell	tan	loose	tan	loose	tan	slight sinter
Waste Paper	white	loose	white/gray	loose	white/black mottled	slight sinter

THOMAS R. MILES CONSULTING DESIGN ENGINEERS
Phone (503) 292-0107
FAX (503) 292-2919

ASH SINTER METHOD

Fuels/Source		No. Samples	600C 1112 F	700C 1292 F	800C 1472 F	900C 1652 F	Alkali lb/MMBtu
WOOD FUELS AND BLENDS							
Hydraco	Wood	10	ASH	ASH	ASH	ASH	0.5 to 1.5
Mendota	15% ag	7	ASH	ASH	ASH	ASH	0.66 to 1.2
Hydraco	20% straw	8	ASH	ASH	ASH	ASH	0.5 to 1.9
	20% straw	1	ASH	ASH	ASH	STICKY	1.31
	20% straw	1	ASH	ASH	STICKY	ASH	0,71
STRAW, FIELD CROP RESIDUES							
Hydraco	straw	1	ASH	ASH	ASH	ASH	1.12
	straw	1	ASH	ASH	ASH	STICKY	1.39
	straw	1	ASH	ASH	STICKY	ASH	1.41
Elkraft	wheat straw	1	ASH	ASH	STICKY	SINTERED	1.57
Hydraco	asparagus fern	1	STICKY	STICKY	ASH	ASH	4.33
NREL	bagasse, IGT	1	STICKY	ASH	ASH	STICKY	0.28
	bagasse, NREL	1	ASH	ASH	ASH	ASH	0.16

PROCEDURE

The samples were tested by the Ash Sinter Method which incorporates visual inspection of the sample at specific temperature levels. The samples were observed after 1 hour at 600, 700, 800 and 900 degrees Centigrade.

PHYSICAL CHARACTERISTICS DEFINITIONS

ASH: Having the characteristics of a common ash. Free flowing and displaying no stickiness.

STICKY: Still a solid, but agglomerated

SINTERED: Appears liquid and solidifies upon removal from heat.